Proceedings of the

7th International Conference

LOCAL MECHANICAL PROPERTIES LMV 2010

November 10-12, 2010

Smolenice Castle, Slovac Republic

Edited by František Lofaj

Organized by the
Institute of Materials Research of the Slovac Academy of Sciences in Košice
in collaboration with
Technical University in Košice

2010

s653

Preface

The 7th International Conference "Local Mechanical Properties - LMV 2010" was held at Smolenice Castle from Nov. 10 till Nov.12, 2010. It continued the series of succesfull LMV meetings held in Košice - 2004 and -2005, Plzeň – Nečtiny -2006, Brno – Šlapanice -2007, Herľany -2008, and Telč -2009, however, several changes occured. The event grew from the original Czech-Slovak meeting into an international workshop and currently reached the status of an international conference due to the substantial increase of the number of participants and number of countries. Secondly, the (almost) only official language of the conference was English for the first time. Finally, generous support from numerous sponsors of the conference indicated not only the importance of the scope of the conference but also emphasized its quality and reputation.

The 7th LMV2010 was organized by Dr. František Lofaj and his team from the Department of Structural Ceramics at the Institute of Materials Research of SAS in Košice in collaboration with Technical University of Košice. The conference was attended by 92 participants who presented 38 oral presentations (2 invited lectures, 2 key note lectures, 5 commercial presentations and 28 regular presentations) and 58 posters.

The scope of the conference focused on research and development in materials engineering, experimental methods, modeling, etc, with the aim to characterize mechanical properties of materials from nano to micro/meso-scale. Contributions on indentation and other methods for hardness and other mechanical properties assessment, measurement of deformations and stresses, time-dependent properties with related microstructure analyses (TEM/ SEM, AFM, X-Ray, etc.) regardless of material type (metals, ceramics, plastics, biomaterials, concrete, etc.) were presented and they are included in the proceedings of the conference.

Declaration

All contributions included in the special issue of this journal have been reviewed prior to publication by the members of the Scientific and Review Boards.

SPONSORS OF THE CONFERENCE

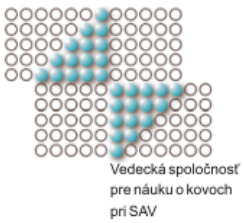

NANOINDENTATION ON ULTRA HIGH PERFORMANCE CONCRETE SYSTEM

JIŘÍ NĚMEČEK[a]*, CHRISTIAN LEHMANN[b], and PATRICK FONTANA[b]

[a] Czech Technical University in Prague, Thákurova 7, 16629 Prague 6, Czech Republic, [b] BAM Federal Institute for Materials Research and Testing, Unter den Eichen 87, 12205 Berlin, Germany
jiri.nemecek@fsv.cvut.cz

Keywords: mechanical properties, nanoindentation, grid indentation, heterogeneous system, ultra high performance concrete

1. Introduction

In the past decade, nanoindentation has become commonly used experimental technique for obtaining quantitative data on elastic and inelastic material properties in small volumes, typically in submicron length scale. The methodology was developed mainly for homogeneous materials or, at least, the homogeneity is assumed far enough from the tested volume in evaluation procedures[1]. Measurement on a heterogeneous system, in which the material phases are intermixed in small volume, is still a challenging task due to several circumstances. First, the preparation of a flat surface on the heterogeneous sample with high differences in stiffness needs special care. Second, the mechanical interaction between the material phases during surface loading is often unavoidable and therefore the extraction of intrinsic properties of individual phases from the heterogeneous system may not be possible. If differences between the stiffnesses of the interacting phases are low, finding of intrinsic properties can be successful using conventional evaluation[1,2]. In other cases, the error in estimating intrinsic properties can reach tens of percent[3,4].

2. Motivation

Many structural materials which are used or are being developed in the construction show high degree of heterogeneity. Ultra high performance concrete (UHPC) is representing an example of such engineering material with a complex microstructure. Overall mechanical properties of UHPC can be tested by conventional methods. However, some phenomena that are interlinked directly with the microstructure can be disclosed exclusively by small scale methods like nanoindentation. Due to enhanced curing conditions at higher temperature (autoclaving) waste materials like fly ash or slag[5,6] can be added to reduce the amount of Portland cement in UHPC. It was found that after autoclaving the samples show some kind of zoning which is exhibited in optical microscope as lighter outer part and darker inner part. It was supposed that the zoning could be caused by an inhomogeneous autoclaving effect in the matrix which in turn could cause also different mechanical behavior of these parts. The zoning was most pronounced in cases when slag was used in the mixture[6]. This finding led us to the idea of testing mechanical resistance of different parts in the sample by micromechanical method, the nanoindentation.

3. Methodology

In order to evaluate the difference in mechanical performance of different zones in the sample (inner and outer parts) grid nanoindentation was employed. Cross sections of the samples were polished and two arbitrarily chosen areas were selected. One in the inner part of the sample and one in the outer part within 4 mm from the sample edge where the zoning was previously observed.

Selected locations were indented by means of massive grid indentation in order to receive large statistical set of data from all material phases. Large number (200–300) of indents was performed on each sample location and elastic properties were computed for individual imprints. The size of indents was chosen to be small (~200 nm in depth). However, it was not possible to keep the indents' size considerably smaller than that of all neighboring features due to extreme microstructural heterogeneity. Therefore, it was not possible to avoid all phase interactions which must be kept in mind and results introduced afterward have to be taken not as individual phase properties but more or less average mechanical properties of the small material volume around the indents. Regardless the indent location, individual results were analyzed by a standard method[1]. Subsequently, histograms of elastic properties of all measurements were plotted and analyzed by means of statistical deconvolution[2,3,7].

4. Sample preparation

Three types of UHPC mixtures were tested. The proportionally uniform composition of the samples (Tab. I) varied in the type of the secondary cementitious materials, aggregate and filler (Tab. II). The water to cement ratio was 0.31 by weight and superplasticizer was used in all cases.

All samples were autoclaved for 6 hours at 180 °C and 12 bar (water vapor saturation) pressure. Heating and cooling took 1 hour each. It is assumed that almost all hydration takes place during the autoclaving period. Then, samples were stored in ambient conditions. Flat surface suitable for nanoindentation was obtained by mechanical polishing before testing.

Table I
Concentrations of sample components (kg m^{-3})

Cement	Micro-silica	Second-ary mat.	Filler	Aggregate (0-2mm)
760	74	76	248	970

Table II
Sample specification

Sample	Secondary material	Filler	Aggregate (0-2mm)
K1-1	class F fly ash	quartz	quartz sand
K1-2	granulated blast furnace slag	quartz	quartz sand
K2-1	class F fly ash	quartz	basaltic sand

5. Measurement

Since matrix properties were of prior interest, indentation locations were selected not to contain large pores or large grains of aggregate. Each location was covered by a rectangular grid of indents with 15 µm spacing in both directions. Maximum indents' depth was prescribed ~200 nm. Loading diagram contained linear loading 24 mN min^{-1}, holding period at the peak for 10 s and linear unloading 24 mN min^{-1}. The insertion of the holding period, in which material creep is demonstrated, is important for unbiasing the unloading stage in case of testing inelastic material[8].

Optical observations showed on the microstructural complexity as illustrated in Figs 1 and 2.

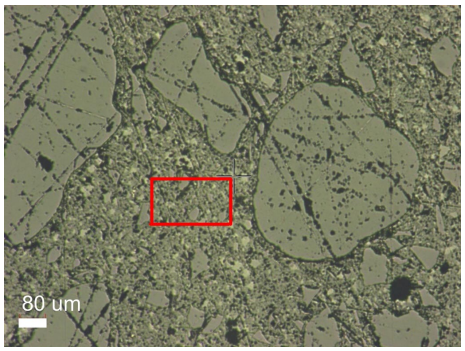

Fig. 1. **Example of the sample microstructure and grid location in the outer zone of sample K1-2**

6. Results

As it was mentioned above, even if the indentation depth was low (~200 nm) it was not possible to avoid interference of the distinct phases in the material due to very high heterogeneity and phase mix. Therefore, the following micromechanical results have to be considered as effective properties of the phase compound within the affected volume. This volume can be estimated as three times maximum depth[2], i.e. ~600 nm.

First, elastic modulus (E) and hardness (H) were evaluated for individual indents[1] using the assumption of constant Poisson's ratio ν=0.2 for all samples. It was found that both elastic modulus and hardness exhibit very similar distributions. Therefore, elastic modulus was used preferably in the following. Maps of E were plotted over the tested area to show on high heterogeneity and representativeness of the selected areas which contain all possible mechanical phases from low to high stiffness (Fig. 3).

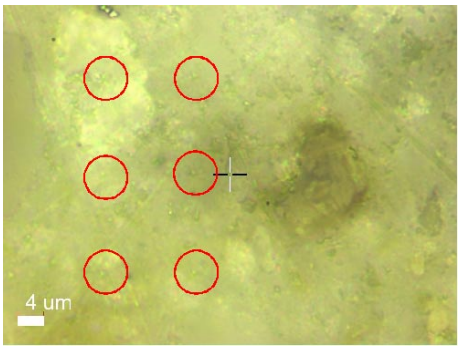

Fig. 2. **Part of the indentation grid in the outer zone of sample K1-2 (slightly visible individual indents are circled)**

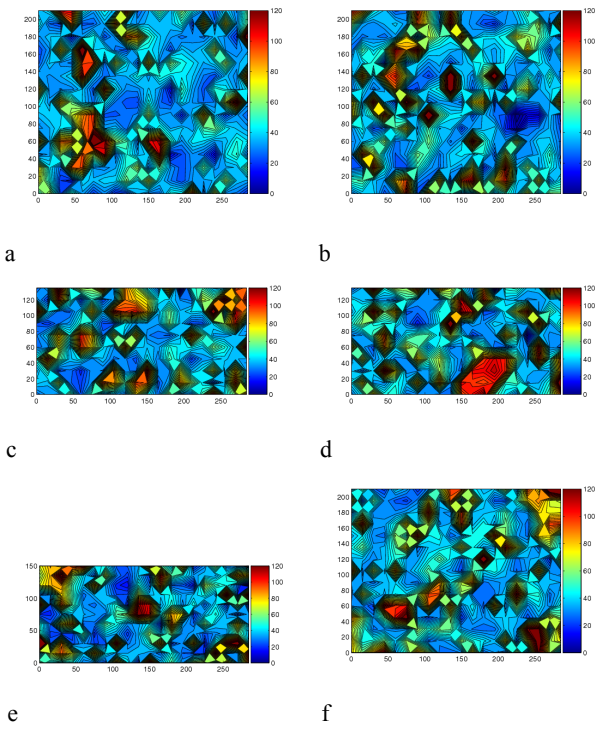

Fig. 3. **Maps of elastic moduli (GPa) over tested areas in a sample inner part (left) and outer part (right). (a-b) belongs to K1-1, (c-d) to K1-2 and (e-f) to K2-1**

Second, loading diagrams (depth-load curves) showed high variation due to the heterogeneity. Therefore, it is reasonable to evaluate the results in the form of histograms of all received parameters which show on the distribution of mechanical phases over the representative areas. Several peaks with high frequency of occurrence could be distinguished (Fig. 4). Afterwards, histograms were plotted in one graph to see the differences between the samples (Fig. 5).

It can be seen in Fig. 5 that all histograms are very similar which shows on similar mechanical behavior of all samples and phases in it. Frequency of occurrence varies a bit. More exact comparison is given by the following deconvolution.

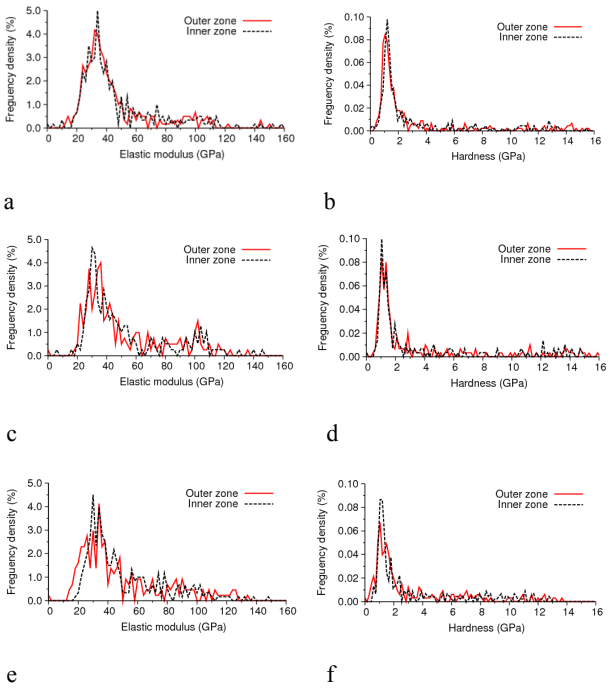

Fig. 4. **Histograms of elastic moduli (left) and hardness (right). (a-b) belongs to K1-1, (c-d) to K1-2 and (e-f) to K2-1**

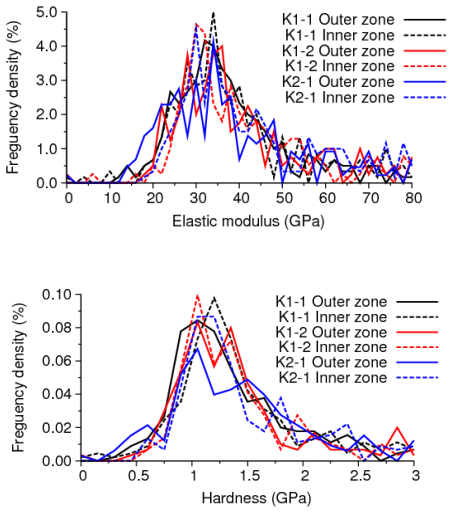

Fig. 5. **Histograms of elastic moduli (top) and hardness (bottom) for all tested locations**

Finally, the histograms of elastic moduli were analyzed by the deconvolution algorithm[2,3,7] in order to separate the overall distribution (whole histogram) into two individual phases. It is supposed that the first phase contains all lower stiffness phases (products of hydration after autoclaving). The second phase contains all the rest, i.e. unhydrated clinkers, quartz, non-reacted fly-ash and other high stiffness phases. It could be possible to perform deconvolution into more than two phases but for the sake of simplicity and clear comparison between the samples, only two (one dominant and the rest) were assumed (see Fig. 6).

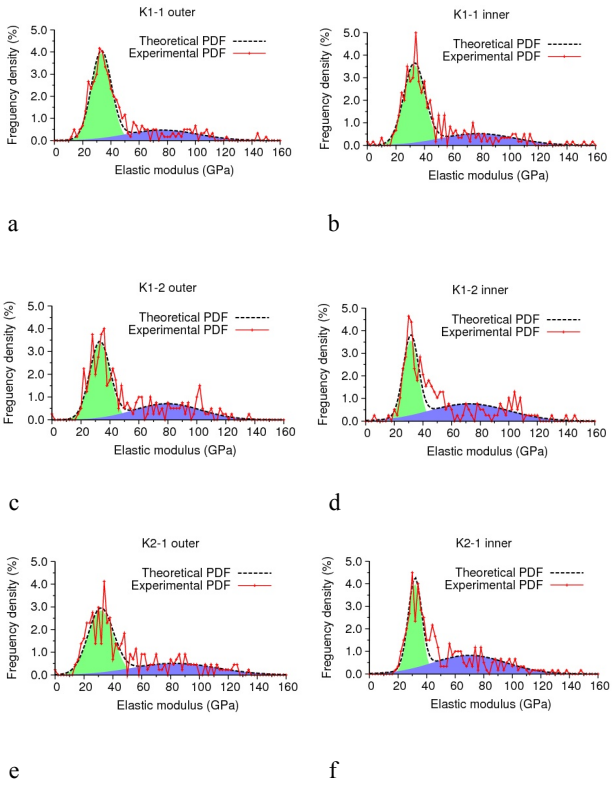

Fig. 6. **Deconvolution of the overall distribution into two individual phases. (a-b) belongs to K1-1, (c-d) to K1-2 and (e-f) to K2-1**

The deconvolution was based on the algorithm[2,3,7] which seeks for n-Gauss distributions in an experimental probability density function (PDF). Random seed and minimizing criteria of the differences between the experimental and theoretical overall PDFs are computed in the algorithm to find the best fit. Table III contains numerical results from the deconvolution also with the estimated volume fractions of the phases.

The first, major phase is characterized with a very similar E~31–33 GPa for all samples and all positions. Therefore, the hypothesis of different mechanical behavior of inner and outer parts in case of slag containing samples (K1-2) was not confirmed. Although the difference in E between the parts was the highest for K1-2 sample, it was still within 5% which is considered to be irrelevant. Volume fractions varied a bit. Higher frequency of the lower stiffness phase was found for

K1-1 and a bit lower for K1-2 and K2-1.Perhaps, it is dependent mainly on the location indented which can contain more or less unreacted material or aggregate. The second phase contains results from all other (higher stiffness) material components and thus the deviation from the mean is high in this case (Tab. III).

Table III
Results of the deconvolution into two phases

	First phase E_1 (GPa)	vol. %	Second phase E_2 (GPa)	vol. %
K1-1 outer	33.20±7.05	69.7	76.25±25.39	30.3
K1-1 inner	32.90±7.45	66.3	77.57±26.00	33.7
K1-2 outer*	33.07±7.00	59.0	79.58±23.15	41.0
K1-2 inner*	31.52±5.22	46.9	72.12±27.73	53.1
K2-1 outer	31.61±8.75	62.4	82.75±29.37	37.6
K2-1 inner	31.81±4.69	47.0	69.93±25.60	53.0

Note: * asterisk denotes slag containing samples K1-2.

7. Conclusions

A very complex microstructure of UHPC samples was studied by means of grid nanoindentation and statistical deconvolution methods. This methodology gives access to the separation of the wide variety of results from this heterogeneous system into limited number of mechanical phases. In this work, differences between the samples and their regions (inner and outer) were studied based on two phase separation. Following major conclusions could be deduced.

- It was found that both elastic modulus (E) and hardness (H) have very similar distributions for reacted parts of the matrix of all samples and all positions with no significant differences between outer and inner parts. The difference in E was found to be within 5%.
- Material properties of unreacted parts and aggregate are also similar for all samples. Their volume fractions are influenced by the selected location for indentation which could contain more or less of these phases.
- Based on low magnification optical images it can be seen that samples contain large amount of porosity. This "large or capillary" porosity is not included in the results and indents laid between the pores. So, if there is some effect of porosity on the overall stiffness or strength of the matrix, this could not be disclosed by nanoindentation.

Finally, it can be concluded that there is probably no significant difference in the mechanical behavior of the sample matrices. Therefore, any differences between the outer and inner parts in terms of their overall stiffness or strength can be caused by different capillary porosity or other effects but the stiffness of the cementitious matrix and their components.

Support of the Czech Science Foundation (GA ČR 103/09/1748) and Ministry of Education of the Czech Republic (MSM 6840770003) is gratefully acknowledged.

REFERENCES

1. Oliver W., Pharr G.: J. Mat. Res. *7* (1992).
2. Constantinides G., Chandran K. R., Ulm F.-J., Vliet K. V.: J. Mater. Sci. Eng., A *430* (2006).
3. Němeček J., Lukeš J.: Chem. Listy *104*, s279 (2010).
4. Kabele P., Davydov D., Jůn P., Němeček J., Jirásek M.: *Proceedings of Concreep 2008*.
5. Lehmann, C., Müller, U., Fontana, P.: *Proceedings of NICOM3, 2009*, 287–293.
6. Fontana P., Lehmann C., Müller U., Meng B.: *Proc. Int. RILEM Conference on Material Science (MatSci), 2010*, Vol. III, 69–77.
7. Němeček J., Šmilauer V., Kopecký L., accepted for publication in Cem. & Concr. Comp., ISSN: 0958-9465.
8. Němeček J.: Mater. Character. *60*, 1028 (2009).

J. Němeček[a], Ch. Lehmann[b], and P. Fontana[b] *([a] Czech Technical University in Prague, Faculty of Civil Engineering, Czech Republic, [b] BAM Federal Institute for Materials Research and Testing, Division "Building Materials", Germany):* **Nanoindentation on Ultra High Performance Concrete**

The paper describes results from nanoindentation on a very heterogeneous structural material, namely ultra high performace concrete (UHPC). Nanoindentation was used to investigate the influence of mixture components and production conditions on the mechanical response of the hydrated matrix after autoclaving. Statistical grid nanoindentation complemented with the deconvolution procedure revealed that the matrix properties of all tested mixtures are very similar without any significant difference in their stiffness or elasticity, respectively.

It is assumed that the sample zoning after autoclaving, which is exhibited in optical microscopy as different color of inner and outer parts, is caused by secondary effects like increased porosity.

MODELLING OF HARDNESS DISTRIBUTION CURVES OBTAINED ON TWO-PHASE MATERIALS BY GRID INDENTATION TECHNIQUE

JIŘÍ BURŠÍK

Institute of Physics of Materials, Academy of Sciences of the Czech Republic, Žižkova 22, 61662 Brno, Czech Republic
bursik@ipm.cz

Keywords: grid indentation, hardness, modelling

1. Introduction

Multiphase materials with fine microstructural features (secondary phase particles, grains of different phases, inclusions, voids, etc.) are challenging for obtaining sound and accurate mechanical characteristics of individual phases. Current advances of instrumented indentation techniques[1] provide the way of measuring the mechanical response of individual phases at the length scale of 10^{-6} m with nanoindenters and even below that with dedicated AFM devices or special sample holders[2] for *in-situ* TEM probing. It is now well established that the response of a material upon the reversal of contact loading provides access to the mechanical properties of the indented material[3].

In the field of instrumented indentation experiments, the so called grid indentation technique (GIT) was proposed[4,5], which consists in making a large array of micro to nanoscale contact experiments and the statistical analysis of the resulting data. GIT uses the advantage of high level of automation of today's nanoindentation instruments; the number of indents in the regular grid is typically of the order of hundreds to thousands[6]. The technique can be conveniently used for heterogeneous materials; however, the proper choice of parameters of the indentation experiment is crucial and critical.

Considering a characteristic size D of structural objects and an indentation depth h, two limiting cases can be identified (Fig. 1). For $h>>D$, the average properties of the composite material are obtained. If $h<<D$, a single indentation test yields properties of the particular constituent phase under indenter. In this case the data allow also the evaluation of volume fraction of constituent phases and construction of 2D maps of the measured mechanical properties. The usual way of processing the frequency distribution curves of mechanical properties obtained by GIT is the multimodal Gaussian fitting[5–7]. The latter limiting case (i.e. $h<<D$) is more rewarding but also more difficult to reach. In practice we can hardly avoid all the phase interfaces and other structural features causing a departure from single phase values and the actual results are often situated in some intermediate state between the two limiting cases.

In this work, the hardness distribution curves obtained by GIT are computer modelled for various volume fractions of spherical particles and for the wide range of indentation loads covering also the intermediate states of possible GIT outputs. The effect of the input parameters on the distribution curves is discussed and potential pitfalls of the routine statistical evaluation by multimodal Gaussian fit are examined.

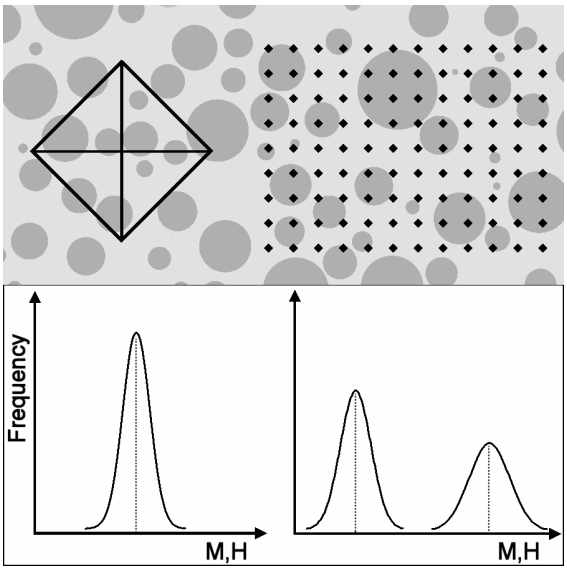

Fig. 1. **The principle of the grid indentation technique for heterogeneous materials and the scheme of the two limiting cases. Large indentation depths (left) lead to the response of the homogenized medium. Small indentation depths (right) allow the evaluation of properties of individual constituents. Horizontal axis most often represents either indentation modulus *M* or indentation hardness *H***

2. Model details

The tested material was modelled as a cube (edge size 1000 arbitrary units) filled with spherical particles. Periodic boundary conditions and log-normal distribution of particle diameters with the median exp(μ)=55 a.u. and the standard deviation σ=0.4 were used (Fig. 2). For three selected levels of particle volume fraction (10, 40 and 60 %), there were 583, 2331 and 3496 particles in the cube, respectively.

Parameters of the two phases were chosen to represent hard particles (p) in a soft matrix (m), namely elastic moduli E_p=380 GPa, E_m=200 GPa, yield points Y_p=8000 MPa, Y_m=667 MPa, Poisson ratios $\nu_p=\nu_m$=0.3. Hardness of the phases was described as

$$H = 3Y \qquad (1)$$

thus making H_p=24 GPa and H_m=2 GPa. Contact radius under indenter a was described as the half-diagonal of the Vickers indentation:

$$a = \sqrt{\frac{1.854P}{4H}} \qquad (2)$$

where P is an applied load. The plastic zone radius c was evaluated according to Johnson's model[8] as

$$c = a\left[\frac{E\tan\beta}{6Y(1-\nu)} + \frac{2}{3}\left(\frac{1-2\nu}{1-\nu}\right)\right]^{1/3} \quad (3)$$

where β is the angle between the indenter flank and the sample surface (22 deg for Vickers tip). The *c*-*P* relation is shown for both phases in Fig. 3.

The graph shows the broad range of applied loads and plastic zone radii used for simulations. The *P* axis scales according to the 'arbitrary unit' of length in the simulation (cube size, particle diameters, plastic zone radius): e.g. if a.u.=nm (resp. mm), the load axis in Fig. 3 scales in μN (resp. N).

The plastic zone volume was adjusted according to the phases under indenter and then the hardness was calculated according to the mixing law proposed by Burnett and Rickerby[9,10]:

$$H = f_p H_p + f_m H_m \quad (4)$$

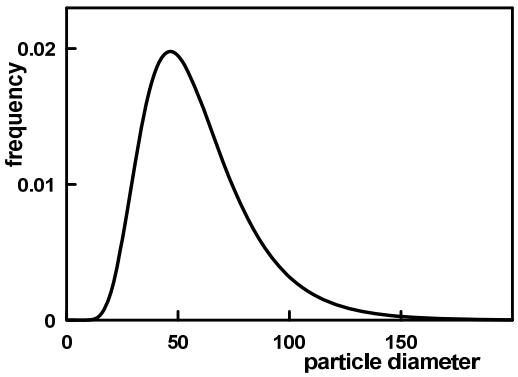

Fig. 2. **The log-normal distribution of particles randomly placed in the modelled cubic block**

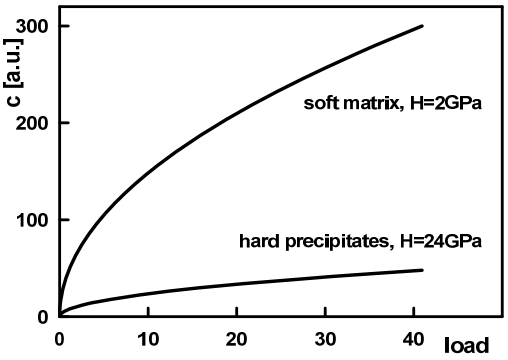

Fig. 3. **The plastic zone radius as depending on the indentation load**

where f_p and f_m are the volume fractions of the phases in the hemispherical plastic zone under the indenter tip. A regular grid of 100×100×100 points was used to simulate the hardness frequency distribution curves (meaning making a 100×100 grid at the cube face, then removing the thin slice and repeating the sequence down the whole cube).

It should be noted that many important practical details of the real indentation process are not dealt with in this model (such as surface roughness, realistic tip geometry, specific material response etc.) and it is focused mainly on the behaviour of hardness frequency distribution curves obtained by grid indentation.

3. Results and discussion

The effect of increasing indentation load is demonstrated on hardness maps in Fig. 4.

Many small particles are averaged out in the map produced at high load. Only inner cores of the large particles retain the true characteristics of the hard phase.

From a series of simulated hardness distributions, several curves were selected to illustrate and discuss important features. In general, the peak of the soft phase is more prone to various artifacts as the plastic zone is larger in soft places and hence the measured value of hardness is more affected by various perturbations in the indentation vicinity.

Starting from the limiting case of the two distinguished peaks of the soft and the hard phase, the first change observed with gradually increasing load is the increasing counts in the right-hand branch of the soft phase peak (Fig. 5).

The peaks still represent well the correct single phase values. However, in practice the grid indentation experiments provide us with typically 10^2 to 10^3 points and the histograms

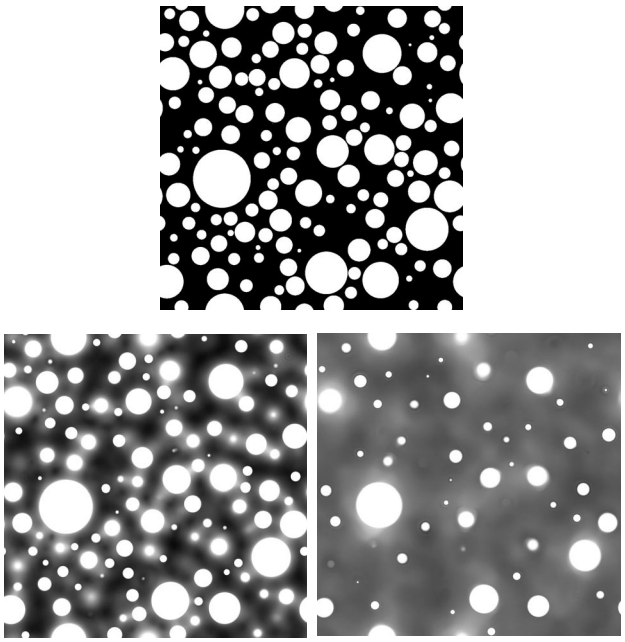

Fig. 4. **The phase map of 40 vol. % sample and two hardness maps produced at medium (*P*=1.37) and high (*P*=10.6) load**

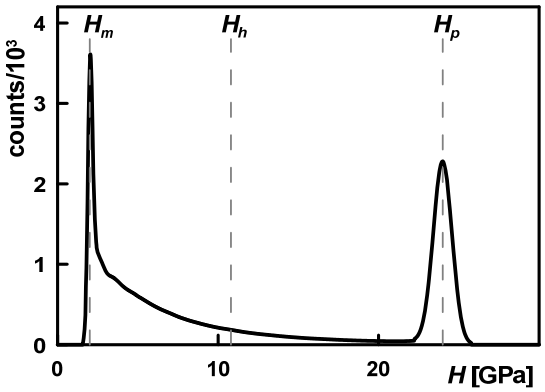

Fig. 5. **The hardness histogram obtained using the load *P*=0.18 a.u. on the model with 40 vol.% of particles.** Dashed vertical lines denote the hardness values of single phases H_m and H_p and the hardness of homogenized medium H_h

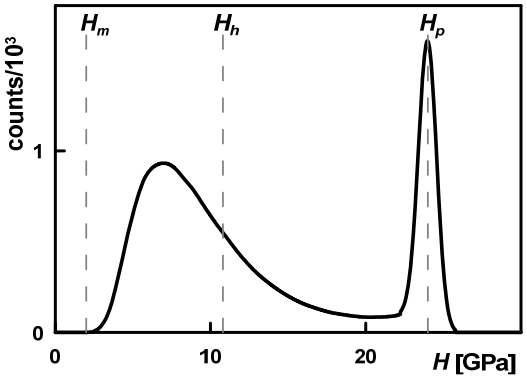

Fig. 6. **The hardness histogram obtained using the load of *P*=1.38 a.u. on the model with 40 vol.% of particles**

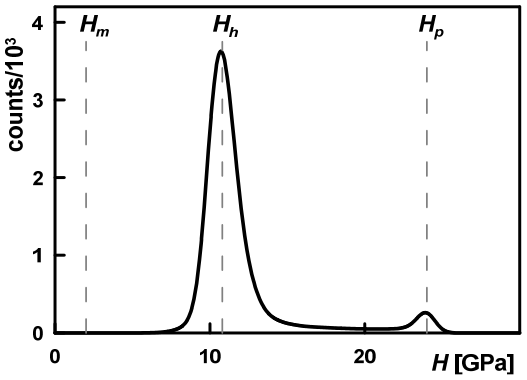

Fig. 7. **The hardness histogram obtained using the load of *P*=18.2 a.u. on the model with 40 vol.% of particles**

are more fuzzy, without clear depiction of the shape (for comparison: 10^6 grid points were used for the modelled histogram in Fig. 5), hence we cannot rely on 'seeing' the correct soft phase peak position. If we attempt to fit the left part of the histogram by a symmetric Gaussian curve, then its mean value is always systematically shifted from the correct peak position to higher values. As a matter of fact, as soon as we leave the ideal case of hitting only single phase regions, the soft phase peak loses its symmetry and fitting it by a symmetric Gaussian curve is questionable.

Further load increase causes the soft phase peak to 'transfuse' into an intermediate peak that gradually shifts across the region between H_m and the hardness of homogenized medium H_h (Fig. 6). The position of the intermediate peak depends on the applied load and does not provide any information about H_m. However, the operator may be mislead by the overall shape of the histogram in Fig. 6 and use the left peak for fitting and evaluation of the soft phase hardness (and perhaps also for the evaluation of the volume fraction). To avoid this pitfall, the hardness distribution curves should be measured at several loads and peak position stability should be checked for.

Yet further load increase causes a distinctive lowering of the hard phase peak and further growth of the intermediate peak. The shifting of the intermediate peak slows down and finally stops at the homogenized medium hardness H_h (Fig. 7.)

Histogram series obtained on materials with 10 and 60 vol.% of particles gave qualitatively similar results. The main quantitative differences were naturally the peak heights and the value of H_h. Another quantitative difference consists in the load values characteristic of various stages depicted in the previous graphs (Fig. 5–7): the characteristic loads are shifted towards higher values for 10 vol.% and in the opposite direction for 60 vol.%.

One more feature worth mentioning was found in a narrow range of loads situated between the cases described in Fig. 5 and Fig. 6, where the soft phase peak is still visible and the intermediate peak is of comparable height. In a result the histograms temporarily show three peaks for a two-phase material (Fig. 8).

Overview of the hardness distribution curves hence offers a rather pessimistic view of the utilization of the grid indentation technique for obtaining characteristics of individual phases beyond the limit $h<<D$: unless the limit is fulfilled (and is it ever, taking into account that h cannot be arbitrarily small due to limitations imposed by both the instrument and the sample?), we cannot rely on the symmetry and/or position of some peaks and even the number of peaks is not always representative of the number of phases.

4. Summary

The hardness distribution curves obtained by grid indentation technique were computer modelled for various volume fractions of spherical particles and a range of indentation loads using a simplified description of the indentation event. The effect of various parameters on the distribution curves

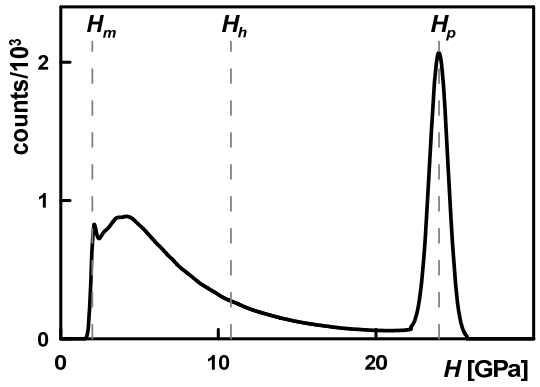

Fig. 8. **The hardness histogram obtained using the load *P*=0.41 a.u. on the model with 40 vol. % of particles**

was discussed and potential pitfalls of their routine statistical evaluation by multimodal Gaussian fit were examined.

The financial support for this work was provided by the Czech Science Foundation (Project 106/09/0700). Vilma Buršíková is acknowledged for stimulating discussions.

REFERENCES

1. Fischer-Cripps A. C.: *Nanoindentation*, Springer Verlag, New York 2003.
2. http://www.nanofactory.com
3. Oliver W. C., Pharr G. M.: J. Mater. Res. *19*, 3 (2004).
4. Constantinides G., Ravi Chandran K. S., Ulm F. J., Van Vliet K. J.: Mater. Sci. Eng., A *430*, 189 (2006).
5. Constantinides G., Ulm F. J.: J. Mech. Phys. Solids *55*, 64 (2007).
6. Randal N. X., Vandamme M., Ulm F. J.: J. Mater. Res. *24*, 679 (2009).
7. Němeček J., Lukeš J.: Chem. Listy *104*, 279 (2010).
8. Johnson K. L.: J. Mech. Phys. Solids *18*, 115 (1970).
9. Burnett P. J., Rickerby D. S.: Thin Solid Films *148*, 41 (1987).
10. Burnett P. J., Rickerby D. S.: Thin Solid Films *148*, 51 (1987).

J. Buršík *(Institute of Physics of Materials, Academy of Sciences of the Czech Republic, Brno):* **Modelling of Hardness Distribution Curves Obtained on Two-Phase Materials by Grid Indentation Technique**

While using a grid indentation technique on a multiphase material, we are often situated somewhere between the two limits of the method, i.e. between obtaining the true material properties of individual constituent phases and obtaining the averaged properties of a composite material. In this work, the hardness distribution curves obtained by the grid indentation technique are computer modelled for various volume fractions of spherical particles, range of indentation loads and various mechanical properties of constituent phases. The effect of these parameters on the distribution curves is discussed and potential pitfalls of their routine statistical evaluation by multimodal Gaussian fit are examined.

MECHANICAL PROPERTIES OF HARD PARTICLES IN SOFT MATRIX

PAVOL ZUBKO[a]*, LADISLAV PEŠEK[a], OLGA BLÁHOVÁ[b]

[a] Technical university of Košice, Department of materials science, Letná 9, Košice, Slovakia, [b] Universtiy of West Bohemia, New Technology Research Center, Plzeň, Univerzitní 8, Czech Republic
pavol.zubko@tuke.sk

Keywords: Hard particles, soft matrix, inclusion, IF steel

1. Introduction

According to recent studies FE (Finite Element) analysis allows us to simulate behaviour of components and materials before their physical existence[1]. For good FE model we need to learn about the properties of all phases and describe how they affect the global properties.

In steels we can find particles, except the mayor phase, which affect the final properties of materials. Hard particles usually delaminate from matrix under loading, soft particles crack. In both cases knowledge of properties of particles are important to correct simulation of material behaviour.

Nanoindentation is a powerful tool to determine mechanical properties in small regions, phases, objects and particles, too.

The aim of the contribution is to determine mechanical properties of particles in an IF steel and to evaluate the influences affecting the precition of the nanoindentation measurement of hard particle in the soft matrix.

2. Experimental material

An interstitial free steel (IF) was used for experiments. In this steel all interstitial elements are bound in the form of stabile inclusions. For purpose of this contribution it will be called the particles. Chemical composition of the investigated steel is in Tab. I.

Table I
Chemical composition of investigated IF steel

C [%]	Mn [%]	Si [%]	P [%]	S [%]	Al [%]	Ti [%]
0.005	0.145	0.0128	0.006	0.006	0.042	0.064

Ferrite polyhedric grains and particles were found in the microstructure, Fig. 1. The particles were identified as TiC(N) particles by the EDX analysis. Size distribution of particles is shown in Fig. 2 and Tab. II.

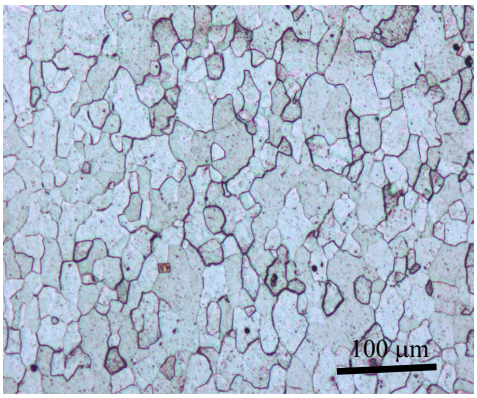

Fig. 1. **Microstructure of investigated IF steel**

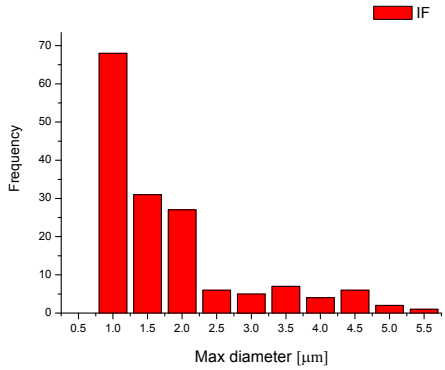

Fig. 2. **Histogram of size distribution of investigated particles**

Table II
Average size of investigated IF steel particles

	Mean diameter [µm]	Perimeter [µm]	Max length [µm]	Area [µm^2]	No.
IF	1.55	3.47	2.05	2.24	158

3. Experimental equipment

First experiments were performed using Shimadzu DUH202 instrument equipped with a Vickers tip[2]. DUH202 is an older equipment and measurements are connected with problems as correct processing of data, which are not affected by first contact selection; area function, thermal drift, etc.

Nevertheless, the data of hardness and Young modulus were measured, Tab. III.

Table III
Average Hardness and Modulus values of IF matrix and particles

	H_{IT} [GPa]	E_{IT} [GPa]
Matrix	1.40±0.12	200±14
TiC(N) particles	5.75±0.49	266±22

Matrix hardness and modulus values are according the literature[3] but TiC(N) particles hardness and modulus values were expected to be double[4,5].

Next experiments were performed using the Nanoindeter XP equipped with a Berkovich tip with rounding ~ 20 nm. Ten measurements in continues stiffness mode were performed on selected particles to the indentation depth of 1 μm. One indent was performed on each particle. Samples for experiments were prepared metallographically.

4. Reusults and discussion

Indentation hardness (H_{IT}), Young modulus (E_{IT}) in relation to indentation depth were monitored (Fig. 4 and Fig. 6). Curves were evaluated by the following way: in area of the peak region a part of curve was determined where the values of hardness and modulus are relatively constant. Values of hardness, modulus, depth and corresponding force together with position of indent after indentation were evaluated for this curve. Results are presented in the Tab. IV. On indentation curves (F-h) were observed changes of loading trend (Fig. 3) and pop-ins (Fig. 5). Those artefacts are connected with delamination of particle-matrix interface, impressing of particle into matrix, cracking of particle etc[6].

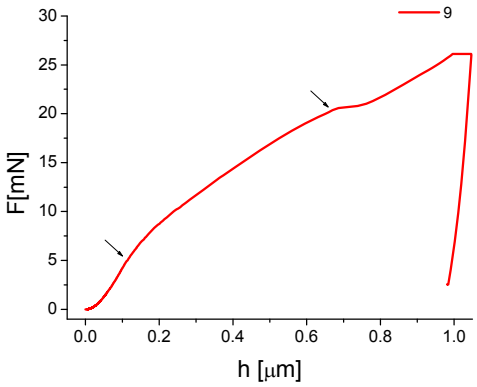

Fig. 3. **Indentation curve of particle no. 9 and particle after indentation**

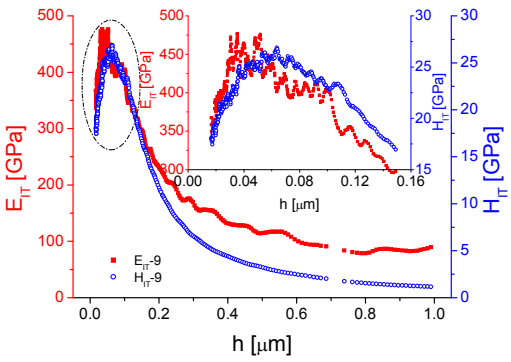

Fig. 4. **Hardness and modulus in relation with indentation depth of particle no. 9**

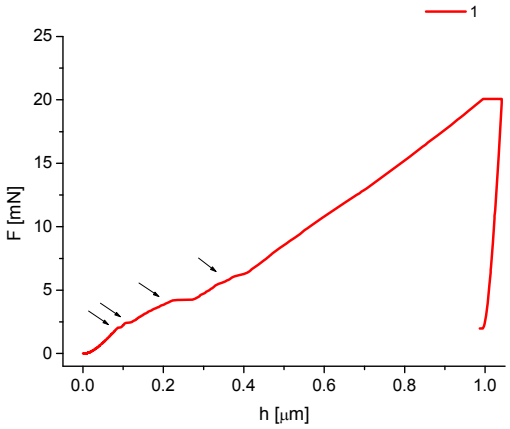

Fig. 5. **Indentation curve of particle no. 1 and particle after indentation**

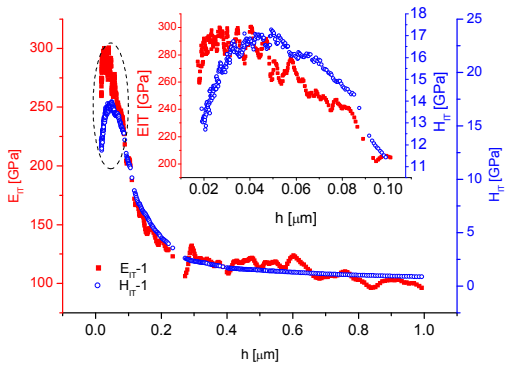

Fig. 6. **Hardness and modulus in relation with indentation depth of particle no. 1**

Table IV
Properties of investigated TiC(N) objects, depth (h) and corresponding force (F) from which were determined values of H_{IT} and E_{IT}, respectively, max perpendicular particle dimesion in the observed plane – b, c

No	H_{IT} [GPa]	E_{IT} [GPa]	h [nm]	F [mN]	b [μm]	c [μm]	Note
1	17	300	20–50	0.3–0.9	3	3	P
2	20	373	30–80	0.6–2.3	3	2	P
3	7	275	10–20	0.05–0.1	5	4	I
4	11	275	15–20	0.07–0.1	3	2	I
5	7	260	30–50	0.4–0.2	4	2	I
6	2	225	300–400	2.3–5.5	5	2	M
7	18	350	30–50	0.5–0.9	4	3	P
8	21	360	20–70	0.2–1.5	9	9	P
9	26	460	30–70	0.2–2.1	4	2	P
10	8	220	70–120	0.7–2.1	4	1	I

P – particle, I – interface, M – matrix

Shape and size of the particle underneath the surface is unknown and depends on basic shape of the particle, on orientation and from its cuts. Finally, effective diameter of particles which resist penetration of indenter is unknown. Results presented in the Tab. IV are with high scatter and are on one side close to matrix values and on other side close to hard TiC (N) coatings. What is correct? What affects the results? One of the many possible influences is impressing of the particle during the indentation into the matrix. If the particle is impressed into the matrix then measured depth (h) is composed from:

$$h = h_i + h_h \qquad (1)$$

indentation depht of the particle into the matrix (h_i) and indentation depth of indenter into the particles (h_h). Suppose that the effective radius of the particle is big enough and the particle is impressed into the matrix only elastically. Indentation of the tip into the particle (h_h) is elasto-plastic :

$$h = h_{ie} + h_{he} + h_{hp} \qquad (2)$$

After expressing[7] the eq. (2) we can achieve following equation:

$$h = \frac{F}{2aE_{rm}} + \sqrt{F}\left(\left(\varepsilon\frac{\sqrt{H_c\pi}}{2E_{rc}}\right) + \left(3\sqrt{3}H_c\tan^2\theta\right)^{-\frac{1}{2}}\right) \qquad (3)$$

In eq. (*3*) there are three unknown parameters: particle hardness (H_c), particle reduced modulus (E_{rc}) and effective radius (*a*) of the particle. An iterative process was used to determine these parameters with following conditions: Iterations were done on all particle measurements, the particles have the same hardness and modulus, radius of the particle can not exceed maximal length of the particle, the cylindrical shape of the particle. The fitting was started at contact point and stopped at first inhomogeneity (pop-in, bending, etc.) on F-h curve. The correctness of eq. (*3*) without particle behaviour term was tested on three different bulk materials, Fig. 7. Calculated and measured data for all three materials are in good agreement.

In Fig. 8, 9 results of simulation using the eq. no (*3*) are presented. Squares symbolize measured curves, dashed lines are simulation of indentation into a bulk material with properties of the particle, solid lines are simulation by the eq. (*3*). The difference between the solid and dashed line describes influence of the particle penetration into the matrix. If this difference is evaluated as stiffness change in relation to reciprocal value of effective radius, it can be seen that relation is linear, Fig. 10. It means that results are strongly influenced by impressing of the particle into the matrix. The influence of the particle size on hardness and modulus values is presented in Fig. 11. The properties measured on the biggest particles could be supposed as the most realistic values and are 30 GPa and 480 GPa for hardness and modulus values, respectively.

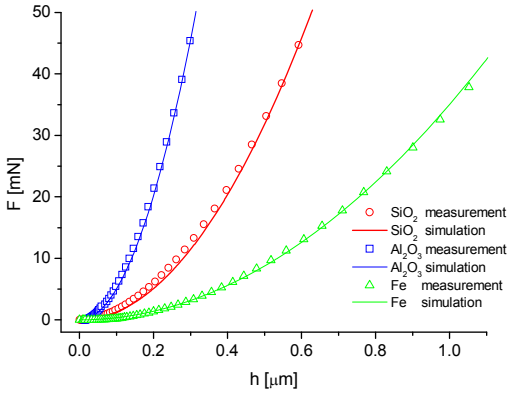

Fig. 7. **Comparison of measurements on bulk materials and simulation by eq. (*3*) without the particle element**

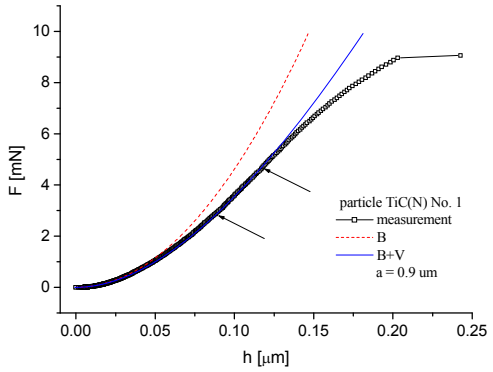

Fig. 8. **Indentation curve of particle no. 9, simulation of bulk material with properties of particle (B) and indented particle (B+V)**

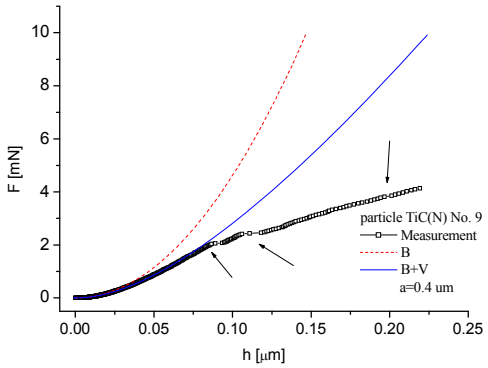

Fig. 9. **Indentation curve of particle no. 9, simulation of bulk material with properties of particle (B) and indented particle (B+V)**

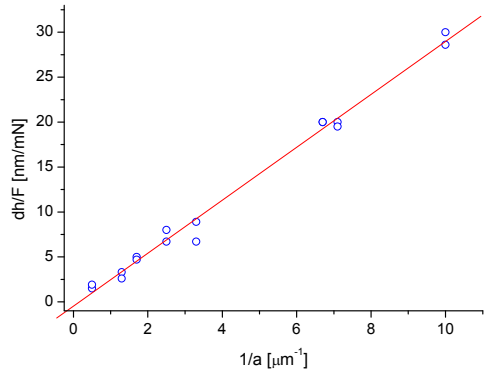

Fig. 10. **Relation between reciprocal value of effective particle radius and stiffness**

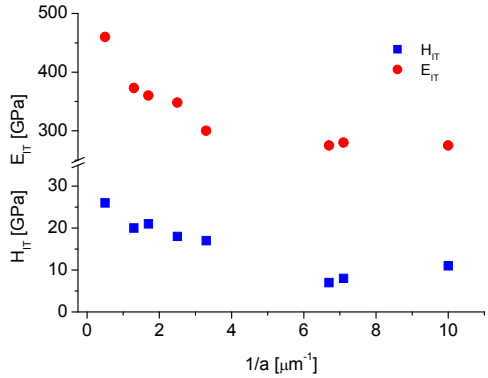

Fig. 11. **Influence of particle effective radius on measured values of hardness and modulus**

5. Conclusions

Following results were obtained from the research presented in this contribution:

– Using DSI method we were able to determine properties of the TiC(N) particles.
– The strong effect of impressing the particles into the matrix during indentation was confirmed.
– The hardness and modulus values of TiC(N) particles are 30 GPa and 480 GPa, respectively.

This work was supported by the grant APVV-0326-07, SK-PL-0019-09, VEGA 1/0846/09.

REFERENCES

1. Mishnaevsky L.: In: *Virtual testing of microstructures as a basis for the optimization of materials*, p. 5–10, IMWF Darmstadt, 2005.
2. Zubko P., Pešek L.: *Fractography of inclusion fractures in deep drawing IF steels. In: Fractography 2003*, (in. Slovak)
3. Tasan C. C., et al.: Acta Mater. *57*, 4957 (2009).
4. An J., Zhang Q. Y.: Surf. Coat. Technol. *200*, 2451 (2005).
5. Hagarová M., et al.: *The Assessment of Properties of PVD Coatings Deposited by ARC and LARC Technology* (in slovak), *In: Vrstvy a povlaky 2009.* Trenčín, Digital Grafhic, 2009.
6. Stus N. V., et al.: J. Alloys Compd. *403*, 305 (2005).
7. Zubko P.: Local mechanical properties in microvolume dimensions of metal materials, *PhD. thesis*, 2008, Košice, in Slovak.

P. Zubko[a], L. Pešek[a], O. Bláhová[b] *([a] Technical university of Košice, Faculty of metallurgy, Department of materials science, Košice, Slovakia, [b] Universtiy of West Bohemia, New Technology Research Center, Plzeň, Czech Republic):* **Mechanical Properties of Hard Particles in Soft Matrix**

The contribution deals with determination of mechanical properties of TiC(N) particles embedded in steel matrix by depth sensing indentation. The system belongs to a hard particle in soft matrix system. It has been shown that this technique can be applied to measure properties of the particles. The influences affecting the accuracy of measurement were described. The measured values of hardness and modulus are H_{IT} = 30 GPa and E_{IT} = 480 GPa, respectively. The physical model of particle behavior during the indentation was presented. Based on this model the influence of the particle size on measured results was determined.

NANOINDENTATION OF TRABECULAR BONE – COMPARISON WITH UNIAXIAL TESTING OF SINGLE TRABECULA

ONDŘEJ JIROUŠEK[a]*, JIŘÍ NĚMEČEK[b], DANIEL KYTÝŘ[a], JIŘÍ KUNECKÝ[a], PETR ZLÁMAL[a], and TOMÁŠ DOKTOR[a]

[a] *Institute of Theoretical and Applied Mechanics, Academy of Sciences of the Czech Republic, v.v.i., Prosecká 76, 190 00 Prague 9,* [b] *Czech Technical University in Prague, Faculty of Civil Engineering, Thákurova 7/2077, 166 29 Prague 6, Czech Republic*
jirousek@itam.cas.cz

Keywords: trabecular bone, nanoindentation, micromechanics, constitutive modelling

1. Introduction

Knowledge of deformation behaviour of trabecular bone in response to mechanical loading is important for better understanding of the relationship between the microstructure and overall mechanical properties. Due to the increased computational power and powerful imaging techniques it is possible to perform numerical simulations with microstructural finite element (FE) models reflecting the true microstructure of the complex material[1]. Information about the microstructure can be obtained using the microfocus computed tomography (micro-CT). The deformation behaviour can be captured applying the micro-CT technique to a sample under gradual loading[2].

For the microstructural FE models it is necessary to measure the material properties at the level of single trabecula. One of the established methods for evaluation of the material properties at this level is nanoindentation[3]. It has been confirmed by several authors that valid microstructural models of trabecular bone can be built using high-resolution micro-CT models and material properties from nanoindentation under wet conditions[4]. The agreement between experiments and micro-FE models has already been published, however, results of experimental investigation using standard mechanical testing of single trabeculae remains scattered. One of the reasons for the high discrepancy in experimental results can be attributed to improper boundary conditions; second reason is difficult precise measurement of the strains. In this study a comparison between the mechanical properties assessed by nanoindentation and properties obtained from tension tests of extracted trabeculae is performed.

2. Materials and Methods

Single trabecula tensile tests

Small blocks of trabecular bone were extracted from proximal human femur (male, 72 years). The blocks were cleaned of marrow and grease in a nonionic detergent in an ultrasonic cleaner at a temperature not exceeding 37 °C. The cleaning was repetitive not to exceed the temperature limit. The sample was then dried at room temperature. Long straight trabeculae were identified in these blocks under a magnifying glass (4× magnification). The trabeculae were carefully extracted using a sharp-tip scalpel. The ends of the trabeculae were dipped in a two-component glue (UHUplus schnellfest 2-K-Epoxidharzkleber, UHU GmbH & Co. KG, Baden, Germany) and stored for 48h at room temperature. The drops of glue at the trabecula ends were used for manipulation with the sample using a pair of tweezers.

The manipulation droplets of glue were used to attach the sample to the end-plates of a laboratory uniaxial tension-compression device specially designed for these experiments. Fast-setting glue (Loctite Super Attak Ultra Plastik, Henkel Ireland Ltd., Ireland) was used for this purpose and the glue was allowed to set for 2 hours prior the experiment at room temperature.

Tension-compression of the sample was provided by means of a precision linear stage M-UMR3.5 with differential micrometer DM11-5 (Newport Corp., USA, sensitivity 0.1 μm, travel range 5 mm) while manipulation (centering) of the fixed end was provided by Y-Z translational stage (Standa Ltd., Lithuania, sensitivity 1 μm, travel range 25 mm). The load was measured using a small-scale load cell FBB350 (FUTEK Advanced Sensor Technology, Inc., USA, load capacity 4.5 N) attached to the Y-Z translational stage.

The samples were tested in displacement-controlled uniaxial tension tests. The load was applied by moving the precision linear stage away from the fixed end of the sample. The whole experiment was captured using a high-resolution CCD camera (VDS Vosskuhler GmbH, Germany) attached to optical microscope (Navitar Imaging Inc., USA). The camera is attached to a PC by firewire cable enabling to capture 15 images per second with 24× magnification.

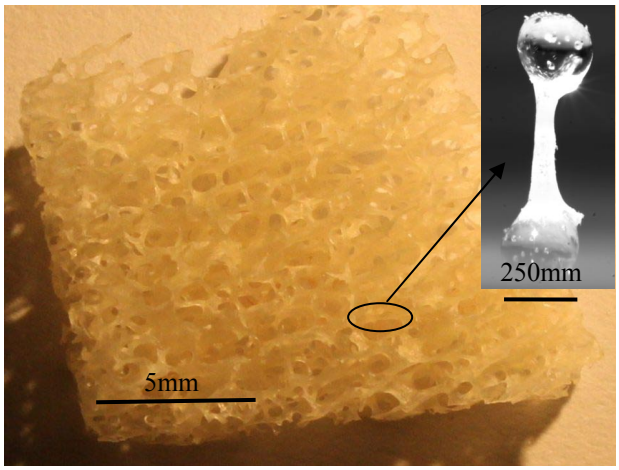

Fig. 1. **A block of trabecular bone after cleaning. Extracted trabecula with droplets of glue covering the ends**

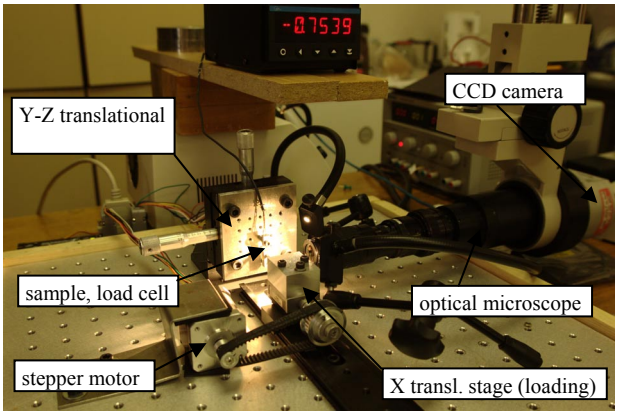

Fig. 2. **Experimental setup for single trabecula tension tests**

Due to the low value of Young's modulus of elasticity of the glue, the strain could not be calculated from the displacements of the end plates. Instead, the strain at the surface of the trabecula was calculated from the sequence of captured images using an image correlation algorithm[5].

Prior the experiment, every sample was captured in two perpendicular projections along its longitudinal axis. The projections were used to generate a finite element (FE) model of each sample. The cross-section of the trabecula was approximated by ellipse with known dimensions of the main axes. These dimensions were calculated from the images taken prior the experiment.

The experiment consisted of 10 cycles of preconditioning immediately followed by tension up to the rupture. The preconditioning was performed to verify the boundary conditions, namely perfect setting of the glue. The preconditioning was controlled by a small displacement value not exceeding the elasticity limit. During the first 10 cycles the force was carefully controlled whether the values for the upper and lower limit is reached in every cycle. If there was change of the measured force exceeding 5 % of the original value during the first 10 cycles, the experiment was considered invalid and the results were excluded.

After successful preconditioning the sample was loaded up to the rupture and the force and sequence of captured images were recorded to the PC.

Total number of samples harvested from the block of trabecular bone was 28. From these 28 samples, 5 samples were damaged or lost during manipulation. From the remaining 23 samples, 7 samples were excluded due to insufficient curing of the glue. Two more samples were excluded due to excessive bending of the sample caused by its inappropriate (highly curved) geometry. Remaining 16 samples were successfully tested in tension and a stress-strain curve for each of the sample was obtained.

Nanoindentation

A small cubic sample of bone tissue was cut from the same anatomical place of the same donor using a diamond blade saw (Isomet 2100, Buehler Ltd., USA). The fat and marrow was removed from the sample using a soft water jet followed by repetitive ultrasonic cleaning. The sample was fixed in low shrinkage epoxy resin (EpoxyCure, Buhler Ltd., USA), polished with diamond discs with grain size 35 and 15 μm followed by monocrystalline diamond suspension with grain size 9, 3 and 1 μm. For the final polishing aluminium-oxide Al_2O_3 suspension with grain size 0.05 μm on a soft cloth was used. Prior the mechanical testing the surface roughness of the sample was measured in a confocal laser scanning microscope (Lext OLS3000, Olympus America Inc., USA). The peak roughness R_p (the highest peak in the roughness profile) of the finished surface was 15 nm.

The sample was then fixed in nanoindenter Nanohardness tester (CSM Instruments, Switzerland) and indented using two different peak forces, 10 mN and 20 mN. For both peak forces a grid of 20 indents was performed with different set of parameters. Apart from the two peak forces, three different loading rates were used (20, 120, 240 mN min^{-1}) and three different holding times (10, 20, 40 s).

For each indent force-depth curves were plotted and hardness and modulus of elasticity were calculated using the Oliver-Pharr method[6]. Results from indents accidentaly placed at the interface between two lamellae were excluded. At average, there were 16.75 successful indents in each set of parameters.

3. Results

From the 16 successfully performed tension tests with isolated trabeculae the strain values were evaluated using DIC method applied to two distant regions. The places for the image correlation were selected using approximately 4/5 of the free length of the sample as the gauge length. The measured force was divided by the cross-sectional area of the sample at the place of the rupture. The area was measured using 10 Mpx camera picture of the imprint of the broken sample. The broken torso of the sample was pressed into a surface of very soft material (modelling clay) to obtain the cross-sectional area. Example of the stress-strain diagram obtained from the tension test is presented in Fig. 4.

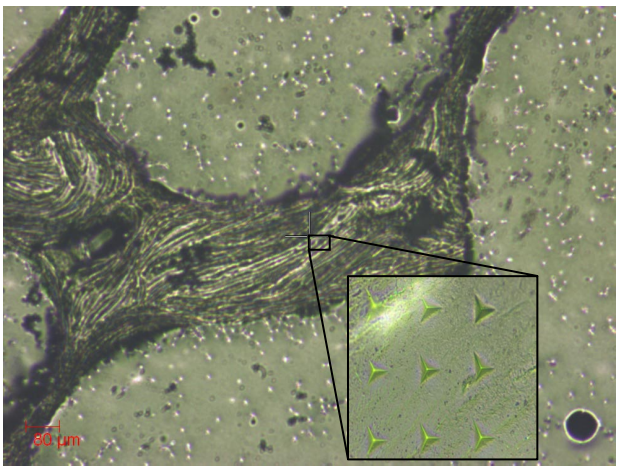

Fig. 3. **Sample trabecula in light microscope showing a grid of indents**

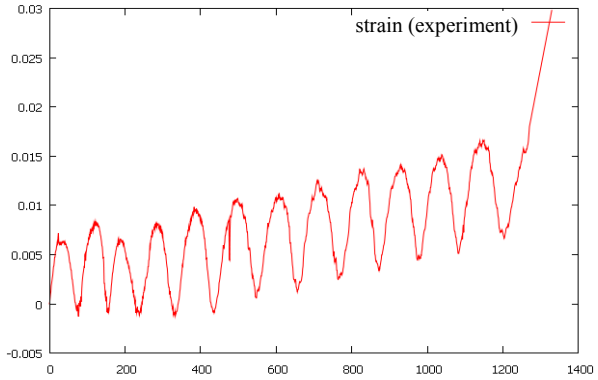

Fig. 4. **Strain assessed using the DIC method (experiment)**

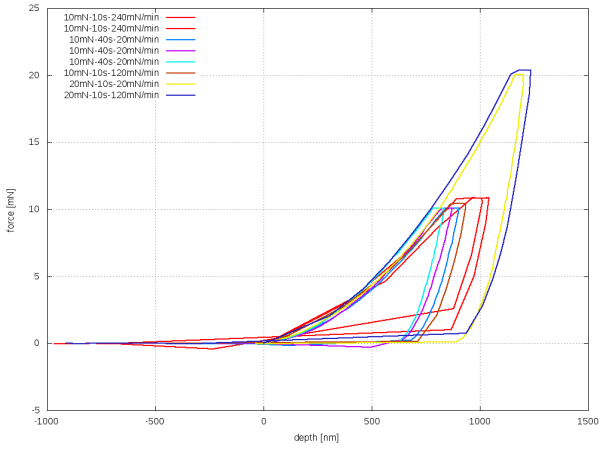

Fig. 5. **Set of depth-force curves obtained by inverse FE modelling for eight selected sets of nanoindentation experiments**

FE simulation of nanoindentation test

For FE simulations of the nanoindentation test a rotationally axisymmetric plane model was used. The Berkovich pyramid indenter was replaced with equivalent cone. The sharp tip of the cone was rounded due to the use of nonlinear contact between indenter and specimen. For the diamond nanoindenter elastic material model (E=1140 GPa, μ=0.04) was used. The elasto-plastic model with von Mises yield criterion and bilinear isotropic hardening was chosen for trabecular bone. This material model is described by four material constants, Young modulus E, Poisson's ratio μ, yield stress σ_y and tangent modulus E_{tan}. Young's modulus and Poisson's ratio were assumed to be the same as in the nanoindentation experiment. Remaining material constants (σ_y, E_{tan}) were evaluated by fitting the nanoindentation curves.

The set of nanoindentation curves with different load speeds, holding times and maximal forces was sampled using linear approximation. Values of force and penetration depth at approximation points were obtained from each nanoindentation curve. The force values with constant increments were prescribed to the model of indenter in each load step of the FE simulation (450 load steps per simulation). Nanoindentation curves obtained from the FE simulation were compared with experimental curves by the least squares method.

Material model identified by the above described fitting procedure was used in FE simulation of the single trabecula tension test. The geometry of the trabecula was approximated using elliptical cross-sections. The lengths of the major and minor axes of the ellipses were estimated from two projections of each trabecula captured by the CCD camera. The volume was discretized by 10-node tetrahedral elements with quadratic shape functions. The model was equipped with the bilinear isotropic hardening model identified from the nanoindentation. The loading was controlled by displacements according to the performed experiments. Obtained relationships between applied displacement and reaction force were compared with results obtained experimentally using the tension tests in terms of the stress-strain diagrams.

Table I
Identified material constants for 8 nanoindentation curves

$\sigma_y = 100.5$ MPa, $E_{\tan} = 898$ MPa

curve #	E [GPa]	μ	loading rate [mN min^{-1}]	max force [mN]	error
1	15.153	0.2	10	240	5716
2	13.959	0.2	10	240	2757
3	16.26	0.2	10	20	722
4	14.849	0.2	10	20	1446
5	17.543	0.2	10	20	2803
6	15.7	0.2	10	120	1945
7	18.482	0.2	20	20	1473
8	18.144	0.2	20	120	2274

$$error = \frac{\sum_{i=1}^{n}(u_i^{\exp} - u_i^{fem})^2}{n}$$

$u_i^{\exp}$ ..penetration depth in experiment (nm)

u_i^{fem} .. penetration depth in FE simulation (nm)

n … number of approximations points

4. Conclusions

Comparison of material properties of human trabecular bone assessed by nanoindentation and tension tests performed on isolated trabeculae was performed. The elasto-plastic material model identified in the FE simulation of nanoindentation test was used in the numerical simulations of the tensile experiments. Obtained response of the FE model was compared with experimentally assessed stress-strain diagrams of the tested samples.

Resulting elastic modulus obtained from nanoindentation (E=16,34±1,76 GPa) and from uniaxial testing (E=9,21±1,26 GPa) gives mean values which differ signifi-

cantly, though the standard deviations are small. This might be caused by extremely irregular shape of tested tensile specimens, and we conclude that the source of error is imprecise calculation (overestimation) of the cross-sectional area of the samples. From the tensile tests of single trabeculae it was also possible to determine the yield stress (σ_y=176±23 MPa) and yield strain (2,85±0,84 %). However, these values cannot be directly compared to nanoindentation.

In this study, dry samples were used due to the difficulties connected to nanoindentation under wet conditions. For the tension tests it is possible to soak the samples in physiological solution prior the experiment (time needed for the experiment is sufficiently short), but it is still a challenge to perform the nanoindentation with wet samples. Performing the described experiments under wet conditions is the aim of our future research.

The research has been supported by the Grant Agency of the Czech Republic (grant No. P105/10/2305), Ministry of Education of the Czech Republic (Research Plan MSM 6840770003) and research plan of the Academy of Sciences of the Czech Republic AV0Z20710524.

REFERENCES

1. Verhulp E., van Rietbergen B., Müller R., Huiskes R.: J. Biomech. *41*, 1479 (2008).
2. Jiroušek O., Jandejsek I., Vavřík D.: J. Inst. 6 (2011), C01039.
3. Rho J.-Y., Tsui T. Y., Phar G. M.: Biomaterials *18*, 1325 (1997).
4. Wolfram U., Wilke H.-J., Zysset P. K: J. Biomech. *43*, 1731 (2010).
5. Lucas B. D., Kanade T.: Proc. Im. Underst. Wshp 121 (1981).
6. Dendorfer S., Maier H. J., Hammer J.: J. Mech. Behavior Biomed. Mater. *2*, 113 (2009).
7. Oliver W. C., Pharr G. M.: J. Mater. Res. *7*, 1564 (1992).

O. Jiroušek[a], J. Němeček[b], D. Kytýř[a], J. Kunecký[a], P. Zlámal[a], and T. Doktor[a] *([a] Institute of Theoretical and Applied Mechanics, Academy of Sciences of the Czech Republic, Prague, [b] Czech Technical University in Prague, Faculty of Civil Engineering, Prague, Czech Republic):* **Nanoindentation of Trabecular Bone – Comparison with Uniaxial Testing of Single Trabecula**

To improve the knowledge about the mechanical properties of trabecular bone and their relationship with the properties of their constituting materials it is necessary to measure the properties at micrometer scale. The published mechanical properties of human trabecular bone vary between 1 GPa and 15 GPa. The cause of this broad discrepancy in results might be in sample preparation, different testing protocols or anisotropy and asymmetry of the micro-samples.

The article deals with a comparison between the properties assessed using nanoindentation and properties measured using uniaxial testing of single trabeculae.

A novel experimental device has been developed which enables to measure single trabeculae in tension and compression with high precision. The strains at the surface of the sample are measured optically using a high-resolution CCD camera. The strain field is evaluated with very precise image correlation algorithm applied to whole surface of the loaded sample.

The mechanical properties measured on micrometer-sized specimens using both methods (nanoindentation and micro-mechanical testing) are then prescribed to FE model of the trabecula sample. The sample is then loaded according to the experimental procedure. The response of the FE model (stress-strain curve) is compared to results from the tensile test.

MICROMECHANICAL PROPERTIES OF POROUS MATERIAL BASED ON METAL FOAM

VLASTIMIL KRÁLÍK* and JIŘÍ NĚMEČEK

Czech Technical University in Prague, Thákurova 7, 166 29 Prague 6, Czech Republic
vlastimil.kralik@fsv.cvut.cz

Keywords: Metal foam, Porous system, Nanoindentation, Micromechanical properties, Elastic properties, Deconvolution

1. Introduction

Traditionally, materials were tested on large samples by macroscopic methods that can give overall (or effective) properties. Together with the development of experimental techniques in the past, microstructural and micromechanical properties have become important in the description of the material behavior since they could give answers on the origin of many macrolevel phenomena.

Structural materials (like cement, lime or gypsum composites as well as metals, wood or plastic) often exhibit large variation in the microstructure of their solid phases. They are also often characterized by a closed or open pore system. Porosity is usually smaller than the solid phase content but the situation is opposite in case of lightweight materials. An exceptional example is metal foam which typically exhibits porosity around 90 % of the sample volume. Its cellular structure is analogous to the natural materials like wood or bones. Metal foams belong to the up-to-date structural materials with high potential to many engineering applications. This highly porous material with a cellular structure is known for its attractive mechanical and physical characteristics such as high stiffness in conjunction with very low weight, high strength, excellent impact energy absorption, high damping capacity and good sound absorption capability.

The usual source material for the production of metal foams is aluminium and aluminium alloys because of low specific density (~2700 kg m^{-3}), low melting point (~660 °C), nonflammability, possibility of recycling and excellent corrosion resistivity.

Products of aluminium foams gained a growing research interest in many engineering branches. They are used in applications ranging from automotive and aerospace industries (Fig. 1) to building industry (e.g. sound proofing panels). Another application of aluminium foams can be found in energy absorption (e.g. the outer shell of motorcycle helmets). More structural and functional applications of metal foams for industrial sectors have been reviewed e.g. by Banhart[1].

Metal foam can be described as a system with stochastically distributed solid phase which in turn brings difficulties in the modeling of different loading cases.

In general, mechanical properties of metal foams are governed by two major factors: (*i*) cell morphology (shape, size and distribution of cells) and (*ii*) material properties of the cell walls[2]. However, measurement of mechanical properties of the cell walls is a difficult problem that cannot be solved with conventional methods due to their small dimensions, low local bearing capacity and local yielding and bending of the cell walls. These problems can be overcome using micromechanical methods in which the load–displacement curve is obtained in the sub-micrometer range.

In this study, nanoindentation was applied to access elastic properties of the distinct phases within the cell walls of a conventional metal foam system.

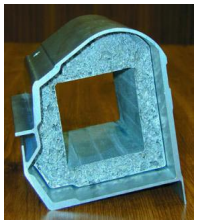

a

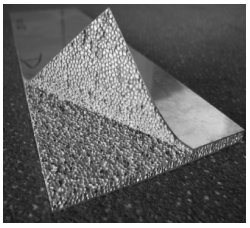

b

Fig. 1. **Examples of aluminium foam components. (a) Reinforcement of car body sill, (b) sandwich panel**

2. Materials and methods

2.1. Tested material

Commercial aluminium foam 'Alporas' (Shinko Wire Co., Ltd) was tested in this study. Alporas is an ultra-light weight material with a closed cell structure. The manufacturing process of the Alporas is a batch casting process[3] in which 1,5 wt.% of calcium is added to the aluminium molten at 680 °C. Calcium serves as a thickening agent which increases viscosity and stabilizes the air bubbles. The alloy is poured into a casting mold and stirred with an admixture of 1,6 wt.% TiH_2 that is used as a blowing agent. Then, the foamed molten material is cooled down. A typical resulting internal structure of the aluminium foam is shown in Fig. 2.

2.2. Specimen preparation

Small Alporas block 14×14×43 mm was firstly embedded into cylindrical mould (30 mm in diameter, 60 mm in height) which was filled with a low viscosity epoxy resin (Struers®). Then, ~5 mm slices were cut by diamond saw and polished with fine SiC papers. Resulting surface roughness was checked with *in-situ* imaging (surface scanning was performed with the same tip as for nanoindentation). Several roughness criteria were used (ref.[4]). For example, arithmetic deviation from the mean is defined as:

$$R_a = \frac{1}{M \cdot N} \sum_{i=1}^{M} \sum_{j=1}^{N} \left| h_{ij} - \bar{h} \right|$$

or quadratic deviation (root-mean-square):

$$R_q = \sqrt{\frac{1}{M \cdot N} \sum_{i=1}^{M} \sum_{j=1}^{N} \left| h_{ij} - \bar{h} \right|^2}$$

In the above equations, M and N are numbers of the measured points in two perpendicular directions with heights h_{ij} ($i=1..N$; $j=1..M$) and $\bar{h}$ is the arithmetic mean from all measured surface heights.

As a rule of thumb, the surface roughness should be kept within 10% of the expected maximum depths used in nanoindentation. In our case, $R_a \approx 24$ nm and $R_q \approx 30$ nm were found on a 20×20 µm scan (Fig. 3) which was acceptable compared to the maximum indentation depths around 300 nm.

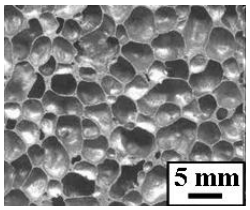

Fig. 2. **Typical structure of aluminium foam 'Alporas'**

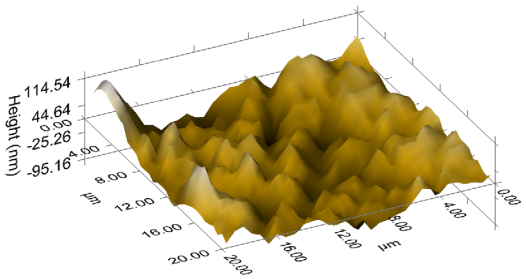

Fig. 3. **3D map of the sample surface on 20×20 µm area**

2.3. ESEM and porosity

The microstrucure of the foam was studied in electron microscope (ESEM). The non-homogeneous solid phase of the cell wall is shown in Fig. 4. Two distinct phases, that exhibit different color in back-scattered electron (BSE) images, can be distinguished. The chemical composition of the two phases was checked with EDX element analysis in ESEM. It was found that the majority of the volume (dark zone) consists of aluminium (~67 wt.%), oxygen (~32 wt.%) and further trace elements (Mg, Ti, Fe, Co, Ni, Cu, Si <2 wt.%). Lighter zones in Fig. 4 consist of Al (~60 wt.%), O (~30 wt.%), Ca (~5 wt.%), Ti (~5 wt.%) and other elements (<1 wt.%). As expected, the majority of the volume (dark zone) is composed of aluminum and aluminium oxide Al_2O_3 (further denoted as Al-rich area). Lighter zones contain significant amount of calcium and titanium (further denoted as Ti-rich area). The non-uniform distribution of these zones shows on inhomogeneous mixing of the admixtures that are added during the production process.

The overall porosity of the sample reaches 90 % (ref.[3]). The large pores have usually round of polyhedral shape with the mean size 4,8 mm (ref.[3]). It can be seen in Fig. 4 that also a smaller part of porosity takes place on microlevel in a micron to submicron range. Further quantification of this 'small' porosity was beyond the scope of this study but it is planned in a near future.

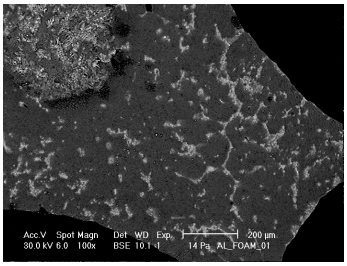

(a)

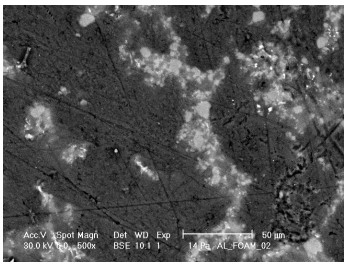

(b)

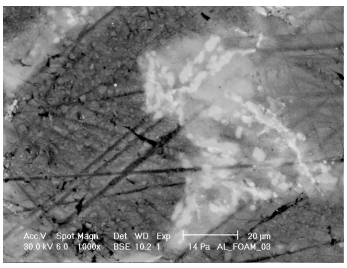

(c)

Fig. 4. **ESEM Images of a cell wall: (a) overall view, (b) and (c) details of Ca/Ti-rich area (light zones)**

2.4. Nanoindentation

The nanoindentation testing was performed using a Hysitron Tribolab system® at the CTU in Prague. This system consists of *in-situ* SPM imaging which was used for scanning the sample surface. Berkovich tip was used for all measurements. Five distant locations were chosen on the sample to capture its heterogeneity. Each location was covered by a series of 10×10 indents with 10 µm spacing (Fig. 5). It yields 500 indents in total which was considered to give suffi-

ciently large statistical set of data. Standard load controlled test of an individual indent consisted of three segments: loading, holding at the peak and unloading. Loading and unloading of this trapezoidal loading function lasted for 5 second, the holding part lasted for 10 seconds. Maximum applied load was 1500 μN.

Elastic constants (hardness and elastic modulus) were evaluated with standard Oliver and Pharr method[5]. Poisson's ratio needed for the estimation of Young's modulus was chosen to be 0,35 for all indents (equivalent to Aluminium[6]).

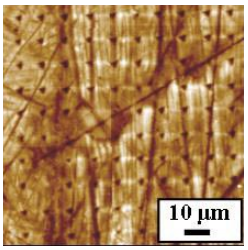

Fig. 5. **Matrix of 10×10 indents scanned with Hysitron Tribolab®**

3. Results

3.1. Statistical results from nanoindentation

An example of a typical loading diagram for Al-rich area (dark zone in Fig. 4) is shown in Fig. 6a. Average contact depth is around 230 nm and maximum depth reaches values around 240 nm. The material volume affected by nanoindentation can be estimated as 3 to 4 times the maximum depth, i.e. < 1 μm (ref.[8]). Variety of results from different positions is shown in Fig. 6b in which a part of curves belongs to Al-rich and a part to Ca/Ti-rich zones.

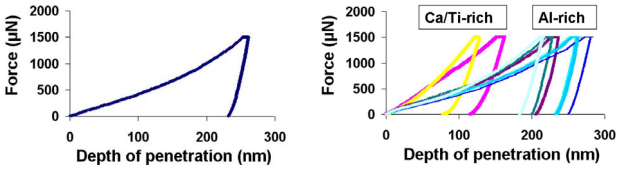

Fig. 6. **(a) Typical loading diagram for Al-rich zone, (b) example of variation in loading diagrams for Ca/Ti-rich zone**

The scatter in the results is affected mainly by the position in different zones and related hardnesses of its constituents. On the other hand, absolute values of elastic constants are affected also by a porosity which is expected to be close to the maximum indentation depth. The porosity is naturally included in the results that are measured for a solid volume consisting this part of the porosity. Overall results are depicted in Fig. 7 in which histogram of all elastic moduli merged from all positions is shown.

It can be seen in Fig. 7 that a significant peak appears around 40 GPa. This value can be considered as a dominant characteristic of a solid phase. More detailed specification is given in the next section. Large scatter in the results can be attributed to the heterogeneous chemical and mechanical

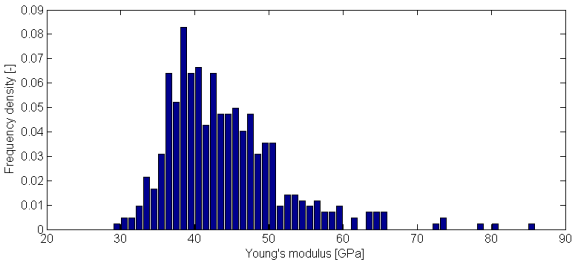

Fig. 7. **Histogram of elastic moduli merged from all positions**

composition (e.g. addition of Ca and Ti) in the sample and also to the porosity as discussed before.

Average mechanical results from all measurements are summarized in the Tab. I.

Evaluated average Young's modulus E lies between 40 to 51 GPa for individual locations. These values and also the dominant characteristic from Fig. 7 (~40 GPa) are much lower than that for pure aluminium (70 GPa, ref.[6]) which is another evidence of the sample heterogeneity and introduced micro porosity. Youngs' moduli of calcium (20 GPa, ref.[6]) and titanium (116 GPa, ref.[6]) are also far from the mean value of E and cannot be found in the overall histogram (Fig. 7) either. It shows on their mechanical interaction within the scale of the nanoindentation. Perhaps, their properties are included in one effective phase (Ca/Ti-rich).

Table I
Average values of micromechanical parameters

Position	Number of indents	Young's modulus [GPa]	St. dev. [GPa]	Hardness [GPa]	St. dev. [GPa]
1	100	43,4	8,69	0,929	0,524
2	100	40,7	4,48	0,737	0,137
3	100	41,2	6,32	0,734	0,099
4	100	51,2	9,21	1,090	0,453
5	100	46,9	7,37	0,941	0,240

3.2. Deconvolution

Statistical results of elastic moduli (Fig. 7) have been further analyzed with a deconvolution technique[7–9] which seeks for parameters of individual phases included in overall results. The deconvolution algorithm searches for n-Gauss distributions in an experimental probability density function – PDF (Fig. 7). Random seed and minimizing criteria of the differences between the experimental and theoretical overall PDFs are computed in the algorithm to find the best fit.

Tab. II contains numerical results from the deconvolution also with the estimated volume fractions of the phases. Two-phase system (one dominant Al-rich phase and one minor Ca/Ti-rich phase) was assumed in the deconvolution.

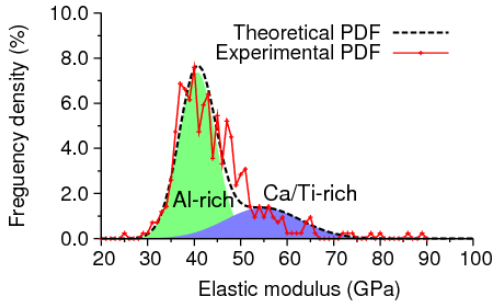

Fig. 8. **Comparison of the experimental probability density function with the results from deconvolution in two phases**

Table II
Elastic moduli (GPa) from deconvolution

Phase	Mean	St. dev.	Volume fraction
1 (Al-rich zone)	40,67	3,93	0,723
2 (Ca/Ti-rich zone)	54,80	8,08	0,277

4. Conclusions

Performed microstructural observations and results from nanoindentation revealed that the heterogeneity included in the aluminium foam at the production process has consequences in its micromechanical behavior. Large scatter of elastic parameters have been obtained. Harder and softer areas measured with nanoindentation can be linked with ESEM analyses and denoted as Al- and Ca/Ti-rich areas. Average mechanical results of a dominant Al-rich phase (40,67 GPa) do not reach values expected for a pure aluminium (~70 GPa). It points out to the fact that a substantial part of the sample porosity can be included in the tested volume (~ 1 μm) and/or softer admixtures influence on the obtained results.

Further research on the microporosity, influence of admixtures and also measurement of inelastic properties is planned in the future. Results should serve as an input data for mathematical modeling of the material.

Support of the Czech Science Foundation (GAČR 103/09/1748) and Agency of the Czech Technical University in Prague, grant No. SGS10/135/OHK1/2T/11, is gratefully acknowledged.

REFERENCES

1. Banhart J.: Progr. Mater. Sci. *46*, 559 (2001).
2. Hasan M. A., Kim A., Lee H.-J.: Compos. Structur. *83*, 180 (2008).
3. Miyoshi T., Itoh M., Akiyama S., Kitahara A., Aluminium foam, "ALPORAS": Mat. Res. Soc. Symp. Proc., Vol. 521, Materials Research Society 1998.
4. ISO 4287-1997, "Geometrical Product Specifications (GPS) – Surface texture: Profile method – Terms, definitions and surface texture parameters"
5. Oliver W., Pharr G.: J. Mater. Res. *7* (1992).
6. WebElements Periodic Table of the Elements. http://www.webelements.com
7. Constantinides G., Chandran K. R., Ulm F.-J., Vliet K. V.: J. Mater. Sci. Eng., A *430* (2006).
8. Němeček J., Lukeš J.: Chem. Listy *104*, s279 (2010).
9. Němeček J., Šmilauer V., Kopecký L., accepted for publication in Cem. & Concr. Comp., ISSN: 0958-9465.

V. Králík, and J. Němeček *(Czech Technical University in Prague):* **Micromechanical Properties of Porous Material Based on Metal Foam**

This paper deals with the study of microstructure and micromechanical properties of a porous aluminium-based material using nanoindentation. ESEM analysis revealed Al- and Ca/Ti-rich areas. Results of elastic moduli and hardness monitored in five distant locations on the solid pore walls. On a large statistical set of measurements analysed using deconvolution method indicated, that average elastic modulus of dominant Al-rich phase is 40.67 GPa and minor Ca/Ti-rich phase 54.80. They are lower than the values for pure aluminium (~70 GPa), possibly due to additional microporosity.

IDENTIFICATION OF STRESS-STRAIN RELATION OF AUSTENITIC STEELS BY INSTRUMENTED INDENTATION

PETR HAUŠILD[a]*, JIŘÍ NOHAVA[b], and ALEŠ MATERNA[a]

[a] *Czech Technical University in Prague, Faculty of Nuclear Sciences and Physical Engineering, Department of Materials, Trojanova 13, 120 00 Praha, Czech Republic,* [b] *CSM Instruments, Rue de la Gare 4, CH-2034 Peseux, Switzerland hausild@fjfi.cvut.cz*

Keywords: Nanoindentation; Stainless steel; Martensitic transformation; Finite element method

1. Introduction

Instrumented indentation with spherical indenter is extensively used for characterization of local mechanical properties of various materials including metals, ceramics and polymers. For elastic-plastic behavior of metals, definitions of indentation stress and representative strain proposed by Tabor[1] are widely accepted and have since been verified by other investigators[2–4].

Indentation (or representative) stress is given by:

$$\sigma_{repr} = \frac{P}{C\,\pi\,a^2} \qquad (1)$$

where P is the load, a is the indentation radius (see Fig. 1) and C is the constraint factor about 3 for most perfectly plastic engineering materials.

Representative (or average) strain is given by:

$$\varepsilon_{repr} = 0.2\frac{a}{R} \qquad (2)$$

where R is the radius of the spherical indenter, prefactor 0.2 was determined empirically[1].

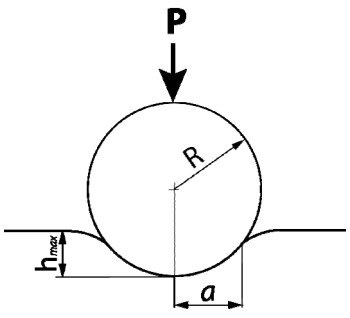

Fig. 1. **Schematic diagram of an indentation by a rigid sphere**

The main assumption of this approach is that the indentation (compressive) stress and strain are similar to their counterparts in uniaxial loading, i.e.:

$$\sigma_{repr} = \sigma_{uniaxial} \quad \text{and} \quad \varepsilon_{repr} = \varepsilon_{uniaxial} \qquad (3)$$

In this paper, the local stress-strain relations of two common austenitic stainless steels (grade A301 and A304) are characterized by instrumented indentation with spherical indenter. The results obtained by indentation are compared with tensile stress-strain curves and analyzed using finite element model. The limitations of such identified relations arise from the indenter shape, uneven contact and non-linear material behavior due to e.g. cracking or phase transformation. Especially AISI 301 steel undergoes at room temperature deformation-induced phase transformation of face-centered cubic γ austenite to body-centered cubic α'-martensite[5]. High internal stresses are generated due to an incompatible transformation strain accompanying the martensitic transformation[6]. The correct interpretation of the measured local properties is therefore essential for good understanding of the material behavior of metastable austenitic steels subjected to plastic strain.

2. Experimental details

Two austenitic stainless steels (AISI 301 and 304) were chosen as an experimental material. The chemical composition is given in Tab. I. The steels were supplied by the ARCELOR-MITTAL as cold rolled sheets (thickness 0.68 mm and 0.8 mm respectively) in the annealed state. Surface of samples was electro-polished in 5 % perchloric acid solution in ethanol at 40 V to avoid the surface layer affected by mechanical grinding and polishing.

Nanoindentation measurements were performed on CSM Instruments NHT Nanoindentation Tester with spherical indenter using instrumented indentation technique. A small indenter radius (5 μm) was chosen to achieve fully plastic deformation under the indent. Single indentation and continuous multi cycle (CMC) indentation with increasing load were performed up to maximum load of 100 mN. Loading time was 10 s per each cycle for CMC, followed by 5 s hold at the maximum load and unloading time 10 s per each cycle. For single indentation, both loading and unloading times were set to 30 s while the hold period at the maximum load was maintained at 5 s.

Table I
Chemical composition of stainless steels (in wt.%)

	C	Cr	Ni	Si	Mn	Mo
A301	0.05	17	7	0.5	1.5	0.1
A304	0.04	18.3	9.2	0.5	1.5	0.18

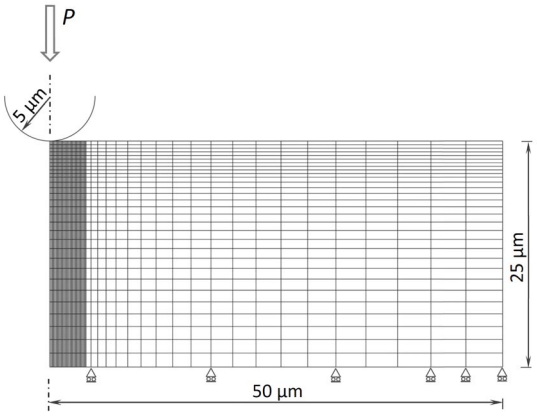

Fig. 2. **Finite element mesh and boundary conditions used for the simulation of indentation experiment**

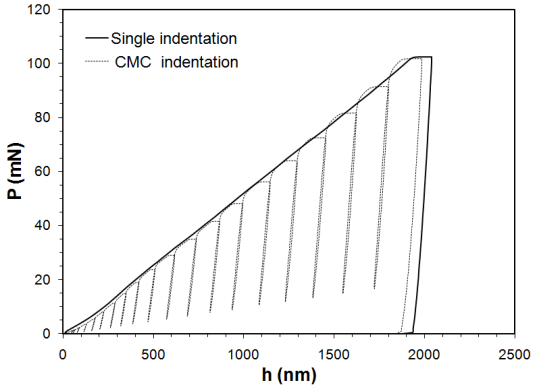

Fig. 3. **Typical single and CMC indentation load *vs* indentation depth curve obtained on A304 stainless steels**

3. Finite element modelling

A forward analysis of Tabor's relations was carried out using finite element method (FEM). FEM model was implemented in Msc.Marc 2010 FEM code. The specimen was modelled by 4000 8-node quadratic axisymmetric elements with the finest mesh (mesh size 100×400 nm) in the region of the indented material (Fig. 2). The indenter was modelled by a rigid contact surface. Elasticity in the indenter was neglected since it is important only for very hard materials (comparable to diamond). The plastic response of the material was governed by von Mises (J2) yield criterion, associated flow rule, isotropic hardening and the constitutive responses obtained from the tensile tests.

4. Results and discussion

Typical load versus indentation depth plot is shown in Fig. 3. Single indentation and continuous multi cycle (CMC) indentation records obtained on both stainless steels are in very good agreement which justifies using indentation stress and indentation radius measured by CMC indentation for the representative stress-representative strain evaluation.

The global responses computed by FEM are compared with the experimental load versus indentation depth curves in Fig. 4. For both steels, the simulated loading parts are in a good agreement with the experimental curves (keep in mind that viscous effects during hold and unload were not considered in FEM modelling).

The small differences between the experimental and simulated loading curve in the case of A301 steel are caused by the transformation induced plasticity which is not taken into account in the modeled material behavior.

Martensitic transformation is a first order phase transformation (accompanied by the volume change).

In the case of intervening such phase transformation, the actual macroscopic (mean) inelastic strain rate, $\dot{\bar{\varepsilon}}_{pl}$, is given by:

$$\dot{\bar{\varepsilon}}_{pl} = (1 - f_m)\dot{\bar{\varepsilon}}_{pa} + f_m\dot{\bar{\varepsilon}}_{pm} + f_m\dot{\bar{\varepsilon}}_{tr} \qquad (4)$$

i.e., consists of the plastic deformation in the austenite ε_{pa}, martensite ε_{pm}, and the transformation induced plasticity ε_{tr} (f_m is the martensitic volume fraction).

The modeled distributions of equivalent plastic strain (at the maximum load) are shown in Fig. 5 and 6 respectively. There is a higher gradient of equivalent plastic strain under the indent in the A304 steel due to the different plastic response. It is also interesting to note the maximum value of equivalent plastic strain (ε_{pl}~0.7) in comparison with representative (mean) strain (ε_{repr}~0.15) obtained from eq. (*2*).

Stress-strain relations obtained using Tabor's formula from nanoindentation experiment are compared with tensile test and FEM modeling in Fig. 7.

In the case of A304 steel, there is almost a perfect fit of tensile curve after some initial stage. The discrepancy for small representative strains (low indentation depths and small

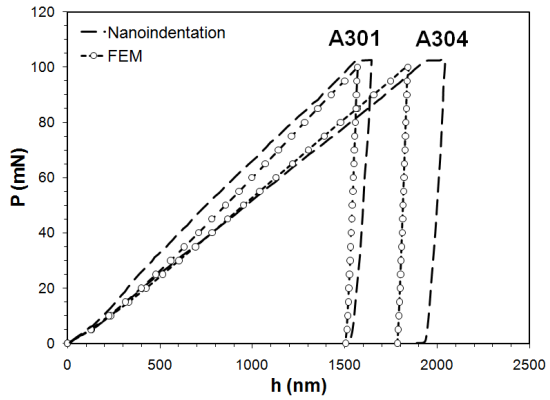

Fig. 4. **Experimental and simulated (FEM) load vs indentation depth curves obtained by single indentation with spherical indenter**

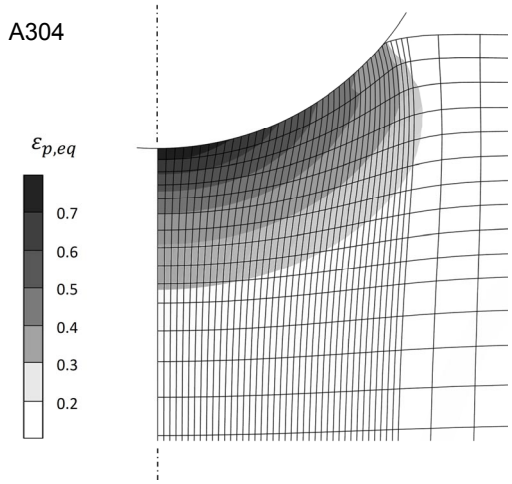

Fig. 5. **Equivalent plastic strain distribution under the indenter in A304 steel computed by FEM model (*P*=100 mN, ε_{repr}=0.15)**

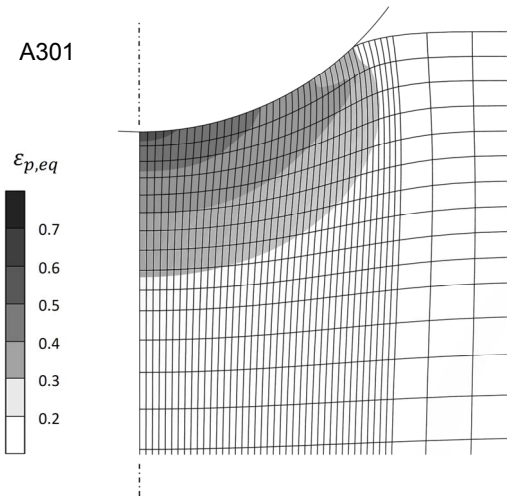

Fig. 6. **Equivalent plastic strain distribution under the indenter in A301 steel computed by FEM model (*P*=100 mN, ε_{repr}=0.14)**

indentation areas) is probably caused by imperfect (worn) indenter radius and/or surface roughness (see Fig. 8b). This could partially be resolved by using larger indenter radius (keeping the low indentation depths but increasing the indentation contact areas) but care must be taken to remain in plastically dominated regime.

In the case of A301 steel, the non-linear material behavior caused by the deformation induced martensitic transformation resulted in a large discrepancy between indentation and tensile test data within the whole interval of interest. In this case, a reverse analysis with much complex materials constitutive behavior must be employed to identify the stress-strain relations.

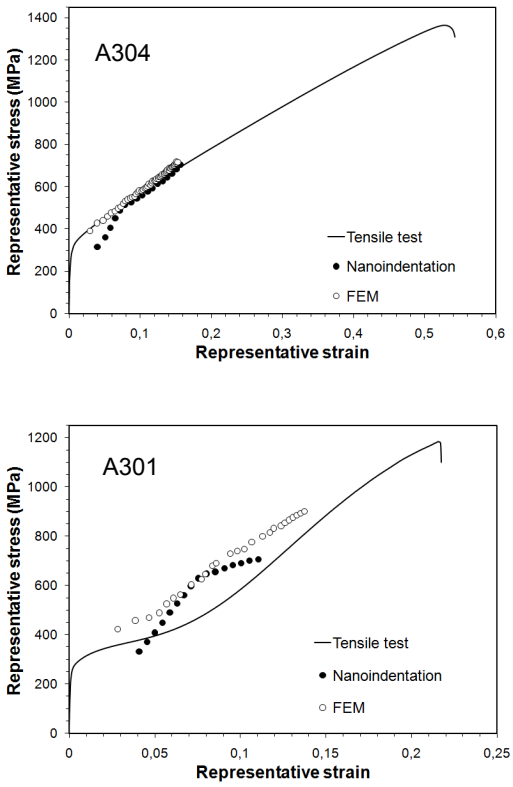

Fig. 7. **Stress-strain relations obtained by tensile test, using Tabor's formula from nanoindentation experiment and FEM model**

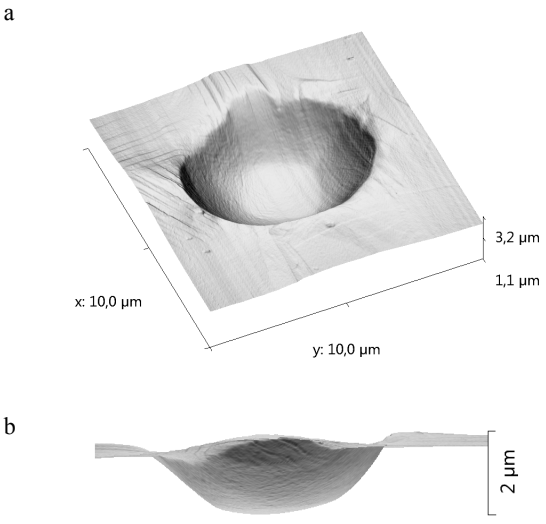

Fig. 8. **Atomic force microscopy image of the indent by 5 µm-radius indenter (a), side view (b). A301 steel, *P*=100 mN**

5. Conclusions

The instrumented indentation technique with a small indenter radius was successfully used for the prediction of the local mechanical behavior of stainless steels in the fully plastic regime.

Indentation experiments were modeled by FEM. FEM simulations reproduced properly the global response of the material to the spherical indentation and allowed us to assess the stress-strain distribution under the indent. FEM simulations showed also the limitations of the instrumented indentation method.

Finally, it must be pointed out that using of Tabor's formula without a full consideration of the character of the indentation process with respect to the elastic-plastic properties of the specimen material can lead to erroneous results especially in the case of intervening phase transformation.

This work was carried out in the frame of research project GA CR 101/09/0702.

REFERENCES

1. Tabor D.: *The Hardness of Metals*, Clarendon Press, Oxford 1951.
2. Johnson K. L.: *Contact mechanics*. Cambridge University Press, 1985.
3. Fischer-Cripps A. C.: J. Mater. Sci. *32*, 727 (1997).
4. Park Y. J., Pharr G. M.: Thin Solid Films *447-448*, 246 (2004).
5. Mangonon Jr., L., Thomas G.: Metall. Trans. *1*, 1577 (1970).
6. Timokhina I., Hodgson P., Pereloma E.: Effect of alloying elements on the microstructure-property relationship in thermomechanically processed C–Mn–Si TRIP steels. In: De Cooman BC, editor. *Proceedings of the international conference on TRIP-aided high strength ferrous alloys, Ghent*, 153–7, 2002.

P. Haušild[a], J. Nohava[b], and A. Materna[a], *([a] Faculty of Nuclear Sciences and Physical Engineering, Czech Technical University in Prague, Czech Republic, [b] CSM Instruments, Switzerland):* **Identification of Stress-Strain Relation of Austenitic Steels by Instrumented Indentation**

In this paper, the local stress-strain relations of two austenitic steels (grade A301 and A304) are characterized by instrumented indentation with spherical indenter. The results obtained by indentation are compared with tensile stress-strain curves and analyzed using finite element model. The limitations of such identified relations arising from the indenter shape, uneven contact and non-linear material behavior due to the stress-induced phase transformation are discussed.

OPPORTUNITIES AND PROBLEMS IN NANOINDENTATION WITH SPHERICAL INDENTERS

JAROSLAV MENČÍK*

University of Pardubice, Studentská 95, 532 10 Pardubice, Czech Republic
jaroslav.mencik@upce.cz

Keywords: nanoindentation, spherical indenter, elastic modulus, stress-strain curve, viscoelasticity, calibration

1. Introduction

The main advantages of indentation with spherical indenters are: *1*) possibility of measurement under low stresses so as to obtain elastic and viscoelastic material parameters without influence of irreversible processes, *2*) gradual increase of stresses and strains with increasing indenter depth, enabling the construction of stress-strain diagrams, *3*) negligible pile-up for small depths of penetration. An important issue is the knowledge of the indenter tip radius, and its calibration is necessary. All these issues are discussed further.

2. Geometry and stresses in elastic contact

Figure 1 shows the geometry of indentation by a spherical indenter. In contrast to pointed indenters (Vickers, Berkovich), the stresses grow gradually with indenter load. Spherical indenters enable measurement under relatively low stresses, with all deformations elastic. For this case, the formulae by Hertz[1] can be used:

$$F = (4/3)E_r R^{1/2} h^{3/2}, \quad h = [(9F^2)/(16RE_r^2)]^{1/3} \qquad (1)$$

F is the load, h – indenter displacement, R – indenter radius, and E_r is the reduced modulus, related to the elastic modulus E and Poisson´s ratio ν of the specimen (no subscript) and indenter (subscript i) as: $1/E_r = (1 - \nu^2)/E + (1 - \nu_i^2)/E_i$. The total depth of penetration h, contact depth h_c, indenter radius R, contact radius a and area A are related as follows:

$$h_c = h/2, \quad A = \pi a^2 = \pi(2Rh_c - h_c^2) \approx 2\pi R h_c \qquad (2)$$

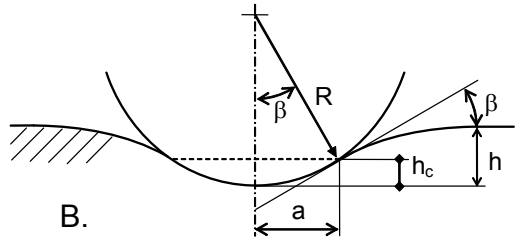

Fig. 1. **Indentation by a spherical indenter – geometry**

the expression at the right holds for small depths. The mean contact pressure („hardness“ in indentation tests),

$$p_m = F/A = F/\pi a^2, \text{ and also} \qquad (3)$$

$$p_m = \pi^{-1}[(16/9)FE_r^2/R^2]^{1/3} = (4/3\pi)E_r(a/R) \qquad (4)$$

The mean contact pressure can be used as a characteristic of contact stresses; see Section 5.

3. Determination of elastic modulus

If the deformations are only elastic, Young modulus can be determined directly from rearranged Eq. (*1*):

$$E_r = (3/4)FR^{-1/2} h^{-3/2} \qquad (5)$$

With respect to the scatter of experimental data, it may be better to calculate E_r as a regression constant in Eq. (*1*), by fitting a group of $F(h)$ data.

If plastic deformations have appeared during the test, Eq. (*5*) may be used as well if the radius R is replaced by the effective radius R_{eff}, obtained from

$$1/R_{eff} = 1/R - 1/R_{res} \qquad (6)$$

where R_{res} is the radius of residual spherical depression; for more see ref.[2,3].

Elastic modulus can also be obtained using the classic Oliver & Pharr[4] approach and formula

$$E_r = [\pi^{1/2}/2\beta]\, S/A^{1/2} \qquad (6)$$

$S = dF/dh$ is the contact stiffness calculated by fitting the upper part of unloading curve, β is an empirical constant (for spherical indenters, β = 1), and A is the contact area, corresponding to the contact depth h_c. This depth can be calculated from the total depth h using the relationship $h_c = h/2$ if the contact is purely elastic. However, Eq. (*6*) can also be used for elastic-plastic contact; in this case the contact depth is obtained as

$$h_c = h - \varepsilon F/S \qquad (7)$$

where $\varepsilon = 0.75$. For all these calculations, the indenter radius $R(h)$ or the area function $A(h_c)$ must be known.

4. Onset of permanent deformations

Permanent deformations can be revealed from the $F(h)$ curve: the load and unload curves do not overlap. The first plastic flow under spherical indenter appears for $p_m = 1.1\ Y$, where Y is the yield stress of the indented material. However, as the material flows first in a small volume beneath surface and is constrained by elastic material around, the deviation of F–h curve from elastic course becomes observable later[5], for $p_m \geq 1.6\ Y$.

The onset of plastic flow is characterised in the $p_m(a/R)$ diagram by the deviation from linearity; cf. Eq. (*4*). An exam-

ple is shown in ref.[3].

An alternative procedure for the detection of the onset of plastic flow was proposed by Chudoba[6].

When preparing elastic-strains tests with a spherical indenter, preliminary information about the yield stress can be obtained from high-load tests, or from a test with a pointed indenter. The parameters for the low-stress spherical contact (F, R) should then be chosen so that the mean contact pressure (3) is several times lower than the „hardness" obtained by a pointed indenter.

5. Stress – strain diagrams

All stress components are proportional to the mean contact pressure p_m, which is thus very suitable for their characterisation. Under a spherical indenter, the contact pressure and strains increase with the depth of indenter penetration, and can be used to construct the stress–strain curves. The representative strain is usually expressed as the ratio of contact radius a and indenter radius r; $\varepsilon_{rep} = 0.2(a/r)$.

The stresses beneath indenter are tri-axial. If the stress-strain curve, based on indentation tests, should resemble the common $\sigma - \varepsilon$ diagram for uniaxial loading, it must be constructed in coordinates $\sigma_{eq} - \varepsilon_{rep}$. The equivalent stress σ_{eq} can be calculated from p_m as

$$\sigma_{eq} = p_m / \Phi(\varepsilon_{rep}, E, Y, \nu\ldots) \qquad (8)$$

the function Φ depends on the degree of deforming (ε_{rep}), on elastic modulus E, yield strength Y and Poisson´s ratio ν. Equation (*8*) is generalization of the relationship between hardness H (= p_m) and uniaxial yield stress Y in soft metals, $H = CY$; the constraint factor C expresses that the mean contact pressure, needed to cause plastic flow, must be higher than the yield stress.

The stress-strain curve (Fig. 2) can be constructed[7] from the $p_m(\varepsilon_{rep})$ data obtained by spherical indenter for a series of loads or using the continuous measurement of properties with depth. It consists of two asymptotes (for small and large strains) and an intermediate part.

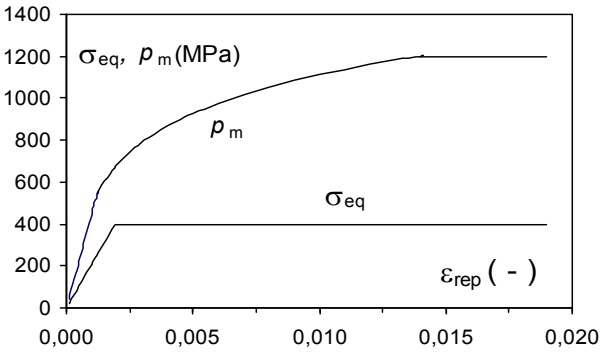

Fig. 2. **Equivalent stress σ_{eq} and mean contact pressure p_m as functions of representative strain ε_{rep}.** (A schematic, after Menčík[7])

Asymptote 1 – elastic deformations. As long as the equivalent stress is lower than the yield strength, the relationship between the equivalent stress and representative strain is linear,

$$\sigma_{eq} = E\,\varepsilon_{rep} \qquad (9)$$

For elastic contact of a sphere with a plane, formula (*4*) can be used. Combination of Eqs. (*8*), (*9*) and (*4*) gives the proportionality constant Φ for $\varepsilon_{rep} = 0.2a/r$:

$$\Phi = 20/(3\pi) \qquad (10)$$

Mesarovic and Fleck[5] have revealed by extensive FEM modeling that the relationship $p_m(\varepsilon_{rep})$ for spherical indentation is linear as long as $p_m < 1.6Y$.

Asymptote 2 – soft materials, full plastic flow. In soft materials ($E/H > 40$), the fully plastic flow is developed soon. In this case, the constraint factor is a constant, $\Phi \approx 3$, and the yield stress is calculated as

$$Y(\varepsilon_{rep}) = \sigma_{eq}(\varepsilon_{rep}) = p_m(\varepsilon_{rep})/3 \qquad (11)$$

Intermediate part – elastic-plastic deformations. For hard materials ($E/H < 40$), or for small representative strain ε_{rep}, the plastically deformed zone is small and surrounded by a relatively large elastic region. The elastic strains are comparable with plastic ones. The constraint factor Φ depends on the ratio of the representative strain (imposed by the indenter) to the material strain capacity, $\varepsilon_{rep}/\varepsilon_Y$. The simplest expression for Φ is based on the model of an infinite elastic–plastic body with a spherical cavity under internal pressure[1]:

$$\Phi = A + B \ln(C\varepsilon_{rep}/\varepsilon_Y) \qquad (12)$$

A, B and C are constants. If ε_Y is not known in advance, it is easier to determine the yield stress $Y(\varepsilon_{rep})$ directly from the expression[8]

$$p_m(\varepsilon_{rep})/Y(\varepsilon_{rep}) = A + B \ln(C\varepsilon_{rep}E/Y_0) \qquad (13)$$

with the constants: $A \approx 4/3$, $B \approx 2/3$, and $C \approx 5/3$ for $\varepsilon_{rep} = 0{,}2a/R$. Equation (*13*) must be solved for Y numerically (for given p_m, ε_{rep} and E). The procedure could be improved, e.g. by considering the influence of Poisson's ratio, see the Johnson's model of expanding cavity[1], or the model by Gao[9], which respects strain hardening, indenter shape and the imprint size.

When constructing the stress-strain curve, it is reasonable first to plot σ_{eq} in a wider range of ε_{rep} using approximations (*9*) – (*13*), and then to find their limits. The constant Φ for elastic deformations (= $20/3\pi$) should be used for $p_m \leq 1.6Y$. An example of curves $p_m(\varepsilon_{rep})$ and $\sigma_{eq}(\varepsilon_{rep})$, obtained for given material data, is depicted in Fig. 2. Vice versa, it is also possible to obtain material parameters from the empirical $p_m(\varepsilon_{rep})$ curve[7,8].

Approximation of the curve $\sigma_{eq}(\varepsilon_{rep})$ or its part by the expression[2]

$$Y(\varepsilon) = Y_0(\varepsilon/\varepsilon_0)^x \qquad (14)$$

enables the determination of strain-hardening index x for elastic-plastic materials.

6. Determination of viscoelastic parameters

In viscoelastic materials, deformations depend not only on the load, but also on its duration. This behaviour can be described by spring-and-dashpot models (Fig. 3), with parameters determined from indentation tests, by fitting the displacement–time data, $h(t)$. In applications, the stresses are usually low and the viscoelastic deformations are reversible and disappear some time after unloading. Therefore, the stresses in the indentation tests for the determination of model parameters should also be low. This cannot be achieved by a pointed indenter, but by a spherical one. A problem is that the $h(t)$ curve for indenter displacement under constant load can often be approximated similarly well by a reversible model with a spring and Kelvin-Voigt bodies, and an irreversible model with a dashpot in series (Fig. 3); its use, however, would be wrong in low-stress applications.

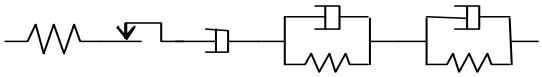

Fig. 3. **Model of a viscoelastic-plastic body (S + D + 2KV)**

The penetration of a spherical indenter under constant load into a viscoelastic body can be described [10–12]:

$$[h(t)]^{3/2} = 3/(4\sqrt{R})F\{C_0 - \Sigma C_j[1 - \rho_j \exp(-t/\tau_j)]\} \qquad (15)$$

the constants C_0, C_1, … C_j characterize the compliances corresponding to retardation (relaxation) times τ_1, … τ_j. The ramp correction factors[10] $\rho_j = (\tau_j/t_R)[\exp(t_R/\tau_j) - 1]$ are used, as the load is never applied instantaneously, but increases to the nominal value F during some time t_R.

If the deformations are fully reversible, the instantaneous compliance, C_0, is related to the reduced elastic (instantaneous) modulus as

$$C_0 = 1 / E_r \qquad (16)$$

7. Pile-up

With sharp indenters or large depths of penetration of a spherical indenter, especially into ductile materials with low ratio of hardness to elastic modulus, the plastically deformed material beneath the indenter is sometimes squeezed up around the indenter, so-called pile-up. The actual contact area is larger than for the same indenter displacement without pile-up, and the elastic modulus and hardness, calculated in the standard way from the F–h data, are wrong. The pile-up can be avoided by using spherical indenters and shallow depths. A comparison of the geometry in both cases follows.

For pointed indenters, the angle β between the undeformed specimen surface and the indenter is 19.7° (= const). For a spherical indenter, the corresponding angle (Fig. 1) grows with the contact depth as

$$\beta = \arccos[1 - (h_c/R)] \qquad (17)$$

The same angle β as for Berkovich indenter is attained with spherical indenter for $h_c = 0.0585\ R$. For example, for a sphere of radius 100 μm, h_c = 5.85 μm. If the contact depth would be only 200 nm, the corresponding contact angle β = 3.62°, and 2.56° for h_c = 100 nm. For such small angles there is no danger of pile-up. The modern devices can measure much smaller depths.

8. Indenter calibration

The accuracy of the determination of material properties by a spherical indenter depends on the accurate knowledge of its radius. Especially for small radii and small depths of penetration the indenter shape often deviates from spherical one, and the radius is not constant (Figs. 4a,b). The differences can amount several tens of percent, see ref.[2] and this section. Therefore, indenter calibration is strongly recommended.

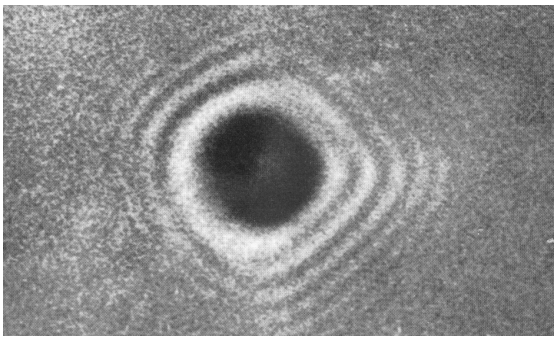

a.

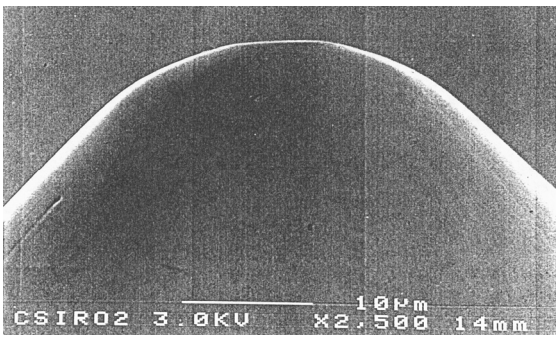

b.

Fig. 4. **a) Interferogram of the tip of a spherical diamond indenter of 50 μm nominal radius.** (After Field & Swain[2]); **b) SEM of the tip of a spherical indenter with 20 μm nominal radius.** (Photo E. Weppelmann[13])

Often, the effective radius R_{eff} is used instead of nominal value. R_{eff} can be obtained for particular F and h values for a specimen with known elastic modulus, using the rearranged Equation (*1*):

$$R_{eff}(h) = (9/16)F^2 E_r^{-2} h^{-3} \qquad (18)$$

This R_{eff} represents the average radius for the total indenter penetration h. If the indenter shape is not exactly spherical, various R_{eff} values would be obtained for various depths of penetration. In this way it is possible to construct the calibration curve $R_{eff}(h)$.

Figure 5 shows calibration curve for a spherical indenter of nominal radius 200 μm. The curve (*18*) was obtained[14]

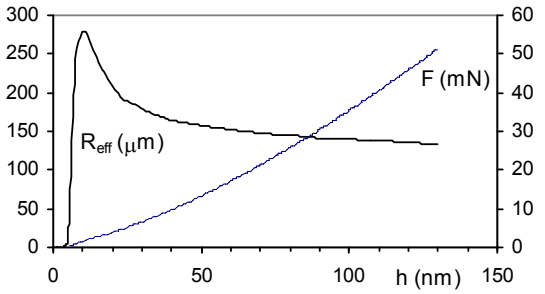

Fig. 5. **Effective radius R_{eff} as a function of penetration depth h. Nominal radius R = 200 μm. Thin curve: $F(h)$.** (After Ref. 14)

from indenter penetration into fused silica, whose reduced modulus was assumed E_r = 70 GPa. The maximum load was F = 50 mN and the corresponding depth h = 130 nm. One can see that the effective radius for this depth (R_{eff} = 134 μm) differs significantly from the nominal value 200 μm. It is also obvious from the graph that this indenter cannot be used for the evaluation of data for depths of penetration less than 10 nm, and that the results for depths up to 20 nm are perhaps not very reliable.

It is also possible to construct the calibration curve for contact area, $A(h)$, for example by inserting $R(h)$ values into Eq. (*2*). Another way uses contact stiffnesses, determined for various depths. Rearrangement of Eq. (*6*) gives for spherical indenters with $\beta = 1$:

$$A(h) = \pi [S(h)]^2/(4E_r^2) \qquad (19)$$

In this case, dynamic contact stiffness may be used as well, determined via a small harmonic signal super-imposed on the basic load (CSM mode). In this way, the calibration curve can be obtained in one test.

The calibration is done mostly on fused silica. For very small depths of penetration, also a danger exists that the elastic modulus in a very thin surface layer (up to several tens of nm), with the properties influenced by polishing, can differ a little from the bulk value. This can be avoided by indenting fresh fracture surfaces, obtained by breaking the source specimen so slowly, that the fracture surfaces are mirror-smooth (a DCDC specimen may be suitable for this purpose[15]). Generally, accurate indenter calibration is crucial for reliable determination of material parameters by spherical indenters from small depths of penetration.

This work was supported by the Grant Agency of Czech Republic, projects GA ČR 103/08/1340 and 103/08/1197.The measurements by Dr. J. Nohava on Si are appreciated.

REFERENCES

1. Johnson K. L.: *Contact mechanics*, Cambridge University Press, Cambridge 1985.
2. Field J., Swain M. V.: J. Mater. Res. *8*, 297 (1993).
3. Kašiarová M., Tatarko P., Hvizdoš P., Dusza J.: *Int. conf. LMV 2010, Smolenice 10.-12.11.2010*, Chem. Listy *105*, s816 (2011).
4. Oliver W. C., Pharr G. M.: J. Mater. Res. *7*, 1564 (1992).
5. Mesarovic S. Dj., Fleck N. A.: Proc. R. Soc. Lond., *A 455*, 2707 (1999).
6. Chudoba T., Schwarzer N., Richter F., Beck U.: Thin Solid Films *377–378*, 366 (2000).
7. Menčík J.: *23rd Danubia Adria Symposium on Exper. Methods in Solid Mechanics, Podbanské, 26 – 29 Sept 2006*, p. 31. Univ. of Žilina, Žilina 2006.
8. Menčík J., Swain M. V.: Materials Forum *18*, 277 (1994).
9. Gao X. L.: J. Mater. Res. *21*, 1317 (2006).
10. Oyen M. L.: Philosophical Magazine *86*, *33-35*, 5625 (2006).
11. Menčík J., He L. H., Swain M. V.: J. Mech. Behav. Biomed. Materials *2*, 318 (2009).
12. Menčík J.: Chem. Listy *104*, s275 (2010).
13. Weppelmann E.: *Observation and analysis of the deformation and fracture… Dissertation*. CSIRO, DAP, Sydney, and University of Karlsruhe (1992).
14. Menčík J., Nohava J.: *Int. conf. LMV 2010, Smolenice 10.-12.11.2010*, Chem. Listy *105*, s834 (2011).
15. Wiederhorn S. M.: personal communication (2010).

J. Menčík *(University of Pardubice, Czech Republic):*
Opportunities and Problems in Nanoindentation with Spherical Indenters

The paper discusses advantages of indentation with spherical indenters: *1*) measurement under low stresses allowing the determination of elastic and viscoelastic material parameters without influence of irreversible processes, *2*) possibility to construct stress-strain diagrams, *3*) negligible pile-up for small depths of penetration. Very important for accuracy of data eva-luation is the knowledge of actual indenter radius. Two methods for indenter calibration were explained.

ELASTIC PROPERTIES OF THIN WC/C COATINGS

FRANTIŠEK LOFAJ[a]*, HARTMUT STADLER[b], GABIKA FUCHSOVÁ[c], PAVOL HVIZDOŠ[a], and ANNAMÁRIA DUSZOVÁ[a]

[a] *Institute of Materials Research of SAS, Watsonova 47, 040 01 Košice, Slovakia,* [b] *Bruker Nano Surfaces Business, Dynamostr. 19, D-68165 Mannheim, Germany,* [c] *Faculty of Manufacturing Technologies of Technical University of Košice in Prešov, Bayerova 1, 080 01 Prešov, Slovakia*
flofaj@imr.saske.sk

Keywords: WC/C, thin coating, nanocystalline structure, elastic modulus mapping, AFM

1. Introduction

Metal- and metal carbide-doped carbon coatings (Me/MeC-C) exhibit interesting mechanical properties because they retain most of the benefits provided by undoped diamond -like-carbon (DLC) while having lower residual stresses and possibility for tailoring their properties[1]. Hardness of these coatings can be increased by applying the concept of „superhardness“. The concept was proposed by Veprek in 1995 (ref.[2]) for nanocrystalline TiN-amorphous Si_3N_4 system, later extended to hydrogenated and non-hydrogenated carbon films doped with nanocrystalline particles of MeC (Me = Ti, Ta, Hf, Nb, W, Cr). This class of coatings exhibits favourable combination of low coefficient of friction (COF), high wear resistance and fracture toughness[3−5]. Hydrogenated WC/a-C:H coatings are commonly prepared by reactive magnetron sputtering of W or WC in Ar-hydrocarbon plasma. They exhibit relatively high elasticity, hardness, wear resistance, good chemical stability, and low COF. Their density, hardness and Young's modulus are inversely proportional to the flow rate and carbon content[5]. The studies on non-hydrogenated nanocomposite WC/a-C coatings are considerably less frequent. Some aspects of their mechanical properties were studied by Yang[3], Liu[4], Zeng, and others[6,7]. Elastic modulus of PE CVD coatings is usually in the range from 120 GPa up to 400 GPa (ref.[8]). Hardness varies from 5 GPa up to superhardness range with typical values of around 15−20 GPa.

Elastic modulus and hardness in thin metallic and non-metallic coatings are often measured using instrumented indentation technique under low loads. The requirements and conditions necessary for their correct measurement without substrate influence are defined in ISO 14577 − Part 4 (ref.[9]). They can be summarized as follows:

- the total penetration depth, h, is less than half of the coating thickness;
- no cracking can occur;
- hardness of the coating is evaluated as a maximum or the plateau that appears in the hardness − penetration depth curve;
- surface roughness, R_a < 5 % h_c (h_c is the penetration depth);
- h_c must be smaller than 10−15 % of the film thickness to prevent substrate influence.

Indentation loads have to be reduced to μN or even nN range depending on the thickness and stiffness of the studied coatings to satisfy the above requirements. Indentation methods were also upgraded from single loading-unloading cycle to so called continuous multi-cycle (CMC) with a predefined number of partial unloadings during loading to the maximum load. Even more sophisticated is the method of sinus loading with relatively high frequency of partial unloading. Both CMC and sinus methods provide full hardness/indentation modulus − penetration depth curve required by ISO standard. However, the reliability of all indentation methods is influenced by the effects of indentation size[10,11], residual stresses[12], and especially by surface roughness[13,14]. The condition set for surface roughness is often not satisfied in the real cases. The consequence of higher roughness is an excessive data scatter. The solution would be the measurement of mechanical properties at considerably smaller x-y scale. Such possibility is offered by recent development of atomic force microscopy (AFM) techniques oriented toward measurement of nanomechanical properties.

AFM mapping of the elastic properties at nanoscale level is possible using „Force Modulation Microscopy“ (FMM) and/or „Peak Force Tapping“ (PFT). FMM uses contact mode imaging superimposed with a sinusoidal cantilever or sample oscillation small enough to keep the tip in contact with the sample, and allows qualitative mechanical property assessment (amplitude and phase shift of the cantilever movement compared to the driving oscillation). PFT uses direct fast force distance curve acquisition by a large sinusoidal z-piezo modulation, periodically contacting and separating tip and sample. The z-movement is synchronized with lateral sample scanning to ensure a controlled maximum impact force down to pN-level, which is used as imaging setpoint. Additional treatment of the realtime force − distance curves obtained during each cycle included in so called „Peak Force Quantitative NanoMechanical“ (PF QNM) mode delivers simultaneously to the topographic height a signal proportional to the elastic modulus and enables (when properly calibrated) even quantitative measurement of elastic properties at a nanoscale level[15]. However, PF QNM has been so far successfully applied only to materials with the stiffness below 70 GPa, e.g. biological tissues and polymers[15].

Therefore, the aims of this work include the investigation of the effect of surface roughness on elastic modulus of the studied nc-WC/a-C coatings from instrumented indentation and mapping of the elastic modulus using PF QNM for comparison.

2. Experimental procedure

The studied nc-WC/a-C coatings were deposited on a set of 7 substrates with the diameter of 55 mm and thickness of

~ 3 mm made from tempered and annealed tool steel (STN 412050). The substrate surfaces were ground flat with a diamond wheel. Five of the substrates were then polished using 15 µm, 6 µm, 3 µm, 1 µm and 0.25 µm diamond slurries. One sample was subsequently ground on #80 SiC paper, two another on 80/63 diamond disc, and polishing cloth with 15 µm diamond slurry, respectively. The remaining 2 substrates remined as-polished.

PECVD WC/C coating with the thickness of around 500 nm has been deposited on all substrates simultaneously. The deposition conditions were as follows: total pressure 3 Pa, current density 1 mA cm^{-2} and bias voltage −5 kV (ref.[16,17]).

"Macro-roughness", R_a, was measured on substrates and coatings as well using contact profilometer (model SJ 201, Mitotuyo) along ten lines 10 mm long and 1 mm apart. The value of R_a was determined as an average of ten measurements. "Micro-roughness" was measured on AFM (model Dimension Icon, Veeco). Two areas with the size of 50 µm × 50 µm were imaged in a tapping mode for each sample. R_a was determined as an average value from ten 10 µm × 10 µm areas arbitrarily distributed on both images.

Indentation modulus, E_{IT}, and indentation hardness, H_{IT}, were investigated using nanoindenter (model NHT, CSM, Switzerland) in sinusoidal loading up to 10 mN. At least 20 indents were made in automatic mode on each sample and corresponding depth profiles were generated. The values of E_{IT} and H_{IT} were determined as an average from the maximum or stable part of a depth profile in each sample. Additional indentation tests were performed on the model polycrystalline material, WC target (97 %, Porexi, Ltd., Ostrava) in sinus mode and on the individual WC grains of the bulk WC-Co (Pramet Šumperk) using single loading – unloading cycle[19].

PF QNM mode on AFM (Dimension Icon, Bruker Co., USA) was used for mapping of the elastic modulus using special AFM probes with the spring constant of around 2000 N m^{-1} and diamond tip. Peak forces were held constant in the low µN-range during acquisition of simultaneous topographical and mechanical data. The values of elastic modulus obtained from the measurements on model materials can be used for the calibration of the images obtained under similar conditions from PF QNM on coatings with nanosized WC crystallites.

3. Results and discussion

The values of macro-roughness of the substrates from contact profilometry and surface area around 100 mm^2 were in the range 24–580 nm whereas micro-roughness from AFM measurements from the area of 2500 mm^2 was 3–304 nm depending on the surface treatment. Analogous values in the coating were 10–660 nm and 16–180 nm, respectively. Although the correlation between R_a of the substrates and coatings is discussed elsewhere[19], the intrinsic roughness of the coatings on the well polished substrates was in the range 10–20 nm. When R_a of the substrates exceeded these values, coatings roughness was determined by the substrate roughness. Obviously, ISO standard requirement that $R_a < 3$ nm can be satisfied in case of 500 nm thin films only with additional lapping.

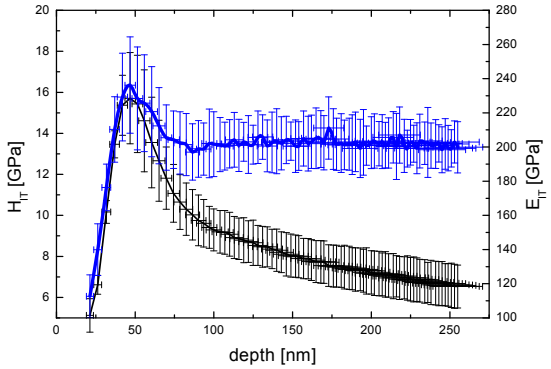

Fig. 1. **Depth profiles of E_{IT} and H_{IT} on WC/C coating**

Fig. 1 summarizes depth profiles of the indentation modulus and hardness in the studied WC/C coatings. Both parameters studied exhibit peak at approximately the same depth of around 50 nm and then their values decrease as the influence of the substrates gets stronger with the penetration depth. The position of the peaks corresponds to 10 % of the coating thickness. Thus, the condition for the determination of the coating properties from indentation tests is in accordance with the ISO requirement. The indentation modulus of the coating at the peak position is approximately 235 ± 29 GPa and its hardness is around 15.8 ± 2.5 GPa.

Fig. 2 shows the variations of E_{IT} of WC/C coating as a function of R_a determined from microscopic area by AFM. The average value of around 220 GPa does not depend on surface roughness in the studied R_a range and only the scatter increases several times when the intrinsic roughness of the coating is exceeded due to substrate roughness. Hardness exhibited the same behavior[18].

The properties measured on WC/C coatings need to be compared with the values obtained on pure WC, which may act as a calibration standard. Fig. 3 shows depth profiles obtained from the bulk polycrystalline WC. Indentation load was up to 400 mN to see the possible indentation size (ISE) effect. Hardness is constant from the depth of around 200 nm and its value is 25.2 ± 2.9 GPa while indentation modulus reaches maximum of ~520 GPa at this depth and than gradually decreases. The average value of E_{IT} is 410 ± 37 GPa. The values correspond to the properties averaged over large number of WC grains in relatively large volume below deep indent formed under relatively high load.

Opposite case would be an instrumented nanoindentation of one WC grain with predefined orientation in e.g. WC-Co sintered carbide. Our detail nanoindentation study on WC-Co[19] confirmed the existence of bimodal distribution of the measured properties. The peak at lower values (H_{IT} ~ 10 GPa) was attributed to Co and that at 29 GPa to an average from larger number of WC grains while neglecting their orientation[19]. The obtained values were different from the averaged bulk values but they are within wide range reported recently for WC grains by Bonache et al.[20]. Variations in the measured properties may be attributed not only to ISE but also to pronounced anisotrophy of the elastic properties of WC grains (H_{IT} > 40 GPa for {1010} and H_{IT} = 25–30 GPa for {0001} orientation) whereas the properties of Co binder (E_{IT} = 210–

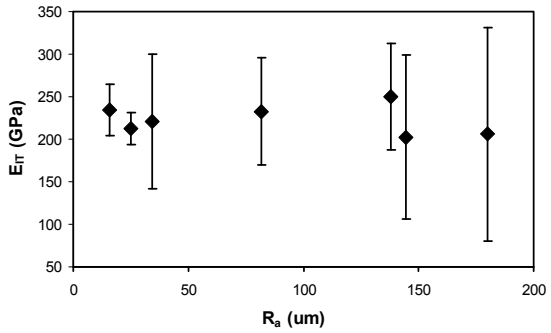

Fig. 2. **The dependencies of the indentation modulus, E_{IT} on coating roughness determined from microscopic area using AFM**

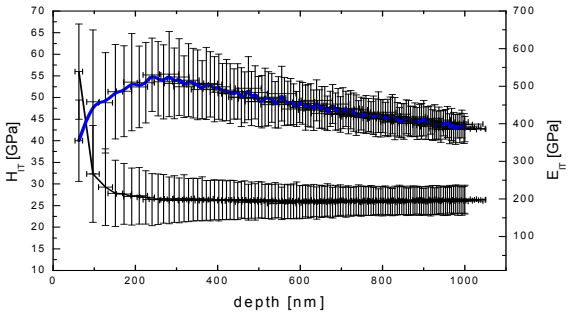

Fig. 3. Depth profiles of the indentation modulus E_{IT} and indentation hardness H_{IT} on bulk WC

290 GPa and H_{IT} = 9–16 GPa) were almost uniform[20].

PF QNM was therefore applied to WC-Co to visualize elastic properties of the individual WC grains and to account for their orientation. The microstructure and the individual grains of WC in WC-Co can be easily revealed using AFM "height" images because of differential polishing of harder WC and softer Co phases. Fig. 4 shows a map of the elastic moduli obtained by PF QNM. The difference between elasticity of WC and Co phase is obvious from the black and white contrast, but contrast varies as well among various WC grains due to Young's modulus anisotrophy. Fine calibration of the absolute values based on the known indentation moduli averaged over individual WC grains with defined orientation is therefore rather difficult. Additional measurements of the elastic moduli of the same WC grains by means of instrumented indentation and subsequently by PF QNM will be performed in the future to solve the problem.

Analogous image in Fig. 5 illustrates relative elastic moduli distribution in the studied nanocomposite WC/C coating deposited on the fine polished substrate. Strong contrast suggests the existence of at least two phases with different elastic moduli: dark (=softer) "grains" with the size up to 50–70 nm separated by a thin continuous net of brighter (=stiffer) phase. This net was independent of surface topography and similar to the (resonance) phase (shift) images obtained in tapping mode earlier[16]. The obtained modulus contrast was

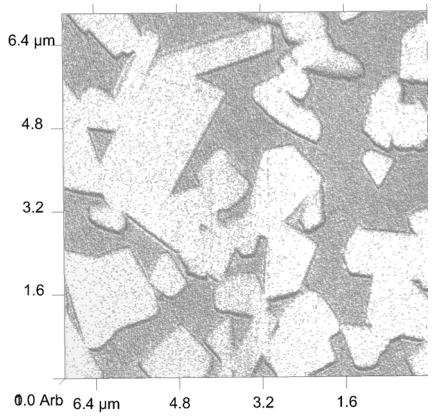

Fig. 4. **Relative elastic moduli distribution in the bulk polycrystalline WC-Co obtained using PF QNM mode**

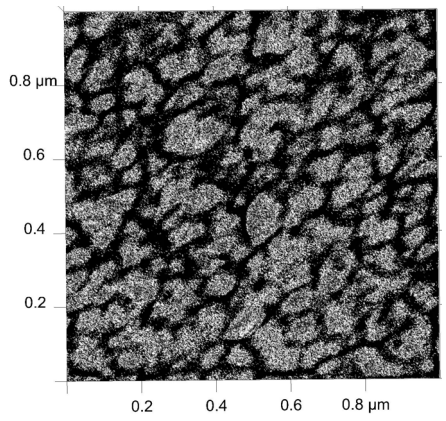

Fig. 5. **PF QNM image of the relative elastic moduli (1 µm × 1 µm) in a thin nanocomposite WC/C coating**

only visible at relatively low imaging forces and vanished at higher load, which indicates real nanoscale dimensions of the components and makes a direct correlation of AFM-based modulus values with data from instrumented indentation difficult. The existence of WC nanocrystals and their agglomerates within the same size range agrees with our earlier transmission electron microscopy observations[16]. The net in Fig. 5 seems to correspond to amorphous carbon phase. However, the determination of the absolute values of elastic moduli is limited by the absence of calibration.

4. Conclusions

Surface roughness substantially increases the scatter of the elastic modulus by instrumented indentation without affecting its average value. Growth kinetics of the studied nanocomposite WC/a-C coatings without the influence of substrate results in surface roughness $R_a \leq 20$ nm. Additional lapping of the coatings seems to be necessary to satisfy ISO standard

requirement on surface roughness in case of nanohardness measurement. An average indentation modulus of around 220 GPa was found on the studied WC/C coatings whereas that of the bulk polycrystalline WC is E_{IT} = 410 ± 37 GPa (hardness is H_{IT} = 25.2 ± 2.9 GPa). PF QNM mode in AFM is capable of elastic modulus mapping of hard materials including WC-Co and WC/C coatings, with the elastic moduli in the range up to 400 GPa. However, additional calibration on WC grains with known orientation is necessary for quantitative measurements of elastic moduli.

The contribution of M. Ferdinandy with coating preparation is gratefully acknowledged. This work was supported by the following projects: APVV 0520-10, VEGA 2/0108/11 and MNT-ERA.NET HANCOC.

REFERENCES

1. Robertson J.: Mater. Sci Eng. R. *37*, 129 (2002).
2. Vepřek S., Reiprich S.: Thin Solid Films *268*, 64 (1995).
3. Yang S., Camino D., Jones A. H. S., Teer D. G.: Surf. Coat. Technol. *124*, 110 (2000).
4. Liu Y., Gubisch M., Spiess L., Schaefer J. A.: J. Nanosci Nanotechnol. *9*, 3499 (2009).
5. Strondl C., Carvalho N. M., De Hosson J. Th. M., van der Kolk G. J.: Surf. Coat. Technol. *162*, 288 (2003).
6. Zeng X. T., Zhang S., Ding X. Z., Teer D. G.: Thin Solid Films *420*, 366 (2002).
7. Konca E., Cheng Y. T., Weiner A. M., Dasch J. M., Alpas A.: Surf. Coat. Technol. *200*, 3996 (2006).
8. Lofaj F., Němeček J., Bláhová O.: Chem. Listy *109*, s271 (2010).
9. ISO 14577-4:2007 Metallic materials - Instrumented indentation test for hardness and material parameters - Part 4 Test method for metallic and non-metallic coatings.
10. Nix W. D.: Mater. Sci. Eng., A *234-6*, 37 (1997).
11. Huang Y., Zhang F., Hwang K. C., Nix W. D., Pharr G. M., Feng G.: J. Mech. Phys. Solids *54*, 1668 (2006).
12. Ling Z, Hou J. P.: Composite Sci. Technol. *67*, 3121 (2007).
13. Jiang W. G., Su J. J., Feng X.-Q.: Eng. Fracture Mech. *75*, 4965 (2008).
14. Bouzakis K. D., Michailidis N., Hadjiyiannis S., Skordaris G., Erkens G.: Mater. Characterization *49*, 149 (2003).
15. http://www.bruker-axs.de/uploads/tx_linkselectorfor pdfpool/PeakForce_Quantitative_Nanomechanical_ Property_Mapping_brochure.pdf
16. Lofaj F., Hviščová P., Duszová A.: Acta Met. Slovaca *16*, 631 (2010).
17. Kottfer D., Olejník F., Pešek L., Mrva P. : Acta Met. Slovaca *10*, 625 (2004).
18. Fuchsová G., Lofaj F., Simkulet V.: Chem. Listy *105*, s796 (2011).
19. Duszová A.: written part of PhD work, 2010.
20. Bonache V., Rayón E., Salvadoe M. D., Busquets D.: Mater. Sci. Eng., A *527*, 2935 (2010).

F. Lofaj[a], H. Stadler[b], G. Fuchsová[c], P. Hvizdoš[a], and A. Duszová[a] *([a] Institute of Materials Research of SAS, Košice, Slovakia; [b] Bruker Nano Surfaces Business, Mannheim, Germany, [c] Faculty of Manufacturing Technologies of Technical University of Košice in Prešov, Slovakia):* **Elastic Properties of Thin WC/C Coatings**

Instrumented indentation and AFM studies of WC/C coatings revealed that surface roughness substantially increases the scatter of the measurements of elastic modulus without affecting its average values. An average indentation modulus of around 220 GPa was found on the studied WC/C coatings whereas that of the bulk polycrystalline WC was E_{IT} = 410 ± 37 GPa (and its hardness was H_{IT} = 25.2 ± 2.9 GPa). PF QNM mode in AFM is capable of qualitative elastic modulus mapping of hard materials including WC-Co and WC/C coatings. However, the calibration on the individual WC grains is necessary for quantitative PF QNM measurements.

MEASUREMENT AND ANALYSIS OF THE HARDNESS OF ALUMINIUM SURFACE LAYERS BY THE NANOINDENTATION AND SCRATCH TESTS

MICHAL ZELEŇÁK[a]*, JAN VALÍČEK[a], JAN BRUMEK[b], PETR HLAVÁČEK[a], BARBORA HALUZÍKOVÁ[a], MICHAL VYLEŽÍK[b], PETRA BÁBKOVÁ[b], MARTA HARNIČÁROVÁ[c], VERONIKA SZARKOVA[d], MILENA KUŠNEROVÁ[a], and VLASTIMIL KUBĚNA[a]

[a] Institute of Physics, Faculty of Mining and Geology, [b] SMID – CPIT, [d] Institute of Economics and control systems, VŠB – Technical University of Ostrava, 17. listopadu, 708 33Ostrava – Poruba, Czech Republic, [c]Faculty of Manufacturing Technologies of Technical University of Košice with a seat in Prešov, Bayerova 1, 080 01Prešov, Slovak Republic
michal.zelenak@vsb.cz

Keywords: nanoindetation, scratch tests, aluminium, mechanical properties, hardness

1. Introduction

Along with the arrival of new modern measurement methods (nanoindentation methods) there is a growing demand for research in mechanical and tribological properties of surface layers of materials. This trend is given by growing requirements for quality of surface layers in various applications of surface engineering (contact loading, protective surface coating, etc.). In this respect nanoindentation tests represent a new tool for researching of surface layers.

Fundamentals of nanoindentation

Nanoindentation and nanoscratch methods are based on immediate recording of load during penetration of an indentation stylus into a material surface in either indentation or scratch mode. From a known geometry of an indenter imprint into the material surface it is possible to determine its mechanical (modulus of elasticity, hardness) as well as tribological (friction coefficient) properties[1,2]. According to the Oliver and Pharr methodology the material hardness can be calculated according to the formula

$$H_{INT} = \frac{P_{\max}}{A(h_c)} = \frac{P_{\max}}{24{,}5 \cdot h_c^2 + \sum_{i=1}^{n} C_n \cdot h_c^{1/2(n-1)}} \qquad (1)$$

where P_{max} is the maximum load, A is the contact indentation area, the constant 24.5 represents the geometry of an indenter, the constant C_n represents a calibration curve for contact indentation area and h_c is a contact indentation depth that is determined according to the formula

$$h_c = h_{\max} - 0{,}75 \times \frac{P_{\max}}{S} \qquad (2)$$

where h_{max} is the maximum indentation depth, 0.75 is a constant depending on the geometry of an indenter, S is the contact stiffness (dP/dH) .

Hardness can also be determined by a scratch test. According to the authors[3] who defined the hardness for transverse circular cross-sections (spheres, cones, parabolas) as

$$H_R = \frac{8 \cdot F_N}{\pi \cdot b^2} \qquad (3)$$

where F_N is a normal component of an acting force, b is a width of the scratch channel groove, a is a radius of an indenter tip, h is a contact indentation depth into the material surface (Fig. 1).

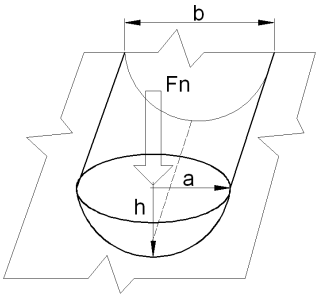

Fig. 1. **Shape of scratch channel groove**

During the scratch testing an indentation stylus penetrates into a material surface and then it is shifted by a translation movement just along one axis (Fig. 2). Due to the fact that the sample surface is not an ideal plane, the hardness can be determined from an immediate component of a normal load related to the respective width of the groove left behind an indenter.

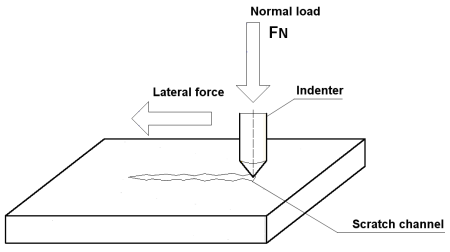

Fig. 2. **Detail of the scratch test**

2. Current state of problem

A contemporary methodology for evaluation of the hardness of the material surface layer through scratch testing is

based upon recording of a normal component of an acting force and an indentation area of the indentation stylus whereas both these parameters are usually not constant. As mentioned above, the hardness for transverse circular cross-sections indenters is determined according to the formula (*3*).

The subject of our research was a determination of hardness through scratch testing with application of the Berkovich tip and identification of mutual relation to determination of hardness through an indentation method. When determining hardness, we go out from the known geometry of the indentation stylus that is defined by the relation (*4*)

$$A = 3\sqrt{3}h^2 \tan^2 65.3^\circ = 24.56h^2 \qquad (4)$$

and alignment of the indentation tip towards direction of scratch channel creation (Fig. 3 a, b).

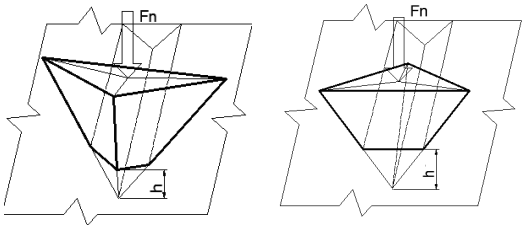

a b

Fig. 3. **a) ideal alignment of the indentation tip b) real alignment of the indentation tip**

Under this assumption a contact area within scratch creation can be modified from relation (*4*) to relation (*5*) where 2/3 of the indenter area is in contact. It is not possible to determine explicitly the proportion of the contact area through an actual alignment of the tip (Fig. 3b). In calculations also the limit situations were considered where only 1/3 of the indenter area would be in contact (*6*).

$$A_{C\mathrm{I}} = 2\sqrt{3}h^2 \tan^2 65.3^\circ \qquad (5)$$

$$A_{C\mathrm{II}} = \sqrt{3}h^2 \tan^2 65.3^\circ \qquad (6)$$

Determination of hardness is made according to the relation (*7*),(*8*),

$$H_S = \frac{F_N}{A_{C\mathrm{I}}} \qquad (7)$$

$$H_S = \frac{F_N}{A_{C\mathrm{II}}} \qquad (8)$$

where F_N is a normal component of an acting force and in the related experiment F_N = const. The contact areas A_{CI}, A_{CII} are functions of the depth h.

3. Experiments

Initial material

An initial material for the realization of experiments was aluminium of EN AW 6060. This structural material is commonly used within various fields of industry, is characterized by medium strength, it is a lightweight material with good corrosion resistance. Aluminium is often being used for decorative purposes. Its disadvantages are poor tribological properties and a low melting point associated with stress strength at higher temperatures and wear. The chemical composition is given in Tab. I.

Table I
Chemical composition of material

	Si	Fe	Cu	Mn	Mg	Cr	Zn	C
[%]	0.3–0.6	0.1–0.3	0.1	0.1	0.35	0.05	0.15	0.15

Preparation of the samples

An aluminium sample with a square cross-section of 10 mm × 10 mm and a height of 5 mm was made through the means of unconventional abrasive waterjet cold cutting technology without thermal influence on the basic material. Consequently, the sample was grinded and polished by using a device Struers Tegra Pol 35. For grinding were used the sandpapers with the grit size of 320, 800, 1000, 1200. A pressure force was of 10 N with a speed of rotation of 200 min^{-1}. A polishing diamond suspense with a grit size of 3 μm and 1 μm was used to polish the sample.

Experimental details on testing

Nanoindentation testing was performed on the Hysitron Triboindentor TI 950 device. The indentation tests were realized with the Berkovich tip. The indentation testing was made with a constant force of 2000 μN, velocity of indenter penetration into the material surface was 400 μN min^{-1}. A total of 60 indents were performed on the sample, 6 indents in a dis-

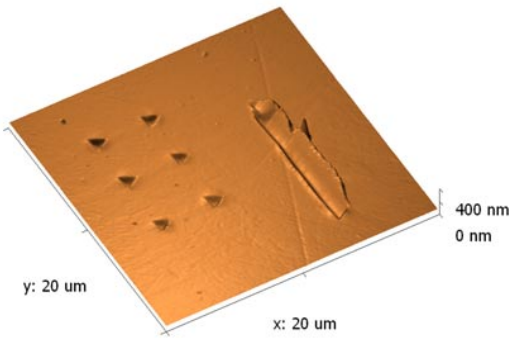

Fig. 4. **Area detail of conducted indentation tests**

tance of 4 μm from each other in 10 areas of testing separated by 100 μm. The Berkovich tip was chosen also for the scratch testing. The scratch testing was made with a constant normal force of 2000 μN, by a translation movement, velocity of indenter penetration into the material surface was 400 μN min^{-1}, evaluated length of the scratch testing was 10 μm, velocity of the indenter shifting through the surface was 0.33 μm s^{-1}, and a total number of scratches was 10. Fig. 4 shows a detail from one area where the indentation tests were performed on the sample.

4. Results

The calculations of the hardness H_{INT} were made according to the relation (*1*) on the basis of the performed indentation tests, measured data and results of calibration. The calculations were made for the selected 36 indents that were not significantly influenced by a quality of surface on the prepared sample. The resulting indentation curves are shown in Fig. 5. The indentation curves demonstrate a range of contact depths *h* running from 115 nm to 140 nm and determine a size of the contact indentation area.

Afterwards 10 scratch tests were performed. Using above mentioned relations (4–7) the hardness H_S was determined from the scratch testing. The results of analysis and captured images confirm that an alignment of the indenter was almost ideal (Fig. 3a). A significant feature for determination of hardness was a record of the normal distance of

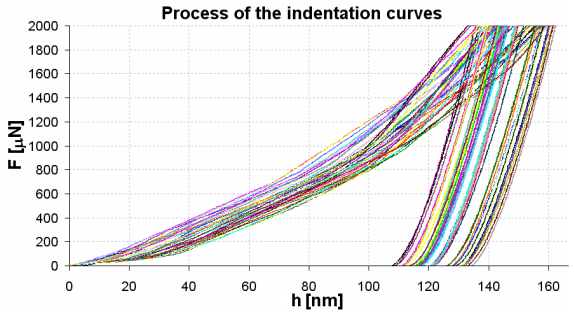

Fig. 5. **Courses of indentation curves**

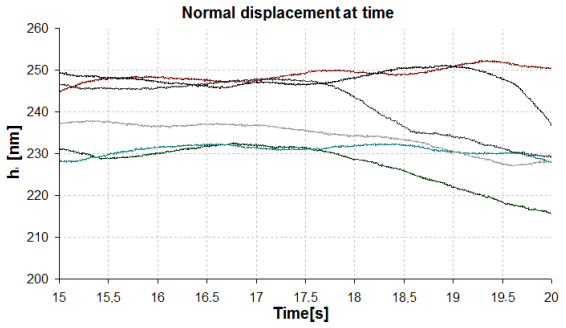

Fig. 6. **Courses of normal displacement during scratch testing**

Table II
Indentation hardness H_{INT} of the surface layer of aluminium compared with the hardness H_S

Nanohardnees H_{INT}	SD	Scratch hardness H_S	SD
2.28	0.09	2.36	0.10
2.45	0.08	2.02	0.39
2.28	0.13	2.29	0.07
2.72	0.34	2.09	0.29
2.55	0.08	1.97	0.37
2.75	0.24	2.22	0.15

indenter depth penetration into the material surface whose amount during creation of the scratch varies depending on a change of surface topography of the sample. In Fig. 6 there is a record of normal depth *h* for 6 selected scratches whose final curves were not significantly influenced by the surface topography.

The results obtained from both tests are summarized in Table II where the values of the hardness H_S are presented only for an ideal geometry of the contact surface.

Based on the analysis results from the indentation and scratch tests H_{INT}, H_s a scatter plot of hardness was determined (Fig. 7).

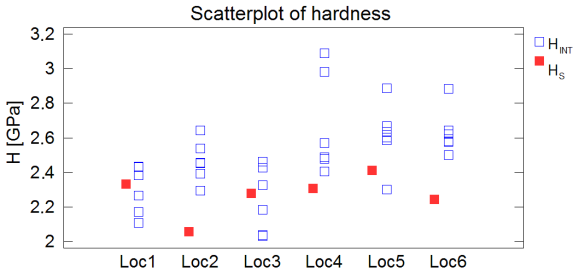

Fig. 7. **Scatterplot of hardness between H_s, H_{INT}**

As can be seen in Fig. 7, it was reached a good correlation between the results for H_{INT} and H_S in the areas of measurement 1, 3, 4 and 5. The accuracy of measurement is in this case very influenced by the quality of surface layer and the range of wear of the indentation tip.

5. Conclusions

This paper presents the results acquired during the evaluation of hardness of surface layers of the EN6060 aluminium alloy through the indentation and scratch tests. During this experiment the Berkovich indenter tip was used for scratch testing. First we designed the geometry of the contact area. The size of contact area was simulated from records of the variable depth. The normal force was constant during the whole testing. A close relationship between indentation H_{INT} and scratch hardness H_s has been determined on the basis of the performed analysis and results presented in Table II (Fig. 7).

Identification of methodology for determination of hardness from indentation and scratch techniques may significantly contribute to evaluation of a specific resistance imposed by a surface layer during exterior loading on other objects. A subject of our future research will be an application of this methodology also for the abrasive waterjet technology.

The work has been supported by projects SGS No. SP/201058, GA ČR No. 101/09/0650, MŠMT No. MSM6198910016, RMTVC No. CZ.1.05/2.1.00/01.0040. Thanks also to the Moravian − Silesian Region for financial support and CEEPUS program CII-PL-0007-05-0910 at the Kielce University of Technology in Poland.

REFERENCES

1. Beegan D., Chowdhury S., Laugier M. T.: Surf. Coat. Technol. *201*, 5804 (2007).
2. Oliver W. C., Pharr G. M.: J. Mater. Res. *7*, 1564 (1992).
3. Ahn K. L. Mittal, R. H. MacQueen: *Adhesion Measurement of Thin Films*, Thick Films and Bulk Coatings. In: K.L. Mittal, Editor, ASTM. Spec. Tech. Publ. 640 (1978), p. 134-137.

M. Zeleňák[a], J. Valíček[a], J. Brumek[b], P. Hlaváček[a], B. Haluzíková[a], M. Vyležík[b], P. Bábková[b], M. Harničárová[c], V. Szarková[d], M. Kušnerová, and V. Kuběna[a] (*[a] Institute of Physics, Faculty of Mining and Geology, [b] SMID – CPIT, [d] Institute of Economics and control systems, VŠB – Technical University of Ostrava, Czech Republic, [c] Faculty of Manufacturing Technologies of Technical University of Košice with a seat in Prešov, Prešov, Slovak Republic):*

Measurement and Analysis of The Hardness of Aluminium Surface Layers by The Nanoindentation and Scratch Tests

The paper deals with an evaluation of mechanical properties of surface layers of aluminium alloy. A *Hysitron TI 950* TriboIndenter was used for a nanomechanical study of surface properties. A purpose was to determine the surface hardness of alloy with a low friction coefficient on the basis of the indentation and scratch tests. A scatter plot of results for the given methods was demostrated on the basis of these measurements. Knowing the hardness (resistivity) of the surface layer can help to a better identification of processes causing wear of surface layers, or to identify the individual components of critical forces of abrasive particles, which cause wear during the abrasive waterjet cutting process.

ADHESION PROPERTIES OF DLC AND TiO_2 THIN FILMS USING SCRATCH TEST METHODS

JAN MIKŠOVSKÝ*, PATRIK KUTÍLEK, JAROSLAV LUKEŠ, ZDENĚK TOLDE, JAN REMSA, TOMÁŠ KOCOUREK, FRANTIŠEK UHEREK, and MIROSLAV JELÍNEK

Czech Technical University in Prague, Faculty of Biomedical Engineering, nam. Sitna 3105, 272 01 Kladno, Czech Republic
jan.miksovsky@fbmi.cvut.cz

Keywords: Diamond-like-carbon (DLC), titanium dioxide (TiO_2), thin films, adhesion, scratch test, standards, standardization

1. Introduction

Diamond like carbon layers are widely used layers in many branches of the industry, including medicine where are used for various implants as biocompatible material. In each application adhesion is very important because after detachment of thin layers from basic materials it does not serve its purpose and remains of the layer could cause additional damage to surrounding tissue in live organism. Adhesion is an important parameter for every coating. There are more methods for its determination, but one of the most used methods is scratch test. Nowadays, micro and nano-scratch tests supplement the classic (macroscopic) scratch test, which is well described in literature.

The progressive load scratch test was seriously suggested for coating adhesion measurements by Perry[2,3], Steinmann and Hintermann[4], Valli[5], etc. Today, the method is widely used by the coating industry and development laboratories. Its usefulness as an adhesion and quality assessment method has been discussed[1,6–10]. The scratch test is generally accepted as a good and an efficient method for quality assessment of coated surfaces, but its use for coating-to-substrate adhesion assessment has been criticised by several authors[10,11].

The scratch test consists of pulling a diamond stylus over the surface of a sample under a normal force, which is increased either stepwise or continuously until failure is observed. The normal load at which this happens is called the critical normal load. It is generally accepted that the test is suitable for coatings of thickness ranging from 0.1 to 20 μm. The scratch test procedures are described in the European, USA and Japan or international standards, which are transposed into the Czech standards. The standards are designed for wide range of different coating materials. Most important standards for quantitative single point scratch testing are:

Czech Republic:

- DIN EN 1071-3 and ČSN EN 1071-3 (727570) – Advanced technical ceramics coatings – Determination of adhesion and other mechanical failure modes.

International:

- ISO 20502 Fine ceramics – Determination of adhesion of ceramic coatings by scratch testing
- ISO N269 (Working Draft) – Fine ceramics coatings – Determination of adhesion.

USA:

- ASTM C1624 (C1624-05) Ceramic coatings – Determination of adhesion and other mechanical failure modes.

Japan:

- JAS JIS R Thin films on glass Substrates – Determination of adhesion.

There are more standards for various materials mainly for paints, varnishes and various polymers.

The types of the failure which are often observed in the scratch test depend critically on the properties of substrate and coating. The material response to loading conditions has been divided into three independent phases by Holmberg[13]. Phase one represents the ploughing of a stylus in the substrate material. The substrate material is deformed by plastic or elastic deformation and a groove is formed. The phase two represents the bending and drawing of a freestanding coating. The bending movements cause stresses and stress release in the coating when drawn between the surfaces. In this phase, the work done for overcoming friction is considered.

The phase three represents pulling and spalling the coating from one point on the surface when its other part is fixed. The increasing pulling force results in cracks at the place of maximum tensile stress. The formation of cracks in the groove of a scratch tester has been shown by e.g. (ref.[1,10,12,14–16]). They can typically be described as angular cracks, parallel cracks, transverse semi-circular cracks, coating chipping, coating spalling and coating breakthrough.

2. Experimental part

Both types of layers DLC and TiO_2 were prepared by Pulsed Laser Deposition with excimer laser with KrF filling (λ = 248 nm and pulse τ = 20 ns).

For DLC layers we used following deposition conditions: Basic substrate was silicon wafer Si(111), pressure in

Table I
Laser energy density used for DLC layer synthesis, number of pulses and measured thicknesses

Sample	Energy density [J cm^{-2}]	Num. pulses [–]	Thicknesses [nm]
DLC-1	10	2400	70 ÷ 80
DLC-2	6	4500	60 ÷ 75
DLC-3	4	5600	60 ÷ 70
DLC-4	2,5	8000	60 ÷ 75

chamber before deposition $1 \cdot 10^{-4}$ Pa, pressure during deposition 0,25 Pa of argon atmosphere with gas flow 10 sccm, temperature 20 °C, target-substrate distance was 50 mm. High purity graphite was used as target material. Laser densities for ablation from target, number of pulses and achieved thicknesses are summarized in Tab. I.

Deposition conditions of TiO_2 layers were: Basic substrate was silicon wafer Si(111), pressure in chamber before deposition at least $1 \cdot 10^{-3}$ Pa, pressure during deposition (10 ÷ 18) Pa of oxygen atmosphere with gas flow around 10 sccm. Depositions were made utilizing radiofrequency discharge (RF) and the temperature during deposition was higher than room temperature due to RF, but less than 100 °C. The target-substrate distance was 40 mm. Pure titanium and pure rutile were used for target basic material. The deposition length was two thousand pulses. For more information see Tab. II.

Table II
Laser energy density used for TiO_2 layer synthesis, target material T-titanium, R-rutile, oxygen O_2 pressure and measured thicknesses

Sample	Energy density [J cm^{-2}]	Target material [nm]	Pressure O_2 [Pa]	Layers thicknesses [nm]
TIO_2-1	3,2	T	18	100 ÷ 120
TIO_2-2	3,2	T	10	65 ÷ 105
TIO_2-3	3,2	R	10	120 ÷ 125
TIO_2-4	3,2	R	18	130 ÷ 140

Mechanical profilometer Alpha-Step IQ (KLA co.) was used for thickness determination, each layer was measured at six places.

For determination of adhesions we used one classic macroscratch tester and two micro/nanoscratch tester. Macroscratch tester REVETEST, scratch tester (CSM co.), nanosclerometric head for scanning probe microscope Solver Next (NT-MDT co.) and Hysitron Triboindenter TI950 with nanoscratch transducer SN5-483-194. For details about testers see Tab. III.

Table III
Summary for load indenter type, load range and scratch length for measurement systems

System	Indenter type [diamond]	Load range	Scratch length
CSM Revetest	Rockwell	1÷200 N	30 mm
Hysitron TI950	Berkovich	Up to 10 mN	10 µm
NT-MTD nanosclerometry head	Berkovich	Up to 150 mN	100 µm

3. Results and discussion

Evaluations of thin films adhesion, which were prepared by PLD technique, were realized at three different devices.

The first system REVETEST (CSM co.) is the standard macroscratch tester which is compatible to CSN EN 1071-3. From this system we obtained normal force, depth of penetration, acoustic emission and friction coefficient and force. The system is equipped with optical microscope with possibility to obtain photography. We used acoustic emission to estimate delamination point and we visually confirmed it from the photography of the scratch. Additionally, we checked penetration force, where we got through the layer to the basic substrate. There was no problem with evaluation of DLC layers and we detected acoustic emission in the point of delamination resp. critical load (F_D), see Tab. IV and Fig. 1.

There were problems with acoustic emission in case of TiO_2 layers because of high counts of droplets in the layers, which was probably the cause of high acoustic emission from the start of the scratch test. Used testing conditions were following: speed 5 mm min^{-1}, loading rate 14 N min^{-1}, tip radius 200 µm for DLC layers. For TiO_2 layers tip radius was 400 µm. Two or more scratches on each sample were made and verified the obtained results.

The second device was Hysitron TI950. This system measures in micro and in nanoscale. In this case was not possible to use standards. Standards do not exist for nanolayers and the Berkovich tip. We obtained lateral force and lateral coordinates, normal force and normal coordinates as time dependency. Information about friction could be evaluated too. Imaging of scratch is provided with SPM technique with the same measuring stylus with contact force 1 µN. Every sample was measured three times with used force ranging from 0 to 3 mN and length of scratch 6 µm. Loading rate was 170 nm s^{-1}. Delamination was not observed in the scanned image. We could only see changes in lateral force from graph dependencies (example of DLC-1 and DLC-3 see in Fig. 1) in place corresponding to the penetration depth (the layers thicknesses). The layers had a good adhesion, which was conclud-

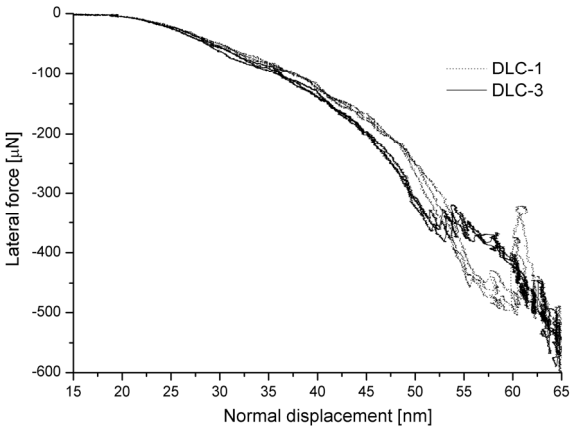

Fig. 1. **Example of dependency of lateral force on normal displacement**

Table IV
Summary of results from three used systems: F_D – delamination force, F_P – penetration force through layer to basic substrate

	CSM Revetest		Hysitron TI950		Nanosclerometric head	
Sample	F_D [N]	F_P [N]	F_D [mN]	F_P [mN]	F_D [mN]	F_P [mN]
DLC-1	6	8	NA	1.5	NA	63
DLC-2	9.5	13	NA	1.25	NA	>75
DLC-3	5	6.5	NA	1.1	NA	75
DLC-4	7.5	9.4	NA	1.25	NA	70
TIO_2-1	1	1	NA	0.75	NA	15
TIO_2-2	10	>25	NA	0.5	NA	33
TIO_2-3	>15	>15	NA	0.8	NA	39
TIO_2-4	4	NA	NA	NA	NA	18

ed from the stylus behaviour. After the stylus penetrated the layer to basic substrate the layer lifted up the stylus (see Fig. 1). We were not able to detect a critical force for TiO_2 and DLC layers, but only a change in the slope of lateral force dependency on a normal displacement corresponding to the layers thicknesses.

The third device we used was nanosclerometric head, which is an extension of AFM microscope Solver Next. This device provided us with the graphic information obtained by SPM technique with high resolution. For obtained images and made scratches same probe was used. Standards were not utilized, because for the Berkovich tip and the nanolayers standards do not exist. Two scratches with different loads were made on each sample. Length of scratches was 50 μm and loads were (0,5 ÷ 40) mN and (35 ÷ 75) mN for DLC layers and (0,5 ÷ 25) mN and (15 ÷ 50) mN for TiO_2 layers. Loading rate was 100 nm s^{-1}. For DLC layers changes were observed in behaviour of the layers. From certain used force the scratching depth grew rapidly, but this behaviour is not connected with adhesion to basic substrate, but with hardness of the layer itself and with the used probe sharpness. This happens because by AFM microscope Solver Next we measured residual depth and not the penetration depth. There was no such effect observed at TiO_2. Force F_P corresponds to penetrations force from the layer to basic substrate and was detected in both cases.

The macroscopic method for DLC layers gave us good results. The same method used for TiO_2 layers is complicated by influence of droplets in layer influencing acoustic emissions and by low contrast of scratch photography for some of these layers, which made difficult to interpret obtained imagines. Another problem with macroscopic scratch is high used force with combination of brittle substrate which caused damage of the sample for higher force than 25 N. This testing could be considered as destructive. For nanoscratch tests there are no classic marks for delamination or loss of adhesion as is described in various standards[12,15–18]. For Hysitron TI950 device, there is the clear change in lateral force/normal displacement dependency for all samples, but only on interface between the layers and basic substrate. Furthermore there is such dependency at TiO_2-1 sample where adhesion and strength of the layer was very low. The results from nanosclerometric head are closer to macroscopic scratch tester in meaning of needed force for penetration through the layer. Delamination or loss of adhesion was not observed for this method.

4. Conclusions

Four DLC and four TiO_2 layers prepared by PLD were measured on three different devices. The results from different devices did not match because of different measuring conditions and used tips, but we found some interesting results for other measurements of thin films by using described macro a nano scratch systems. The layers thickness determined by scratch testing was in an agreement with the measurement done with mechanical profilometer. Normal forces necessary to penetrate the layers were determined for all samples and devices used. Using CSM Revetest macroscopic scratch tester we were able to evaluate the measurement to determine the delamination force i.e. determine the quality of adhesion of nano layers in accordance with standard EN 1071-3.

This work was supported by grant of Ministry of Education, Youth and Sports of the Czech Republic MSM 6840770012 and by Grant Agency of Czech Technical University, Prague, No. SGS10/222/OHK4/2T/17.

REFERENCES

1. Bull S. J.: Surf. Coat. Technol. *50*, 1991.
2. Perry A.: Thin Solid Films 78, 1981.
3. Perry A.: Thin Solid Films 107, 1983.
4. Steinmann P., Hintermann H.: J. Vac. Sci. Technol. A3 (1985).
5. Valli J.: J. Vac. Sci. Technol. A3 (6) (1985).
6. Valli J.: J. Vac. Sci. Technol. A4 (6) (1986).
7. Valli J., Mäkelä U., Matthews A.: Surf. Eng. *2* (1) (1986).
8. Perry A.: Surf. Eng. *2* (3) (1986).
9. Bull S. J., Rickerby D., Matthews A., Leyland A., Pace A., Valli J.: Surf. Coat. Technol. *36* (1988).
10. Von Stebut J., Rezakhanlou R., Anoun K., Michel H., Gantois M.: Thin Solid Films 181 (1989).

11. Bromark M., Larsson M., Hedenquist P., Olsson M., Hogmark S.: Surf. Coat. Technol. 52 (1992).
12. European Standard EN1071-3: Advanced technical ceramics—methods of tests for ceramic coatings. Part 3. Determination of adhesion and other mechanical failure modes by scratch test.
13. Holmberg K.: Tribologia—Finn. J. Tribol. 19 (3) (2000).
14. Hedenquist P., Olsson M., Jacobson S., Hogmark S.: Surf. Coat. Technol. 41 (1990).
15. ASTM Standard C1624 (C1624-05): Ceramic coatings – Determination of adhesion and other mechanical failure modes.
16. International standards ISO 20502: Fine ceramics – Determination of adhesion of ceramic coatings by scratch testing
17. Japanese standard JAS JIS R: Thin films on glass Substrates – Determination of adhesion.
18. CSN EN 1071-3 (727570): Advanced technical ceramics coatings – Determination of adhesion and other mechanical failure modes.

J. Mikšovský[a,b], P. Kutílek[a], J. Lukeš[c], Z. Tolde[d], J. Remsa[a,b], T. Kocourek[a,b], F. Uherek[e], and M. Jelínek[a,b]
([a] Czech Technical University in Prague, Faculty of Biomedical Engineering, Kladno, [b] Institute of Physics ASCR, Prague, [c] Faculty of Mechanical Engineering, Czech Technical University in Prague, Prague, [d] Czech Technical University in Prague, Innovation Centre for Diagnostics And Application of Materials, Prague, Czech Republic, [e] International Laser Center, Bratislava, Slovakia): **Adhesion Properties of DLC and TiO_2 Thin Films Using Scratch Test Methods**

One of the important parameters of thin films made on various types of basic substrates is adhesion of these films to basic material. In this article, we focused on the study of the actual problem of adhesion of diamond-like-carbon films (DLC) and adhesion of titanium dioxide (TiO_2). The used deposition technique was Pulsed laser deposition (PLD) and the basic substrates were silicon wafers Si(111). We prepared testing samples of DLC with various deposition energies. The thicknesses of these tested films were several tens of nanometres. The TiO_2 testing samples were prepared with various deposition conditions and thicknesses in range of 60÷130 nanometres. On these samples we tested adhesion properties by various techniques based on scratch tests on various instruments in several different laboratory departments in the Czech Republic. For the individual instruments we observed and compared abilities of these systems to evaluate adhesion of thin films with thickness of 100 nanometres and less. For evaluation we used Czech, International and USA standards for ceramic and metallic materials.

EFFECT OF MICROSTRUCTURE OF Cu-Al_2O_3 COMPOSITE ON NANO-HARDNESS AND WEAR PARAMETERS

PAVOL HVIZDOŠ* and MICHAL BESTERCI

Institute of Materials Research, Slovak Academy of Sciences, Watsonova 47, 04001 Košice, Slovak Republic
phvizdos@imr.saske.sk

Keywords: Cu-Al_2O_3, ECAP, nanocomposite, wear

1. Introduction

Copper based materials are widely used in friction parts of machines, such as washers, bearing liners, etc. For these applications properties such as high strength and ductility, fatigue strength, wear resistance, etc., are necessary. To this end an approach of creating composites using hard dispersoid particles is often used[1].

Another way how such desirable properties can be achieved is creating very fine, submicron-grained microstructures[2]. Such microstructures can be prepared by inducing severe plastic deformation[3]. Very promising technique for preparation of these structures is ECAP (Equal Channel Angular Pressing) which results in very fine grained microstructure (nanostructure) by multiple pressings through the die[4].

The aim of the present study is to compare the hardness and wear of two copper based micro/nano-composites with 5 % alumina nanograins and different matrix grain sizes.

2. Experimental Materials

Reaction milling and mechanical alloying was used to prepare the samples. Cu powder with the calculated addition of Al was homogenized by attrition in oxidizing atmosphere. The distribution of the obtained CuO was uniform. Subsequent treatment at 750 °C induced the reaction of CuO with the added Al powder and led to the formation of Al_2O_3 particles. The remaining CuO was reduced by attrition in a mixture of H_2 + H_2O (rate 1:100). The powder was compacted using cold pressing and hot extrusion at 750–800 °C. This material was composed of micron sized grains of Cu and nanoparticles of Al2O3 and it is designated as Cu1.

Initial material with 5 vol.% Al_2O_3 was pressed through two right angled (90°) channels and transformed by the ECAP into a nanocomposite material. Resulting nanosized Cu-Al_2O_3 is denoted as Cu2.

3. Experimental Methods

Instrumented indentation was carried out on a nano-indentation tester TTX-NHT (CSM Instruments). Berkovich pyramid diamond tip was used in sinus mode loading of 5 Hz frequency and 5 mN load amplitude. Loads up to 100 mN were applied. The resulting load-penetration (P-h) curves were evaluated according to the analysis of Oliver and Pharr[5] and values of hardness and elastic modulus as functions of depth as well as elastic and plastic deformation energies were calculated. Up to 20 indentations were performed and the obtained data were statistically evaluated.

Wear testing was performed on a High Temperature Tribometer THT, (CSM Instruments), using ball-on-disk technique. The sample was fixed on a turntable with adjustable rotational speed. The tangential force exerted on the holder was measured and the coefficient of friction was recorded as function of distance/time/laps. Also the position of the holder was measured in order to evaluate the displacement due to material removed by wear. As friction partners steel balls with 6 mm diameter were used. The loading of 1 N was applied using a dead weight system. The nominal wear track radius was 2 mm, the sliding speed was set to 5 cm/s and the overall sliding distance was 100 m. Testing was done in air at room temperature in dry conditions. After the tests, both tribological partners (the steel ball and the sample) were observed using light and SEM microscopy. The depth and shape of the wear tracks were measured by a stylus profilometer (Mitutoyo SJ-201) at minimum three locations, the average wear track cross section area was calculated and subsequently the volume of the removed material was estimated. The wear rates were then expressed as the volume loss per distance and load (mm^3/m.N) and compared for both material systems.

4. Results

Microstructure of both materials was studied using TEM thin foils, in order to reliably identify the nanosized phases.

Fig. 1 shows TEM micrographs of the microstructures of experimental materials. Typical grain size in the material Cu1 was about 1–2 microns whereas in the material Cu2 it was from 100 to 200 nm.

Fig. 2 compares depth profiles of modulus of elasticity in Cu1 and Cu2 as measured by the instrumented indentation. In both cases these values were about 105 GPa at depths more than 1 μm, which corresponds to the elasticity of bulk copper. Smaller values at depths of penetration bellow 1 μm can be partly attributed to insufficient smoothness of the ground surface which was not highly polished. Another factor is the dislocation density, which during the testing increased under the indenter tip with increasing load until it reached the saturation point. The differences between the two materials were small, within the error range. Slightly higher values in Cu2 in smaller depths are caused by higher density of pre-existing dislocations in this highly plastically deformed material.

The difference in the case of hardness values was more pronounced (Fig. 3). Here, in both materials, the hardness start at higher values but also with very high scatter, which is caused by errors of measurement at very low loads and depths. For depths above 400 nm, however, the data show clearly two different levels of hardness, 2.28 GPa and 2.69 GPa for Cu1 and Cu2, respectively. This difference is

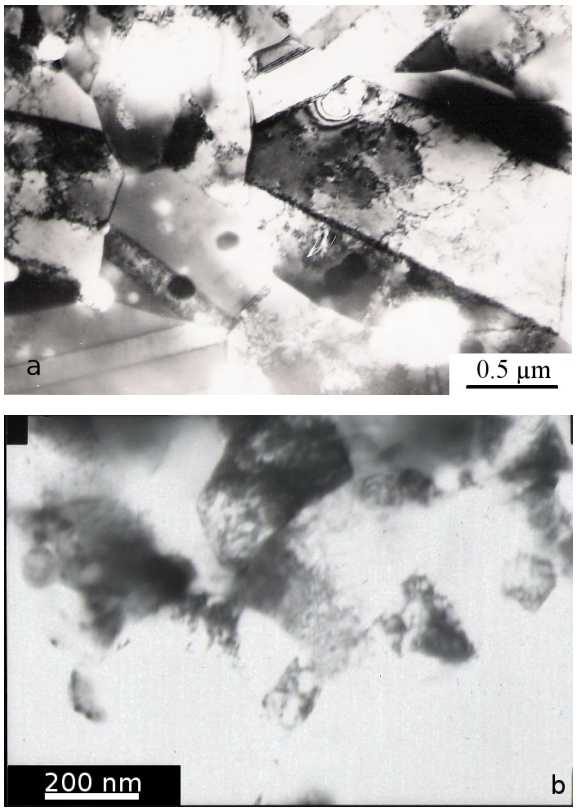

Fig. 1. **TEM micrographs, showing microstructure of (a) Cu1, and (b) Cu2**

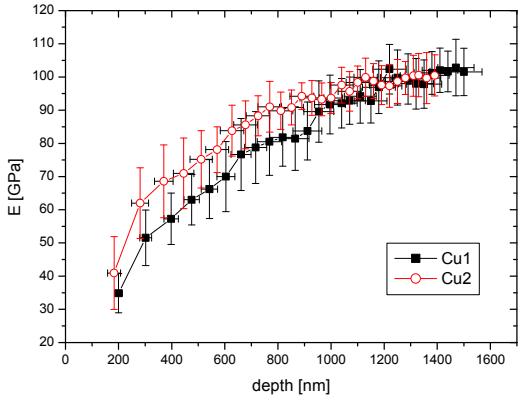

Fig. 2. **Modulus of elasticity vs depth for Cu1 and Cu2**

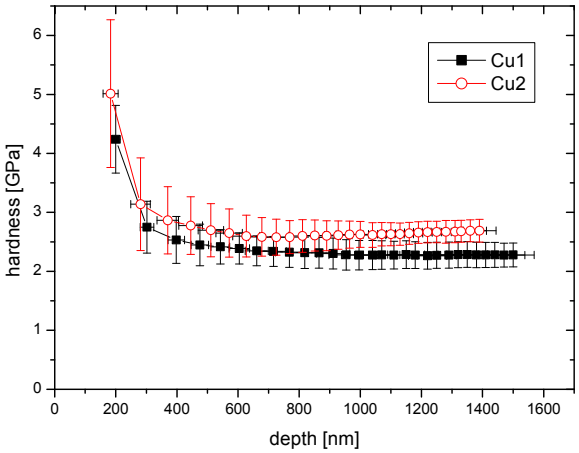

Fig. 3. **Depth profile of nano-hardness for both experimental materials**

statistically significant as it is greater than the scatter of the data.

From the load penetration (P-h) curves also the elastic (W_e), plastic, and total (W_t) energies of indentation were calculated. The differences between Cu1 and Cu2 are summarized in Table I. The elastic energy in indentation of Cu2 was higher than that of Cu1 even though its total indentation energy was lower. This behaviour was highly reproducible, as it is indicated by small scatter values (Tab. I).

It can be summarized that while the elasticity was in both cases very similar, the refinement of the matrix copper grains lead to a measurable increase of hardness and substantial increase of the ability for elastic recovery of the nanocomposite.

Table I
Indentation deformation energies

	Cu1	Cu2
W_t [nJ]	60.57 ± 2.11	47.30 ± 1.95
W_e [nJ]	5.57 ± 0.11	7.04 ± 0.17
W_e/W_t	0.092 ± 0.003	0.149 ± 0.005

Friction behaviour of both materials was in terms of coefficient of friction (COF) very similar (Fig. 4). At the beginning the COF started at low values, usually 0.12, which were very stable. After short running-in phase (2 to 10 meters of sliding distance) macroscopic failure of the surface began to take place and COF values rapidly rose up to 0.45–0.60, the values typical for steel-copper dry friction contact[6,7]. This level of friction then remained stable till the end of the test, up to 100 m sliding distance (nearly 8000 laps). The average values of COF in this wear regime were 0.55±0.02 for Cu1 and 0.58±0.03 for Cu2, respectively (Fig. 5).

Fig. 5 also compares the wear rates of both materials. It shows that the material Cu2 is about 3 times more wear resistant than the other one. This finding is analogous to literature data[8] for pure copper with submicro and nanocrystalline microstructures. Fig. 6 shows the wear tracks in both materials, photographed immediately after the test with the debris

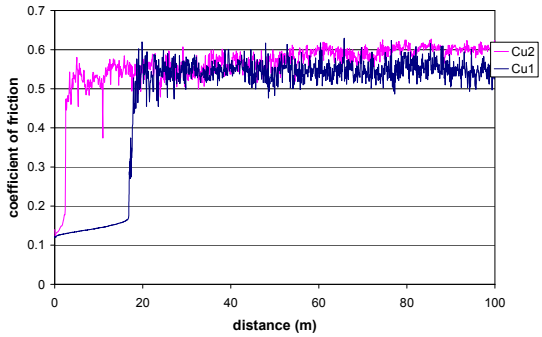

Fig. 4. **Coefficient of friction along the sliding distance**

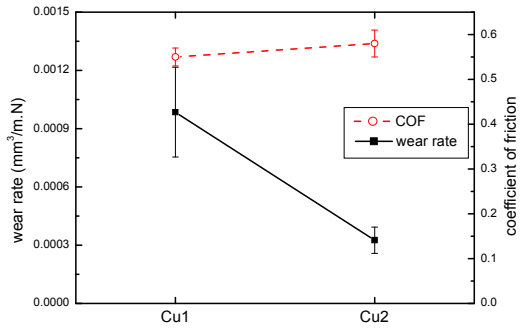

Fig. 5. **Coefficient of friction and wear rates of the experimental materials**

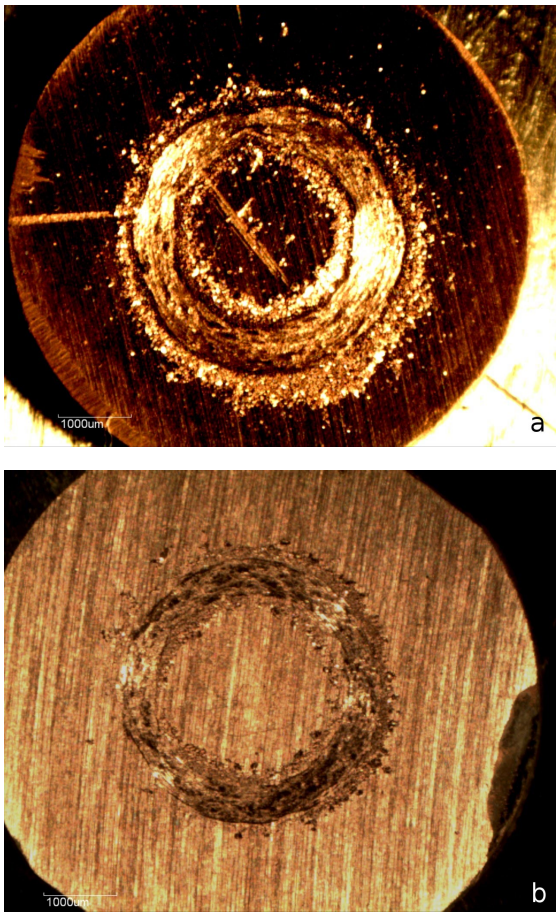

Fig. 6. **Wear tracks, together with wear debris, in Cu1 (a) and Cu2 (b)**

still present. The difference is immediately visible – the track in the Cu1 is larger and also the amount of wear debris around it is considerably greater (Fig. 6a) than in Cu2 (Fig. 6b).

The material was lost almost exclusively on the side of the copper discs; the steel balls were after the tests virtually intact. There were no circular worn caps present and in fact, it appears that part of the wear damage was due to adhesion of copper grains to the steel surface. This corresponds to the mechanism of copper transfer to the steel surface as it was established for coarse grained copper[9].

Details of the morphology of the worn areas in copper wear tracks are presented in SEM micrographs – Fig. 7. In both materials one can identify smooth and scarred areas, with presence of ductile and granular type of damage. The difference between the two materials is in the amount of the mentioned mechanisms. The worn surface of the material Cu1 (micro) is much smoother, in the material Cu2 granular features and fine particles are more frequently observed. SEM analysis showed, that in the present conditions mechanisms of 'mild' wear, as described in[8,10], were typical for both materials.

It can be concluded that the wear mechanisms are in both materials qualitatively the same, but the material with coarser grains contains more ductile damage.

5. Conclusions

Two Cu + 5 % Al_2O_3 composites with different size of the matrix grains were prepared. The hardness and elasticity was measured by instrumented nanoindentation, wear testing was carried out using pin-on-disc method and the friction and wear properties of both materials were compared. The results indicate that while both materials retained basically equal modulus of elasticity, corresponding to ordinary copper, the material with finer grains was significantly harder. The friction coefficients in both cases were very similar, corresponding to copper-steel sliding contact. The wear rates as well as the micrographic analyses indicate that in both cases mild wear of copper took place. The values of wear rates in terms

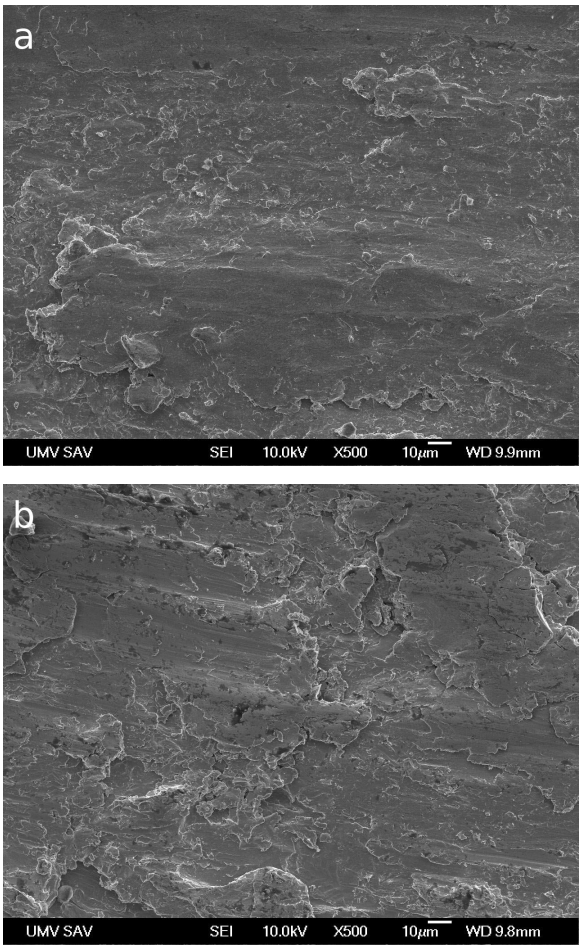

Fig. 7. **Details of wear tracks– (a) Cu1, (b) Cu2**

of the volume loss, however, were markedly different. It was shown that by ECAPing (i.e. by modification of microstructure – refinement of grains and introduction of the dislocations) the hardness and wear resistance can be improved significantly.

This work was realized within the frame of the project „Centre of Excellence of Advanced Materials with Nano- and Submicron-Structure", which is supported by the Operational Program "Research and Development" financed through European Regional Development Fund. The experiments could be carried out thanks to the projects VEGA 2/0120/10, 2/0025/11 and APVV-0520-10.

REFERENCES

1. Besterci M., Kováč L.: Int. J. Mater. Product Technol. *18*, 26 (2003).
2. Gleiter H.: Nanostruct. Mater. *1*, 1 (1992).
3. Valiev R. Z., Krasilnikov N. A., Tsenev N. K.: Mater. Sci. Eng., A *137*, 35 (1991).
4. Besterci M., Kvačkaj T., Kočiško R., Sülleiová K.: Int. J. Mater. Product Technol., in press.
5. Oliver W. C., Pharr G. M.: J. Mater. Res. *7*, 1564 (1992).
6. http://www.engineeringtoolbox.com/friction-coefficients-d_778.html
7. Marui E., Endo H.: Wear *249*, 582 (2001).
8. Sadykov F. A, Barykin N. P., Aslanyan I. R.: Wear, *225–229*, 649 (1999).
9. Syed Asif S. A, Bismas S. K., Pramila Bai B. N.: Scripta Met. et Mater. *24*, 1351 (1990).
10. Antoniou R., Borland D. W.: Mater. Sci. Eng. *93*, 57 (1987).

P. Hvizdoš and M. Besterci, *(Institute of Materials Research, Slovak Academy of Sciences):* **Effect of Microstructure of Cu-Al_2O_3 Composite on Nano-Hardness and Wear Parameters**

Two copper based composites with different grain size were studied: microCu-Al_2O_3 composite (grain size 1–2 microns), and nanoCu-Al_2O_3 nanocomposite prepared from microCu-Al_2O_3 by ECAP. This procedure resulted in 100–200 nm grain size.

Hardness and elastic modulus were measured by instrumented nanoindentation, the wear characteristics were evaluated using pin-on-disk method.

The results showed that the elastic modulus of the two materials was the same, similarly as the friction coefficient. However, it was found that by ECAPing the nanohardness increased due to refinement of the grains (increased density of grain boundaries) and thus the wear resistance improved by 200 %.

THE INFLUENCE OF ELEVATED TEMPERATURE ON COEFFICIENT OF FRICTION OF HVOF SPRAYED COATINGS MEASURED BY PIN-ON-DISC TEST

ROSTISLAV MEDLÍN* and ŠÁRKA HOUDKOVÁ

New Technologies - Research Centre, University of West Bohemia, Univerzitní 8, 306 14 Plzeň, Czech Republic
medlin@ntc.zcu.cz

Keywords: HVOF, coating, sliding, wear, pin-on-disc, CoF

1. Introduction

The friction between a piston, piston rings and a cylinder is responsible for almost 55 % of total power loss in engines. The decrease of friction in the piston area leads to a significant fuel saving and also to the emission reduction. The application of thermally sprayed coating is one possible way to decrease the friction and wear of engines.

From tribological point of view the engine system of piston, piston rings and cylinder is quite complicated. Together with the counterpart the piston ring makes a friction couple that should meet the requirements of low friction, wear and a long durability. During running, the system parts are submitted to the three-body abrasion, caused by the contamination of lubricant by solid particles. Compare to the rotational movement, the reciprocating linear movement is much more demanding due to sudden changes of direction, velocity, surface roughness and supply of lubricant. More to that, the piston rings surface is exposed to demanding chemical and thermal conditions. The study of the influence of elevated temperature on the sliding friction behavior of HVOF (High Velocity Oxygen Fuel) sprayed coatings are subject of this paper.

The technology of thermal spraying enables to create the surface coating approximately 50 μm thick, which provides the functional surface protection of the coated parts. The HVOF technology offers the possibility of creating the coatings of materials based on the principle of hardmetals with high wear resistance and favorable sliding properties. Such a combination predestinates the HVOF sprayed coatings for sliding applications, such as pistons of combustion engines, pumps and other hydraulic devices. In this application area they are used on a regular basis. By this reason, the wear resistance and the friction properties of these coatings were intensively studied under various conditions[1–4]. For severe wear applications, the HVOF sprayed hardmetal coatings are generally acknowledged as the best choice. Hardmetals offer an advantageous combination of wear and corrosion resistance with good friction properties. Some of them are also suited for elevated temperatures. They properties make them to be the good possibility for application in the piston-piston rings-cylinder system, as it was confirmed in previous works[5–7].

2. Experimental

Seven types of coating materials were chosen as potential candidates for engine parts application. The coating was sprayed by HP/HVOF JP-5000® (TAFA) spraying technology in the ŠKODA VÝZKUM s.r.o. in Plzeň, using the standard preparation procedure on the grit blasted substrate of carbon steel (ČSN 11 523) and the previously optimized spraying parameters. The average as-sprayed coatings thickness was 450 μm, surface grinding and polishing moves maximal 50 μm of thickness away. The coatings composition and basic mechanical properties are summarized in the Table I, the microstructures in the Fig. 2.

The coating sliding wear and friction properties were evaluated in the partner organization New Technology Center of University of West Bohemia in Plzeň (NTC ZČU), by the pin-on-disc test according to ASTM G-99, using High Temperature Tribometer produced by CSM Instruments SA. Even thought linear movement is more damaging than rotational movement, there can be seen relations between responses of testing materials and behavior of used materials.

The test was provided on the polished coating surface with the roughness Ra varying between 0,05–0,25. (see Table I) as original surface of piston rings used in engines. The testing used parameters are summarized in the Table II.

Working temperature of piston-rings in fuel-engine is calculated and measured about 350 °C (see Fig. 1) therefore temperature for piston-rings testing materials were used on that value.

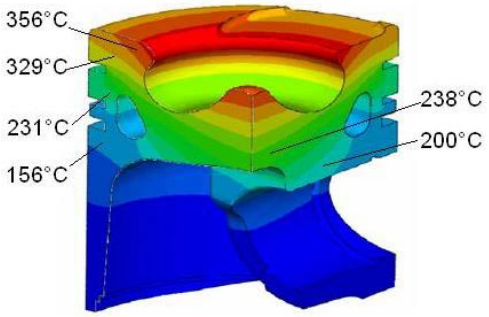

Fig. 1. **Temperature distribution in the piston**

The dry condition was chosen for the measurements to simulate the most demanding extreme situation of lack of lubricants that can cause the most severe wear of the coated parts. The results of influence of lubricants on the measured parameters can be found elsewhere[8].

Table I
Coatings mechanical properties

Coating	Surface roughness Ra	Micro-hardness HV0,3	Hardness HR15N
CoMoCrSi	0,13	705 ± 52	80,1 ± 1,9
NiCrMoWFe	0,05	420 ± 26	76,0 ± 1,7
WC-17%Co	0,25	1485 ± 88	90,0 ± 0,3
WC-20%CrC-7%Ni	0,10	829 ± 112	87,0 ± 0,9
Cr_3C_2-25%CoNiCrAlY	0,10	848 ± 30	85,3 ± 0,9
Cr_3C_2-25%NiCr	0,16	1030 ± 114	84,0 ± 0,5
Cr_3C_2-35%NiCr	0,14	811 ± 33	82,4 ± 0,9

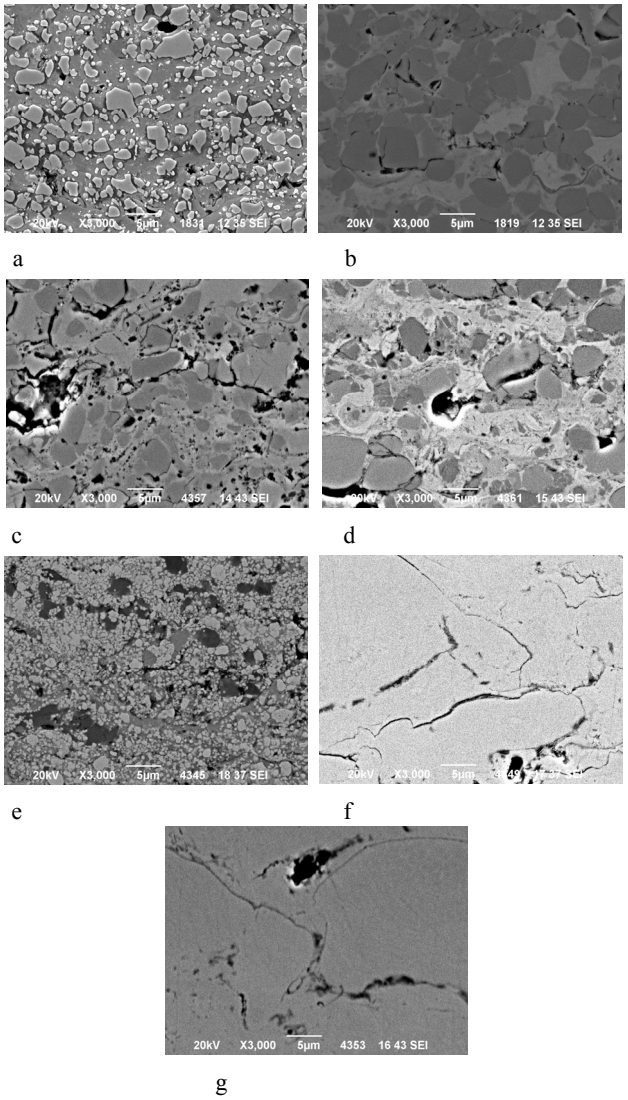

Fig. 2. **Microstructure of examined coatings a)WC-17%Co, b) Cr_3C_2-25%NiCr, c) Cr_3C_2-35%NiCr, d) Cr_3C_2-25%CoNiCrAlY, e) WC-20%CrC-7%Ni, f) CoMoCrSi, e) NiCrMoWFe**

Table II
Pin on disc test parameters

Pin	Al_2O_3 and Steel ball, ∅ 6 mm
Speed	0.1 m s^{-1}
Number of cycles	30 000
Pin load	10 N
Wear track diagonal	2, 3.5 and 5 mm
Temperature	20 °C, 350 °C
Lubrication	Dry

3. Results

The measured results of coefficient of friction (CoF) values are summarized in the Table III and the CoF detail progressions in dependence on the number of cycles are compared for all evaluated materials measured at room and elevated temperatures in the Fig. 3.

Table III
a) Pin on disc test CoF results for Steel Ball

Coating	CoF of Steel Ball	
	20 °C	350 °C
CoMoCrSi	0,710 ± 0,138	0,798 ± 0,010
NiCrMoWFe	0,732 ± 0	0,701 ± 0,006
WC-17%Co	0,780 ± 0,011	0,610 ± 0,008
WC-20%CrC-7%Ni	0,759 ± 0,002	0,611 ± 0,019
CrC-25%CoNiCrAlY	0,547 ± 0,002	0,630 ± 0,005
CrC-25%NiCr	0,713 ± 0,090	0,552 ± 0,004
CrC-35%NiCr	0,612 ± 0,029	0,614 ± 0,009

b) Pin on disc test CoF results for Al_2O_3 Ball

Coating	CoF of Al_2O_3 Ball	
	20 °C	350 °C
CoMoCrSi	0,685 ± 0,008	0,605 ± 0,138
NiCrMoWFe	0,666 ± 0	0,642 ± 0,013
WC-17%Co	0,364 ± 0,020	0,547 ± 0,026
WC-20%CrC-7%Ni	0,482 ± 0,0005	0,808 ± 0,007
CrC-25%CoNiCrAlY	0,684 ± 0,0005	0,616 ± 0,008
CrC-25%NiCr	0,671 ± 0,012	0,539 ± 0,0005
CrC-35%NiCr	0,605 ± 0,027	0,555 ± 0,017

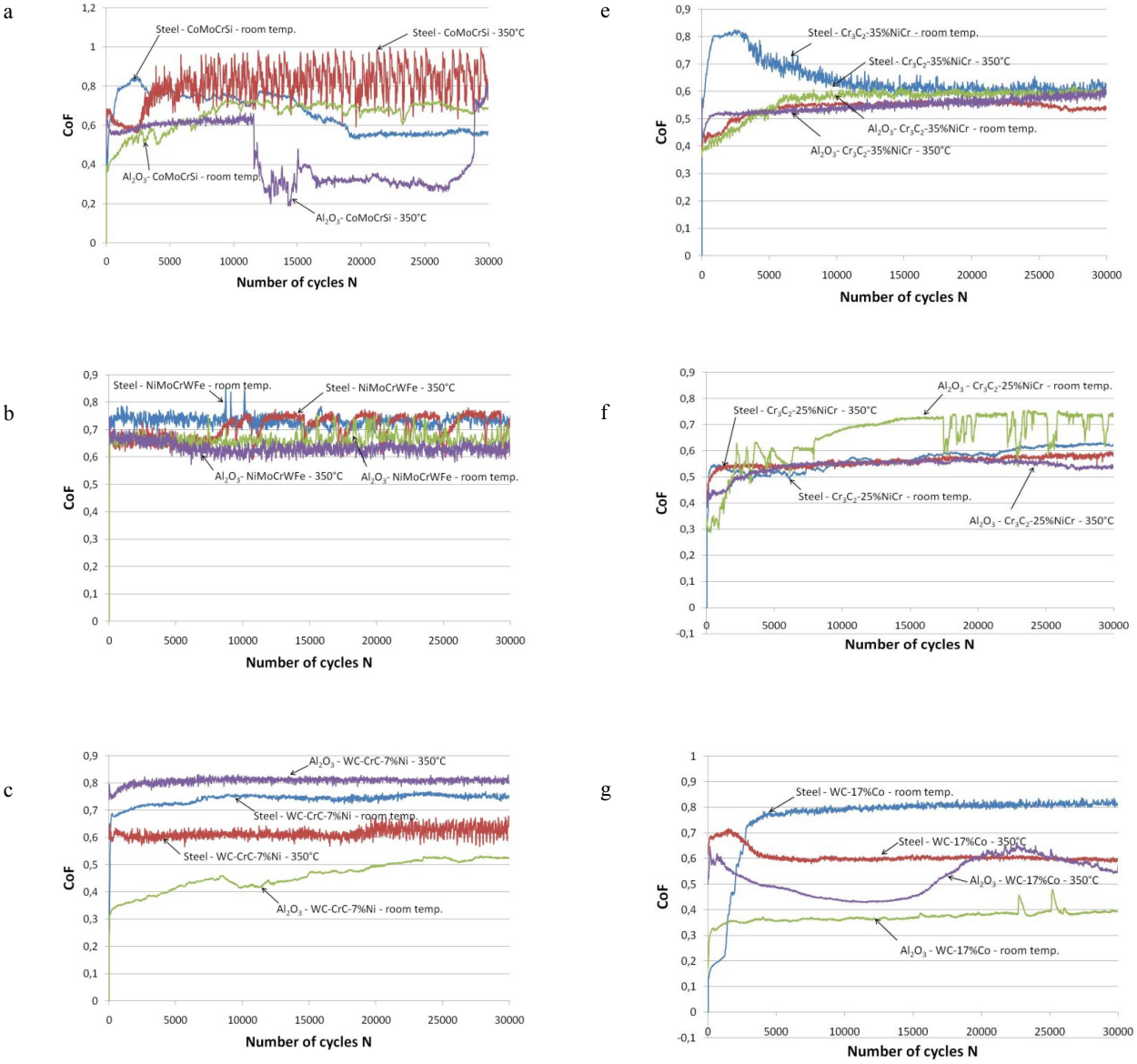

Fig. 3. **The progression of CoF in dependence on the number of cycles of examined coatings a) CoMoCrSi, b) NiCrMoWFe, c) WC-20%CrC-7%Ni, d) Cr_3C_2-25%CoNiCrAlY, e) Cr_3C_2-35% NiCr, f) Cr_3C_2-25%NiCr, g) WC-17%Co**

In Tab. IV are oxygen volume measured SEM Quanta 200 from FEI with EDAX EPMA with EDS detector on free surface and inside of ball tracks after tribology experiment for Steel and Al_2O_3 ball. The increasing oxygen content points to the creation of the oxidic tribofilm that can influence the coefficient of friction values. With EDS on rough surface of Ball track it may L series of Cr energy X-ray peaks overlay with Oxygen energy peak because they have similar energy. Cr are determined from K-series and L/K series intensity ratio are sensitive to surface roughness. Cr-Oxide film creation on surface was indicated in previous work[3].

Table IV
a) Oxygen volume in coatings for 20 °C

Coating	Oxygen volume [wt.%]		
	Free surface	Steel Ball	Al_2O_3 Ball
CoMoCrSi	0.00	17.03	3.43
NiCrMoWFe	0.00	0.00	0.19
WC-17%Co	1.42	12.89	1.30
WC-20%CrC-7%Ni	0.31	0.00	0.61
CrC-25%CoNiCrAlY	0.71	0.45	4.16
CrC-25%NiCr	1.68	0.72	39.79
CrC-35%NiCr	0.00	3.11	0.00

b) Oxygen volume in coatings for 350 °C

Coating	Oxygen volume [wt.%]		
	Free surface	Steel Ball	Al_2O_3 Ball
CoMoCrSi	2.01	2.46	3.25
NiCrMoWFe	0.00	0.00	12.23
WC-17%Co	3.07	7.64	5.79
WC-20%CrC-7%Ni	3.26	5.41	4.13
CrC-25%CoNiCrAlY	1.06	15.82	0.00
CrC-25%NiCr	1.80	2.39	8.10
CrC-35%NiCr	1.66	2.76	0.00

Wear mechanisms investigated by SEM were usual. For carbide materials there were marks of erosion of carbides from material and then abrasion from eroded carbides in wear track, in metal alloys abrasion and surface fatigue (Fig. 4).

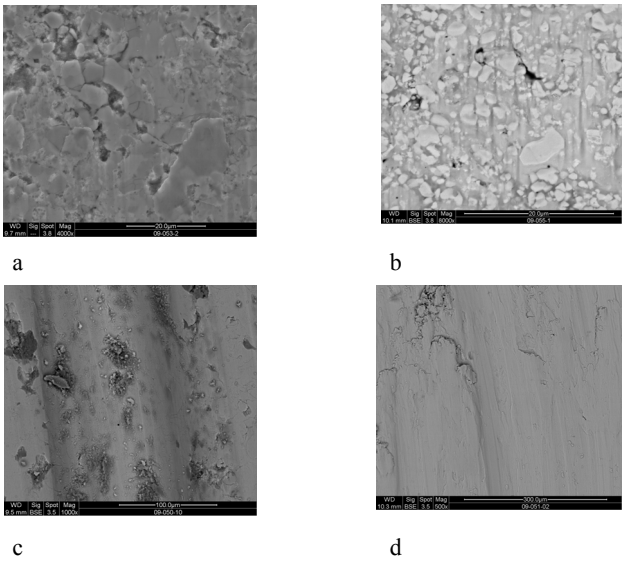

Fig. 4. **Wear mechanisms of sprayed coatings observed by SEM. Erosion (a) and subsequently abrasion (b) of carbides in wear track for carbide materials and abrasion (c) and surface fatigue with adhesion, material transfer and pits (d) for metal alloys**

4. Discussion

The values and the progression of CoF change significantlyy with the increase of temperature. While for room temperature and Al_2O_3 counterpart the lowest CoF values shown the WC-based coatings and the CrC-based coatings shown the highest CoF values, for increased temperature it is backwards. The increased temperature causes the creation of oxidic film on the surface of CrC-based coatings that consist from Cr_2O_3, eventually $NiCr_2O_4$ (ref.[9]). Its CoF value range between 0,25–0,3 (ref.[10]), and it is well adhered to the coating surface. The WC-based coatings create at elevated temperature $CoWO_4$ a WO_3 oxides[9], that are poorly adhered to the coatings surface and tends to fall.

The CoMoCrSi coating on the CoF progression illustrates well the situation, where the creation of oxidical tribofilm causes the sudden decrease the CoF value. The tribofilm was at the end of the test ripped off, and the CoF increase immediately on its origin value. It is phenomenon that appears in the case of poorly adhered tribofilms[10].

Compare to the Al_2O_3 counterpart, the behavior in the contact with the steel counterpart changed especially for WC-based coatings, where the CoF is lower for higher temperature than for room temperature, while for Al_2O_3 counterpart it is contrariwise. The CrC-based coating had at elevated temperature similar behavior for Al_2O_3 and steel counterpart, the CoF values is in the range of 0,5–0,65, its progression is smooth, without significant fluctuation.

In the case of WC-CrC-Ni coating, the elevated temperature brings the increase of CoF for both counterparts. The created oxidic tribofilm does not have the expected positive effect as in the case of CrC-based coatings.

The NiMoCrWFe coating has stable behavior in all conditions. Due to its relatively low hardness it can be assumed, that the CoF value is determined more in consequence of plastic deformation during counterpart movement, and the counterpart material and surrounding temperature has not a big influence.

5. Conclusion

The measured results show that the presumption beneficial influence of Cr content in the coatings composition on their frictional properties can be confirmed only for hardmetal coatings. All CrC-based coatings with Cr in the matrix show with elevated test temperature decrease of CoF value (in the case of Al_2O_3 counterpart), or at least the unchanged behavior. More than the absolute CoF value the CoF progression is considerable due to its potential to predict the behavior in the following cycles. The Cr_2O_3 – which is together with $NiCr_2O_4$ the most probable oxide[4,9] – adheres strongly to the coating's surface and it is in correlation with CoF values measured in this study – characterized by CoF values in between 0.25–0.5 (ref.[10]). The alloy coatings with Cr content – CoMoCrSi and NiCrMoWFe – show no difference in the friction behavior even if the oxide tribofilm was measured by SEM EPMA. The WC-based coatings both show the increase of CoF with increasing temperature. Their oxidation behavior is not propitious for the application at elevated temperature. The combined WC-CrC-Ni hardmetal does not fulfill the

expectations, its behavior is not exceed the simpler WC-based and CrC-based coatings. The alloy coatings does are either not enough wear resistant (NiMoCrWFe) or unstable in CoF progression (CoMoCrSi). With respect to the results it can be said that the application requirement mentioned in the beginning meet from the suggested candidates only CrC-based hardmetals and that can be recommended for application on piston rings.

This work was supported by the Ministry of Industry and Trade of the Czech Republic no. FT-TA5/07.

REFERENCES

1. Bolelli G., et al.: Surf. Coat. Technol. *200*, 2995 (2006).
2. Picas A., Forn A., Matthäus G.: Wear *261*, 477 (2006).
3. Houdková Š., Zahálka F., Kašparová M.: Mater. Sci. Forum *567-568*, 229 (2007).
4. Berger L.-M., et al.: *In Conf. Proc. Int. Thermal Spray Conf. & Exhibition ITSC 2004*, DVS-Verlag, 2004, p.10.
5. Barbezat G.: *International Thermal Spray Conference (2004) May 10–12, Osaka*, Japan, Thermal Spray 2004: Advances in Technology and Application, Ed. B. R. Marple, C. Moreau, Pub. ASM International, Materials Park, OH, USA, 2004.
6. Herbst-Dederichs C.: Thermal spray solutions for Engine Piston Rings, Thermal Spray 2003: Advancing the Science and Applying the Technology, *International Thermal Spray Conference (2003) 5-8 May, Orlando*, Florida, (B. R. Marple, C. Moreau, ed.). Pub. ASM International, Materials Park, OH, USA, 2003, pp. 129–138.
7. Rastergar F., Richardson D. E.: Surf. Coat. Technol. *90*, 156 (1997).
8. Houdková Š., Zábranská I., Zahálka F.: *Metal 2009, 19.-21.5. 2009, Hradec nad Moravicí*, p. 258–265.
9. Berger L.-M., Zieris R., Saaro S.: *Conf. Proc. Int. Thermal Spray Confernce & Exhibition ITSC 2005, 2-4 May 2005, Basel*, Switzerland, Düsseldorf: DVS-Verlag, (2005), CD, pp. 969–976.
10. Buschnan B.: *Introduction to Tribology*, J. Wiley, New York 2002.

R. Medlín, and Š. Houdková *(New Technologies - Research Centre, University of West Bohemia, Plzeň, Czech Republic):*
The Influence of Elevated Temperature on CoF of HVOF Sprayed Coatings Measured by Pin-on-Disc Test

The pin-on-disc test according to ASTM G-99 was provided on selected thermally sprayed coatings to determine and describe their sliding wear behavior under elevated temperature. The progression of coefficient of friction was measured against two types of counterpart material, at room temperature and at 350°. After the test, the mechanisms of wear were studied by SEM and EDX. It was confirmed, that the content of Cr in the coatings is the most important factor causing the decrease of coefficient of friction with elevated temperature.

MICROSTRUCTURE BASED HARDENING MODEL FOR TRANSFORMATION INDUCED PLASTICITY (TRIP) STEELS

HENDRIK QUADE, ULRICH PRAHL, and WOLFGANG BLECK

Department of Ferrous Metallurgy at RWTH Aachen University, Intzestraße 1, 52072 Aachen, Germany
hendrik.quade@iehk.rwth-aachen.de
ulrich.prahl@iehk.rwth-aachen.de
wolfgang.bleck@iehk.rwth-aachen.de

Keywords: TRIP steels, phase transformation law

1. Introduction

Multi phase steels especially TRIP steels combine a high strength and a high formability, which is a condition for deep drawing parts in the automotive industry. The TRansformation-Induced-Plasticity-effect (TRIP) is responsible for an extra work hardening during straining and the energy absorption during this effect enables an application to crash relevant components. But the damage behaviour of TRIP steels is poorly understood and the application of them is restricted.

2. Motivation and aim

This work presents a microstructural numerical investigation of the influence of the TRIP effect and its different contributions to the evolution of the microstructure to get a better understanding of the microstructural damage mechanisms and to ensure an application in automotive parts.

Due to industrial conditions of processing routes TRIP steel sheets show a change of the morphology over the sheet thickness, which therefore results in a change of failure mechanisms within the part. The reasons for this are segregation and banding effects within the sheet.

Fig. 1 shows such resultant failure mechanisms in two different industrial TRIP sheets (left: debonding of hard martensitic bands from the surrounding ferritic matrix, right: cleavage fracture zones surrounded by a ductile network of voids). Typically, TRIP steels consist of a ferritic / bainitic-ferritic matrix with embedded islands of retained austenite and some martensite (see Fig. 2).

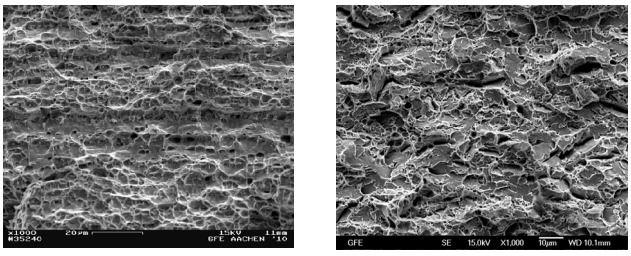

Fig. 1. **Different failure mechanisms at sheet centre of different TRIP steels (left: debonding of hard martensitic bands from ferritic matrix, right: cleavage fracture zones in a ductile network)**

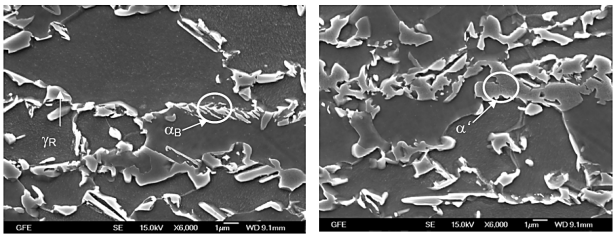

Fig. 2. **SEM image of a TRIP microstructure**

During deformation, these retained austenite grains undergoe a phase transformation to the harder phase martensite. The locations of these grains in the microstructure are of major importance because they influence the impact of the TRIP effect, the microstructural localization and therefore the macroscopical deformability of the material.

3. Phase transformation law and microstructural finite element model

Different deformation mechanisms occur within different temperature ranges. Below the martensite start temperature M_s, martensite can be formed by cooling. Above M_s, an additional driving force is needed and phase transformation can be achieved by deformation of the microstructure. Within this range, martensite is formed at same nucleation sites as during cooling.

Above a so called M^{σ}_s-temperature, martensite is formed at intersections of shear-bands consisting of ε martensite with hcp crystal structure. These shear bands emerge after plastic deformation of retained austenite (see Fig. 3).

The presented model considers the TRIP effect in the strain-induced regime which is based on the phenomenologi-

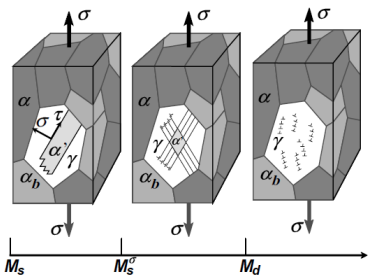

Fig. 3. **Deformation** mechanisms in dependence of the temperature[1] (between M_s and M^{σ}_s – **stress-assisted martensite formation, between M^{σ}_s and M_d – strain-induced martensite formation)**

cal model of Olson and Cohen[2]. According to Iwamoto et al., the plastic strain rate is defined as the sum of the plastic strain rate which is induced by slip deformation in austenite and martensite and the transformation strain rate which is induced by phase transformation[3]. The constitutive model is based on the publication of Sierra and Nemes[4]. The transformation plastic strain rate is divided into two parts, the deviatoric contribution related to the shape change, and the dilatational contribution related to the volume change. Hence, the overall plastic strain rate tensor is given by the following expression:

$$\dot{\varepsilon}_{ij}^{p} = \dot{\varepsilon}_{ij}^{pslip} + \dot{\varepsilon}_{ij}^{ptrans} = \dot{\varepsilon}_{ij}^{pslip} + \dot{\varepsilon}_{ij}^{pshape} + \dot{\varepsilon}_{ij}^{pdilat} \quad , \tag{1}$$

with the slip deformation plastic strain rate tensor:

$$\dot{\varepsilon}_{ij}^{pslip} = \dot{\bar{\varepsilon}}^{pslip} \frac{\partial F}{\partial \sigma_{ij}}. \tag{2}$$

The shape change plastic strain rate tensor is defined as follows:

$$\dot{\varepsilon}_{ij}^{pshape} = R\dot{f}^{m} \frac{\partial F}{\partial \sigma_{ij}}, \tag{3}$$

with the magnitude of shape change:

$$R = R_0 + R_1\left(\frac{\bar{\sigma}}{\sigma_{ya}}\right), \tag{4}$$

the yield stress of the parent austenitic phase is σ_{ya} and the dimensionless constants are R_0 and R_1. The increase in martensite volume fraction $\dot{f}^{m}$ is determined by plastic strain in the austenite and is written in the following form:

$$\dot{f}^{m} = A\left(1 - f^{m}\right)\dot{\bar{\varepsilon}}_{a}^{pslip} \quad , \tag{5}$$

with the equivalent plastic strain rate in austenite due to slip deformation $\dot{\bar{\varepsilon}}_{a}^{pslip}$, and A is defined as follows:

$$A = \alpha\eta\left(f^{sb}\right)^{n-1}\left(1 - f^{sb}\right), \tag{6}$$

with the volume fraction of shear bands f^{sb} and the hardening exponent n. α is a temperature dependent coefficient which is defined by:

$$\alpha = \alpha_1 T^2 + \alpha_2 T + \alpha_3 - \alpha_4 \Sigma, \tag{7}$$

where $\alpha_{1\text{-}4}$ are material constants, T is the temperature and Σ is the stress triaxiality. The driving force for martensite formation η is also dependent on the stress state and given by the following equation:

$$\eta = \eta_1 + \eta_2 \Sigma, \tag{8}$$

with the constants η_{1-2}.

Finally, the dilatational plastic strain rate tensor is expressed by:

$$\dot{\varepsilon}_{ij}^{pdilat} = \frac{1}{3}\Delta\upsilon\dot{f}^{m}\delta_{ij}, \tag{9}$$

where $\Delta\nu$ accounts for the volume change which lies in a range between 0.02–0.05 and δ_{ij} is the well known Kronecker delta.

The constitutive law which describes the behaviour of the composite similar material is given by:

$$\dot{\sigma}_{ij} = D_{ijkl}^{e}\dot{\varepsilon}_{kl} - P_{ij}\dot{\bar{\varepsilon}}^{p} - Q_{ij}\Delta\upsilon\dot{f}^{m} \quad , \tag{10}$$

with

$$P_{ij} = \frac{E}{1+\upsilon}\frac{\partial F}{\partial \sigma_{ij}} \quad ,$$

and

$$Q_{ij} = -P_{ij}\Sigma + \frac{1}{3}\delta_{ij}\frac{E}{1-2\upsilon} \quad .$$

$\dot{\sigma}_{ij}$ is the rate of Cauchy stress, D_{ijkl}^{e} is the elastic stiffness tensor, E is the Young's modulus and ν is the Poisson's ratio.

The phase transformation was used as a user defined material subroutine (UMAT) within the commercial finite element package ABAQUS®.

A TRIP microstructure was simplified to a 2 phase microstructure consisting of retained austenite islands embedded in a ferritic matrix. The principal can be seen in Fig. 4. The simplified microstructure (upper right image) was nearly created from a given SEM image (upper left image). For mesh generation, at first a geometry file was created (IGES file) by using a Voronoi cell generator (see lower left image). Finally, the mesh was built by a geometry export into the meshing tool

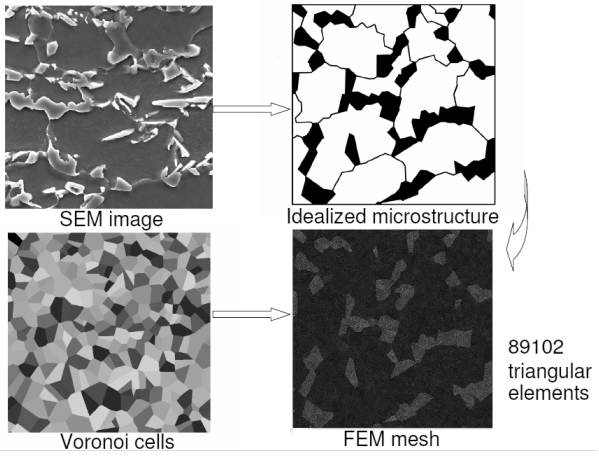

Fig. 4. **Principle of the mesh generation for investigation of a simplified TRIP microstructure with consideration of morphology**

Table I
Model materials for investigation of influence factors

A	B	C	D
Stress-state independent martensitic formation	Stress-state independent shear band formation	No shape change	No volume dilatation
η_2=0	α_4=0	R_0, R_1=0	$\Delta\nu$=0
$\eta = \eta_1$	$\alpha = \alpha_1 T^2 + \alpha_2 T + \alpha_3$	$\dot{\varepsilon}_{ij}^{shape} = 0$	$\dot{\varepsilon}_{ij}^{dilat} = 0$

Hypermesh® and the material properties were given according to the upper right image. The final mesh consists of 89102 triangular elements and the calculations were taken out under a plane strain condition. To investigate the influence of different contributions to the TRIP effect, 4 material models were investigated[4]. The isotropic elastoplastic constitutive law of the ferritic matrix was kept constant, but the retained austenite stability was modified by adjusting of certain material parameters. The different assumptions are given in Table I.

4. Results and discussion

Fig. 5 shows the martensite volume fraction and Fig. 6 the Von Mises stress distribution after uniaxial tension with applied homogeneous boundary conditions until 10% deformation of the microstructure by consideration of all effects. By viewing the distribution of martensite volume fraction it can be seen a more or less influence of the morphology on phase transformation and stress distribution. The volume fraction ranges from about 0.2 to 0.7 over the whole material and deviates more or less within the grains.

Big grains are preferred for an early transformation because they have longer interfaces which allow higher stress transferences than smaller ones. Besides, there is a strong influence of position and orientation of the grains within the microstructure. Because the position alters stress distribution within the matrix and consequently strain localization which emerges as shear-bands of high plastic strains. That means the position influences the local stresses and therefore the phase transformation.

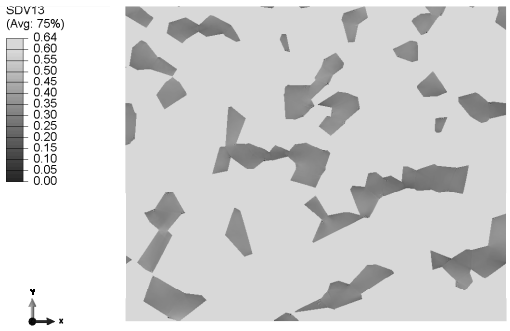

Fig. 5. **Distribution of martensite volume fraction after 10% deformation (uniaxial tension in x direction with homogeneous boundary conditions) by consideration of all contributions to the TRIP effect**

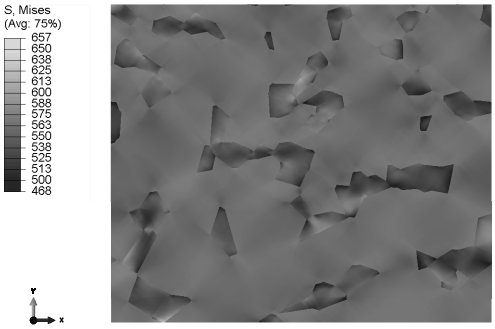

Fig. 6. **Stress distribution after 10% deformation (uniaxial tension in x direction with homogeneous boundary conditions) by consideration of all contributions to the TRIP effect**

In addition it can be seen that locations with high martensite contents have higher stresses due to their increased strength (see Fig. 6). This increased strength occurs suddenly because of a rapid phase transformation. During deformation, the phase transformation alters the stress distribution within the matrix and therefore changes the accumulation of plastic strain and damage which postpones the final failure. To investigate the influence of different contributions to the TRIP effect, some parameters in the model definition were set to zero (see Table I). In material A there is no consideration of the influence of stress triaxiality on phase transformation (see equation (*8*)). As already mentioned, the strain induced phase transformation assumes that martensite forms at the intersection of shear-bands. To investigate this effect the influence of stress triaxiality on shear-band formation was neglected in material B. In material C and D the Greenwood-Johnson effect was investigated, where material C assumes no shape change (see equation (*3*)) and material D allows no volume dilatation (see equation (*9*)) during martensite formation.

Material A and D show that stress-state independent martensitic formation and volume dilatation have a minor influence on phase transformation than the influence of stress state dependent shear-band formation and shape change (see Fig. 7). In comparison to all active mechanisms, the martensite fractions in material A, B and D are not as high as by consideration of all effects.

The neglecting of influence of stress-state on shear-band formation results in a significant lower martensite volume fraction. That means that the formation of shear-bands has a major importance for the TRIP effect. A shape-change free phase transformation results in much higher martensite content, because the matrix does not need to oppose a strong resistance against the lattice change.

Like in the previous results it can also be seen that high martensite volume fractions lead to higher local stresses due

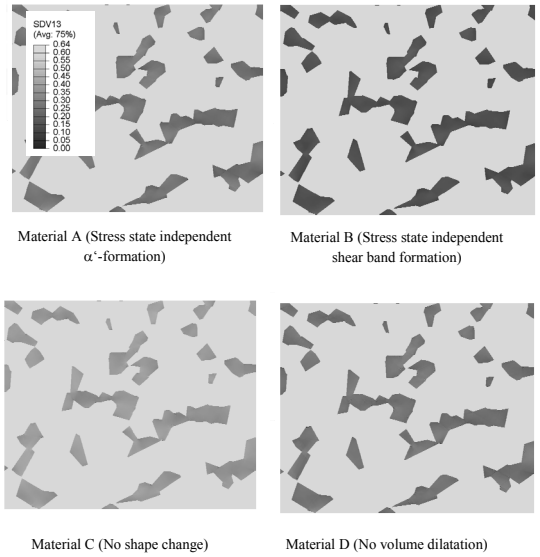

Fig. 7. **Martensite volume fractions in the different material models**

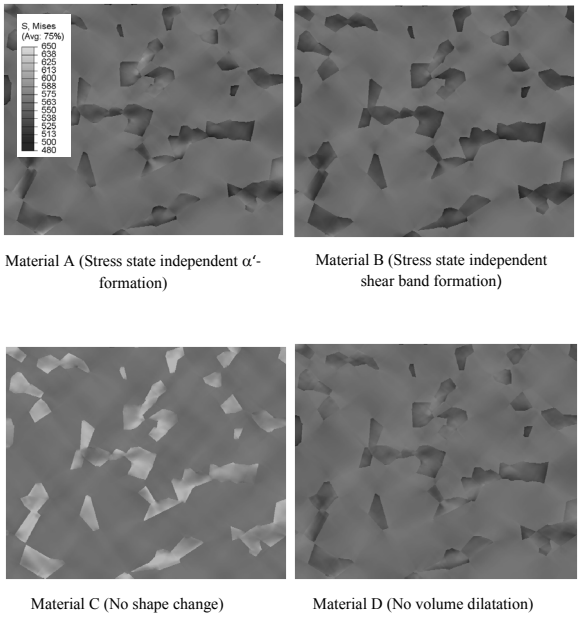

Fig. 8. **Von Mises stress distribution in the different material models**

to increased strength (see Fig. 8). A strong deviation of stress distribution within the grain gives a heterogeneous stress distribution within the matrix material.

5. Conclusion

The numerical investigations showed a strong influence of the morphology on the phase transformation. Therefore a local consideration of the microstructure is required. The probability of shear-band formation and the shapechange during transformation play a major role for the TRIP effect.

The partial transformation within the austenitic grains results in a heterogeneous distribution of the stress fields. Therefore the further increase in martensite content is influenced.

This research was carried out under the Project No. MC2.07293 in the framework of the Research Program of the Materials innovation institute M2i (http://www.m2i.nl).

The author wants to thank Piet Kok and Frank Korver (Tata steel) for the provision of the Voronoi cell generator. In addition he wants to acknowledge Robinson Sierra and James Nemes for providing the UMAT subroutine of the phase transformation law for the finite element package ABAQUS®.

REFERENCES

1. De Cooman B. C.: Current Opinion in Solid State and Mater. Sci. *8*, 285 (2004).
2. Olson G.B., Cohen M.: J. Less-Common Metals *28*, 107 (1972).
3. Iwamoto T., Tsuta T., Tomita Y.: Int. J. Mech. Sci. *40*, 173 (1998).
4. Sierra R., Nemes J.A. : Int. J. Mech. Sci. *50*, 649 (2008).

H. Quade, U. Prahl, and W. Bleck *(Department of Ferrous Metallurgy at RWTH Aachen University, Germany):*
Microstructure Based Hardening Model for Transformation Induced Plasticity (TRIP) Steels

A model is presented which takes the strain-induced martensite formation in low-alloyed TRIP steels into account. A parameter study is conducted to demonstrate the influence of individual mechanisms (e.g. volume dilatation). A correlation between martensite volume fraction and local stresses is depicted.

QUALITY EVALUATION OF RESISTANCE SPOT WELDS OF HOT-DIP GALVANIZED SHEETS IN CORROSIVE ENVIRONMENT

ĽUBOŠ KAŠČÁK[a]*, JANETTE BREZINOVÁ[a], MAROŠ HALAMA[b], and JÁN VIŇÁŠ[a]

[a] *Technical University of Košice, Faculty of Mechanical Engineering, Department of Technology and Materials, Mäsiarska 74, 040 01 Košice,* [b] *Technical University of Košice, Faculty of Metallurgy, Department of Materials Science, Slovakia*
lubos.kascak@tuke.sk

Keywords: spot welding, tensile strength, microhardness, corrosion potential

1. Introduction

Significant contribution to rapid development of the automotive industry is provided by continuous improvement of quality and performance parameters of produced vehicles. One of the important requirements for materials used for vehicles is their corrosion resistance, which leads to the increasing share of the automobile parts with protective, especially zinc coatings[1,2]. Galvanized sheet produced by zinc electrolyzing or dipping shows very good resistance to atmospheric corrosion. Surface treatment by galvanizing ensures good corrosion resistance of metal chassis and allows producers to offer more than 10 year life guarantee of the chassis[3,4]. However, this type of surface treatment causes considerable problems for joining metal chassis. Conventional methods (MIG welding, resistance spot welding), but also unconventional methods (laser welding) lead to evaporation of protective layers near weld due to the heat and loss of the corrosion resistance of the welded parts[3].

The aim of the contribution is to analyse quality of welds on galvanized sheets and their corrosive properties. Protective efficiency of zinc coatings for automobile sheets was evaluated, based on the determination of their electrochemical characteristics in passivated and non-passivated state, as well as their corrosion resistance in simulated corrosion environments.

2. Materials and methods

Following materials were investigated:
1) sample A: DX54D+Z
– sheet thickness 0.70 mm; zinc coated 140 g m^{-2}
– surface treatment: non-passivated
– use: for exterior body panels for cars – DACIA LOGAN – roof

2) sample B: DX54D+Z
– sheet thickness: 0.70 mm; zinc coated 140 g m^{-2}
– surface treatment: passivated Cr3+
– use: for exterior body panels for cars – DACIA LOGAN – doors

Test samples were cut to size 90 × 40 mm according to STN EN 051 122, length of lapping was 30 mm. Spot welding was carried out on pneumatic spot-welder BPK 20 with welding electrodes CuCr with 5 mm diameter. Selection of the welding parameters was based on the recommendations of British Standard (BS 1140) for spot welding of coated sheets and knowledge of weld growth mechanism[5]. However, the correction of the parameters was necessary, for the specific spot-welder. Welding parameters were: contact force Fz =2.6 kN, welding time t = 14 periods, welding current 85 kA (ref.[1,2]). Tensile tests according to STN 05 1122 were used for the evaluation of mechanical properties of spot welds before and after the exposure to the corrosive environments. The test of spots and full penetration welded joints were carried out on a test machine TIRA-test 2300, (VEB TIW Rauenstein).

The samples for microhardness evaluation were prepared according to ISO 6507-1 and ISO 6507-2. Microhardness on the cross scratch patterns was measured according to STN EN 1043-2 for hardness evaluation of particular areas of the weld and its transient phases.

The tests were carried out on Shimadzu Bubo microhardness tester with indenter Vickers under a load of 0.01 kN. Intender load time was 10 s.

The microhardness was measured on cross scratch patterns according to scheme in Fig. 1. Three measurements were carried out: in the base material, heat affected zone and weld metal in DX54D+Z.

Welds were exposed to salty environment of 5% NaCl solution and ecological solution Solmag used during winter season on roads. The above environments simulated conditions of vehicle operation[6–8]. Gravimetric method was used for the evaluation of the corrosion processes. Potentiodynamic polarization curves were measured for determination of the electrochemical characteristics of these materials. The values of Ek – corrosion potential by Tafel, Ik – corrosion current density and Rp – polarization resistance were measured. Electrochemical characteristics of the tested samples were evaluated before exposure to the corrosive environment and after 240, 480 and 720 hrs of exposure according to Tafel and Stern method. A computer-controlled potentiostat/galvanostat VOLTALAB 21 PGP201 (producer Radiometer Analytical, Denmark) with software VOLTAMASTER 4 was used for potentiodynamic measurement; a schematic diagram of appa-

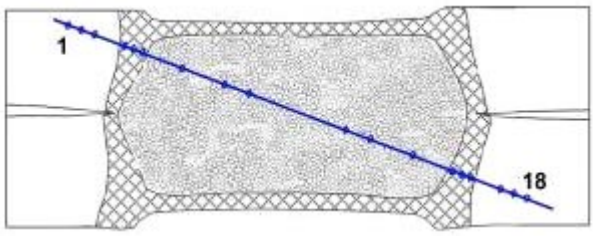

Fig. 1. **Hardness measurement process**[1]

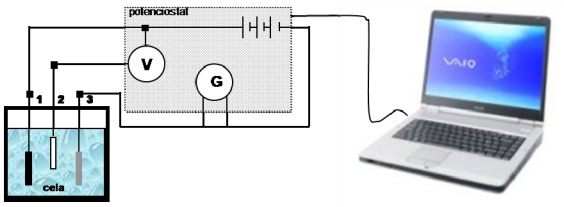

Fig. 2. **Scheme of measurement of base corrosion characteristic with linear voltammetry method;** V – voltmeter, G – ammeter, 1 – sample, 2 – SCE – saturated calomel electrode, 3 – Pt – auxiliary electrode

ratus in three-electrode configuration is in Fig. 2. Scanning electron microscope JEOL JSM - 7000F was used for microscopic observations.

3. Results

Fig. 3 shows that the force determining the strength of spot welds before their exposure to the corrosive environments was ~ 11 % higher in material B in passivated state than in the case A in nonpassivated state. Both materials were exposed to the corrosive environment of 5% NaCl solution, after which increased carrying capacity of welds was observed in material B (passivated state). When the values of F_{max} before and after the exposure to the corrosive environment are compared, strength increase was found in for both types of spot-welds (for samples A by ±0.45 %, and samples B by ±5.1 %). Both materials were exposed to the corrosive environment of ecological solution Solmag, after which increased carrying capacity of welds was observed in material B (passivated state).

Fig. 4 shows the macrostructure of the cross-section of the weld. No signs of defects and, heat affected areas and local flashing of the Zn layer in the contact place of welding electrodes can be seen.

Fig. 5 illustrates the formation of the zinc corrosion products on the surface of the test samples after the corrosion tests in NaCl environments. It is possible to observe white zinc hydroxide, products of corrosion, which was confirmed by EDX analysis.

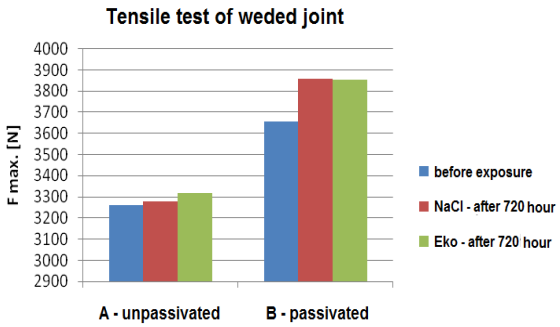

Fig. 3. **Average values of maximum strenght of A and B samples**

Fig. 4. **Macrostructure of the cross section of the weld**

The factors causing formation of white corrosion on zinc layer are condensation of air moisture, and the effect of the electrolyte.

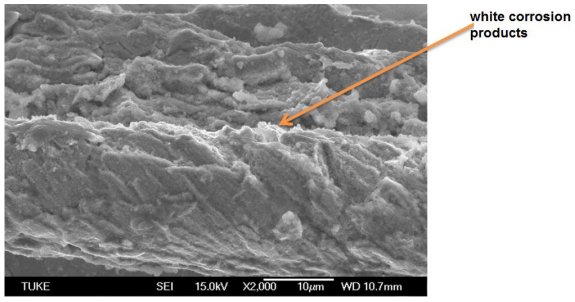

Fig. 5. **SEM of Zn layer on sample surface after corrosion test**

The measured values of microhardness are represented in Fig.6.

The measurements show that changes in parameters of resistance spot welding do not cause significant microhardness changes in the weld metal or heat affected zone of DX54D+Z steel.

Agresive environment does not influence microhardness of welds.

Galvanized sheet behaves like a galvanic cell when the moisture is present, where zinc layer with lower electric potential is the anode and steel represents the cathode. Oxygen is very important factor in the atmospheric corrosion because

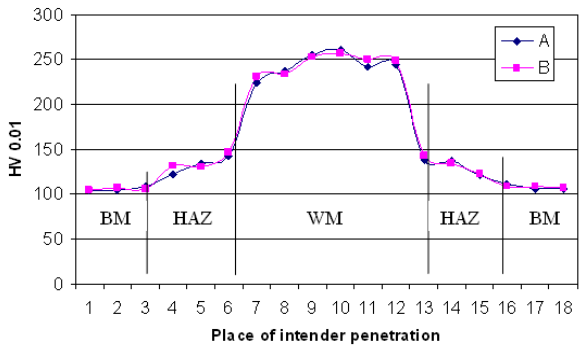

Fig. 6. **Microhardness profile in materials A and B;** BM – base material, HAZ – heat affected zone, WM – weld metal

the thin layers of moisture act as diffusion barriers into the condensed moisture[9]. Therefore, reaching the dew point is not necessary for the electrochemical reaction. As a result, very thin layer of electrolyte solution (0.005 to 0.15 mm) forms on a metal surface already at a low humidity (corrosion humidity ~ 60 %).

When the samples were exposed to the environment of 5% NaCl solution for up to 240 hours, their weight increased due to formation of corrosion products, mainly zinc. However, when the exposure of samples to chloride environment exceeded 240 hours, there was a significant weight loss of zinc coating, caused by release of corrosion products into the electrolyte. The protective efficiency of zinc coating is significantly reduced in the aggressive environment. The comparison of weight losses of A and B samples in 5% NaCl solution showed a difference of 53.66 %, Fig. 7. It indicates that the passivated samples are more resistant to mass loss than non-passivated in 5% NaCl solution.

When the samples were exposed to the environment of the ecological solution Solmag, their weight did not significantly change during the time of exposure. The potentiodynamic polarization curves of the samples measured in both states (non-passivated and passivated surface) evaluated by Tafel method are shown in Fig. 8.

Non-passivated zinc-coated sheet (A) and passivated zinc-coated sheet (B) in 5% NaCl solution after 720 hours exposure show the same corrosion current densities Jk, i.e. passivation is effective only in the early phase of exposure, Fig. 8.

The influence of chloride corrosive environment on galvanized sheets is so intense, that after several tens of hours‘ exposure there is no significant difference between passivated and non-passivated surface in zinc-coated steel sheet.

An interesting phenomenon occured between 240 to 480 hours of passivated zinc-coated steel‘s exposure in non-aggressive environment, when the corrosion products show a high polarization resistance Rp to corrosion current flow (1.2–1.6 MΩ; see Fig. 9). However, after 720 hours of exposure, this passive layer is damaged even in low-aggressive environment and the “run-off” effect of zinc (emmissions of Zn into the environment) predominates.

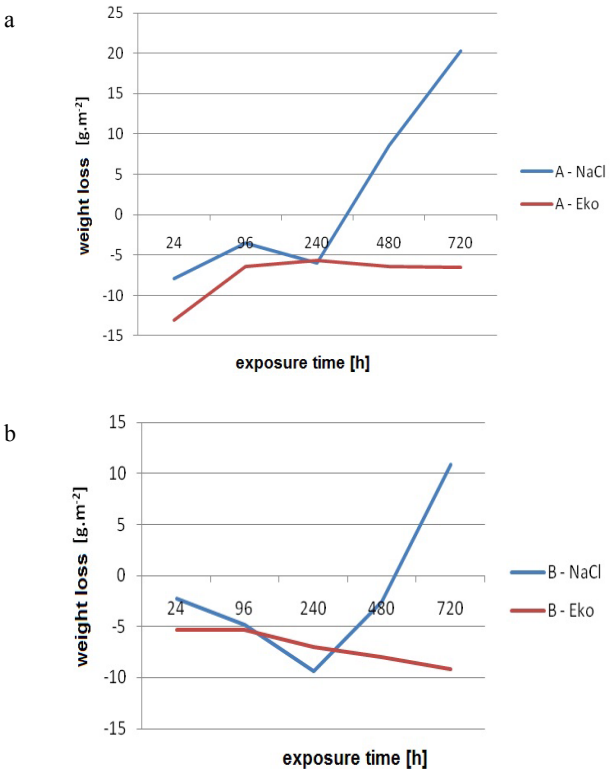

Fig. 7. **Weight loss in corrosion enviroments;** a) material A; b) material B

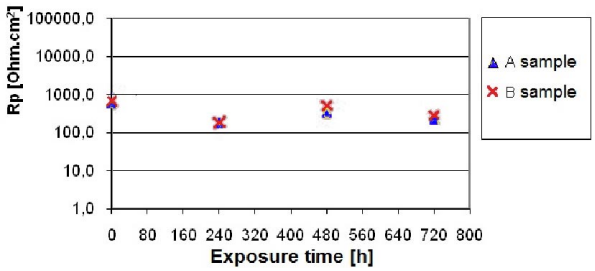

Fig. 9. **Stern method for determination of Rp**

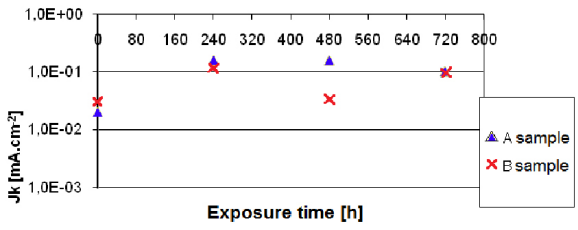

Fig. 8. **Tafel method for determination of Jk**

4. Conclusion

Welds on passivated sheets have higher carrying capacity in their initial state than the welds on non-passivated sheets. After exposure of samples to both corrosive environments the welds on passivated samples have higher carrying capacity. This increase is caused by zinc corrosion products, which, despite their low adhesion to the substrate, increase the strength of welds.

The measured values of microhardness shown in Table 5 are in accordance with the observed microstructures and their components. The maximum values were measured in the sample in WM (261 HV 0,01). This value corresponds to

microhardness of a dominant beintic compound in the weld metal. The change of microhardness in the weld metal was continuous and it corresponded to mixing the weld metal of particular types of steel.

Microscopic analysis proved high-quality of welds, which also showed that optimum technological parameters of welding were used. Local flashing of zinc layer was observed in the contact place of welding electrodes. After exposure of samples to corrosive environments, zinc corrosion products, so-called "white corrosion", formed, as a result of condensation of air moisture or effect of the electrolyte.

The weight of samples exposed to ecological solution Solmag during corrosion tests increases in consequence of accrued zinc corrosion products, and the corrosion process is slower than when exposed to NaCl solution. In the relatively aggressive corrosive environment of NaCl there occurs significant weight loss. The potentiodynamic electrochemical measurements show that both types of sheets have the same corrosion current densities after 720 hours of exposure. That indicates that passivation is useful only in the early phase of exposure of materials to corrosive environment. Corrosion products with a high polarization resistance Rp form on the surface of the passivated samples, keeping their favorable properties up to approximately 500 hours of exposure to corrosive environment.

The contribution was elaborated within the Research Projects VEGA No. 1/0206/08 and No. 1/0510/10.

REFERENCES

1. Viňáš J., Kaščák Ľ.: Transfer inovácií *8*, 112 (2005).
2. Kaščák Ľ., Viňáš J.: Scientific Papers of University of Rzeszow *273*, 127 (2010).
3. Zhang H., Senkara J.: *Resistance Welding: Fundamentals and Applications*, Taylor&Francis Group, New York 2006.
4. Tumuluru D. M.: Welding J. *86*, 161 (2007).
5. Harlin N., Jones T. B., Parker J. D.: J. Mater. Proces. Technol. *143-144*, 448 (2003).
6. Aslanlar S.: Mater. Design *27*, 125 (2006).
7. Mabbutt S. et al.: Progres in Organic Coatings *59*, 192 (2007).
8. Chang B. H., Shi Y. W., Dong J.: Welding Res. Supplement, *1999*, 275.
9. Šulek M.: *Diplomová práca*, Technická univerzita. Košice 2010.

Ľ. Kaščák, J. Brezinová, M. Halama, and J. Viňáš, *(Technical University of Košice, Faculty of Mechanical Engineering, Department of Technology and Materials, Slovakia):*
Quality Evaluation of Resistance Spot Welds of Hot-Dip Galvanized Sheets in Corrosive Environment

The contribution dealt with the evaluation of quality of resistance spot welds. Steel sheets of DX54D+Z were used for experiments. Welds on passivated sheets have higher carrying capacity in their initial state than the welds on non-passivated sheets. This increase is caused by zinc corrosion products, which increase the strength of welds. The weight of samples exposed to ecological solution Solmag during corrosion tests increases in consequence of accrued zinc corrosion products, and the corrosion process is slower than when exposed to NaCl solution. Both types of sheets have the same corrosion current densities after 720 hours of exposure.

THERMAL EFFECTS ON STEELS AT DIFFERENT METHODS OF SEPARATION

DAVID MAŇAS, MIROSLAV MAŇAS, MICHAL STANĚK, ŠTEPÁN ŠANDA, and VLADIMÍR PATA

Tomas Bata University in Zlin , nam. T.G.Masaryka 5555, 760 01 Zlin, Czech Republic
dmanas@ft.utb.cz

Keywords: microhardness, plasma cutting, laser cutting, flame cutting, Vickers hardness

1. Intruduction

As regards material separation methods, more sophisticated and effective methods are used today beside the classical ones. The new everyday development and changes of modern electronic technology and machine tool engineering brings new generations of many different products. Global development of these methods plays a vital role in the industrial process.

The cutting of material is usually the first operation that has to be done when producing some component. There are different types and methods of steel cutting. The most common methods of material splitting are cutting by water jet, laser, plasma and flame. In some cases, the heat caused by cutting influences the outer layers of the processed material.

Among two other common methods of cutting there are cutting by tools with defined geometry and abrasive processing – such as grinding or sanding. Some progressive methods could be also applied using physical, electrical and chemical processes as well as other sources of energy for removal of the material.

All these methods of material splitting force us to explore their impact to the qualities of cut material, especially to the layer that is in direct contact with the cutting tool. Learning about changes in structure and qualities of processed materials could assist in development of material separation and processing technologies.

1.1. Testing of micro-hardness

Development of hardness measurement methods for individual structural parts – measurement of micro-hardness – was an important requirement for studying the structure of solids. Micro-hardness testing devices are inbuilt in metallographic microscopes or they are used as stand-alone devices[1].

Measurement of micro-hardness is done by pushing of the diamond body, shaped in Vickers or Knoop pyramid, into the surface of measured body by forces ranged from 1 g (0,009807 N) to 1000 g (9,807 N). While common testing of (macro) hardness according to Vickers is done by means of load of 10 N to 1200 N, the forces weaker than 10 N were used first in 1932, when such testing was done at the National Physical Laboratory in UK.

The accuracy of measurement is lower as the applied forces are weaker (smaller size of the dint). Moreover, as the load force weakens and enters the area of micro-hardness, the Vickers hardness is no more depending on the power of applied load (unlike in macro-hardness that is measured according to geometric similarity of individual dints)[1].

1.2. Micro-hardness according to Vickers

Test of hardness according to Vickers is prescribed by European standard ČSN EN ISO 6507-1, for three different areas of testing load (Tab. I)[1].

Table I
Hardness according to Vickers – areas of testing load for metals

Area of testing load F [N]	Symbol of hardness	Previous marking (ISO 6507-1:1982)
$F \geq 49{,}03$	≥ HV 5	Test of hardness according to Vickers
$1{,}961 \leq F < 49{,}03$	0,2 to < HV 5	Test of hardness according to Vickers with low load
$0{,}09807 \leq F < 1{,}961$	HV 0,01 to < HV 0,2	Test of micro-hardness according to Vickers

The penetrating body – made of diamond shaped as a regular tetragonal pyramid with the square base and with preset vertex angle (136°) between opposite walls – is pushed against the surface of testing body[1,2]. Then, the diagonal size of the dint left after load removal is measured (Fig. 1).

$$F = 0{,}1891 \times \left(F / d^2\right) \qquad (1)$$

where F – Testing load in N, d – Arithmetic average of two diagonals d_1, d_2 in mm.

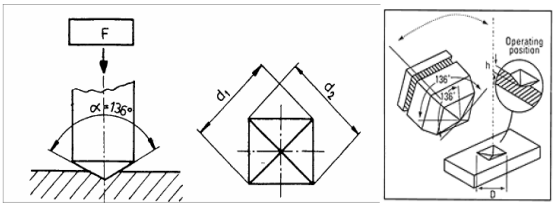

Fig. 1. **The basic principle of hardness testing according to Vickers**

Vickers´ hardness is then expressed as the ratio of the testing load applied to dint area in form of regular tetragonal pyramid with square base and the vertex angle equal to the angle of penetrating body (136°).

Hardness measurement by applying low load and testing of micro-hardness require exact measuring of dint diagonals. Evaluated testing sample has to have smooth and even surface, without flakes, lubricants and foreign particles. Evaluated sample is thus prepared as a metallographic scratch pattern, i.e. no deformation or thermal influence to the surface must occur. Generally, the preparation is done by wet grinding and then by polishing on diamond pastes or by electro-polishing. Exact method of sample preparation is chosen according to respective materials.

Thickness of testing body or layer has to be at least 1,5 times longer than the diagonal length of the dint[1,2].

2. Experimental part

There were three methods of material cutting selected in the experimental part. All three methods have a thermal impact to the outer layer. Steel 11373 was selected for testing of thermal influence in the cutting area. The testing samples were made by using the technology of cutting by laser, plasma and flame. The sample preparation was done in companies specialized to these technologies of material cutting[2].

2.1. Micro-hardness testing according to Vickers

A device used for micro-hardness testing is called micro -hardness tester.

The modern digital device can measure d_1 as well as d_2 dimensions directly in digital form; then a computer computes the average of d_1 and d_2, which is followed by HV computing and further data processing, so that different needs are met. At the same time, the whole micro-hardness testing process is controlled digitally so that highly effective and exact measurement can be obtained.

Fig. 2. **Micro-hardness tester with computer**

Table II
Chemical composure of steel 11373

Steel label	Chemical composure [%]		
	C	P	S
ČSN 11373	0,17	0,045	0,045

Table III
Measurement conditions

Sample material	Steel 11373
Load	200 g (HV 0,2 F=1,961N)
Load time	10 s

Micro-hardness testing of structural components and phases is one of the most important tools used in metallographic industry. By means of micro-hardness testing, individual structural components could be identified relatively exactly, such as lower and upper bainit, lowly and highly carbonated martenzit etc.

The measurement is done by means of digital micro-hardness tester DM 2D from AFFRI (Fig. 2). Measurement conditions are stated in the Tab. III above. The tester is able to measure the hardness according to Vickers as well as according to Knoop. An inbuilt 16bit monolithic high-power microprocessor equipped by photomechanical software was used. Its power can be fully adjusted according to the needs of micro-hardness testing in new century[2–6].

2.2. Sample preparation

As the sample surface must have a metallic shine and the surface roughness must not excess Ra 0.2, the sample preparation is very important step. In general, the sample could be fixed in a gripping or set into spaces and after grinding by soft grindstone, the sample has to be sanded by metallographic sand papers of different numbers so that the dint could be clearly seen[3–6].

2.3. Laser

Testing samples were made by means of TRUMPF laser. The power used for preparation of the testing sample was 2400 W amd pressure 0,6 bar. The temperature in controlled cutting process reaches up to 10^6 °C, (cutting speed was 2,7 m min^{-1}). Maximum power of respective laser is 5 KW with accuracy of 0,1 mm.

The original structure of measured sample was a pearlitic one, respectively ferrite-pearlitic, with hardness ranging from 170 HV to 180 HV. Cutting by laser has a thermal impact on the original pearlitic structure and changes it to bainitic structure. The change is caused by great difference in temperature between the cutting area and the surrounding environment. The temperature in the cutting area is approximately 106 °C. The standard temperature of the surrounding environment is 22 °C, which causes very quick cooling creating the non-equilibrium state (hardening) in the cutting area and thus creating the structure of bainit. The measured hardness value in the cutting area was approximately 340 HV (Fig. 3) that corresponds to structure of upper bainit. Due to the characteristics of the tested material (11373), especially due to its low contain of carbon (0,17 %), lower values of

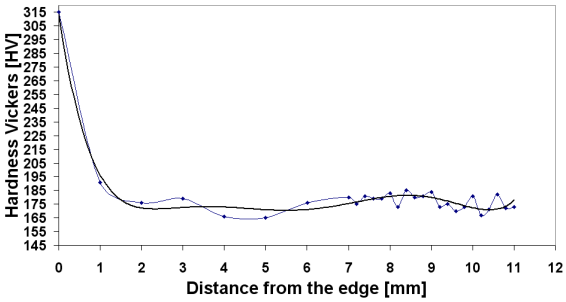

Fig. 3. **Change of micro-hardness** (cutting by laser)

hardness can be expected. The measured values show that the depth of the influenced layer is up to 1–1,5 mm. The changes of hardness are insignificant in greater distance from the cutting line (Fig. 3).

2.4. Flame

The original structure of measured sample was pearlitic, respectively ferrite-pearlitic, with hardness ranging from 160 HV to 165 HV. Cutting by flame creates the temperature of 3000 °C with accuracy of 0,5–1 mm. Environment temperature was 22 °C. The temperature difference between the cutting area and its surrounding environment is not high enough to have an impact on nearest environment around the cutting line. The cutting is followed by cooling process on open air, thus lowering the cooling speed. This enables the creation an equilibrium state of coarse-grained pearlitic structure with globular cementite. Baling of cementite is caused by the surface tension. This change in structure causes decrease in hardness to value of 165 HV as seen in Fig. 4.

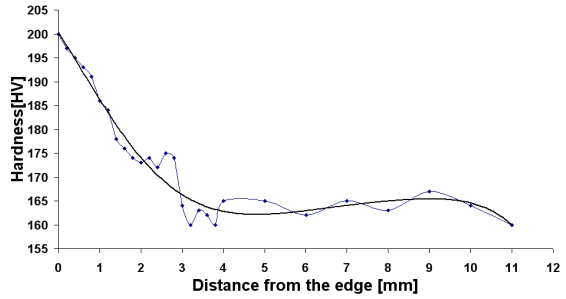

Fig. 4. **Change of micro-hardness (cutting by flame)**

2.5 Plasma

Plasmatic torch is a device for creating highly heated gaseous stream of ions and electrons (plasma). This jet stream is heated to very high temperature (over 30.000 °C) by arc discharge and it streams in high speed from a narrow jet. The plasma ray can be deflected by means of magnetic field and accelerated by means of electric field. The splitting of testing material was done by means of higher (30.000 °C) and lower temperature (20.000 °C).

Cutting by plasma creates the temperature about 30.000 °C in the cutting area and generator was used 100 A, Ar/H_2. Environment temperature was 22 °C. Despite the great difference between the temperatures in the cutting area and the surrounding environment, no significant changes on the surface layer around the incision line have occurred. This could be caused by very low content of carbon (0,17 %) and by slower speed of cooling that has not reached the critical speed and thus a non-equilibrium state (hardening) was not reached. On the opposite side, the lower speed of cooling occurred causing the creation of very fine pearlitic structure with hardness around 255 HV. Micro-hardness values could be seen in Fig. 5.

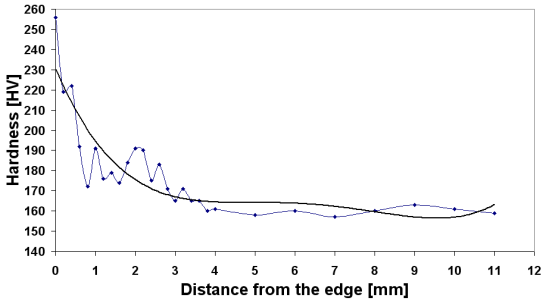

Fig. 5. **Change of micro-hardness** (cutting by plasma, 30 000 °C)

The original structure of measured sample was pearlitic respectively ferrite-pearlitic with hardness ranging from 170 HV to 180 HV (Fig. 6) while cutting by plasma at temperature of 20.000 °C. Cutting by plasma creates the temperature about 20.000 °C in the cutting area. The cutting was performed by means of the torch pictured in Fig. 6. Environment temperature was 22 °C. As in the previous cutting method by plasma, despite the great difference between the temperatures in the cutting area and the surrounding environment, no significant changes on the surface layer around the incision line has occurred. This was probably caused by slower cooling when the final structure was created in a very fine pearlitic structure with hardness of around 230 HV (Fig. 6). In case of

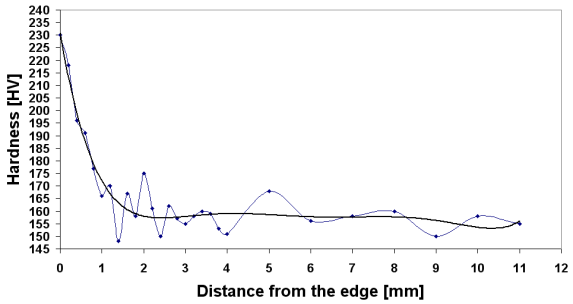

Fig. 6. **Change of micro-hardness** (plasma cutting, 20 000 °C)

slightest speeding up of the cooling, the speed of cooling would reach the critical value and thus the process would create a non-equilibrium structure (bainit). By applying the lower temperature in the cutting line, the slight decrease of hardness occurred as could be seen in Fig. 6.

3. Conclusion

This work is focused mainly on issues connected with using of different methods of thermal material cutting and their impact to the surface layers. Three basic types of cutting were prepared. Laser cutting technology was used together with cutting by plasma and by flame. In cutting by plasma, two different cutting temperatures were applied, i.e. 30.000 ° C and 20.000 °C. Testing samples were sanded and then prepared to micro-hardness testing. The testing was done on Micro-hardness tester DM-2D. The measurement results were displayed in graphic and then evaluated.

The results show that testing bodies cut by laser shown the hardness of 340 HV. Maximum thickness of the layer influenced by cutting was 1−1,5 mm (plasma and flame 3 mm). Deeper layers were not influenced by cutting procedure and the hardness remained unchanged. In plasmatic cutting, the tested material was influenced by the cutting procedure only very slightly. The thickness of the influenced layer was almost the same as in laser cutting. The lowest micro-hardness values were shown in cutting by flame. The depth of influenced layer was more than three times greater than in cutting by laser or by plasma. This was caused especially by selected material containing only 0,17 % of carbon. Steels with such low carbon content are practically non-hardenable.

This article was written with support of Ministry of Industry of Czech Republic as a part of the project called Development of the system for evaluation of hardness testing with stress on the research of new possibilities of polymer material characteristics analysis and application of the results on the market FR-TI1/487.

REFERENCES

1. Doležal P., Pacal B.: *Hodnocení mikrotvrdosti struktur materiálů*. VUT, Brno 2000.
2. Staněk M., Maňas M., Maňas D., Sanda S.: Chem. Listy *103*, 91 (2009).
3. Staněk M., Maňas M., Maňas D.: Novel Trends in Rheology III, AIP, New York, USA, p. 75−85, (2009).
4. Staněk M.: *Plastics and Rubber XLVII. 5 – 6*, 142, (2010).
5. Zamfirova G., Dimitrova A.: Polym. Test. *19*, 533 (2000).
6. Bláhová O., Medlín R., Říha J.: *Conference proceeding Metal 2009, Ostrava*. p. 359. Tanger, 2009.

D. Maňas, M. Maňas, M. Staněk, S. Šanda, and V. Pata *(Tomas Bata University in Zlin, Zlin, Czech Republic):* **Thermal Effects on Steels at Different Methods of Separation**

The submitted article describes the effects of a thermal separation of material on the properties of the surface layers. The separation of material is an integral part of a preparation of all final products. During cutting the surface layer of the separated material is effected, which then has an influence on the sequence of the following operations. Three methods of thermal separation of material were selected for the experiment described in the article -a method of laser, plasma and flame cutting. The temperatures for plasma cutting were 30 000 °C and 20 000 °C. The material selected for these three methods was a common steel 11 373, which is industrially produced and processed. The effect on the material was shown by measuring micro-hardness using the micro-hardness tester DM 2D.

HARDNESS OF PLASMA NITRIDED LAYERS CREATED AT DIFFERENT CONDITIONS

ZDENĚK POKORNÝ[a]*, JAROMÍR KADLEC[a], VOJTĚCH HRUBÝ[a], MIROSLAV POSPÍCHAL[a], DUNG. Q. TRAN[a], TEREZA MRÁZKOVÁ[a], and LACSLO FECSO[b]

[a] Department of Mechanical Engineering, University of Defence, Brno, Czech Republic, [b] Department of Engineering, Miklós Zrynyi Defence University, Budapest, Hungary
pokorny.zdenek@centrum.cz

Keywords: plasma nitriding, cavity, nitrided layer, microhardness

1. Introduction

The plasma nitriding is a method of surface hardening using d.c. glow discharge to improve elemental nitrogen to the surface of steel with subsequent diffusion into the bulk of material[1]. Generally, two layers are created during plasma nitriding process. The compound layer is consisted of ε-$Fe_{2-3}N$ and γ-Fe_4N phases[2]. This type of layer has been very hard, but unfortunately brittle with good friction and anticorrosion properties[3]. The thickness and hardness of γ´-Fe_4N depends on quantity and quality of nitride-formed elements[4,5].

The composition of nitrided layers can be effectively influenced by chemical composition of nitriding atmosphere. The carbon alloy steels have been generally used in automobile industry for their high hardness and strength. Low corrosion resistance sometimes limits their industrial application. Plasma nitriding process is a chemical-heat treatment widely used to increase the surface hardness, fatigue strength, wear and corrosion resistance of steels[1–3]. Parameters of plasma nitriding layer are not dependent only on process parameters of nitriding, such as duration, temperature, pressure, voltage and nitrogen potential, but also dependent upon the substrate alloy type and in this case of selected alloy on their microstructure[6].

The aim of study was to research the creation of nitrided layer inside the cavity with the diameter of 6 and 8 mm at pressure 4 mbar. This study deals with mechanical properties of nitriding layers inside the cavities after plasma nitriding process.

2. Experimental

Bars of 32CrMoV12-10 steel in an untreated state were cylinder bored with diameters of 6 and 8 mm. The samples of length 500 mm were heat treated (HT) in accordance with Tab. I.

A microhardness of an untreated material of samples was 580 $HV_{0,05}$. Plasma nitriding was carried out on PN 60/60 RÜBIG appliance in accordance with following parameters from Tab. II. The charge was consisted of 2 cylindrical samples (cavities) which were plasma nitrided at the pressure of 4 mbar for 6 hours.

Table I
Temperatures of heat-treatment

Procedure	Temperature [°C]
Salt quenching	940
Salt tempering	650

Table II
Parameters of plasma nitriding process

Temperature [^oC]	500
Duration [h]	6
Gas flow H_2/N_2 [$l.min^{-1}$]	24/8
Bias [V]	530
Pressure [mbar]	4
Pulse length [μs]	100

After plasma nitriding process, the samples with the diameters of 6 and 8 mm were cut off. The length of the first sample was 30 mm, each other was 12 mm. The lengths of the samples were 30, 42, 54, 66, 78, 90, 102, 114, 126, 138, 150, 162, 174, 186, 198, 210, 222, 234, 246, 258 mm which is shown in Fig. 1. All samples were wet grounded using silicon carbide paper with grit from 80 down to 2000 and subsequently polished.

Glow discharge optical spectroscopy (GDOES) measurement was performed in the LECO SA-2000 optical emission spectroscopy analyser with argon glow discharge plasma excitation source and mentioned calibration of nitrogen: JK41-1N and NSC4A standards. The chemical composition of material was measured by GDOES/Bulk method and the nominal composition is displayed in Tab. III. The depth profile was evaluated by GDOES/QDP method and is shown in Fig. 2.

The microhardness was measured by Vickers microhardness method on the automatic microhardness tester LM 247 AT LECO at 50 g load and 10 s dwell time. The major Vickers microhardness numbers were derived from five measurements such an average value according to Fig. 3 and the result is displayed in Fig. 4.

Following equation was used for calculation of Nht thickness X (Eq. (*1*)) in accordance with DIN 50190

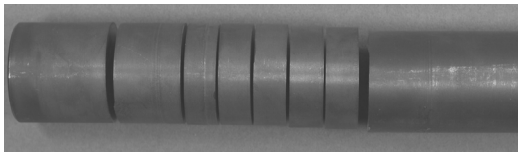

Fig. 1. **Image of cutting samples**

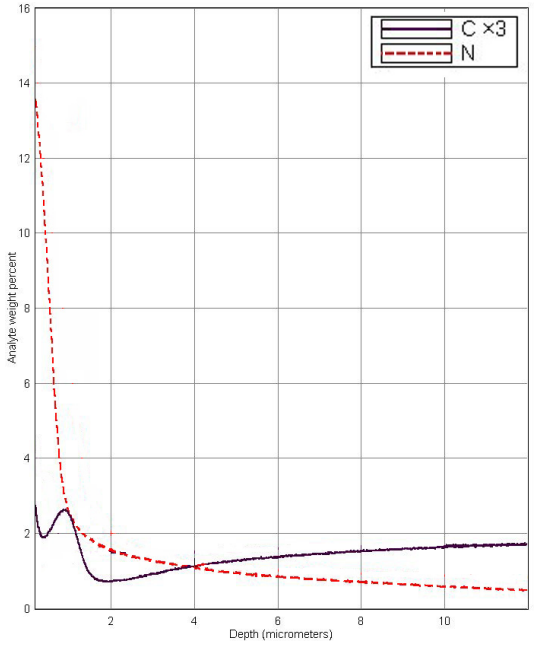

Fig. 2. **GDOES depth profile of plasma nitrided sample after 6 hours**

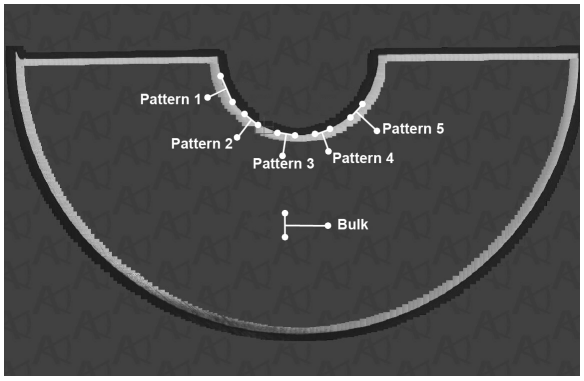

Fig. 3. **Image of measured specimen**

standard[8]:

$$X = [(Y * 0.1) * 10] + 50 \qquad (1)$$

where X is Nht thickness in mm, Y is the average microhardness number from five indentation´s patterns in HV 0.05 [kg].

Confocal laser microscope LEXT OLS 3000 with outstanding resolution of 0.12 µm and magnification range from 120× to 12400× was used for observation and cross-structure documentation and compound layer evaluation. Cross-section structure of chemical etched material is shown in Fig. 4.

Instrumental hardness measurements were carried out on a Zwick Universal testing machine with a hardness measurement head (Zwick ZHU 2.5). The initial head speed approaching the sample was 300 mm min^{-1}. After the head touched the sample, the approach speed of the diamond indenter until initial contact with the specimen was 50 mm min^{-1}. Indentations were made on the surface of sample. The tests were carried out at 100 N indenter loads. Working test force has been maintained for 12 s. The result values of universal hardness were calculated as an average value of 5 measurements.

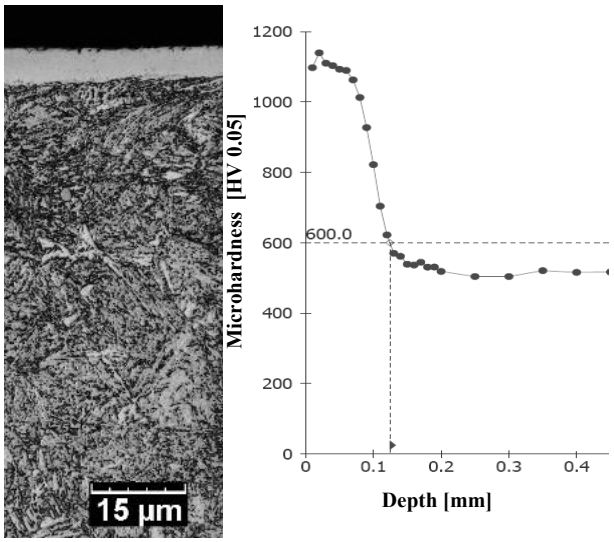

Fig. 4. **The chemically etched (by NITAL) confocal cross-sectional microstructure (diameter of 6 mm in length 30 mm) with microhardness depth profile of a plasma nitrided layer**

Table III
Chemical composition of 32CrMoV12-10 steel

C	Mn	Si	Cr	Mo	V	P	S
GDOES/Bulk							
0,30	0,47	0,25	2,95	0,89	0,28	0,002	0,001
DIN standard							
0,30	<	<	2,80	0,80	0,25	<	<
0,35	0,60	0,35	3,20	1,20	0,35	0,025	0,010

The universal hardness was evaluated automatically by software (TestXpert®) and was expressed as volume hardness[9]. Universal hardness was measured on HT nitrided and NHT nitrided samples (Fig. 5, 6).

Vickers indentor was used for indentation test. Following equation was used in calculating universal hardness HM (Eq. (*2*)).

$$HM = \frac{F_2}{f_{IT} * h_2} \qquad (2)$$

where HM is universal hardness in N mm^{-2}, F_2 force at the

point of load application after dwell time in N, f_{IT} is factor for indentor (26,43 for Vickers), h_2 is indentation depth at the maximum force in mm[9].

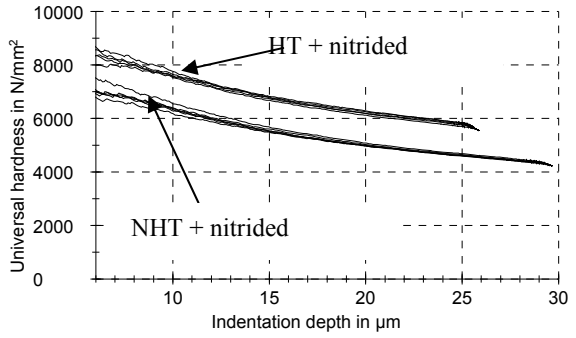

Fig. 5. **Universal hardness – depth graph for nitrided heat-treated surface and nitrided non heat-treated sample**

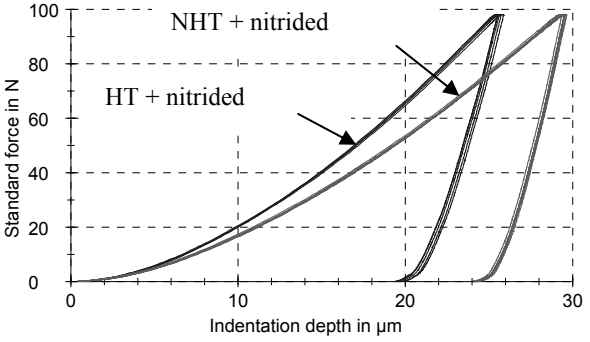

Fig. 6. **Loading and unloading behavior on heat-treated nitrided and no heat-treated plasma nitrided sample**

3. Results

Heat-treated samples with diameters of 6 and 8 mm, which were plasma nitrided at pressures of 4 mbar, were investigated and subsequently compared.

Microhardness of depth profiles of plasma nitrided layers confirmed the enhancement of microhardness more than 500 $HV_{0,05}$ which is shown in Fig. 4. Nht thickness of plasma nitrided layer was measured in accordance with DIN 50190 standard[8]. The samples with the diameter of 8 mm attained Nht thickness 0.10 mm in length 30 mm (Fig. 7). The values of Nht thickness irregularly decreased with increasing length of nitriding. Nht thickness was 0.02 mm in length 234 mm. In next sample, no nitrided layer was found.

In case of cavity with diameter of 6 mm, in length 30 mm the Nht thickness achieved 0.12 mm (Fig. 7).

The last value of Nht thickness of nitrided layer 0.04 mm was measured in length 138 mm.

Nitrided layer was lengthened from 138 (cavity 6 mm) to 234 mm (cavity 8 mm) in order to increasing of diameter (Fig. 7). The length of nitrided layer in cylindrical cavity is decreased with the decreasing diameter of cavity.

Evaluation of universal hardness measurement showed that plasma nitriding increase surfaces hardness of ferrous materials (Fig. 5, 6). Especially in Fig. 5, 6 are visible the changes of hardness of nitrided layers what is represented by higher depth of indentation. Also microhardness depth profiles (Fig. 4).

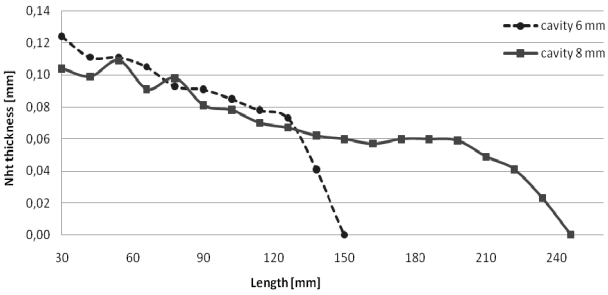

Fig. 7. **Nht thickness of various diameters after plasma nitriding process (pressure 4 mbar)**

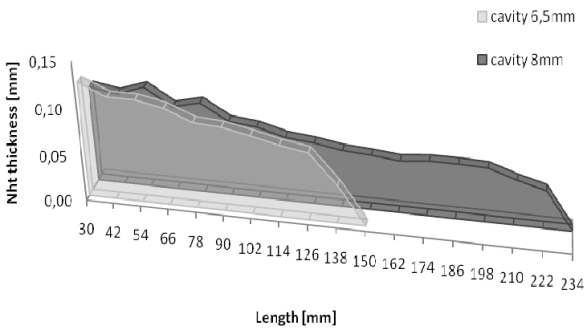

Fig. 8. **The diffusion profile of bored plasma nitrided samples**

4. Conclusion

After plasma nitriding process the nitrided layers were created. This layer consisted of compound layer and diffusion layer (Fig. 4).

The mechanical properties of created nitrided layer were researched and compared with no nitrided material. Experiments showed that plasma nitriding process increase the surface hardness about 100 % in case of material 32CrMoV12-10.

This fact is displayed in Fig. 4, 5, 6. The length of nitriding was 234 mm in case of cavity with diameter of 8 and 138 mm in case of cavity with diameter of 6 mm (Fig. 8).

Results of experiment show that diameter of cavity caused change of length of nitriding. It was proven that the diameter of cavity has remarkable influence on the plasma nitriding in length in accordance with Fig. 8. Peaks which

were established during plasma nitriding process concern of plasma density and content of nitrogen. Generally, thickness of compound layer, Nht thickness of diffusion layer and concentration of nitrogen are dependent each other.

Experiment showed that plasma nitriding process is applicable not only for flat surfaces but for cavities too. Much hardness layers are created in HT materials than in NHT materials (Fig. 5, 6). These created nitrided layers improve corrosion resistance and mechanical properties of steel.

The work was supported by a research project of the Ministry of Defence of the Czech Republic, project No. MO0FVT 0000404 and Specific research Modern materials in special technology.

REFERENCES

1. Akbari A., Mohammadzadeh R., Templier C., Riviere J. P.: Surf. Coat. Technol. *204*, 4114 (2010).
2. Joska Z., Kadlec J., et al.: Key Eng. Mater. *465*, 255 (2011).
3. Pokorny Z., Hruby V.: Key Eng. Mater. *465*, 267 (2011).
4. Pye D., v knize: *Practical nitriding and ferritic nitrocarburizing. 2nd. ed., Ohio: ASM International materials park, 2003. 256p.*
5. Kadlec J., Dvorak M.: Strength Mater. *40*, 118 (2008).
6. Jelinek M., Kocourek T., Kadlec J., Bulir, J.: Laser Phys. *10*, 1330 (2003).
7. Joska Z., Pospichal M., et al: Chem. Listy *104*, 322 (2010).
8. DIN 50190-4:1999, *Hardness depth of heat-treated parts - Part 4: Determination of the diffusion hardening depth and the diffusion depth.*
9. ČSN ISO 14577-1 *Kovové materiály – Instrumentovaná vnikací zkouška stanovení tvrdosti a materiálových parametrů – Část 1: Zkušební metoda* (*Metalic materials – Instrumected indentation test for hardness and materials parameters – Part 1: Test method*).

Z. Pokorný[a], J. Kadlec[a], V. Hrubý[a], M. Pospíchal[a], D. Q. Tran[a], T. Mrázková[a], and L. Fecso[b] *([a] Department of Mechanical Engineering, University of Defence, Brno, Czech Republic, [b] Department of Engineering, Miklós Zrynyi University of Defence, Budapest, Hungary):* **Hardness of Plasma Nitrided Layers Created at Different Conditions**

The nitriding behaviour of heat-treated alloyed carbon steel was carried out on two cylinders samples with different diameters. The influence of microstructure and nitriding conditions on the thickness and hardness of nitrided layer were investigated. Prior to nitriding, cylinders samples were quenched and tempered. Plasma nitriding was performed at 500 °C for 6 hours with mixture of H_2 and N_2 in plasma nitriding furnace. Structure and mechanical properties of nitrided layers were characterized using optical spectrometry, optical microscopy and microhardness testing. Plasma nitriding process increased the surface hardness of samples by 100 %. The nitrided depth was also estimated using cross-sectional microhardness profiles. The results show that plasma nitriding creates a nitrided layer consisting of compound layer and nitrogen diffusion layer.

MICROFRACTOGRAPHY OF FISH-EYE FRACTURES IN NITRIDED STEEL

KAREL SLÁMEČKA*, JAROSLAV POKLUDA, KATEŘINA BONAVENTUROVÁ, and LADISLAV ČELKO

Brno University of Technology, Faculty of Mechanical Engineering, Technická 2, 616 69 Brno, Czech Republic
slamecka@fme.vutbr.cz

Keywords: Fractography, fish-eye cracks, bending-torsion fatigue, striations, nitrided steel

1. Introduction

Nitriding is important industrial technology that is used to improve key properties of engineering components, especially the surface hardness, the fatigue strength and the wear and corrosion resistance[1-5]. The procedure is characterized by adsorption of nitrogen and its subsequent diffusion into the material bulk resulting in the formation of a thin brittle compound layer (the so-called white layer) and a subsurface diffusion zone harbouring a compressive residual stress field caused by the lattice distorsion. Due to the enhanced strength of the nitrided layer and restrained moveability of dislocations within the diffusion zone, the subsurface crack initiation and growth in the form of the so-called fish-eye crack is the predominant failure mechanism, usually in both the high-cycle fatigue (HCF) and the low-cycle fatigue (LCF) region. Analogous fracture behaviour has been reported for other surface hardening procedures, such as carburization or shot peening[6,7]. Moreover, fish-eye crack is a typical feature of gigacycle fatigue (GCF), where the transition of failure initiation from surface into the interior is connected with a significant change in the slope of the S-N curve[8-10].

In general, the fish-eye crack initiation is associated with an interior defect in the material. Most frequently, the crack initiates on the internal inclusion, usually by decohesion of the inclusion-matrix interface. The fish-eye crack looks bright to the naked eye or in the optical microscope, whereas the region outside seems to be grey. The difference in colour is, most probably, caused by the change of the growth micromechanism from the fatigue crack propagation in the near vacuum to the environmentally assisted growth when the crack front approaches the low-toughness nitrided layer and causes its breaking[3]. In the GCF domain, the dark area (often termed 'optically dark area' or 'fine granular area') usually exists in the centre, inside which the crack initiation site is located. Some authors attribute its origin to the microscale fatigue fracture caused by cyclic stress coupled with the internal hydrogen trapped by the inclusion, although the controversy still exists in this matter[9].

The question concerning the time span of the fish-eye crack initiation period in the GCF region has been tackled by several researches. The results of the deterministic model based on the Paris-Hertzberg-McClintock crack growth rate[10,11], which have been recently experimentally confirmed by the infrared pyrometry measurements[12], showed that the propagation stage of the crack constitutes only a small part of the total fatigue lifetime. In this paper, after a brief summary of main results of study on biaxial fatigue of nitrided steel, the microfractography is used to analyse the fish-eye crack propagation mechanism and also to address the above mentioned question in the HCF domain by extrapolating the local crack growth rate curve to the overall fish-eye crack region.

2. Experimental details

The fatigue experiments were carried out on cylindrical specimens made of plasma nitrided high-strength low-alloy Cr-Al-Mo steel (equivalent to EN 37CrAlMo6). The chemical composition (wt.%) of the base material was as follows: C: 0.357 %, Mn: 0.468 %, Cr: 1.49 %, Mo: 0.194 %, V: 0.01 %, Cu: 0.072 %, Al: 1.4 %, W: 0.032 %, Si: 0.292 %, P: 0.006 %, S: 0.006 %, Fe: balance. Specimens were annealed (920 °C, 25 min, air), quenched (930 °C, 25 min, oil) and tempered (650 °C, 25 min, air). The micropulse plasma nitriding was applied in two steps: cleaning (510 °C, 30 min) and nitriding (515 °C, 8 hours). The procedure resulted in yield strength σ_y = 870 MPa, ultimate tensile strength σ_u = 1020 MPa, and in the depth of the diffusion layer $h_{dl} \approx 200$ μm and the thickness of the white layer $h_{wl} \approx 3$ μm. The microstructure of the nitrided layer and the core region is presented in Fig. 1, the inclusions within the material observed in the light and dark field are shown as Fig. 2.

Fatigue experiments were carried out on the testing stand MZGS-200. Sinusoidal symmetrical bending (5 specimens), torsion (3 specimens) and synchronous in-phase bending-torsion loading (15 specimens) were applied at a frequency f = 29 Hz. All specimens were fractured in the HCF domain with the number of cycles to failure, N_f, in the range of $(2.0\times10^5;\ 6.1\times10^6)$ cycles. The results of extended experi-

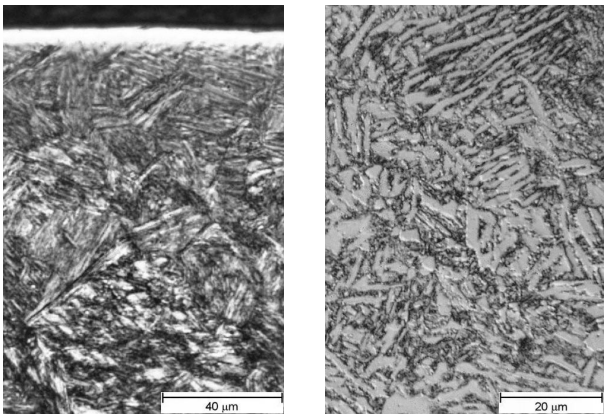

Fig. 1. **Microstructure of the the nitrided layer (left) and the base material in the core (right)**

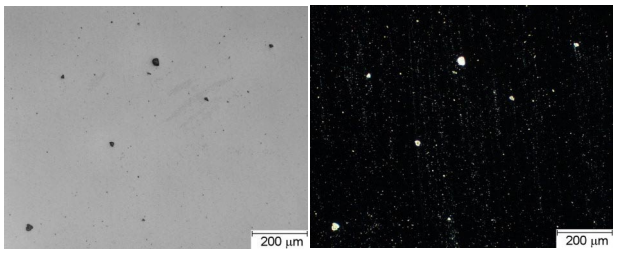

Fig. 2. **Inclusions within the material observed in the bright and dark field**

mental investigation of the influence of nitriding on the fatigue life under biaxial fatigue loading and also under the conventional push-pull loading of different *R*-ratios were presented elsewhere[5]. Sufficient to note here that for all loading regimes the micropulse plasma nitriding was found to increase the fatigue resistance by about 25 % in both LCF and HCF regions.

Examination of fracture surfaces was performed in the scanning electron microscope (SEM). The spatial geometry and morphology of the fish-eye cracks were also studied by means of the optical profilometry and stereophotogrammetry.

3. Results

Fractographical examination revealed that all specimens failed due to the internal fish-eye type of fracture. The initiation sites were always found at non-metallic inclusion located in the interior of the specimen. The average inclusion diameter was 37±14 μm and the distance of the centre of inclusion from the free specimen surface, *h*, was in the range of 420–1040 μm. The stages of the crack initiation, the crack propagation and the final fracture were usually well defined, as shown in SEM image in Fig. 3.

The studied fish-eye cracks were more or less of an elliptical shape. Carefull analysis has shown, however, that the crack growth towards the free surface was always at least

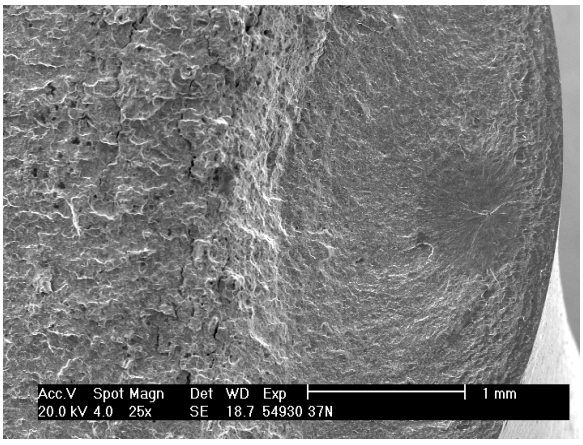

Fig. 3. **SEM macrophoto of the fish-eye crack in the specimen fractured under combined bending-torsion loading regime with the loading ratio z = 0.27 (σ_a = 850 MPa, τ_a = 310 MPa, N_f = 2.6×10^5 cycles)**

partially reduced due to the increasing residual compressive stresses[13]. This retardation effect was prominent especially for the fish-eye cracks initiated at inclusions in depths $h < 0.7$ mm.

The deflection of the fish-eye crack plane from the plane perpendicular to the specimen axis was almost negligible (less than 5°) in the radial direction. On the other hand, the inclination angle in the tangential direction, α_t, varied as a function of the loading ratio $z = \tau_a / (\sigma_a + \tau_a)$, where σ_a is the bending amplitude and τ_a is the torsion amplitude, Fig. 4. Despite the higher scatter of α_t for combined bending-torsion loading regimes, the crack front clearly tends to propagate under pure mode I loading.

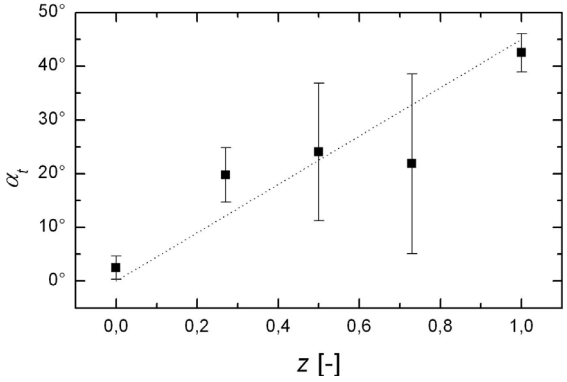

Fig. 4. **The inclination angle, α_t, as a function of the loading ratio, z**

An example of the local fracture topography is shown as Fig. 5, where fracture profiles intersecting the centre of the fish-eye crack from Fig. 3 in the tangential and radial directions are plotted. Nearly same values of the root mean square roughness, R_q, calculated as the standart deviation of residual *z*-coordinates show similarity between both directions.

The predominant role of mode I micromechanism has been confirmed by the presence of the striations field located in the immediate vicinity of the inclusion in the fish-eye centre, Fig. 6. The distinct striation pattern reveals a presence of a softer material near the inclusion, which could be created by a depletion of alloying elements and carbon due to their diffusion towards the incoherent inclusion/matrix interface. Very

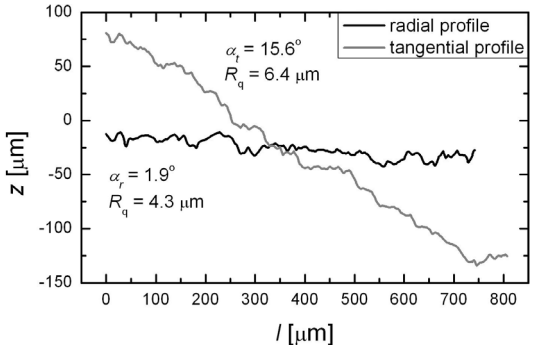

Fig. 5. **Radial and tangential fracture profiles intersecting the centre of the fish-eye crack from Fig. 3**

low striations spacing near the fish-eye centre (less than 100 nm) reveals a continuous crack front propagation even at very low crack growth rates.

Fig. 7 shows the plot of logarithm of the striations spacing, d, vs. the logarithm of the root square of the crack length, a. Note the reasonable linearity suggesting that data are in the Paris region. It is generally agreed that in this region the striations spacing (microscopic fatigue crack growth rate) corresponds to the macroscopic crack growth rate, da/dn, as exactly one striation is formed at each applied loading cycle[14]. This fact may be used in the estimation of the timespan of the crack growth period. Following assumptions are made:

(i) The crack grows into the specimen interior starting from the initial lentgth, a_i, which is equal to the halfsize of the inclusion (13.6 μm), up to the final length, a_f, equal to the halfsize of the fish-eye (450 μm). The initial crack growth rate corresponds to conventional 'operational' definition of the fatigue crack growth threshold, i.e. 10^{-10} m/cycle. Since the transition short/long crack in the high-strength steels is in order of tens mm in magnitude, the crack can be assumed to be a long one already from the beginning. This is also supported by the existence of striations in the very vicinity of the inclusion/matrix interface. The number of cycles for crack growth outside the fish-eye can clearly be neglected.

(ii) It is assumed that the crack growth rate is proportional to the square root of the crack length (the dependence of the shape factor on the crack length is neglected). This simplification seems to be reasonable particularly in the threshold region (the longest period very close to the inclusion), where neither the shape factor of the crack front nor the stress change too much.

Consequently, the crack growth has been modeled by a simplified Klesnil-Lukáš type of relationship[15]:

$$\mathrm{d}a/\mathrm{d}n = B\left(a^m - a_i^m\right) \qquad (1)$$

where $B = (5.98 \pm 4.62) \times 10^{-8}$ and $m = 4.80 \pm 0.24$ are constants obtained by fitting striations spacing data (both a and d given in μm units). By integrating this equation from the initial lenth a_i to the final length a_f, it was found that the propagation stage of the fish-eye crack is N_p = <522, 15957> cycles, which is 1~7 % of the total fatigue lifetime.

4. Summary

The microfractography has been used to analyse the fish-eye crack propagation mechanism under biaxial bending-torsion fatigue and to estimate the time span of the crack growth period. The analysis of the fish-eye crack orientation and the local roughness measurements leads to the conclusion that the cracks propagate predominantly by mode I micro-mechanism. The extrapolation of the local crack growth rate to the overall fish-eye crack region revealed that the propagation stage of the fish-eye crack constitutes only 1~7 % of the total fatigue lifetime.

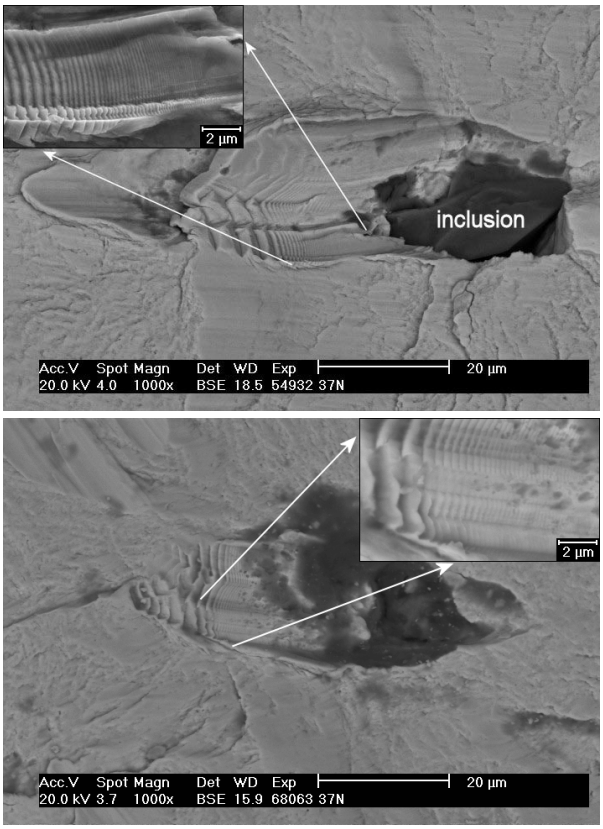

Fig. 6. **Microphotographs of mating fracture surfaces showing the striations near the centre of the fish-eye crack from Fig. 3**

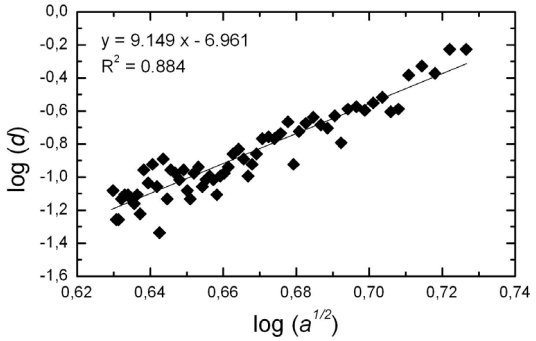

Fig. 7. **Plot of the logarithm of striations spacing, *d*, vs. the logarithm of the root square of the crack length, *a***

The authors greatly acknowledge the financial support provided by Brno University of Technology (Project FSI-S-10 -64) and the Czech Science Foundation (Project 106/08/ P366).

REFERENCES

1. De la Cruz P., Odén M., Ericsson T.: Mater. Sci. Eng. *A242*, 181 (1998).
2. Genel K., Demirkol M., Çapa M.: Mater. Sci. Eng. A279, 207 (2000).
3. Limodin N., Verreman Y.: Mate. Sci. Eng. *A435-436*, 460 (2006).
4. Sirin S. Y., Sirin K., Kaluc E.: Mater. Charact. *59*, 351 (2008).
5. Pokluda J., Dvořák I., Horáková H., Major Š.: In: (Johnson W.S., ed.) *Proc. Fatigue 06*, Elsevier (CD), Atlanta, Georgia 2006, pp. 0601A_24.
6. Agarwal N., Kahn H., Avishai A., Michal G., Ernst F., Heuer A. H.: Acta Mater. *55*, 5572 (2007).
7. Shiozawa K., Lu L. T.: In: (Stanzl-Tschegg S., Mayer H., ed.), *Proc. Fatigue in the very high cycle regime*, Institute of Metrology and Physics, Austria 2001, pp.165.
8. Terentev V. F.: Metal Sci. Heat Treat. *46*, 244 (2004).
9. Huang Z., Wagner D., Bathias C., Paris P. C.: Acta Mater. *58*, 6046 (2010).
10. Wang Q. Y., Bathias C., Kawagoishi N., Chen Q.: Int. J. Fat. *24*, 1269 (2002).
11. Marines-Garcia I., Paris P. C., Tada H., Bathias C.: Mater. Sci. Eng. *A468-470*, 120 (2007).
12. Ranc N., Wagner D., Paris P. C.: Acta Mater. *56*, 4012 (2008).
13. Slámečka K., Pokluda J., Kianicová M., Major Š., Dvořák I.: Int. J. Fat. *32*, 921 (2010).
14. Ruckert C. O. F. T., Tarpani J. R., Bose Filho W. W., Spinelli D.: Int. J. Fract. *142*, 233 (2006).
15. Klesnil M., Lukáš P.: *Fatigue of Metallic Materials.* Elsevier, Oxford 1980.

K. Slámečka, J. Pokluda, K. Bonaventurová, and L. Čelko *(Brno University of Technology, Faculty of Mechanical Engineering):* **Microfractography of Fish-Eye Fractures in Nitrided Steel**

The paper presents results of the micro-fractographical study of fish-eye cracks that were formed in plasma-nitrided specimens under symmetrical bending, symmetrical torsion and biaxial in-phase bending-torsion loading regimes. Analysis of the local striation field found near the inclusion in the center of the fish-eye crack together with the local roughness measurements support the hypothesis that the cracks propagate predominantly by mode I micromechanisms. Moreover, the extrapolation of the local crack growth rate curve to the overall fish-eye crack region suggests that similarly to the gigacycle fatigue, the most of the fatigue life is spent on the initiation of the interior microcrack.

POLYPROPYLENE NANOCOMPOSITES STUDIED BY LOCAL MICRO- AND NANO-MECHANICAL MEASUREMENTS

GALINA ZAMFIROVA[a], O. BLAHOVA[b], J. MINSTER[c]*, and V. GAYDAROV[a]

[a] *Transport University "T. Kableshkov", Geo Milev str. 158, 1574 Sofia, Bulgaria,* [b] *New Technology Research Centre, University of West Bohemia, Univerzitní 8, 306 14 Plzeň,* [c] *Institute of Theoretical and Applied Mechanics of the AS CR, v. v. i., Prosecka 76, 190 00 Prague, Czech Republic*
gzamfirova@mail.bg, minster@itam.cas.cz, blahova@ntc.zcu.cz

Keywords: polypropylene, carbon nanotubes, Vickers microhardness, total microhardness, nanoindentation

1. Introduction

Micro- and nanoindentation study of nanostructured polymer composite materials is a modern scientific approach allowing simple and very fast determination of some important mechanical properties. There is a huge variety of possible interactions between polymer matrix and filler, and as a consequence there can be a wide range of behaviour in the mechanical properties of the composites. The additive law[1] applied to the components of the composite often deviates from the experimental results. For a common composition the real mechanical properties decrease with the increasing content of a filler[2]. However, in some composite materials, containing fibres or oriented fillers, the reinforcing effect could be observed[3,4]. Nanocomposite materials occupy a special position among reinforced materials, e.g. when the reinforced effect is due to the large interfacial area and nano-dimensions of the filler, leading to manifestation of the scale factor[5].

The aim of this work is to use the micro- and nanoindentation technique to determine the resistance against plastic and elastic deformation of isotactic polypropylene (iPP) and nanocomposite filled with carbon nanotubes.

2. Experimental

Material: A commercial masterbatch of 20 wt.% multiwalled carbon nanotubes (MWCNT) in polypropylene (Hyperion Catalysis Int.) was used. The dimensions of the nanotubes were: 10 to 15 nm in diameter and 1 to 10 μm in lengths. Isotactic polypropylene (iPP) Buplen 6231 (Lukoil Neftochim) with density, ρ = 901 kg m^{-3} was used as the matrix polymer.

The masterbatch was diluted to various carbon nanotube concentrations in the range of 0.05 to 3 wt.% with virgin iPP at a melt temperature of 200 °C. The composites were extruded and further calandered as sheets about 1.5 mm in thickness at a melt temperature of 230 °C. Samples with dimensions of 10×10 mm were cut for microhardness measurements.

Methods: The measuring equipment for microindentation measurement was a mhp-160 Vickers microhardness device supplied with a Vickers indenter and attached to a UN-2 microscope. Vickers microhardness and total microhardness were measured at a load of 20 g, 40 g, 80 g and 160 g. The loading process consists in the loading time 10 s and the hold time 10 s. At least ten imprints were made for each point of the figures. The relative error for all microhardness measurements is less than 5 %.

It was established that the viscoelastic deformation component is, in relation to the elastoplastic component, negligibly small and consequently it was ignored in these short-term measurements. Due to the short hold time during the microhardness measurements the creep processes were also neglected. The following microhardness characteristics were measured:

– Vickers microhardness (*MHV*), connected with the irreversible deformation component and providing information about the plastic properties of the sample. *MHV* is calculated according to the equation:

$$MHV = KP/d^2 \qquad (1)$$

where d is the projected diagonal length of the imprint after releasing the indentor, P is applied load and K is a constant, depending on the geometry of the pyramid;

– Total microhardness (*MHT*), which can be considered as a measure of the local total material resistance against penetration and related to the total deformation, including elastic, plastic and viscoelastic components[6], is calculated according to the equation:

$$MHT = KP/D^2 \qquad (2)$$

where D is the projected diagonal length of the indentation in the loaded state.

The measuring equipment for nanoindentation measurement was the XP Nano Indenter supplied with a Berkovich indenter. All time-dependent measurements were made in the creep regime as an indentation under a step load ($P(t)=P_oH(t)$, where $H(t)$ is the Heaviside unit step function) for a period of 600 s and loading P_o = 200 mN. The initial loading rate in the load range 0–200 mN was 125 mN s^{-1}. The creep compliance $D(t)$ can then be directly deduced[7] from the equation:

$$D(t) = \frac{2h^2(t)}{\pi(1-\nu^2)P_0 \tan\alpha} \qquad (3)$$

with displacement into surface $h(t)$, constant Poisson´s ratio ν and effective face angle of the indenter α. All measurements were performed at room temperature. Fig. 1 shows a typical loading diagram of the indentation creep test with a constant load (47 indents).

3. Results and discussion

Fig. 2 shows the *MHV* dependencies as a function of the filler quantity measured at various loads. The first MWCNT portions raise the microhardness very rapidly. After 0.1 % MWCNT this increase becomes smoother. These dependences can be approximated by two straight lines *a* and *b* with

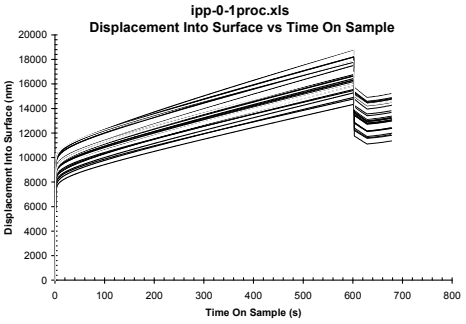

Fig. 1. **Indentation creep tests of the material with MWCNT 0.1 %**

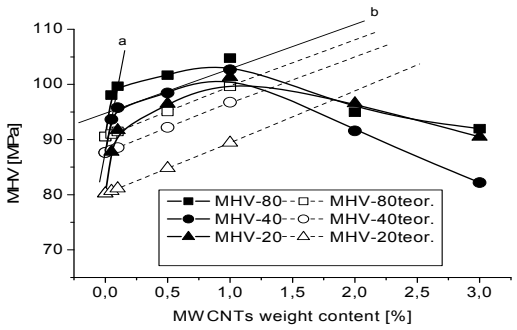

Fig. 2. **MHV vs. filler quantity under various loads**

different slopes as shown for the dependence measured at load 40 g, which means that the reinforcing effect of the filler is governed by a different mechanism.

The theoretical Vickers microhardness values were calculated according to the parallel additive model applied often for polymer blends, compositions and semicrystal polymers[1]. The following formula was used:

$$MHV = w_f MHV_f + (1-w_f) MHV_{iPP} \quad (4)$$

where *MHV* is a composite microhardness, MHV_{iPP} and MHV_f are the intrinsic microhardness of the pure iPP and carbon nanotubes respectively and w_c is the filler fraction. The value of 1GPa was used for MHV_f[1]. The theoretical Vickers microhardness values are plotted with dashed lines in Fig. 2. They are absolutely parallel to each other, as a result of the application of the additive law, but an interesting fact is that they are almost parallel to the experimental data for composites containing from 0.1 % to 1 % nanofiller. Hence in the area where *MHV* increases more smoothly the reinforcment mechanism is due to the principle of additivity. The rapid enhancement of *MHV* at very small MWCNT content can be attributed to changes in the crystal structure of the polymer matrix, i.e. to qualitative changes in the PP structure. Previous microscopic investigations[8] and microphotographs have shown that the PP spherolites become smaller with the first portion of nanofiller.

MWCNT concentrations higher than 1 % do not increase the *MHV* values. On the contrary, the *MHV* values decrease. This is because of the occurrence of percolation processes and, as a consequence, there is lower filler activity. The percolation of the nanoparticles is proved by rheological measurements[8].

The influence of the MWCNT content on the *MHT* for various applied loads is shown in Fig. 3. Again there is a considerable increase in *MHT* when there is a small quantity of MWCNT and after a content of 0.1 % the increase becomes slower and the dependences can be approximated by two straight lines crossing at about 0.1 % MWCNT. The *MHV* and *MHT* increase expressed as a percentage are close together, in the range from 20–25 %. Knowing that Total microhardness expresses general resistance against deformation including reversible and irreversible deformation, and that *MHV* is resistance only against irreversible deformation, the similar percentage increase in *MHV* and *MHT* values means that the nanofiller predominately improves resistance against irreversible (plastic) deformation. According to many authors, plastic deformation during penetration in semicrystal polymers predominantly affects the crystal parts of the sample[1]. It can therefore be supposed that the nanofiller influences the crystal phase, strengthening its resistance against penetration. Changes in the crystal phase that could enhance the Vickers microhardness might be: increasing the quantity and/or the perfectibility of the crystals, increasing the lamella thickness or changes in allotropic modification. As was mentioned above, in this case the nanotubes are nuclei formation agents facilitating the crystallisation process, and they help to build the PP crystal phase with a better resistance against plastic deformation. Thus, rapid enhancement of the *MHV* of the nanocomposites at a very small MWCNT content can be attributed not to the inherent *MHV* values of the filler, but to changes in the crystal structure of the polymer matrix. After 1% filler content, a slow decrease takes place.

The results of the nanoindentation measurements of the concentration dependence of hardness (*H*) are plotted in Fig. 4. The curves pass through a maximum for samples containing 0.1 % MWCNT. Fig. 5 shows the concentration dependencies of modulus of elasticity *E* and instantaneous compliance *J*, which pass through the extreme at the same concentration. This trend of both characteristics is to be expected, because it is theoretically predetermined from the well-known correlation between Vickers hardness and modulus of elasticity, $MHV = a.E^b$, where a and b are material constants. This power relation was extended for Total microhardness[9] with various values of constants a and b. These results confirm the general validity of the dependences in this case for hardness determined by the Oliver-Pharr method.

For comparison the three hardness characteristics *MHV*, *MHT* and *H* measured at loading 20 g as a function of the filler content of the nanocomposites are plotted in Fig. 6. The values of *MHV* range from 80 MPa to 100 MPa. The values of *MHT* range from 1,2 MPa to 2 MPa. The data for *H* occupies a medium position in the interval 20–30 MPa. These at first sight large differences are due to a different approach for determining them and consequently their different physical nature.

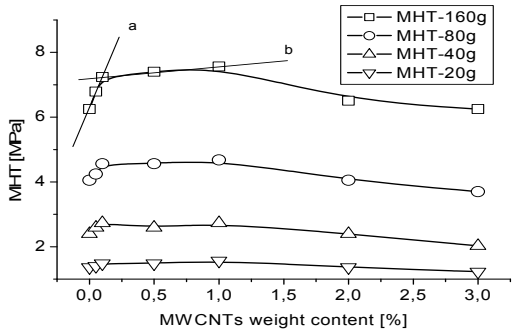

Fig. 3. **MHT vs. filler quantity at various loads**

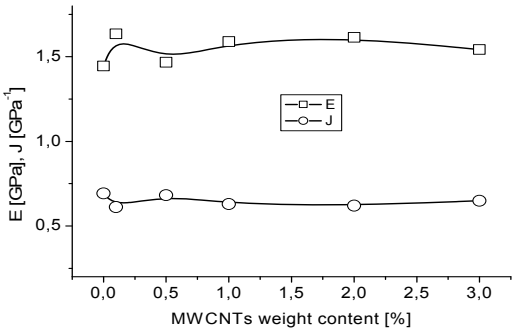

Fig. 5. **Modulus of elasticity, E, and instantaneous compliance, J, vs. the MWCNT weight content**

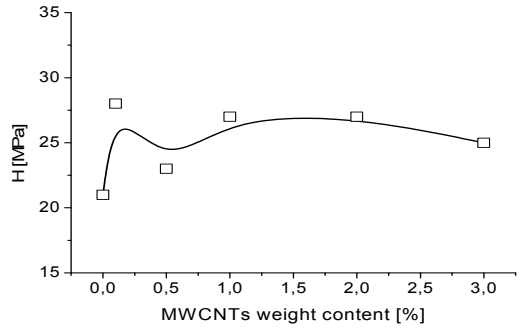

Fig. 4. **Hardness obtained by the Oliver-Pharr method vs. the MWCNT weight content**

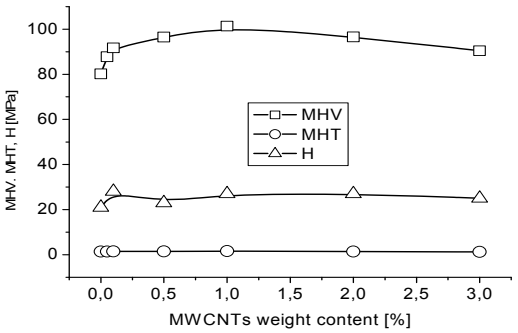

Fig. 6. **Comparison of hardness characteristics: MHV, MHT and H, measured at loading 20 g as a function of the filler content**

– The value of *MHT* is calculated on the basis of the depth of indentation in the loaded state, and it includes elastic, plastic and viscoelastic material resistance against the penetrating pyramid, and also the total resistance of the deformed material in the vicinity of the pyramid, i.e. resistance against the so-called "sink-in" effect.

– Hardness *H*, obtained by the Oliver – Pharr method, is calculated on the basis of the contact surface, or the contact depth, and so the influence of the „sink-in" effect is avoided. The physical meaning of this characteristic is similar to *MHT*, but its value is larger because the material deformation around the indenter is not taken into account.

– The *MHV* values are the highest because they are calculated on the basis of the diagonals of the relaxed imprint after the indenter is extracted, and so they express the resistance only against plastic deformation.

Viscoelastic creep compliance histories of the measured polypropylene nanocomposites derived from indentation creep tests according to[7,10] (3) are plotted in Fig. 7. The number of implemented indents varied from 36 (MWCNT 3 %) to 73 (MWCNT 1 %). In agreement with the statements relevant for instantaneous mechanical properties, the filler content 0.1 wt.% MWCNT has the most positive influence on time-dependent behaviour. The viscoelastic compliance history for the pure matrix represents the upper limit for all investigated filler contents.

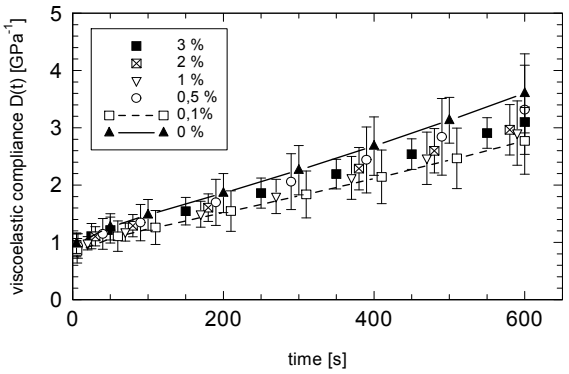

Fig. 7. **Comparison of the viscoelastic creep compliance histories derived from instrumented indentation for various filler contents**

4. Conclusions

It has been established that small weight fractions of MWCNT, up to 0.1 %, significantly increase the Vickers microhardness and the Total microhardness, as well as the hardness obtained by the Oliver − Pharr method. The small filler content positively influnces also the time-dependent properties. This effect is due to changes in the crystal phase of the polypropylene matrix as a consequence of the nucleation effect of the MWCNT. This increases its resistance against irreversible deformation and raises its modulus of elasticity.

A further increase in MWCNT content in the composit untill 1 % leads to a smoother increase in microhardness, obeying the additive law, i.e. there are no essential changes in the structure of the polymer matrix.

The increase in the Total microhardness of the MWCNT/iPP nanocomposite is due to the increase of the Vickers microhardness.

A further increase in MWCNT content after 1 % leads to decreasing Vickers microhardness and Total microhardness. After this concentration threshold, percolation processes take place and the effectiveness of the nanofiller decreases drastically. The total resistance against penetration even becomes worse than the total resistence of the non-filled samples.

The different approaches of the two indentation methods and the correlation between the used indentation parameters have been discussed in terms of their physical nature.

This study has been supported by NSF- Bulgaria, (D002 -138/2008-2011) and by GAAV CR (grant No IAA 200710801).

REFERENCES

1. Baltá Calleja F. J., Fakirov S.: in *Microhardness of Polymers,* Cambridge University Press, Cambrige 2000.
2. Zamfirova G., Gaydarov V., Perena J. M., Cerrada M. L., Benavente R.: *Proceedings of the 11-th Int. Conf. on Mech. and Tech. of Composite Materials Sofia, 2006.* Bulgaria, p. 379-384, (2006).
3. Minkova L., Yordanov H., Zamfirova G., Magagnini P. L.: Colloid Polym. Sci. *4*, 280, 358 (2002).
4. Gaydarov V., Zamfirova G., Fambri L.: NDT Days 2008, Sozopol, Bulgaria, 97 (2008).
5. Zamfirova G., Gaydarov V.: *Proceedings of the 10-th Int. Conf. on Mech. and Tech. of Composite Materials Sofia, 2003.* Bulgaria, 399 (2003).
6. Zamfirova G., Dimitrova A.: Polymer Testing *19*, 533 (2000).
7. Knauss W.G., Emri I., Lu H.: Mechanics of Polymers: Viscoelasticity, in *SpringerHandbook of Experimental Solid Mechanics*, (W. N. Sharpe, ed.). Chapter 3, pp. 49–96, Springer, 2008.
8. Kotsilkova R., Ivanov E., Krusteva E., Silvestre C., Cimmino S., and Duraccio D.: J. Appl. Polym. Sci. *115*, 3576 (2009).
9. Zamfirova G., Lorenzo V., Benavente R., Pereña J. M.: J. Appl. Polym. Sci. 88, 1794 (2003).
10. Minster J., Blahova O., Lukes J., Nemecek J.: Mech. Time-Depend Mater. *14*, 243 (2010).

G. Zamfirova[a], O. Blahova[b], J. Minster[c], and V. Gaydarov[a] *([a] Transport University "T. Kableshkov", Sofia, Bulgaria, [b] New Technology Research Centre, University of West Bohemia, Plzeň, [c] Institute of Theoretical and Applied Mechanics of the AS CR, Prague, Czech Republic):* **Polypropylene Nanocomposites Studied by Local Micro- and Nano-mechanical Measurements**

This paper reports on a micro- and nano-indentation investigation of iPP filled with multiwall carbon nanotubes (MWCNT) in the range of 0.1–3 wt.%. Vickers microhardness and Total microhardness were determined using a mhp-150 microhardness tester and a NU-2 light microscope. Elastic modulus, instantaneous compliance and hardness were obtained using an XP Nano Indenter. It was established that a small weight fractions of MWCNT (0.1 wt.%) significantly improves the microindentation parameters.

A comparison of the results of the two measuring techniques showed a relatively large difference in hardness values. This may be related to the different physical nature of the measured microhardness characteristic. There is a discussion presented of the similarity and/or difference in the microhardness values from the viewpoint of the trend of concentration dependencies and also their physical peculiarities.

COMPARISON OF MECHANICAL PROPERTIES OF CFRP LAMINATE OBTAINED FROM FULL-SCALE TEST AND EXTRAPOLATED FROM LOCAL MEASUREMENT

JAROSLAV VALACH[a]*, DANIEL KYTÝŘ[a], TOMÁŠ DOKTOR[a], KLÁRA SEKYROVÁ[a], VLASTIMIL KRÁLÍK[b], and JIŘÍ NĚMEČEK[b]

[a] *Czech Technical University in Prague, Faculty of Transportation Sciences, Na Florenci 25, 110 00 Prague 1,* [b] *Czech Technical University in Prague, Faculty of Civil Engineering, Thákurova 7, 166 29 Prague 6*
valach@fd.cvut.cz

Keywords: CRFP laminate, fatigue test, nanoindentation

1. Introduction

Since from the very beginning of aviation, the research was focused on lightweight and strong materials. Due to continuous research and investment, various novel materials successfully compete with once dominating light metal alloys. In comparison with metals, composites offer favorable strength to density and stiffness to density ratios and also superior fracture toughness properties implied by nature of their micro-structure. However, the behavior of the applied materials is sufficiently known to be operated safely in civil aircraft, a complete understanding of these materials is yet to be built. One example supporting this statement are difficulties in generalization of observations and tests of the materials' degradation properties. The difficulties arise from composites heterogeneity, engaging several damage mechanisms acting at several scales and also from the long-time experiments necessary for study of materials' degradation processes.

The research presented in this paper is a part of an extensive investigation of the fatigue behavior of the special class of carbon fibre reinforced plastics (CFRP) represented by carbon fibre in polyphenylene sulfide thermoplastics matrix (C/PPS) composites used in the aircraft industry.

The main aim of the paper is to show correlation between decrease of the material's stiffness during cyclic loading and the associated changes in the matrix properties.

2. Problem and material overview

From the technical point of view the material's degradation due to external loading ultimately manifests itself in the decrease of the strength. As this property cannot be determined nondestructively, other mechanical properties of the materials, are used as damage indicators[1]. Prominent role among these indicators is assigned to the measurement of modulus of elasticity: damage accumulation causes weakening of the material's internal bonds and increase of its compliance or, equivalently, decrease of its stiffness[2].

The concepts, as classified e.g. in a review paper[3], can be divided into the three groups: fatigue life investigation, residual stiffness determination and damage accumulation measurement. The first one constructs S-N curve relating strength to the number of cycles, but ignoring detailed model of the damage process in the material, this approach does not discriminate between fatigue of metals and other materials, however it is obvious that underlying mechanisms differ fundamentally. The second approach builds criteria based upon phenomenological description of the remaining strength or stiffness; it is considered the most suitable for experimental investigation as it yields nondestructively measurable property. Finally, the third approach studies a detectable property of material directly associated with damage accumulation from micromechanical viewpoint. According to the above mentioned classification, the presented results intend to demonstrate a connection between residual stiffness and damage mechanism.

The C/PPS composite is a relatively new material; it is quasi-isotropic 8-ply of carbon fabric bonded by thermoplastic matrix, a notable difference from more common composites based on epoxy resin. Its modulus to weight and strength to weight ratios favors this material for hi-tech application. The composite under investigation contains the carbon fibers prepared from PAN (Poly acrylonitrile), which are among those of the highest stiffness from the range from 40 to 400 GPa known from literature[4–6]. The reasons for this striking variation are different manufacturing methods adopted by industry. In contrast to glass fibres the carbon ones are highly anisotropic and design of composite takes often an advantage from this fact. Further details of mechanical and other properties can be found in materials datasheets[7].

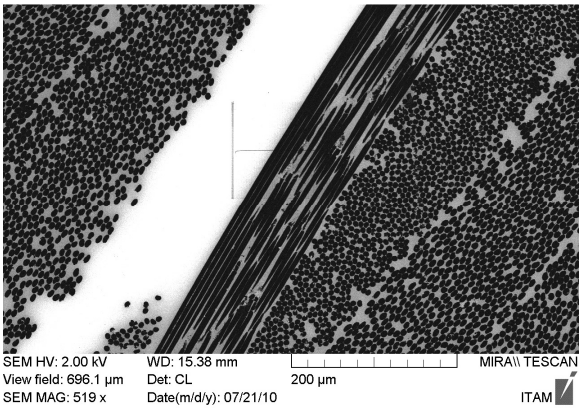

Fig. 1. **SEM micrograph of CFRP taken in CL regime depicts in high contrast density of fibers in various plies as well as their orientation. Ellipses of cross section of the fibers indicate the angle of cut in relation to axis of fibre**

3. Experimental procedure

The experiments were carried out on typical tensile specimen (depicted in cross section in Fig. 1 and in overall view

in Fig. 2) with rectangular cross-section 25×2.5 mm and total length 250 mm. For the fatigue testing servo-hydraulic Instron 1603 loading machine was used. The outputs of the force and displacement transducers were captured with 10 Hz sampling frequency. A sinusoidal force with 3 Hz frequency was applied. According to chosen stress level (76 % of limit tensile strength) mean loading force value (13 kN) and amplitude (12 kN) were set up. Fatigue experiment was six times interrupted at predefined intervals and number of cycles in order to determine damage indicators, i.e. to measure the stiffness.

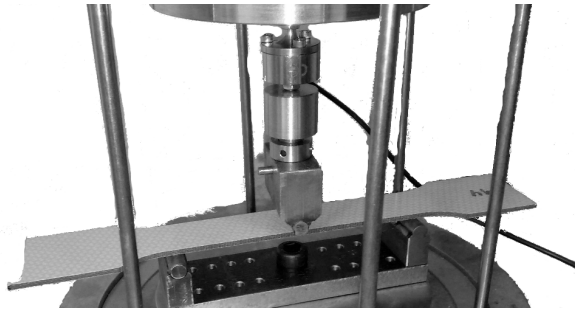

Fig. 2. **Three point bending testing device**

The stiffness was determined using three point bending (3PB) and from the ultrasound (US) measurement. Although different physical principles are involved in the both methods for elastic modulus determination, the results are very close for the intact specimens.

The experiment was carried out using testing device USG 20 (Krompholz Geotron Elektronik, FRG) used with a 250 kHz transducer (USG-T) and receiver (USE-T). The velocity of the longitudinal ultrasonic waves' propagation depends on the mechanical properties of the material, therefore the Young's modulus can be obtained from the formula for coupling elasticity modulus E_{ad}

$$E_{ad} = \rho v^2$$

in which, v stands for the wave velocity and ρ is the material density.

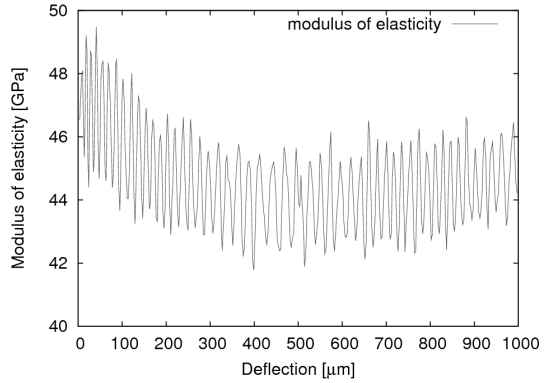

Fig. 3. **Values of Young's modulus during the 3PB test**

Three point bending measurements were performed using an uniaxial loading device as shown in Fig. 2. The loading run was controlled by displacement with maximal deflection value 1000 μm. The support span was 120 mm. The Young's modulus was calculated using the incremental metod. Fig. 3 shows values of Young's modulus acquired in 3PB test. The values corresponding to deflections 0 to 100 μm were excluded because of settlement of the experimental setup.

4. Nanoindentation

Nanoindentation plays a unique role in the presented investigation due to its ability to distinguish between fibres and matrix and to measure these properties separately. Considering the components' properties evolution, their contribution to the composite degradation can be estimated to identify the primary cause of breakdown.

The nanoindentation was carried out on the intact specimen and on the ruptured one (indicated in Fig. 4).

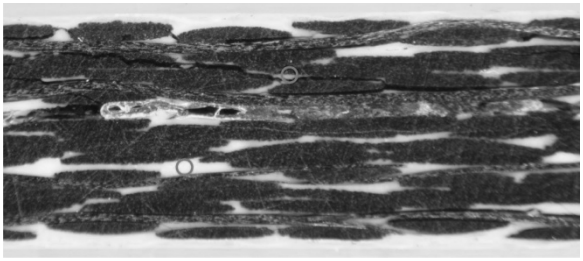

Fig. 4. **Polished surface from the ruptured specimen. A production imperfection is clearly visible. During rupture the delamination cracks were created, some of them are clearly visible above the inclusion. Location of nano indentation are marked by circles**

To conform nanoindentation requirements, the cross section surface was carefully polished to provide desired flatness and smoothness. Scanning Probe Microscopy (SPM) was used to obtain the information about the surface roughness before testing. Achieved value of the surface roughness was 30 nm or less.

For the tests, Hysitron TriboIndenter Ti750 (Hysitron, Inc.) with Berkovich tip diamond indenter (three-sided pyramid) was used. The duration of the loading phase was 5 s and the maximum loading force 1000 μN was kept for 10 s. The duration of the unloading phase lastex for 5 s. Twenty five indents were performed in a 5×5 grid. Comparison of nanoindentation loading curves of intact and ruptured specimen is shown in Fig. 5.

The nanoindentation into carbon fiber yields the results of E=18 GPa in the longitudinal cross section and E=25 GPa in the transversal cross section. The difference between these values can be explained by the effect of internal fiber structure and compliant matrix that surrounds relatively stiff and elastic fibers. The carbon fibre can be imagined as a bundle of narrow carbon (graphite) ribbons that rearrange easily during the penetration of indenter.

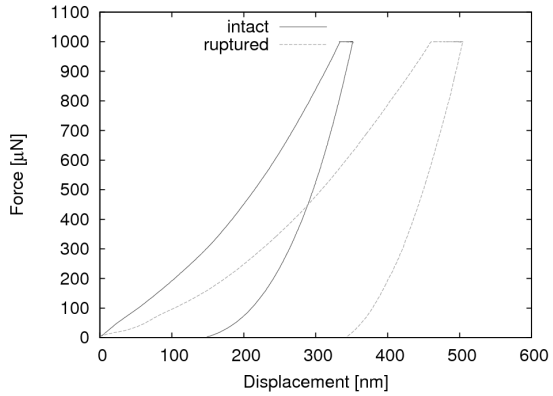

Fig. 5. **Nanoindentation loading curves**

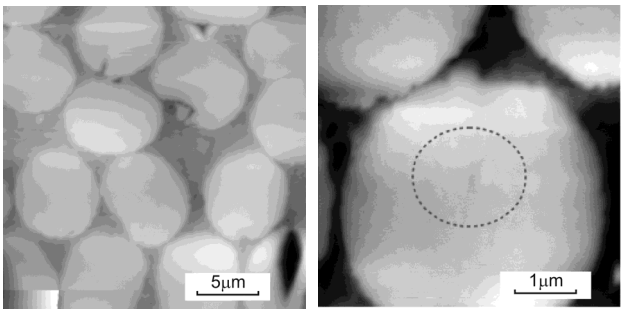

Fig. 6. **Nanoindentation of fibres in the transversal cross section**

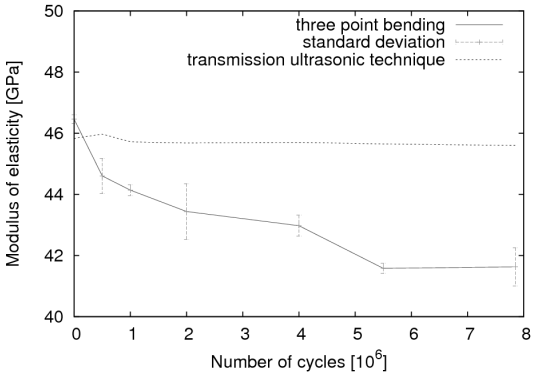

Fig. 7. **Comparison of static and dynamic moduli of elasticity evolution in fatigue testing**

Table I
Comparison of the Young's modulus decrease obtained by different techniques

Techniuqe/Young's modulus [GPa]	Intact specimen	Ruptured specimen
Overall properties		
Ultrasound	45.83	45.61
Three point bending	46.46	41.63
Matrix properties		
Nanoindentation	5.63	4.09

This behavior also clarifies the observed fact that nanoindenter tool does not leave any traces on carbon fiber (see Fig. 5). Indents in the matrix were clearly visible, therefore the nanoindentation tests of the matrix were used for the observation of the degradation process.

5. Results

The fatigue testing was terminated after 789,183 cycles when the specimen was ruptured. The degradation of the Young's modulus during the cyclic loading is depicted in Fig. 7 and listed in Tab. I.

Comparing two macro-mechanical measurements, the following observations were made: values of the adiabatical modulus of elasticity remain at various stages of the fatigue test within the range of measurement error the same, while the stiffness derived from flexure test decreases.

The decrease in stiffness values as measured by the 3PB test and the fact of different values obtained by the US tests are caused by different physiscal background of the used measurement techniques. The dynamic modulus of elasticity depends on the pressure wave velocity in material. This principle naturally suppresses the influence of many defects, as it tends to close cracks and detour broken fibers. In contrast with this measurement, the bending tests "activates" defects on the strained side of the specimen, exposing hidden faults. The stiffness' invariability in US measurement reveals fully elastic behavior and integrity of carbon fibres and their bonds to the matrix. The lack of broken fibres and delamination points toward the properties of the matrix accounting for the damage accumulation as the only component that can deteriorate and be responsible for the flexural stiffness decrease. Micromechanically, the matrix transfers loads across the volume of the composite. Shear compliance of the matrix as a softer component of the composite is responsible for the shear properties of the whole composite. This hypothesis was verified by matrix nanoindentation in the beginning and in the end of the fatigue test.

6. Discussion and conclusions

Successful comparison of macro- and micro- measurement presented in this paper brings in a hope of more fundamental understanding of the processes during fatigue loading. Obtained results couple nondestructively measurable damage indicators with the changes in microstructure and component's properties. The measurement proved prominent role of the matrix in the composite's properties fatigue degradation.

The presented study describes the possibity of assessment of the fatigue behavior using the micromechanical testing. But the problems that occured show on some limitations of used techniques. For more complex description of the dis-

tinct components in the composite material, nanoindentation and microtensile tests of separated phases can be helpful.

The research has been supported by Grant Agency of the Czech Technical University in Prague (grants No. SGS10/218/OHK2/2T/16, SGS10/135/OHK1/2T/11), by the Grant Agency of the Academy of Sciences (grant No. IAA200710801) and by research plan of the Ministry of Education, Youth and Sports MSM6840770043.

REFERENCES

1. Van Paepegem W., De Baere I., Lamkanfi E., Degrieck J.: *Poisson's ratio as a sensitive indicator of (fatigue) damage in fibre-reinforced plastics*, Fatigue & Fracture of Engineering Materials & Structures 30(4), 269–276, Wiley Online Library, 2007.
2. Vasiliev V. V., Morozov E. V.: *Mechanics and analysis of composite material*, Elsevier (2001).
3. Degrieck J., Van Paepegem W.: Appl. Mech. Rev. *54*, 279 (2001).
4. Maurin R., Davies P., Baral N., Baley C.: Appl. Compos. Mater. *15*, 61 (2008).
5. Kriz R. D., Stinchcomb W. W.: Exp. Mech. *19*, 41 (1979).
6. Kelly A.: Compos. Sci. Technol. *65*, 2285 (2005).
7. Airbus: *AIMS - Airbus Material Specification*, Airbus S.A.S (2007).

J. Valach[a], D. Kytýř[a], T. Doktor[a], K. Sekyrová[a], V. Králík[b], and J. Němeček[b], *([a] Czech Technical University in Prague, Faculty of Transportation Science, Prague, [b] Czech Technical University in Prague, Faculty of Civil Engineering, Prague, Czech Republic):* **Comparison of Mechanical Properties of CFRP Laminate Obtained from Full-Scale Test and Extrapolated from Local Measurement**

The presented paper outlines experimental investigation that is a part of an extensive research plan of study of fatigue properties of aerospace industry grade CRFP laminates. These materials are relatively novel and their long-term behavior and degradation are not yet completely described. Deterioration of this complex material in cyclic loading conditions is to be evaluated by several criteria based on evolution of certain of mechanical properties. Among the criteria is a decrease of modulus of elasticity. In order to reliably detect the changes in this property sensitive three point bending experimental setup was prepared, calibrated and compared to the results of the independent ultrasound method yielding the dynamical modulus of elasticity. Simultaneously, the local mechanical properties were studied by nanoindentation in order to set a reference point for a successive measurement after fatigue tests.

3D REPLICATION OF SURFACE STRUCTURES BY RAPID PROTOTYPING TECHNIQUE

VLADIMÍR PATA*, MIROSLAV MAŇAS, DAVID MAŇAS, and MICHAL STANĚK

Tomas Bata University in Zlin, Nam. T. G. Masaryka 5555, 760 01 Zlin, Czech Republic
pata@ft.utb.cz

Keywords: Surface structure, replication, rapid prototyping

1. Introduction

The replication of surface structures is a process which can be widely applied for the assessment of the surface quality of technical components made from metal and polymer material from the point of visualization[1,2].
There are a number of manufacturers focusing on the production of single purpose machines which scan and then assess the surface quality according to the relevant ISO standards in both 2D and 3D. The result is either numerical parameters of the surface quality or special graphs, which can, however, be very difficult to interpret for a user who does not specialize in the assessment of the surface quality. It is also necessary to take into account the fact that it is rather complicated to achieve the same conditions for reproducibility of measurements of the surface quality. Visualization of the scanned surface is at present only possible by using single purpose programmes supplied together with the machine which, however, lack compatibility with each other.

1.1. Surface mask

The principle of 3D replications of surface structure of the specimen structure is using 3D scanner with the defined step in axis **x** and **y**. The specimen used for surface replication is covered by a mask made from thin elastic material, which has a hole of rectangular shape whose edges correspond with the size of the scanned surface – see Fig. 1.

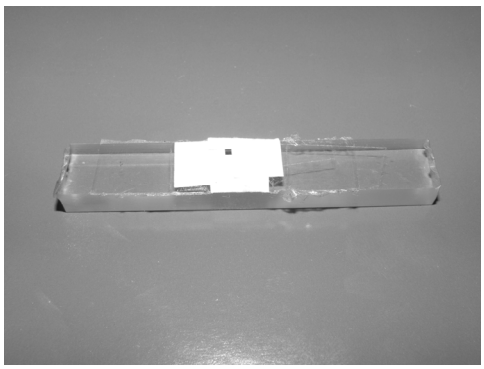

Fig. 1. **Specimen with applied mask**

1.2. Technique for scanning the surface coordinates

The next step is to scan the coordinates of the surface using the three dimensional matrix x,y,z. This matrix is then exported through ASCII file and adjusted by single-purpose programme for rapid prototyping process, in which we obtain the required replication of the scanned surface structure at a selected scale. Besides rapid prototyping technique it is also possible to use the import of the data adjusted as above into a CAD programme, generate automatically the relevant tool paths and make the replication of the surface structure using a CNC milling machine. The size of the replicated surface is limited only by the parameters of rapid prototyping, or the CNC milling machine.

2. Examples of practical applications

The applicability of the above mentioned process of surface structure replication was confirmed on one example in which microhardness of a specimen made from polymethylmetacrylate, commercially known as Plexiglass, is measured and assessed. After the measurement of microhardness the tested specimen shows an imprint of a pyramid. The diagonals of the pyramid are 0.020 mm and its height 0.015 mm. Because of relaxation of the specimen material the imprint is deformed, which needs to be visualized and then assessed. The methods used so far could be visualized only by using an electron microscope, e.g. SEM. When the surface was covered by a mask made from paper with a hole in the shape of a square of 0.6 mm, the surface was scanned by 3D scanner of Tailor Hobson with a CLA scanner with a step in axis x and y 0.0005 mm. After the scan, the three dimensional matrix of coordinates was transferred to the above mentioned single-purpose programme and then adjusted for 3D print using the rapid prototyping technique.
Fig. 2 shows a surface visualized in 3D using the commercial programme Talymap of Taylor Hobson and Fig. 3 shows the replication of the surface of the specimen with the imprint after the relaxation.

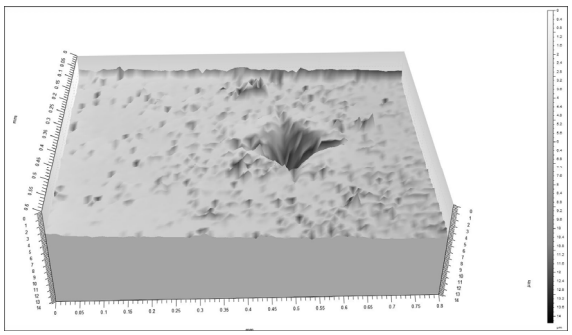

Fig. 2. **The surface of the specimen made by Talymap programme**

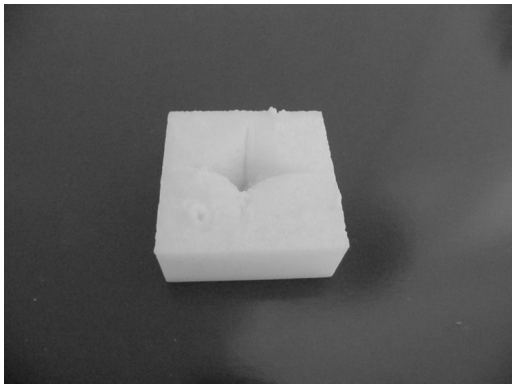

Fig. 3. **Replication of the specimen surface using the rapid prototyping technique**

Fig. 4 shows 3D image of the structure of a specimen made from steel 12020, which was machined by face milling technique. The size of the scanned surface is 4 mm × 2 mm. Fig. 5 is its 3D replication made by the same technological process.

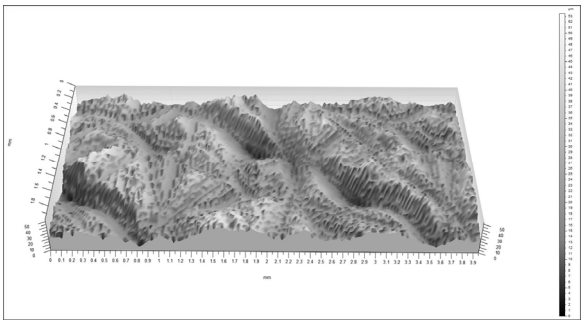

Fig. 4. **3D image of the specimen surface made by Talymap programme**

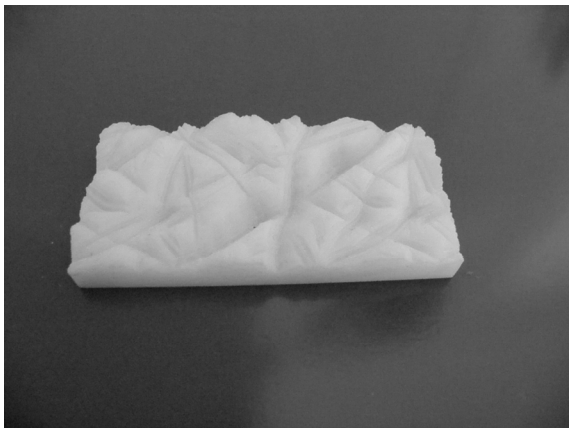

Fig. 5. **3D replication of the surface structure of the specimen created by rapid prototyping technique**

3. Conclusion

The process of replication of surface structures described above is very suitable in the instances when it is necessary to make 3D replication of the assessed surface, which is mainly interesting from the tribological point of view.

Next, it is possible to replicate different defects at a selected scale which occur on the surface of specimens and lower its quality, such as scratches, cracks, fissures, etc. This is very useful in the field of "Forensic Engineering[3–5]". Using 3D replication helps to visualize defects, which are on the specimen, and hence it is not necessary to use special projection or photo documentary techniques.

This article is supported by the European Regional V & V center in the project CEBIA – Tech, no. CZ. 1. 05/2. 1. 00/03. 0089 and the internal grant of TBU in Zlín No. IGA/10FT/11//D funded from the resources of specific university research.

REFERENCES

1. Manas D., Manas M., Stanek, M., Pata V.: Wear of Tire Treads. *Archives of Materials Science* Volume 28 (1–4), 2007 Pages 81 – 89, Committee of Materials Science of the Polish Academy of Sciences, Warszawa, Poland.
2. Manas D., Stanek M., Manas M., Pata V., Javorik J.: KGK, Kautsch. Gummi Kunstst. *62*, 240 (2009).
3. Manas D., Manas M., Stanek M., Zaludek M., Sanda S., Javorik J., Pata V.: Chem. Listy *103*, 72 (2009).
4. Manas D., Manas M., Stanek M., Pata V.: *International Rubber Conference – IRC 2008*, 20 – *23.10.2008, Kuala Lumpur*, Malaysia, p.37–48.
5. Manas D., Pata V., Manas M., Stanek M.: *8th Fall Rubber Colloquium 2008*, *Hannover,* 26 – 28.11.2008, Germany, p.93–94.

V. Pata, M. Maňas, D. Maňas, and M. Staněk *(Tomas Bata University in Zlin, Zlin, Czech Republic):* **3D Replication of Surface Structures by Rapid Prototyping Technique**

The article describes the possibilities of 3D replications of surface structures by the rapid prototyping technique. It presents the method of masking the surface of the specimen in order to make the scanning of the required structure more precise. Next, it describes the method of scanning and assessing the data through the surface matrix. Finally, the above is documented by 3D replications of a specimen made from "polymethylmetacrylate" which was used for the assessment of microhardness, and a specimen from steel 12020 machined by the face milling technique.

USE OF THE INDENTATION TESTS FOR THE EVALUATION OF MACHINABILITY OF MATERIALS DURING ABRASIVE WATERJET CUTTING

PETR HLAVÁČEK [a]*, JAN VALÍČEK[a], JAN BRUMEK[b], MICHAL ZELEŇÁK[a], BARBORA HALUZÍKOVÁ[a], MARTA HARNIČÁROVÁ[c], and VERONIKA SZARKOVÁ[d]

[a] Institute of Physics, Faculty of Mining and Geology, VŠB-TUO, 17. listopadu, 708 33 Ostrava - Poruba, Czech Republic; [b] SMID - CPIT, VŠB - TUO, 17.listopadu, 708 33 Ostrava - Poruba, Czech Republic; [c] Faculty of Manufacturing Technologies of Technical University of Košice with a seat in Presov, Bayerova 1, 080 01 Prešov, Slovak Republic; [d] Institute of Economics and control systems, Faculty of Mining and Geology, VŠB - TUO, 17. listopadu, 708 33 Ostrava - Poruba, Czech Republic
petr.hlavacek@vsb.cz

Keywords: hydroabrasive erosion, machinability, instrumented indentation test

1. Introduction

The hydroabrasive machining is a technological process which used a high pressure waterjet with addition of abrasive material with a purpose of a controlled abrasive action. It is used to cut almost any material. The hydroabrasive machining can be carried out either by a suspension abrasive waterjet (Abrasive Slurry Jet – ASJ) or more often by an abrasive waterjet (Abrasive Water Jet – AWJ)[1]. In this work the experiments were performed by the AWJ technology, but a proposed methodology for the materials machinability can be generalized and used also in the ASJ technology.

The AWJ is used to accelerate the abrasive particles (mostly garnet) for disintegration of materials. The abrasive waterjet has many outstanding features that make it ideal for use in a wide range of applications. There is no heat affected zone during the abrasive waterjet machining (the maximum temperature of cut is about 70 °C). This feature is used for example to secure the disposal of munitions[2]. Very low cutting forces (below 50 N) affect the process of machining, so that mechanical stresses do not arise and also there are no residual stresses within the machined material[3].

2. Evaluation of the materials machinability

The term machinability is used for the cumulative effects of physical properties and chemical composition of materials on the process flow and economic or qualitative results of the machining process. The machinability generally can be considered in terms of an impact of material on the intensity of tool wear, energy balance of the cutting process and their effects on the chip and new surface formation within the conventional machining technologies. Knowledge of the machinability can be used for prediction, control and optimization of technological parameters of the machining process.

Current state of the evaluation of the materials machinability in the AWJ technology

For the evaluation of the materials machinability in the abrasive waterjet technology, there are many models for prediction, control and optimization[5–8]. Hashish was one of the first pioneers in this field, who has proposed a comprehensive model for prediction of parameters by the hydroabrasive machining[5]. The machinability evaluation criterion in almost of all models is a maximum depth of cut h that can be attained with the given technological parameters. As an alternative the machinability evaluation on the basis of the achieved surface roughness can be used[9].

Currently, most authors use a model of Zeng and Kim[6]. They have defined the machinability of different materials as a "Machinability Number N_M". On the basis of extensive experimental testing they have determined an empirical formula for calculating the machinability in the form of

$$N_M = \frac{hCD^{0.618}u^{0.866}q}{P_w^{1.25}m_w^{0.687}m^{0.343}} \qquad (1)$$

where h – depth of cut, C – scale factor of the machinability, D – focusing tube diameter, u – cutting speed, P_w – pressure of water, m_w – mass flow rate, m – mass flow rate of abrasive , q – degree of cut quality[6].

A level of quality cut q is chosen in the range of 1 to 5. The value of $q = 1$ corresponds to the quality of rough cut and the value of $q = 5$ corresponds to a high surface quality. This model has spread around the world due to its simplicity and many international companies are using this model for optimization of the process parameters in the hydroabrasive machining[1]. A disadvantage of this method of the machinability evaluation is that is based on a subjective quality assessment.

New methodology for the machinability evaluation of materials by the AWJ

A new methodology for the machinability evaluation of materials in the AWJ technology is based on a comparison of a unit volume of material removal.

A newly designed machinability test for the AWJ can be broken down into the following 10 steps:

1. Mass measurement m_1 of tested material with an accuracy of ± 0.01 g.
2. On the basis of the geometric dimensions of tested sample its volume V ± 5 % is determined.
3. Using the equation (*2*) the density ρ of material being tested is determined

$$\rho = m_1 / V \qquad (2)$$

Note: if the density ρ is known, the step 2 and 3 can be omitted.

4. On the material being tested a test cut creating a groove in the material is performed. The groove so created is the amount of removed material. When the groove is being created, there must not be cut through the whole thickness of the material. Fig. 1 shows the groove profile created in aluminum alloy.
5. After the groove has been created, it is necessary to dry the sample by airflow. In case of absorbent materials (such as different geomaterials), the sample must be dried in an oven.
6. Measuring of the final mass m_2 of material being tested.
7. Determination of the mass removal rate by the equation (*3*)

$$\Delta m = m_1 - m_2 \tag{3}$$

8. On the basis of the equation (*4*) the volume of material removal is determined

$$\Delta V = \Delta m / \rho \tag{4}$$

9. Selection of a unit volume of material removal

$$\Delta V_U = \Delta V / L \tag{5}$$

where L is a length of the groove being tested.
Note: A unit volume of material removal can be determined by measuring the geometric dimensions of the groove by an optical profilometer. Fig. 1 shows the groove measured by an optical profilometer FRT MicroProf.
10. If we know the unit volume of material removal, an index of machinability M_I can be established

$$M_I = \frac{\Delta V_U}{\Delta V_{Uet}} \tag{6}$$

where ΔV_{Uet} is the unit volume of material removal of etalon material.
Note: For materials with the machinability index of less than one, their machinability is worse than the machinability of etalon material. On the contrary, materials with a higher machinability index as one are better for machining than etalon material. Low carbon steel of EN S355J0 was chosen for the etalon material. Given that the different kinds of steel have the machinability index very small, there will be no big mistake, when using of low carbon steel as the etalon material.

a

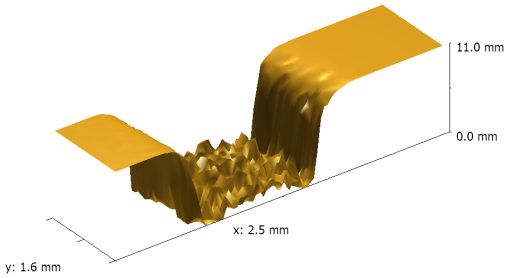

b

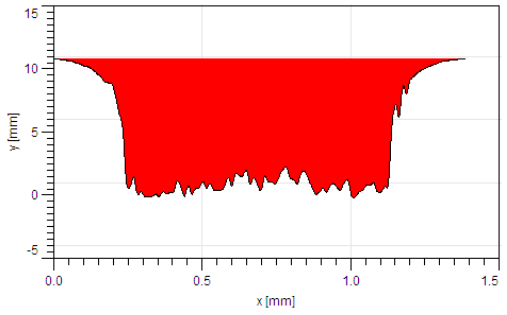

Fig. 1. a) **3D visualization of the groove created by the hydroabrasive machining** b) **representation of the groove profile**

3. Material and methods

Used materials

The experimental part was mainly focused on testing of metallic materials. These were as follows: stainless steel AISI 309, AISI 304 stainless steel, low carbon steel of EN S355J0, pure titanium Grade 2, CuZn40Pb2 brass, aluminum alloy AlMgSi0, 5.

These materials create a group of materials being classified as tough materials. From a group of materials that are known as brittle, was used silicate glass and Silesian granite.

Measurement of mechanical properties

In order to understand the machinability of materials by the hydroabrasive machining, it is important to investigate a relationship between the machinability values and physical-mechanical properties of materials. For example we logically consider that the machinability has a relationship with the material hardness. An important parameter is the modulus of elasticity giving information about the elastic behavior of material. The modulus of elasticity shall be usually determined on the basis of the uniaxial tensile test. A suitable alternative to this test is to identify the modulus of elasticity by an instrumented indentation test. The instrumented indentation tests are used for the determination of a wide range of mechanical parameters of material. The most commonly they are used to determine the material hardness. Hardness is described as a material's resistance to entry of foreign particles. Another parameter that can be determined by these tests is the above mentioned modulus of elasticity. The modulus of elasticity is determined from a relief curve.

Microhardness tester from CSM Instruments company was used. A diamond pyramid indenter was used to carry out tests according to Vickers. An advantage of the Vickers test is particularly a low sensitivity of the measured values to a loading force. A maximum loading force of 3000 μN lasting 10 seconds was used in experiments. For each material 10 indentation tests were carried out, from which it was calculated a mean value.

4. Results and discussion

Verification of the newly proposed methodology for the machinability evaluation

To verify accuracy of the obtained results a model of the machinability evaluation proposed by Zeng and Kim was used. Fig. 2 illustrates dependence between the machinability index M_I and machinability according to Zeng and Kim.

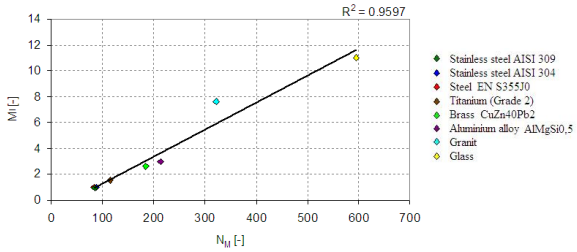

Fig. 2. **Dependence of the machinability index M_I on the machinability parameter N_M**

In Fig. 2 it can be seen that the machinability values being determined by the new methodology M_I are in close agreement with the machinability being determined by Zeng and Kim N_M (ref. [6]).

On the basis of this close agreement it can be determined the correlation equation for the calculation between the two types of machinability may be written

$$N_M = 46.22 M_I + 44.56 \qquad (7)$$

Use of this relation is very convenient, because the vast majority of devices that are used in a number of companies around the world are programmed to use the parameter of machinability according to Zeng and Kim. The advantage of using the new methodology for the materials machinability evaluation by the AWJ is in that, it can help to eliminate the subjective assessment of surface quality *q*. Another advantage is that this method is the least sensitive to a change of the technological parameters during testing.

Effect of mechanical properties on the machinability

If it is possible to find a link between the mechanical properties and machinability of the material, it would be possible to predict the machinability from these properties. This would help to avoid the time-consuming and cost expensive testing of machinability for each material. In Fig. 3 dependence between the observed index of machinability and Vickers hardness *HV* is shown.

In Fig. 3 a clear relationship between the material hardness *HV* and machinability index M_I can be seen. Following this it can be concluded that with an increase of the material hardness the machinability of material is being deteriorated. A match between the experimentally measured data and the correlation equation is 89 %.

Fig. 4 shows a relationship between the observed index machinability M_I and the modulus of elasticity *E*.

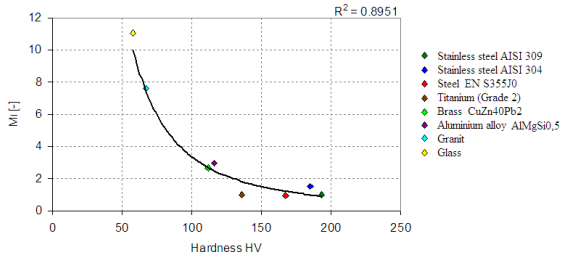

Fig. 3. **Relation machinability index M_I for hardness *HV***

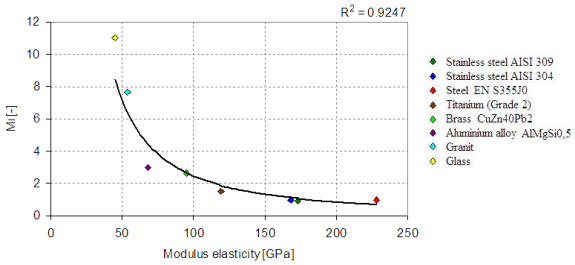

Fig. 4. **Relation machinability index M_I for modulus of elasticity**

From Fig. 4 a clear relationship between the index of machinability M_R and the modulus of elasticity *E* can be seen. The correlation coefficient in this case is even higher and thus 92 %.

Proposal of the materials machinability parameter M_P

Given that both the material hardness and the modulus of elasticity are in inverse proportion to the materials machinability, a new materials machinability parameter M_P has been proposed in equation form of

$$M_P = \frac{E \cdot HV}{E_{et} \cdot HV_{et}} \qquad (8)$$

where E_{et} is the modulus of elasticity of the etalon and HV_{et} is Vickers hardness of the etalon.

Fig. 5 shows dependence between the machinability index M_I and the newly materials machinability parameter being proposed.

Fig. 5 shows a good match between the machinability index M_I and the materials machinability parameter M_P. The correlation coefficient is close to 99 %.

$$M_I = 0.975 M_P^{-1.0484} \qquad (9)$$

If the relation (*9*) is generalized to the equation form (*10*), we can say that the machinability index M_I is approximately equal to the inverse value of materials machinability parameter M_P.

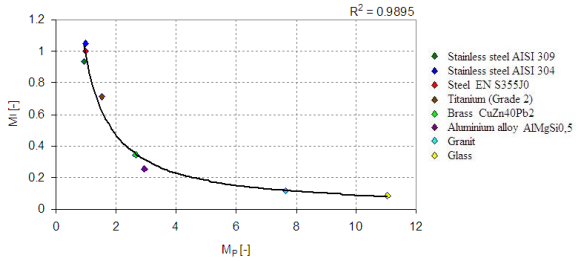

Fig. 5. **Dependence of the index of machinability M_I on the material machinability parameter M_P**

$$M_I \cong 1/M_P \tag{10}$$

5. Conclusions

In this paper we propose the new methodology for the machinability evaluation of materials by the hydroabrasive machining, which is based on the comparison of the unit volume of material removal. The advantages of using the new methodology for the machinability evaluation in the AWJ lies in the fact that compared to others methods this method is accurately quantified and there is no subjective assessment of surface quality q. Another advantage is that this method is the least sensitive to the changes of the technological parameters during testing. It is relatively simple, not expensive and rapid test that requires no special equipment. Verification of the newly proposed methodology was performed by comparing the machinability indexes with the values of machinability according to Zeng and Kim, where a very good match between parameters has been achieved. Therefore the correlation equation for the calculation between the machinability index M_I and machinability according to Zeng and Kim has been proposed. In this paper the effects of mechanical parameters on the machinability are also evaluated. A clear dependence of the machinability on the material hardness and also on the modulus of elasticity has been proved. The new materials machinability parameter M_P has been proposed. This parameter can be used to predict the materials machinability in the AWJ technology provided that the modulus of elasticity and Vickers hardness are known.

The work has been supported by projects SGS No. SP/201058, GA ČR No. 101/09/0650, RMTVC No. CZ.1.05/2.1.00/01.0040. Thanks also to the Moravian - Silesian Region for financial support and CEEPUS program CII-PL-0007-05-0910 at the Kielce University of Technology in Poland.

REFERENCES

1. Liu H. T.: J. of Man. Pro. *12*, 8 (2010).
2. Kmeč J., et al.: Technical Gazette *17*, 383 (2010).
3. Hassan A. I., et al.*:* Int. J. of Mach. T. & Man *44*, 595 (2004).
4. Meng H., et al.: Wear *181-183*, 443 (1995).
5. Hashish M. A.: J. Eng. Mater. Technol. *111*, 154 (1989).
6. Zeng J., Kim T.: *7th American Water Jet Conference*, p. 175−189, USA, Washington 1993.
7. Capello E., Groppeti R.: *7th American Water Jet Conference*, p. 157−174, USA, Washington 1993.
8. El-Domianty A. A., et al.: Int. J. Adv. Manuf. Tech*. 13*, 172 (1997).
9. Hlaváček P., et al.: Strojarstvo *51*, 273 (2009).

P. Hlaváček[a], J. Valíček[a], J. Brumek[b], M. Zeleňák[a], B. Haluzíková[a], M. Harničárová[c], and V. Szarková[d] *([a] Institute of Physics, VŠB-TUO, Czech Republic; [b] SMID - CPIT, VŠB - TUO, Czech Republic; [c] Faculty of Manufac. Technologies of Technical University of Košice with a seat in Prešov, Slovak Republic; [d] Institute of Economics and control systems, VŠB - TUO, Czech Republic):* **Use of the Indentation Tests for the Evaluation of Machinability of Materials during Abrasive Waterjet Cutting**

The paper deals with the possibilities of using the indetation tests for the evaluation of machinability of materials during abrasive water jet cutting. Indentation tests are used to simulate the interaction between abrasive particles and material during the process of abrasive water jet cutting. On the basis of these tests the machinability of materials can be characterized. The machinability of materials is very important for optimization of the technological process parameters of abrasive water jet cutting, which affect the quality, performance and economy of the entire process.

SURFACE INTEGRITY AND TRIBOLOGICAL BEHAVIOUR OF HARDENED STEELS

ZDENEK PALA[a], NIKOLAJ GANEV[b], KAMIL KOLAŘÍK[c], OLGA BLÁHOVÁ[d], and JAN JERSÁK[e]

[a] Department of solid state engineering, FNSPE, CTU in Prague, Trojanova 13, 120 00 Prague, [b] Department of solid state engineering, FNSPE, CTU in Prague, Trojanova 13, 120 00 Prague, [c] Department of solid state engineering, FNSPE, CTU in Prague, Trojanova 13, 120 00 Prague, [d] Department of mechanics, Faculty of applied sciences, University of West Bohemia, Univerzitní 22, 306 14 Pilsen, [e] Department of machining and assembly, Faculty of mechanical engineering, Technical University of Liberec, Studentská 2, 461 17 Liberec , Czech Republic
zdenek.pala@fjfi.cvut.cz, nikolaj.ganev@fjfi.cvut.cz, kamil.kolarik@fjfi.cvut.cz, blahova@kme.zcu.cz, jan.jersak@vslib.cz

Keywords: residual stresses, milling, friction, surface roughness

1. Introduction

Crystal structure undoubtedly belongs to the crucial factors influencing the local mechanical properties of a solid body. Yet perfect crystals are virtually nonexistent[1] and, hence, defects are a common matter. When a polycrystalline material is considered, such "crystallographic factors" as grain size and grain boundaries must be taken into account. Moreover, internal or residual stresses are often present. Occurrence of these stresses is facilitated by processes of inhomogeneous plastic deformation and/or by the presence and temporal evolution of thermal fields and/or the existence of phase transformations[2]. However, residual stresses have rarely been taken into account when mechanical properties, wear and friction are studied, and traditionally only microstructure, surface morphology, microhardness and roughness represent the group of investigated parameters.

The surface area of a solid body is extremely important and its qualities are paramount for numerous applications. It is often a challenge to choose the magnitudes that would serve best to assess the suitability of the surface for its putative usage. The last decade has seen the term surface integrity[3] in the crosshairs of material science. It encompasses not only traditional surface characteristics, but also more novel ones such as macroscopic and microscopic residual stresses, grain size, texture and dislocation density. The aim of the introduction of a new set of characteristics was to improve understanding of the role played by surface structure and microstructure in which they determine above all the mechanical properties and preordain the future behaviour of the whole body in a given environment.

It would be especially beneficial to establish the mutual relationship between surface integrity on one hand and wear and friction on the other. This would facilitate the optimisation of surface treatment processes leading to improved fatigue and longer service life. Nevertheless, the direct, general and even qualitative links mentioned above are lacking and, according to some material scientists[4], may be boldly rendered as only wishful thinking. Yet there have been attempts[5] to elucidate such links for certain type of material structure with a given real structure, i.e. deviations from the perfect structure of ideally crystalline material which covers diverse areas ranging from macroscopic parameters to nano-scopic ones.

In our contribution, we strive to analyse the surface by means of four surface integrity parameters, i.e. macroscopic and microscopic residual stresses, roughness and microhardness, and compare them with the results of tribological investigations. This research has not only academic purposes, but also serves as vital information for decision making by our industrial partner when the most appropriate tool tips for implementation in its horizontal milling machine have to be selected.

2. Experimental

2.1. Samples

The surface layers of three pairs of samples were investigated. The samples were in the form of two parts of guide gibs from steel ČSN 14100.3 (59 – 61 HRC) embedded into a cast iron bed (ČSN 422425). These samples were subjected to side milling by tool tips produced by three manufacturers and marked as *SA2*, *SA3*, *SE2*, *SE3*, *WA2*, and *WA3*. Table I shows the working and cutting parameters of applied milling where a_p [mm] is depth of cut, n – number of cuts, d [min] – tool´s diameter, f [mm min^{-1}] – shift, v_c [m min^{-1}] is cutting speed, and f_z [mm] – feed per tooth.

Table I
Working and cutting conditions for investigated surfaces

Sample	a_p	n	d	f	v_c	f_z
SA2	0.5	4	100	570	300	0.10
SA3	0.3	7				
SE2	0.5	3	63	1050	350	0.10
SE3	0.3	7				
WA2	0.5	3	160	500	60	0.17
WA3	0.3	7				

2.2. X-ray diffraction

Macroscopic and microscopic residual stress data were furnished by X-ray diffraction which is acknowledged to be a suitable and accurate tool. The measurements were performed on a θ/θ goniometer X´Pert PRO with *CrKα* radiation.

The diffraction line {*211*} of *α-Fe* phase was analysed. The ***sin²ψ*** method [6] with nine different tilt angles ψ was used. The X-ray elastic constants $½s_2 = 5.76 \cdot 10^{-6}$ MPa^{-1}, $-s_1 = 1.25 \cdot 10^{-6}$ MPa^{-1} were used in macroscopic stress calculations of biaxial state. The single line Voigt function method[7] was applied for corrections of instrumental broadening and the determination of microstrains and particle size. The microstress σ^{micro} could be calculated from the microstrains e using Hooke's law ($\sigma = e\,E$) with the Young modulus E = 216 GPa in order to be comparable with macroscopic residual stress.

2.3. Hardness and roughness measurements

The measurements were made on a *Buehler MICROMET 2100* microhardness tester with a 200 g load, which was assessed as the optimal load with regard to indentation readability from all the investigated surfaces.

Surface roughness was analysed using a *MITUTOYO SURFTEST 2000* contact profilometer. A trace 4.0 mm long was evaluated with cut off length of 0.8 mm to obtain surface roughness data.

2.4. Tribology measurements

In order to analyse friction and wear, the pin-on-disc test was used. During this test, the coefficient of friction was continuously monitored as wear occured; material removal was determined by weighing and measuring the profile of the resulting wear track. The operating conditions were set to simulate, as precisely as possible, those in a working process.

The measurement of friction coefficient was undertaken using a *CSM High Temperature Tribometer*. The specimens' surfaces after the pin-on-disc test were observed by light microscopy and scanning electron microscopy.

The friction tests were performed with two different layouts (Fig. 1) using a "polymer"cylinder with diameter 5.5 mm. The tests were carried out using a 2 N constant load and a linear relative speed dependent on radius of track (speed = radius/2). In the first case, the cylinder and the weight holder formed an angle of 45° in the plane formed by the axis of the holder and the sensing arm (Fig. 1, left). In the second case, the cylinder and the weight holder formed an angle of 45° in the plane perpendicular to the plane formed by the axis of the holder and the sensing arm (Fig. 1, right). The wear test was performed with 5,000 laps at room temperature.

3. Results

The obtained surface integrity characteristics are summarised in Table II. The values of macroscopic residual stress along the cut's shift direction σ_L, perpedicular cut's shift direction σ_T, microstrains ε_{micro} and surface roughness *Ra* are averages from measurements in three areas chosen on the investigated surfaces. The hardness *HV0.2* is a mean value from 18 locations on the analysed surface.

The experimental error of macroscopic residual stress´ measurements $\Delta\sigma$ does not exceed 20 MPa, $\Delta\varepsilon_{micro} < 3 \cdot 10^{-4}$, and the 95 % confident interval of *HV0.2* is smaller than 1 % of the values below.

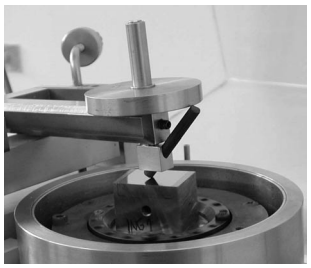

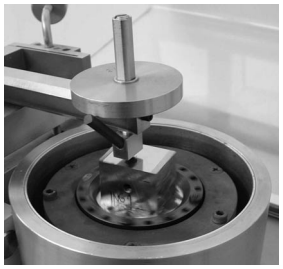

Fig. 1. **Pin-on-disc test layout**

Table II
Results of surface integrity parameters on the measured surfaces

Sample	σ_L [MPa]	σ_T [MPa]	ε_{micro} [$\times 10^{-4}$]	*Ra* [μm]	*HV0.2*
SA2	– 113	– 137	29.7	0.23	769
SA3	– 150	– 179	28.4	0.22	762
SE2	– 353	– 125	24.7	0.09	762
SE3	+ 31	+ 311	30.4	0.14	758
WA2	– 451	– 520	35.9	0.75	835
WA3	– 390	– 395	36.7	0.71	818

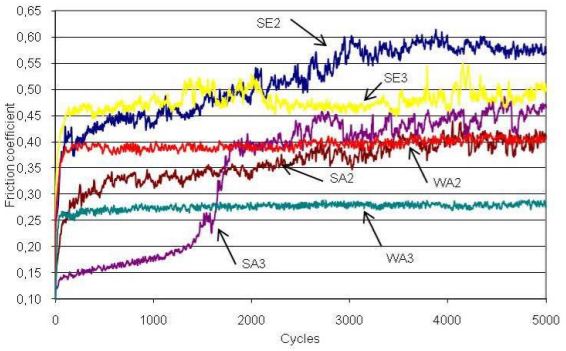

Fig. 2. **Friction coefficient curves for layout 1**

Comparisons of friction coefficient curves at different radii for all samples are in Figs. 2 and 3.

4. Discussion

It has been shown[8] that, in general, compressive residual stresses can favourably reinforce dynamic strength by about 50 %; on the other hand, tensile stresses could reduce the dynamic strength by about 30 %. The advantageous effect can be derived from a mechanical model of counterbalancing, when residual stresses mitigate the adverse effects of tensile load stresses[9] that occur during the lifetime. The concept of

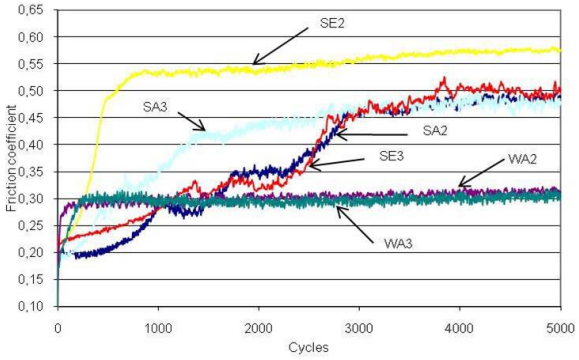

Fig. 3. **Friction coefficient curves for layout 2**

compressive stresses as an elastically compressed lattice would also explain their beneficial role in corrosion resistance.

In the studied case, favourable compressive macroscopic stresses were obtained on all the samples with the exception of surface *SE3*, where tensile residual stresses were found. At the same time, this sample showed significant anisotropy and $\sigma_T = 10\ \sigma_L$. As can be seen from Tab. I & II, only in the case of the tool *SE* is surface residual stress very sensitive to the cutting depth a_p, i.e. when a_p changed from 0.5 mm to 0.3 mm compressive RS of – 353 MPa converts to tensile RS of + 31 MPa. These observations could be explained by the small tool diameter and big shift resulting in a cutting forces' distribution different from the case of *SA* and *WA* tools.

The *WA* tools generate the highest compressive residual stresses and the biggest values of microhardness and microstrains. These facts give evidence of a predominant effect of inhomogeneous plastic deformation of surface layers during cutting in comparison to thermal influence, which is apparently a consequence of the (5–6 times) slower cutting speed and the (4 times) greater number of teeth with respect to the remaining two tools.

In the case of side milling, surface microrelief is a result of the tool's revolving and relative feed of the tool and a workpiece, and thus depends on the measuring direction. The values *Ra* in Tab. II are obtained in the direction of cut's shift (σ_L). As can be seen from Tab. II, the depth of cut does not have any impact on the surface roughness and *Ra* primarily depends on the tool's diameter, its feed and cutting speed.

The obtained average surface hardness of 770–860 HV0.2 corresponds to the values expected for the hardened 14100 steel. This demonstrates that no additional hardening took place as a result of plastic deformation during machining. The temperature on the surface increases with increasing cutting speed, which leads to a microhardness decrease (see Tab. II) of the technologically influenced subsurface layer. In all the investigated cases, deeper cuts (a_p = 0.5 mm) lead to slightly higher microhardness HV0.2 in comparison to a_p = 0.3 mm, even though the differences are within the experimental precision.

Although the values of tribology test parameters are higher than the operational ones for components in contact, the specimen material (steel) showed no damage. The material from the cylinder (polymer) was transferred onto the steel surface in all tests, but the most visible wear traces were on *WA* samples.

Samples *WA2* and *WA3* showed the highest surface roughness, i.e. more than 0.7 μm *Ra*, along with the most uniform or less scattered friction coefficients curves in both layouts. According to Tab. I, these two samples are distinguished by the highest compressive residual stresses.

It is worth emphasising that the highest friction coefficient was obtained for *SE* samples with the lowest roughness while the lowest friction coefficient for *WA* samples with the highest roughness.

Pondering the differences between the two tribology test layouts used, the lower scatter of friction coefficient was determined for layout no. 2.

5. Conclusions

The performed analyses facilitate drawing these main conlusions:

- The surfaces of all analysed samples are homogeneous from the point of view of studied surface integrity characteristics.
- The high roughness in *WA* surfaces does not negatively influence friction coefficient. In a similar matter, low roughness (*SE*) leads to high friction coefficient.
- The best, i.e. the lowest, scatter of friction coefficient curves was recorded on surfaces with the highest roughness (*WA*).
- The lowest friction coefficients were found in surfaces milled with the *WA* tool that, at the same time, is distinguished by the highest compressive residual stresses.
- Increasing cutting speed leads to a rise in temperature at the cutting zone which results in a decrease of measured microhardness.
- The change of the cutting depth from 0.3 to 0.5 mm does not have any impact on the surface roughness values.

The research was supported by Project № 101/09/0702 of the Czech Science Foundation and by Project MSM 6840770021 of the Ministry of Education, Youth and Sports of the Czech Republic.

REFERENCES

1. Welzel U., Ligot J., Lamparter P., et al.: J. Appl. Cryst. *38*, 1 (2005).
2. Mahdi M., Zhang L. C.: J. Mater. Process. Technol. *95*, 238 (1999).
3. Leskovar P., Peklenik J.: CIRP Anals – Man. Tech. *31*, 447 (1982).
4. Persson B. N. J.: *Sliding Friction - Physical Principles and Applications*, Springer-Verlag, Berlin 1998.
5. Williams J.: *Engineering Tribology*, Cambridge University Press, New York 2005.
6. Hauk V. et al.: *Structural and Residual Stress Analysis by Nondestructive Methods*, Elsevier Science B. V., 1997.

7. de Keijser Th. H., Langford J. I., Mittemeijer E. J., Vogels A. B. P.: J. Appl. Cryst. *15*, 308 (1982).
8. Youtsos A. G.: *Residual stress and its effect on fracture and fatigue*, Springer 2006.
9. Abu-Nabah B. A., Nagy P. B.: NDT&E International *40*, 405 (2007).

Z. Pala[a], N. Ganev[b], K. Kolařík[c], O. Bláhová[d], and J. Jersák[e] *([a] Department of solid state engineering, FNSPE, CTU in Prague, [b] Department of solid state engineering, FNSPE, CTU in Prague, [c] Department of solid state engineering, FNSPE, CTU in Prague, [d] Department of mechanics, Faculty of applied sciences, University of West Bohemia, [e] Department of machining and assembly, Faculty of mechanical engineering, Technical University of Liberec):* **Surface Integrity and Tribological Behaviour of Hardened Steel.**

A comparison between the results of tribological investigations and four surface integrity parameters, i.e. macroscopic and microscopic residual stresses, roughness and microhardness, was performed. The samples in the form of two parts of guide gibs from steel embedded into a cast iron bed were subjected to side milling by three different tool tips. The performed analysis yields some mutual relationships between surface integrity and friction coefficient, e.g. low roughness lead to high friction coefficient, the highest compressive residual stresses were found for the lowest friction coefficients, or increasing cutting speed leads to a decrease in microhardness.

EFFECT OF INDICATION LIQUIDS ON BRITTLE-FRACTURE PROPERTIES OF VITREOUS ENAMEL COATING

KAMILA HRABOVSKÁ[a]*, JITKA PODJUKLOVÁ[b], ONDŘEJ ŽIVOTSKÝ[a], KARLA BARČOVÁ[a], IVO ŠTĚPÁNEK[c], VRATISLAV BÁRTEK[b], and TOMÁŠ LANÍK[b]

[a] Institute of Physics, [b] Faculty of mechanical Engineering VŠB -Technical University of Ostrava, 17. listopadu 15, 708 33 Ostrava Poruba, [c] Faculty of mechanical Engineering, University of West Bohemia in Pilsen, Univerzitní 8, 306 14 Plzen, Czech Republic
kamila.hrabovska@vsb.cz

Keywords: vitreous enamel coating, steel, microhardness, mechanical properties, indication liquid

1. Introduction

Enamel coatings belong to the category of vitreous ceramic covering crusts providing very high resistance of steel substrates against damage and corrosion. This type of coatings can be used in energetic, environmental, or agricultural machinery, in architectonic design and civil engineering, in car industry, health service, and in products of consumer goods[1–6]. However, creating a compact enamel coatings without faults is the essential precondition for using its functional properties[2,3].

Undesirable faults of coatings may occur e.g. by selection of an unsuitable foundation substrate, type of enamel coat, or by the technological procedure of enamelling. One of the most serious problems is the hydrogen faults (fish scales) created by the hydrogen penetrating to the surface of the coat from the steel – enamel boundary[1].

Low voltage test (LVT) is usually performed to verify surface properties of the enamel coatings and to determine material defects (according to the ČSN EN ISO 8289 standard). The LVT test is realized using indication liquids (containing water, water-soluble salts and surfactant) as and electricaly conductive solutions. Unfortunately, the testing standard does not indicate any way of cleaning the coat from indication liquids. Long-time treatment of the indicating liquids after LVT testing may cause the damage of the surface layer and the creation of faults detected by customer´s acceptance test[7–13].

The main aim of this paper is to investigate the influence of indication liquids on brittle – fracture and mechanical properties of the under-coat and top-coat enamels. To realize this aim a number of modern experimental methods were applied (expecially scratch and nano-indentation test).

2. Sample preparation

For experimental testing, a steel plate was used as the substrate with the following properties: the quality of kosmalt E 300T (produced by U.S. Steel Košice) and the thickness of 3 mm (chemical composition (weight %): C: 0.041; Si: 0.02; S: 0.007; N: 0.006; Mn: 0.241; P: 0.010; Al: 0.052; Ti: 0.067; Cr: 0.023; Mo: 0.005; V: 0.005). The surface of hot-rolled steel plate was treated by mechanical shot blasting to obtain the surface cleanliness of Sa 2.5 (ČSN EN ISO 12944-4) and additionally degreased for 5 minutes in the degreasing alkali liquid Simple Green with the concentration of 1:10 and the concentrate pH of 9.4.

The 24 hour-old enamel slurry was applied on degreased steel substrate by pneumatic spraying, dried at the temperature of 100 °C for 5 minutes, and subsequently burned at the temperature of 820 °C for 8 minutes. Consequently the samples were cooled in air at the temperature of 20 °C. In accordance to the colour were distinguished two types of enamels: the grey (basic under-coat) and the green (top-coat). The consistence of both enamels is 1750 kg m^{-3} and main chemical composition (wt.%): 25 quartz ground, 8 clay MIC, 0.4 boric acid, 0.3 Sb_2O_3, 0.05 K_2CO_3, 0.15 $NaNO_2$ and 56 water. Undercoat enamel layer forms the function interlayer in enamel-metal system. Due to higher content of elements (Si, Ni, Ca, K …) it caused increasing adhesion of glassy phase to the substrate and strongly influences a surface design of final product[14–19].

Surface properties of three different samples were investigated. Sample 1 is the initial degreased steel substrate covering by grey under-coat and green top-coat enamel layers without the exposure of any indication liquids. Sample 2 containes the same enamel layers as sample 1, but the surface was additionally treated by the NaCl indication liquid (30 g NaCl per 1 l water + liquid tenside). Surface treatment of the sample 3 was performed using $NaNO_2$ indication liquid (30 g $NaNO_2$ per 1 l water + liquid tenside). Average electrical conductivities of NaCl and $NaNO_2$ enriched liquids were determined to 50.858 mS and 50.231 mS with pH of 8.02 and 8.19. Such prepared samples were waterproofly packed according to the storage prescripts of manufacturing, time of exposure of indication liquids was chosen for 3 weeks at the laboratory temperature of 20 °C. This time period represents the usual time interval between the production output check of the enamel coat and the customer's acceptance of the product. The thickness of both layers of enamel coating (under-coat and top-coat) is 200 μm.

3. Experimental methods

Microhardness measurements and fracture toughness

Microhardness is defined as a resistance of material to local plastic deformation, which is established by the loading of surface by an indenter. To determine the H_V parameter describing the microhardness using the Vickers method was used Hanemann microhardness tester (NEOPHOT 2 optical microscope) with a diamond pyramid indenter with the apex angle of 136°. Indenter was impressed perpendicularly to the surface of investigated coat with the force of 1 N during the

time of 10 s (ref.[14–19]).

Using microhardness measurements were defined critical values of the stress intensity coeficient K_Ic for investigated samples. At this value of stress intensity the crack does not propagate. Fracture toughness is an indication of the amount of stress required to propagate a preexisting flaw. It is a very important material property since the occurrence of flaws is not completely avoidable in the processing, fabrication, or service of a material/component. Flaws may appear as cracks. On the basic of the resultant values microhardness and Palmquist crack length (Fig. 1) we determined the fracture toughness K_Ic (equation (*1*)).

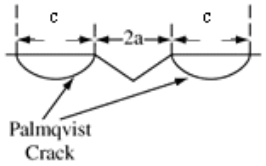

Fig. 1. **Palmqvist Crack formation by Vickers indentation**

Palmqvist crack formula used for the evalution of the fracture toughness[14]:

$$K_{IC} = 0.035\left(\frac{c}{a}\right)^{-\frac{1}{2}}\left(\frac{Ek}{H_v}\right)^{\frac{2}{5}}\left(\frac{H_v a^{\frac{1}{2}}}{k}\right) \qquad (1)$$

for:

$$0{,}25 < \frac{c}{a} < 1{,}5$$

E – Young modulus, H_v – microhardness, a – half diagonal length of the microindentation, k – constraint factor ≈ 3, c – total crack length.

Resistance to shot (shot firing test) and abrasion (by ball tester)

Shot firing tests were provided using steel ball with diameter of 5 mm fired towards on enamel surface with the increasing impact force in the range 10–90 N. Adhesion of vitreous enamel coating was obtained according to the Wegner instrument in compliance with ČSN ISO 4532 (945050) standard.

A rotating steel ball with diameter of 30 mm affecting a certain place of the enamel coat surface was used for test checking the resistance to abrasion.

Surface roughness

ČSN ISO 4287 standard was used for evaluation of the surface roughness. Coating roughness (as a deviation with the rexpect to the mean line of the profile) is defined by 2 main parameters: Ra – mean arithmetic deviation of the profile and Rz – miximum height of the profile. Our measurements were performed using the contact profilometer Mitutoyo, SurfTest SJ-301 with mobile measurement head fitted by a retractable diamond stylus sensor (5 μm/0,2 mils radius) and working at load of 4 mN.

Scratch, static and nano indentation test

A scratch indentation test was carried out by means of a diamond indenter of the Rockwell type (cone) with the apex angle of 120° and radius of curvature of 0.5 mm. The value of normal loading affecting the indenter was changing with constant speed and the table with the fixed sample under the indenter was moving with the same speed as well. The range of normal force from 40 N to 80 N was used for the evaluation.

During the measuring process, the course of an acoustic emission signal depending on the acting of normal force was recorded. However, signals of the acoustic emission follow the deformation and fracture processes and provide integral information on the current dynamic state of material. After finishing the scratch test, we documented the morphology of failures with the help of a light microscope with highlighting of the failure by means of polarization and the Nomarsky differential contrast. Existence of brittle fractures was confirmed at the scratch indentation test and experimental analysis of the acoustic emission signal without sample moving (static indentation test). These surface-sensitive methods enabled to obtain the dependence of acting loading as a function of penetrating depth of the enamel. This experiment was done by means of the Nanoindenter SHIMADZU DUH – 202, the device with the following parameters: – indenter loading: 0.01–200 g (with the accuracy of 0.002 g), – depth of indentor penetration: 0–10 μm (with the accuracy of 0.001 μm).

3. Results and discussions

Differences between the surface structure of the initial steel plates before and after degreasing process are shown in Fig. 2. The as-prepared non-degreased plate exhibits dirty surface with the crack-type faults. The uniformity of shot blasting process proved positively influence of the adhesion to the vitreous enamel coating for degreased sample.

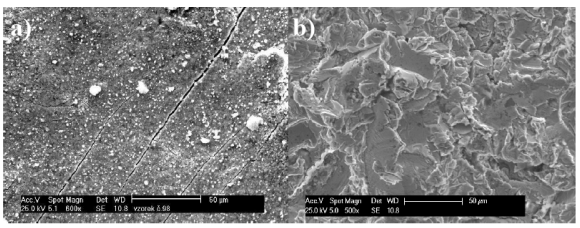

Fig. 2. **SEM analysis of the a) non-degreased and b) degreased, shot blasted raw steel plate surface**

Chemical element analysis and SEM micrographs of enamel slurries are compared in Tab. I and Fig. 3.

Experimental results clearly confirmed negative influence of indication liquids exposure on brittle-fracture properties of vitreous enamel coatings. Table II shows that sample 2 and sample 3 parameters of microhardness, fracture toughness, roughness of the coat and its adhesion are markedly deteriorated in comparison to reference sample 1. In the case of microhardness test the microscopic analysis showed in Fig. 4 indicate a visible damage of the surface, microcracks and conchoidal fractures with numerous Wallner lines ob-

Table I
Chemical analysis of the enamel slurry of grey basic enamel and green top enamel

Chemical element	grey under-coat	green top- coat
	total weight percentage Wt [%]	total weight percentage Wt [%]
O	32,76	29,57
Na	9,96	10,14
Al	6,05	7,26
Si	38,96	34,32
K	1,92	0,41
Ca	5,49	3,24
Ti	1,12	3,26
Fe	2,15	2,48
Co	0,46	2,63
Ni	1,13	-
Cr	-	6,68
Total	100	100

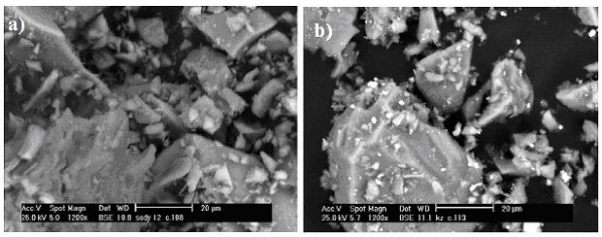

Fig. 3. **SEM analysis of the enamel slurry of grey basic enamel (a) and green top enamel (b)**

served in the neighbourhood of diagonals originated after the impress of Hanemann indenter. Such fractures are typical for brittle vitreous materials with low fracture toughness. In diagonals of an indenter impression the presence of radial Palmquist cracks, with lengths used to determination the fracture toughness K_Ic, can be seen. Decreasing values of bursting force strength F_P confirm the reduction of adhesion of enamel coats to the steel substrate, conversely from profilographs substantial increase of surface roughness (measured parameters of Ra and Rz are approximately 1,5 times higher in comparison to reference sample) were observed. But it must be stressed that marked difference between samples 2 and 3 was not proved using these methods.

As a result of rotating-ball test was detected the length of the damage region L after 6000 rotations of ball that are marked in Fig. 5 for samples 1, 2 and 3. Resistance to abrasion was sole test, at which the sample 2 exhibits better mechanical properties than sample 3. At Fig. 5 are visible regions of the damage without the circle shape (corresponding to the surface roughness). Their measured lengths L for samples 1, 2, and 3 were estimated to 210 µm, 270 µm, and

Table II
Average values of microhardness, fracture toughness, bursting force by the shot firing test, and surface roughness of the vitreous enamel coat before and after the exposure to indication liquid

	Sample 1 without indication liquids	Sample 2 indication liquid NaCl	Sample 3 indication liquid $NaNO_2$
$HV_{0,1}$ [MPa]	6749,58	7341,39	7450,89
K_{IC} [MPa.m$^{1/2}$]	0,85	0,79	0,80
Bursting force Fp [N]	90	75	80
Surface Roughness [um]	Ra = 0,27 Rz = 1,55	Ra = 0,44 Rz = 2,27	Ra = 0,38 Rz = 2,33

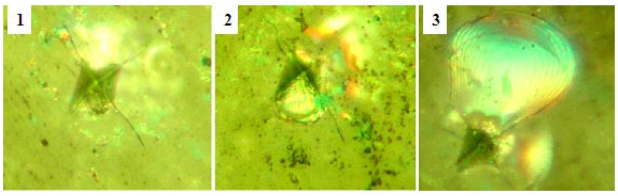

Fig. 4. **Impress of the Hanemann microhardness tester into the surface of enamel coats. Enlarged 1000 times**

300 µm, respectively. In accordance with previous results showing the higher microhardness and lower fracture toughness, the ball test was connected with the crumbling of the particles of the coats, especially for samples 2 and 3. The highes damage was observed for the sample 3 with the higher value of microhardness. It is a typical phenomenon for vitreous enamel coatings.

Results of the scratch test, when the normal force ranges from 40 N to 80 N: The sample 3 exhibits a slow penetration of the indenter into the surface. The scratch was slowly spreading and near the normal loading of 40 N, there was a visible formation of cracks across the scratch. With increasing normal loading, the cracks gradually grew and failures in the surroundings of cracks occurred even at higher normal forces. During acting of the normal force from 0 N to 40 N, the sample 2 showed a similar process, with the difference

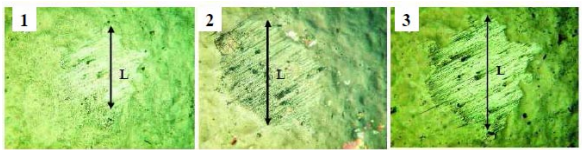

Fig. 5. **Regions of the coat damage with determined damage lengths L after the ball test. Enlarged 100 times**

that cracks were formed at lower normal force. At higher values of normal forces, the most significant failure in the surroundings of the cracks was observed. In contrast, the sample without the exposure of indication liquids (sample 1) embodies the highest resistance and the highest hardening with regard to the width of the scratch. Very shallow cracks are formed at around 40 N. These results were supported by the acoustic emission measurements. We found out that signal courses at all samples have similar character, the first and the latest responses were detected about the forces of 6 N and 12 N in the case of samples 2 and 1, respectively. The graph of static indentation test is shown in Fig. 7. Maximal normal loading of 100 N showed substantial cracking of the sample surface, where the indication fluid with the NaCl content acted (denoted by line with circles). The reference sample (full line) is without distinct failure and the sample with the $NaNO_2$ content (line with square) shows, except small marks at the beginning of the curve and around the values of 35 N and 48 N, gradual increase of small brittle fractures from 78 N of normal loading. The highest depth at nano indentation test (about 4,5 μm) was determined for NaCl enriched sample (see Fig. 8), while at the reference sample 1 and the sample 3 with the $NaNO_2$ content the indenter penetrates into the similar depth of 4,3 μm. 4,4 % difference of penetration depth is a strong influence in the nano-scale. Based on the results of indentation tests we can conclude that indication liquid with NaCl strongly influences surface quality and properties of enamel coatings. These conclusions are supported by the fact that when the samples were unpacked after 3 weeks, surface of the sample 2 observed by optical microscope showed the origin of colour thin plan-parallel layer in the surroundings of the coat fault, which penetrates up to the steel substrate. This layer obviously comes from the reaction of indication liquid with NaCl content and the iron oxides. Note that this phenomenon was not visible at sample 3.

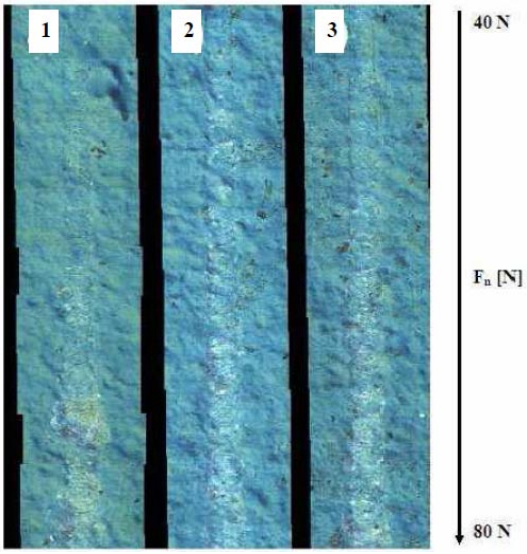

Fig. 6. **Scratch indentation test of vitreous enamel coat before (1) and after (2, 3) exposure to the indication liquid containing NaCl and NaNO2, respectively**

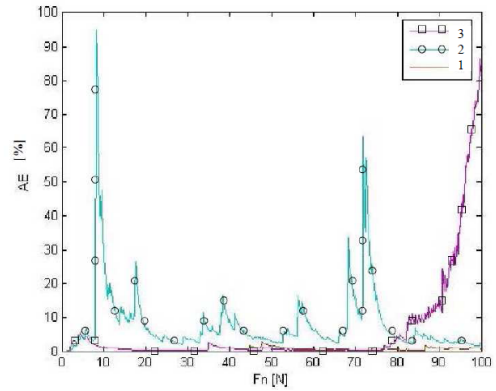

Fig. 7. **Static indentation test – full line and lines with circles and squares correspond to the acoustic emission signals detected from samples 1, 2, and 3, respectively**

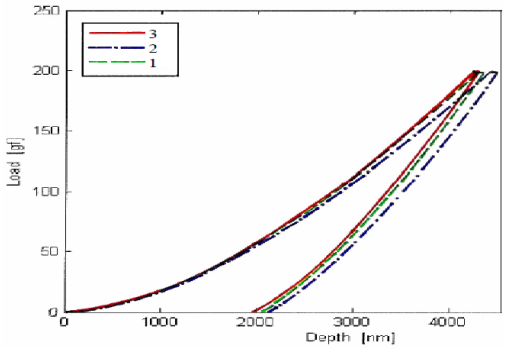

Fig. 8. **Depiction of an indentation curve – dependence of force intensity and deformation during the nano-indentation test with the maximal normal loading of 200 g**

4. Conclusion

Indication liquids are substances used for identifying faults in vitreous enamel coats. Results presented in this paper confirm that their long-time exposure cause the corrosion of vitreous part of enamel coating and in this way significantly decrease final quality of the enamel coat surface. According to these facts, residue of indication liquids after the LVT should be included into the whole process of production monitoring and controlling the quality of vitreous enamel coats at producers. Moreover, mechanical properties of enamel products with deteriorate brittle-fracture parameters often become worse during the transport to the customer.

Acknowledgments – MŠMT ME 08083, MSM6198910016, SP2011/26, CZ.1.05/2.1.00/01.0040.

REFERENCES

1. Podjuklova J.: *Studium vlastností systémem kov-sklovitý smaltový povlak*, VŠB-TUO, 44 (2000).

2. Yatsenko E. A., Ryabova A. V., Zubekhin A. P., Guzii V. A.: Glass Ceram. *54*, 1-2 (1997).
3. Podjuklova J., Mohyla M.: Acta Metall. Slovaca *6*, 380 (2000).
4. Hrabovska K., Barcova K., Podjuklova J., Sionko M.: Acta Mechanica Slovaca *9*, 67 (2005).
5. Yang X., Jha A., Brydson R., Cochrane R. C.: Mater. Sci. Eng. *A366*, 254 (2004).
6. Zhang T., Bao Y., Gawne D. T.: J. Eur. Ceram. Soc. *23*, 1019 (2003).
7. Curtis T.: Shreir's Corrosion, Chapter 3.28, 2330 (2010).
8. Oliver S., Proctor B. A., May C. A.: Shreir's Corrosion *3*, 2306 (2009).
9. Protasova L. G., Kosenko V. G., Farafontova E. P.: Glass Ceram. *60*, 229 (2003).
10. Barcova K., Mashlan M., Zboril R., Filip J., Podjuklova J., Hrabovska K., Schaaf P.: Surf. Coat. Technol. *201*, 1836 (2006).
11. Barcova K., Mashlan M., Zboril R., Hrabovska K.: *AIP Conference proceedings*, (M. Gracia, J.F. Marco, F. Plazaola, ed.). American Institute of Physics 765, 120 (2005).
12. Yang X., Jha A., Brydson R., Cochrane R. C.: *An analysis of the microstructure and interfacial chemistry of steel–enamel interface*. 33–45, (2003).
13. Bouše V.: *Smalty a jejich použití v protikorozní ochraně*, SNTL, Praha 1986.
14. Menčík J.: *Pevnost a lom skla a keramiky*, SNTL, Praha 1990.
15. Hrabovská K., Podjuklová J., Barčová K., Dobrovodská L., Pelikánová K.: Email *4*, 57 (2008).
16. Hrabovská K., Podjuklová J., Pelikánová K., Dobrovodská L., Laník T., Viliamsová J.: Acta Mechanica Slovaca *4 – B*, 126 (2008).
17. Barcova K., Zboril R., Mashlan M., Jiraskova Y., Filip J., Lunacek J., Hrabovska K.: Surf. Interface Anal. *38*, 413 (2006).
18. Hrabovská K., Podjuklová J., Barčová K., Dobrovodská L., Pelikánová K.: Solid State Phenomena *147 -149*, 856 (2009).
19. Dietzel A.: Glass Email *73*, 63 (1940).

K. Hrabovská[a], J. Podjuklová[b], O. Životský[a], K. Barčová[a], I. Štěpánek[c], V. Bártek[b], and T. Laník[b] *([a] Institute of Physics, VŠB-Technical University of Ostrava, Ostrava, [b] Faculty of mechanical Engineering, VŠB-Technical University of Ostrava, Ostrava, [c] Faculty of mechanical Engineering, University of West Bohemia in Pilsen, Plzen, Czech Republic):* **Effect of Indication Liquids on Brittle-Fracture Properties of Vitreous Enamel Coatings**

Vitreous enamel coatings are created by the process of burning at temperature above 800 °C after the application of an enamel slip on metal substrate. To detect the faults and cracks in the coat, which penetrate up to the steel substrate, the coat surface is covered by different types of indication liquids. In this paper we observed the influence of two types of indication liquids on the brittle-fracture of under and top vitreous enamel coatings. Results show that long-time exposure of indication liquids negatively influences brittle-fracture properties. Hence we recommend careful removing of indication liquids from the enamel surface immediately after the low voltage test.

LOCAL STUDIES OF CAST IRON MACHINED SURFACES

ANTONÍN KŘÍŽ

University of West Bohemia, Univerzitní 22, 30614, Plzeň, Czech Republic
kriz@kmm.zcu.cz

Keywords: surface integrity, machined surfaces, special drilling tool, surface morphology

1. Introduction

Chip removal belongs to the machining processes where higher surface quality is required. The surface used to be evaluated to a very limited extent, mostly involving roughness characteristics. Description of surface is more accurate if it includes not only Ra roughness but also additional surface characteristics, in particular the areal roughness. Nowadays, tools, instruments and experience are available that allow better characterization of the state of surface and correlations with resulting properties. Comprehensive examination of machined surfaces is based on state of the art knowledge which is often summarized in the surface integrity concept. The techniques include scratch testing, nanoindentation hardness measurement, cyclic impact testing and local corrosion testing.

1.1. Surface Integrity Concept

Surface integrity exploration is based on the set of instruments at the author's department and on the cooperation with the Department of Machining Technology at the Faculty of Mechanical Engineering of the University of West Bohemia in Plzeň. This cooperation expands to include practical applications thanks to scientific and industrial projects concerning both machining accuracy and the state of surface. Application of surface integrity to practical issues requires a very cautious approach. First, the results obtained are extensive and may not be always relevant to practical use. Second, they might be conflicting. The state of surface used to be described by means of roughness characteristics. Surface and sub-surface defects received some attention as well. In more profound studies, these were even correlated with the material's fatigue behaviour. The comprehensive nature of those results requires that they are treated in an appropriate context and with proper correlations. Measurement of residual stresses may serve as an example[2,4–6]. The problems arise in selection of a method of determining residual stresses with certain (in)accuracy. Others are related to its interpretation and usability in practice. In the real world, problems might occur with the usability of solely residual stress-based findings for rejecting non-conforming products or for predicting service properties. Four years ago, there was only one company on the European market offering defined finishing of machined surfaces, the Baublies AG[1]. Its contribution consists in developing a standalone roller burnishing tool which offered numerous advantages. One of the most important ones is the fact that it is adjustable within a certain range of diameters and this adjustability is useful for worn rollers as well. On the other hand, it also has its drawbacks: the drilled hole must have certain characteristics related not only to accuracy but also surface morphology and hardness. It cannot be used as a combination tool either. Another drawback is its high price which is many times higher than the prices of drills and even broaches. Despite these drawbacks, this company's range of products has no competitor in Europe. This company can boast not only market innovations but also scientific contribution, as it was its product range which introduced the surface integrity concept into engineering practice. Although the American standard on surface integrity, ANSI B211.1 1986, has been presented three years ago, it has been used very little in practice.

This is why broader description of individual properties is necessary. At first sight, these may lead to conflicting findings but in wider context they will be more accurate than mere residual stress measurement whose interpretation is difficult and often impossible. Theoretical aspects of the individual factors of surface integrity are covered in the standard and presented in a number of papers[2–4]. This study aims to describe a specific evaluation of machined surface of drilled holes in a cast iron, focusing both on the resulting accuracy and other surface integrity aspects.

2. Experimental Procedure

This study was aimed at the surface integrity of drilled holes with the depth of 3D where the required tolerance grade was IT6 – IT7. The studied material was gray cast iron. Testing samples were cylinders with the following dimensions: d = 26 mm, l = 36 mm. Three types of drills denoted A, B and C from different companies were used for hole drilling into the cylinders. After drilling, the cylinders were cut along their axis to allow analysis of the machined surface.

The following factors were monitored: surface topography measurement, surface roughness, surface microstructure, microhardness, nanoindentation hardness, scratch, corrosion and impact resistance.

3. Results and Discussion

3.1. Surface Topography

Optical micrographs of surfaces of holes were compared visually and by means of image analysis software.

The surface of the hole drilled with the tool A exhibited dark spots where the machined surface was pulled out during drilling, and light areas where no extraction occurred. Sharp edges of graphite flakes are locations of high stress concentration, contributing to the pull-out of graphite particles or even parts of surface attached to them (see Fig. 1). Analysed surfaces showed parallel markings running at about 30° to the axis of the cylinder, regardless of the tool used. These are

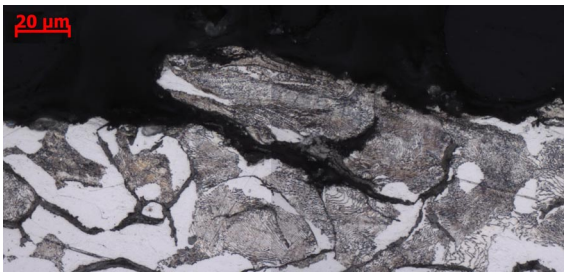

Fig. 1. **Micrography of pull-out of surface in the drilled hole**

probably traces of surface deformation caused by the tool flank while the tool was being removed from the hole. These irregularities can be regarded as undesirable effects impairing the quality of the machined surface. Such surface defects can be detected only using light or scanning confocal microscope, image analysis and measuring areal roughness because they do not affect roughness values. Despite, a number of authors accept roughness values as decisive data for description of surface state. The roughness data cannot be regarded as conclusive, as it does not reflect the actual condition of the surface.

The amount of extracted surface depends on the stress state and on the forces between the tool and machined surface. It is assumed that the higher the internal stress (particularly the tensile stress) in the machined surface, the greater the amount of graphite pulled out together with the matrix by the drilling tool and the greater the depth from which the material is extracted. The quality of the machined surface is impaired by this process. This finding implies that the time-consuming measurement of residual stresses may not be necessary. It is the heterogeneous microstructure of grey cast iron for which this approach proves effective, as the location of material pull-out is governed by the location of graphite under the surface (Fig. 1). The surface relief is affected by the state of microstructure in a definite manner. The study of the surface is useful also for revealing the internal structure which changes in dependence on the introduced stress and temperature. These relations proved true mainly during drilling of D2 tool steel when, with certain machining parameters, the drilled surface re-hardened and its hardness increased markedly again (Fig. 2).

3.2. Surface and Subsurface Microhardness

Microhardness of specimens was measured along two lines located about 50 µm apart and in 50 µm distance from and parallel to the surface. The first line was just beneath the machined surface and in the plastic deformation zone created by the cutting tool. The second line of indentations was in the unaffected material. By comparing average hardnesses along both lines and average standard deviations, one can assess the state of the material surface after machining. Hardness was measured as HV0.015 microhardness.

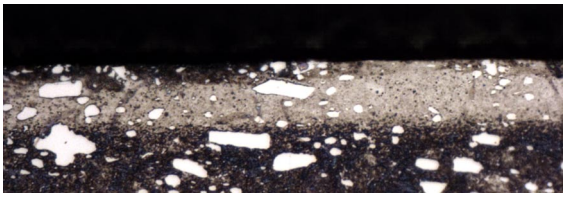

Fig. 2. **Surface hardened to the depth of 30 µm. D2 steel with surface hardness of HV0.01 = 1.107**

The results show that changes in hardness of the material were not consistent. In some cases, hardness of the machined surface decreased, despite the expected influence of plastic deformation. In this case, certain impact of the tool wear cannot be ruled out, as under normal conditions, i.e. normal machining temperature, cast iron should not exhibit softening. The decline may also be explained by the effects of the cutting process, which does not introduce sufficient amount of strain or even lacks the parameters to make the material strengthen above its initial level. The tool A retained its initial parameters throughout the cutting process. The tool B lost its ability to cause work hardening in the material at the end of the drilling process. The tool C with its special geometry caused the material to harden gradually. Compared with C45 steel which was also tested in the present project, the increase in the amount of deformation in cast iron is much smaller.

3.3. Surface and Subsurface Nanohardness

Nanoindentation measurements are carried out in the material unaffected by drilling and in the machined surface. Unlike in the case of conventional microhardness measurement, the effect of hardening was found in all surfaces of drilled holes. The average increase in nanoindentation microhardness HIT in the affected zone was 47 % compared to unaffected material. With the tool A, this increase was 55 %. From the viewpoint of elastic-plastic strain ratio, highest values were found for the tool B: 27.2 %. For the tool C, the elastic-plastic strain ratio was the smallest (24.2 %).

3.4. Scratch Testing

Scratch testing is typically used for assessing the adhesive-cohesive behaviour of thin film-substrate systems. However, it can be employed also fin the case of drilling-affected surface layers. The purpose of measurement was not only to determine the surface hardness but also the surface uniformity along the entire hole depth of 36 mm. Two 18 mm scratches were created on the surface under a constant load of 40 N. Scratch channel volumes were measured using Olympus Lext 3100 confocal microscope at the magnification of 200×.

Volumes of scratch channels on the machined surface of the cast iron show that the largest value (indicating the lowest surface hardness) is associated with the element machined by the tool A. In contrast, the lowest scratch channel volume was found in the element drilled with the tool B. Scratch channel volumes are not very different. The differences are within the measurement error range, which is why these results do not confirm the earlier conclusion that the tool A produces the softest surface.

Results of this analysis have been included in this paper on purpose, although they do not correspond to the above findings and are in contradiction to the assumption that

scratch channels are less deep in materials with higher hardness. This contradiction illustrates the difficulties inherent to characterising comprehensive properties of real-world surfaces in relation to surface integrity.

3.5. Corrosion Resistance Tests

The purpose of the corrosion test was to assess the impact of the state of machined surface on the corrosion behaviour. This simple corrosion test does not clearly indicate if the dominant aspect is the surface topography or the activation energy increased by plastic deformation. The most rapid corrosion was seen in specimens drilled with the tool B. The other drilled holes showed very similar results. After finding additional correlations, it was shown that the surface created by the tool B contains more defects, pull-out regions and higher hardness. In this case, the surface relief proved more significant than the plastic strain introduced, as the latter was negligible in the machined surfaces.

3.6. Cyclic Impact Test

Impact resistance of hole surfaces was evaluated by means of the cyclic impact test. It consists in cyclic impact loading of the surface. The blows are repeated with certain pre-defined frequency and energy.

The examined surfaces were subjected to identical loads consisting in 5,000 impacts with the lowest energy available in the setup. The purpose of the test was to measure the properties of those surface areas where different effects of the cutting tools were expected. The test created an impact crater which was then examined. The crater dimensions were measured and characteristics of degradation processes were determined (surface layer delamination, cracks).

The craters were observed in a light microscope and using a scanning electron microscope (SEM).

The dimensions of craters did not differ significantly. It is due to the fact that the state of machined surfaces does not vary enough under the presently used impact test conditions to be detected. SEM examination of defects in the crater revealed that the surface machined with the tool C was of higher quality than those created by the other two tools. Thus, a surface machined with high-quality tools has negligible influence on degradation processes under impact loads in ordinary service. Detecting the state of machined surfaces more accurately would require much lower energy of the impact body than in the current test.

4. Conclusions

The concept of surface integrity encompasses various methods to obtain comprehensive image of the state of machined surface. Unfortunately, some results can be conflicting and difficult to classify without contradictions. This may be due to lack of accuracy of measurement but one cannot exclude effects of unknown factors which have different impact in different types of measurement. The former cause can be eliminated by larger number of measurements and by statistical processing of results, taking account of the standard deviation. The latter causes are difficult to identify. They can only be eliminated through better understanding of undergoing processes. This applies to, for instance, the corrosion tests where the results depend on competing effects. Despite these difficulties, surface integrity data are valuable for academic but also for practical applications. In this case, it applies to evaluation of surfaces created by specially designed "finishing" drills. The surface integrity concept will be further developed based on the collaboration of the academic sphere and manufacturers and users of cutting tools.

This paper is one of the outcomes of the project No. FI-IM4/226, which is co-funded by the Ministry of Industry and Trade of the Czech Republic and the company HOFMEISTER s.r.o.

REFERENCES

1. Website of the company Baublies AG available online at: http://www.baublies.com/de/index.html, accessed 2 Aug 2010.
2. Kříž A., Šimeček J.: *Conference proceedings of Vrstvy a Povlaky, Rožnov pod Radhoštěm, 2009.* LISS a.s., 2009, pp. 36-42.
3. Kříž A.: Integrita povrchu a její význam v praktickém použití. Available on-line at: http://www.ateam.zcu.cz, accessed 2 Dec 2009.
4. Kříž A., Šimeček J.: *Conference proceedings of Tepelné zpracování. Jihlava, 2009.* Ecosond, 2009, pp. 1-6.
5. Bumbálek B.: Integrita povrchu a její význam pro posouzení vhodnosti dané plochy pro její funkci. Online at http://www.ateam.zcu.cz, accessed 2 Dec 2009.
6. Stephenson D. J.: Surface Integrity Control During The Precision Machining Of Brittle Materials, available online at http://www.azom.com, accessed 2 Dec 2009.

A. Kříž *(University of West Bohemia, Plzeň, Czech Republic):* **Local Studies of Cast Iron Machined Surfaces**

The surface integrity concept represents a comprehensive characterization of all influences affecting the surface properties and the end-use properties of a product.

This paper describes practical application of the concept of surface integrity to holes drilled in gray cast iron with special tools.

MEASUREMENT OF LOCAL DEFORMATION FIELDS IN DENTAL COMPOSITES USING 3D OPTICAL SYSTEM

MILOS MILOSEVIC[a], VESNA MILETIC[b]*, NENAD MITROVIC[a], DRAGICA MANOJLOVIC[b], TATJANA SAVIC STANKOVIC[b], and TASKO MANESKI[c]

[a] *Innovation Center of Faculty of Mechanical Engineering, University of Belgrade, Kraljice Marije 16, 11000 Belgrade, Serbia,* [b] *School of Dentistry, University of Belgrade, Rankeova 4, 11000 Belgrade, Serbia*
[c] *Faculty of Mechanical Engineering, University of Belgrade, Belgrade, Kraljice Marije 16, 11000 Belgrade, Serbia*
vesna.miletic@gmail.com

Keywords: dental composites, polymerization shrinkage, deformation, light curing units, digital correlation

1. Introduction

Polymerization shrinkage remains one of the most important disadvantages of dental composites and leads to the loss of marginal integrity of the tooth-restoration interface[1]. Shrinkage is caused by shortening the intra-molecular distances between monomer units in the polymer compared to intermolecular distances between free monomers. The formation of microgaps between the cavity walls and the restoration allows the penetration of salivary fluids and microorganisms which may lead to secondary caries. Attempts have been made to develop low-shrinkage composites based on the silorane technology[2,3]. However, polymerization shrinkage has not been eliminated even in the most contemporary materials available on the market.

A variety of contact or non-contact methods have been used to study polymerization shrinkage of dental composites. Recently, digital image correlation based on a single-camera system has been used for this purpose.[4]

The aim of this study was to investigate the possibility to analyze local deformation fields of a dental composite upon polymerization using 3D optical system of digital image correlation based on two cameras.

2. Materials and Methods

A conventional, microhybrid composite Filtek Z250 (3M ESPE, St. Paul, MN, USA) was used in the study. It contains about 20 wt.% of dimethacrylate monomers: Bisphenol A diglycidyl ether dimethacrylate (BisGMA), Diurethane dimethacrylate (UDMA), Bisphenol A polyethylene glycol diether dimethacrylate (BisEMA6), Triethylene glycol dimethacrylate (TEGDMA), and about 80 wt.% of silane treated ceramic fillers.

The material was placed in custom-made Teflon molds. The surface facing the cameras was sprayed with a fine layer of black paint to produce irregular-shaped speckles used as reference points for ease of tracking and analysis by the image correlation system. The unsprayed surface of each sample, opposite the one facing the cameras, was light cured for 40 s using a conventional halogen light curing unit at an intensity of 450 mW cm^{-2} and 1 mm tip-to-surface distance. Standardized conditions were created by mounting each mold onto a fixating device that allowed maintaining the same distance from the cameras. Also, the light curing unit was fixed in a holder at the specified distance from each sample. Fig. 1 and 2 illustrate the experimental setup.

The digital image correlation system (Aramis 2M, GOM, Braunschweig, Germany) consisted of two digital cameras with the resolution of 1600×1200 pixels and maximum frame rate of 12 Hz and specialist software. Other parts of this system were the stand, device for charging and taking pictures and a PC.

Prior to starting the experiment, system callibration was performed using the callibration panel, depending on the chosen measurement volume. This volume was chosen based on the dimensions of the measured local area, and all other dimensions were set based on it in accordance with the tables in the instruction manual[5]. Once the measurement volume and the camera position were successfully aligned during callibration, the measurement could commence.

Digital images of each sample were taken immediately before and after light curing. Afterwards, the computations were applied by the software and various software tools

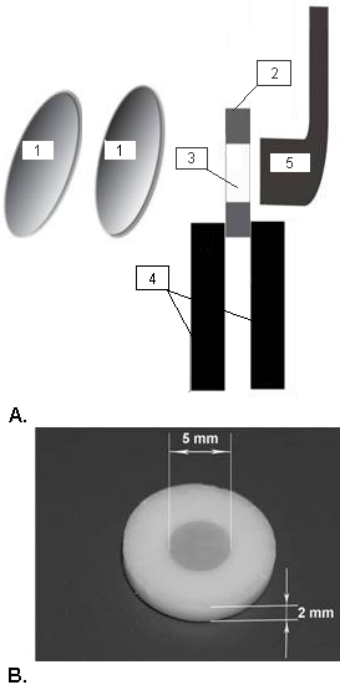

Fig. 1. **A. Scheme of the experimental setup.** 1 – Cameras; 2 – Teflon mold; 3 – Sample; 4 – Sample holder; 5 – Light curing unit. B. Sample, 2 mm thick and 5 mm in diameter, in a Teflon mold

Fig. 2. **Experimental setup.** 1 – Cameras; 2 – Teflon mold; 3 – Sample; 4 – Sample holder; 5 – Light curing unit

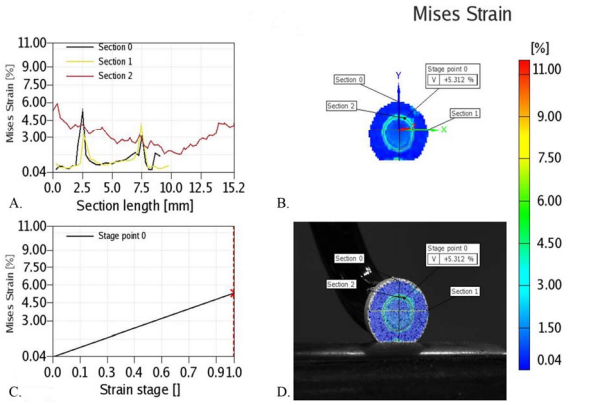

Fig. 3. **Local deformation fields of Filtek Z 250 – software-generated distribution of Mises strains.** A. Section diagram of Mises strains across the x, y and z axis (Sections 0 and 1) and along the periphery of the sample (Section 2); B. Camera image of stress distribution; C. Stage point showing linear strain of a randomly selected point on Section 2; D. Photograph of a sample taken by the cameras

enabled subsequent data processing, such as data filtering, or interpolation, if needed. For diagramatic presentation of results, different types of primitives could be formed inside each state (part of a plane, part of a circle, curved part), or inside the whole object.

3. Results

Polymerization shrinkage of Filtek Z250 is illustrated in Fig. 3 which is a typical Aramis report. The report contains the most important data of the performed measurements and consists of four elements:

A. Section diagram (Multi-Section) shows one or more sections of the current load stage. This diagram shows the selected visualization (Mises strain) with respect to the length of the section per stage. Several sections are displayed in different colours, showing values for the entire section which can be further examined.

B. Camera images (project images) are of particular importance for objects with distinct 3D structure as they can be rotated to an optimal position in the 3D view, and therefore appear to be 3D in the report.

C. Stage point diagram (Multi-Stage-Point) shows one or more stage points through load stages. The current stage is displayed on the bottom left as well as on the bar scale.

D. Visualization of the deformation with an image of Strain overlay (project image). A photograph of a real object is displayed along with the picture processes by the software. The pictures are overlapped, so local zones with largest deformations can be easily spotted.

In the case of Filtek Z250 used in the present study, local deformations were presented as Mises strains. Non-uniform distribution of these strains was observed with higher strains along the periphery and lower strains in central parts of each sample. Mises strains were plotted as a function of distance along each section. The peripheral strain values were between 2 % and 6 % with the average of 3.5 %. The central strain values were about 1–1.5 %.

4. Discussion

Polymerization shrinkage of dental composites has been measured using contact methods, such as water or mercury dilatometry[6,7], strain gauges[1], a linear voltage differential transducer[8] or bonded discs[9]. These involve contact of the material with a liquid or solid medium. Contact methods may introduce additional forces, gravitational or adhesive, and consequently deformations of non-shrinkage origin. Non-contact methods involve laser scanning[10], video imaging[11] and digital image correlation[4], all of which are devoid of any contact between the material and the measuring medium. Recently, laser displacement method was used to determine polymerization shrinkage of flowable and universal dental composites. This method comprised a diffuse-reflection, high-precision laser sensor head which detected dimensional changes of materials placed in glass tubes[10]. In another study, polymerization shrinkage of dental composites was measured using digital image correlation based on a single camera which allowed dimensional changes to be determined in x and y axes but not in the z axis. This out-of-plane shrinkage ε_z was then assumed to be equal to the transverse shrinkage ε_y and used to calculate volumetric shrinkage. The authors pointed out that the use of a two-camera system would allow exact measurement of local deformations in z axis and a more precise determination of the volumetric shrinkage[4].

In the present study, Aramis, the two-camera system, was used in a standardized setup which allowed reproducibility of experimental conditions and control of variables such as sample thickness, distance from the light curing unit, light intensity and the distance between the sample and the cameras.

Aramis is a non-contact and material independent measuring system providing, for static or dynamically loaded test objects, local 3D surface coordinates, displacements and velocities, strain values and strain rates.

The system is applied in solving problems when analyzing local structure integrity, determining local properties of materials, veryfing and refining numerical calculations etc.[12] It is suitable for analysis of irregular object geometries made of various materials, such as metal, composite, gum, wood, organic materials, biomaterials, and for analysis of hyper-elastic materials[4,12,13].

Measurements based on multiple Aramis sensors were proven beneficial for multiple applications, for example measuring exact thickness reduction in tensile test situations with two Aramis sensors, but also for synchronous capturing of a complete object or multiple areas, typically if non-homogeneous materials are involved or complex loading situations have to be captured. For capturing fast sequences, multiple Aramis sensors can be adjusted to observe the same area and can be triggered sequentially to capture data with high local resolution and fast data rates. The possibility to combine data captured by multiple Aramis sensors and transformation of these measurement data in customized coordinate systems gives a clear view about object behaviour. In addition, data can easily be integrated or compared with data generated by numerical simulations.

The present results indicated non-uniform distribution of local deformation fields in dental composites with greater deformations peripherally and smaller deformations centrally. Plotting strain values as a function of distance along sample periphery further elucidates heterogeneous nature of local deformation fields. Non-uniform shrinkage deformations were not previously noticed with the aforementioned contact methods and were only reported with the digital image correlation method.

Non-uniform deformations of dental composites have important clinical implications, particularly in Class II and MOD cavities which have different cavity depths. It seems impossible to predict the zones of greatest deformations within the material in clinical conditions where numerous variables are involved. Some of these are operator-wise, such as the placement of the material or light-curing regime, and some are tooth-wise, such as the quality of tooth tissues at various positions within the cavity. Therefore, more research is necessary to understand *in situ* polymerization shrinkage of dental composites.

5. Conclusion

Polymerization of dental composites is characterized by heterogeneous deformation patterns with variable shrinkage values at different locations within the material. Digital image correlation using 3D optical system is a promising tool enabling qualitative and quantitative mapping of local deformation fields in dental composites.

REFERENCES

1. Fleming G. J., Khan S., Afzal O., Palin W. M., Burke F. J.: J. Dent. *35*, 97 (2007).
2. Eick J. D., Kotha S. P., Chappelow C. C., Kilway K. V., Giese G. J., Glaros A. G., Pinzino C. S.: Dent. Mater. *23*, 1011 (2007).
3. Ilie N., Hickel R.: Dent. Mater. J. *25*, 445 (2006).
4. Li J., Fok A. S. L., Satterthwaite J., Watts D. C.: Dent. Mater. *25*, 582 (2009).
5. ARAMIS, Hardware, aramis_hw_en_rev-c, 2007, User information.
6. Feilzer A. J., Dauvillier B. S.: J. Dent. Res. *82*, 824 (2003).
7. Skrtic D., Stansbury J. W., Antonucci J. M.: Biomaterials *24*, 2443 (2003).
8. Watts D. C., Cash A. J.: Dent. Mater. *7*, 281 (1991).
9. Atai M., Watts D. C.: Dent. Mater. *22*, 785 (2006).
10. Miyasaka T., Okamura H.: Dent. Mater J. *28*, 544 (2009).
11. Sharp L. J., Choi I. B., Lee T. E., Sy A., Suh B. I.: J. Dent. *31*, 97 (2003).
12. Ahn B., Kim J.: Med. Image Anal. *14*, 138 (2010).
13. Hogstrom P., Ringsberg J., Johnson E.: Int. J. Impact Eng. *36*, 1194 (2009).

M. Milosevic[a], V. Miletic[b], N. Mitrovic[a], D. Manojlovic[b], T. Savic Stankovic[b], and T. Maneski[c], (*[a] Innovation Center of Faculty of Mechanical Engineering, University of Belgrade, Serbia, [b] School of Dentistry, University of Belgrade, Serbia; [c] Faculty of Mechanical Engineering, University of Belgrade, Belgrade, Serbia):* **Measurement of Local Deformation Fields in Dental Composites Using 3D Optical System**

Polymerization shrinkage is the single most important local deformation of dental composites that has a substantial effect on the quality of the tooth-restoration interface in clinical conditions. The aim of this study was to investigate the possibility to analyze local deformation fields of a dental composite upon polymerization using the 3D optical method of digital image correlation with two cameras. Conventional, microhybrid composite samples were prepared in custom-made Teflon molds and polymerized with a conventional halogen light. Local deformation fields were determined using the two-camera system, Aramis 2M, by correlating sample dimensions before and after polymerization. The greatest deformations of up to 6 % with the average of 3.5 % were observed along the periphery of the samples in contrast to substantially lower deformations of about 1–1.5 % in the central parts. Polymerization of dental composites yields heterogeneous deformation with variations in shrinkage values. The 3D optical system is a promising tool enabling qualitative and quantitative mapping of local deformation fields in dental composites.

EVALUATION OF THE LOCAL TENSILE PROPERTIES OF AUSTENITE-FERRITE WELDED JOINT

RADOMIR JOVICIC[a], ALEKSANDAR SEDMAK[b]*, KATARINA COLIC[a], MILOS MILOSEVIC[a], and NENAD MITROVIC[a]

[a] *Innovation Center of Faculty of Mechanical Engineering, University of Belgrade, Kraljice Marije 16, 11000, Belgrade, Serbia,* [b] *Faculty of Mechanical Engineering, University of Belgrade, Belgrade, Kraljice Marije 16, 11000 Belgrade, Serbia*
asedmak@mas.bg.ac.rs

Keywords: weldment heterogeneity, tensile test, numerical simulation, finite element method, strain gauges

1. Introduction

Integrity analysis of welded joints requires knowledge of complex stress and strain distribution in a heterogeneous material, consisting of weld metal (WM), heat-affected-zone (HAZ) and base metal (BM) of different microstructure and mechanical properties[1–5]. This is even more complex problem when two different base metals are welded, like in the case of ferrite-austenite welded joint[6].

Due to very complex microstructure of HAZ and its extremely small size compared to WM and BM it is not possible to determine the tensile properties of HAZ. This problem is also more pronounced if ferrite-austenite welded joint is analysed, because two different HAZ are involved[7]. Therefore, the HAZs tensile properties have to be estimated. In this paper will be presented an estimation procedure of the HAZs tensile properties, based on numerical simulation of an experiment.

2. Materials and methods

One plate, dimensions (1000×1000×12 mm) was welded and used for experimental investigation, out of which tensile testing and microhardness measure-ment are presented here. The shielded manual metal arc welding (SMAW) process was used.

Vickers microhardness measurements, with load 10 N, were carried out to determine the local mismatch levels for various regions of weld metal and HAZ, as shown in Fig. 1.

Empirical formula between micro hardness and yield strength for the ferritic steels:

$$\sigma_{0,2}=3.18\times HV-168[MPa] \quad (1)$$

indicates that the yield strength is proportional to the microhardness. Although no literature data was available for the austenite microstructure, a similar formula was assumed, based on the known yield strength of the WM:

$$\sigma_{0,2}=2.30\times HV-145\ [MPa] \quad (2)$$

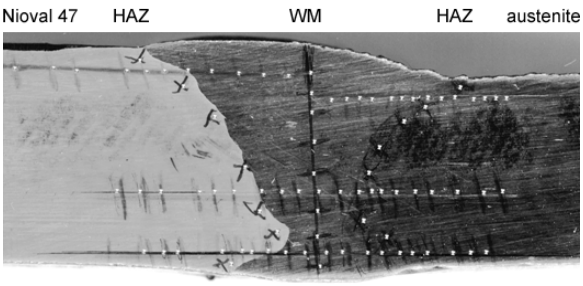

Fig. 1. **Microhardness measurements**

Results for the hardness measurement (average from several values at different positions) and yield strength predictions are shown in Tab. I.

Table I
Results for HV and $\sigma_{0,2}$ [MPa]

	BM - 4572	BM - Nioval	WM	CGHAZ-ferrite
HV	195	190	295	228
YS	355	455	545	550
	FGHAZ-ferrite	CGHAZ-austenite	FGHAZ-austenite	
HV	170	218	166	
YS	400	400	300	

Full thickness flat tensile specimens were machined from two base metals and tested to determine the stress-strain curves. The weld metal itself was tested by using a specimen with circular cross-section, whereas the whole welded joint behaviour was assessed by the flat specimen. The results indicate different behaviour of two base metals – continuous curve for 4572 steel and the curve with a yielding behaviour for Nioval. Anyhow, one should notice large difference when comparing the weld metal round and flat specimens, being a consequence of different directions being tested – in the first case it was the weldment direction and in the second one it was perpendicular to the weldment. Having in mind the practical application of the weldment, the second one was taken as the relevant.

According to the results, the modulus of elasticity, yield strength and hardening coefficient were determined and given in the Tab. II for both base metals and the weld metal as well. The hardening coefficient were determined as the ratio of the difference between the ultimate tensile strength and yield strength and 1/2 of total strain (4572), 2/3 (Nioval) or 4/7 (weld metal)[6,7].

Table II
Tensile properties for two base metals and fm

Material	Yield Strength $\sigma_{0.2}$ [MPa]	Ultimate Stress σ_u [MPa]	A_5 [%]	ref. A_5 [%]	E, [GPa]	H', [MPa]
4572	335	670	48	24	193	1400
Nioval	455	616	33	22	207	730
FM	545	685	35	20	193	700

3. Experimental procedure

In order to evaluate strain distribution, 2 tensile panels have been instrumented with strain gages.

Fig. 2. **Experimental setup**

A total of 12 strain gages and 4 strain chains were used for each tensile panel, positioned at each side of the specimen, Fig. 2, 3.

The strain chain has 10 strain gages of 0.625 mm length and 12 mm length for the chain. The strain chains were cut in two pieces (5 strain gages each) in order to cover two HAZs as precise as possible. In this way three SG actually covered each HAZ, with one SG at the end points of HAZs and the remaining third one in the center of HAZs. The forth SG was positioned in the MW and the fifth one in the BM. A personal computer (iBook Mac) collected the test data via multi channel data acquisitions.

The results are shown in Tab. III for all four measurements at four sides of a specimen (up, down, left, right). Bold numbers indicate strain chain measurements, whereas the bold & italic numbers indicate the SC fifth point being in BMs. The average of four measurements is also given in Tab. III and used as the relevant data for the comparison with numerical results.

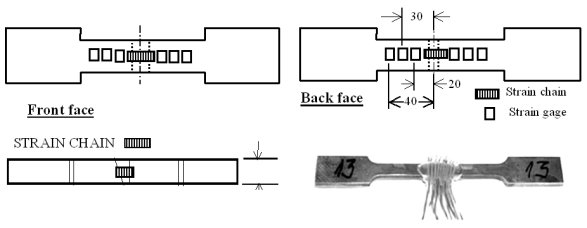

Fig. 3. **Strain gages positioned at tensile panel faces**

Table III
Experimental results (up, down, left, right)

mat.	2	2	2	2	2,7	7,6	6,3	3
up	11.40	12.38	12.88	***10.65***	**7.47**	**4.78**	**3.81**	**2.12**
down	11.22	11.82	12.82	***10.11***	**7.72**	**4.83**	**4.19**	**2.00**
left	11.08	12.10	12.41	***11.44***	**7.85**	**4.77**	**4.22**	**2.29**
right	11.82	12.26	12.57	***12.00***	**7.96**	**5.14**	**4.26**	**2.47**
ave.	11.38	12.18	12.67	***11.05***	**7.75**	**4.88**	**4.12**	**2.22**
mat.	3	3,5	5,4	4,1	1	1	1	1
up	**1.60**	**1.36**	**2.77**	**3.45**	***3.62***	6.42	6.04	7.34
down	**1.60**	**1.26**	**2.71**	**3.63**	***4.36***	5.40	5.91	5.99
left	**1.77**	**1.60**	**2.37**	**4.15**	***6.06***	5.92	5.73	7.97
right	**1.67**	**1.62**	**2.83**	**4.53**	***6.12***	6.18	5.14	6.86
ave.	**1.66**	**1.46**	**2.67**	**3.94**	***5.04***	5.98	6.27	7.04

Material are denoted from 1 to 7 in accordance with the finite element model (1 and 2 are base metals, ferrite and austenite, respectively, 3 is the weld metal, 4 and 5 the HAZ at the ferrite BM side, and 6 and 7 the HAZ at the austenite BM side).

4. Numerical simulation

The finite element method has been used to simulate the strain distributions obtained experimentally. The three-dimensional model of V-joint (45°) specimen without crack is shown in Fig. 4.

The three-dimensional isoparametric finite ele-ments with 20 nodes were used to create a mesh. The maximum remote stress was 425 MPa. The specimen was modeled with seven materials, as defined in Tab. IV.

The heat affected zones were divided into two regions – fine grain HAZ (FG HAZ) and coarse grain HAZ (CG HAZ). Tensile properties of CG HAZ and FG HAZ, needed for the calculation (yield strength Re and hardening coefficient H'),

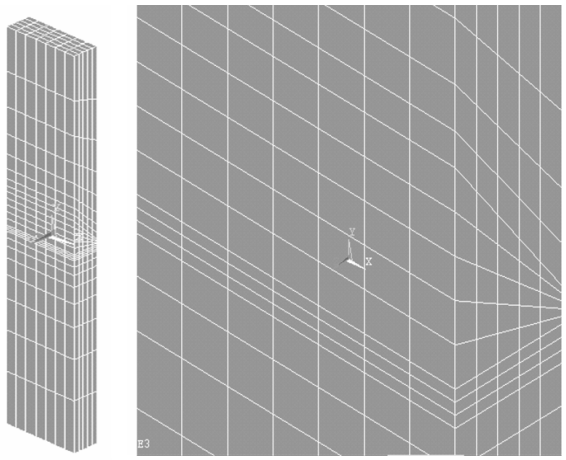

Fig. 4. **The FE Model**

Table IV
Data of iteration procedure for property estimation, YS (MPa), H′ (MPa)

	BM - 4572 2	BM-Nioval 1	WM 3	CGHAZ-f 5	FGHAZ-f 4	CGHAZ-a 6	FGHAZ-a 7
1	355. 1400	455. 730	545. 700	550. 300	400. 1000	400. 400	300. 1000
2	355. 1400	455. 730	545. 700	650. 400	400. 1000	400. 400	300. 1000
3	355. 1400	455. 730	545. 700	650. 400	450. 1200	400. 400	300. 1000
4	355. 1400	455. 730	545. 700	650. 400	450. 1200	630. 400	300. 1000
5	355. 1400	455. 730	545. 700	650. 400	450. 1200	630. 500	400. 1600

Table V
Data of iteration procedure for strains

					Strain ε_y (%) for σ=425 MPa (points 1–12)							
mat.	2	2	2	2	2	2,7	7	7,6	6	6,3	3	3
exp.		11.38	12.18	12.67	11.05	7.75		4.88		4.12	2.22	
5.it.	8.49	11.88	12.44	11.92		7.10	5.54	4.99	4.15	4.09	2.76	1.53
4.it.	8.49	11.88	12.44	11.92		7.70	6.64	6.91	4.15	4.09	2.76	1.53
3.it.	8.49	11.88	12.44	11.92		7.70	6.64	7.91	6.45	6.20	2.76	1.53
2.it.	8.49	11.88	12.44	11.92		7.70	6.64	7.91	6.45	6.20	2.76	1.53
1.it.	8.49	11.88	12.44	11.92		7.70	6.64	7.91	6.45	6.20	2.76	1.53
point	1	2	3	4	5	6	7	8	9	10	11	12
					Strain ε_y (%) for σ=425 MPa (points 12–23)							
mat.	3	3	3,5	5	5,4	4	4,1	1	1	1	1	1
exp.		1.66	1.46		2.67		3.94	5.04	5.98	6.27	7.04	
5.it.	1.53	1.35	1.41	1.42	3.19	4.06	4.04		6.36	6.70	6.34	2.80
4.it.	1.53	1.35	1.41	1.42	3.19	4.06	4.04		6.36	6.70	6.34	2.80
3.it.	1.53	1.35	1.41	1.42	3.19	4.06	4.04		6.36	6.70	6.34	2.80
2.it.	1.53	1.35	1.41	1.42	3.69	4.56	4.54		6.36	6.70	6.34	2.80
1.it.	1.53	1.35	2.21	2.22	4.10	4.56	4.54		6.36	6.70	6.34	2.80
point	12	13	14	15	16	17	18	19	20	21	22	23

were varied until nu-merical strain distributions matched closely enough the experimental ones. Five different sets of ten-sile properties were used to match the experi-mental strain distribution, as shown in Tab. V. In the case of hardening coefficient one can notice that even for BMs and WM some variation had to be made. The results of this procedure are given in Tab. V.

5. Results and discussion

One should notice the following regarding points as defined in the bottom row of Tab. V: 1 & 23 are given only for as numerical, because they were too close to grips (boundary conditions can explain low values); 2,3,4 & 22,21,20 gives matching results for BMs; 5 & 19 – only experimental, too close to HAZ (no node at these positions); 6,8,10,11 & 18,16,14,13 matching results for HAZs and WM; 7,9 & 17,15 – only numerical, no space in HAZs for SG; 12 – only numerical, no space in WM for SG.

The basic aim was to simulate the experiment and compare displacements, strains and stresses, having in mind specimen heterogeneity, and specific behaviour of base metals (ferrite BM with higher yield strength σ_Y but strengthening coefficient H' than austenite BM) and weld metal with the highest σ_Y and strengthening coefficient H' similar to the ferrite BM, not to mention two HAZs with two different regions – CG and FG.

Based on the comparison of numerical and experimental results one can see that minimum seven different materials (WM, two BMs, two CGHAZ and two FGHAZ) should be modeled in the case of austenite-ferrite welded joint. Since it was neither possible to extract tensile specimens from small regions like CG and FG HAZs[2,3], nor would be the microhardness measurement appropriate procedure in this case, an iteration procedure has been applied, providing reliable results for all 7 regions.

One should notice that not only these two basic tensile properties differ, but the whole tensile behavior as well[6,7]. It is

also to be noted that the austenite BM has the largest strengthening modulus and the smallest yield strength, whereas the WM has the smallest strengthening modulus and the largest yield strength. Finally, one should keep in mind that heat-affected-zones in both base metals, being heterogeneous even by themselves, present yet another source of material heterogeneity, which is modeled here by taking into account the fine grain and coarse grain regions.

6. Conclusion

Experimental and numerical models have been used in this study. Experimental analysis has been limited to welded tensile panels made from dissimilar base metals. Numerical analysis, detailed three-dimensional finite element model of the same welded tensile plate, without surface crack, has been performed. Based on these analyses, the following conclusions may be drawn:

• Three-dimensional finite element analysis is essential for analysis of welded joint behaviour, even without presence of a crack, because of complex material behavior, involving different yield strength and strengthening levels.

• The original iterative method for evaluation of elastic-plastic properties of different regions in the weldment has been introduced, based on matching of numerical and experimental results. This method turned out to be very efficient.

• The iterative method proved that HAZ has to be modeled with at least two different regions, coarse-grain and fine-grain, for precise evaluation of elastic-plastic properties.

• The iterative method should be improved in order to get next step automatically on the basis of the previous one and its difference in comparison to the experimental results. This procedure has to be verified with more examples and eventually introduced as a convenient method for this purpose.

REFERENCES

1. Maneski T., Sedmak A.: Struct. Integr. Life *1*. 107 (2001).
2. Adziev T., Sedmak A., Adziev G., Arsic M.: Struct. Integr. Life *2*, 20 (2002).
3. Adziev G., Sedmak A.: Struct. Integr. Life *3*, 93 (2003).
4. Manjgo M., Sedmak A., Grujic B.: Struct. Integr. Life *8*, 149 (2008).
5. Gubeljak N., Predan J., Rak I., Kozak D.: Struct. Integr. Life *9*, 157 (2009).
6. Jovicic R.: Analysis of crack effect on structural integrity of ferrite-austenite welded joints. *D.Sc. thesis,* Faculty of Mechanical Engineering, University of Belgrade (2004).
7. Jovicic R., Prokic-Cvetkovic R., Popovic O.: Struct. Integr. Life *5*, 89 (2005).

R. Jovicic[a], A. Sedmak[b], K. Colic[a], M. Milosevic[a], and N. Mitrovic[a] *([a] Innovation Center of Faculty of Mechanical Engineering, University of Belgrade, [b] Faculty of Mechanical Engineering, University of Belgrade):* **Evaluation of The Local Tensile Properties of Austenite-Ferrite Welded Joint**

Local mechanical properties (Yield Strength Re and Hardening Coefficient H') of austenite-ferrite welded joint has been evaluated by using finite element method to simulate the strain distributions obtained experimentally by tensile test using strain chains and strain gages. The three-dimensional model of V-joint (45°) specimen has been used with seven materials, simulating both base metals (BM), the weld metal (WM) and two sub-regions of two heat-affected zones (HAZ) – fine grain (FG) and coarse grain (CG) HAZ. Tensile properties of CG HAZ and FG HAZ, needed for the calculation, were varied until numerical strain distributions matched closely enough the experimental ones, whereas tensile properties of BMs and WM were kept constant. Five different sets of tensile properties were used to match the experimental strain distribution. In this way local tensile properties of the whole austenite-ferrite welded joint have been evaluated.

ELASTIC MECHANICAL PROPERTIES OF FIBER REINFORCED COMPOSITE MATERIALS

EVA KORMANÍKOVÁ, and KAMILA KOTRASOVÁ*

Technical University of Košice, Civil Engineering Faculty, Vysokoškolská 4, 042 00 Košice, Slovak Republic
eva.kormanikova@tuke.sk, kamila.kotrasova@tuke.sk

Keywords: analytical homogenization, numerical homogenization, unidirectional lamina, effective elastic moduli

1. Introduction

For heterogeneous materials such as composites, a large number of material properties are needed. The values of these properties change as a function of the volume fraction of reinforcement. An alternative to the experimental determination of these properties is usage of homogenization techniques. Many analytical techniques of homogenization are based on the equivalent eingestrain method, which considers the problem of a single ellipsoidal inclusion embedded in an infinite elastic medium. The Eshelby solution develops a method, which considers a random distribution of inclusions in an infinite medium. Homogenization of composites with periodic microstructure has been accomplished by using various techniques including an extension of the Eshelby inclusion problem, the Fourier series technioque, and variational principles[1].

2. Micromechanics models

Micromechanical models can be classified into empirical, semiempirical, analytical and numerical.

2.1. Voigt and Reuss model

When an unidirectional lamina is acted upon by either a tensile or compression load parallel to the fibers, it can be assumed that the strains on the fibers, matrix and composite in the loading direction are the same. Mechanical model has a parallel arrangement of fibers and matrix (Voigt-model) (Fig. 1)[2].

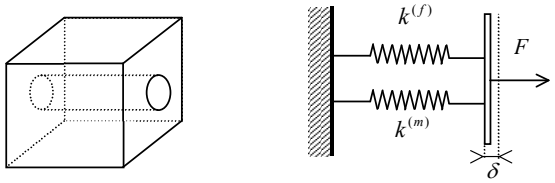

Fig. 1. **The Voigt-model**

The effective modulus E_1 and effective Poisson´s ratio ν_{12} can be written as follows:

$$E_1 = E^{(f)}\xi + E^{(m)}(1-\xi) \qquad (1)$$
$$\nu_{12} = \nu^{(f)}\xi + \nu^{(m)}(1-\xi)$$

where subscripts *f* and *m* refer to the fibre and matrix respectively; ξ is a volume fraction of reinforcement.

The mechanical model in Fig. 2 has an arrangement in a series of the fiber and matrix (Reuss-model), and the resultant load and the stress are equal for all phases.

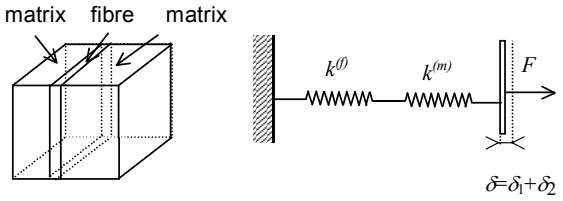

Fig. 2. **The Reuss-model**

The effective transverse modulus E_2 and in-plane shear modulus G_{12} can be written as follows

$$E_2 = \frac{E^{(f)}E^{(m)}}{E^{(m)}\xi + E^{(f)}(1-\xi)} \qquad (2)$$
$$G_{12} = \frac{G^{(f)}G^{(m)}}{G^{(m)}\xi + G^{(f)}(1-\xi)}.$$

2.2. Halpin and Tsai model

Effective elastic moduli related to loading in the fibre direction E_1 and ν_{12} are dominated by the fibers. All estimations in this case and experimental results are very close to the rule of mixtures estimation. But the value obtained for the transverse Young´s modulus and in-plane shear modulus do not agree well with the experimental results. Semi-empirical relationships have been developed to overcome the difficulties with complicated mathematical equations. The most useful semi-empirical models are those by Halpin and Tsai. Halpin and Tsai proposed equations that are general and simple in the formulation

$$E_2 = E^{(m)}\frac{1+\zeta_E\eta_E.\xi}{1-\eta_E\xi} \qquad G_{12} = G^{(m)}\frac{1+\zeta_E\eta_G\xi}{1-\eta_G\xi} \qquad (3)$$

where

$$\eta_E = \frac{E^{(f)}/E^{(m)} - 1}{E^{(f)}/E^{(m)} + \zeta_E} \qquad \eta_G = \frac{G^{(f)}/G^{(m)} - 1}{G^{(f)}/G^{(m)} + \zeta_E} \tag{4}$$

ζ_E is called a reinforcing factor that depends on geometry of the fibers, packing arrangement of the fibers and loading conditions. The factor ζ_E is between 1 and 2. But only when a reliable experimental value of E_2 is available for composite, the factor ζ_E can be derived for this case and can be used to predict E_2 for a range of fibers volume ratio of the same composite.

2.3. Periodic microstructure model

If the composite has periodic microstructure, then Fourier series can be used to estimate all the components of the stiffness tensor of the composite. Explicit formulas for a composite reinforced by long circular cylindrical fibres, which are periodically arranged in a square array a_2=a_3 (Fig. 3), are written in the following way[3].

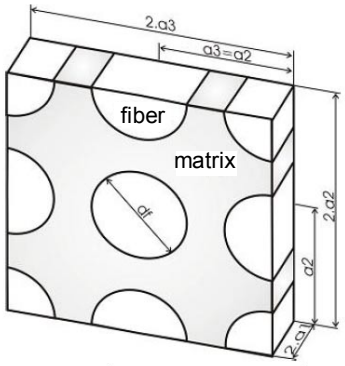

Fig. 3. **The periodic microstructure model**

Because the microstructure has square symmetry, the stiffness tensor has six unique coefficients given by

$$C_{11} = \lambda^{(m)} + 2\mu^{(m)} - \frac{\xi}{D}\left(\frac{S_3^2}{\mu^{(m)2}} - \frac{2S_6S_3}{\mu^{(m)2}g} - \frac{aS_3}{\mu^{(m)}c} + \frac{S_6^2 - S_7^2}{\mu^{(m)2}g^2} + \frac{aS_6 + bS_7}{\mu^{(m)}gc} + \frac{a^2 - b^2}{4c^2} \right)$$

$$C_{12} = \lambda^{(m)} + \frac{\xi}{D} b \left(\frac{S_3}{2c\mu^{(m)}} - \frac{S_6 - S_7}{2c\mu^{(m)}g} - \frac{a+b}{4c^2} \right)$$

$$C_{22} = \lambda^{(m)} + 2\mu^{(m)} - \frac{\xi}{D}\left(-\frac{aS_3}{2\mu^{(m)}c} + \frac{aS_6}{2\mu^{(m)}gc} + \frac{a^2 - b^2}{4c^2} \right)$$

$$C_{66} = \mu^{(m)} - \xi\left(-\frac{S_3}{\mu^{(m)}} + \left(\mu^{(m)} - \mu^{(f)}\right)^{-1} \right)^{-1}$$

$$C_{23} = \lambda^{(m)} + \frac{\xi}{D}\left(\frac{aS_7}{2\mu^{(m)}gc} - \frac{ba + b^2}{4c^2} \right) \tag{5}$$

$$C_{44} = \mu^{(m)} - \xi\left(\frac{2S_3}{\mu^{(m)}} + \left(\mu^{(m)} - \mu^{(f)}\right)^{-1} + \frac{4S_7}{\mu^{(m)}\left(2 - 2\nu^{(m)}\right)} \right)^{-1}$$

where

$$D = \frac{aS_3^2}{2\mu^{(m)2}c} - \frac{aS_6S_3}{\mu^{(m)2}gc} + \frac{a\left(S_6^2 - S_7^2\right)}{2\mu^{(m)2}g^2c} + \frac{S_3\left(b^2 - a^2\right)}{2\mu^{(m)}c^2} + \frac{S_6\left(a^2 - b^2\right) + S_7\left(ab + b^2\right)}{2\mu^{(m)}gc^2} + \frac{\left(a^3 - 2b^3 - 3ab^2\right)}{8c^3} \tag{6}$$

and

$$\begin{aligned} a &= \mu^{(f)} - \mu^{(m)} - 2\mu^{(f)}\nu^{(m)} + 2\mu^{(m)}\nu^{(f)} \\ b &= -\mu^{(m)}\nu^{(m)} + \mu^{(f)}\nu^{(f)} + 2\mu^{(m)}\nu^{(m)}\nu^{(f)} - 2\mu^{(f)}\nu^{(f)}\nu^{(m)} \\ c &= \left(\mu^{(m)} - \mu^{(f)}\right)\left(\mu^{(f)} - \mu^{(m)} + \mu^{(f)}\nu^{(f)} - \mu^{(m)}\nu^{(m)} + 2\mu^{(m)}\nu^{(f)} - 2\mu^{(f)}\nu^{(m)} + 2\mu^{(m)}\nu^{(f)}\nu^{(m)} - 2\mu^{(f)}\nu^{(m)}\nu^{(f)}\right) \\ g &= \left(2 - 2\nu^{(m)}\right) \end{aligned} \tag{7}$$

Assuming the fiber and matrix are both isotropic, the Lame's constants of both materials are obtained by

$$\lambda = \frac{E}{(1+\nu)(1-2\nu)} \qquad \mu = G \tag{8}$$

For a composite reinforced by long circular cylindrical fibers, periodically arranged in a square array the constants S_i, i=3, 6, 7 are given as follows

$$\begin{aligned} S_3 &= 0.49247 - 0.47603\xi - 0.02748\xi^2 \\ S_6 &= 0.36844 - 0.14944\xi - 0.27152\xi^2 \\ S_7 &= 0.12346 - 0.32035\xi + 0.23517\xi^2 \end{aligned} \tag{9}$$

2.4. Numerical homogenization

Most composites have random arrangement of the fibers. Random microstructure results in transversely isotropic properties at a meso-scale. An analysis of composites with random microstructure can be done by using of fictitious periodic microstructure. A simple alternative is to assume that the random microstructure is well approximated by the hexagonal microstructure in Fig. 4.

For calculation of C_{ij} (i, j = 1–3) we used the quarter FEM model and for calculation of C_{ij} (i, j = 4–6) we used full model in Fig. 5.

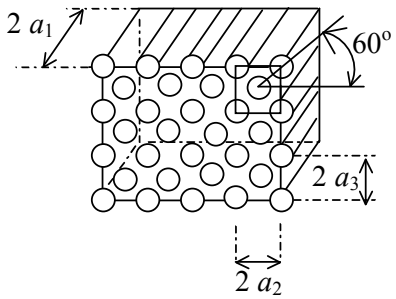

Fig. 4. **The hexagonal microstructure model**

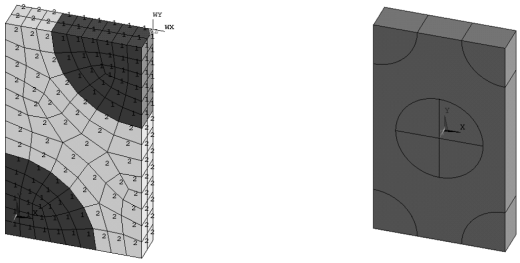

Fig. 5. **The hexagonal microstructure FEA quarter and full models**

Further alternative is the periodical microstructure with square arrangement of fibers in the representative volume element (RVE)[3,4] in Fig.6.

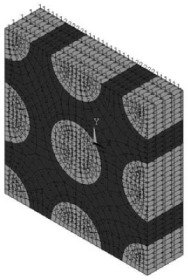

Fig. 6. **The periodic square microstructure FEA model**

Analysis of microstructure yields the transversely isotropic stiffness tensor

$$\begin{Bmatrix} \bar{\sigma}_1 \\ \bar{\sigma}_2 \\ \bar{\sigma}_3 \\ \bar{\tau}_4 \\ \bar{\tau}_5 \\ \bar{\tau}_6 \end{Bmatrix} = \begin{bmatrix} C_{11} & C_{12} & C_{12} & 0 & 0 & 0 \\ C_{12} & C_{22} & C_{23} & 0 & 0 & 0 \\ C_{12} & C_{23} & C_{22} & 0 & 0 & 0 \\ 0 & 0 & 0 & \frac{1}{2}(C_{22}-C_{23}) & 0 & 0 \\ 0 & 0 & 0 & 0 & C_{66} & 0 \\ 0 & 0 & 0 & 0 & 0 & C_{66} \end{bmatrix} \begin{Bmatrix} \bar{\varepsilon}_1 \\ \bar{\varepsilon}_2 \\ \bar{\varepsilon}_3 \\ \bar{\gamma}_4 \\ \bar{\gamma}_5 \\ \bar{\gamma}_6 \end{Bmatrix} \tag{10}$$

Elastic properties of the homogenized material can be computed by[5]

$$E_1 = C_{11} - 2C_{12}^2/(C_{22}+C_{23}) \tag{11}$$

$$\nu_{12} = C_{12}/(C_{22}+C_{23})$$

$$E_2 = \left(C_{11}(C_{22}+C_{23}) - 2C_{12}^2\right)(C_{22}-C_{23})/\left(C_{11}C_{22}-C_{12}^2\right)$$

$$G_{12} = C_{66}$$

$$\nu_{23} = \left(C_{11}C_{23}-C_{12}^2\right)/\left(C_{11}C_{22}-C_{12}^2\right)$$

$$G_{23} = C_{44}$$

$$G_{23} = C_{44} = \frac{1}{2}(C_{22}-C_{23})$$

In order to evaluate the elastic matrix **C** of the composite, RVE is subjected to an average strain. The volume average of the strain in RVE equals the applied strain

$$\bar{\varepsilon}_{ij} = \frac{1}{V}\int_V \varepsilon_{ij}\,dV \tag{12}$$

The components of the tensor **C** are determined by solving three elastic models of RVE with parameters (a_1, a_2, a_3) subjected to boundary conditions. By using an unit value of an applied strain, it is possible to compute the stress field, whose average gives the required components of the elastic matrix as

$$C_{ij} = \bar{\sigma}_i = \frac{1}{V}\int_V \sigma_i\,dV \qquad \varepsilon_j^0 = 1 \tag{13}$$

The coefficients in **C** are found by setting a different problem for each column of **C**.

In order to determine the components C_{i1} with i = 1, 2, 3, the following strain is applied to stretch of RVE in the fiber direction x_1:

$$\varepsilon_1^0 = 1 \qquad \varepsilon_2^0 = \varepsilon_3^0 = \gamma_4^0 = \gamma_5^0 = \gamma_6^0 = 0 \tag{14}$$

The following boundary conditions on displacements can be

used:

$$u_1(a_1,x_2,x_3)=a_1 \qquad u_1(0,x_2,x_3)=0 \qquad (15)$$
$$u_2(x_1,a_2,x_3)=0 \qquad u_2(x_1,0,x_3)=0$$
$$u_3(x_1,x_2,a_3)=0 \qquad u_3(x_1,x_2,0)=0$$

The coefficients C_{i1} are found by using

$$C_{i1}=\overline{\sigma}_i \qquad (16)$$

In order to determine the components C_{i2} with i = 1, 2, 3, the following strain is applied to stretch the RVE in the direction x_2:

$$\varepsilon_2^0=1 \qquad \varepsilon_1^0=\varepsilon_3^0=\gamma_4^0=\gamma_5^0=\gamma_6^0=0 \qquad (17)$$

The following boundary conditions on displacements can be used

$$u_1(a_1,x_2,x_3)=0 \qquad u_1(0,x_2,x_3)=0 \qquad (18)$$
$$u_2(x_1,a_2,x_3)=a_2 \qquad u_2(x_1,0,x_3)=0$$
$$u_3(x_1,x_2,a_3)=0 \qquad u_3(x_1,x_2,0)=0$$

The coefficients C_{i2} are found by using the equation

$$C_{i2}=\overline{\sigma}_i \qquad (19)$$

In order to determine the components C_{i3} with I = 1, 2, 3, the following strain is applied to stretch RVE in the direction x_3:

$$\varepsilon_3^0=1 \qquad \varepsilon_1^0=\varepsilon_2^0=\gamma_4^0=\gamma_5^0=\gamma_6^0=0 \qquad (20)$$

The following boundary conditions on displacements can be used:

$$u_1(a_1,x_2,x_3)=0 \qquad u_1(0,x_2,x_3)=0 \qquad (21)$$
$$u_2(x_1,a_2,x_3)=0 \qquad u_2(x_1,0,x_3)=0$$
$$u_3(x_1,x_2,a_3)=a_3 \qquad u_3(x_1,x_2,0)=0$$

The coefficients C_{i3} are found by using

$$C_{i3}=\overline{\sigma}_i \qquad (22)$$

The coefficient C_{66} is calculated using (Equation (*10*)) written as

$$C_{66}=\overline{\sigma}_6=\frac{1}{V}\int_V \sigma_6 dV$$

In order to determine the component C_{66}, the following strain is applied to RVE.

$$\gamma_6^0=\varepsilon_{12}^0+\varepsilon_{21}^0=1 \qquad \varepsilon_1^0=\varepsilon_2^0=\varepsilon_3^0=\gamma_4^0=\gamma_5^0=0 \qquad (23)$$

The boundary must by enforced by using coupling constraint equations[5].

2.5. Laminated representative volume element

A simile procedure to that used to obtain RVE at the micro-scale can be used to analyze laminates on the meso-scale. In this case, RVE represents a laminate. Therefore, the through-thickness direction should remain free to expand along the thickness. In general, the RVE (Fig. 7) must include the whole thickness. For symmetrical laminates subjected to in-plane loads, RVE can be defined with half the thickness using symmetry boundary conditions.

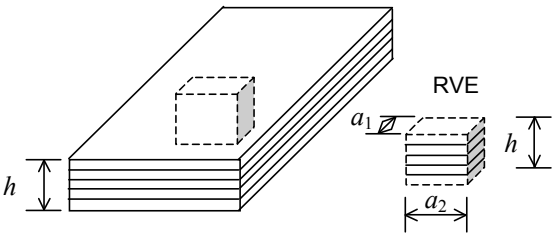

Fig. 7. **The laminated representative volume element**

3. Results and discussion

Asn an example, E_1, E_2, ν_{12}, and G_{12} are computed for an unidirectional composite with isotropic fibers E_f = 241 GPa, ν_f = 0.2, and isotropic matrix E_m = 3.12 GPa, ν_m = 0.38 with fiber volume fraction ξ = 0.4 and ζ_E = 1.5. The fiber diameter is d_f = 7 μm.

Next, E_x, E_y, ν_{xy}, and G_{xy} are computed for a $[0/45/-45/90]_S$ laminate with the layer thickness 0.125 mm and with given properties calculated by the numerical hexagonal model.Elastic properties of the homogenized material are shown in Table I. The effective elastic properties of the laminated RVE are shown in Table II.

Table I
Summary of results

	Voigt-Reuss model	Halpin and Tsai model	Periodic analytical model	Hexagon. numeric. model	Periodic numeric. model
E_1 [GPa]	98.270	98.270	98.306	98.302	98.305
E_2 [GPa]	5.156	8.0505	7.792	7.479	8.990
ν_{12}	0.308	0.308	0.298	0.298	0.299
G_{12} [GPa]	1.870	2.929	2.594	2.583	2.601

Table II
Summary of results

E_x [GPa]	E_y [GPa]	G_{xy} [GPa]	ν_{xy}
37.296	37.296	14.042	0.328

4. Conclusion

The paper compares two approaches of homogenization of an unidirectional lamina. In a frame of the numerical homogenization, the best results were obtained from the hexagonal microstructure model. In a frame of the analytical homogenization, the best results were obtained from the periodic microstructure model. This model is suitable for analytical approach of modelling of the unidirectional lamina. The results obtained from this model are very similar to the results obtained from the numerical model. The example is solved in program ANSYS by FEM[5].

The scientific research and the paper presented as its result were supported by the Project NFP 26220220051 and Project VEGA 1/0201/11.

REFERENCES

1. Gürdal Z., Haftka R. T., Hajela P.: *Design and Optimization of Laminated Composite Material,* J. Wiley & Sons, 1999.
2. Altenbach H., Altenbach J., Kissing W.: *Structural Analysis of Laminate and Sandwich Beams and Plates*, Lublin, 2001.
3. Luciano R., Barbero E. J.: Int. J. Solids Sruct. *31*, 2933 (1995).
4. Žmindák M., Novák P., Melicher R.: Numerical simulation of 3D elastostatic inclusion problems using boundary meshless methods, In.: Mechanika kompozitních materiálů a konstrukcí, 2008, pp. 32–43.
5. Barbero Ever J.: *Finite element analysis of composite materials*, CRC Press, Taylor&Francis Group, 2008.

E. Kormaníková, and K. Kotrasová *(Technical University of Košice, Civil Engineering Faculty, Slovakia):* **Elastic Mechanical Properties of Fiber Reinforced Composite Materials**

The paper describes analytical and numerical approaches of modelling of an unidirectional lamina. In a frame of the analytical homogenization, Voigt-model, Reuss-model, Halpin-Tsai semi-empirical model and periodic microstructure model are described. In a frame of the numerical homogenization, finite element model with hexagonal and square periodical array is described. Comparison of these approaches is also presented.

EVALUATION OF AU THIN FILMS DEPOSITED ON THE POLYSTYRENE SUBSTRATE

PETRA BUBLÍKOVÁ[a], OLGA BLÁHOVÁ[a], ROSTISLAV MEDLÍN[a], PETR SLEPIČKA[b], and VÁCLAV ŠVORČÍK[b]

[a] *New Technologies - Research Centre, University of West Bohemia, Univerzitní 8, 306 14 Plzeň,* [b] *Department of Solid State Engineering, Institute of Chemical Technology, 166 28 Prague, Czech Republic*
blahova@ntc.zcu.cz

Keywords: Au/polystyrene composite, diode sputtering, nanoindentation, scratch testing

1. Introduction

The requirements of miniaturisation and amplification of electric signal brought about the need for materials with low electrical resistance and higher electrical and thermal conductivity. Electronic parts made from the metal-polymer composites exhibit suitable combination of the resistance to mechanical stresses, elevated temperatures and chemical attack[1]. Among them, Au/polystyrene (PS) is interesting for various microelectronics applications due to special electrical, optical and photo-physical properties of Au. The other applications of these composites can be found in biotechnology, like biosensors. The thickness of thin gold films ranges from a few tens of nanometres up to several micrometres. Polymers are used for stabilization of unstable metal particles which have unique electrical properties[1,5]. However, the difference in the character of metal and polymer causes weak bonding between them. This problem can be resolved by the modification of the polymer substrate.

Several techniques (physical, chemical or their combination) are used for the improvements of the adhesion and mechanical properties of the whole system[1–4]. The adhesion between metal and polymer is often improved by physical modifications using plasma discharge, laser, ultraviolet light, high-energy electrons or ion irradiation[5,6].

The main aim of this study is to examine the influence of different times of Au sputtering (t_s) and the influence of the Ar plasma treatment and ageing on selected mechanical properties of Au/PS composites.

2. Experimental procedure

Materials

Biaxially-oriented polystyrene (PS, supplied by Goodfellow, Ltd. UK; density ρ = 1.05 g cm^{-3}) in the form of 50 μm-thick foils with the size of 2 × 2 cm^2 was used as a substrate. The PS samples were modified in a diode plasma discharge (Fig. 1) using Balzers SCD 050 device for Ar plasma (the gas purity was 99.997 %, the Ar flow approx. 0.3 l s^{-1}, pressure of 10 Pa, electrode distance of 50 mm and its area 48 cm^2, the chamber volume was around 1,000 cm^3 and the plasma volume was 240 cm^3). The discharge power of 8.3 W was used and the treatment was carried out at the room temperature with an exposure time of 240 s. Several some samples were left for 7 days to age. Gold deposition occurred with two different sputtering times of 100 s and 300 s. The pristine (PS - 100 s Au and PS - 300 s Au), plasma modified (PS - 100 s Au, modified and PS - 300 s Au, modified), and aged plasma modified (PS - 100 s Au, modified, aged 7 days and PS - 300 s Au, modified, aged 7 days) PS samples were covered with 50 nm thin Au layer deposited from an Au target (99.995 %) by diode sputtering (BAL-TEC SCD 050) at room temperature (Fig. 2). The sputtering parameters of were: Ar pressure of 4 Pa, 50 mm electrode distance, 20 mA current.

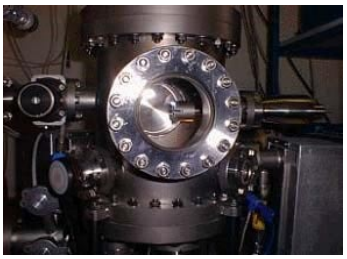

Fig. 1. **The chamber for plasma modification of polymers**

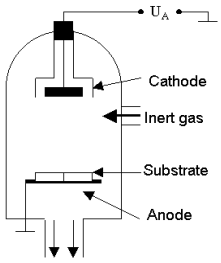

Fig. 2. **The principle of diode sputtering**

Techniques

Instrumented indentation measurement of hardness and elastic modulus and the nanoscratch tests were carried out using the NanoIndenter XP to estimate the resistance of the materials to indenter penetration. Indents and scratches were created with the Berkovich indenter[9]. According to the IIT (Instrumented Indentation Testing) method, the elastic modulus E and hardness H of tested material were determined as functions of displacement into the surface h. Indentation hardness H_{IT} is calculated using the following formula:

$$H_{IT} = \frac{F_{\max}}{c \cdot h_c^2} \qquad (1)$$

where F_{max} is the maximum load, c indicates a constant dependent on the shape of the indenter used and h_c is the contact depth[9]. The calculation of the elastic modulus E is the following:

$$\frac{1}{E_r} = \frac{1-\nu^2}{E} + \frac{1-\nu_i^2}{E_i} \qquad (2)$$

where E, ν are the elastic modulus and Poisson's ratio for the tested material, respectively; E_i, ν_i are the elastic modulus and

Poisson's ratio for the material of the indenter, respectively. E_r is the reduced elastic modulus which is calculated as follows:

$$E_r = \frac{\sqrt{\pi} \cdot S}{2 \cdot \beta \cdot \sqrt{c \cdot h_c^2}} \qquad (3)$$

S is the contact stiffness, β is the correction constant for various shapes of indenters[9].

The indentation modulus is especially important for the evaluation of thin films because it is normally not identical to the values known for bulk materials. During nanoindentation of thin films, a small oscillating load with a frequency of 0.05−200 Hz and amplitude of 60 nN − 300 mN was superimposed onto the primary load. The method is called CSM (Continuous Stiffness Measurement) method. The system analysed dynamic response of tested material, measuring the contact stiffness S, and changes in mechanical values during loading as a function of penetration depth.

Scratch testing is one of the most widely used testing methods for the investigation of the adhesion and other mechanical properties of thin film-substrate structures. The standard for scratch testing was created for hard thin films like TiN with the thickness of several μm, where the critical forces are in the order of a few tens of Newton. The principle of the scratch test is a relative motion of the support with the sample against an indenter, which is loaded with a selected normal force[6]. The acting forces, the normal force F_N, lateral force F_L and friction force F_t are shown in Fig. 3. In this work, the tested films were 50 nm thick and were deposited on soft polystyrene foils. The applied constant forces F_N were chosen <50 mN based on the previous studies of polymeric substrates. The tests in this force range are called nanoscratch tests. Three different forces, 1 mN, 10 mN and 50 mN, were used for constant force nanoscratch tests and the force from 1 mN to 10 mN was applied during the rising force nanoscratch test. The lengths of scratches of 200 μm for constant force and 400 μm for the rising force type of scratches were selected.

Scanning electron microscopy (SEM, Quanta 200) was used for scratch morphology visualization[8] immediately after testing in order to eliminate the relaxation which is known to occur in polymeric materials.

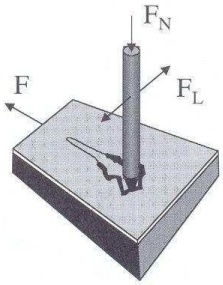

Fig. 3. **The principle of scratch testing**

3. Results and discussion

Fig. 4 and Fig. 5 show the dependence of the average values of hardness and elastic modulus on the penetration depth for all investigated samples. The graphs in these figures and Table I with average values from measurement prove the influence of different sputtering times, t_s, modification of the substrate and ageing on the mechanical properties.

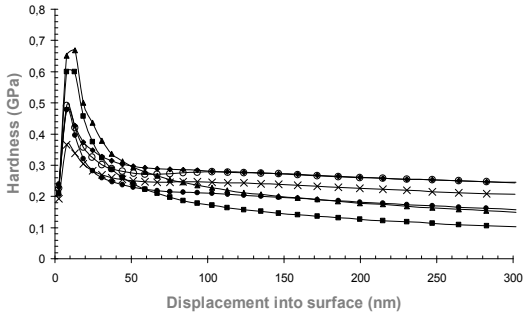

Fig. 4. **Dependence of indentation hardness on the penetration depth**

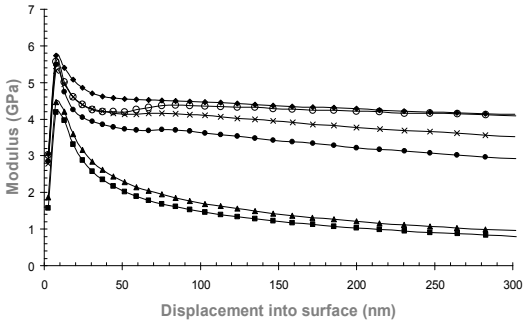

Fig. 5. **Dependence of indentation modulus on the penetratation depth**

Table I
Average values of mechanical properties [GPa]

Samples	PS - 100s Au	PS - 100s Au, mod.	PS - 100s Au, mod., aged	PS - 300s Au	PS - 300s Au, mod.	PS - 300s Au, mod., aged
Hardness	0.48	0.60	0.67	0.37	0.49	0.48
Modulus	5.73	4.19	4.46	5.32	4.61	5.48

Samples with the sputtering time t_s = 100 s mostly showed higher hardness and lower values of elastic modulus with the exception of elastic modulus for pristine PS as shown in Table I. In most cases, hardness was higher and elastic modulus was lower in comparison with the pristine PS due to modification and ageing.

The nanoscratch tests with the constant force yielded the dependence of average depth of penetration into the material along the scratch groove (Fig. 6, a–c).

The corresponding penetration depth values averaged for each stress along the scratch path are compared in Table II.

Fig. 7 shows SEM images of the scratches produced under the highest applied load F_N = 50 mN in each sample whereas Fig. 8 illustrates the differences in scratch morphology between the plasma modified PS with t_s = 100 s and plasma modified PS with t_s = 300 s under the constant force F_N = 10 mN. Obviously, the samples with t_s = 300s exhibit better resistance to penetration of the indenter in almost all cases.

Table II
The average values of penetration depth after scratch tests under different constant load

Applied force [mN]	The average value of penetration into the material [μm]					
	PS - 100s Au	PS - 100s Au, mod.	PS - 100s Au, mod., aged	PS - 300s Au	PS - 300s Au, mod.	PS - 300s Au, mod., aged
1	1.20	1.85	0.53	0.46	0.42	0.51
10	10.30	12.31	3.87	3.49	1.87	2.46
50	8.30	20.54	5.72	12.95	5.31	5.85

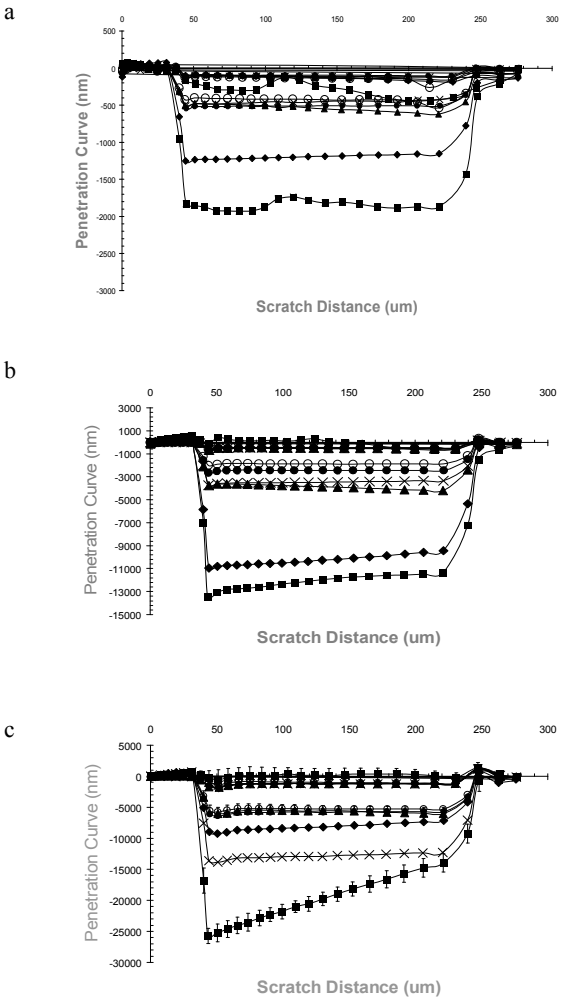

Fig. 6. **The dependence of an average depth of penetration along the of scratch length under the applied normal load: a) - F_N = 1 mN, b) - F_N = 10 mN, and c) - F_N = 50 mN**

In the process of creation of the scratches with the rising force, the tip was gradually loaded from 1 to 10 mN. Fig. 9 a and Fig. 9 b depict the comparison of the scratches on plasma modified PS- Au samples to indicate the effect of sputtering time. In both cases, the surface was revealed immediately after the first contact of the indenter with the surface occurred. The critical load is also in the range of milinewton.

Although the above results provide some absolute values, they cannot be considered as "standard mechanical properties" values for thin films. Nanoindentation measurement and scratch test values are predominantly intended for qualitative comparison of tested samples and determining the influ-

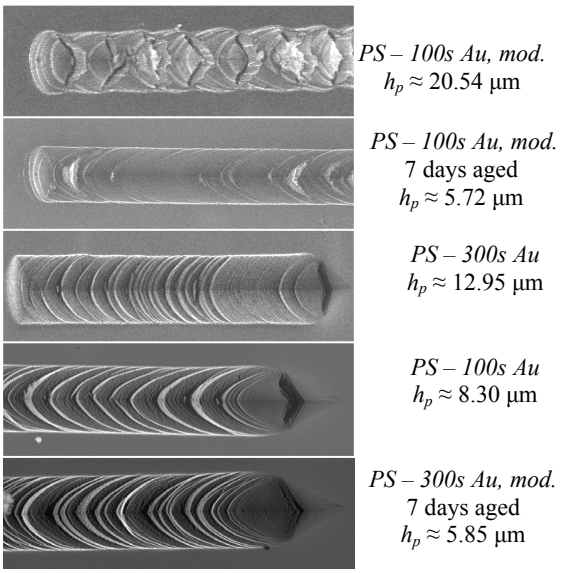

Fig. 7. **SEM images of scratch paths on the 50 nm Au nano-layer for the normal load F_N = 50 mN**

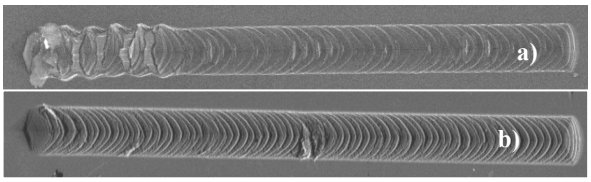

Fig. 8. **The effect of different sputtering times t_s on scratch paths in the plasma modified PS 50 nm Au nanolayer under the constant force F_N = 10 mN: a) t_s =100 s, b) t_s =300 s**

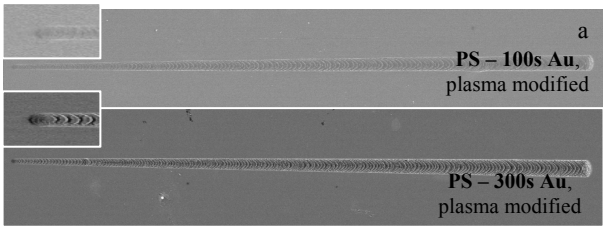

Fig. 9. **SEM images of the rising force scratch paths on the 50 nm Au nano-layer deposited on the plasma modified PS (force F_N = 0 - 50 mN**

ence of sputtering time, plasma modification and ageing on mechanical properties of the whole composite system.

4. Conclusions

Instrumented indentation hardness, modulus of elasticity, and depth of penetration into the surface during the scratch test were investigated on the samples of polystyrene with thin Au nanolayer. Higher hardness and predominantly lower values of elastic modulus were found for the sputtering time t_s = 100 s compared to the samples sputtered for t_s = 300 s. Plasma treatment and ageing of PS increased the values of hardness and reduced elastic modulus in comparison with the pristine PS (with the exception of the specimen marked PS - 300 s Au - modified and aged, where the elastic modulus was higher than that of pristine PS.

Scratch testing showed that the plasma modified PS with the time t_s = 300 s has the best resistance to penetration under all applied forces. In most cases, ageing has significant influence on the resistance to penetration. Plasma modified samples with t_s = 300 s have better resistance to penetration than the pristine PS, whereas samples with t_s = 100 s have poorer resistance to penetration. Samples with t_s = 300 s show the best results in scratch testing.

This work was supported by the GA CR under the projects 106/09/0125 and 106/09/P046.

REFERENCES

1. http://physics.ujep.cz/CZ/view.php?cisloclanku=2007020005.
2. Švorčík V., Kotál V., Slepička P., Bláhová O., Šutta P.: Polym. Eng. Sci. *46*, 1326 (2006).
3. Kotál V., Švorčík V., Slepička P., Bláhová O., Šutta P., Hnatowicz V.: Plasma Proc. Polym. *4*, 69 (2007).
4. Gross B., Grycz B., Miklóssy K.: *Technika plazmatu*. Praha 1967.
5. Švorčík V., Chaloupka A., Záruba K., Král V., Bláhová O., Macková A.: Nucl. Instrum. Meth. B *267*, 2484 (2009).
6. Slepička P., Kolská Z., Náhlík J., Hnatowicz V., Švorčík V.: Surf. Interf. Anal. *41*, 741 (2009).
7. Siegel J., Slepička P., Heitz J., Kolská Z., Sajdl P., Švorčík V.: Appl. Surf. Sci. *256*, 2205 (2010).
8. Customer Care Kit MTS system Corporation. USA 2004.
9. ISO14577-1:2002, Metallic materials-Instrumented indentation test for hardness and materials parameters - Part 1: Test method.

P. Bublíková[a], O. Bláhová[a], R. Medlín[a], P. Slepička[b], and V. Švorčík[b] *([a] New Technologies - Research Centre, University of West Bohemia, Plzeň, [b] Department of Solid State Engineering, Institute of Chemical Technology, Prague, Czech Republic):* **Evaluation of Au Thin Films Deposited on The Polystyrene Substrate**

The instrumented indentation and scratch tests were applied to polystyrene substrates with thin Au layer to examine the influence of different times of Au sputtering (t_s) and the influence of the Ar plasma treatment and ageing in these composites. Higher hardness and predominantly lower values of elastic modulus were found for the sputtering time t_s = 100 s compared to the samples sputtered for t_s = 300 s. Plasma treatment and ageing of PS usually increased the values of hardness and reduced elastic modulus in comparison with the pristine PS. Scratch resistance is affected by plasma treatment and ageing.

DETERMINATION THE CRACK GROWTH RESISTANCE OF AUTOMOTIVE STEEL SHEETS

ĽUBOMÍR AMBRIŠKO* and LADISLAV PEŠEK

Department of Material Science, Faculty of Metallurgy, Technical University of Košice, Park Komenského 11, 043 85 Košice, Slovakia
lubomir.ambrisko@tuke.sk

Keywords: stable crack growth, R-curve, videoextensometry, thin steel sheets, CTOD

1. Introduction

Materials for the automotive body (1–2 mm thin) in the crash event must have high resistance toward crack growth initiated by the crash and guarantee the safety. Evaluation the crack growth resistance is well developed for bigger thicknesses, but not for thin sheet materials.

The crack growth resistance of a ductile material characterises R-curve by continuously recording the toughness in dependence on crack growth, Δa. Fracture toughness is commonly expressed in terms of the J-integral[1]. Relationship between the applied value of J and the amount of stable crack extension is known as the J_R-curve. The full J_R-curve is a material property and is indicative of the materials toughness[2].

The tearing modulus parameter is a measure of the resistance of the material to tearing and an indication of the stability of crack growth. The tearing modulus T represents a dimensionless form of the J_R-curve slope[3]. Use of the J_R-curve for stable crack growth is popular, although it is accepted that the J_R-curve may depend on the geometry of the specimen or the component[4]. The range of validity, i.e. of geometry independence is obviously much larger for the crack tip opening displacement CTOD resistance curve δ_R-curve[5].

Local deformation at the crack tip occurs in 1st stage of ductile tearing by notch tip blunting. Dimensions of sharp notch with tip radius 0.1 mm increase by blunting; before crack initiation the stretch zone[6] of the steels investigated reaches dimensions 0.1 – 0.2 × 0.4 – 1.3 mm. By followed stable crack growth CTOD increases. CTOD of the steels investigated reaches 1.5 – 5 mm at the end of ductile tearing by crack extension Δa=4 mm.

The aim of experiments was to analyze the influence of the microstructure, the rolling direction and loading rate on the crack growth resistance.

2. Material and methods

The materials used in this study are three grades of thin automotive steel sheets: XSG, HR 45 and DP, Fig. 1. XSG is a deep drawing interstitial free steel with ferrite microstructure (C=0.0013 %). HR 45 is a microalloyed steel with ferrite-pearlite microstructure (C=0.16 %) and DP is a dual phase steel with ferrite-martensite microstructure (C=0.072 %). Thickness t and mechanical properties of the steels investigated are shown in Tab. I.

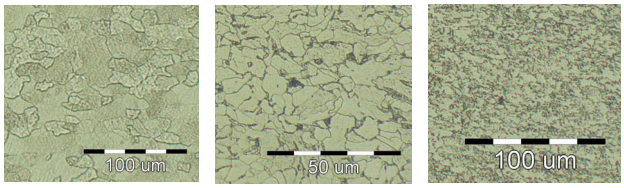

a) XSG b) HR 45 c) DP

Fig. 1. **Microstructure of the investigated steels**

Table I
Mechanical properties of the steels investigated

Grade	t [mm]	R_e [MPa]	R_m [MPa]	A [%]
XSG	1.95	182	299	45.2
HR 45	1.80	382	493	24.7
DP	1.60	357	580	24.5

Stable crack growth was monitored with videoextensometry techniques on the CT (Compact Tension) specimens with an electrospark prepared notch (tip radius 0.1 mm) or a fatigue precracks. Specimens with spot welds[7] in the fixative hole area and with anti-buckling plates were loaded by eccentric tension on material testing machine FP 100/1, whereby the deformation in area around the notch was recorded by a non-contact displacement measurement – a videoextensometry technique[8]. Opening of the notch was determined by continual recording the co-ordinates of centre of gravity of the dots by appropriate software. The crack growth Δa, in both directions perpendicular and parallel to the rolling direction, was evaluated with program MATLAB on recorded images. Opening of the notch has been recalculated at CTOD by plastic hinge model, used equations are published in[9]. J-integral values using[10] were determined.

3. Results

Experiments were performed using three automotive zinc coated steel grades. From obtained data J_R-curves and δ_R-curves were evaluated. Max. J-integral as well as CTOD were found in XSG steel.

The R-curve slope characterizes the stable crack growth resistance. In Fig. 2 are presented the crack growth resistance characteristics of the steels investigated (dCTOD/da, T modulus). The crack growth resistance characteristic – T modulus of the steels investigated by the crack growth in direction perpendicular to the rolling direction (LT orienta-

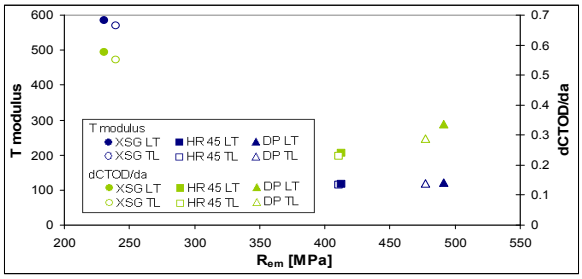

Fig. 2. **The crack growth resistance characteristics of the steels investigated**

tion) is bigger of 2 % as by the crack growth in the rolling direction (TL orientation). Bigger differences (3–14 %) were determined for dCTOD/da.

CT specimen usually has notch end with a fatigue precrack. In this work were used CT specimens with an electrospark prepared notch. In ref.[11] was no particular difference in the crack propagation characteristics of both fatigue precracked and sharp V-notched specimens with notch radius 0.1 mm. δ_R-curve of steels used for both an electrospark notch and a fatigue precrack are in Fig. 3. For slope dCTOD/da of steels investigated weren't determined important differences.

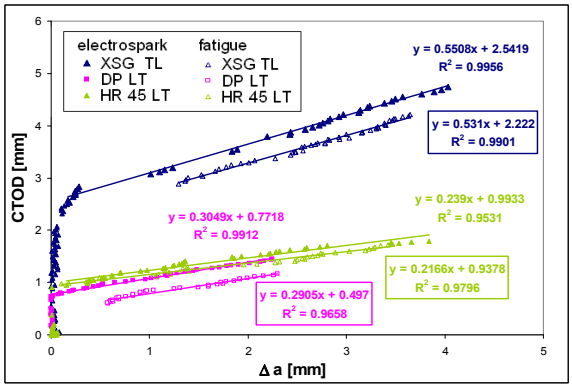

Fig. 3. **δ_R-curve of steels investigated for both an electrospark prepared notch and a fatigue precrack**

The influence of various loading rates (1.3, 130 and 1000 mm min^{-1}) on the crack growth resistance – slope dCTOD/da was determined for XSG steel. Slope dCTOD/da increases with loading rate increasing. By the loading rate of 1000 mm min^{-1} dCTOD/da for XSG reaches the highest values (more than 8 % as by loading rate of 130 mm min^{-1}; more than 10 % as by 1.3 mm min^{-1}). By the loading rate of 130 mm min^{-1} dCTOD/da reaches higher values of 2 % as by loading rate of 1.3 mm min^{-1}.

4. Conclusions

The crack growth resistance depends on steel grade, on the crack orientation to the rolling direction as well as on the loading rate. The crack growth resistance of steel XSG (IF steel) is the highest, for both parameters dCTOD/da and T modulus. The crack growth resistance (T modulus) of XSG steel is higher by 80 % than that of both HR 45 (ferrite-pearlite steel) and DP (dual phase steel). Differences between the crack growth resistance of steels investigated are result of microstructure and mechanical properties. The crack growth resistance is higher for crack growth perpendicular to the rolling direction compared with parallel direction.

No important differences in the stable crack growth characteristic (dCTOD/da) of both fatigue precracked and electrospark notched specimens of steels investigated were observed.

This work was performed within the frame of the APVV Project No. APVV – 0326 – 07.

REFERENCES

1. Aberkane M., Ouibrahim A., Pluvinage G., Azari Z.: Strength Mater. *35*, No. 4 (2003).
2. Saxena A.: *Nonlinear fracture mechanics for engineers*, CRC Press, 1. ed., 1998.
3. *ASM Handbook*, Volume 19, Fatigue and fracture, ASM International, 1997.
4. Dhar S., Marie S., Chapuliot S.: Int. J. Pressure Vessels Piping *85* (2008).
5. Brodka W., Anuschewski P., Schneider I.: Eng. Failure Anal. *17* (2010).
6. Ambriško Ľ., Pešek L.: In: Acta Metallurgica Slovaca – Conference, *2* (2010).
7. Kaščák Ľ., Viňáš J.: Acta Mechanica Slovaca *12*, č. 3-A PRO-TECH-MA (2008).
8. Pešek L.: In: *Lokální mechanické vlastnosti 2006, Plzeň – Nečtiny, 8.-10.11.2006*, ZČU v Plzni.
9. Methods for Crack Opening Displacement (COD) Testing, BS 5762, British Standards Institution, London, 1979.
10. ESIS Recommendations for Determining the Fracture Resistance of Ductile Materials, ESIS P1-92, ESIS Delft, 1992.
11. Kayamori Y., Hillmansen S., Crofton P. S. J., Smith R. A.: Mater. Sci. Forum *539-543* (2007).

Ľ. Ambriško and L. Pešek *(Technical University of Košice, Faculty of Metallurgy, Department of Material Science):* **Determination the Crack Growth Resistance of Automotive Steel Sheets**

This paper deals with determination of the crack growth resistance of automotive steel sheets. Stable crack growth was monitored with videoextensometry techniques on CT (Compact Tension) specimens with various orientation of notch (parallel to rolling direction, perpendicular to rolling direction). Specimens of three steel grades with a fatigue precracks and with an electrospark produced notches were loaded by eccentric tension by loading rate 1.3 mm min^{-1}. From obtained data the local deformation at the crack tip CTOD (Crack Tip Opening Displacement), J-integral and crack growth Δa were specified and afterwards the R-curves were established. From R-curves the resistance of the stable crack growth for each material was determined.

CHARACTERISATION OF MECHANICAL PROPERTIES OF S-PHASE COATINGS PRODUCED BY MAGNETRON SPUTTERING DEPOSITION

JOLANTA BARANOWSKA and SEBASTIAN FRYSKA*

Institute of Materials Science and Engineering, West Pomeranian University of Technology, 70-310 Szczecin, al. Piastów 19, Poland
sebastian.fryska@zut.edu.pl

Keywords: S-phase, reactive magnetron sputtering, microstructure, mechanical properties

1. Introduction

S-phase is a phase with very high hardness and good corrosion resistance that has a large potential for many applications. It can be obtained using various methods, including gas and plasma nitriding of austenitic stainless steel as the most common ones[1–4]. However, layers produced at such conditions have a gradient structure, which makes it difficult to characterise properties of layers as a function of nitrogen content. S-phase coatings obtained by reactive magnetron sputter deposition (PVD) are homogeneous in a bulk and can be produced in an effective way even at a very low temperature.

There are few publications that present a possibility to obtain such coatings by reactive magnetron sputtering[5–9]. As it was observed in previous investigations[10,11] layers obtained by this method have a very strong texture. The <100> direction perpendicular to substrate surface was a preferred direction of crystal growth. However, it is possible to modify the microstructure of coatings by changes of sputtering deposition parameters. The main objective of this work was to evaluate how changes in microstructure of S-phase coatings can influence its mechanical properties.

2. Experimental

The coatings were produced using an unbalanced DC-magnetron sputtering system equipped with three magnets. Substrates (ϕ 28 mm, 4 mm thick) and targets (ϕ 50 mm) were made of AISI 316 steel. During the experiments the following parameters were kept constant: temperature – 200 °C, N:Ar ratio – 3:10, sputtering time – 30 min. Two different total pressures were applied – 0.53 and 1.07 Pa and two different plasma power densities – 10 and 20 W cm^{-2}. Moreover, a different numbers of targets were used during deposition (1, 2 or 3). Samples before depositions were mechanically ground and polished. Final polishing step was conducted with 0.05 μm alumina slurry by means of vibrational polishing machine to eliminate surface deformation leading to ferrite formation in subsurface layer. The current paper presents only selected results to discuss how coating morphology affects their properties. The following techniques were used to characterise the coatings:

a) X-ray diffraction (XRD) with Bragg-Brentano geometry for the range of 2 theta angles between 20–120° with CuKα radiation (X'pert Panalytical);
b) Electron microprobe spectrometry (EPMS WDS) to measure nitrogen content in the coatings (IBEX Noran Instruments);
c) Glow discharge optical emission spectroscopy (GD-OES – Horiba Yvon Jobin) to estimate elements distribution in the coatings;
d) Hardness measurements by nanoindentation with a Berkovich tip (XP– MTS NanoInstruments). The continuous stiffness measurement technique was applied to determine hardness changes across the coatings. The load was gradually increased to obtain a maximum penetration depth of ca. 2.9 μm. The maximum load of 490–545 mN was reached. A set of 25 measurements was performed for each coating.
e) Coating thickness was estimated by means of profilometer (Dektak 8M – Veeco) by measuring the step between coated and uncoated part of the substrate that remained covered during deposition. The same instrument was used to evaluate roughness of the coatings.

3. Results and discussion

Deposition of the coatings did not change geometry of the surface. Roughness of the coatings varied in the same range as for non-treated surface: Ra=0.008–0.025 μm. XRD analysis demonstrated that all the coatings were composed of S-phase. Essential differences in peaks position and texture were observed, however, depending on the deposition parameters. Fig. 1 presents a comparison of diffraction patterns obtained for different gas pressure values when 2 or 3 targets were used. When lower pressure (0.53 Pa) was applied coatings were composed of S-phase grains with (200) planes parallel to substrate surface only (lines 1 and 3, Fig. 1). An increase of the pressure (1.07 Pa) changed the texture: grains with planes (111) parallel to the surface were dominant in these coatings (lines 2 and 4, Fig. 1).

Increasing the number of targets at the same time as total pressure caused the shift in the S-phase peaks position toward higher 2theta angles regardless of the kind of texture observed (lines 1 and 3, 2 and 4, in Fig. 1 and Fig. 2). It means a decrease in S-phase lattice parameter due to lower nitrogen content. This phenomenon can be explained by higher quantity of metal ions in comparison to nitrogen supply from plasma.

It was also observed that S-phase peaks with much higher intensity were registered when one target was used during deposition (Fig. 2). It can suggest much bigger crystallites size in these coatings. Usually, a higher number of targets used during deposition means that much higher quantity of metal ions is sputtered toward the substrate. In this way the

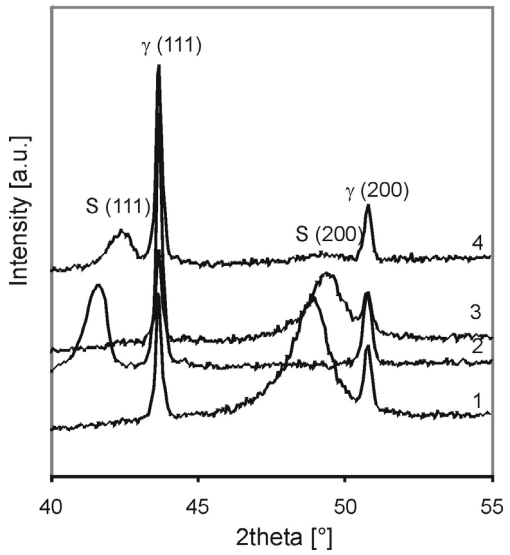

Fig. 1. **Diffraction patterns for samples deposited with the following parameters:** p=10 W cm^{-2}, 1 – 2 targets, 0.53 Pa; 2 – 2 targets, 1.07 Pa; 3 – 3 targets, 0.53 Pa; 4 – 3 targets, 1.07 Pa

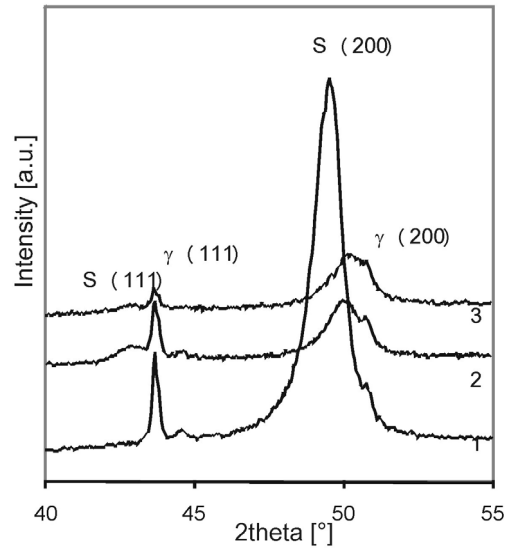

Fig. 2. **Diffraction patterns for samples deposited with the following parameters:** pressure = 0.53 Pa, p=20 W cm^{-2}: 1 – 1 target; 2 – 2 targets; 3 – 3 targets

number of nuclei is also increased leading to formation of much finer crystallite structure as it was observed in current studies.

When lower plasma power density was applied in the experiments (10 W cm^{-2}) there were no changes in a texture observed for 0.53 Pa pressure. However, an increase of plasma power density up to 20 W cm^{-2}, for the same number of targets also led to production of grains with (111) planes parallel to the surface (Fig. 3).

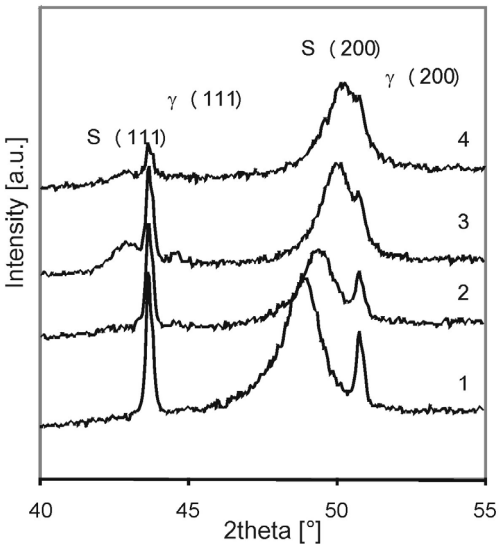

Fig. 3. **Diffraction patterns for samples deposited with the following parameters:** pressure = 0.53 Pa, 1 – 2 targets, 10 W cm^{-2}, 2 – 3 targets, 10 W cm^{-2}, 3 – 2 targets, 20 W cm^{-2}, 4 – 3 targets, 20 W cm^{-2}

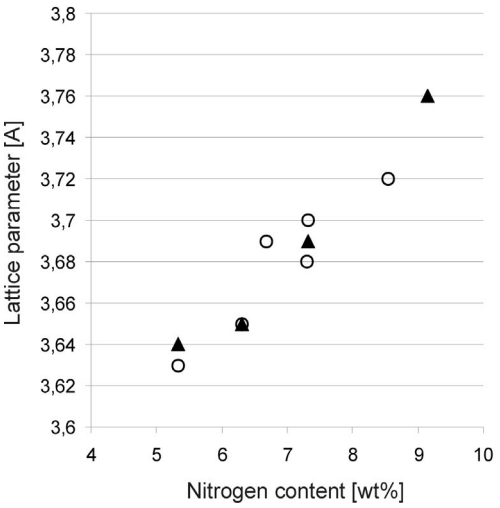

Fig. 4. **Changes of lattice parameter in function of nitrogen content:** triangle – lattice parameter measured for (111) planes, circle – for (200) planes

Positions of S-phase peaks in diffraction patterns correspond well to nitrogen content measured by WDS methods (Fig. 4), even though the measurements on thin coatings are affected by the substrate influence. Only small differences in lattice parameters measured for (111) and (200) peaks can be observed. In case of S-phase produced by nitriding this differ-

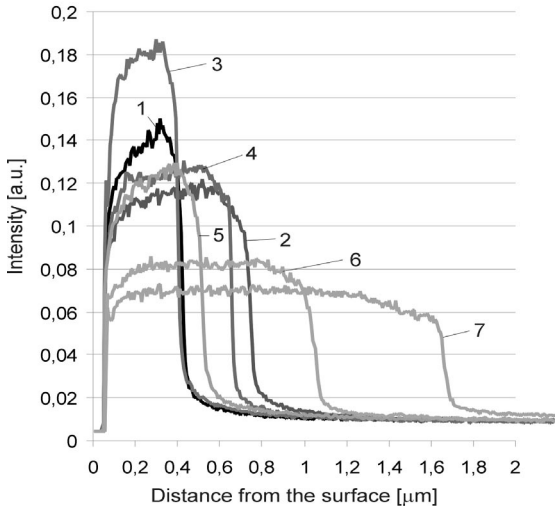

Fig. 5. **Nitrogen profiles in analysed coatings (GDOES):** 1 – 2 targets, 0.53 Pa, 10 mW cm^{-2}, 2 – 3 targets, 0.53 Pa, 10 mW cm^{-2}, 3 – 2 targets, 1.07 Pa, 10 mW cm^{-2}, 4 – 3 targets, 1.07 Pa, 10 mW cm^{-2}, 5 – 1 target, 0.53 Pa, 20 mW cm^{-2}, 6 – 2 targets, 0.53 Pa, 20 mW cm^{-2}, 7 – 3 targets, 0.53 Pa, 20 mW cm^{-2}

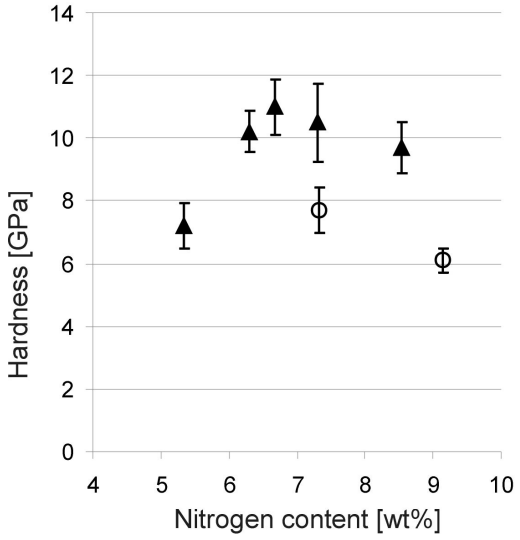

Fig. 6. **Hardness of the coatings as a function of nitrogen content:** triangles – coatings with a (200) texture, circles – coatings with a (111) texture

ence can be up to 10 % due to strong stresses generated during layer formation[3,4].

An analysis of nitrogen profiles obtained by GDOES technique confirmed differences in nitrogen content (Fig. 5), but it also showed that WDS analysis underestimated nitrogen content due to small thickness of the layer (thinner than the depth of the analysed area). The thickness varied in the range between 300 and 1800 nm. Thickness of the coatings depended on depositing parameters. A rate of deposition was increasing with an increasing number of targets, plasma power density and total pressure.

Microstructural changes induced by different process parameters influenced mechanical properties of the coatings. In case of coatings with (200) texture, small influence of nitrogen content on hardness can be observed (Fig. 6 – triangles). Hardness increases from 6 GPa up to 11 GPa with nitrogen content. Then it drops below 10 GPa. It suggests the existence of a maximum of hardness observed by others[6]. However, the drop in the hardness in the coating with the highest nitrogen content, which was relatively thin (Fig. 5 – line 3), can be strongly influenced by substrate with much lower hardness than the coatings.

However, a drop in hardness is also observed for coatings with a (111) texture with higher nitrogen content (Fig. 6 – circles). It can be caused by the same effect as above, but after having analysed the hardness profiles obtained by continuous stiffness measurements (Fig. 7) this hypothesis was rejected. Coating 3, which has a comparable thickness to coating 1 but has much higher nitrogen content (Fig. 5), has a significantly lower hardness. The coating 5 which has a comparable nitrogen content to that of coating 4 which is slightly thicker, has much higher hardness. These coatings with a (111) texture were obtained at higher pressure of depo-

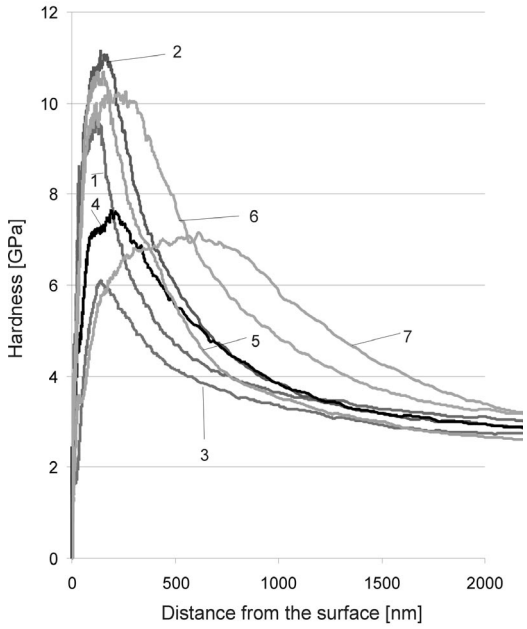

Fig. 7. **Hardness profile measured by nanoindentation from the coating surface**: 1 – 2 targets, 0.53 Pa, 10 mW cm^{-2}, 2 – 3 targets, 0.53 Pa, 10 mW cm^{-2}, 3 – 2 targets, 1.07 Pa, 10 mW cm^{-2}, 4 – 3 targets, 1.07 Pa, 10 mW cm^{-2}, 5 – 1 target, 0.53 Pa, 20 mW cm^{-2}, 6 – 2 targets, 0.53 Pa, 20 mW cm^{-2}, 7 – 3 targets, 0.53 Pa, 20 mW cm^{-2}

sition which means also under higher nitrogen partial pressure (0.24 Pa). Dahm et al.[6] observed that an increase of nitrogen partial pressure led to formation of coatings with lower hardness. No explanation to this fact was given. According to the

present investigation changes in hardness can be attributed to changes in grain texture formed in the coatings. Similar relationship was observed for Young modulus, which was much lower for coatings with a (111) texture.

Mechanical properties of single crystals depend on crystallographic direction. In fcc structure the maximum modulus is in direction <111> while the minimum value is in direction <100>[12]. It is contradictory to the observations made in the present investigations. Therefore, it can be suggested that much finer microstructural differences related to the type of the texture formed during deposition could be responsible for changes in mechanical properties, which will be the subject of further investigations.

4. Conclusions

1. The reactive magnetron sputtering deposition enables S-phase coatings to be produced and these coatings do not demonstrate deformations of a crystal cell typical for other processes of S-phase formation.
2. An increase of such parameters as total and nitrogen partial pressure, plasma power density and metal ion supply influences positively the rate of deposition, but also has an important effect on layer morphology. An increase of nitrogen partial pressure changes the coatings' texture. The growth of the crystals proceeds along <111> direction instead of <100> observed for lower pressure.
3. A kind of texture produced in S-phase coatings can have an influence on coatings mechanical properties. Higher hardness was measured for coatings with a (200) texture than with a (111) texture. However, this effect is not related directly to orientation of the crystals dominating the coatings.

The authors would like to acknowledge the financial support of Polish Research Committee in a period of 2009-2012.

REFERENCES

1. Fewell M. P. Mitchell D. R. G., Priest J. M., Short K. T., Collins G. A.: Surf. Coat. Technol. *131*, 300 (2000).
2. Baranowska J.: Surf. Coat. Technol. *180-181*, 293 (2003).
3. Christiansen Th., Somers M. A. J.: Struers J. Metallography *9*, 1 (2006)
4. Maendl S., Rauschenbach B.: Def. Diff. Forum *188-190*, 372 (2001).
5. Terwagne G., Colaux J., Collins G. A., Bodart F.: Thin Solid Films *377-378*, 441 (2000).
6. Dahm K. L, Dearnley P. A.: Surf. Eng. *12*, 61 (1996).
7. Dahm K. L, Anderson I. A., Dearlney P. A.: Surf. Eng. *11*, 138 (1995).
8. Dahm K. L, Dearnley P. A: Proc. Inst. Mech. Eng. *214*, 181 (2000)
9. Kappaganthu S. R., Sun Y.: J. Cystal Growth. *267*, 385 (2004).
10. Baranowska J., Fryska S., Przekop J., Suszko T.: Adv. Manuf. Sci. Technol. *33*, 59 (2009).
11. Baranowska J., Fryska S., Przekop J., Suszko T.: Elektronika *9*, 19 (2009).
12. Noyan I. C., Cohen J. B.: *Residual Stresses*. Springer, Berlin 1987.

J. Baranowska and S. Fryska *(Institute of Materials Science and Engineering, West Pomeranian University of Technology, Szczecin, Poland):* **Characterisation of Mechanical Properties of S-Phase Coatings Produced by Magnetron Sputtering Deposition**

The paper presents the results of the investigations of mechanical properties of S-phase produced by reactive magnetron sputter deposition. It was demonstrated that texture of the coatings, which depended on deposition parameters, had an influence on coatings' hardness. Higher hardness was measured for coatings with a (200) than with a (111) texture.

PREPARATION OF STAINLESS STEEL/TiC COMPOSITE BY SELECTIVE LASER MELTING

ANNA BIEDUNKIEWICZ*, WITOLD BIEDUNKIEWICZ, PAWEŁ FIGIEL, and DARIUSZ GRZESIAK

West Pomeranian University of Technology Szczecin,Piastow Ave.17; 70-310 Szczecin, Poland
Anna.Biedunkiewicz@zut.edu.pl

Keywords: nanocomposite, TiC, sol-gel, SLM, FEM

1. Introduction

Metal matrix composites (MMCs) are in the focus of intensive research and development world wide for many industrial applications, where weight reduction along with the improvement in elastic moduli, strength, thermal stability, wear resistance and service life are required[1–4]. One of the ways for obtaining functional nanocomposite materials is the technology based on the selective laser melting of the powders. This method belongs to promising rapid prototyping (RP) processes due to its ability to fabricate three-dimensional (3D) metal parts directly according to CAD model[5].

Our work presents an experimental investigation of the synthesis and characterization of nanocrystalline TiC prepared by sol-gel method and composite stainless steel/TiC prepared by SLS/M method using stainless steel powder and pure titanium carbide powder as raw materials.

2. Experimental details

The original way of ceramic nanomaterials synthesis based on non-hydrolytic sol-gel method was elaborated[6,7]. Using carbonized and purified nc-TiC particles the technology of the production of the nanocomposite structures based on the Selective Laser Sintering/Melting (SLS/M) technology was worked out. The MCP HEK Realizer II device was applied. Suitable gear and the modification of the parameters of the laser energy delivering allowed to use the device for work in the Partial Melting technology. Such configuration enables the research on obtainment of the nanocomposite material. As matrix the stainless steel 1.4404 (AISI 316L) was used and as the filler (nanoparticles) was nc-TiC0.85. Samples were subjected to hardness tests for quick estimation of the mechanical parameters. Chosen samples with highest hardness were submitted to observations on the scanning microscope. Several variables are used in the nanocomposite manufacturing researches. This allows to get coherent, functional material and in the further researches it will let to optimize the materials properties. Controlled process variables can be divided on two groups – material parameters (percent share of the filler and the matrix) and process parameters (the power of the laser, the exposure time, melted layer thickness). The powder was prepared in two ways: manual mixing and ball-milling method. In the SLM process following parameters was used: TiC/steel ratio: 0.5–0.8 wt.%, the power of the laser: 2500–5000 mA; the exposure time: 200–400 μs, sintered layer thickness: 50–75 μm. The solid products were investigated by XRD method. Nanoparticles size, chemical and phase composition were determined with the following techniques: XRD (PANalytical PW3040/60 X'Pert Pro), TEM (JEOL JEM 1200EX), SEM (JEOL JSM 6100), EDX (Oxford Instruments, ISIS 300). Hardness and modulus measurements were performed on MTS Nano Indenter XP using Brekovich tip.

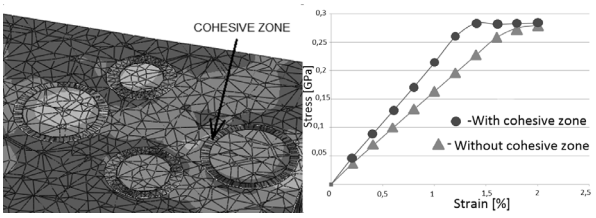

a b

Fig. 1. **a) Additional interphase – cohesive zone, b) Stress – strain curves comparison**

2.1. FEM model

In the aim of the improvement of the nanocomposite parameters, FEM model has been worked out. FEM model was developed by the state-of-the-art linear and nonlinear multi-scale material modelling software, which is applied to generating multiphase structures together with boundary. For the regard of the „super hardness" phenomena, which is observed in nanocrystallite composites, the cohesive zone mechanism was used. It is enable additional effects, which appears on the boundary of separate phases of the composite. This effect was modelled as additional interphase with special mechanical properties, which was react on matrix and filler nanoparticles (Fig. 1a). The global structure of the nanocomposite was treated as isotropic and because of that it wasn't necessary to create the model of whole sample, it was limited to „Representative Volume Element" (RVE). RVE is the segment of the structure, which is big enough to avoid the size influence during the analysis and small enough to reach satisfy calculation time. The size of RVE is chosen individually.

Two models has been developed, both with the same parameters except application of cohesive zone in one of them. The TiC particles was modelled as linear elastic (Young modulus $E = 250$ GPa, Poisson's ratio $\nu = 0.3$) while the matrix was modelled as elastoplastic ($E = 193$ GPa, $\nu = 0.3$, Yield stress = 205 MPa and experimentally determined stress-strain curve). Uniaxial Dirichlet type of boundary condition was applied to the models (2 % tension). The result 'stress –

strain' chart with curves from both models is shown in Fig. 1b.

4. Result and conclusion

The average nc-TiC crystallites size was 40 nm (Fig. 2). The manual mixing of the powder before its introduction to Realizer II device enabled obtainment of non-porous composite with homogeneous dispersion of nc-TiC particles in steel matrix applying the following sintering parameters: TiC/steel ratio up to 60 wt.%, power of the laser = 5000 mA, exposure time: 200–400 μs.

Composite materials obtained by SLM technique, containing purified nc-$TiC_{0.85}$ in steel matrix, were characterized by good dispersion of TiC nanoparticles in matrix and three times higher hardness than stainless steel. The SEM image of the composite is presented in Fig. 3. In order to increase the ratio of nanoparticles in steel matrix, maintaining at the same time their homogeneous distribution, the ball-milling of nc-TiC and steel powders was used. After the sintering process

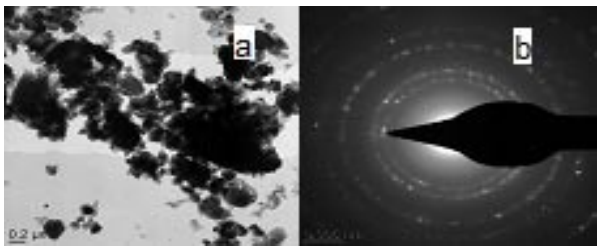

a b

Fig. 2. **a) TEM micrograph, and b) electron diffraction image of purified nc-TiC powder**

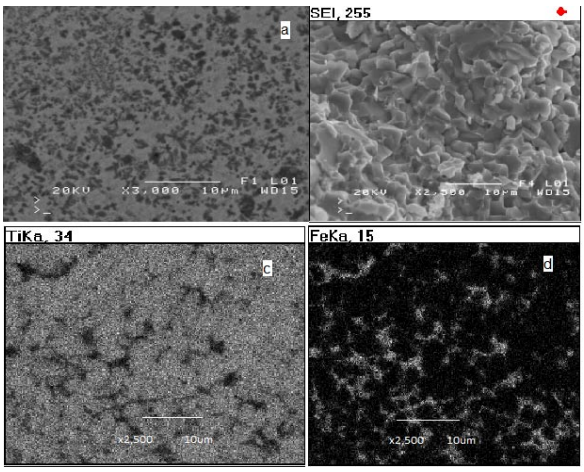

Fig. 3. **a) SEM cross-section image of steel/TiC composite sample; b) SEM microstructure of sintered nanocrystalline TiC sample; c) mapping of Ti; d) Fe distribution**

nc-TiC, austenite, small amounts of ferrite and trace amounts of carbides of M_7C_3 type, derived from conversions proceeding in material of steel powder in SLM process, were identified in the brittle and porous composite .

Presented FEM model is fitted to one specify sample made by SLM technique. It will be extended to other samples with different parameters and used to optimisation of the structure.

Financial support of the work by the Ministry of Science and Higher Education within the project No. N N507 444334, 2008-2011, is gratefully acknowledged.

REFERENCES

1. Tong L., Reddy R. G.: Metall. Mater. Trans. B, *37B*, 531 (2006).
2. Surender M., Balasubramaniam R., Basu B.: Surf. Coat. Technol. *187*, 93 (2004).
3. Pagounis E., Lindroos V. K.: Mater. Sci. Eng., A *246*, 221 (1998).
4. Das K., Bandyopadhyay T. K, Das S.: J. Mater. Sci. *37*, 3881 (2002).
5. Wang Li.: J. Southeast Univ. *20*, 846 (2004).
6. Biedunkiewicz A., Gabriel U., Figiel P., Grzesiak D.: J. Therm. Anal. Calorim. *101*, 701 (2010).
7. Biedunkiewicz A., Wysiecki M., Noworol P.: Polish Patent; P200978 (2008).

A. Biedunkiewicz, W. Biedunkiewicz, P. Figiel, and D. Grzesiak *(West Pomeranian University of Technology, Szczecin, Poland):* **Preparation of Stainless Steel TiC Composite by Selective Laser Melting**

SLM method was used to prepare stainless steel/ TiC composite. The samples were fabricated from 1.4404 stainless steel powder and nanocrystalline TiC powder synthesized by sol-gel method. In the aim of the improvement of the nanocomposite parameters, FEM model has been worked out. Nanoindentation was used to determine composition and hardness of this material. Chemical, structural and mechanical properties were investigated using scanning electron microscopy (SEM), transmission electron microscopy (TEM), and X -ray diffraction (XRD). Good dispersion of titanium carbide in steel matrix and significant increase hardness were obtained using purified, high stoichiometry nc-TiC for composite manufacturing by SLS/M method. The results were used to obtain finite element model of the nanocomposite structure.

EVALUATION OF THERMAL SPRAYED COATINGS PROPERTIES IN TERMS OF EROSIVE WEAR

JANETTE BREZINOVÁ*, ANNA GUZANOVÁ, MARIÁN EGRI, and JOZEF MALEJČÍK

Technical University in Košice, Faculty of Mechanical Engineering, Department of Technology and Materials, Mäsiarska 74, 040 01 Košice, Slovakia
janette.brezinova@tuke.sk

Keywords: BOF hood, thermal spraying, erosive wear, mass loss

Introduction

In steel making, inner parts of oxygen converter hood are subject to extreme wear. Converter hood material is exposed to set of unique factors related to temperature and gas rate variation, dust particles load etc. For inner hood side protection there are various types of protective coatings used with aim to enlarge hood lifespan[1−6].

This report deals with research results focused on analysis of renovative layers applied by thermal spraying.

Materials and methods

Experimental protective layers were applied on the base material of P235 GH (1.0405) ISO 2605 – heat-resistant carbon steel with specific properties, used for making pipes for energy and chemical equipment.

There were two types of cladding layers applied by thermal spraying technology on this base material: S – NiCr 80/20 and DURMAT – AS – 761. Before coatings application, test samples were pre-treated by pneumatic abrasive blast cleaning: blasting medium – brown corundum, grain size 0.71 mm, blasting angle 75°, air pressure 0.6 MPa, distance testing sample – blasting notule 250 mm. The surface roughness of blasted samples was evaluated by contact roughness tester according to STN EN ISO 4287. Vickers microhardness test of cladding and also base material was evaluated on metallographic cross-sections according to STN EN ISO 6507, testing equipment DUH 202 SHIMADZU. Tested coating was exposed to erosive wear simulated by abrasive grit blasting with aim to simulate operating conditions at two blasting angles: 45° and 75°. Used blasting medium – brown corundum with grain size 0.9 mm. One erosive cycle equals to 5 cycles of blasting medium in blasting equipment.

Results and discussion

Surface of the base material after grit blasting with angular blasting medium is characterized by typical morphology – undirected, isotropy surface. This morphology is suitable for functional coating application, because it provides higher adhesion to substrate. Blasted surface roughness was: Ra 11.42 μm and Rz 72.89 μm. Fig. 1 shows appearance of the surface blasted by brown corundum.

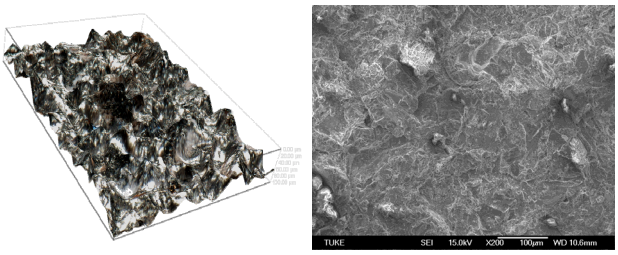

Fig. 1. **3D view and SEM of grit blasted surface**

Microscopic analysis proved characteristic sandwich structure of both evaluated coatings, Fig. 2, 3.

Microhardness measurement pattern is shown in Fig. 4. Experimentally determined microhardness of base material was 281 HV 0.01. Microhardness of coating made of DURMAT-AS-761 was higher (810 HV 0.5, Fig. 5) in comparison with Ni-Cr 80/20 coating (775 HV 0.5, Fig. 6), resulting from material properties, chemical composition and structure of particular materials. It is possible to assume that higher microhardness values provide higher wear resistance of coatings.

Fig. 7 shows mass loss Wh (g) of particular coatings at blasting angle 75° and 45°. Lower wear of both coating was achieved at 75° blasting angle. Lower blasting angle leads to more intensive material wear.

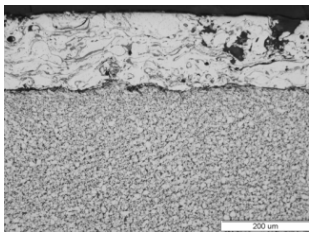

Fig. 2. **Cross-section of coating S – NiCro 80/20**

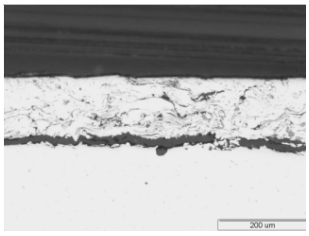

Fig. 3. **Cross-section of coating DURMAT- AS – 761**

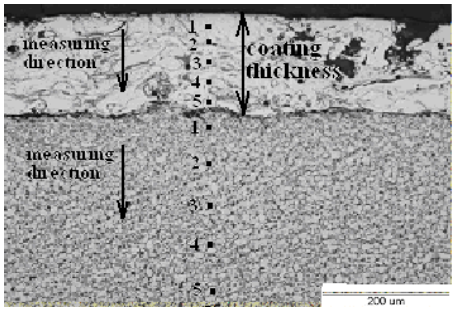

Fig. 4. **Microhardness measurement pattern**

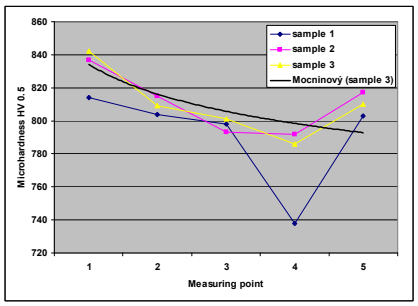

Fig. 5. **Microhardness of** DURMAT – AS – 761 coating

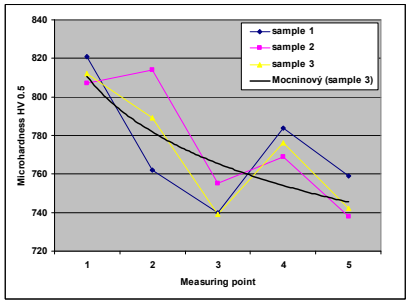

Fig. 6. **Microhardness of Ni-Cr 80/20 coating**

Notched abrasive grain can cause crack generation and failure of coatings, resulting in stress concentration and coating separation. Erosive wear test was carried out up to 5 cycles, when coating was completely removed. DURMAT-AS-761 coating showed high wear resistance resulting from its material properties, chemical composition and material structure along with its microhardness.

Conclusion

Microscopic analysis proved typical sandwich structure on both of the evaluated coatings.

Experimentally determined microhardness of the base material was 281 HV 0.01. Microhardness of new tested coating, DURMAT-AS-761, was higher (810 HV 0.5), in comparison with Ni-Cr 80/20 coatings (775 HV 0.5); it results from their material characteristics, chemical composition and structure. It can be assumed that higher microhardness values provide higher wear resistance of coatings.

Erosive wear test proved lower mass loss at 75° blasting angle for both of evaluated coatings. Lower blasting angle causes more intensive material reduction.

At places of abrasive impact, some cracks and coating failures can appear resulting in stress concentration and coating separation.

Achieved results showed, that new coating marked DURMAT-AS-761 has better properties in comparison with previously used coating from perspective of chemical composition, microhardness and also erosive wear evaluation.

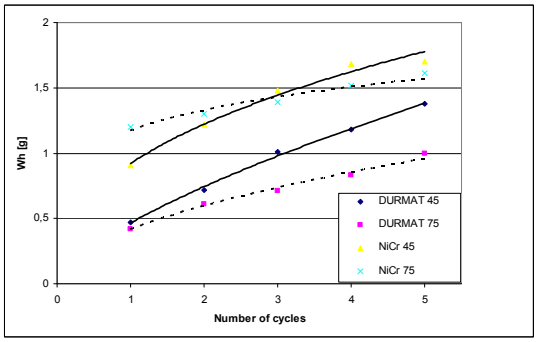

Fig. 7. **Mass loss of samples coated by DURMAT-AS-761 and Ni-Cr 80/20**

This work was done within the scientific project VEGA No. 1/0510/10.

REFERENCES

1. Makida Y., Tobe S., Ando M., Tochigy J., Sonoya K., Wakabayashi T., Yokohamashi J.: Extension of service life of gas turbine blade by ternary TBC coating. *ITSC 2002*, Essen 2002.
2. Jones R. L.: J. Therm. Spray Technol. *6*, 1 (1997).
3. Pershin V., Lufitha M., Mostaghimi J., Chandra S.: Proceedings from *Materials sollutions 2001*, *Thermal spray symposium, Ottawa 2001*.
4. Matějíček J., Neufuss K., Ctibor P., Rohan P., Dubský J., Chráska P., Brožek V.: *ITSC 2002, Essen*.
5. Jiang X., Wan Y., Herman H., Sampath S.: Thin Solid Films *385*, 1 (2001).
6. Fukumoto M., Huang Y., Ohwatari M.: Flattening mechanism in thermal spraying particle impinging on flat substrate in Coddet, C. (ed.). *Thermal spray meeting the chalenges of 21st century*, ASM, Materials park, 401, 1998.

J. Brezinová, A. Guzanová, M. Egri, and J. Malejčík
(Technical university in Košice, Faculty of Mechanical Engineering, Department of Technology and Materials, Slovakia):
Evaluation of Properties of Thermal Sprayed Coatings in Terms of Erosive Wear

The paper presents results of research aimed at analyzing the characteristics of the renovation layers applied by thermal spraying technology. There were experimentally determined properties of the currently used coating based on Ni-Cr 80/20 and a new coating DURMAT-AS-761 applied in form of filled wire. Quality of renovation layers was evaluated by metallographic analysis, EDX method, microhardness measurements and gravimetric method in terms of erosive wear. Contribution was based on the practice problems in order to increase the lifetime of the BOF (Basic Oxygen Furnace) hood.

CHARACTERIZATION OF SINTERED Ag NANOPOWDER JOINTS USING NANOINDENTATION TESTS

JIŘÍ BURŠÍK[a]*, JIŘÍ SOPOUŠEK[b], VILMA BURŠÍKOVÁ[c], ALEŠ STÝSKALÍK[b], and DAVID ŠKODA[b]

[a] *Institute of Physics of Materials, Academy of Sciences of the Czech Republic, Žižkova 22, 616 62 Brno,* [b] *Department of Chemistry, Faculty of Science, Masaryk University, Kotlářská 2, 611 37 Brno,* [c] *R&D Center for Low-cost Plasma and Nanotechnology Surface Modifications, Faculty of Science, Masaryk University, Kotlářská 2, 611 37 Brno, Czech Republic*
bursik@ipm.cz

Keywords: solder, silver nanopowder, nanoindentation

1. Introduction

Since 2006, when regulations enforcing lead-free solders were implemented into the EU legislation, there is an ongoing drive to find the best lead-free alternatives. It turns out that there is no single replacement, which would cover all technical applications.

Melting temperature of a solder is of the primary concern for both economical and technological reasons. The melting point of bulk silver (as an example of low-toxic material) is 962 °C, which is far too high even in a category of high-temperature solders (defined by $T_m \geq 230$ °C and limited by 350 °C due to polymer materials used in electronic industry). However, the effect of lowering melting point of powders with decreasing particle size[1–3] can be turned to advantage in this case. We have synthesized a silver nanopowder. We have prepared model joints and studied the nanopowder sintering and local mechanical properties.

2. Experimental

Silver nanopowder was prepared by a chemical wet synthesis from chemicals of high purity. Its characterization by means of transmission electron microscopy[4] revealed the prevailing particle diameter around 20 nm. Copper disks 5.5 mm in diameter were punched from a sheet, etched in acid ethanol (0.5 ml 98 wt.% H_2SO_4 and 100 ml 95 wt.% ethanol) at 60 °C and finally washed in 60 °C ethanol to remove surface oxides. A layer of silver nanopowder suspension in toluene was put on one of the Cu disks and covered by another one. The sandwich structures were annealed at temperatures 200, 250, 300 and 350 °C for 1.5 hour in the furnace LAC1200. Metallographic cross-sections were prepared from annealed samples and studied using a JEOL JSM 6460 scanning electron microscope (SEM). Microhardness and other mechanical properties of sintered Ag layers were measured by instrumented indentation technique using a Fischerscope H100 depth sensing indentation tester equipped with Berkovich indenter. The accuracy of the depth measurement was about ± 2 nm.

3. Results and discussion

Instrumented indentation tests were performed on cross sections to characterize local mechanical properties of sintered Ag layers. The optimum testing load range from 5 to 10 mN was chosen so that the extent of the plastic zone size around the indenter estimated using the Johnson's spherical cavity model[5] approach was several times lower than the sintered nanosilver layer thickness. This estimation was made for the single crystalline silver. The indentation tests were made in the central part of sintered nanoAg layer in order to avoid the influence of the surrounding copper plates (Fig. 1).

According to SEM observations the silver layer showed nanocrystalline character but also some porosity depending on the preparation conditions. In the case of ultrafine-grained (UFG) materials, the yield stress is higher compared to an ordinary polycrystalline bulk material. This is in accordance with the well-known Hall-Petch relation[6] between the yield stress σ_Y and the grain size d. The hardness of the sintered nanoAg layers was 4 to 8 times higher than the hardness of the single crystalline silver, hence proving the UFG character of Ag sintered layers.

The results of indentation tests showed a large scatter of measured values because of the heterogeneous nanoAg grain size and sample porosity. In order to assess the quality of the nanoAg layers the frequency diagrams of sample mechanical parameters were evaluated. In Fig. 2 and 3 the frequency diagrams of hardness and Young's modulus results obtained on 4 samples annealed in temperature range from 200 to 350 °C are shown.

Despite the sintered silver layer in the sample annealed at 350 °C exhibited the largest pores, its average hardness was the highest, because the pore distance was not smaller than the plastic zone radius. This fact caused the high scatter in hardness values and the relatively low Young's modulus (the radius of elastically deformed zone being larger than the pore distance) in sample S350. On the other hand, the highest values of the Young's modulus (between 60 and 70 GPa) were achieved after annealing at 250 °C, indicating that at this annealing temperature probably the lowest porosity of the sintered layer was attained. SEM observations of S250 revealed a homogeneous distribution of very fine pores. The pore distance was lower, than the plastic zone radius. Hence both hardness and Young's modulus were smoothly affected by the pore occurrence. This is in a good accordance with the higher modulus, lower hardness and lower scatter of measured values obtained on sample annealed at 250 °C (compared to those annealed at 350 °C).

The comparison of the values shown above with the results obtained previously on sandwiches prepared using a commercial Ag nanopowders[7] [$H = 600 \pm 200$ MPa and $E = 35 \pm 15$ GPa] shows better mechanical properties of the whole series of recently produced Ag layers.

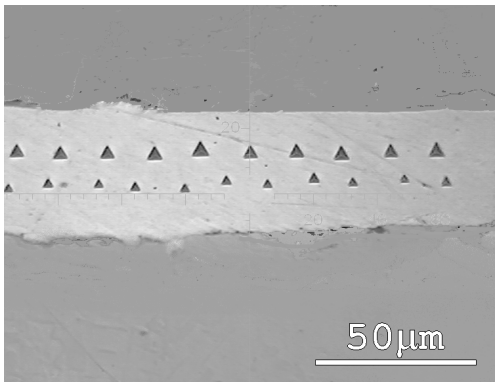

Fig. 1. **Light microscopy image of indentation prints made on sample S350 with applied loads 5 and 10 mN**

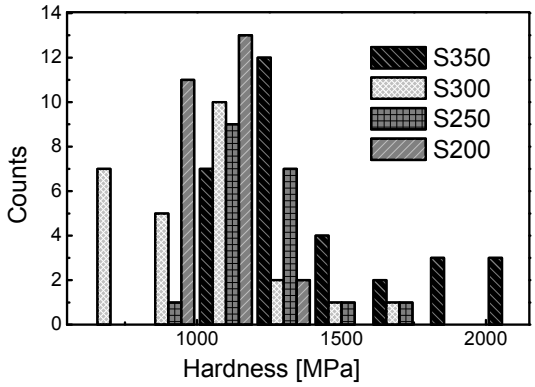

Fig. 2. **Hardness frequency diagrams for samples annealed at 200, 250, 300 and 350 °C.** The testing load was 5 mN

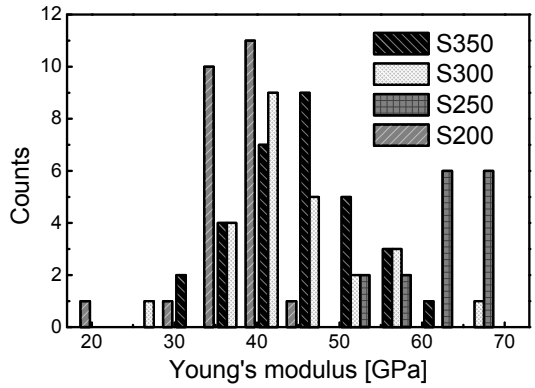

Fig. 3. **Young's modulus frequency diagrams for samples annealed at 200, 250, 300 and 350 °C.** The results were obtained using the testing load of 5 mN

4. Summary

Model joints, i.e. sandwiches consisting of copper disks with Ag nanopowder interlayer annealed at various temperatures from 200 to 350 °C were studied in this work. The highest hardness values of sintered nanoAg were obtained in case of sandwiches annealed at 350 °C. The highest values of the Young's modulus were achieved after annealing at 250 °C, indicating the lowest porosity of the sintered layer.

The financial support was provided by the Czech Science Foundation (Project 106/09/0700).

REFERENCES

1. Youn J. I., Ha W., Kim Y.: J. Adv. Mater. Res. *15-17*, 995 (2007).
2. Pawlow P.: Z. Phys. Chem. *65*, 545 (1909).
3. Buffat P., Borel J.-P.: Phys. Rev. A *13*, 2287 (1976).
4. Buršík J. Sopoušek J., Zálešák J., Buršíková V.: In: *Proceedings of NANOCON 2010*, on CD-ROM, Ostrava, TANGER, 2010.
5. Johnson K. L.: J. Mech. Phys. Solids *18*, 115 (1970).
6. Hall E. O.: Proc. Phys. Soc. B *64*, 747 (1951).
7. Buršík J., Sopoušek J., Buršíková V., Zálešák J.: In: *Proceedings of NANOCON 2009*, on CD-ROM, Ostrava, TANGER, 2009.

J. Buršík[a], J. Sopoušek[b], V. Buršíková[c], A. Stýskalík[b], and D. Škoda[b] *([a] Institute of Physics of Materials, ASCR, Brno, [b] Department of Chemistry, Faculty of Science, Masaryk University, [c] CEPLANT, DPE, Faculty of Science, Masaryk University, Brno, Czech Republic):* **Characterization of Sintered Ag Nanopowder Joints Using Nanoindentation Tests**

Sandwiches consisting of copper disks with Ag nanopowder interlayer annealed at various temperatures from 200 to 350 °C were studied. The main emphasis was placed on the characterization of quality of the sintered Ag layers by means of nanoindentation experiments. The highest hardness values were obtained after annealing at 350 °C. The highest values of the Young's modulus were achieved after annealing at 250 °C, indicating the lowest porosity of the sintered layer.

MECHANICAL PROPERTIES OF ALUMINOSILICATE SYSTEMS BASED ON ALKALI ACTIVATION OF INDUSTRIAL BY-PRODUCTS

LUKÁŠ BUZEK*, JAROMÍR WASSERBAUER, MARTIN ZMRZLÝ, and FRANTIŠEK ŠOUKAL

Brno University of Technology, Faculty of Chemistry, Centre for Materials Research CZ.1.05/2.1.00/01.0012, Purkyňova 464/118, Brno, CZ-61200, Czech Republic
xcbuzek@fch.vutbr.cz

Keywords: geopolymer, carbonation, strength

1. Introduction

The chemical stability of geopolymer binder such as attacked by sulphates, seawater, chlorides, acid media, frost-thaw cycles, high temperatures, and so on was proved. Another important consideration in connection with concrete durability is carbonation[1].

The aim of the present research is to study the carbonation of fly ash/slag binders and explain the influence of quality used raw materials on the mechanical properties.

2. Experimental

Low calcium fly ash (LCFA) obtained from Czech power plant and finely blast furnace slag (BFS) were used as the base materials. Alkali activators used in this study were potassium hydroxide in flake form dissolved in water to form 16M water solution and potassium water glass (K_2O=8.2 %, SiO_2=19.8 % and water=72.0 %). Both of the solutions were mixed together and then poured into a solid fly ash/slag mixture. Time of the mixing takes 3 minutes. Material was elaborated into steel molds of 2×2×10 cm. Specimens were cured in molds at laboratory temperature for 24 hours.

The carbonated depths were observed by light optical microscope Olympus BX 50 in the polarized reflected light. Mechanical properties were carried out by means of compressive strength tester DESTTEST 3310. Morphological observations and elemental compositions of samples were obtained using a Zeiss Ultra Plus 55 Scanning Electron Microscope (SEM) equipped with an energy dispersive analyzer (EDX).

3. Results and discussion

It is well known that the main hydration product of alkali activated fly ash/slag systems is C–S–H gel with a low C/S~1 ratio containing alkaline and aluminate ions in the structure. The carbonation of C–S–H can be expressed as follows:

$$C–S–H + CO_3^{2-} \rightarrow CaCO_3 + xSiO_2 \cdot nH_2O + 2OH^-$$

On the other hand fully hydrated Portland cement pastes, consist roughly of 70 % C–S–H with a high C/S ratio, 20 % $Ca(OH)_2$, 7 % AFt and 3 % AFm. The carbonation of $Ca(OH)_2$ describe this chemical reaction[2]:

$$Ca(OH)_2 + CO_3^{2-} \rightarrow CaCO_3 + 2OH^-$$

In the atmosphere containing 20 % CO_2 at 70 % relative humidity, carbonate precipitation is much more intense in Portland cement paste contains a higher Ca content susceptible to interaction with H_2CO_3. Carbonation takes place in both the portlandite and in the C–S–H gel. The $CaCO_3$ precipitated in the pores prevents or hinders the passage of CO_2 into deeper layers of the mortar. Whereas in alkali activated fly ash/slag pastes, carbonation occurs directly in the C–S–H gel, which means a deterioration of mechanical properties[3].

3.1. Light optical microscope (LOM)

Light optical microscope was used for observation of fly ash/slag geopolymer binders with different kinds of BFS. The first sample was prepared from fresh blast furnace slag and cured in the lab conditions for 28 days. The fracture area showed on the outer edge of the specimen 1 mm deep carbonated front. However the second samples with the same composition and curing conditions, but using of BFS stored 1 year in the plastic drums showed fully carbonated fracture area.

3.2. Mechanical properties

Compressive strength evolutions of the pastes are shown in Fig. 1. Samples prepared from different kinds of slags (black plots – fresh BFS, grey plots – 1 year old BFS) exhibit very similar strength evolution until 7 days. However after 28 days, the compressive strength of the samples with the old slag is lower and the results of flexural failure test surprisingly show the decrease of strength.

3.3. Scanning electron microscopy (SEM)

The process of carbonation of fly ash/slag geopolymer binders was examined in SEM. The image in secondary electrons mode, Fig. 2, shows fracture area of sample composed of 1 year old BFS. EDX analysis of the binder C–S–H phase (place 1) indicate very small C/S ratio. The unreacted parti-

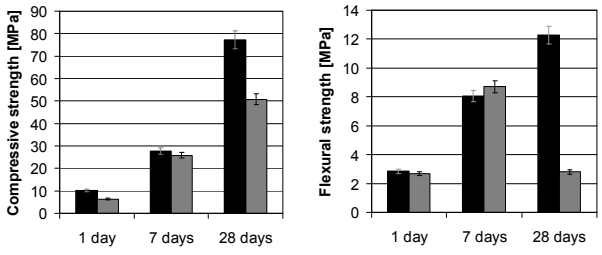

Fig. 1. **Compressive (left) and flexural (right) strength development of alkali activated LCFA/BFS**

cles of fly ashes (place 3) and slags (place 4) are still well incorporated into the geopolymer matrix.

On the surface were observed whitish particles with a very high K content, whose chemical composition corresponded to K_2CO_3 (place 2).

According to the theoretical structure of geopolymer materials[4], the alkaline ions are presented in solvated form and for that reason the bond in the structure is weak. This fact explains the tendency of alkali activated systems to the formation of efflorescences. Potassium alkaline activator does not give rise to visible hydrates in comparison with Na-activator which created visible $Na_2CO_3 \cdot nH_2O$.

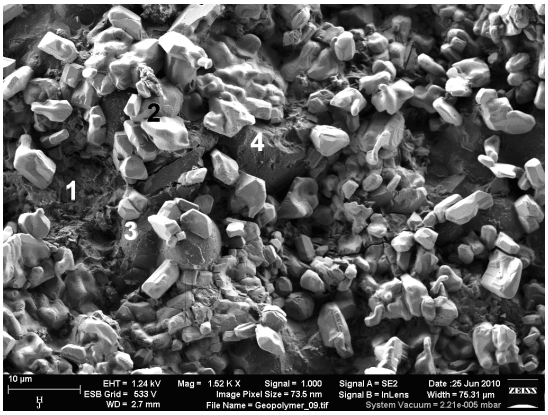

Fig. 2. **Morphology of carbonated fracture area**

The binder phases (C–S–H gel) in geopolymers with various quality of BFS are different. When fresh BFS is used as raw material, there is a greater deal of binder phase with higher C/S ratio. The higher Ca content in the CSH gel may generate greater amounts of $CaCO_3$ during carbonation, and this product might precipitate into and cover the pores of the mortar as well as case of hydrated OPC. When the base material is the 1 year old BFS, the main binder phase is amorphous decalcified CSH gel with very low C/S caused binder softening and some deterioration of strength was observed.

4. Conclusion

Characterization of microstructure and the differentiation of various rising phases in the edge and interior of the geopolymer provide a good basis for local mechanical properties measurements. Once we described the microstructure, we can continue with micro-hardness and nanoindentation testing. So the next step of our research will be characterization of strength of interfaces between structure phases and characterization of the carbonation depth relative to the bulk geopolymer paste matrix and also provide one means of estimating the width of the carbonation.

Geopolymer binder properties depend on the nature of the blast furnace slag. LCFA/BFS-based geopolymer has an excellent potential for its application in building industry, but it is necessary to control chemical properties of raw materials.

This work was supported by the project "Centre for Materials Research at FCH BUT" No. CZ.1.05/2.1.00/01.0012 from ERDF.

REFERENCES

1. Puertas F., Palacios M., Vázquez T.: J. Mater. Sci. *41*, 3071 (2006).
2. Shi C., Krivenko P.V., Roy D., v knize: *Alkali-Activates Cements and Concretes*, kap. 7, s. 208. Taylor & Francis, Abingdon 2006.
3. Palacios M., Puertas F.: J. Am. Ceram. Soc. *89*, 3211 (2006).
4. Barbosa V. F. F., Mackenzie K. J. D., Thaumaturgo C.: Int. J. Inorg. Mater. *2*, 309 (2000).

L. Buzek, J. Wasserbauer, M. Zmrzlý, and F. Šoukal *(Centre for Materials Research, Brno University of Technology, Faculty of Chemistry, Brno, Czech Republic):* **Mechanical Properties of Aluminosilicate Systems Based on Alkali Activation of Industrial By-Products**

This paper deals which mechanical properties in relation to structure of heterogeneous material (geopolymer). The testing material was inorganic aluminosilicate polymer, called geopolymer, synthesized from the alkali activation of fly ash/slag mixtures. Effect of quality used raw materials that influence the compressive and flexural strength of hardened geopolymer was discussed. The study of the microstructure was based on LOM and SEM-EDX analyses.

INSTRUMENTED INDENTATION OF Al_2O_3-SiC NANOCOMPOSITES

ERIKA CSEHOVÁ[a]*, JÁN DUSZA[a], APICHART LIMPICHAIPANIT[b], and RICHARD TODD[b]

[a] *Institute of Materials Research, Slovak Academy of Sciences, Watsonova 47, 043 53 Košice, Slovak Republic,* [b] *Department of Materials, University of Oxford, Oxford, United Kingdom; ecsehova@imr.saske.sk*

Keywords: Al_2O_3-SiC, ISE, micro/nano-hardness

1. Introduction

It is well known that the apparent hardness of a solid usually depends on the applied test load. This phenomenon, known as the indentation size effect (ISE), involves a decrease in the measured apparent hardness with increasing applied test load, i.e., with increasing indentation size. The works focused mainly on the analyses of the micro- or macro-hardness data and little effort has been devoted to examine the applicability of these equations to the nanoindentation data obtained using instrumental indentation test[1].

The instrumental hardness, "*H*" is defined as the ratio of the peak load, P_{max}, to the project area of the indentation impression, A_c,

$$H = \frac{P_{max}}{A_c} = \frac{P_{max}}{24.5 h_c^2} \quad (1)$$

where h_c is the contact depth most often determined by Oliver and Pharr method[2].

The most widely used empirical equation for describing the ISE is the Meyer's law, in the form:

$$P_{max} = A h_c^n \quad (2)$$

where A and n are constants that can be derived directly from curve fitting of the experimental data in the relationship $ln\ h_c$ vs. $ln\ P_{max}$. If $n < 2$ there is an ISE on hardness and when $n = 2$, the hardness is independent of the applied load.

According to Hays and Kendall[3] there exists a minimum level of the applied test load, W, named the test-specimen resistance, below which permanent deformation due to indentation does not initiate, and only elastic deformation occurs. They introduced an effective indentation load, $P_{eff} = P_{max} - W$, and proposed the relationship;

$$P_{max} - W = A_1 h_c^2 \quad (3)$$

where W and A_1 are constants independent of the test load for a given material.

Li and Bradt in their PSR (proportional specimen resistance) model[4] suggested that the test-specimen resistance, W, during indentation is not a constant, as was proposed by Hays and Kendall, but increase linearly with the indentation size and is directly proportional to it according to the relationship;

$$W = a_1 h_c \quad (4)$$

and the effective indentation load and the indentation dimension are therefore related as follows:

$$P_{eff} = P_{max} - W = P_{max} - a_1 h_c = a_2 h_c^2 \quad (5)$$

where the parameters a_1 and a_2 can be related to the elastic and the plastic properties of the test material. The term a_2 in the linear fits describes the load independent hardness, so called „true hardness", H_0.

The coefficients of the proportional specimen resistance (PSR) a_1 and a_2, can be evaluated through the linear regression of "P_{max}/h_c" versus "h_c",

$$\frac{P_{max}}{h_c} = a_1 + a_2 h_c \quad (6)$$

For the nanoindentation test with a Berkovich indenter, H_0 can be calculated:

$$H_0 = \left(P_{max} - a_1 h_c\right)/(24.5 h_c^2)\Big) \quad (7)$$

Gong et al.[5] suggested a modified PSR model based on the consideration of the effect of the machining-induced residual stresses at the surface during the indentation in the form

$$P_{max} = a_0 + a_1 h_c + a_2 h_c^2 \quad (8)$$

where a_0 is a constant related to the surface residual stresses associated with the surface machining and polishing and a_1 and a_2 are the same parameters as in the PSR model. Similarly, the parameters of the modified PSR were obtained by conventional polynomial regression of the plot P vs. d and H_0-values were calculated according to the equation:

$$H_0 = \left(P_{max} - a_0 - a_1 h_c\right)/(24.5 h_c^2)\Big) \quad (9)$$

The aim of the present work is to investigate the load dependence of the measured instrumental Berkovich hardness of Al_2O_3-SiC composites, to examine the ISE using different models and to compare this to the ISE observed during conventional Vickers hardness test.

2. Experimental procedure

The materials used in this investigation were alumina (A) and Al_2O_3-SiC composites with the addition of 5 vol.% (A5)

Table I
Best-fit results of the parameters

Meyer´s Law Eq. (*2*)		Hays-Kendall approach Eq. (*3*)		PSR model Eq. (*6*) and Eq. (*7*)			Modified PSR model Eq. (*8*) and Eq. (*9*)			
	n	*W* (mN)	A_1 (mN/nm^2)	a_1 (mN/nm)	a_2 (mN/nm^2)	HV_0 (GPa)	a_0 (mN)	a_1 (mN/nm)	a_2 (mN/nm^2)	HV_0 (GPa)
A	1.62	3.03	3.53×10^{-4}	0.0764	3.02×10^{-4}	10.7 ±5.7	-8. 37	0.149	2.23×10^{-4}	9.75 ±3.8
A5	1.70	8.84	5.82×10^{-4}	0.0615	5.23×10^{-4}	20.7 ±3.0	-7.39	0.129	4.41×10^{-4}	20.79 ±9.1
A10	1.68	17.38	6.31×10^{-4}	0.0582	5.74×10^{-4}	21.3 ±2.1	-5.61	0.108	5.09×10^{-4}	24.19 ±9.9

and 10 vol.% (A10) SiC, processed at the University of Oxford, United Kingdom[6].

The CMC^{TM} (Continuous Multi Cycle) method was applied using Nano Hardness Tester (CSM-Instruments SA) with Berkovich diamond indenter. In each test run, the indenter was driven into the specimen surface under a peak load gradually increased from 5 mN to 400 mN, unloaded gradually to 10 % of the peak load after being held at peak load for 10 s, and then driven again into the specimen surface to a higher value of the peak load. At least 15 test runs were recorded on each sample.

3. Results and discussion

The results of the hardness measurement and of the applied ISE models are illustrated in Fig. 1 and in Table I. The hardness decreased with increasing peak load and exhibited a typical indentation size effect which was most evident for alumina ($n = 1.62$). The behaviour of the composites is very similar, ($n = 1.68$ and $n = 1.70$). These results are in good agreement with the results of conventional Vickers hardness tests (from 1 N to 49.05 N), performed on the same materials, according to which the most significant ISE is in alumina ($n = 1.83$) and in the composites the ISE is less pronounced ($n = 1.92$ and $n = 1.93$) (ref.[7]).

By comparing these results it is visible that the ISE is more pronounced during the instrumental test in the lower interval of applied loads. As regards the indentation module, for alumina the values decrease with increasing load from approximately 300 GPa to 100 GPa and for composites from 500 GPa to 300 GPa. The ISE of various types of ceramics has recently been investigated using nanoindentation data measured in the peak-load range from 7.5 to 500 mN by Peng et al.[1]. Our results show good agreement with their results in the case of Hays - Kendall model, however the values obtained for *W* are too high, mainly for the composite with 10 vol.% of SiC. According to the results, both the PSR and modified PSR models underestimate the true hardness for alumina and overestimate the true hardness for composites. For ceramics investigated in the present work the PSR model applied for conventional Vickers hardness data results in the best estimation of true hardness values[7].

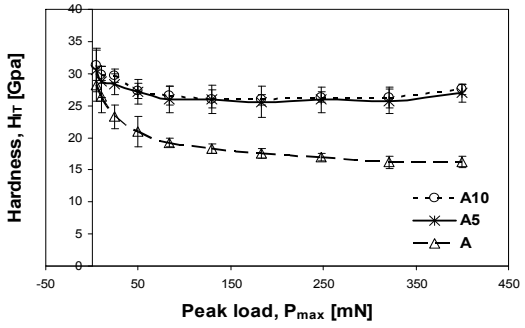

Fig. 1. **Influence of P_{max} on hardness**

4. Conclusions

The load-dependence of the nano/micro instrumental Berkovich hardness of alumina and Al_2O_3-SiC composites has been investigated. Similar ISE was found as in the case of conventional Vickers hardness test for all systems. The Hays - Kendall approach results in high *W* values and the PSR and modified PSR models in low true hardness for alumina and high true hardness for composites.

This work was supported by APVV LPP 0174-07, VEGA 2/0088/08 and MNT-ERA.NET HANCOC.

REFERENCES

1. Peng Z., Gong J., Miao H.: J. Eur. Ceram. Soc. *24*, 2193 (2004).
2. Oliver W. C., Pharr G. M.: J. Mater. Res. *7*, 1564 (1992).
3. Hays C., Kendall E. G.: Metall. *6*, 275 (1973).
4. Li H., Bradt R. C.: J. Mater. Sci. *28*, 917 (1993).
5. Gong J., Wu J., Guan Z.: J. Eur. Ceram. Soc. *19*, 2625 (1999).
6. Limpichaipanit A., Todd R. I.: J. Eur. Ceram. Soc. *29*, 2841 (2009).
7. Csehova E., Dusza J., Limpichaipanit A., Todd R., Metallic materials, in press.

E. Csehová[a]*, J. Dusza[a], A. Limpichaipanit[b], and R. Todd[b] *([a] IMR, SAS, Košice, Slovak Republic, [b] Department of Materials, Oxford, United Kingdom):* **Instrumented Indentation of Al_2O_3-SiC Nanocomposites**

The load dependence of instrumental Berkovich hardness has been investigated and the indentation size effect has been analyzed during the hardness test of alumina and Al_2O_3-SiC nanocomposites in the load range from 5 mN to 400 mN. As regards the load dependence of hardness the results are in agreement with the results of conventional Vickers hardness test.

INDENTATION SIZE EFFECT IN BASAL AND PRISMATIC PLANES OF Si_3N_4 CRYSTALS

ERIKA CSEHOVÁ[a]*, ANNAMÁRIA DUSZOVÁ[a], PAVOL HVIZDOŠ[a], FRANTIŠEK LOFAJ[a], JÁN DUSZA[a], and PAVOL ŠAJGALÍK[b]

[a] *Institute of Materials Research, Slovak Academy of Sciences, Watsonova 47, 040 01 Košice;* [b] *Institute of Inorganic Chemistry, Slovak Academy of Sciences, Bratislava, Slovak Republic*
ecsehova@imr.saske.sk

Keywords: Si_3N_4 grains, CMC Indentation Test

1. Introduction

Hardness is one of the most important selection criteria for structural ceramics for engineering applications. However, hardness and microhardness of ceramics including Si_3N_4 vary widely, depending on the densification method, porosity, chemical composition, crystallographic orientation, etc. In addition in many cases an indentation size effect (ISE) has been found: the measured hardness increases with decreasing indentation load. Although relatively much effort has been devoted to understanding the hardness of polycrystalline Si_3N_4 based ceramics, the number of investigations of the microhardness of α- and β-Si_3N_4 single crystals is significantly lower and only little attention has been paid to the hardness of individual grains in sintered polycrystalline Si_3N_4 (ref.[1,2]).

The aim of the present contribution is to study the influence of the grain orientation and indentation load on the Berkovich indentation hardness and modulus of individual grains of a Si_3N_4 poly-crystal in a load range from 10 to 70 mN.

2. Experimental procedure

Si_3N_4 ceramics with Y_2O_3 as sintering additive was prepared by hot pressing at IACH SAS Bratislava[3].

The hardness measurements were performed using Nano Hardness Tester (CSM-Instruments SA) with Berkovich diamond indenter (α = 65.3 ± 0.3°). The indentation hardness and modulus, H_{IT}, E_{IT} were obtained by standard method in a load range from 10 mN to 70 mN. For a particular load at least five indentation tests were recorded on each grain. Large Si_3N_4 grains with the basal plane (0001) parallel to the sample surface, or with prismatic planes [e.g. (1010), (1120)] parallel to the sample surface, were selected for the indentation, Fig. 1. The hardness and ISE was evaluated according to the procedure described in (ref.[4]). Beside the stepwise loading regime single indentations have been realized, too, Fig. 2.

3. Results and discussion

The material has a bimodal grain size distribution, with large grains up to 10 μm in diameter and small ones < 1 μm in diameter.

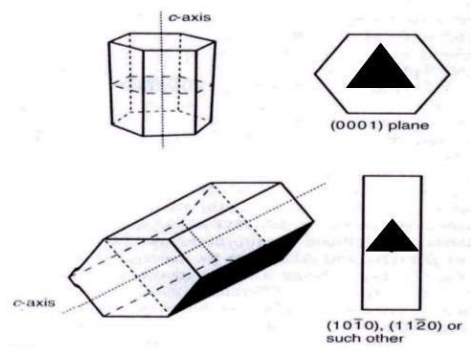

Fig. 1. **Schematic illustration of the planes used for Berkovich indentation**

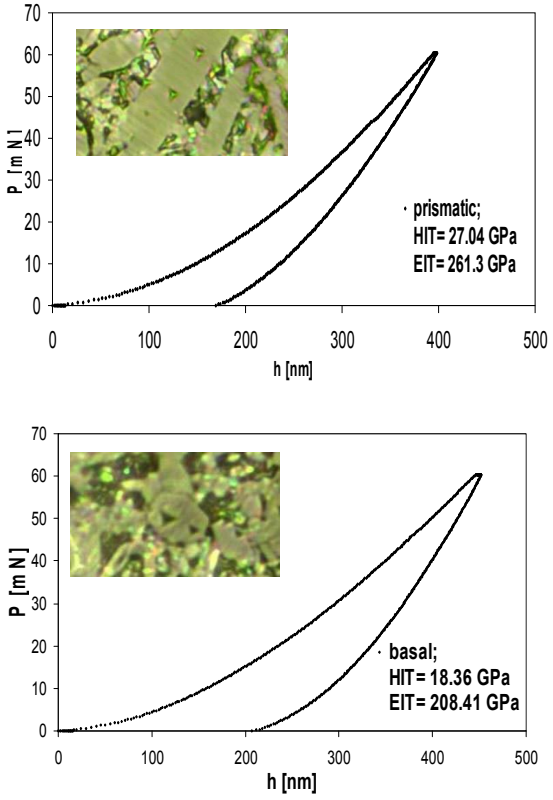

Fig. 2. **Load-displacement curves under a peak load of 60 mN at indentation of prismatic and basal planes**

The results of the indentation hardness H_{IT} measurements are summarized in Fig. 3. Similarly, as in the case of conventional Vickers test[1] there exist a significant difference in the instrumental indentation hardness measured on the basal and prismatic planes. The hardness on both planes increases with decreasing load, however this dependence is more pronounced at prismatic planes (n = 1.64 and n = 1.8).

Similar behavior was found for indentation modulus E_{IT} according to Oliver and Pharr method (see Fig. 4), which also decreases with increasing loads for both planes. The indentation modulus measured at prismatic planes is also higher than the modulus of basal planes, however the difference is significantly lower than in the case of indentation hardness.

Previous studies tried to relate the Meyer's index, n, to the microstructure parameters. Babini et al.[5] in the study on the Vickers hardness behaviour of hot-pressed Si_3N_4-based ceramics found that the n value increases as grain size increases. Applying the Proportional specimen resistance[4] (PSR) model to the experimental results describe the load independent, so called „true hardness", which was found for Si_3N_4 prismatic and basal planes, 15.3 ± 5.5 GPa and 13.75 ± 3.5 GPa, respectively. In this model, the test-specimen resistance to permanent deformation is assumed not to be a constant, but increase linearly with the indentation size. It seems that this model slightly underestimates the hardness at both planes of silicon nitride. Traditional Vickers hardness as a function of the indentation load and of grain orientation was studied in individual grains of a gas pressure sintered[6] (GPS) polycrystalline silicon nitride using indentation loads in the range from 1 to 50 g. The indentation load size effect (ISE) was more evident in the prismatic planes of the grains which is in good agreement with our results. Similarly we confirmed that the threshold load for indent formation is below 5 mN for both basal and prismatic planes of Si_3N_4 grains. As regards the indentation modulus, our results are different comparing to the results of Hay et al.[7] who found significantly higher indentation modulus for the basal planes of β-silicon nitride grains than for the prismatic planes.

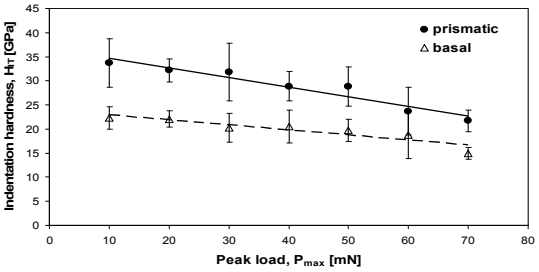

Fig. 3. **Indentation hardness vs. the peak load at basal and prismatic planes**

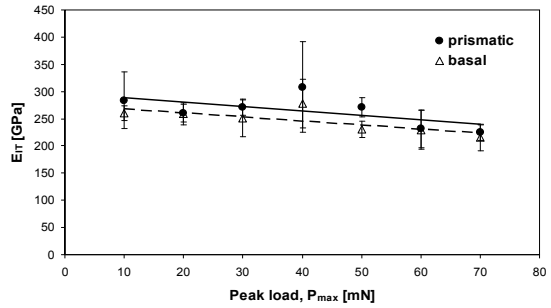

Fig. 4. **Indentation modulus versus the peak load**

4. Conclusions

A distinct indentation size effect was found for the indentation hardness in individual silicon nitride grains of a polycrystalline silicon nitride. This effect was slightly more pronounced for prismatic planes (n = 1.64) of the grains compared to the basal planes (n = 1.8). The indentation modulus decreases with the increasing indentation load.

This work was partly supported by APVV LPP 0174-07, APVV-0034-07, VEGA 2/0088/08 and MNT-ERA.NET HANCOC.

REFERENCES

1. Dusza J., Eschner T., Rundgren K.: J. Mater. Sci. Lett. *16*, 664 (1997).
2. Lofaj F., Rundgren K., Okada A., Kawamoto H.: Prakt. Metallogr. *30*, 515 (1999).
3. Hnatko M., Lojanová Š., et al.: Int. J. Mater. Res. *97/6*, 772 (2006).
4. Peng Z., Gong J., Miao H.: J. Eur. Ceram. Soc. *24*, 2193 (2004).
5. Babini G. N., Bellosi A., Galassi C.: J. Mater. Sci. *22*, 1687 (1987).
6. Dusza J., Steen M.: J. Am. Ceram. Soc. *81*, 3022 (1998).
7. Hay J., Sun E., Pharr G., Becher P., Alexander K.: J. Am. Ceram. Soc. *81*, 2661 (1998).

E. Csehová[a]*, A. Duszová[a], P. Hvizdoš[a], , F. Lofaj[a], J. Dusza[a], and P. Šajgalík[b] *([a] IMR, SAS, Košice, [b] IICH, SAS, Bratislava, Slovak Republic):* **Load-Size Effect in Basel and Prismatic Planes of Si_3N_4 Crystals**

The influence of the grain orientation and indentation load on the indentation Berkovich hardness in individual grains of a Si_3N_4 polycrystal has been investigated. A distinct indentation size effect was found with n = 1.64 for prismatic planes and n = 1.8 for basal planes. The indentation modulus is slightly higher at prismatic planes in comparison to the basal planes.

EFFECT OF SOFT DRINKS ON ENAMEL MECHANICAL PROPERTIES

RADIM ČTVRTLÍK*[a], JULIA MOROZOVA[b], ZDEŇKA ZAPLETALOVÁ[b], and VÁCLAV RANC[c]

[a] *Regional Centre of Advanced Technologies and Materials, Joint Laboratory of Optics of Palacky University and Institute of Physics of Academy of Science of the Czech Republic, Faculty of Science, Palacky University, 17. listopadu 12, 771 46 Olomouc, Czech Republic,* [b] *Clinic of Dentistry, Palacký University, Palackého 2, 772 00, Olomouc,* [c] *Department of Analytical Chemistry, Palacký University, 17. listopadu 12, 771 46 Olomouc, Czech Republic*
ctvrtlik@fzu.cz

Keywords: enamel, dental erosion, nanoindentation, hardness, elastic modulus

1. Introduction

During the last 20 years we can observe a substantial increase of different soft drinks and fruit juices' consumption. According to Lussi[1] the consumption of these beverages in Europe is more than 50 % of total nonalcoholic drinks consumption. The majority of these beverages contain citric, phosphoric, carbonic acids. Their pH is usually lower than 4.0.

Frequent consumption of acid beverages may lead to dental erosions[2]. Erosive potential of these drinks depends on the low pH level as well on buffer capacity – as the amount of alkaline, which is necessary for drink's acids neutralization. The remaining components of food and beverages such as calcium, phosphate and fluoride may further reduce their erosive potential.

Our work is aimed to determine both soft drinks and fruit juices influence on the physical properties of dental enamel. The original Czech soft drink Kofola, Coca Cola and an orange juice were chosen for testing. In addition the influence of yoghurt on the dental surface was also investigated.

2. Experimental details

40 enamel samples (5×3×1.5 mm) were prepared from buccal and oral intact surfaces of freshly extracted human molars using a micromotor and a diamond disc with copious water cooling. After extraction the teeth were disinfected in 0.5 % solution of chloramin T. Buccal as well as oral surfaces of the teeth were polished with Opti Disc Polishing Discs (KerrHawe, Switzerland) from Medium up to Extra Fine. Prepared specimens were retained in the mineral solution of this content: 1.5 mmol l^{-1} $CaCl_2$, 1.0 mmol l^{-1} KH_2PO_4, 50 mmol l^{-1} NaCl at temperature 4 °C. The enamel samples were randomly assigned to 4 groups ($n = 10$). Each of the groups was initially used as baseline. After that the samples of all the groups were immersed to 4 different solutions. The first group samples were immersed into the original Czech soft drink Kofola (Kofola, a.s., Krnov, Czech Republic), second group into Coca Cola (Coca-Cola HBC Czech Republic, s.r.o.), third group of samples into orange juice (Hello, Nivnice, Czech Republic) and fourth group of samples into natural yoghurt (Olma, Czech Republic).

The values of pH and buffer capacity were determined using pH meter InoLab pH 730 (InoLab, Germany). The determination of buffer capacity was based on a standard addition of basic solution of ammonium hydroxide, $c = 0.2$ mol l^{-1}. From the change of pH, buffer capacity was determined.

The determination of total calcium level in yoghurt was based on a volumetric method. As a chelation agent, the solution of ethylendiaminetetraacetic acid (EDTA) was used at the concentration of 0.2 mol l^{-1}. Exactly 0.5 g of respective yoghurt was added to 10 ml of water and sonificated 5 minutes at 25 °C. Suspension was then filtrated and calcium was determined using Murexid as indicator.

The nanoindentation experiments were performed using NanoTest NT600 instrument[3] equipped with Berkovich indenter using the indentation load of 10 mN with loading/unloading rate of 0.5 mN s^{-1}. Six indentations per test were performed on each specimen with spacing of 30 μm. The hardness and reduced elastic modulus were determined from indentations curves according to the analysis developed by Oliver and Pharr[4]. The average values of hardness and reduced elastic modulus were calculated at least from 4 independent measurements.

Nanoindentation measurements were performed on each specimen before (base-line) and after the treatment of investigated beverages and yoghurt. The specimens were immersed for 5 min. Subsequently they were rinsed with distilled water for 10 s and immediately dried by air. All of the beverages and yoghurt had room temperature. Optical microscopy was used in order to measure the same enamel area before and after the treatment.

3. Results

The average values of enamel nanoindentation hardness and effective elastic modulus are depicted in Fig. 1 and Fig. 2. The white/gray bars represent mechanical properties before/after 5 min exposure of different beverages and yoghurt. It is apparent that enamel hardness and modulus decrease after exposure to investigated soft drinks and orange juice. The most significant reduction of hardness was observed for Coca-Cola 43.6 ± 14.4 % and orange juice 41.7 ± 3.4 %. Kofola leads to the hardness decrease of 33.4 ± 5.1 %, whereas yoghurt effect is not significant. In spite of the yoghurt's pH is 4.40, it does not erode the dental surface. The yoghurt improves hard dental tissues because it contains calcium and phosphate, which are the common components of hard dental tissues.

The values of pH and buffer capacity are summarized in Tab. I. The content of calcium in the yoghurt was approx. 50 mg/100 g.

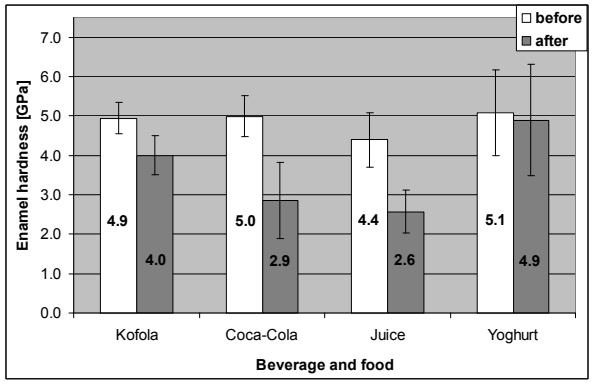

Fig. 1. **Enamel nanoindentation hardness before and after 5 min exposure to different beverages and yoghurt**

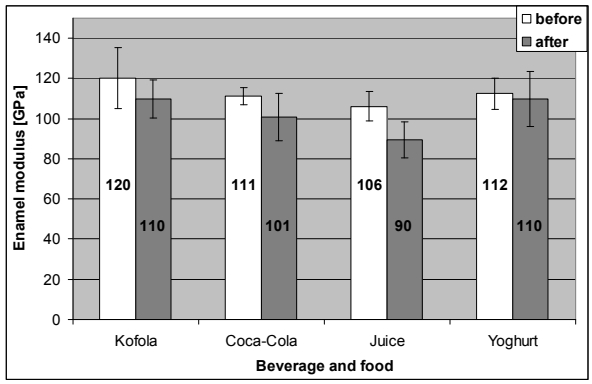

Fig. 2. **Enamel effective elastic modulus before and after 5 min exposure to different beverages and yoghurt**

Table I
Summary of pH and buffer capacity of different beverages and yoghurt

Beverage/food	pH [−]	Buffer capacity 10^{-3} [−]
Kofola	2.65	1.52
Coca-Cola	2.60	1.58
Orange juice	3.74	5.26
Yoghurt	4.40	2.02

5. Conclusion

Acidic foodstuffs and beverages are considered as risk factors in the dietary erosions of teeth. Our results show that hardness of human enamel was significantly decreased after 5 min exposure to acid beverages (Kofola, Coca-Cola, orange juice). The most significant reduction of hardness was observed for Coca-Cola 43.6 ± 14.4 % and orange juice 41.7 ± 3.4 %. Acidic food as yoghurt did not erode the enamel, because of its mineral content (calcium and phosphate).

The authors gratefully acknowledge the support by the Operational Program Research and Development for Innovations - European Regional Development Fund (project CZ.1.05/2.1.00/03.0058 of the Ministry of Education, Youth and Sports of the Czech Republic).This work was also supported by the Academy of Sciences of the Czech Republic, research project No. KAN301370701, project 1M06002 of Ministry of Education, Youth and Sports of the Czech Republic.

REFERENCES

1. Lussi A.: *Dental Erosion from Diagnosis to Therapy.* Karger, Basel 2006.
2. Wongkhantee S., Patanapiradej V., Maneenut C., Tantbirojn D.: J. Dent. *34*, 214 (2006).
3. Čtvrtlík R., Stranyánek M., Boháč P., Jastrabík L.: Mater. Struct. *13*, 90 (2006).
4. Oliver W. C., Pharr G. M.: J. Mater. Res. *7*, 1564 (1992).

R. Čtvrtlík[a], J. Morozova[b], Z. Zapletalová[b], and V. Ranc[c] *([a] Regional Centre of Advanced Technologies and Materials, Joint Laboratory of Optics of Palacky University and Institute of Physics of Academy of Science of the Czech Republic, Faculty of Science, Palacky University, Olomouc, Czech Republic, [b] Clinic of Dentistry, Palacký University, [c] Department of Analytical Chemistry, Palacký University, Czech Republic):* **Effect of Soft Drinks on Enamel Mechanical Properties**

The tooth enamel is exposed to various mechanical and chemical factors. In this respect, the dental erosion connected with dietary factors is of considerable importance. The aim of this in vitro study is to investigate the effect of specific soft drinks (Kofola, Coca-Cola), orange juice and yoghurt on mechanical properties of human molar enamel. Hardness and reduced elastic modulus were measured using nanoindentation technique. It was found out that the exposure of enamel to soft drinks leads to degradation of mechanical properties. Short time (5 min) exposure to Coca-Cola resulted in 43.6 ± 14.4 % degradation of enamel strength. Acidic food as yoghurt did not erode the enamel, because of its mineral content (calcium and phosphate).

CYCLIC DEFORMATION RESPONSE OF AZ31 MAGNESIUM ALLOY AFTER CORROSION DEGRADATION

PAVEL DOLEŽAL*, JOSEF ZAPLETAL, MIROSLAVA HORYNOVÁ, PAVEL GEJDOŠ, and LADISLAV ČELKO

Brno University of Technology, Technická 2, Brno, Czech Republic
dolezal@fme.vutbr.cz

Keywords: alloy AZ31, corrosion attack, fatigue crack initiation, cyclic deformation response

1. Introduction

Advantages of magnesium alloys are high specific strength and specific stiffness, but major problem limiting their use in structural applications is the high corrosion susceptibility[1,2]. Studies concerning effect of corrosion on the mechanical behaviour are limited and they are mostly focused on corrosion fatigue. Experiments considering mechanical loading of component with prior corrosion damage are also important. They simulate situation, when components are put into operation after corrosion exposures (e. g during their processing or shipping). Local corrosion attack act as stress concentrator, facilitates defect initiation and reduces the lifetime of a component[3].

2. Experimental material

The experimental material used was magnesium alloy AZ31 (2.68 % Al, 1.1 % Zn, 0.35 % Mn, 0.01 % max. other - each), obtained by the method of squeeze casting. The basic mechanical properties established via tensile test are given in Table I.

From the results of a local analysis of chemical composition and from data in the literature[1,4] it follows that the structure of alloy AZ31 is formed by solid solution δ, intermediate phase γ ($Mg_{17}Al_{12}$), eutectic, and AlMn-based particles.

Table I
Tensile properties of AZ31 alloy

	E [GPa]	$R_{p0,2}$ [MPa]	R_m [MPa]	A [%]	Z [%]
AZ31	38.3	64.2	174	8.8	9.0

3. Corrosion degradation

Corrosion degradation of test specimens for fatigue testing and reference specimens for the determination of corrosion rate was carried out in a spray of neutral 5 % solution of sodium chloride.

The corrosion rate of flat reference specimens was established on the basis of mass losses as 0.12 mm/year. From the viewpoint of local corrosion attack it was established that the depth of corrosion attack in the reference specimens corresponded to 91 μm for an exposure time of 480 h, and 213 μm for an exposure time of 1000 h. The maximum depth of corrosion attack in the fatigue specimens was 257 μm for the 480 hour exposure and 864 μm for the 1000 hour exposure.

4. Cyclic deformation response

The fatigue behaviour of bare and pre-corroded (480 and 1000 hour exposure) magnesium alloy AZ31 in the stress amplitude control mode was determined on a servo-hydraulic testing system. Experiments were conducted in the range of proof stress amplitudes from 30 to 110 MPa at a constant frequency of 3 Hz, or 20 Hz for amplitudes lower than 65 MPa. The symmetrical sine cycle (R = –1) was used. The number of cycles to fracture, N_f, was determined on the basis of the criterion of the 5 % change of effective modulus E_{eff}.

Fractographic analysis of uncorroded fatigue specimens revealed that fatigue cracks initiated preferentially at inclusions. In the pre-corroded specimens, crack initiation and crack growth occurred at the area with maximum local corrosion attack (Fig. 1).

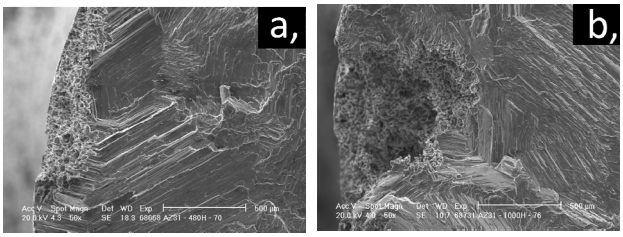

Fig. 1. **Fracture surface of pre-corroded fatigue specimens after a, 480 hrs exposure b, 1000 hrs exposure**

Experimental points of the cyclic deformation curve (Fig. 2) were fitted to exponential regression function (*1*) while equation (*2*) was used to establish the cyclic yield point $R_{p0.2}'$ (Table II). It follows from Fig. 2 that due to corrosion degradation the cyclic plasticity of the alloy under study was not affected and that the material hardened cyclically, which is also corroborated by the $R_m/R_{p0.2}$ ratio, which is greater than the value 1.4.

$$\sigma_a = K' \cdot \varepsilon_{ap}^{n'} \qquad (1)$$

$$R_{p0,2}' = K' \cdot 0{,}002^{n'} \qquad (2)$$

Table II
Parameters of cyclic deformation curve

K' [MPa]	n' [-]	$R_{p0,2}$' [MPa]
426.04	0.233	100.32

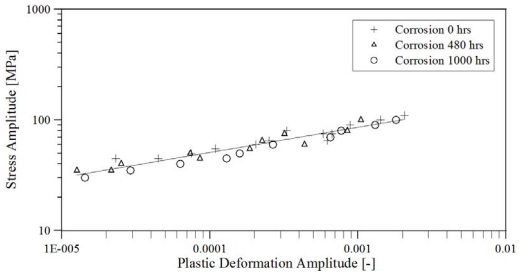

Fig. 2. **Cyclic deformation curve**

The Woehler-Basquin and the derived Manson-Coffin curves are shown in Fig. 3. Each dependence relation is fitted in standard way by means of regression analysis by an exponential curve (equations (*3*) and (*4*)) and the fatigue parameters established are given in Table III.

$$\sigma_a = \sigma_f' \cdot (2N_f)^b \qquad (3)$$

$$\varepsilon_{ap} = \varepsilon_f' \cdot (2N_f)^c \qquad (4)$$

Table III
Fatigue parameters

Corrosion [h]	σ_f' [MPa]	b [-]	ε_f' [-]	c [-]
0	410.52	-0.169	1.454	-0.787
480	411.92	-0.177	1.312	-0.813
1000	425.3	-0.197	0.696	-0.785

From the obtained dependence of stress amplitude and plastic deformation amplitude on the number of half-cycles to fracture it follows unambiguously that with increasing time of corrosion degradation the fatigue lifetime decreases. This effect is given by the local corrosion attack on the surface, which is responsible for the easier initiation of fatigue cracks with subsequent propagation of the leading crack. Fatigue crack initiation is more pronounced at lower loading-cycle levels.

Due to the larger local corrosion attack in the case of longer corrosion time the Woehler-Basquin curves get slightly steeper and the exponent of fatigue strength *b* increases. The major differences between the obtained fatigue strength σ_f and fatigue ductility ε_f may be due to the structural and chemical heterogeneity of the cast material.

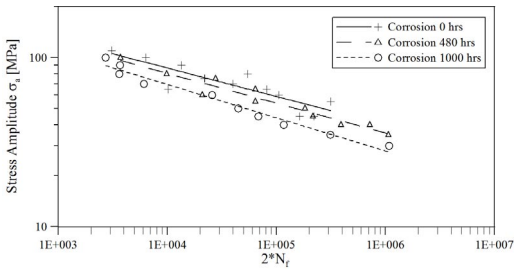

Fig. 3a. **Woehler-Basquin curves**

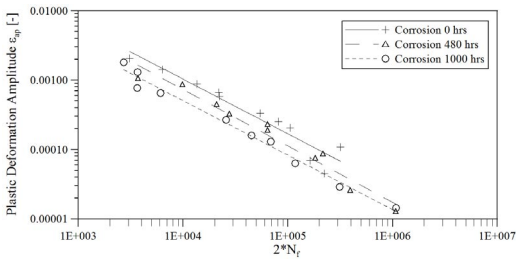

Fig. 3b. **Derived Manson-Coffin curves**

5. Conclusions

Cyclic deformation response was not affected by local corrosion attack.

It follows from the Basquin relation that the fatigue life curve steepness increases due to larger local corrosion attack. The steepness of the curves in Manson-Coffin's relation is not affected markedly by the corrosion exposure, while ε_f' decreases at the same time.

The fatigue limit for 10^5 cycles drops due to corrosion degradation from 52.1 MPa in as-cast state to 47.5 MPa after 480 hours and further down to 38.4 MPa after 1000 hours of corrosion.

Fatigue life decrease due to local corrosion attack resulting in notch effect related with local increasing of cyclic plastic deformation and reduction of crack initiation phase to smaller number of cycles.

Acknowledgments – Czech Science Foundation (grant GACR 101/09/P576), MSMT (project MEB 0810122 and MSM 1M0556), BUT (project FSI-J-10-38).

REFERENCES

1. Hasegawa S. et al.: Int. J. Fatigue *29*, 1839 (2007).
2. Ishihara S. et al: Mater. Sci. Eng., *A 468-470*, 214 (2007).
3. Chamos A. et al.: Mater. Design 9, *31*, 4130 (2010).
4. Zhang B., Zhang Z.: Transaction of Nonferous Metals 2, *20*, 439 (2010).

P. Doležal, J. Zapletal, M. Horynová, P. Gejdoš, and L. Čelko *(Brno University of Technology, Czech Republic):* **Cyclic Deformation Response of AZ31 Magnesium Alloy after Corrosion Degradation**

Cyclic deformation response and low fatigue behaviour of bare and pre-corroded magnesium alloy AZ31was studied under stress amplitude control. Pre-corroded specimens had been exposed to spray of 5 % solution of sodium chloride for 480 and 1000 hours.

Fatigue limit drops from 52.1 MPa to 47.5 MPa (480 hrs) and 38.4 MPa (1000 hrs). Fatigue life decrease due to corrosion damage is pronounced at low stress amplitudes, whereas the durability attained at higher amplitudes is practically the same.

MONITORING OF MATERIAL SURFACE POLISHING PROCEDURE USING CONFOCAL MICROSCOPE

MICHAELA DUDÍKOVÁ[a], DANIEL KYTÝŘ[b]*, TOMÁŠ DOKTOR[b], and ONDŘEJ JIROUŠEK[b]

[a] Czech Technical University in Prague, Klokner Institute, Šolínova 7, 166 08 Prague 6 – Dejvice, [b] Academy of Sciences of the Czech Republic, Institute of Theoretical and Applied Mechanics, Prosecká 76, 190 00 Prague 9, Czech Republic dudikova@klok.cvut.cz

Keywords: roughness reduction, sample preparation, confocal microscope, surface roughness criteria

1. Introduction

Results of microscopic material testing (e.g. nanoindentation) are highly influenced by the precision of sample preparation. This paper is focused on optimizing of the preparation of sample surface for nanoindentation. Two different types of material were considered in this study. First one, a representative of porous material trabecular bone was chosen. As representatives of compact materials samples of fibre composite and asbestos-free plates were used. Surface average roughness smaller than 50 nm is requested for successful nanoindantion for abovementioned three types of material. The change in surface roughness was monitored during the preparation process by confocal microscope. Effect of grain size, load and duration time of grinding on surface roughness was analyzed.

2. Materials and methods

Tested samples (6 specimena in a group for each material) were fixed by cold mounting. Using low shrinkage Epoxy-Cure (Buehler, Ltd., Düsseldorf, Germany) mounting compound with hardening time 6 h. TegraPol-11 (Struers, Ltd., Willich, Germany) grinding and polishing machine with maximal speed 120 rpm and maximal grinding head force 20 N was used for surface preparation. Diamond grinding discs with grain size 35 and 15 µm and monocrystalline diamond suspension with grain size 9, 6, 3 and 1 µm were used for grinding following the empiciral grinding rule[1] of half grain size in the next step. According to Buehler's recommendation[2] grinding head force 5 N, speed 120 rpm and duration time 240s was used in each step. For the final polishing aluminum-oxide Al_2O_3 suspension with grain size 0.05 µm was used. The influence of grinding and polishing to surface roughness is depicted in Fig. 1.

3. Roughness analysis

Monitoring of the roughness reduction was performed using a Confocal Laser Scanning Microscope LEXT OLS3000 (Olympus, Inc., Tokyo, Japan). This device performes the reconstruction of the scanned surface using a laser beam. Results of the scanning are represented by a 2D matrix of heights, calculated surface characteristics (e.g. average roughness, mean squared roughness, largest peak height, largest valley depth) and high resolution images. The physical size of the scanned area was 640×480 with magnification 480×.

The roughness analysis using the 2D matrix of heights was performed in regions corresponding with the size of a rectangle covered by the array of indentors used for nanoindentation tests[3,4].

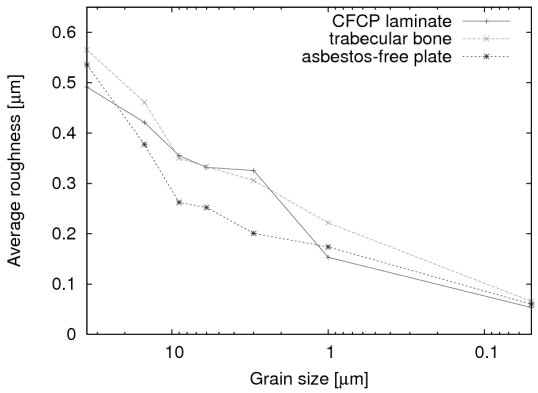

Fig. 1. **Grinding procedure before optimization**

4. Optimization of the polishing procedure

Satisfactory values of final roughness were obtained, but a low roughness reduction by grinding using 9, 6 and 3 µm suspensions was observed. Therefore changes in the grinding procedure were suggested. The influence of grinding head force on abrasion rate and surface roughness was analyzed. Achieved abrasion rates are listed in Tab. I.

Influence of pressure force on surface roughness was not observed. In accordance with these results, the grinding step

Table I
Abrasion rates for different abrasive types

Abrasive type	Load [N]	Abrasion [µm min^{-1}]
15 µm diamond disk	5	20 ± 3
15 µm diamond disk	10	35 ± 4
3 µm diamond suspension	5	1.1 ± 0.2
3 µm diamond suspension	10	1.7 ± 0.4
3 µm diamond suspension	15	2.4 ± 0.4

Table II
Optimized grinding procedure

Abrasive/size	Load [N]	Speed [rpm]	Time [s]
35 μm diamond disk	5	120	120
15 μm diamond disk	5	120	120
9 μm diamond suspension	15	120	360
3 μm diamond suspension	10	120	240
1 μm diamond suspension	5	120	240
0.05 μm SiO_2 suspension	2.5	100	300

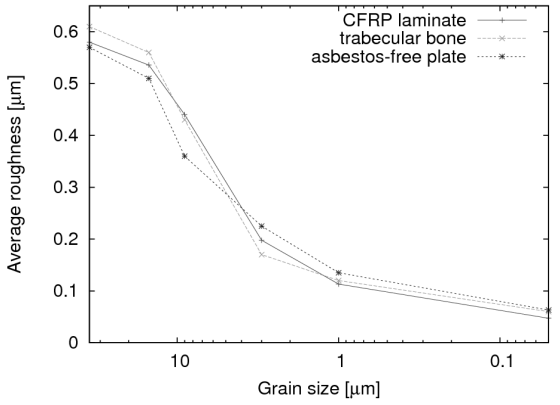

Fig. 2. **Optimized grinding procedure**

with grindstone-size 6 μm was omitted and duration time of the other steps was optimized. The improved grinding procedure is described in Tab. II.

The region of low reduction of surface roughness was removed (Fig. 2).

5. Conclusions

In this work, optimization of grinding procedure for three representative materials for microstructural testing was performed. Roughness reduction during the original grinding procedure was monitored using a confocal microscope and according to the obtained results the procedure was optimized. In case of the initial concatenation of grinding steps a slow progress in the middle of the procedure was observed. Number of grinding steps was reduced and optimal forces and grinding times were estimated. Using the optimized polishing procedure equal values of final surface roughness were reached and shorter time (26 % reduction) and with smaller amount of grinding substances (14 % volume saving) required.

The research has been supported by Grant Agency of the Czech Technical University in Prague (grant No. SGS10/227/OHK1/2T/31), by the Grant Agency of the Czech Republic (grant No. P105/10/2305) and research plan of the Academy of science of the Czech Republic AV0Z20710524.

REFERENCES

1. Brinksmeier E., Mutlugunes Y., Klocke F., Aurich J. C., Shore P., and Ohmori H.: *Ultra-precision grinding*, CIRP Annals - Manufacturing Technology, volume 59 (2010).
2. Buhler: *The Science Behind Materials Preparation*, Buhler ltd. (2004).
3. Němeček J.: Mater. Character. *60*, (2009).
4. Zlámal P., Kytýř D., Jiroušek O.: *Calibration on material model for trabecular bone verified by time-lapse X-Ray microtomography*, *Proc. of the 7th IASTED intern. conf. on Biomedical engineering*, ACTA Press (2010).

M. Dudíková[a], D. Kytýř[b], T. Doktor[b], and O. Jiroušek[b] *([a] Czech Technical University in Prague, Klokner Institute, Prague, [b] Academy of Sciences of the Czech republic, Institute of Theoretical and Applied Mechanics, Prague, Czech Republic):* **Monitoring of Material Surface Polishing Procedure Using Confocal Microscope**

Article deals with monitoring and optimization of roughness reduction procedure used for preparation of samples for nanoindentation tests. The aim of the research was to measure roughness reduction effect of various combination of grindstones, polishing time, pressure and speed. Suitable procedure with respect to time and cost for three different materials was proposed. For porous materials trabecular bone was chosen, fibre composite as and asbestos-free plates compact ones. Roughness measurement was performed by contactless method using a confocal microscope. Number of grinding steps was reduced and optimal forces and times of grinding were estimated.

MICROSTRUCTURE PARAMETERS VERSUS INDENTATION SIZE EFFECT IN WC-Co HARDMETALS

ANNAMÁRIA DUSZOVÁ, PETER HORŇÁK, VLADIMÍR STOYKA, PAVOL HVIZDOŠ, FRANTIŠEK LOFAJ, and JÁN DUSZA

Institute of Materials Research of SAS, Košice, Slovak Republic

Keywords: WC-Co, microstructure, hardness, ISE

1. Introduction

Cemented carbides are widely used as cutting, forming and machining tools in different areas of industry because of their high hardness and strength, good fracture tougness and excellent wear resistance. Their mechanical properties are determined by their microstructure parameters but are also dependent on the testing methods[1].

Hardness is one of the most important characteristic of cemented carbides. The apparent hardness of ceramics and ceramics based composites depends on the applied test load, it decreases with increasing load, which is called "load size effect" or "indentation size effect" (ISE). The hardness on the other side strongly depends on the microstructure of these materials and exhibits significant scatter, especially at low indentation loads[2].

The aim of the present contribution is to study the influence of the applied load on the hardness, indentation modulus and their scatter in WC-Co systems with different microstructure parameters during the instrumental hardness test in the load range from 5 mN to 440 mN.

2. Experimental procedure

The experimental materials were supplied by Pramet Sumperk. Four systems have been prepared using standard processing routes with different microstructure parameters. Their microstructure has been evaluated using standard ceramographic procedures – cutting, grinding, polishing and SEM observation, (Fig. 1.) The microstructure parameters as volume fraction of Co binder – f_{Co}, mean grain size of WC – D_{WC}, mean free path in binder – L_{Co} and contiguity – C_{WC}, have been calculated using standard point/line analysis[3].

The CMC^{TM} (Continuous Multi Cycle) method was applied using Nano Hardness Tester (CSM-Instruments SA) with Berkovich diamond indenter. In each test run, the indenter was driven into the specimen surface under a load gradually increased from 5 mN to 450 mN with 10 stops at predefined loads. At each stop the indent was unloaded gradually to 10 % of the load after being held at that load for 10 s, and then driven again into the specimen surface to a higher value. At least 15 test runs were recorded on each samples. Single cycle indentations have been realized in the same load interval. The calculation of the indentation hardness and the evaluation of the ISE have been realized according to the methods described[4]. Traditional Vickers hardness was measured in the load interval from 0.98 N to 298 N.

3. Results and discussion

Characteristic microstructures of systems WC-Co 35 and WC-Co 60 systems are illustrated in Fig. 1 and the microstructure parameters for all investigated materials together with their Vickers hardness are summarized in Tab. I.

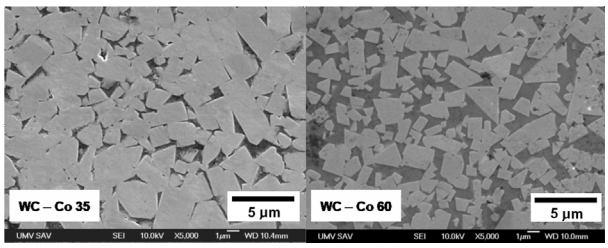

Fig. 1. **Characteristic microstructure of the systems WC-Co 35 and WC-Co 60 (bright – WC, dark – Co)**

Table I
Microstructure parameters and Vickers hardness with standard deviations of the studied WC-Co systems

	f_{Co} [%]	D_{WC} [µm]	L_{Co} [µm]	C_{WC} [−]	HV30 [kg mm^{-2}]
WC-Co 20	12.5	1.51	0.34	0.39	994/12
WC-Co 35	10.7	1.69	0.29	0.37	1191/31
WC-Co 60	35.3	1.07	0.76	0.23	826 /13
WC-Co 110	10.8	0.81	0.20	0.52	1330/39

According to Table I, the volume fractions of the binder are similar in WC-Co 20, WC-Co 35 and WC-Co 110 (around 11.0 vol%) and only WC-Co 60 has significantly higher f_{Co} with the value of 35.3 vol%.

The results of the instrumented indentation test are illustrated in Figs. 2-4. The increased value in hardness at the highest penetration depth is Fig. 2 an artefact. It seems that the ISE is not significant for the studied materials. In all systems however the scatter in hardness values increased with decreasing load significantly, especially at loads below 100 mN. The hardness values of the WC-Co 20, WC-Co 35 and WC-Co 110 are very similar within the whole load range. The lowest ISE was observed in the system WC-Co 110.

The lowest hardness was found in WC-Co 60 for all indentation loads. The indentation modulus decreased with increased loads for all systems, with evident differences

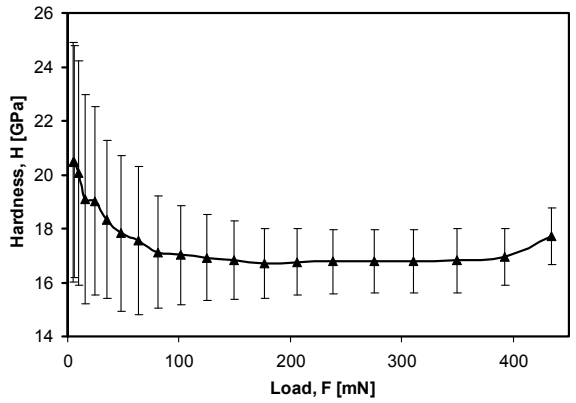

Fig. 2. **Influence of the load on the hardness for WC-Co 35**

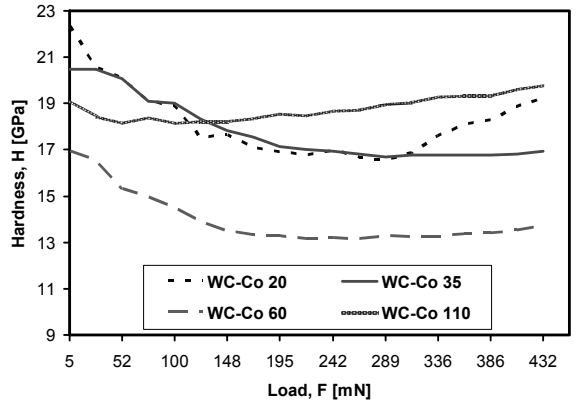

Fig. 3. **Influence of the load on the hardness for all systems**

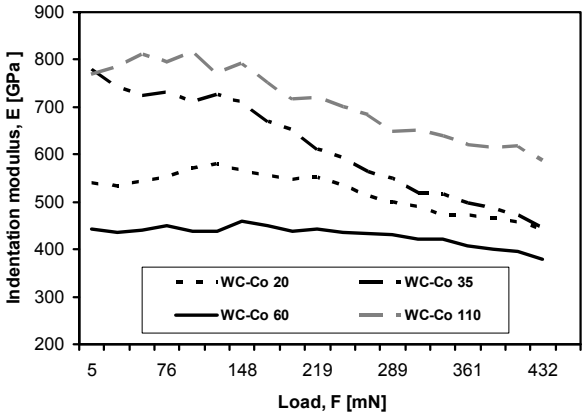

Fig. 4. **Influence of the load on the indentation modulus**

between systems, and with a probably strong relationship to the individual microstructure parameters.

The scatter in traditional Vickers macro hardness at loads > 0.98 N is caused mainly by the scatter in indent size measurement. Below 100 mN, when the indent size became smaller, the volume of the deformed area below the indents contains less WC grains and Co areas with different size/ properties and the scatter is increasing. At very low loads (cca 10 mN), the indent size is comparable or smaller than the D_{WC} and L_{Co} and the scatter is significant, caused by the very different hardness and elastic modulus of the individual phases.

Recently Bonache et. al[5] found differences as high as 100 % in the hardness and indentation modulus of WC crystals measured at different crystallographic orientations. Our preliminary results partly confirmed these facts. This can contribute additionally to the high scatter at very low loads, which will be the object of our future investigation.

4. Conclusions

The differences in microstructure parameters of the studied WC-Co systems, beside the system 60, result only in relative small differences in their hardness but in larger differences in their indentation modulus. The volume fraction of binder, f_{Co} determines the hardness at higher loads and the mean free path in binder, L_{Co}, mean grain size of WC, D_{WC}, and the crystallographic orientation of WC grains the nanohardness at loads < 25 mN. The ISE is more significant in the case of instrumented modulus.

This work was supported by APVV-0520-10, VEGA 2/0108/11 and MNT-ERA.NET HANCOC.

REFERENCES

1. Exner H. E.: Inst. Met. Rev. *4*, 149 (1979).
2. Dusza J.: *PhD Thesis*, IMR SAS, (1983)
3. Gurland J., in: *Practical Applications of Quantitative Metallography* 839, ASTM STP, p. 65, (1984).
4. Peng Z., Gong J., Miao H.: J. Europ. Ceram. Soc. *24*, 2193 (2004).
5. Bonache V., Rayón E., Savlador M. D., Busquets D.: Mater. Sci. Eng., *A 527*, 2935 (2010).

A. Duszová, P. Horňák, V. Stoyka, P. Hvizdoš, F. Lofaj, and J. Dusza *(IMR, SAS, Košice, Slovak Republic)*:
Microstructure Parameters vs. Indentation Size Effect in WC-Co Hardmetals

The influence of the applied load on the hardness, indentation modulus and their scatter in WC-Co systems with different microstructure parameters has been investigated. The indentation size effect was not significant and the microstructures influenced more significantly the indentation modulus. The scatter in hardness values increases at low indentation loads.

EFFECT OF LIGHT ABSORPTION ON INDENTATION MODULUS OF DENTAL FILLING COMPOSITES

RENATA EICHLEROVÁ*, JAROSLAV LUKEŠ, JOSEF ŠEPITKA, and SVATAVA KONVIČKOVÁ

Department of Mechanics, Biomechanics and Mechatronics, Faculty of Mechanical Engineering, CTU in Prague, Technická 4, 166 07 Prague 6, Czech Republic
eichlerova.renata@seznam.cz

Keywords: nanoindentation, dental filling composites, light absorption

1. Introduction

In many branches such as biomechanics, orofacial surgery and material engineering FEM analyses are used for different problem solving[1]. These analyses are used for the dental fillings lifetime improvement in order to prevent fracture of filling, loss of filling and creating of secondary caries on the tooth-filling interface. These failures are caused by the stress as an effect of the light activated polymerization process and occlusal loading. Several studies deal with optimization analyses and try to decrease the polymerization residual stresses in filling by different shaping of the cavity and/or by the manner how the cavity is filled[2]. These analyses require knowledge of exact mechanical properties of all materials used for FEM model including the dental filling composites. This work is focused on effect of polymerization light absorption on elastic modulus evaluating at a different depth of the material. As the most suitable method for local mechanical properties determination the nanoindentation method was chosen.

2. Materials and methods

Cylindrical specimens were made from dental filling composites (Filtek™ Supreme XT, Filtek™ Silorane and Charisma) with different chemical composition. The material was pushed into the epoxy mould, Fig. 1, covered by a transparent plastic film and pressed by a glass slide. Polymerization of the material was activated by the use of light curing unit (Translux Power BlueTM, Hereaus Kulzer GmbH, Germany) for time period according to instructions for use. Each specimen was irradiated only from one side in order to simulate real conditions in tooth. These specimens were halved (diamond cut-off wheel, Ø150 × 0,4 × Ø12,7 mm, low speed, Struers) in order to evaluate effect of light absorption to elastic modulus at different depth of the material. The surface of the cut face was finished mechanically in grinding machine with abrasive papers of subsequently decreasing abrasiveness up to 4000-grit and then was polished[3]. Thus prepared specimens were stick on magnetic metal thin plate in order to prevent movement of specimen during indentation.

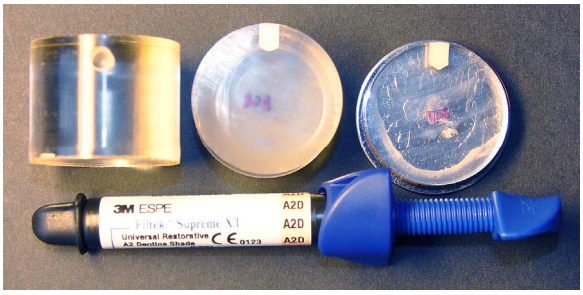

Fig. 1. **A halved epoxy mould with composite specimen**

NanoDMA load controlled experiment was performed on Hysitron's TriboLab® system (Hysitron, Inc., Minneapolis, USA) at the CTU in Prague. During the test a sinusoidal force was applied to a sample and the resultant amplitude and displacement were measured. Harmonic loading with dynamic load amplitude 0.02 mN was specified for a harmonic frequency 5–150 Hz. During the nanoDMA experiment was applied static load with maximum force P_{max} = 2 mN. A diamond tip (E_i = 1141 [GPa] and ν_i = 0.07) was used for experimental measurements in room temperature conditions. The indentation matrix 3×7 (about separation of 15×15 μm) was placed in every 0.5 mm of depth to a value of 3.5 mm under the irradiated surface. The procedure of dynamic data analysis was adopted from Asif et.al.[4]. An automatically calculated data of the damping coefficient C_S and the contact stiffness K_S of the specimen are than used to determine the viscoelastic properties. The reduced storage modulus E_r', the reduced loss modulus E_r'' of the specimen, and their ratio tanδ can be calculated by equations (*1*), (*2*) and (*3*), respectively:

$$E_r' = \frac{K_S\sqrt{\pi}}{2A_C} \qquad E_r'' = \frac{\omega C_S\sqrt{\pi}}{2\sqrt{A_C}} \qquad \tan\delta = \frac{\omega C_S}{K_S} \qquad (1, 2, 3)$$

where A_C is the contact area based on tip area function related to contact depth at quasistatic loading, and ω is the frequency [rad/s]. The storage and loss modulus of the sample E_s' and E_s'', respectively, are related to the reduced storage and loss modulus according to equations (*4*) and (*5*):

$$\frac{1}{E_r'} = \frac{\left(1-\nu_i^2\right)}{E_i} + \frac{\left(1-\nu_s^2\right)}{E_s'} \qquad (4)$$

$$\frac{1}{E_r''} = \frac{\left(1-\nu_i^2\right)}{E_i} + \frac{\left(1-\nu_s^2\right)}{E_s''} \qquad (5)$$

where the subscripts *i* and *s* refer to the indenter and sample materials, respectively, and ν is the Poisson´s ratio. Poisson's ratios of the material were determined from the measured ultrasonic velocities and the densities of the materials. Experi-

mental measurement was carried out and analysed according to ultrasonic technique description[5]. Poisson´s ratios were set as $\nu_s = 0.285$ for Filtek™ Supreme XT, $\nu_s = 0.28$ for Filtek™ Silorane, and $\nu_s = 0.3$ for Charisma.

3. Results

The values of reduced storage modulus and loss modulus are desired results of nanoDMA analyses. The typical example of average values of moduli of material Charisma is presented in Fig. 2. For all materials the ratio of storage and loss modulus didn`t reach over ten percent and the range of variation coefficient was around 10 ± 5 %.

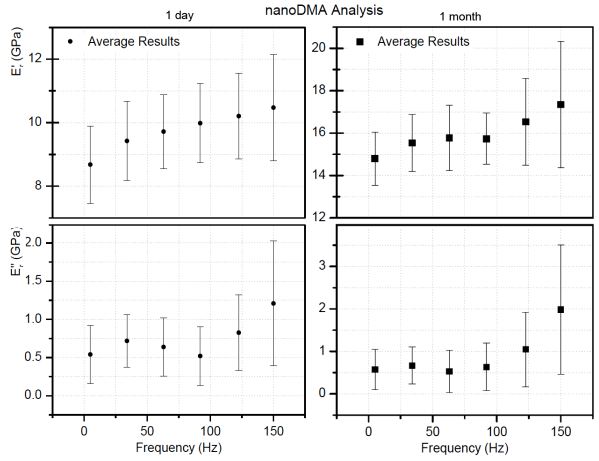

Fig. 2. **Reduced storage and loss moduli of Charisma measured one day (left) and one month (right) after manufacturing**

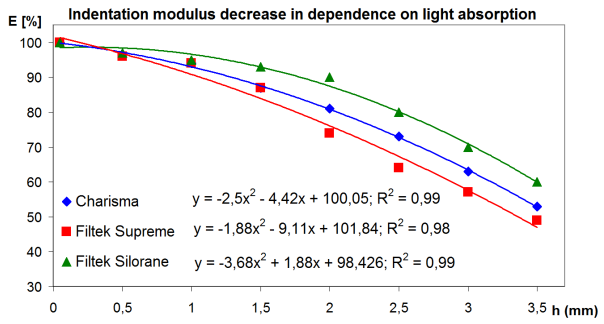

Fig. 3. **The percentage expressed decrease of complex indentation modulus *E* in dependence on depth *h***

The mean values of complex moduli E [GPa] measured one day after specimens manufacturing on the upper layers are: $E = 14.5$ for Filtek™ Supreme XT; $E = 11.8$ for Filtek™ Silorane; $E = 6.9$ for Charisma. The decrease of values of complex moduli in dependence on depth h [mm] is presented in Fig. 3.

4. Discussion

Good repeatability of measurements was observed for low frequency of 50 Hz and in range 50–100 Hz. For frequencies higher than 100 Hz the standard deviation was increasing. The ratio of storage and loss modulus increase in time. It means that the elastic behaviour of the material is more significant whereas the viscous component is supressed.

5. Conclusion

Dynamic indentation method nanoDMA proper for viscoelastic properties testing was successfully applied on dental filling composites. The polymerization depth that is guaranteed by producer was in accord with obtained results. The smaller decrease of modulus caused by light absorption was observed in depth to 1.5 mm and more significant decrease in range of depth 1.5–3.5 mm.

The research was supported by the Ministry of Education project: Transdisciplinary research in Biomedical Engineering II, No. MSM 6840770012, and by the Grant Agency of the Czech Technical University in Prague, grant No. SGS10/247/OHK2/3T/12.

REFERENCES

1. Baca V., Horak Z., et. al.: Compa. (Med. engineering & physic) *30*, 924 (2008).
2. Kowalczyk P.: Influen. (Dental Materials) *25*, 83 (2009).
3. Válová M.: TechMat 2010.
4. Asif S.A.S., et. al.: Review of Sci. In. *70*, 2408 (1999).
5. Goldmann T.: *Mech. prop.*, 1st ed., Saarbrücke: Lambert Academic Publishing AG & Co. KG, 2010. 115 p.

R. Eichlerová, J. Lukeš, S. Konvičková, and J. Šepitka *(Department of Mechanics, Biomechanics and Mechatronics, Faculty of Mechanical Engineering, CTU in Prague, Czech Republic):* **Effect of Light Absorption on Indentation Modulus of Dental Filling Composites**

The intent of this study was to evaluate elastic modulus of three dental filling composites. NanoDMA was focused on mechanical properties of upper irradiated layers of the specimens and on deeper layers where the intensity of polymerization radiation decreased. The nanoindentation testing was performed using a Hysitron's TriboLab®. Poisson`s ratios of composites were obtained by ultrasonic measurement of mechanical properties of the same materials. First observation showed decrease in modulus due to light absorption.

THE EFFECT OF SURFACE ROUGHNESS ON NANOINDENTATION

GABIKA FUCHSOVÁ[a], FRANTIŠEK LOFAJ[b], and VLADIMÍR SIMKULET[a]

[a] *Faculty of Manufacturing Technologies of Technical University of Košice with a seat in Presov, Bayerova 1, 080 01 Prešov,* [b] *Institute of Materials Research of SAS, Watsonova 47, 040 01 Košice, Slovakia*
flofaj@imr.saske.sk

Keywords: nanoindentation, surface roughness, WC-C coating, nanohardness, indentation modulus

1. Introduction

Nanoindentation measurement is strongly affected by surface roughness. The reason is that the depth of penetration is determined from the zero point of initial contact of the indenter with the surface. Natural roughness of real surfaces causes uncertainty in the determination of the zero point and subsequently, of contact area with the surface asperities at shallow indentation depths which significantly increases the data scatter. The analytical models usually involve elastic or completely plastic contact and often take into consideration the statistical variation in asperity height in real surfaces[1].

ISO 14577-1 standard requires that the surface roughness, R_a, is below 5 % of indentation depth, h (ref.[2]). In the case of thin coatings, an additional requirements of ISO 14577-4 is that the h is below 10 % of the coating thickness, d, to avoid substrate effects[3]. However, real coatings often exhibit roughness, which does not satisfy this requirement. Therefore, the aim of this work is to investigate the effect of substrate and coating roughness on nanoindentation data.

2. Experimental procedure

The material of the substrate was a rod of tool steel 12 050. Seven samples with the diameter of 55 mm and thickness of around 4 mm were machined from the rod, tempered from 860 °C into oil and annealed at 200 °C. Their surfaces were ground with a diamond wheel with the grain size of around 100 μm. Two samples in the as-ground (A-G) state were used as the representatives of the highest surface roughness, and the remaining samples were polished up to 1 μm. Two of them represented the lowest surface roughness. Subsequently, one sample was ground on #80 SiC paper, another one on 80/63 diamond disc and the last one on the polishing cloth with 15 μm diamond spray. "Macro-roughness", R_a, was measured using contact profilometer (model SJ 201, Mitotuyo) on ten lines with the length of 10 mm each. The distance between the lines was 1 mm. The value of R_a was determined as an average of these ten measurements. "Micro-roughness" was measured using an atomic force microscope (model Dimension Icon, Veeco). Two areas with the size of 50 μm × 50 μm were imaged in a tapping mode for each sample. R_a was determined as an average value from ten 10 μm × 10 μm areas arbitrarily distributed on both images.

Nanohardness, H_{IT}, and indentation modulus, E_{IT}, of the substrates were investigated using nanoindenter (model NHT, CSM, Switzerland) in sinusoidal loading mode up to 10 mN, 100 mN and partial unloading (Continuous Multi-Cycle – CMC) mode up to 400 mN. At least 20 indents were made in automatic mode on each sample and corresponding depth profiles were generated. The extreme curves were excluded from further analysis. The values of hardness and indentation modulus were determined as an average from the stable part of each depth profile.

PECVD WC-C coating with the thickness of around 500 nm has been deposited on all substrates simultaneously. The deposition conditions were as follows: total pressure 3 Pa, current density 1 mA cm^{-2} and bias voltage −5 kV. The roughness of the coatings was measured using the same methods as in the case of substrates. Nanoindentation tests were performed in sinus mode only up to 10 mN to satisfy 10 % indentation depth limit applied to coatings.

3. Results and discussion

Tab. I summarizes roughness data from the contact profilometer on the substrates and coatings. The range of R_a in the substrates is 0.02–0.6 μm whereas it is 0.1–0.6 μm in the coatings. Tab. II shows similar data for R_a obtained from AFM. The roughness range is 3–300 nm in the very local areas (10 μ m x 10 μm) free of any deposition artifacts. Coating roughness is often higher than the substrate roughness both in nano- and micro- range, especially at low R_a. The ratio of R_a of the coating and substrate is in Fig. 1. The roughness of the coating is dominant on well polished substrates and this effect is greatly suppressed when roughness of the substrate exceeds 130 nm. The same is valid for AFM measurements from Tab. II. This data suggests that large "coating grains" grew on flat surfaces due to limited number of nucleation sites. *Vice versa*, rough surfaces provide increased nucleation site density and the resulting coating consists of smaller grains, therefore, R_a is determined by the roughness of the substrate. Fig. 2 shows the dependence of nanohardness measured in sinusoidal loading mode up to 10 mN on the substrates with different roughness. Hardness varies from 4.5 GPa up to ~11 GPa. The dependency on R_a is not pronounced, and it is hidden in the

Table I
Roughness data on the substrates and corresponding coatings obtained by contact profilometry

	1 μm	1 μm	15 μm	80/63	80SiC	A-G	A-G
$R_{a\ \text{substrate}}$ [μm]	0.024	0.024	0.135	0.412	0.45	0.502	0.573
$R_{a\ \text{coating}}$ [μm]	0.098	0.099	0.175	0.662	0.522	0.555	0.623

Table II
Roughness data on the substrates and coatings from AFM

	1µm	1µm	15µm	80/63	80SiC	A-G	A-G
$R_{a\ substrate}$ [nm]	2,993	3,855	104,74	195,84	303,84	146,06	139,3
$R_{a\ coating}$ [nm]	24,858	15,93	81,78	179,8	34,41	144,46	137,79

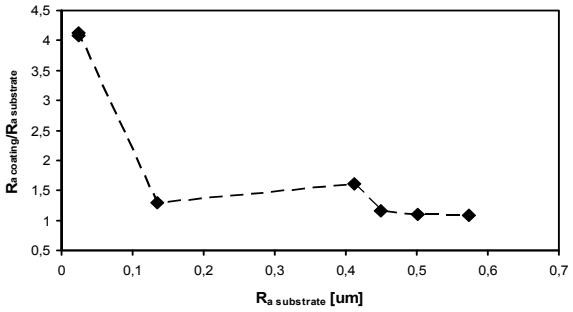

Fig. 1. **Relative change of the surface macro-roughness of the coatings as a function of substrate macro-roughness**

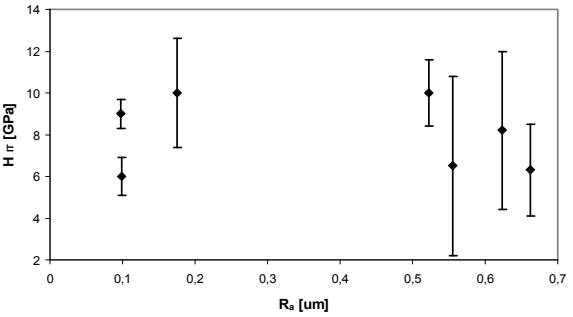

Fig. 2. **Indentation hardness vs. surface macro-roughness of steel substrates**

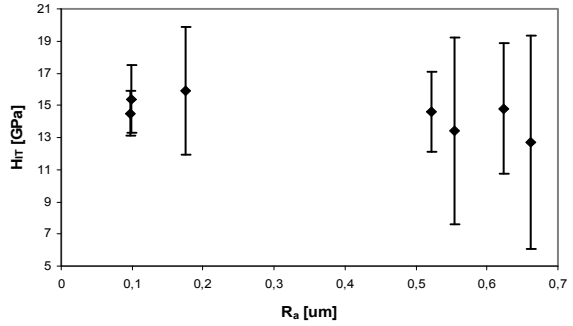

Fig. 3. **Indentation hardness vs. surface macro-roughness of WC-C coatings**

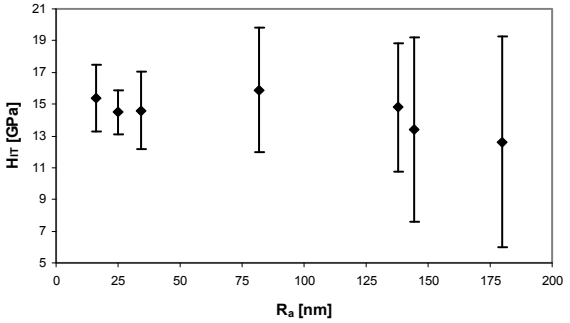

Fig. 4. **Indentation hardness vs. surface nano-roughness of WC-C coatings**

data scatter, which increases with R_a. Hardness of the coating determined at the same conditions exhibits the same behavior regardless of the macro- or nano-roughness level (Fig. 3 and Fig. 4, respectively). The main effect of R_a increase is the substantial increase of data scatter, especially in the case of nano-roughness measured using AFM. Indentation modulus exhibited the same behavior both in the substrate and in the coating.

4. Conclusions

Surface roughness of the examined WC-C coating increases on substrates with smaller roughness, probably due to unconstrained growth at the limited number of nucleation sites. Hardness (and indentation modulus) of steel substrates and WC-C coatings does not depend on R_a within the studied R_a range but R_a increase substantially increases the scatter of the measurements.

This work was supported by APVV-0520-10, VEGA 2/0108/11 and MNT-ERANET HANCOC Projects.

REFERENCES

1. Fischer-Cripps A. C.: *Nanoindentation*, Springer-Verlag, New York 2004.
2. ISO 14577 - 1:2002:E, Metallic materials – Instrumented indentation test for hardness and materials parameters – Part 1 Test method, ISO, 2002.
3. ISO 14577 - 4:2007:E, Metallic materials – Instrumented indentation test for hardness and materials parametrs – Part 4 Test method for metallic and non/metallic coatings, ISO, 2007.

G. Fuchsová[a], F. Lofaj[b], and V. Simkulet[a] *([a] Faculty of Manufacturing Technologies of Technical University of Košice with a seat in Prešov; [b] Institute of Materials Research of SAS, Slovakia):* **The Effect of Surface Roughness on Nanoindentation**

Current study revealed that surface roughness of WC-C coating increases with steel substrate roughness reduction and nanohardness (and indentation modulus) of substrates and coatings does not depend on R_a, it only substantially increases the scatter of the measurements.

MEASUREMENT OF PARAMETERS DETERMINING MECHANICAL PROPERTIES OF GRAINS WITH PARTICULAR ORIENTATION IN NON-ORIENTED ELECTROTECHNICAL STEELS

PETRA GAVENDOVÁ, FRANTIŠEK KOVÁČ, IVAN PETRYSHYNETS, and VLADIMÍR STOYKA

Institute of Materials Research, Slovak Academy of Sciences, Watsonova 47, 040 01 Košice, Slovak Republic
pgavendova@imr.saske.sk

Keywords: spherical indentation, crystallographic texture

1. Introduction

The non-oriented (NO) steels are mainly used as core materials for rotating equipments[1]. Important parameters that determine good magnetic properties of electrical steels are crystallographic texture, grain size and chemical composition[2]. These properties of NO steels are provided by (100) [0vw] so called "rotating" cub texture. However, this texture state is not achieved in the practice so far. It is important to notice that maximal attention in the field of the research and development of NO steels is concentrated on achievement of the cube texture component intensity in the plane of the steel sheet.

2. Experimental material and procedure

As experimental material was used NO electrical steel (FC) that was taken from industrial line after cold rolling with 74 % of deformation and subsequent recrystallization annealing in laboratory conditions (800 °C/10 min). The chemical conception of the experimental material is presented in Table I.

The study was carried out with nanoindentation testing method. To determine the hardness a triangular Berkovich indenter has been used. The sample were measured with the Quasi Continuous Stiffness Measurement (QCSM) module at a maximum force of 100mN. The QCSM module allows measuring the contact stiffness depth – dependent at one and the same position of the sample. In addition, the sensitivity of the measurements will be raised in the small force range, so that stiffness values may be readily determined even for very small forces and depths. In order to determine stress-strain curves a spherical indenter with radius 21 μm has been used. The measurements have been carried out using a new method where the stress-strain curve of metals is determined with a neural network from indentation measurement with spherical indenter[3].

Table I
Chemical composition of investigated steel FC

Element	C	Mn	Si	P	S	Al	N
wt.%	0.006	0.24	1	0.07	0.009	0.013	0.011

3. Results and discussion

The microstructure of the investigated steel obtained after laboratory heat treatment is presented in Fig. 1. This sample was subjected to annealing at 950 °C/5 min. As one can see, the material is characterized by columnar microstructure with average grain size about 200 μm.

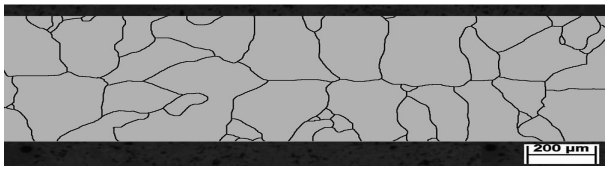

Fig. 1. **Microstructure of FC material**

The micro and nano-indentation were carried out in the FC material passed the laboratory annealing. It means that investigated grains in material characterized by single crystals oriented in space with low defects (dislocation) density. Inverse Pole Figure (IPF) map of the cross section-plane obtained from the sample in Fig. 1b is presented in Fig. 2. This map is used for defined of grains crystallographic orientation in investigated material. We have chosen one grain from each orientation; G (011), D(111), C(001) in which was performed nanoindentation measurements.

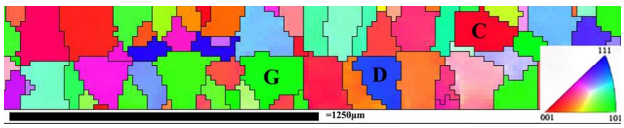

Fig. 2. **IPF map representing the columnar grains in cross – section of FC steel**

Hardness results

Five measurements were carried out in every grain (C, D, G). As one can see, there is the significant difference in hardness values and modulus values between the grain orientations Fig. 3.

Measurement of stress – strain curves

The 9 measurements in a 3 × 3 array in a distance of 50 μm have been carried out in each grain. Fig. 4a, b, c show the impressions.

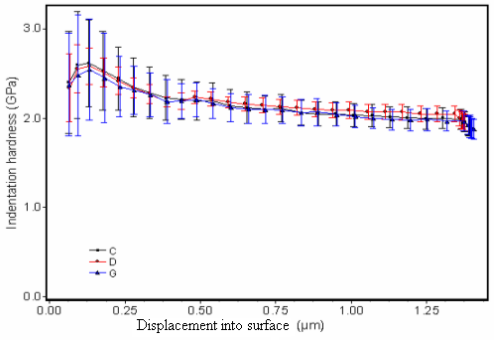

Fig. 3. **Comparison of depth-dependent hardness results for all 3 grains**

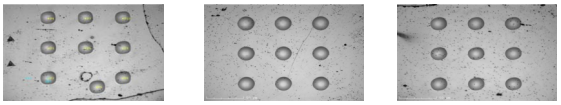

a b c

Fig. 4. **a) Indentation array in grain C, b) Indentation array in grain D, c) Indentation array in grain G**

It can be seen that not all indents are rotationally symmetric. This is the influence of the crystallographic orientation. The measurement curves have been averaged and only the average curve has been analyzed Fig. 5. As one can see between the individual grain orientations is a significant difference and each of these grain orientations have different intensity of deformation.

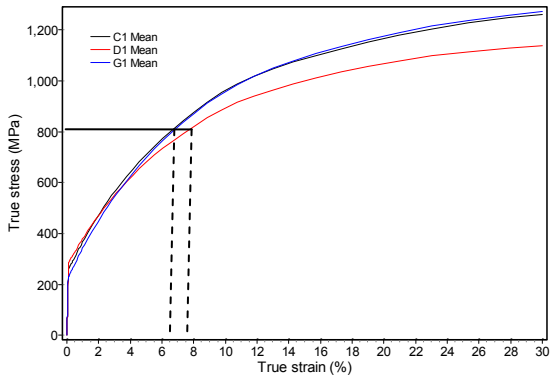

Fig. 5. **Comparison of the mean stress-strain curves from all three grains**

4. Conclusions

On the basis of differences in deformation behaviour of grains with particular crystalografic orientation it can be suggested, that for a given deformation stress the highest value of strain will be reached in D(111) orientated grains.

This fact is important in optimizing the degree of temper rolling for strain induced grain growth in non-oriented electrotechnical steel. For the investigated steel the recommended deformation is over 6 %.

This work was carried out within the frame of the project "Technology of preparation of electrotechnical steels possessing high permeability for high affectivity electromotors", ITMS 26220220037 financed through European Regional Development Fund. Special thanks are due to Dr. Tomas Chudoba for nanoindentation measurements and Franziska Kairat from ASMEC Advanced Surface Mechanics GmbH.

REFERENCES

1. Castro S. F., Gallego J., Landgraf F. J. G., Kestenbach H. -J.: Mater. Sci. Eng., A *427*, 301 (2006).
2. Džubinsky M., Sidor J., Kovač F.: Mater. Sci. Eng., A *385*, 449 (2004).
3. Tyulyukovskiy E., Huber N.: J. Mater. Res *21*, 664 (2006).

P. Gavendová, F. Kováč, I. Petryshynets, and V. Stoyka *(Institute of Materials Research, Slovak Academy of Sciences, Košice, Slovakia):* **Measurement of Parameters Determining Mechanical Properties of Grains with Particular Orientation in Non-Oriented Electrotechnical Steels**

The aim of the present work is to determine the difference in mechanical properties between the grains possessing three predefined orientations (with (100); (110) and (111) planes perpendicular to the loading) by the spherical indentation method. By means of spherical indentatiom technique was measured a significant differences in deformation behavior between grain orientations in polycrystalline material, which is more difficult to determine by another method (such as microhardness test or uniaxial tensile test).

DIAGNOSTICS OF DEFECTS IN THE FORGED BLADES USED IN POWER INDUSTRY

PAVLÍNA HÁJKOVÁ[a], JIŘÍ JANOVEC[a], JAN SIEGL[b], BOHUMIL SMOLA[c], and MICHAELA VYROUBALOVÁ[a]

[a] CTU in Prague, Faculty of Mechanical Engineering Karlovo nám. 13, 121 32 Prague 2, [b] CTU in Prague, Faculty of Nuclear Sciences and Physical Engineering, Trojanova 13, 120 00 Prague 2, [c] Charles Univesity in Prague, Faculty of Mathematics and Physics, Ke Karlovu 5, 121 16 Praha 2, Czech Republic
pavlina.hajkova@fs.cvut.cz, jiri.janovec@fs.cvut.cz, michaela.vyroubalova@fs.cvut.cz, jan.siegl@fjfi.cvut.cz, bohumil.smola@mff.cuni.cz

Keywords: Blades, Cr-martensitic steel , power plant, microstructure, fractography analysis

1. Introduction

The purpose of this paper is to determine the causes of cracks on forged blades, designed for turbine wheels of low pressure parts in 1,000 MW turbines. Visual inspection identified cracks in the middle of shovel blades (Fig. 1, No. 1), in the transition area of the lock (Fig. 1, No. 2) and in the area of upper groove lock (Fig. 1, No. 3) developed during the final machining operations. The blades were manufactured by die forging of stainless steel X12CrNiMoV12-3 (the numerical designation 1.4938). The initial semiproduct was rod KR 110 mm, pre-forging was done at temperatures from 950 to 1050 °C and then finaly forged at temperatures form 900 to 1100 °C. At the end of forging the straightening of blades was performed. The blades were then heat treated 1020 °C / oil + 620 °C / water and annealed to achieve a stress relief at 580 °C in order to meet regulatory requirements for yield strength min. 800 MPa, ultimate strength of 1000 MPa, elongation min. 14 % and the notch toughness of 55 J in longitudinal direction.

2. Experimental

Cracks, which were found in three areas of blades, were first identified using a magnetic method (see Fig. 1). Consequently, microstructural analysis of undamaged blades and blades with cracks was carried on a light microscope (Zeiss Neophot 32) and TEM (JEOL JEM2000FX and EDS microanalyzer LINK AN10000).

Samples for microstructural analysis were taken from areas around the cracks and the leaf blades lock in the transverse and longitudinal direction. Samples for light microscopy were metallographically prepared by standard and chemically etched (Vilalla Bain). The structures were taken at magnifications of 100, 200 and 500 times. The microstructure of the basic material had the typical structure of Cr tempered martensitic steel (see Fig. 2) and showed characteristicss of needle-like structure of martensitic phase. Dispersivity and orderliness of carbide phases did not show significant roughness nor orientation or localization of carbides in the areas of original austenite grains. Cracks were filled with corrosion products with different morphologies. At the crack tip and in the region of the secondary propagation, cracks had intergranular course, were homogeneous and black colored. In the region of crack root they were wider, grayish and non-integral, which is typical for cracking of wustit phase (FeO). Observed cracks had the character of cracks resulting from the heat.

Fig. 1. **Cracks identified by magnetic method in three areas**

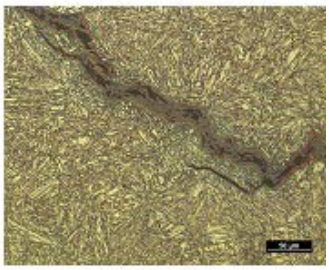

Fig. 2. **Crack in the region of blade lock and martensitic structure of matrix**

Thin foils for TEM were prepared by standard[1] and subsequently electropolished in a 6% $HClO_4$ in methanol at –35 °C and current 150 mA.

The analysis confirmed the martensitic structure with needle-like morphology and increased density of dislocations. In the fracture surfaces of interfaces within the martensite grains the large amount of $M_{23}C_6$ type carbide particles was observed, which precipitated during steel processing. Within intact blades the occurence of carbide particles was lower[1].

Control of chemical composition of the material and the original cast blades was conducted on quantometer ARL 3460 OE. The results showed compliance with the chemical composition of all blades[1]. Samples for microchemical analysis that was completed in Camebax MICRO microanalyzer were taken from corrosively attacked cracks surface. The results confirmed the presence of iron oxides. Oxides also showed a reduced concentration of Cr. Their formation therefore had to happen at temperatures of 1000−1100 °C at high temperature oxidation where highly porous wustidu was created.

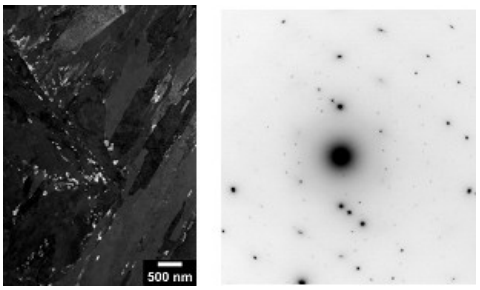

Fig. 3. **a) Carbide particles $M_{23}C_6$ in dark field; b) microdiffraction from the carbide indicated in Fig. 3a, zone [021] of carbide $M_{23}C_6$**

Fractographic analysis of samples with forging cracks was performed, images were obtained by scanning electron microscope JSM 840A and JSM 5510 LV. Samples were taken from the leaf blade with the original parts surfaces after forging (A) and the blade lock (B). Two zones were observed within the sample A that differed by the degrees of coloration, which identified different layer micromorphology. Zone I contained corrosion products and Zone II contained high temperature oxides. The fracture surface showed a mixed fracture with a significant proportion of intercrystallic decohesion (Fig. 4). Transkrystallic failure could not be unambiguously determined due to the layer of corrosion products, which was unremovable. The shape of the technological fracture beginning of B sample suggested that the fracture itself branched repeatedly along the grain boundaries and locally also the spread across the grain boundaries was observed. On the fracture surface signs of decohesion were found and locally also a transcrystallic quazi-brittle fracture was observed. The analysis of samples A and B implied that cracks were formed during forging, increased C content in the crack tip showed the influence of oil quenching.

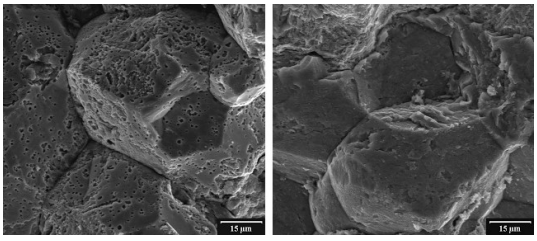

Fig. 4. **Occurence of micromorphological characters of intercrystallic fracture of sample A (left zone I, right zone II)**

Finally the mechanical properties were inspected. All measurements met the requirements[2].

3. Discussion and conclusions

No significant deviations from the material requirements, which could lead to cracks in the forged blades, were found by the analyses. Observed cracks were typical for those resulting from the heat during the two processes. Forging initiated the formation of intercrystalic cracks and austenitization annealing lead to the growth of thicker oxides. The cracking occurred due to improper forging procedure, where most likely an interval of forging temperatures was not kept. Susceptibility to fracture may be attributed to the high incidence of $M_{23}C_6$ carbides, which precipitated during steel processing. For blades with no cracks carbide phase occurred in much smaller quantities. Modified Cr martensitic steels showed significant carbide precipitation in supercooled austenite in the range of 700−800 °C while delays were tens of minutes. From the nature of the defects it can be assumed that the failure was caused by the finishing of forging process including straightening of blades within the forging temperatures interval.

This paper has been supported by the CTU project: SGS number SGS10/258/OHK2/3T/12, Research program MSM6840770021 and Development project "Using electron and light microscopy for modern methods of diagnostics of technical materials".

REFERENCES

1. Janovec J., et al.: Reasons of failure and their character in forging blade LP 3A TG 1000MW. [Research report]. Prague: CTU, Faculty of Mech. Eng. 2010. 11-10. 40p. (in Czech).
2. Hájková P., et al.: Mater. Technol. *44*, 227 (2010).

P. Hájková[a], J. Janovec[a], J. Siegl[b], B. Smola[c], and M. Vyroubalová[a] *([a] CTU in Prague, Faculty of Mech. Eng., [b] CTU in Prague, Faculty of Nuc. Scien. and Phys. Eng., [c] CU in Prague, Faculty of Math. and Phys., Czech Republic):*
Diagnostics of Defects in The Forged Blades Used in Power Industry

The subject of this article is to determine the causes of cracks and their character within the forged blades of turbine wheels of low-pressure parts in power plant. From the Cr-martensitic stainless steel forged samples of blades were prepared. Visual inspection discovered surface cracks that were caused by drop forging. Causes of forging cracks in terms of microstructure and chemical composition were analyzed. Also fracture surfaces of samples of damaged blades were documented and fractography analysis was performed.

CONTACT STRENGTH AND CRACK FORMATION IN MONOLITHIC SiC AND $MoSi_2$

LUCIA HEGEDÜSOVÁ*, LADISLAV CENIGA, and JÁN DUSZA

Institute of Materials Research, Slovak Academy of Sciences, Watsonova 47, 040 01 Košice, Slovak Republic
lhegedusova@imr.saske.sk

Keywords: contact test, microstructure, cone cracks

1. Introduction

Conventional tensile tests for determination of strength of ceramics describe failure behaviour related to a simple stress state which is mostly uniaxial with insignificant gradients. Considering practical applications, mechanical loading leads to an inhomogeneous multi-axial stress state which can be simulated by line or point loading. The line or point loading is induced by two opposite rollers or spheres, respectively. Weibull analysis[1] is commonly used for describing strength of brittle ceramics. It is defined by the characteristic strength σ_0 and the Weibull parameter m which is the measure of the scatter in strength values. The Fett's theory[2] which defines relationships between parameters of the Weibull analysis for the four-point bending test ($\sigma_{0,\mathrm{bend}}$, m_{bend}) and single-cycle contact test using rollers ($\sigma_{0,\mathrm{cont,r}}$ $m_{\mathrm{cont,r}}$) suggests

$$m_{bend} \approx 2\, m_{cont,r} \quad , \quad \sigma_{0,bend} \approx \sigma_{0,cont,r} \qquad (1)$$

The characteristic strength $\sigma_{0,\mathrm{bend}}$ and $\sigma_{0,\mathrm{cont,r}}$ results from experimental values of σ_{bend} and $\sigma_{\mathrm{cont,r}}$, respectively, defined as[2]

$$\sigma_{bend} = \frac{3P(S_1 - S_2)}{2tW^2} \quad , \quad \sigma_{cont,r} = \frac{1.96P}{tW} \qquad (2)$$

S_1 and S_2 represent outer and inner spans, respectively. W and t are dimensions of a sample along directions parallel and perpendicular to a direction of the applied force P at failure, respectively. Finally, the stress $\sigma_{\mathrm{cont,s}}$ along with the Young's modulus E have the forms[3]

$$\sigma_{cont,s} = \frac{1-2\nu_m}{3\pi}\left[\frac{6PE^2}{R^2}\right]^{1/3} \quad , \quad \frac{1}{E} = \frac{1-\nu_s^2}{E_s} + \frac{1-\nu_m^2}{E_m} \qquad (3)$$

where E_s, ν_s and E_m, ν_m are the Young's modulus, the Poisson's ratio for the spheres and a ceramic material, respectively.

The paper deals with the determination of contact strength of two monolithic ceramic materials using opposite rollers and spheres methods as well as with the verification of the Fett's theory validity.

2. Experimental materials and tests

Two monolithic ceramics have been investigated: (*1*) silicon carbide (SiC) prepared at the Institute of Inorganic Chemistry, Bratislava, Slovakia; (*2*) $MoSi_2$ prepared at Cesiwid, Erlangen, Germany.

Microstructure of the materials was studied using scanning electron microscopy on polished and etched samples. The bending test was applied at S_1 = 40 mm, S_2 = 20 mm. The contact mode by standard hardened steel rollers with the diameter D = 3 mm was applied to specimens with the dimensions $W \times t \times L$=3×4×(10-15) mm. The load P of this test increased up to a value of the specimens. The contact mode by standard hardened steel spheres with the radius R = 2.5 mm was applied to specimens with the dimensions $W \times t \times L$=3×4×25 mm. In this case, a load increase was stopped at P = 4.9 kN, i.e. prior to failure of specimens with an aim to investigate a character of cracks. With regard to Eq.(*3*), material parameters of SiC, $MoSi_2$ and standard hardened steel (SHS) of spheres were used[4].

3. Results and discussion

Microstructure of SiC consists of fine submicron-sized equiaxed grains with a low aspect ratio, with inter-granular phase located at thin grain boundary films as well as at triple junctions. Three different phases are identified in $MoSi_2$, i.e. $MoSi_2$ grains with average size of 7 μm, amorphous SiO_2, and low amount of Mo_5Si_3. The SiO_2 particles are represent at triple junctions of the $MoSi_2$ grains, and occasionally precipitates in the $MoSi_2$ grains. Pores with size of 25 μm are the only defects present. Table I presents the Weibull characteristics for the investigated materials. The Fett's theory is not valid for SiC due to the presence of significant processing defects with size of 200 μm in contrast to $MoSi_2$ with the processing flaws with size of 40 μm. The contact strength between spheres is significantly higher in comparison with the bending strength for both materials. $MoSi_2$ with lower fracture toughness exhibits $\sigma_{0,cont,s} / \sigma_{0,bend} = 8.3$, and SiC exhibits this ratio approx. 7.6. In contrast to the contact test by rollers, a correlation between the bending mode and the contact mode by spheres can not be defined. Fig. 1 shows SEM micrographs of cross section views of (a) SiC and (b) $MoSi_2$ loaded by the contact test using spheres for R = 2.5 mm, up to P = 4.9 kN and P = 1 kN, respectively. SiC exhibits multiple cone cracks with a perpendicular behaviour below a contact surface, followed by a linear behaviour. These cone cracks arise to a critical size during the loading and they are a reason of the failure and strength degradation. Multi-crack formation is connected with deformation of spheres and with an enlarged contact surface at the load increase.

Table I
Weibull characteristics of SiC, $MoSi_2$, (see Eqs. (*1*)-(*3*))

Material	$\sigma_{0,bend}$ [GPa]	$\sigma_{0,cont,r}$ [GPa]	m_{bend}	$m_{cont,r}$
SiC	437.1	617.1	10.6	8.9
$MoSi_2$	236.4	261.3	6.9	3.6
Material	$\sigma_{cont,s}$ [GPa]	$m_{cont,s}$	$\sigma_{0,cont,r}$ / $\sigma_{0,bend}$	m_{bend} / $m_{cont,r}$
SiC	3327.6	20.5	1.4	1.2
$MoSi_2$	1966.8	83.5	1.1	1.9

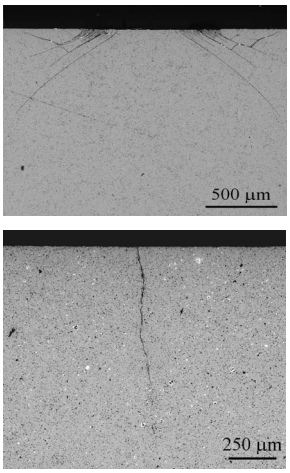

Fig. 1. **SEM micrographs of cross section v of (a) SiC and (b) $MoSi_2$ loaded during contact test using spheres with R = 2.5 mm, up to P = 4.9 kN and P = 1 kN, respectively**

Fig. 1 shows SEM micrographs of cross section views of (a) SiC and (b) $MoSi_2$ loaded by the contact test using spheres for R = 2.5 mm, up to P = 4.9 kN and P = 1 kN, respectively. SiC exhibits multiple cone cracks with a perpendicular course below a contact surface, followed by a linear course. These cone cracks as a reason of the failure and strength degradation arise to a critical size during the load. This multi-crack formation is connected with deformation of spheres and with an enlarged contact surface at the load increase. $MoSi_2$ exhibits different behaviour, i.e. no characteristic cone cracks are formed, and the median crack perpendicular to a contact surface is observed only (see Fig. 1b). The median crack is a reason of lower contact strength and very high Weibull modulus compared to SiC (see Tab. I). In contrast to brittle SiC, this different behaviour is a consequence of a quasi-plastic character of $MoSi_2$ during the contact test between spheres[5]. During the contact mode by rollers, the materials exhibit lateral, median and contact end cracks.

4. Conclusions

The Fett's theory was proved for $MoSi_2$ but is not valid in the case of SiC due to presence of large processing defects. SiC exhibits multiple cone cracks and high contact strength during the test between spheres. In contrast to SiC, the $MoSi_2$ behaves as quasi-plastic materials and exhibits a median crack during the contact test by spheres, which is the reason of lower contact strength and higher Weibull modulus. The contact strength between rollers are similar to bending strength of both materials.

This work was supported by the Slovak Research and Development Agency under the contract No. APVV-0520-10; by VEGA 2/0088/08; and by MNT-ERANET HANCOC.

REFERENCES

1. EN 843-1 Advanced Technical Ceramics: Determination of Flexure Strength, CEN, 2006.
2. Fett T., Munz D.: Eng. Fract. Mech. *69*, 1353 (2002).
3. Fett T., Ernst E., Munz D.: J. Mater. Sci. Lett. *21*, 1955 (2002).
4. Skočovský P.; Bokůvka O., Palček P.: *Materials Science*; kap. 5, s. 268. EDIS, Žilina 1996.
5. Alfredsson B., Olsson M.: Fatig. Fract. Eng. Mater. Struct. *22*, 225 (1999).

L. Hegedüsová, L. Ceniga, and J. Dusza *(Institute of Materials Research, Slovak Academy of Sciences, Košice, Slovak Republic):* **Contact Strength and Crack Formation in Monolithic SiC and $MoSi_2$**

The paper deals with a determination of contact strength of monolithic ceramic materials (SiC, $MoSi_2$) using rollers or spheres. SiC exhibits multiple cone cracks and high contact strength during the test between spheres. In contrast to SiC, the $MoSi_2$ ceramics behaves as a quasi-plastic material and exhibits median crack formation during the contact test by spheres, which is a reason of lower contact strength and higher Weibull modulus. The contact strength between rollers are similar to bending strength of both materials. The Fett's theory which was suggested for brittle (ceramic) materials is shown to be also valid for quasi-plastic materials. In case of ceramic materials with large processing flaws, this theory can not be considered.

VICKERS INDENTATION FRACTURE TOUGHNESS OF HVOF SPRAYED WC-BASED COATINGS

ŠÁRKA HOUDKOVÁ[a]*, OLGA BLÁHOVÁ[a], FRANTIŠEK ZAHÁLKA[b], and MICHAELA KAŠPAROVÁ[b]

[a] New Technologies Research Centre, University of West Bohemia, Univerzitní 8, 306 14, Plzeň, [b] ŠKODA VÝZKUM s.r.o, Tylova 51, 30000, Plzeň, Czech Republic
houdkov@ntc.zcu.cz

Keywords: HVOF, coating, IFT, WC-Co

1. Introduction

The high hardness and the resistance against the spreading of cracks are crucial properties of all kinds of materials, intended as wear resistant. While hardness is a well known and easily measured parameter, the measurement of fracture toughness still remains rather problematic in the case of coating materials. In the paper, fracture toughness of the HVOF sprayed WC-12%Co and WC-17%Co coating was evaluated by the Vickers indentation test in dependence on used load. The applicability of using different equations is discussed with respect to the size indentation effect of IFT.

2. Experimental

The WC-Co coatings were sprayed by the HVOF TAFA JP5000 spraying equipment onto a grid blasted steel surface, using a spraying procedure standard in ŠKODA VÝZKUM s.r.o. The thickness of the coatings varied from 350 to 400 μm. The cross sections of the samples, embedded in an epoxy resin, were mechanically grinded and polished using the Struers automatic polishing machine. The CSEM Scratch Tester, equipped with the Vickers indentor, was used to make the indentations in to the coatings cross sections. The 25, 50, 75, 100, 125, 150, 175 and 200 N loads were used, for each load 16–20 indents were made in dependence on their size. The space between the individual indents equaled at least 3 indents diagonal to avoid their mutual affecting.

The lengths of indents diagonals, as well as the lengths of cracks (Fig. 1), were measured by NICON EPIPHOT 200 microscope with software LUCIA. For the K_{Ic} calculations, the equations proposed by Chicot[2] at condition of the Palmqvist, Intermediate and Radial-median cracking mode were used:

For Radial-median cracks:

$$K_{Ic(R-M)} = 0{,}0154\left(\frac{E}{H_v}\right)^{1/2}\left(\frac{L}{c^{3/2}}\right) \qquad (1)$$

For Palmqvist cracks:

$$K_{Ic(P)} = 0{,}0089\left(\frac{E}{H_v}\right)^{2/5}\left(\frac{L}{al^{1/2}}\right) \qquad (2)$$

For Intermediate cracks:

$$K_{Ic(M-M)} = (0{,}0074 - 0{,}0043q)f\left(\frac{E}{H_v}\right)\frac{L}{a^q c^{1{,}5-q}} \qquad (3)$$

where L is the used load [N], E is the elastic modulus, Hv is the Vickers hardness, and q is the coefficient, developed by Chicot[2], involving the Mayers low of indentation size effect.

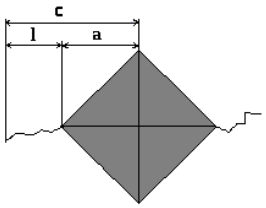

Fig. 1. **Schematic picture of the Vickers indent with cracks spreading in the anisotropic microstructure thermally sprayed coatings**

While in the Ponton-Rolings work[1], the Palmqvist and Radial-median cracking mode was recognized according to ratio c/a (c/a < 2.8 for Palmqvist cracks and c/a > 2.8 for Radial-median cracks), Chicot[2] recommended using the experimental slope of the linear representation of ln c versus ln L. If it corresponds to 2/3, Equation 1 should be used, if it corresponds to 2(1−1/n), where n is the Meyer's index characterization of the Indentation Size Effect, Equation 2 should be used. If none of the theoretical and experimental slopes corresponds, the equation for intermediate cracking mode should be used.

The E/H ratio used in this work was determined by the MTS Nanoindentor as an average value of the E/H ratio in the range defined from the depth of indentation 2–8 μm. The used E/H ratio values were 17.3 for WC-12%Co and 17.2 for WC-17%Co. The measurement of the E/H ratio of cermet HVOF coatings using dept-sensing indentation, realized at NTC ZČU, is described in[3].

3. Results and discussion

The results of K_{IC} calculations are summarized in the Fig. 2, 3 and 4. In the case of WC-12%Co the transition between he Palmqvist and Radial-median cracks according the coandition of c/a ~ 2.5 is at indentation load 75 N, in the case of WC-17%Co at 125 N. It means that for lower loads, the Eq. (*1*) should be used, while for higher loads the Eq. (*2*) is

proper. From the experimental data it is clearly understood, that the K_{IC} calculated according Eq. (*1*) and (*2*) are load dependent in the same manner as the Vickers microhardness. Incorporating the Mayer index to the K_{IC} equation, the load dependance dissolved. The K_{IC} value is constant accross all range of used load and the unique average value can be determined, which is not possible to do for K_{IC} determined according Eq. (*1*) and (*2*). On the other hand, the value of K_{IC} (M-M) is very low due to high value of the q index.

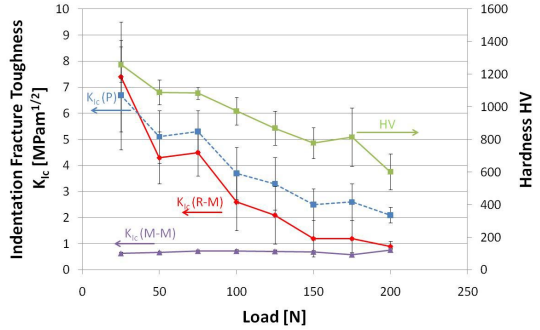

Fig. 2. **The load dependence of measured HV and K_{IC} of WC-12% Co coating**

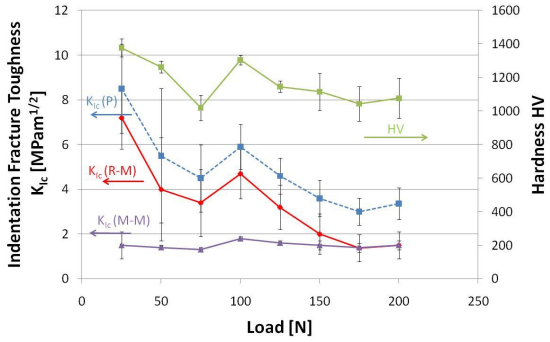

Fig. 3. **The load dependence of measured HV and K_{IC} of WC-17% Co coating**

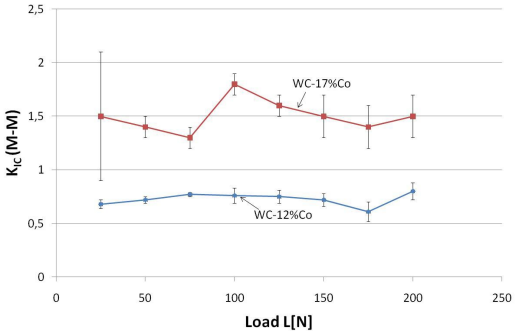

Fig. 4. **Comparison of K_{IC} (M-M) results for WC-based coatings**

Comparing the K_{IC} values of the two WC-based coatings with different Co content, the lower fracture toughness of coating with lower Co content met the expectation. The unique average value of K_{IC} (M-M) from all measurement without the respect to used load are 0.72 ± 0.05 for WC-12% Co and 1.53 ± 0.15 for WC-17%Co.

4. Conclusion

The study of WC-based HVOF coatings Vickers fracture toughness showed a strong load dependence of K_{IC} values, calculated according to usually used equations. Distinction on the cracks on Palmqvist or Radial-median according to the rule of c/a ~ 2.5, or according to the slope of the c – L dependance is useless regarding the selection of the proper K_{IC} equation. The equation, proposed by Chicot[2] for intermediate cracking mode is load independent in the all range of used load. It enables to determine one unique K_{IC} value, comparable with measurement at different loads. The differnece between the coatings with different Co content match the expectations – the K_{IC} of WC-17%Co is higher compare to K_{IC} of WC-12%Co. The used method enables to evaluate the fracture toughness of thermall sprayed coatings and represent the influence of their microstructural features. The unique load-independent K_{IC} value is favourable for comparing the results measured at different load conditions.

This work was supported by the Ministry of Industry and Trade of the Czech Republic no. FT-TA5/07.

REFERENCES

1. Ponton C. B., Rawlings R. D.: Mater. Sci. Technol. *5*, 865 (1989).
2. Chicot D., Duarte G., Tricoteaux A., Jorgowski B., Leriche A., Lasage J.: Mater. Sci. Eng., *A 257*, 65 (2009).
3. Houdková Š., Bláhová O., Zahálka F.: Chem. Listy *103*, s318 (2009).

Š. Houdková, O. Bláhová, M. Kašparová, and F. Zahálka *(NTC ZČU, ŠKODA VÝZKUM s.r.o.):* **Vickers Indentation Fracture Toughness of HVOF Sprayed WC-Based Coatings**

The Vickers indentation fracture toughness of HVOF sprayed WC-12%Co and WC-17%Co coatings was evaluated in dependence on used load. Three different equations for K_{IC} value vas used and their results compared. It was shown, that while usually used equations for both Radial-median and Palmqvist crack modes are strongly dependent on used load, the equation for intermediate cracking mode incorporating the Mayer index, is load-independent and enable the comparison of results.

ANALYSIS OF PRECIPITATION PROCESSES IN AUSTENITIC CAST STEEL WITH NIOBIUM

RENATA CHYLIŃSKA*, MAŁGORZATA GARBIAK, PERIKLIS CHRISTODOULOU, and BOGDAN PIEKARSKI

Institute of Materials Science and Engineering, West Pomeranian University of Technology, Piastow 19 Av., 70 -310 Szczecin, Poland
Renata.Chylinska@zut.edu.pl

Keywords: austenitic cast steel, microhardness, precipitation

1. Introduction

The creep resistance of austenitic cast steel is raised, among others, by addition of niobium introduced to its chemical composition. The addition of niobium not only changes the phase composition but also the course of the precipitation processes.

The paper presents an example of practical application of the results of random microhardness measurements in evaluation of changes that take place in the microstructure of niobium-stabilised Ni-Cr cast steel during aging.

2. Theoretical and experimental results

Microhardness measurements taken at different points in the specimen (a metallographic polished section) enable plotting the hardness density distribution, which reflects local microstructure of the examined material. Once determined, this distribution will prove the presence of different structural constituents[1].

The interpretation of the results of measurements depends largely on the size of an indentation mark left by the hardness tester, referred to the geometry of alloy microstructure (Fig. 1). For example, indentations of an area larger than the size of the precipitates present in alloy matrix represent an "average" matrix microhardness and volume fraction of the precipitates (Fig. 1a). In the case of indentations smaller than the size of the precipitates, the measurements can be used in evaluation of the actual volume fraction of these precipitates.

The microhardness density distribution for a three-phase material is shown in Figure 1b. The area under the curves corresponds to the content of individual phases or microstructural constituents; their sum equals a unity. If hardness was measured with an indenter leaving in the examined material an indentation mark much larger than that shown in Fig. 1a, the measurement would reflect only the properties of a microstructure consisting of: A – matrix, B – primary carbides, and C – secondary carbides.

Specimens for test were made from cast steel of the chemical composition shown in Table I.

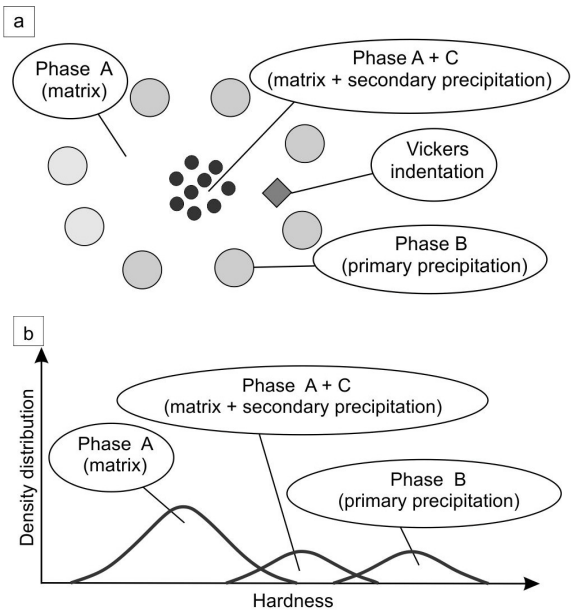

Fig. 1. **Microhardness density distribution for a three-phase material and indentation size reflecting the size of the precipitates: a) scheme of the microstructure, b) theoretical microhardness density distribution;** A – matrix, B – primary carbides, C – secondary carbides

Table I
Chemical composition of cast steel, wt.%

C	Si	Mn	Cu	P	S	Cr	Ni	Nb
0,31	1,91	0,96	0,22	0,015	0,010	18,2	29,3	1,84

Cast steel was melted in an open induction furnace and poured into sand moulds[2]. The specimens cut out from the ingots were subjected to annealing in the air at a temperature of 600 °C for 10, 100 and 500 hours.

Microhardness was measured on unetched metallographic sections using Vickers measuring technique (10 G, 10 s). The measurements were taken at random, applying each time a grid of 200 measuring points distributed at even spacing along the three parallel straight lines.

At 600 °C, the cast steel microstructure is composed of an austenitic matrix with large precipitates of NbC carbides and small precipitates of $M_{23}C_6$[2] type chromium carbides (Fig. 2).

The microhardness density distribution in specimen after annealing for 500 hours is shown in Fig. 3. Fig. 4 shows microhardness density distribution obtained in the alloy matrix after annealing for 10 and 100 hours.

Hardness distributions were obtained by averaging the measurements taken in the vicinity of a given point (25 neighbouring points).

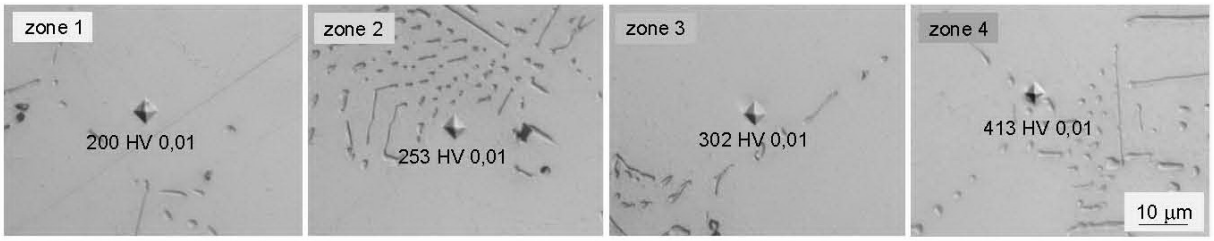

Fig. 2. **Microstructure of cast steel, examples of indentations − 600 °C/ 500 hrs** (microhardness density distribution results see Fig. 3)

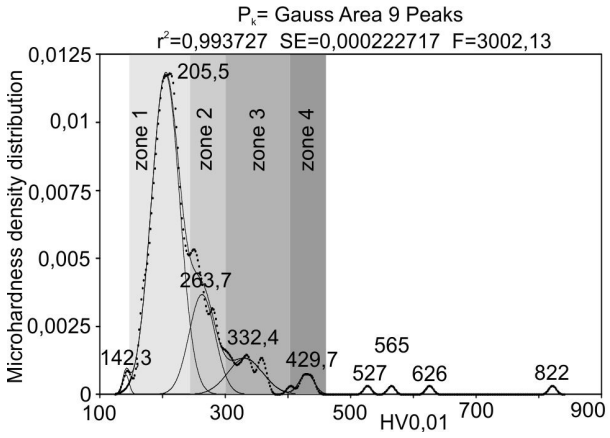

Fig. 3. **Microhardness density distribution results presented in graphic form − 600 °C/ 500 hrs**

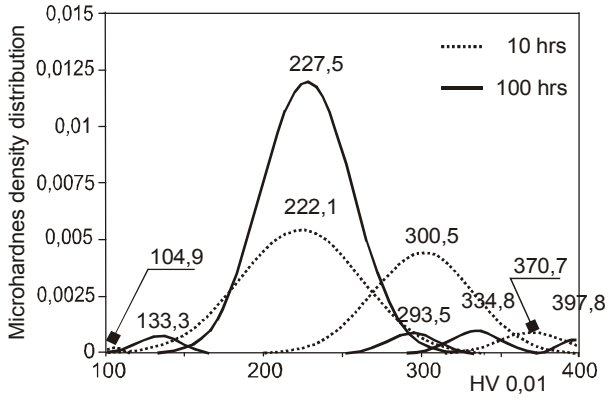

Fig. 4. **Graphic representation of the results of measurements of the microhardness HV density distribution in cast steel matrix**

Processing of the results was done on an S-Plus[3] software. Next, the individual constituents were determined using a PeakFit[4] programme.

The dotted line (Fig. 3) represents the hardness density distribution obtained in the examined specimen. The solid line is the sum of distributions identified from an analysis of the dotted line. Numbers above the peaks represent the hardness levels at which the peak reaches its maximum.

Each of the peaks marked in zones 1–4 (see Fig. 3) and peaks shown in Fig. 4 corresponds to a distribution of the matrix hardness, which depends on the number of the secondary precipitates and on their size distribution. The sum of the areas under the four peaks is equivalent to a volume fraction of the matrix in the alloy. Other peaks in Fig. 3 correspond to the areas where the primary precipitates occur.

During annealing the fraction of secondary precipitates in the matrix changes and leads to the increase or decrease of the area size under the individual peaks (see 10 hrs and 100 hrs of annealing, Fig. 4).

3. Conclusions

Studies have confirmed that the results of random microhardness measurements can be effectively used to trace changes in the cast steel microstructure during aging.

REFERENCES

1. Christodoulou P., Garbiak M., Piekarski B.: Mater. Sci. Eng., *A457* (2007).
2. Garbiak M.: Estimated effect of niobium and titanium on structure and mechanical properties of 30Ni-18Cr cast steel, *PhD thesis*, SUT-Szczecin, Poland, 2006 (in Polish).
3. Chambers J. M., Hastie T. J.: Statistical models in S. Chapman & Hall Inc. 1993.
4. http://www.sigmaplot.com/products/peakfit/peak%20fitting.php.

R. Chylińska, M. Garbiak, P. Christodoulou, and B. Piekarski *(Institute of Materials Science and Engineering, West Pomeranian University of Technology in Szczecin, Poland):* **Analysis of Precipitation Processes in Austenitic Cast Steel with Niobium**

The paper presents an example of how to process the results of the random HV 0.01 microhardness measurements taken in 30Ni-18Cr-type cast steel with 1.84 % niobium annealed at a temperature of 600 °C. Studies have proved that, in most cases, the microhardness measurements reflect the microhardness of a structure that is a mixture of matrix and secondary precipitates or of matrix and primary precipitates.

DEGRADATION OF IRON SUPERALLOYS H39WM CATALYTIC PIPE IN STEAM REFORMING CONDITIONS

WALENTY JASIŃSKI*

West Pomeranian University of Technology in Szczecin, Al. Piastów 17, 70-310 Szczecin, Poland
walenty.jasinski@zut.edu.pl

Keywords: superalloys, reforming, phase transformation

1. Introduction

Primary Steam Reforming Furnaces are used to convert mixture of hydrocarbons and steam into hydrogen-rich gases which can be used for the production of ammonia, methanol, etc. The process gas passes under pressure via vertical tubes filled with catalyst. Because high temperature is required to maintain the required chemical reactions, the tubes are heated up to 660 ÷ 850 °C by burners in a large furnace, which results in temperature gradients along the tube (Fig. 1). The internal pressure of the process gas is simultaneously maintained in the range 2.75 ÷ 4.15 MPa (ref.[1]).

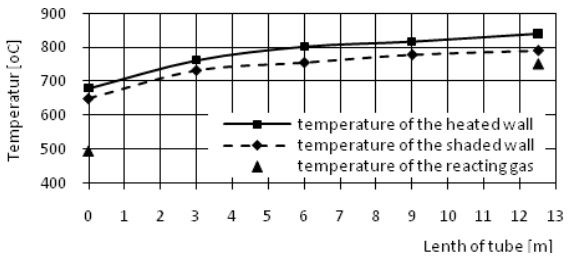

Fig. 1. **Distribution of temperature along of catalytic tube**

The tubes used in steam reforming with the length of 13 meters were assembled together by welding of segments. The segments of tubes were made by centrifugal casting of austenitic chromium-nickel cast steels stabilized with additions of niobium, titanium and zirconium and rare elements[2]. The stability of dendritic microstructure, microsegregation as well as the dispersion of carbides undergo changes during exploitation. The long-lasting influence of elevated temperature causes precipitation of the intermetallic phases in the austenitic matrix. This results in a degradation of mechanical properties of pipe material as well as in enhancement of creep process. Two important types of precipitates that can occur are carbides and topologically closed-packed (TCP) phases. TCP phases, particularly σ and G phases, are generally undesirable[1,2]. Therefore the chemistry of the second, third, and forth generation superalloys were designed in such a way that σ and G phase do not form[2]. The aim of the current work is to investigate the changes in the microstructure and properties of H39WM catalytic pipe after 88000 h exploitation.

2. Experimental procedure

The investigations were carried out on a pipe with the size of ϕ 140 × 12 mm made by centrifugal casting from H39WM (25 % Cr, 35 % Ni, 0.85 % Nb, 0.15 % Ti) superalloy. The test samples taken from the inlet area and 1.65, 3.5, 6.0, 8.5, and 12.5 m apart from the inlet, were subjected hardness testing, metallographic and X-ray examinations. The Brinell hardness measurements were conducted on HPO 250 hardness tester (Heckert VEB Werkstoffprüfmaschinen) and MIC 10 portable hardness tester (Krautkramer) in accordance with EN ISO 6506-4:2005 standard. Metallographic studies were performed on cross sections perpendicular to tube axis using light (Nikon EPIPHOT 200) and scanning electron (Jeol JSM-6100 with EDS LINK ISIS 300) microscopy. The polished samples have been etched by Murakami solution which dyes brown σ phase and chromium carbide, while MC carbides type get bright tint.

3. Results

Metallographic observations of the material in as-cast state showed austenitic matrix with a network of eutectic carbides precipitated initially during the solidification process and distributed at the dendrite and grain boundaries with fine-grained eutectic (Fig. 2). Dendritic columnar austenite grains were oriented almost perpendiculary to the tube walls.

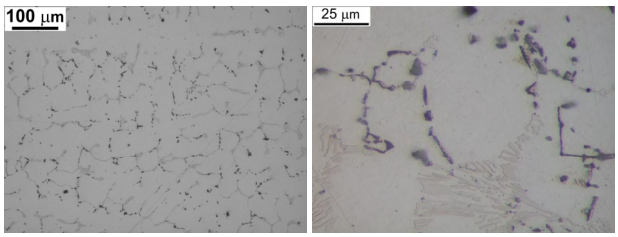

a b

Fig. 2. **Microstructure of superalloy H39WM - as cast, Murakami etched**

X-ray analysis in as-cast state shows the presence of austenite and eutectic NbC and $(Cr,Fe)_{23}C_6$ type carbides, which agrees with the findings in Fe-Ni-Cr alloys[1,3]. Some changes in the hardness of H39WM were observed after 88000 h exploitation due to disappearance of dendrite structure and precipitation, spheroidization and coagulation of intermetallic phases (Figs. 3÷5). Microstructure and hardness obtained from both testers (HPO and MIC 10) show good correlation with local temperature of the pipe in service.

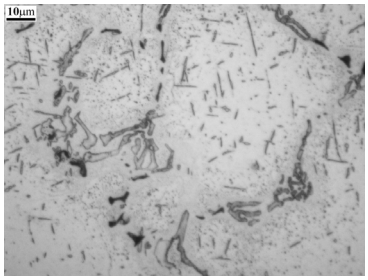

Fig. 3. **Microstructure of superalloy H39WM at a distance of 1,65 m from the inlet after 88000 h of work, Murakami etched**

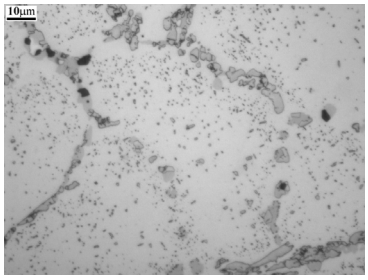

Fig. 4. **Microstructure of superalloy H39WM at a distance of 8,5 m from the inlet after 88000 h of work, Murakami etched**

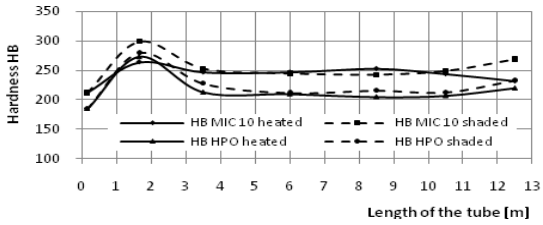

Fig. 5. **The Brinell hardness along the catalytic pipe length**

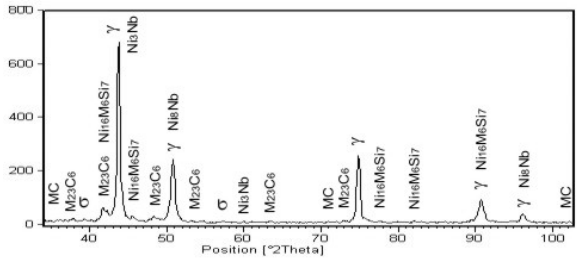

Fig. 6. **The diffractogram of superalloy H39WM at a distance of 8,5 m from the inlet after 88000 h exploitation**

The fine arrays of secondary carbides σ(FeCr) and G ($Ni_{16}M_6Si_7$) where M = Nb, Ti, Zr, precipitated heterogeneously within the dendrites and grains from as cast supersaturated matrix. The needle-shaped and globular precipitates of σ phase and fine secondary carbides G phase were visible inside the grains of austenite and at boundaries containing eutectic. An EDX analysis of σ phase precipitates revealed significant amount of chromium, lower than in matrix amount of iron, and a slightly higher amount of silicon[2,3]. X-ray diffraction on samples after 88000 h exploitation confirmed the presence of NbC, $M_{23}C_6$, σ and G phases (Fig. 6).

4. Conclusions

The use of H39WM superalloys under elevated temperatures causes the changes in microstructure toward more equilibrium state. These changes depend on the temperature and time of exploitation and they influence on the mechanical properties of the tube. The highest hardness and content of intermetalic phases in a tube oparating for 88000 h were found in the zone 1.65 m from the inlet. However, needle shaped σ phase precipitation did not occur in the region working at a temperature above 815 °C. The transformation of NbC carbides into Ni_3Nb and into G phases ($Ni_{16}M_6Si_7$), cause hardness reduction and possibility of creep initiation.

REFERENCES

1. Jones J. J.: *Improved Reformer Furnace Efficiency by Changing the Tube Alloy*, Technical papers, Paralloy Limited.
2. Mikułowski B.: *Heat resistance alloys – Superalloy*, Publication of AGH, Kraków 1997 (in Polish)
3. Jasiński W.: Adv. Manufacturing Sci. Technol. *30*, 41 (2006).

W. Jasiński (*West Pomeranian University of Technology in Szczecin, Poland):* **Degradation of Iron Superalloys H39WM Catalytic Pipe in Steam Reforming Conditions**

The hydrogen to ammonia synthesis in the chemical plants occurs in a process of endothermic thermal-catalytic decomposition of methane with water steam. The process is carried out in reformer‘s pipes made from austenitic cast steel with nickel catalyst under pressure up to 4,0 MPa and temperature up to 780 °C. The long-lasting influence of increased temperature causes the spheroidization precipitation of the intermetallic phases in alloyed austenite matrix. The stability of casting dendrite microstructure disappears. This results in a decrease of the mechanical properties of the pipe material as well as in the enhamcement of creep. Microstructure and properties show good correlations with the local temperature of the pipe.

CHARACTERISTICS OF DUPLEX SYSTEM CrN COATING ON PLASMA NITRIDED STAINLESS STEEL 316L

ZDENĚK JOSKA*, JAROMÍR KADLEC MIROSLAV POSPÍCHAL and Q. DUNG TRAN

Department of Mechanical Engineering, University of Defence in Brno, Kounicova 65, 662 10 Brno, Czech Republic
joska.zdenek@email.cz

Keywords: Stainless steel, duplex coating, adhesion, chemical composition, mechanical properties

Introduction

Austenitic stainless steels are very attractive and important materials, which are used in many industrial applications due to combination of good corrosion resistance, cryogenic properties, high temperature strength, ductility and biocompatibility. However, stainless steels have low hardness and poor abrasive wear which limit their application[1–3]. Enhancing the surface hardness of austenitic stainless steels is at present the subject of intensive research. Plasma nitriding is one of various surface treatment techniques which improve surface hardness without decreasing corrosion resistance[1,2,5,6]. An interstitial supersaturating metastable phase called S phase, is generated by this technique. The S phase has very high hardness, good wear resistance and good corrosion resistance. Thin hard and superhard PVD coatings were developed to protect substrates against wear and corrosion[2,4,5].

CrN coating is known for its high ductility and fracture toughness, lower coefficient of friction and excellent resistance to oxidation and corrosion. The mechanical properties of these thin coatings are reduced when they are applied on stainless steel. To overcome this limitation, thermochemical treatments prior to the hard-coating deposition were undertaken[4,5]. This duplex surface treatment significantly improves the surface and sub-surface properties, which were unobtainable through any individual technique.

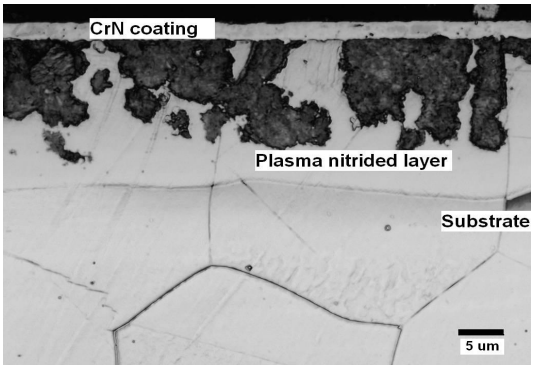

Fig. 1. **The chemically etched (by aqua - regia) cross-section showing the morphology of the duplex coating in a confocal micrograph**

2. Experimental material and surface treatment

Samples of an AISI 316L stainless steel in the untreated state had the diameter of 30 mm and a thickness of 7 mm. The substrate had a microhardness of about 230 HV. Before the plasma nitriding process, the samples were wet ground using silicon carbide paper from 120 down to 4000 grit and finally polished with 1 μm diamond paste. Plasma nitriding was carried out in PN 60/60 Rübig equipment with these parameters: temperature of 510 °C, duration 6 h, pressure 320 Pa, gas mixture of H_2 flow 8 l min^{-1} and N_2 flow 24 l min^{-1}, pulse length 100 μm, voltage 520 V. The pre-nitrided samples were afterwards coated with CrN coatings in PVD industrial equipment, CrN coatings were deposited on the specimens in PLATIT Pl 1000 equipment by cathodic arc evaporation system using 2 chromium targets. The deposition system was installed with a three-fold substrate rotation mechanism to produce a uniform coating on the surface of the samples. The deposition procedure included 20 min of Ar plasma ion cleaning and 15 min of Cr plasma ion cleaning. During the deposition only nitrogen was fed to the chamber at a pressure of 0.8 Pa. The temperature of deposition was held at 450 °C. Applied substrate DC bias was 50 V. Arc current at the Cr target was 160 A.

3. Experimental methods

Depth profiles of plasma nitrided layer and PVD coatings were measured by GDOES/QDP method. GDOES measurements were performed in a LECO SA-2000. Calibration of nitrogen: JK41-1N and NSC4A standards. Confocal laser microscope LEXT OLS 3000 was used for observation of the cross section morphology of duplex coatings and craters after adhesion Rockwell tests. The surface hardness of duplex systems was evaluated by a Vickers microhardness test in a LECO automatic microhardness tester LM 247 AT. Adhe-

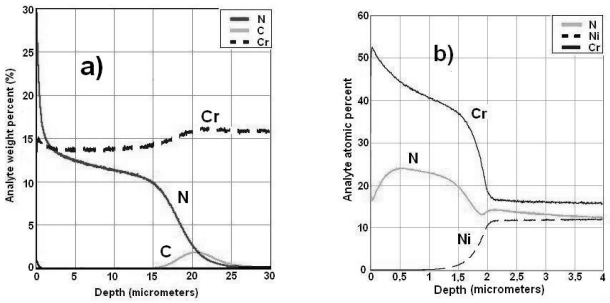

Fig. 2. **GDOES depth profile of a) plasma nitrided layer b) CrN coating on nitrided surface**

sion test was performed on the duplex coatings as a standard Rockwell test, while using a load of 150 kg and a diamond Rockwell indenter of 0.2 mm in diameter to assess the vertical adhesion of the coatings.

4. Experimental results

Fig. 1 shows an optical micrograph of a cross-section of the surface of an AISI 316L sample treated by a combination of a plasma nitriding and a PVD coating. The plasma nitriding process formed a nitrided layer of 25 μm thickness. The CrN coatings subsequently deposited by PVD have the thicknesses of 1.3 and 2.5 μm. Depth profiles of the plasma nitrided layer (Fig. 2a.) for both carbon and nitrogen are in good agreement with the proposed plasma treatment schedule. Carbon and nitrogen contents decrease along the layer depth (from surface to substrate). For carbon concentration there is a local maximum twenty micrometers from the surface. In the CrN coating on nitrided surface (Fig. 2b) constant nitride concentration was found in the coating between 20–15 at.% which gradually decreases in the substrate material in value 15 at.%. Indentation adhesion tests were performed by Rockwell indentation test (Fig. 4). The sample shows good adhesion in range HF1 and HF2, without any delamination of coatings. The surface hardness of duplex treated samples (Fig. 3) rapidly increased: the highest values 3400 $HV_{0.01}$ were found in the duplex treated sample with the CrN coating of 2.5 μm. The same coating deposited on non-treated surface reached only 1500 $HV_{0.01}$.

5. Conclusion

Duplex surface treatment consisted of deposition of a plasma nitrided layer and subsequently successful deposition of a CrN coating. The analysis carried out by using GDOES/QDP method was in a good agreement with observation of the metallographic cross-section and microhardness measurement. The thickness of the nitrided layer was 25 μm and microhardness values were around 1150 $HV_{0.05}$. The surface hardness of duplex coatings reached 3400 $HV_{0.01}$. Rockwell adhesion test shows that the plasma nitrided layer contributes to good adhesion of the CrN coating, which has then better adhesion than on a non-nitrided substrate.

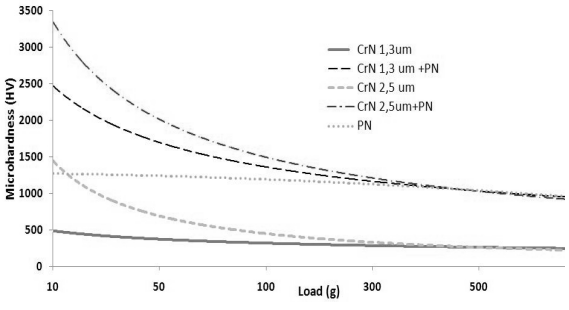

Fig. 3. **Surface microhardness of treated samples**

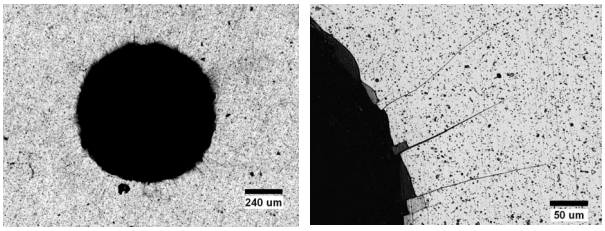

Fig. 4. **Rockwell indentation test of duplex coating**

The work was supported by a research project by Ministry of Defence of the Czech Republic, the project No. MO0FVT 0000404 and Specific research Modern materials in special technology.

REFERENCES

1. Lo K. H., Shek C. H., Lai J. K. L.: Mater. Sci. Eng. R: Reports *65*, 39 (2009).
2. De Las Heras E.,. Egidi D. A, Corengiea P., et al: Coat. Technol. *202*, 2945 (2008).
3. Czerwiec T., Renevier N., Michel H.: Surf. Coat. Technol. *131*, 267 (2000).
4. Jelinek M., Kocourek T., et al: Laser Physics *15*, 211 (2005).
5. Joska Z., Pospichal M., et al: Chem. Listy *104*, 322 (2010).
6. Kadlec J., Dvorak M.: Strength Mater. *40*, 118 (2008).

Z. Joska, J. Kadlec, M. Pospíchal, and Q. Dung Tran *(University of Defence Brno, Czech Republic):* **Characteristics of Duplex System CrN Coating on Plasma Nitrided Stainless Steel 316L**

A combination of plasma nitriding and PVD coating as surface treatment has been used to improve material properties like hardness, without an influence on the corrosion performance. In this article a duplex treatment was investigated. Duplex treatment consists of plasma nitriding and deposition of a CrN coating on AISI 316L stainless steel. This study covers the microstructure, chemical composition and mechanical properties of this duplex system. Chemical composition and depth profiles were investigated by GDOES methods, microstructure was explored by confocal microscopy, adhesion by the indentation test and surface hardness was measured by microhardness testing. Analysis and discussion of the results showed that combination of these two processes improves considerably the surface hardness.

STUDY OF MICROSTRUCTURE AND MECHANICAL PROPERTIES OF ALUMINUM ALLOY AlSi7Mg0.6 AFTER DIFFERENT COOLING METHODS

MARTIN JULIŠ*, SIMONA POSPÍŠILOVÁ, JOSEF ZAPLETAL, and TOMÁŠ PODRÁBSKÝ

Brno University of Technology, Technická 2896/2, 616 69 Brno, Czech Republic
julis@fme.vutbr.cz

Keywords: AlSi7Mg0.6, solidification rate, heat removal rate, controlled cooling, image analysis, DAS

1. Introduction

Until now it was routine in the design of aircraft components to produce the assembly compositions of several separate elements, which are then joined into one unit but at the price of the waste material more than 95 % in their manufacture. Therefore, the modern trend of production mentioned units is the precision investment casting[1,2], which puts high requirements on the quality and properties of common materials.

The aim of the present work is to verify the effect of solidification rate and heat removal rate from the cast during crystallization (cooling rate) on the structure and local mechanical properties of the alloy AlSi7Mg0.6.

2. Experimental details

The plate tensile test specimen (see white arrow in Fig. 1) were cast by method of precision investment casting from alloy AlSi7Mg0.6. The chemical composition of experimental material corresponds to the material standard. The ceramic shell was cooled after casting in several ways; cast A (casting and free cooling in the casting field); cast B (casting and controlled cooling in the casting field); cast C (casting and controlled intensive cooling in the casting field); cast D (casting in the furnace in isolation and cooling as the sample B). Then, the castings were heat treated to T6 condition (solution annealing at 530 °C/8 h/water and age hardening at 160 °C/8 h).

The yield strength $R_{p0.2}$, the ultimate tensile strength R_m and elongation A_{20} were obtained using universal tensile test equipment TIRA TEST 2300. The plate tensile test specimen with rectangle cross section (4 × 10 mm) and length L_0 (35 mm) were used. The microstructure was observed by light microscopy (LM). The influence of cooling rate on microstructure was studied by DAS (dendritic arm spacing) measurements and porosity evaluation. Both were obtained by image analysis with software Olympus Analysis Five.

Fig. 1. **Wax model for casting of the test specimens**

3. Experimental results

The dendritic microstructure of specimen A is shown in Fig. 2. The casting defects, most often pores, were occured in specimen sections.

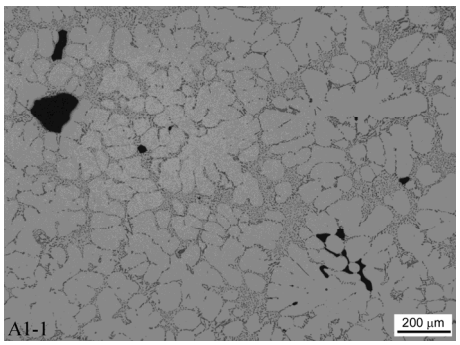

Fig. 2. **Microstructure of sample A (casting + free cooling), LM**

The DAS values were obtained by observing 10 different places from each sample and each field of view were evaluated by image analysis. There were measured up to 300 individual dendritic spaces (of secondary dendritic arm) in each field of view. The DAS values were obtained from median of the total measurements of each sample. The microstructures of samples A–D were similar, but size of DAS and number of pores were different. The results of DAS measurements are shown in Table I.

The indicator of the quality of the castings is the porosity evaluation. The maximum pore size, mean pore size, elon-

Table I
The results of DAS measurements [µm]

Sample A	Sample B	Sample C	Sample D
66.68	50.22	43.69	52.37

gation, the shape of pores and the average area of pores were observed using image analysis by parameters as maximal diameter, mean diameter, elongation, shape factor and area (see Fig. 3).

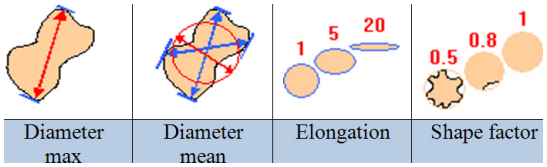

Fig. 3. **Graphic display of the parameters for porosity evaluation**

The maximum pore size (diameter max.) is always the maximum value of the biggest pore [μm] found on observed sample. Other values (diameter mean, elongation etc.) correspond to median. The average pore volume (porosity) is expressed as the ratio of the area of all measured pores to area of the field of view in percentage. The results of porosity evaluation are shown in Table II.

Table II
The results of porosity evaluation

Sample	Diameter max	Diameter mean	Elongation	Shape factor	Porosity
	[μm]	[μm]	[-]	[-]	[%]
A	308.55	23.28	1.78	0.64	1.68
B	163.26	21.80	1.40	0.66	0.70
C	207.56	17.93	1.82	0.67	0.54
D	206.87	15.96	1.66	0.55	0.68

Table III
Comparison of mechanical properties, DAS and porosity

Sample	A_{20}	R_m	$Rp_{0.2}$	DAS	Porosity
	[%]	[MPa]	[MPa]	[μm]	[%]
C	4.6	300	241	43.69	0.54
D	4.2	287	235	52.37	0.68
B	3.9	290	239	50.22	0.70
A	2.4	276	234	66.68	1.68

Futhermore, the mechanical properties of specimens after different cooling methods were obtained. Table III presents the results of mechanical properties after static tensile tests. The engineering stress – strain curve is shown in Fig. 4. The origins of particular curves are shifted by reason of clarity.

4. Discussion and summary

On account of microstructure and evaluation of DAS and porosity of all samples it was found, the best results were performed by casting and controlled intensive cooling in the

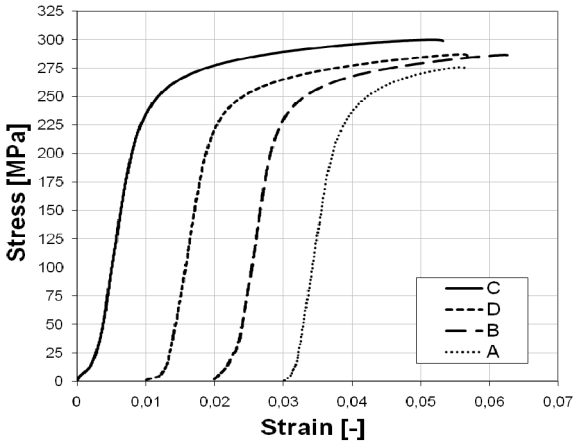

Fig. 4. **Engineering stress – strain curve after tensile tests**

casting field (casting C); the smallest values of DAS were obtained. Beyond, the biggest values of DAS was achieved by A cooling method.

By comparison of particular DAS values with smallest deviations were also proved the positive effect of method C on uniform size of dendrites in casting. The bigest scatter of DAS values were found in method A.

The minimum porosity (0.54 %) was found in specimen C. The satisfactory results were performed also by cooling methods B and D. The biggest porosity was found out in specimen A.

The results of mechanical properties after static tensile tests correspond to the results obtained from the microstructure observation and also DAS and porosity evaluation. The optimal combination of mechanical properties was achieved by cooling method C.

Research was supported by Ministry of Education, Youth and Sports of the Czech Republic (projects 1M2560471601 and MEB0810123) and Brno University of Technology (project of specific research FSI-S-10-46).

REFERENCES

1. Michna Š., Lukáč I., Očenášek V.: *Encyklopedie hliníku*, 720 p. Adin s.r.o., Prešov 2005.
2. Zapletal J., Věchet S., Kohout J., Liškutín P.: *Communications* 1/2009, pp.17–21.

M. Juliš, S. Pospíšilová, J. Zapletal, and T. Podrábský *(Brno University of Technology, Czech Republic):*
Study of Microstructure and Mechanical Properties of Aluminum Alloys AlSi7Mg0.6 after Different Cooling Methods

The paper deals with the evaluation of microstructure using image analysis and mechanical properties of aluminum alloy AlSi7Mg0.6 after different cooling methods. The aim of the present work is to verify the effect of solidification rate and cooling rate on the structure and local mechanical properties of the alloy AlSi7Mg0.6.

STUDY OF SURFACE RELIEF EVOLUTION IN CYCLICALLY STRAINED SUPERALLOY IN738LC USING ADVANCED EXPERIMENTAL TECHNIQUES

MARTIN JULIŠ[a]*, DAVID KUSMIČ[b], SIMONA POSPÍŠILOVÁ[a], STANISLAV PRŮŠA[a], KAREL OBRTLÍK[c], JIŘÍ DLUHOŠ[d], and TOMÁŠ PODRÁBSKÝ[a]

[a] *Brno University of Technology, Technická 2896/2, 616 69 Brno,* [b] *University of Defence, Kounicova 65, 602 00 Brno,* [c] *Institute of Physics of Materials, Academy of Sciences of the Czech Republic, Žižkova 22, 616 62 Brno,* [d] *DemoLab and Applications, Tescan, s.r.o., Libušina třída 21, 623 00 Brno, Czech Republic*
julis@fme.vutbr.cz

Keywords: Inconel 738LC, low cycle fatigue, intrusion, extrusion, surface relief, slip marking

1. Introduction

From the previously published works[1,2] the surface relief inside the persistent slip markings (PSMs) is mainly characterized by the existence of isolated deep and narrow intrusions and slight hilly extrusions in the case of nickel-base superalloys. However, much of the PSMs show only a weak surface relief.

In order to study initial stages of surface relief formation and evolution, low cycle fatigue tests were interrupted after 5, 15 and 35 cycles. Each interruption was followed by observation of the surface relief of specimens, using several techniques.

The main aim of the present work was to study surface topography in the early stages of fatigue damage and to compare results obtained with selected observation techniques.

2. Experimental details

The surface relief evolution within PSMs was observed on button-end cylindrical specimens (Fig. 1) of cast polycrystalline nickel base superalloy IN738LC after low-cycle fatigue at room temperature. Specimens were fatigued with a constant total strain amplitude (ε_a = 0.4 %) with fully reversed total strain cycle ($R_\varepsilon = -1$).

Specimens were cyclically loaded by a limited and predetermined number of cycles (5, 15, 35 cycles). After each test the surface relief was studied in the vicinity of a shallow scratch previously created on the surface in the central part of the specimen (see arrow in Fig. 1). The precisely marked locations were observed using the confocal laser scanning microscope LEXT Olympus OLS 3000 (CLSM) and scanning electron microscope TESCAN MIRA3 (SEM). The surface relief formed was also observed by AFM microscope – Nanosurf EasyScan2. The places for the detailed observation were chosen after 5 cycles when the first fine slip markings appeared.

Fig. 1. **The test specimen, the arrow shows area of observation**

3. Results

Fig. 2 shows SEM image with a detail of the surface relief after 5 cycles. The slip marking which intersects the scratch is indicated by the white arrow. The width of the slip marking is approximately 10 nm.

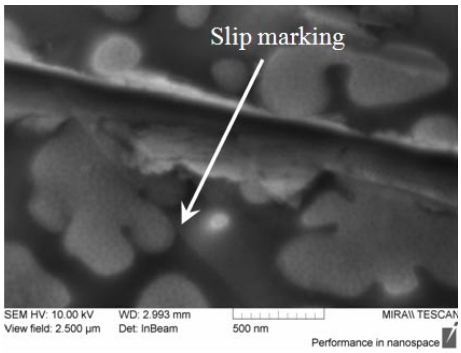

Fig. 2. **Detail of slip marking intersecting the scratch (SEM)**

Using the other observation techniques (CLSM and AFM) the slip marking could not be displayed at this stage of surface relief evolution. Very low width of PSMs and negligible surface relief are under the resolution of the techniques.

With the increasing number of cycles and associated increase in surface relief, CLSM and AFM could identify the slip markings. The CLSM image of the surface relief after 250 cycles is displayed in Fig. 3. PSMs lying amost perpendicularly to the previously created scratch are clearly visible. The detail of the examined area, marked by the black rectangle in Fig. 3, is shown in Fig. 4a after 10 cycles using AFM. Two PSMs can be seen perpendicularly to the auxiliary scratch. The white dash line perpendicular to the left PSM represents the section in which the surface profile was measured by AFM – see Fig. 4b. The arrow in Fig. 4b indicates a shallow intrusion in the profile. The intrusion reached a depth of 0.07 µm after 10 cycles.

PSM profiles were also measured by CLSM. In longitudinal profiles, the height and depth of the surface relief were measured in a plane perpendicular to the specimen surface parallel to the slip marking through its center. It was found that the generated slip marking contained a significant number of narrow isolated intrusions. With increasing number of cycles the intrusions deepened and interconnected.

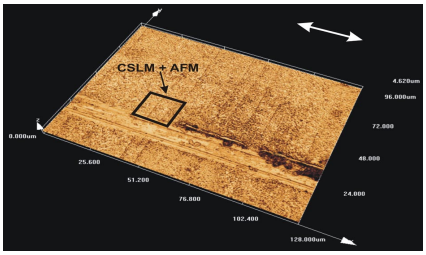

Fig. 3. **The surface relief after 250 cycles (CLSM). The area that was observed in detail is marked by a rectangle**

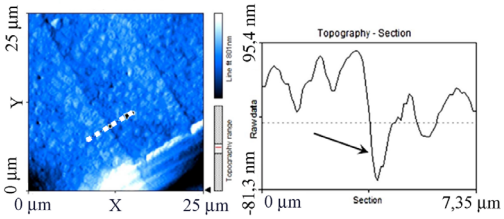

Fig. 4. a) **Detail of PSM on the surface after 10 cycles (AFM).** b) **The surface profile perpendicular to the PSM in the section marked with the white dash line in Fig. 4a. The black arrow indicates an intrusion**

Fig. 5 shows longitudinal profiles within the slip marking denoted by the white dash line in Fig. 4a after 120 and 250 cycles. Surface relief profile of the matrix is obtained in a section parallel to the slip marking in the distance of 2 µm from its center. The average intrusion depth after 120 cycles was 0.38 µm and after 250 cycles was 0.54 µm.

Deepening and widening of individual intrusions with increasing number of cycles is apparent in Fig. 5. Intrusions show a tendency to link and to form a long shallow intrusion or microcrack inside the slip marking. The present findings correspond to previously published data on stainless steells, as well as to models of initiation of fatigue microcracks[3].

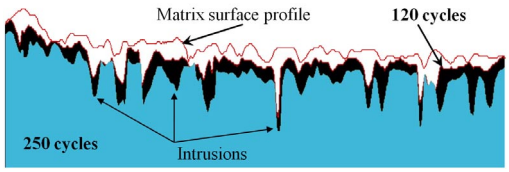

Fig. 5. **The longitudinal profiles of PSM (see left PSM in Fig. 4a marked by the white dash line) after 120 and 250 cycles**

4. Discussion and summary

The CLSM technique has proved an effective tool to obtaine quantitative data on the formation of surface relief and the initiation of fatigue microcracks. This technique is able to analyze detailed surface topography of observed slip markings, particularly the depth of intrusions. On the other hand, the measured values of fine intrusions and extrusions may differ from their actual size regarding to the limited resolution in X, Y axis. Tescan FEG-SEM technique was successfully applied to acquire qualitative data in initial stages of surface relief evolution. The other techniques can not be applied for reasons of limited resolution. On the other hand this method can not be used to evaluate quantitatively theintrusion and extrusion size. AFM is a proper technique to measure the height of extrusions. But tip dimensions result in the distorted extrusion shape and direct quantitative data on intrusions can not be obtained at all. Therefore, a combination of several imaging techniques is necessary to acquire more realistic dimensions of the surface relief inside the slip markings during cyclic straining.

Research was supported by Ministry of Education, Youth and Sports of the Czech Republic (project 2E08017 and MEB0810123 – mobility of CZ-SK researchers and project MO0FVT0000404), Czech Science Foundation (project 106/09/P522 and P107/11/2065), by Brno University of Technology (project of specific research FSI-S-10-46).

REFERENCES

1. Obrtlík K., Man J., Petrenec M., Polák J., in: *Fatigue 2002*, EMAS, West Midlands, United Kingdom, 2002, pp. 963–970.
2. Obrtlík K., Juliš M., Man J., Podrábský T., Polák J.: J. Phys.: Conference Series 240, IOP Publishing Ltd. 2010.
3. Polák J., Man J., Obrtlík K.: Int. J. Fatigue 25, 1027 (2003).

M. Juliš[a], D. Kusmič[b], S. Pospíšilová[a], S. Průša[a], K. Obrtlík[c], J. Dluhoš[d], and T. Podrábský[a] *([a] Brno University of Technology, [b] University of Defence, [c] Institute of Physics of Materials, [d] Tescan, s.r.o.):* **Study of Surface Relief Evolution in Cyclically Strained Superalloy IN738LC Using advanced Experimental Techniques**

The present paper is focused on the study of surface relief within persistent slip markings on cast polycrystalline nickel base superalloy Inconel 738LC during low cycle fatigue tests. The surface relief was studied using confocal scanning laser microscopy, scanning electron microscopy and atomic force microscopy.

INFLUENCE OF THE ADDITION OF SiC NANOPARTICLES ON THE HARDNESS AND ELASTIC MODULUS OF Si_3N_4 COMPOSITES MEASURED BY INDENTATION METHOD

MONIKA KAŠIAROVÁ*, PAVOL HVIZDOŠ, PETER TATARKO, and JÁN DUSZA

Institute of Materials Research, Slovak Academy of Sciences, Watsonova 47, 04001 Košice, Slovak Republic
mkasiarova@imr.saske.sk

Keywords: silicon nitride, ceramic nanocomposite, indentation, spherical indentor, hardnes and elastic modulus

1. Introduction

Although structural ceramics have a number of excellent properties, which allow their applications as parts and tools for different combinations of load and temperatures, wider application is still limited by their brittleness, low flaw tolerance and low reliability. One of the ways to improve their mechanical properties is the incorporation of nanoparticles into ceramic matrix.

Silicon nitride and silicon carbide are the promising materials for structural application because of their hardness, wear resistance, excellent high temperature strength and creep behaviour.

Newly developed materials are often prepared in limited quantities and shapes unsuitable for extensive mechanical testing. The utilization of a depth sensing indentation methods has introduced the advantage of load and depth measurement during the indentation cycle. This enables, using simple and fast measurement, to evaluate not only hardness, but also elastic modulus, yield behaviour, plasticity, the onset of other irreversible deformation processes such as cracking or pressure induced phase transformations, time dependent phenomena such as creep and recovery and the energy absorbed during indentation[1].

The aim of the study was to investigate some mechanical properties of Si_3N_4-SiC nanocomposites using depth sensing indentation.

2. Experimental materials and methods

Two kinds of composites with different amounts of SiC nanoparticles were prepared from the mixture of powders listed in Table I. Beside nanocomposites, also a monolithic Si_3N_4 was studied. Samples were hot-pressed under a specific heating regime, atmosphere and mechanical pressure regime at 1750 °C for 2 h. The details of the fabrication procedure are described elsewhere[2].

For the indentation study pieces with dimensions of 3×4 ×15 mm[3], polished to the 0.25 μm were used.

The nanoindentation tests, using the depth sensing technique (DST), were carried out on UMIS 2000 (made by CSIRO Australia) ultramicroindentation system at room temperature in ambient air. Multiple partial unloading method, developed by Field and Swain[3] and studied in detail by Bushby[1], was used.

Table I
Composition of the starting powders

Samples	Composition [wt.%]			
	Si_3N_4	Y_2O_3	C	SiO_2
Si_3N_4	94.05	4.95		1.0
Si_3N_4-1wt.%SiC	93.23	4.91	0.43	1.43
Si_3N_4-5wt.%SiC	84.13	4.43	4.05	7.39

Spherical diamond indenter with nominal radius R_i = 7 μm, modulus of elasticity 1150 GPa and the Poisson's ratio 0.07 was used. Loading force up to 300 mN in 30 incremental steps was applied, each step was followed by 25 % unloading. Altogether 20 tests were perfomed.

The modulus of elasticity of the material was calculated for each step's penetration depth, assuming Poisson's ratio ν_m = 0.2. The hardness was calculated at loads from 270 to 300 mN which induced stresses well above the transition point. The partial unloading procedure also allows an indentation stress-strain curves to be generated, where the mean pressure (P_m) is taken as indentation stress, and indentation strain is expressed as the ratio of radius of diamond sphere indenter in contact with material surface and nominal radius of sphere a/R_i. The details of the calculation procedure are described elsewhere[4].

3. Results and discussion

Table II summarizes the values of hardness, elastic modulus and yielding points of studied materials measured by indentation method by diamond spherical indentor.

Table II
Values of hardness, elastic modulus and yielding stress

Material	Hardness [GPa]	Elastic modulus [GPa]	Yielding point [GPa]
Si_3N_4	21.8 ± 0.7	254 ± 10	14.8 ± 1.6
Si_3N_4-1wt.% SiC	23.4 ± 1.3	299 ± 12	15.2 ± 2.0
Si_3N_4-5wt.% SiC	28.3 ± 0.7	322 ± 11	20.7 ± 2.1

Hardness values of both nanocomposites are higher compared to monolithic Si_3N_4. DST method resulted in value of monolithic silicon nitride H_{IT} =21.8 GPa, that agree with the literature hardness data[5] for high density HPSN (22 GPa). The addition of SiC particles (27–33 GPa) has positive influence on the value of hardness.

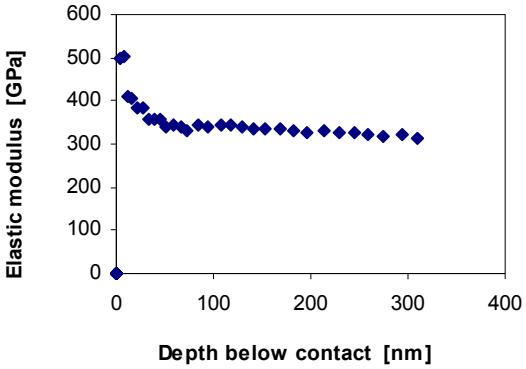

Fig. 1. **Modulus of elasticity of Si_3N_4-5wt.% SiC measured by depth sensing method of indentation**

Fig. 1 shows the values of modulus of elasticity calculated from the depth sensing indentation techniques. The relatively large scatter of values at very low loads (penetration depths < 15 nm) is caused by errors in reading of the depth which is close to the instrument resolution limits. Average values obtained from indentation are summarized in Tab. II. Results show same dependence than for the hardness: the increase of modulus of elasticity with the increasing amounts of SiC nanoparticles.

The indentation stress-strain curve (Fig. 2) shows similar features to a tensile or compressive stress strain curves. The initial portion is linear and corresponds to purely elastic deformation.

Yielding point can be identified as the deviation from this elastic behaviour. In our tests (see Tab. II) these values ranged from 14.8 GPa to 19.0 GPa. This information for ceramics and glasses is unique because conventional tensile or compressive tests normally result in catastrophic failure at much lower stresses.

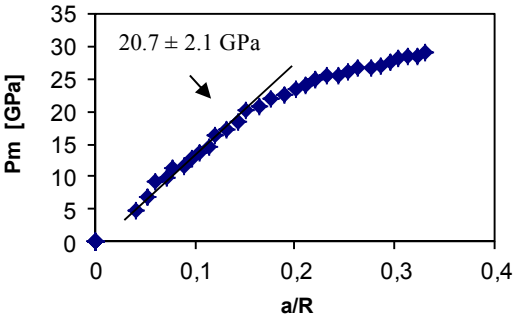

Fig. 2. **Indentation stress-strain curve of Si_3N_4-5wt.% SiC measured by using multiple partial unloading method**

4. Conclusions

Mechanical properties and deformation behavior of Si_3N_4-SiC nanocomposites were investigated by instrumented indentation with sphere. Method of partial unloading allowed to explore contact stress-strain behaviour, hardness, and modulus of elasticity. The values of hardness and elastic modulus of Si_3N_4-SiC composites measured by indentation technique increased with the increasing amount of SiC particles. The same beaviour was observed for a yielding point estimated from indentation stress-strain curves. The addition of SiC nanoparticles into silicon nitride matrix increased the all of studied mechanical properties.

The work was supported by the Slovak Grant Agency project No. 2/0156/10, APVV-0171-06, LPP-0203-07 and by Centrum of Excellence NANOSMART.

REFERENCES

1. Bushby A. J.: Nondestr. Test. Eval. *17*, 213 (2001).
2. Hnatko M., Galusek D., Šajgalík P.: J. Eur. Ceram. Soc. *24*, 189 (2004).
3. Field J. S., Swain M. V.: J. Mater. Res. *8*, 297 (1993).
4. Hvizdoš P., Kašiarová M., Dusza J., Hnatko M., Šajgalík P.: J. Eur. Ceram. Soc. *24*, 3345 (2004).
5. Richerson D. W., v knize: *Modern Ceramic Engineering*, Marcel Dekker, New York 1992.

M. Kašiarová, P. Hvizdoš, P. Tatarko, and J. Dusza *(Institute of Materials Research, Slovak Academy of Sciences):* **Influence of The Addition of SiC Nanoparticles on The Hardness and Elastic Modulus of Si_3N_4 Composites Measured by Indentation Method**

Mechanical properties of Si_3N_4/SiC nanocomposites with different amount of SiC particles were investigated by nanoindentation with spherical diamond indenter. Depth sensing technique was used to measure the values of hardness and elastic modulus. Indentation with the spherical indenter also enabled to investigate the elastic-to-elastic/plastic transition phenomena that are extremely difficult to study by using other methods.

SHEAR STRENGTH OF THERMALLY SPRAYED COATINGS

MICHAELA KAŠPAROVÁ, JOSEF VOLÁK, FRANTIŠEK ZAHÁLKA, and ŠÁRKA HOUDKOVÁ

ŠKODA VÝZKUM Ltd., Tylova 1/57, 316 00 Plzeň, Czech Republic
michaela.kasparova@skodavyzkum.cz

Keywords: shear strength, thermally sprayed coatings, cohesion, adhesion

1. Introduction

The test of tensile adhesive strength of thermally sprayed coatings is commonly used method but it has some limits namely the necessity of samples bonding using adhesive or glues with high tensile strength. In the dependency on the coating chemical composition and microstructure, the values of the bond strength can be artificial improved due to adhesive penetration in coating porosity and formation the chemical compounds. These negative effects can be eliminated using the shear tests without adhesives. These tests are closer to real situation than tensile bond strength test. Several methods and systems arrangement for shear loading were designed and described e.g. in ref.[1–3]. The shear test according to EN 15340 is the most commonly used test for measuring the shear strength of coatings. Other methods e.g. in ref.[5,6] are described (punch test, indentation test, pre-notched four-point bending test, non-destructive methods). The main purpose of the shear tests is to determine the resistance against shear loading on the coating-substrate interface (adhesive strength) or the strength of the coating itself (cohesive strength).

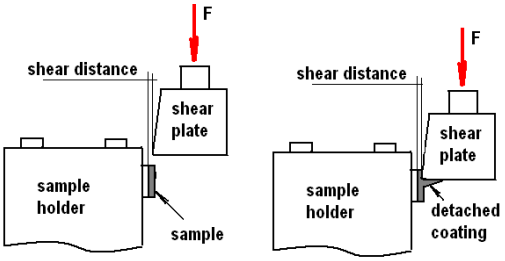

Fig. 1. **Principle of the shear test**

The purpose of this study was to modify the shear coating strength test in accordance with ČSN EN 15340 Standard, where the coating is uniformly loaded in parallel to the coating/substrate interface. The principle of the test is depicted in Fig. 1. With respect to the substrate roughness, the shear distance must be 50 μm ± 20 μm from the substrate. Lyphout et al.[4] evaluated the influence of the shear distance on the shear strength of the coating. They mentioned increasing of shear strength by about 45 MPa when the shear distance was 140 μm comparing to the shear distance of 60 μm.

During the shear tests the coating is loaded with smooth moving of the shear tool at a constant velocity till fracture occurs and the load drops down. The first maximum of the load curve defines the resistance to the shear stress.

2. Experiment

2.1. Samples preparation

The commercially available (15–45 μm) Triballoy 400 (CoMoCrSi), Stellite Alloy 6 (CoCrWCSi) and 13 % Cr were deposited on low-carbon steel substrates of 40×50×30 mm in size. Trib400 and Stellite were prepared using the JP-5000 HP/HVOF technology and 13 % Cr using the arc spray technology. The substrates were cleaned by grit-blasting with (0,8–1 mm) brown corundum. The TTN 24 Sand Blaster was used, the blasting distance was 12 cm and the blasted pressure was 6 atm. The substrate roughness was R_a = 9 μm. The coatings were sprayed using the optimized spray parameters. The final coatings thickness was 500 ± 50 μm for all sprayed samples. After spraying, the samples were cut for the shear test by the water jet to the size of 5×10×30 mm.

2.2. Experimental measurements

The shear strength of coatings was measured in accordance with ČSN EN 15340 Standard. The coating located on one facing surface of the tested sample was loaded with the compression stress by the loading velocity of 50 μm s^{-1}. The sample fixing was ensured using two screws in the special tool, which prevents sample movement in all directions. The microstructure was investigated using scanning and light microscope on the coatings cross sections.

3. Results and discussion

Typical shear curves for the tested samples are shown in Fig. 2. The shear force of Stellite coating was 1900 MPa and that of Triballoy400 was 1945 MPa, while the shear strength of arc sprayed 13 % Cr coating was lower, 1500 MPa. Seven measurements for each coating were performed. Average values of the shear test are mentioned in Tab. I. The shear strength of the HVOF coatings compared to the arc technology is higher due to homogenous, compact and dense structure with low content of oxides and un-melted particles, see Fig. 2. The fracture appearance in the coatings after the shear test is also documented in Fig. 3. It is evident that both HVOF coatings were fractured adhesively or adhesively-cohesively. It means that the coating was either fully detached from the substrate the crack propagated inside the coating. In the case of 13 % Cr coating, the elastic behaviour was found, see

Table I
Summary of the shear tests

Coating	Shear force F_{max} [N]	Shear strength σ_{max} [MPa]	Failure
Stellite	1900±180	38±3.6	a-c
Trib 400	1945±166	39±3.3	a-c
13%Cr	1350±140	27±2.8	a-c

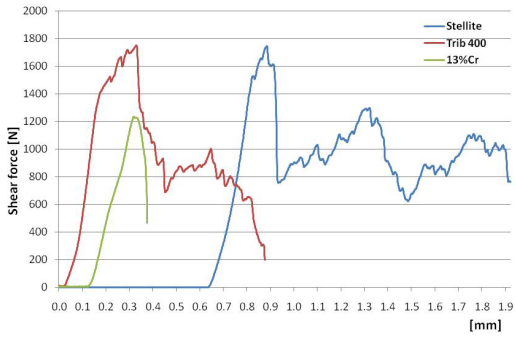

Fig. 2. **Record of the shear curves**
*shear modes definitions are stated in ČSN EN 15340 Standard

Fig. 2, because only the coating deflection for all tested samples occurred after the coating detaching.

Different failure modes can be observed during the shear test. They are caused by different modes of crack propagation in the coating during the shear stress action*. The different crack types are influenced by the coating material, adhesion properties between substrate and coating and the cohesion properties between the coating phases. The curves for the HVOF coatings were mostly in mode 2, which means that the coating adhesion is higher than its cohesion. In failure of mode 3, the coating is separated into small parts by the shear plate from the ground material. This behavior is typical for coatings with high hardness. However, the failure mode 1 was also observed for those coatings (the coatings detach along the whole coating-substrate interface). For the 13 % Cr coating, only the failure in mode 3b was observed, which means that the coating separate in large parts by the shear plates.

4. Conclusion

The shear test used for the evaluation of the shear strength of thermally sprayed coatings is convenient method for fast, easy and objective investigation of one of the coating parameters that relates to the coating strength properties and lifetime. The HVOF coatings exhibit higher shear strength compared to arc coatings due to more compact and denser microstructure and higher bond strength to the base material. It was achieved by high impact velocity and kinetic energy of impinging particles on the substrate.

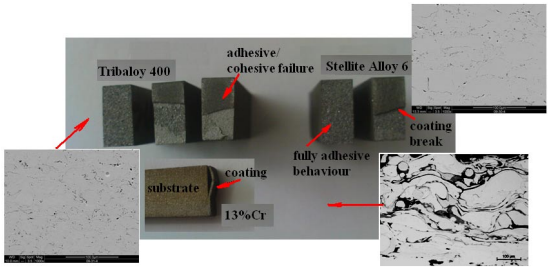

Fig. 3. **Documentation of coating fracture after the shear test**

This work was supported by the project No. VZ/MSM 4771868401.

REFERENCES

1. Callus P. J., Berndt C. C.: *Proceedings of 12th International Thermal Spray Conference, London*, UK (1989) 69 -76.
2. Era H., Otsubo F., Uchida T., Fukuda S., Kishitake K.: J. Mater. Sci. Eng. *A251*, 166 (1998).
3. Grutzner H., Dvorak M., Siegmann S., Nassentstein K.: *ITSC 2004 Thermal Spray Solutions – Advances in Technology and Applications*, Osaka, Japan, DVS, (2004), p. 364–368.
4. Lyphout C., Nylén P., Wigren J.: *Char. of Adhesion Strength and residual Stresse of HVOF sprayed Inconel 71/ for Aerospace Repair Applications*, ITSC 2007, p. 588–593.
5. Sakata K. et al.: *Effect of diffusion treatment on the interface microstructure between ts cobalt-based self-fluxing alloy coating and steel substrate*, ITSC 2008, p.696–700.
6. Ducos M., Bossuat B., Walesyek H., Canal B.: *Non-destructive testing of the coating-substrate interface of thermally-sprayed industrial parts*, ITSC (2005) p. 1041 –1046.

M. Kašparová, J. Volák, F. Zahálka, and Š. Houdková *(ŠKODA VÝZKUM Ltd., Plzeň, Czech Republic)*: **Shear Strength of Thermally Sprayed Coatings**

HVOF-coatings of Stellit Alloy 6 and Trib400 and the arc-coating of 13 % Cr were investigated using shear tests in accordance with EN 15340 Standard. The shear curves and the maximal shear forces were recorded and compared with each other. Also the fracture appearance after the tensile tests was documented using scanning electron microscopy. The results give beneficial information about adhesive-cohesive behaviour of thermally sprayed coatings which facilitate to predicate mainly the shear, impact resistance and coatings lifetime.

INFLUENCE OF TEMPERATURE ON MICROHARDNESS OF ALUMINIUM-BASED COMPOSITES PRODUCED BY CONTROLLED HYPEREUTECTIC REACTION IN Al-Ni BINARY SYSTEM

LENKA KLAKURKOVÁ[a,*], LADISLAV ČELKO[a], KAREL SLÁMEČKA[b], PAVEL DOLEŽAL[a], and JIŘÍ ŠVEJCAR[a]

[a] Institute of Materials Science and Engineering, [b] Institute of Physical Engineering, Faculty of Mechanical Engineering, Brno University of Technology, Technická 2896/2, 616 69 Brno, Czech Republic
klakurkova@fme.vutbr.cz

Keywords: Al-rich intermetallics, aluminium-based composites, hypereutectic alloys, microhardness

1. Introduction

In the Ni–Al binary system, the majority of scientific attention is focused on the development of NiAl and Ni_3Al phases. The Ni–Al binary system also contains other three, less known phases. The $NiAl_3$, Ni_2Al_3 and Ni_5Al_3 phases are not considered for use in high-temperature applications mainly due to their lower melting points being 854 °C, 1133 °C and approx. 700 °C, respectively[1–4]. New information about their formation and degradation mechanisms, morphology, and distribution, physical and mechanical properties can be, however, successfully used for strengthening of Al composites, Ni/Al/Ni interconnections, and layered structures design[5,6].

This contribution is focused on local mechanical properties represented by microhardness of Al substrate and strengthening Al-rich intermetallic phases produced from deposited Ni sacrificial coatings after the annealing in a wide range of temperatures encompassing the solid and/or molten state of the aluminium substrate.

2. Experimental

Aluminium sheet of commercial purity (99.5 wt.%) was used as a substrate. A commercially available nickel (99.7 wt.%) powder was deposited onto the substrate using High Velocity OxyFuel technique. The thickness of deposited coating was in the range of 250–300 μm. Subsequent annealing in the temperature ranges 600–630 °C (solid state), 640–660 °C (semi-solid state) and above 660 °C (liquid state of aluminium) with appropriate dwells was applied regarding to Al-rich aluminides Ni_2Al_9, $NiAl_3$ and Ni_2Al_3 formation at the coating-substrate interface and/or at the aluminium substrate.

The resulting microstructures were obtained by scanning electron microscopes (JEOL-840A, Philips XL-30). Local mechanical properties, represented by microhardness of the aluminium substrate and intermetallics formed, after the annealing was measured by the microhardness tester (LECO LM 247AT).

3. Results

At the temperatures below the Al + $NiAl_3$ eutectic melting point (639.9 °C), aluminium from the substrate diffuse primarily toward the coating and forms the $NiAl_3$ and Ni_2Al_3 layers, see Figs. 1a and 1b. In dependence on the temperature heigh the different annealing times were used to their formation. Their thicknesses increase markedly faster at higher temperatures applied. Nickel diffuse from the rating into the substrate and form $NiAl_3$ and/or Ni_2Al_9 intermetallic particles. These take up only 2.5 vol.% at maximum.

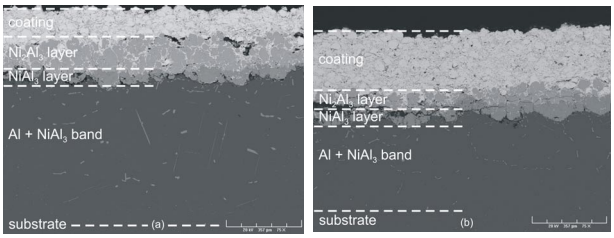

Fig. 1. **Coating-substrate interface after annealing (a) 600 °C / 500 hrs, (b) 630 °C / 50 hrs – SEM-BSE**

In the range of 640–660 °C, the onset of liquid aluminium phase can be expected. The nickel coating dissolves in aluminium substrate. Total thickness of the original coating deposited onto the substrate decreases during annealing. Discontinuous Ni_2Al_3 and $NiAl_3$ layers start to form at these interfaces, see Figs. 2a and 2b. The region denoted as Al + $NiAl_3$ band consists of Al + $NiAl_3$ eutectic and primary $NiAl_3$ particles. Strengthening phases formed in the substrate occupy 20 vol.%. Below 645 °C, the Al + $NiAl_3$ eutectic was never observed, see the system at lower temperatures.

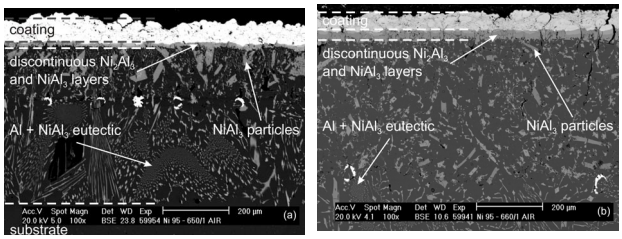

Fig. 2. **Coating-substrate interface after annealing (a) 650 °C / 60 min, (b) 660 °C / 60 min – SEM-BSE**

At temperatures exceeding 660 °C, the Al substrate is completely in the liquid state. The dimensions of Al substrate body do not change dramatically, because of the existence of oxide cover which keeps the substrate compact. In the first minutes of annealing the coating is almost or completely dis-

solved in the substrate, see Figs. 3a and 3b. At the temperatures higher than 800 °C, significantly higher amount of $NiAl_3$ particles was formed. The growth rate of eutectic band thickness could be also governed by dwell time at annealing temperature. The strengthening phases occupy up to 35 vol.% of the substrate on average.

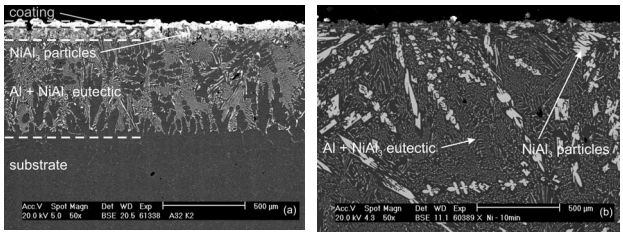

Fig. 3. **Coating-substrate interface after annealing (a) 700 °C / 10 min, (b) 800 °C / 10 min – SEM-BSE**

Measured and averaged values of microhardness of selected structural parts are presented in Fig. 4. Significant drop in hardness of primary $NiAl_3$ particles down to the range of 600–650 HV is observed at temperatures of 650 and 700 °C. The drop of microhardness within this range can result from contribution of the substrate iron-based impurities, which participates on the primary $NiAl_3$ stoichiometric compound formation. At the same temperatures finer morphology of Al + $NiAl_3$ eutectic formation was observed. Above the 650 °C, where the Al + $NiAl_3$ eutectic region starts to form, the hardness 75 HV remains stable. The aluminium substrate harndess of about 40 HV was measured with increasing temperature of the Al-Ni hypereutectic composite formation.

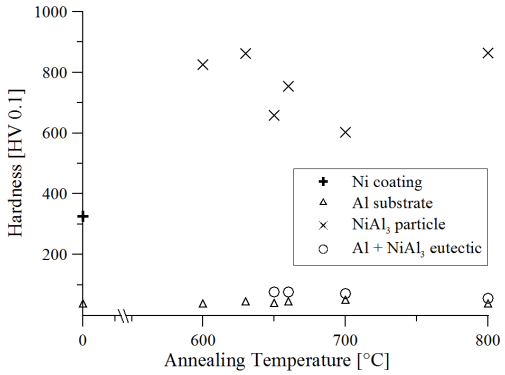

Fig. 4. **Hardness of selected structural parts**

The composite hypereutectic alloy prepared from sacrificial nickel coatings at the temperature of 700 °C seems to be the most interested choice because of the formation of finer Al + $NiAl_3$ eutectic.

4. Conclusions

- The hardness of primary $NiAl_3$ phase change markedly at the temperatures of 650 and 700 °C.
- The optimal condition for processing of Al–Ni composites from sacrificial coatings is at the temperature of 700 °C.
- To form the layered structures containing Al-rich intermetallics, the temperatures below the eutectic melting point can be used.
- The origin of layers and/or composite, are diffusion-driven and can be governed by the annealing dwell.

This work was financially supported by the Czech Science Foundation Project No. 106/09/P513.

REFERENCES

1. Morsi K.: Mat. Sci. Eng. A *299*, 1 (2001).
2. Tamarin Y.: *Protective Coatings for Turbine Blades*. ASM International, Ohio 2002.
3. Čelko L., Klakurková L., Man O., Švejcar J.: Mater. Manuf. Proc. *24*, 1155 (2009).
4. Garg S. P., Kale G. B., Patil R. V., Kundu T.: Intermetallics *7*, 901 (1999).
5. Gonzalez G., Lara-Rodriguez G. A., Sandoval-Jimenéz A., Saikaly W., Charai A.: Mater. Char. *59*, 1607 (2008).
6. Čelko L., Klakurková L., Švejcar J.: Def. Diff. Forum. *297-301*, 771 (2010).

L. Klakurková[a], L. Čelko[a], K. Slámečka[b], P. Doležal[a], and J. Švejcar[a] *([a] Institute of Materials Science and Engineering, [b] Institute of Physical Engineering, Faculty of Mechanical Engineering, Brno University of Technology, Brno, Czech Republic):* **Influence of Temperature on Microhardness of Aluminium-Based Composites Produced by Controlled Hypereutectic Reaction in Al-Ni Binary System**

Aluminium matrix composites were prepared by High Velocity OxyFuel spraying of nickel powder onto the aluminium sheet's surface followed by annealing in a range of temperatures 600–630 °C (solid state), 640–660 °C (semi-solid state) and above 660 °C (liquid state of aluminium). The Ni_2Al_3 and Ni Al_3 intermetallic layers were formed at the interface between original Ni coating and Al matrix. Moreover, Ni diffused into the aluminium matrix and caused strengthening of $NiAl_3$ and Ni_2Al_9 particles. Local mechanical properties represented by microhardness of aluminium matrix and intermetallic phases formed were measured.

INFLUENCE OF DEFORMATION DEGREE ON LOCAL DEFORMATION HETEROGENEITY DURING THIN SHEET ROLLING

RÓBERT KOČIŠKO[a], JÚLIUS BACSÓ[a], JANA BIDULSKÁ[a*], ANDREA KOVÁČOVÁ[a], PETER BELLA[a], and MÁRIA MOLNÁROVÁ[b]

[a] Department of Metals Forming, Faculty of Metallurgy, Technical University of Košice, 042 00, Košice, [b] Institute of materials research, Slovak Academy of Sciences, 040 01, Košice, Slovakia
jana.bidulska@tuke.sk

Keywords: FEM, cold rolling, deformation heterogeneity

1. Introduction

The non-uniform deformation is always being formed throughout deformation band volume during rolling process[1,2]. The non-uniform deformation reduces the strain of core parts contributing to structural non-homogeneity through the thickness of sheet such as non-uniform grain size, anisotropy, etc. These aspects also contribute to the structural non-homogeneity through sheet thickness such as non-uniform grain diameter, and the anisotropy. On the other hand, non-uniform deformation through the thickness of thin sheet represents the different energy areas resulting in the development of the recovery processes in the further processing. It is possible to achieve precisely defined deformation non-homogeneity through the thin sheet thickness by means of the controlled rolling.

Geometric ratio l_d/h_s (l_d – length of contact arc, h_s – medium thickness of the sample) has the greatest impact on the distribution of deformation through thickness of semi-product. When l_d/h_s ratio is low, influence of rigid ends (the rolling of thick plates) has preferential effect and the friction importance is relatively small. However, when l_d/h_s ratio is high frictional forces have significant impact. J. J. Tarnovskij divided rolling conditions based on l_d/h_s folow[3]:

I. $l_d/h_s < 0.2$ the compressive deformation is concentrated below the surface,
II. $0.15–0.2 < l_d/h_s < 0.6–0.7$ the compressive deformation penetrates to the core gradually,
III. $0.6–0.7 < l_d/h_s < 2–3$ the compressive deformation penetrates to the core gradually, following increase of spread in core parts leads to the formation of convex shape of the side walls,
IV. $l_d/h_s > 2–3$ the friction cones overlap together in the center part and thereby flow stress increases as well as convex shape of side walls.

The penetration of plastic deformation during thin sheets rolling can be also analysed using numerical simulations based on finite element method (FEM). Although the basic theoretical relationships between geometric ratio and penetration of plastic deformation are well known only few works have verified them or extended the theory on the impact of friction. FEM was used for: determining the distribution of rolling pressure along the strip width[4], the mathematical simulation of elastic entry and existence of regions in a roll bite zone[5], the study of a hot rolling process, the approach is based on thermo-mechanical analysis[6], the study of cold rolling of thin sheet with different friction conditions[7], determining the on-line accurate mean value of both friction coefficient and flow stress for anisotropic materials during cold rolling[8].
The aim of this study is to find out local penetration of plastic deformation during thin sheet rolling using FEM. The degree of plastic deformation and contact friction are variable parameters.

2. Experimental procedure

Rolling process of thin sheet was simulated using the software product Deform. The treshold conditions were defined by laboratory experiment[9]. The working rolls with diameter D = 210 mm were defined as a perfectly rigid body. The rotational speed of rolls was 8 rad, what is the rolling speed 0.83 m s^{-1}. The finite element mesh had 11850 node number for sample with input thickness h = 1.5 mm and length l = 50 mm. Number of elements through sample thickness was 25. The sample was defined as a plastic material. The experimental material is characterized as the C-Mn-Si steel. Flow stress is defined by equation $\bar{\sigma} = \bar{\sigma}(\bar{\varepsilon}, \dot{\varepsilon}, T)$, where $\bar{\sigma}$ is flow stress, $\bar{\varepsilon}$ is effective plastic strain, $\dot{\varepsilon}$ is effective strain rate, T is temperature. The average yield stress is 202 MPa. The elastic properties of samples are defined by Poisson's ratio 0.3 and Young's modulus 2.1×10^5 MPa.

The calculations of thin sheet rolling process were carried out by using different degrees of deformation 2 %, 4 %, 6 %, 8 % and 10 %. Three values of the contact friction coefficient f = 0.1; 0.6 and 0.9 were applied for all degrees of deformation.

3. Results and discussion

The amount of non-uniform deformation during process of thin sheet rolling is mostly influenced by geometric ratio l_d/h_s as well as friction coefficient. The change of geometric ratio for rolls diameter D = 210 mm was guaranteed by amount of the reduction (h). When degree of deformation is 2, 4, 6, 8, 10 %, l_d/h_s ratio is in the range 1.2–2.8 mm that falls into two areas based on Tarnovskij model. Fig. 1 shows the effective strain in dependence on degree of plastic deformation and change of contact friction. Distribution of effective strain was analysed through sample thickness. The highest effective strain intensity was below the surface (about 20 % of the total thickness of the plate) and decreases towards the core of the sheet gradually. The deformation degree had negligible influence on the effective strain heterogeneity between samples surface and core ($\Delta\varphi$). Distribution of effective deformation through material thickness calculated by mathematical simulations was

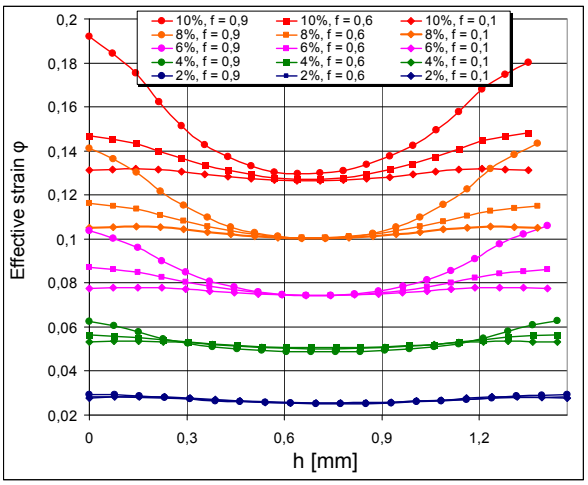

Fig. 1. **Effective strain in dependence on the degree of deformation and contact friction level**

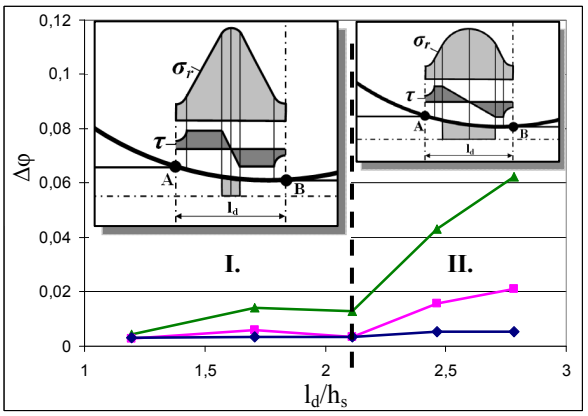

Fig. 2. **Effective strain between samples surface and core (Δφ). depending on l_d/h_s and the contact friction**

confirmed by experimental microhardness measurements presented by authors[9].

The contact friction coefficient for different geometric ratios l_d/h_s had influence on the Δφ more significantly, as seen in Fig. 2. The dependence in terms of friction is possible to divide into two areas:

I. $l_d/h_s < 2.1$ – in this area the friction has negligible influence on Δφ, band adhesion is concentrated only in narrow range around the neutral plane along l_d, substantial part of l_d is formed by band slip. Moreover, backward slip zone and forward slip zone are also observed.

II. $l_d/h_s > 2.1$ – in this area friction has significant influence on Δφ, adhesion band makes main part of l_d, slip band is being minimized while backward slip zone and forward slip zone are preserved.

4. Conclusion

When friction is low (f = 0.1), l_d/h_s ratio has negligible influence on the plastic deformation heterogeneity during thin sheet rolling. Significant influence of contact friction appears when $f > 0.6$ at $l_d/h_s > 2.1$. These threshold values cause extension of adhesion zone along l_d and resulting in the enhancement of non-uniform effective strain between the center and edge of the sheet.

This work was realized within the frame of the project „Technological preparation of electrotechnical steels with high permeability for electrodrives with higher efficiency“, which is supported by the Operational Program “Research and Development” ITMS 26220220037, financed through European Regional Development Fund.

REFERENCES

1. Zamyslovský Z.: Hutnícke listy *2*, 101 (1971).
2. Kvačkaj T.: Neue hütte *6/7–92*, 225 (1992).
3. Kollerová M., Žídek M., Dědek V., Počta B.: *Valcovanie*, Alfa, Bratislava 1991.
4. Liu X., Shi X., Li S., Xu J., Wang G.: J. Iron Steel Res. Int. *14*, 22 (2007).
5. Jiang Z. Y., Tieu A. K., Lu C.: J. Mater. Process. Technol. *146*, 167 (2004).
6. Galantuccia L. M., Tricarico L.: J. Mater. Process. Technol. *92–93*, 494 (1999).
7. Jiang Z. Y., Tieu A. K.: Tribol. Int. *37*, 185 (2004).
8. Han H.: J. Mater. Process. Technol. *159*, 401 (2005).
9. Gavendová P., Kováč F., Stoyka V., Petryshynets I., Kvačkaj T.: Acta Metallurgica Slovaca *16*, 181 (2010).

R. Kočiško[a], J. Bacsó[a], J. Bidulská[a], A. Kováčová[a], P. Bella[a], and M. Molnárová[b] *([a] Department of Metals Forming, Faculty of Metallurgy, Technical University of Košice, [b] Institute of materials research, Slovak Academy of Sciences, Košice, Slovakia):* **Influence of Deformation Degree on Local Deformation Heterogeneity During Thin Sheet Rolling**

The cold rolling process of thin sheet was simulated by a two-dimensional rigid-plastic finite element method (FEM) to find out local penetration of plastic deformation during thin sheet rolling. It was found of that the deformation degree had negligible influence on the effective strain heterogeneity between surface and core samples (Δφ) in dependence on the degree of plastic deformation and contact friction. The contact friction coefficient for different geometric ratios l_d/h_s influenced Δφ more significantly.

INDENTATION THERMAL SHOCK RESISTANCE OF Si_3N_4/CNT COMPOSITES

ALEXANDRA KOVALČÍKOVÁ[a]*, TAPASZTÓ ORSOLYA[b], CSABA BALÁZSI[b], and JÁN DUSZA[a]

[a] *Institute of Materials Research, Slovak Academy of Sciences, Watsonova 47, 040 01 Košice, Slovak Republic,* [b] *Ceramics and Composites Laboratory, Research Institute for Technical Physics and Materials Science, Hungarian Academy of Science, Konkoly-Thege ut 29-33, 1121 Budapest, Hungary*
akovalcikova@imr.saske.sk

Keywords: Si_3N_4/CNT composites, indentation thermal shock resistance, crack propagation

1. Introduction

Carbon nanotubes (CNTs) offer new possibilities to improve the functional and mechanical properties of advanced ceramics thanks to their small diameter, large aspect ratio, low mass and excellent mechanical, electrical and thermal properties[1]. During the last decade new ceramic/carbon nanotube composites have been developed and a number of authors have reported improved mechanical and functional properties in the case of ceramic/CNT composites compared to the monolithic material[2]. Three main problems have been recognized during these investigations: dispersion of the CNTs in the matrix, densification of the composites and degradation of the CNTs.

However, only few researchers have been concerned with thermal properties of carbon nanotube composites in ceramic systems. In convectional testing thermal shock resistance (TSR) is quantified by measuring of residual strength of polished specimens after quenching. This standardized method requires a large number of prepared samples, it cannot allow multiple shock measurements. For these reasons an alternative indentation-quench method has been developed[3]. In this technique, the TSR is measured by studying the propagation of median/radial cracks around a Vickers indentation after single or repeated quenching. The critical temperature difference DTc, of the material can be defined with reference to the number of propagating cracks and the amount of crack extension.

The main aim of this study is an estimation of indentation TSR of Si_3N_4/CNT composites.

2. Experimental procedure and materials

Si_3N_4, Al_2O_3 and Y_2O_3 were used as starting powders. Different amount of CNTs were added in addition to batches (1 and 3 wt.%). The powder mixtures together with the added CNTs were milled in ethanol for 3 h. The batches were dried and sieved. Green samples were obtained by dry pressing at 220 MPa. The samples without CNT were fabricated in the same manner. HIP was performed at 1700 °C in high purity nitrogen at gas pressure 20 MPa.

For the investigation of TSR the indentation-quench method was used. The length of the cracks was measured using optical microscopy. After the indentation the samples were heated in a vertical tube furnace in air to the required temperature and held there for 25 min. Then the specimens were rapidly immersed into a ~20 °C water bath. Final radial crack lengths were then measured with optical microscope. The procedure was repeated at increasing quenching temperatures ΔT, up to the critical value of ΔTc at which radial crack became unstable and the specimen failed.

3. Results

The microstructure of sintered CNT composites (Fig. 1) consisted mainly of β-Si_3N_4 grains (several micro meters in length) and nanotubes. The CNTs are located mainly in the inter-granular positions and they have a good contact to the surface of silicon nitride grains. The dispersion of nanotubes is still far from optimum, in most of the cases they are in interconnected groups.

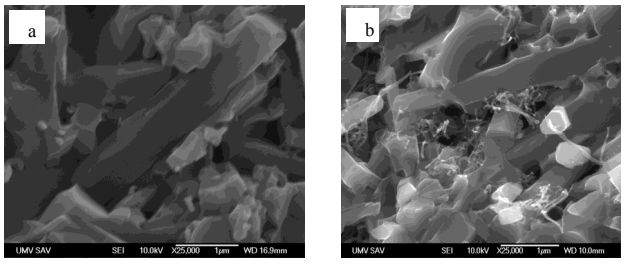

Fig. 1. **Fracture surfaces of HIP samples (a) Si_3N_4 reference sample, (b) CNT/Si_3N_4 composties with 3 % CNT**

The initial cracks size for silicon nitrides samples were ≈ 120 μm at indentation load 98.1 N. The dependence of radial crack growth on temperature for tested materials is plotted in Fig. 2. There are visible three different areas which characterize the crack evolution after quenching: a) an initial radial cracks growing slightly with increasing ΔT (area to ΔT ~ 200 °C); b) a radial crack growing stable extension (area ΔT 200–700 °C); c) a radial crack growing unstable extension and the specimens failed. A critical temperature ΔT_c when the Si_3N_4 failed is ~ 780 °C. In the case of Si_3N_4/CNT reinforced composites the initial crack length was above 125–130 μm. Again are visible different areas which characterize the crack evolution after quenching: a) an initial radial cracks growing slightly with increasing ΔT (area to ΔT ~ 250 °C for SN-CNT1, to ΔT ~ 200 °C for SN-CNT2); b) a radial crack growing stable extension (area ΔT 250–700 °C for SN-CNT1, ΔT 200–600 °C for SN-CNT2; c) a radial crack growing unstable extension and the specimens failed (ΔT_c~ 870 °C for SN-CNT1 and ΔT_c~ 620 °C for SN-CNT2).

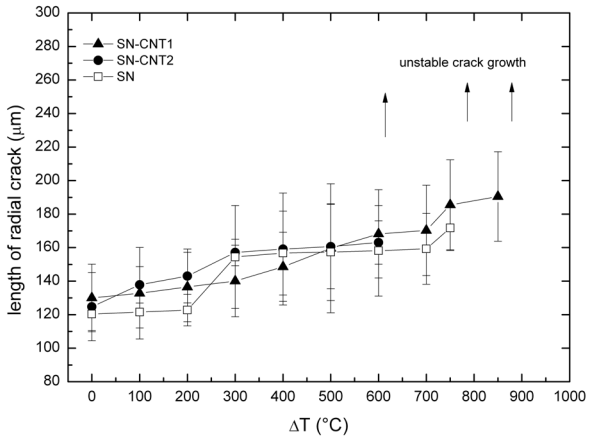

Fig. 2. **Crack propagation at thermal shock tests**

With increasing the CNT content a decrease of TSR has been observed. TSR can be improved by the increased flexural strength and fracture toughness and by decreased Young's modulus and coefficient of thermal expansion. Because fracture toughness for Si_3N_4/CNT (6.0 MPa $m^{1/2}$) does not differ significantly from the values of Si_3N_4 (6.3 MPa $m^{1/2}$), the reason for lower TSR could be degraded strength values by CNT dispersions due to insufficient densification[4]. The other possible reason is a difference in thermal properties of the materials- thermal expansion coefficients of Si_3N_4 (3.10^{-6} K^{-1}) and CNTs ($1.6–2.6.10^{-5}$ K^{-1}). Microfractographic observation of thermally shocked specimens with Vickers indentation showed well defined radial crack pattern. The propagation of Vickers indentation crack of SN-CNT1 before and after thermal shock at $\Delta T = 870$ °C is shown in Fig. 3. These cracks increased in size with increasing temperature, but always reached instability first in the longitudinal direction.This indicates a slightly higher tension in the transverse direction, consistent with some edge effect in the thermal transfer process (via r_0 in the Biot coefficient)[5].

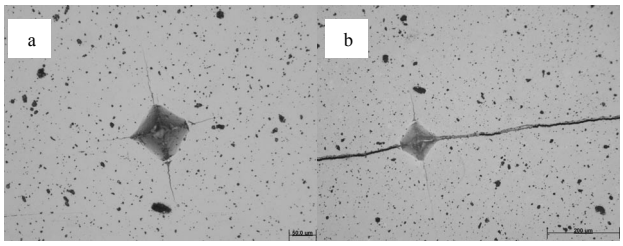

Fig. 3. **Vickers indentation crack of SN-CNT1, (a) before thermal shock, (b) after thermal shock (ΔT = 870 °C)**

4. Conclusion

With increasing the carbon nanotube content a decrease of thermal shock resistance has been observed. The reason for lower TSR could be degraded strength values by CNT dispersions due to insufficient densification and different thermal expansion coefficients of Si_3N_4 and CNTs.

This work was financed by the Slovak Government through the project LPP 0203-07 and by MNT-ERA.NET HANCOC.

REFERENCES

1. Merkoci A.: Microchim. Acta *152*, 157 (2006).
2. Tatami J., Katashima T., Komeya K., Meguro T., Wakihara T.: J. Am. Ceram. Soc. *88*, 2889 (2005).
3. Andersson T., Rowcliffe D. J.: J. Am. Ceram. Soc. *79*, 1509 (1996).
4. Balázsi Cs., Kónya Z.,Wéber F., Biró L. P., Arató P.: Mater. Sci. Eng. *C23*, 1133 (2003).
5. Lee S. K., Moretti J. D., Readey M. J., Lawn B. R.: J. Am. Ceram. Soc. *85*, 279 (2002).

A. Kovalčíková[a], T. Orsolya[b], Cs. Balázsi[b], and J. Dusza[a] *([a] Institute of Materials Research, Slovak Academy of Sciences, Košice, Slovak Republic, [b] Ceramics and Composites Laboratory, Research Institute for Technical Physics and Materials Science, Hungarian Academy of Science, Budapest, Hungary):* **Indentation Thermal Shock Resistance of Si_3N_4/ CNT Composites**

The influence of carbon nanotubes on the thermal shock resistance of the multiwall carbon nanotube reinforced silicon nitride composites has been investigated. Silicon nitride based composites with different amount (1 or 3 wt.%) of carbon nanotubes have been prepared by hot isostatic pressing. The adition of 1 wt.% CNTs enhanced the thermal shock resistance of the composite, however, CNT content increase up to 3 wt.% reduced its thermal shock resistance.

UNIVERSAL HARDNESS TEST APPLIED TO PM MATERIALS PREPARED FROM COATED POWDERS

MIRIAM KUPKOVÁ[a]*, MARTIN KUPKA[b], SUSANNE STROBL[c], and PAVOL HVIZDOŠ[a]

[a] Institute of Materials Research of SAS, Watsonova 47, Košice, [b] Institute of Experimental Physics of SAS, Watsonova 47, Košice, Slovakia, [c] Institute of Chemical Technology of Inorganic Materials, TU Vienna, Vienna, Austria
mkupkova@imr.saske.sk

Keywords: powder metallurgy, Cu-coated Fe powder, compaction, sintering, micromechanical properties

1. Introduction

Copper is an important alloying element in ferrous powder metallurgy (PM) due to its hardening effect (solid solution, precipitation) and for allowing the liquid phase sintering[1].

In order to distribute the alloying element uniformly, iron powder particles are often coated with a copper layer. The coating, in addition, removes the segregation of elements during transport and processing of the powders, it reduces harmful dustiness in the PM industry. The coatings also prevent powders from further oxidation, improve compressibility and enhance dimensional stability upon sintering.

To estimate the effective macroscopic properties of microheterogeneous materials, it is important to know the distribution, volume fractions and properties of individual phases constituting the material. However, the distinction of individual phases and determination of their mechanical properties is not straightforward and some indirect method has to be involved[2].

Nanoindentation has emerged as an important method for evaluation of the mechanical response of small material volumes to applied loading.

In the current investigation, nanoindentation tests are used extensively to determine the distribution of mechanical properties within the (sub)surface regions of the both "green" compacted and sintered cylinders prepared from Fe + 12 wt.% Cu coated powders.

2. Materials and experimental methods

Water-atomized iron powder, Höganäs ASC 100.29 grade, fraction 63−180 μm, was used as a starting raw material.

Iron particles were immersed into an aqueous electrolyte which contained coppersulfate and sulphuric acid. After stirring for several minutes, copper layer was deposited on surfaces of iron particles by cementation process. The required copper amount (12 wt.%) was controlled by the copper sulfate content in the electrolyte. More details on the fabrication and characteristics of the powders were presented elsewhere[1].

The powders obtained were cold-pressed into cylindrical compacts 10 mm in diameter and with heights of about 10 mm. The compaction pressure was 600 MPa. The lubricant was not added to the powder, zinc stearate was used as a die wall lubricant. Compacts were sintered in Marsch laboratory furnace at sintering temperature of 1120 °C for 60 minutes, in the atmosphere of 90 % N_2 – 10 % H_2.

To prepare for examinations, the samples were cut, mounted, ground, polished and nital-etched. The microstructure of the samples was analysed by a light optical microscope (OLYMPUS GX71, Japan).

The hardness and indentation elastic modulus were determined from the load-displacement curves, measured by the TTX-NHT apparatus with diamond Berkovich tip and analysed by the method developed by Oliver and Pharr[3]. The maximum load of 100 mN was chosen. The indentations were repeated twenty times for each sample. The irregular curves were excluded from analysis. Despite this, each thereinafter mentioned value represents an arithmetic average from at least 15 repeated measurements.

3. Results

At the temperature of 1120 °C, only about 8 wt.% of Cu may be dissolved in a solid iron. So, when the Fe + 12 wt.% Cu compact undergoes sintering at 1120 °C, the copper-rich liquid phase is permanently present. The melt penetrates into contacts between iron particles as well as along the grain boundaries into the interior of particles. This can cause particles to disintegrate. The disintegration leads to increased mobility of single grains and enables renewed (secondary) rearrangement.

As a result, the pore size, shape and distribution start to change. Pores are closing, spheroidizing and coalescing. Sintered compacts have thus got higher density (7.23 g cm^{-3}) than "green" ones (7.12 g cm^{-3}).

Simultaneously, the solid-state diffusion and solution-precipitation take place. The diffusion of copper into iron causes particles to become strengthened. This results in final sintered compacts consisting of hardened Fe particles bonded by a soft copper-based matrix.

Metallographic examination of the microstructure of compacted samples demonstrated that in "green" compacts the particle surfaces were almost completely covered with a copper (Fig. 1a). After sintering at the temperature of 1120 °C, the samples revealed a microgradient structure (Fig. 1b). After etching by nital, the Fe cores of original powder particles are less affected and the regions around, consisting of the Fe-Cu solid solution, are more attacked by the etching reagent (dark).

The changes in the mechanical properties are in close relation to these microstructures. Fig. 2 presents the average values of indentation hardness and indentation modulus. Pronounced differences in the indentation hardness and indentation modulus are observed for the "green" and sintered samples.

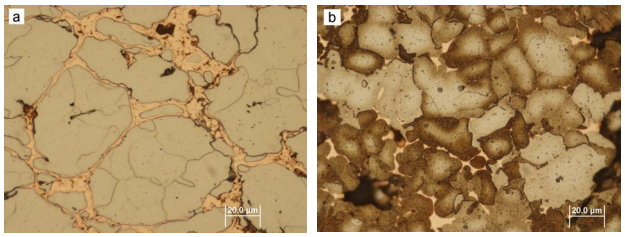

Fig. 1. **Structure of samples compacted at 600 MPa from iron powders coated with 12 wt.% of Cu. Sample in a "green" state (a) and (b) sintered at temperature 1120 °C and nital etched, LOM**

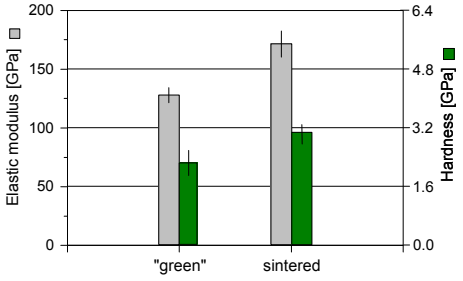

Fig. 2. **Indentation modulus and indentation hardness for samples prepared from 12 wt.% Cu coated iron powders**

The hardness and modulus are improved for sintered samples. They are strengthened by copper precipitation and by the formation of solid solution with iron.

4. Conclusion

In principle, the DSI method seems to be suitable for determining the "local" properties of PM samples.

Elastic properties are determined from the data obtained during unloading of the indentation. The indentation elastic modulus, E_{IT}, can be calculated from the slope of the upper portion of the unloading curve.

If the total measured compliance (the reciprocal of the slope of unloading curve) consists only of the compliance of contact between indenter and surface grain, the calculated elastic modulus corresponds to the Young's modulus E_m of the grain's material,

$$E_{IT} \approx E_m \qquad (1)$$

To allow for the "granular"character of the sample surface, we considered the total measured compliance as composed of two contributions – the compliance of the contact between indenter and the surface grain and the compliance of contact between the surface grain and the adjacent subsurface grain. Then we found that

$$E_{IT} \approx \frac{E_m}{1+2\left[\left(1+\frac{1-\nu_i^2}{1-\nu_m^2}\frac{E_m}{E_i}\right)\frac{r}{R}\right]^{1/3}} \qquad (2)$$

E_i and v_i are the Young's modulus and Poisson's ratio for the material of indenter; E_m and v_m are those for the grain's material. R is the radius of grain; r represents the radius of curvature of the indenter's tip.

The expression (*2*) shows that the indentation elastic modulus (i) does not exceed the modulus of grain's material, and (ii) should change with the size of grains. This change represents the goal of further investigations.

This work was supported by VEGA grant 2/0129/09 of the Slovak Grant Agency.

REFERENCES

1. Strobl S., Gierl C., Konnegger T., Kupková M., Kabátová M.: Powder Metall. Progress *6*, 149 (2006).
2. Němeček J., Lukeš J.: Chem. Listy *104*, 279 (2009).
3. Oliver W. C., Pharr G. M.: J. Mater. Res. *7*, 1546 (1992).

M. Kupková[a], M. Kupka[b], S. Strobl[c], and P. Hvizdoš[a]
([a] Institute of Materials Research of SAS, Košice, [b]Institute of Experimental Physics of SAS, Košice, Slovakia, [c] Institute of Chemical Technology of Inorganic Materials, TU, Vienna, Austria): **Universal Hardness Test Applied to PM Materials Prepared from Coated Powders**

Iron powder particles were coated with copper by cementation. The resultant powder contained 12 wt.% of copper. The coated powder was then compressed into cylindrical samples and sintered. Sintered samples possessed microgradient structure with a copper concentration decreasing from the surface towards the interior of iron grains. The hardness and elastic modulus of individual grains in both "green" and sintered samples were determined by the depth sensitive indentation method. The properties of sintered samples were found better than those of the "green" ones. To estimate the effect of "granular" structure of samples on measured properties, the relation for an indentation modulus based on a simple model was proposed.

IMPROVEMENT OF MECHANICAL PROPERTIES OF TPE BY IRRADIATION

MIROSLAV MAŇAS*, DAVID MAŇAS, MICHAL STANĚK, ŠTEPÁN ŠANDA, and VLADIMÍR PATA

Tomas Bata University in Zlin, nam. T.G.Masaryka 5555, 760 01 Zlin, Czech Republic
dmanas@ft.utb.cz

Keywords: thermoplastic elastomer, irradiation, mechanical properties

1. Introduction

The cross-linking of rubbers and thermoplastic polymers is a well-proven process of the improvement of the thermal properties. The chemical cross-linking or rubber vulcanization is normally induced by the effect of heating after processing with the presence of a curing agent. The cross-linking process for thermosets is very similar. In thermosets the polymer molecules are also chemically linked due to heat after processing.

Cross-linked rubbers have a wide-meshed molecular network that keeps them soft and their properties change only slightly on a wide temperature scale. On the other hand, thermosets are characterized by a very narrow-meshed network. Due to this fact they hardly change their high level of stiffness on a wide temperature scale.

The irradiation cross-linking of thermoplastic materials via electron beam or cobalt 60 (gamma rays) is proceeding separately after the processing. The cross-linking level can be adjusted by the irradiation dosage and often by means of a cross-linking booster (Fig. 1).

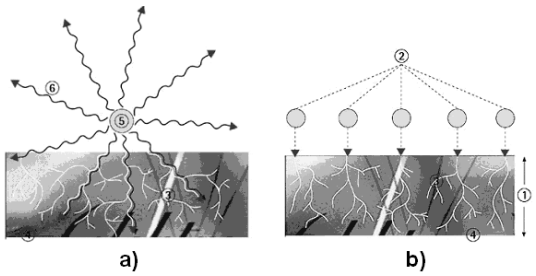

Fig. 1. **Design of Gamma rays (a) and Electron rays (b);** a) 3 – secondary electrons, 4 – irradiated material, 5 – encapsulated Co – 60 radiation source, 6 – Gamma rays, b) 1 – penetration depth of electron, 2 – primary electron, 3 – secondary electron, 4 – irradiated material

The main deference between beta and gamma rays lies in their different abilities of penetrating the irradiated material. Gamma rays have a high penetration capacity. The penetration capacity of electron rays depends on the energy of the accelerated electrons (Fig. 2).

Due to electron accelerators, the required dose can be applied within seconds, whereas several hours are required in the gamma radiation plant[1].

Cobalt 60 serves as the source of radiation in the gamma radiation plant. Many of these radiation sources are arranged in a frame in such a way that the radiation field is as uniform as possible. The products on pallets are conveyed trough the radiation field. The radiation dose is applied gradually, that is to say, in several stages, whereby the palleted products are conveyed around the Co – 60 radiation sources several times. This process also permits the application of different radiation doses from one product type to another. It can be used for irradiation of polyolefines, polyesters, halogen polymer and polyamides from thermoplastics group, elastomers and thermoplastic elastomers[2]. Some of them need the addition of crosslinking agent. The dimensional stability, strength, chemical resistance and wear of polymers can be improved by irradiation. Irradiation cross-linking normally creates higher strength as well as reduced creep under load if the application temperature is above the glass transition temperature (Tg) and below the former melting point[3]. Irradiation cross-linking leads to a huge improvement in resistance to most of the chemicals and it often leads to the improvement of the wear behaviour.

2. Experimental

Properties of unirradiated (natural) and irradiated TPE – E with the doses up to 199 kGy have been compared. Injection molding machine Arburg 420 C Allrounder Advance has been used for sample preparation[4,5]. Tested polymer: Thermoplastic elastomer TPE-E.

Tensile test has been carried out on the Zwick 1456 tensile testing machine according CSN EN ISO 527 - 1, 527 - 2 standard. Test Xpert standard software was used for test evaluation.Testing samples have been irradiated by the dose of 0, 66, 99, 132, 165 and 199 kGy.

3. Results and discussion

For easier and faster comparison of the measured values, so called dimensionless values ([-]) expressed as the ratio of separate measurements to the maximum value reached during the given measurements were used (Fig. 2 and Fig. 3).

3.1. Tensile strength, elongation

The dose of irradiation influence mechanical properties of monitored properties. The tensile strength is the highest with the dose of 66 kGy and with the higher dose falls of with the dose higher than 132 kGy oscillate tensile strength around the same value as in the case of not irradiated polymer.

The elongation is markedly influenced by irradiation. Higher dose of irradiation leads to important reduction of elongation. By the dose of 199 kGy is the reduction of elonga-

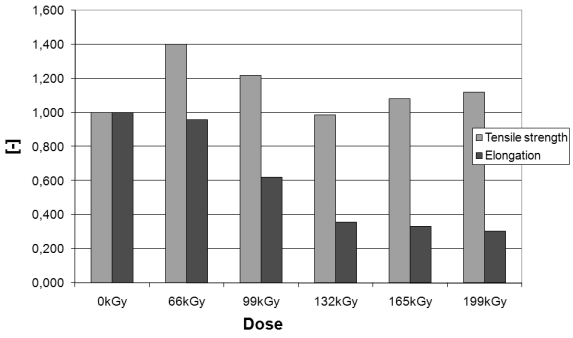

Fig. 2. **Comparison of tensile strength and elongation**

tion is four time in comparison with the unirradiated TPE-E (Fig. 2).

3.2. Modulus

Modulus of elasticity of irradiated thermoplastic elastomer TPE-E rises with the dose of irradiation. The highest difference between irradiated and unirradiated thermoplastic elastomer reached to 50 % with the dose of 199 kGy (Fig. 3).

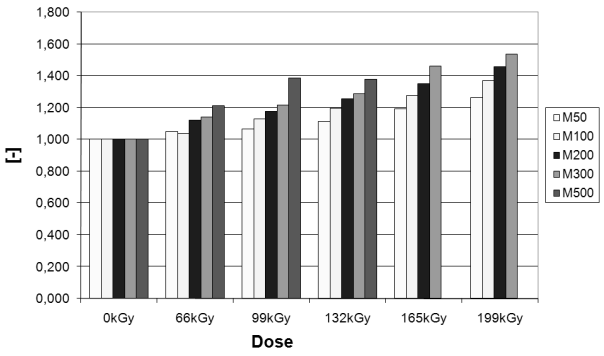

Fig. 3. **Comparison of modulus of elasticity**

4. Conclusion

The differences of mechanical properties of irradiated and natural thermoplastic elastomers TPE-E have been found out. Advantage of irradiation process laies in possibility to carry out the process on the final products, e.g. injection molded parts, extruded or thermoformed products. In other hand it is necessary to have in mind, that irradiation is and additional process which need additional cost. It is necessary to take in account all benefits/cost resulting from the irradiation process already during the design stage of the polymer part.

The energy of accelerated electrons effect the penetration ability of radiation.Thus only defined zone of the polymer product can be affected. The properties of polymer product would be controlled in this way.

This article is financially supported by the Czech Ministry of Education, Youth and Sports in the R&D project under the title 'Modelling and Control of Processing Procedures of Natural and Synthetic Polymers', No. MSM 7088352102 and 'CEBIA Tech', No. CZ.1.05/2.1.00/03.0089.

REFERENCES

1. Drobný J. G.: *Radiation Technology for Polymers*. CRC Press, Boca Raton 2003.
2. Crawford R. J.: *Plastic Engineering - 3 rd Edition*. Butterworth – Heinemann, Oxford 1998.
3. Dole M.: *The radiation chemistry of macromolecules*. Academic Press, New York and London 1972.
4. Stanek M., Manas M., Manas D., Sanda S.: Chem. Listy *103*, 91 (2009).
5. Stanek M., Manas M., Manas D.: *Mold Cavity Roughness vs. Flow of Polymer.* Novel Trends in Rheology III, AIP, New York, USA, p.75–85, (2009).

M. Maňas, D. Maňas, M. Staněk, Š. Šanda, and V. Pata *(Tomas Bata University in Zlin, Zlin, Czech Republic):* **Improvement of Mechanical Properties of TPE by Irradiation**

The article describes the effect of irradiation on properties of thermoplastic elastomer. The irradiation leads to huge improvement of their mechanical properties. The changes of properties depend on the dose of irradiation.The modulus of elasticity goes up to 50 % wheras the elongation drops to four times with the dose of irradiation of 196 kGy.

THE EFFECT OF VARIOUS NON-LINEAR MATRIX TYPES ON MECHANICAL PROPERTIES OF PARTICULATE COMPOSITE

ZDENĚK MAJER*, and EVA NOVOTNÁ

Brno University of Technology, Technická 2896/2, 616 69 Brno, Czech Republic
majer@fme.vutbr.cz

Keywords: polymer composite, Young´s modulus, rigid particles, non-linear matrix, FEM

1. Introduction

In this article polymeric particulate composites are studied. The polymeric particulate composites, especially with the polypropylene matrix (PP) and mineral fillers (rigid particles), are of great practical importance due to the possibility both of modifying many different mechanical properties and reducing the price/volume ratio of resulting material[1,2]. The properties of the matrix and rigid particles (especially size, shape and material properties) can have a significant effect on the global behavior of the composite. The change of the general material properties of the particulate composites (i. e. elastic modulus or yield stress) is the principal motivation for investigation composites filled by rigid particulate[3].

Numerical calculations are considered a perfect homogeneous distribution of the particles in the matrix[4,5].

2. Numerical model

The numerical model was created with respect a few general terms[6]: (i) particles should be of small size (less than 5 μm), (ii) aspect ratio must be close to unity to avoid high stress concentration, (iii) particles must debond prior to the yield strain of the matrix polymer in order to change the stress state of the matrix material and (iv) particles must be dispersed homogeneously in the polymer matrix.

The deformation behavior of a two-phase composite (soft matrix and rigid particle) with homogeneously distributed particles was numerically simulated on a microscopic scale using the finite element program ANSYS (see Fig. 1a). The finite element model was three dimensional with periodic boundary conditions on each side of the representative volume element model (RVE). The representative volume element was pulled from 27 unit cells. The calculated configuration corresponding to perfect adhesion between particles and matrix was considered. For simulations only one to eight model was used, see Fig. 1b.

For the numerical modeling the following assumptions were valid: the spherical shape of the particles, the regular distribution of the particles and the perfect adhesion between particle and matrix.

The mesh of finite elements was created using 20-node elements; this corresponds to the SOLID95 ANSYS element. In fact, the critical locations were situated at the boundary between the particles and the matrix. The mesh was created to be more accurate in these zones and more dispersed in the matrix. The number of elements depends on the volume filler fraction (from pure matrix up to volume filler fraction 40 %); it was included between 100 000 and 300 000.

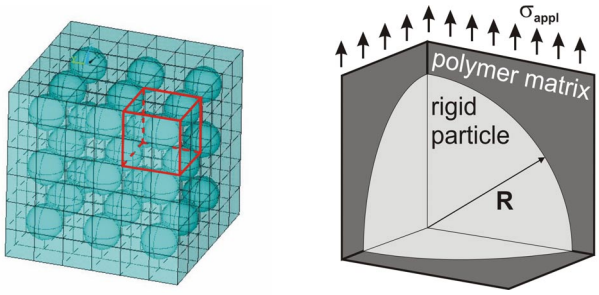

Fig. 1. **a) Homogeneously distributed particles in representative volume element (RVE) considered for numerical simulations (one unit cell in red contour); b) one eight of the unit cell = FEM model**

3. Experiment

The matrix of measured composite was copolymer PP SHAC KMT 6100 (produce by Shell International Chemical Co. Ltd.). This material is used for injection of various products (i. e. tools, cars components, equipment of household)[7].

As rigid fillers were used magnesium hydroxide in two commercial available versions; company named KISUMA 5AU and MAGNIFIN H 10. In addition MAGNIFIN H 10 was modified by 2.5 % stearic acid named ASTRA. In fact, three different types of composites and pure natrix were measured (see Tab. I).

The ideal size of particles from experiment was determined too (see Fig. 2). According to Fig. 2 size dispersion was detrminated and it can be said that assumption of particle size 1 μm was correct and valid.

Table I
Different types of materials identification

Material	S	F2	F4	F6	S2	S4	S6	N2	N4	N6
Filler	---	KISUMA 5AU companymodified			MAGNIFIN H 10 modified			MAGNIFIN H 10 unmodified		
[%] VFF	0	20	40	60	20	40	60	20	40	60

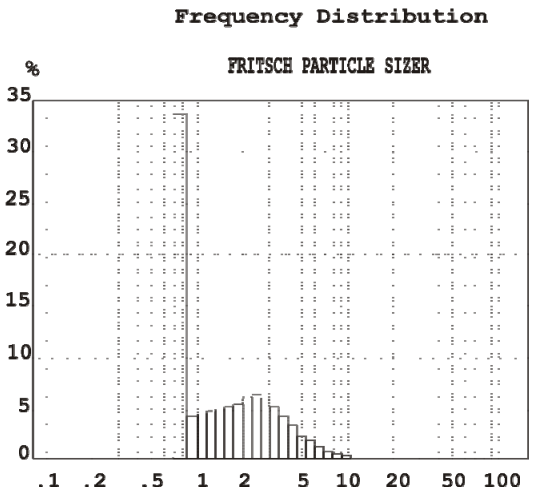

Fig. 2. **Distribution of particles size for KISUMA 5AU filler**

4. Results and discussion

The polymeric particulate composites with the polypropylene matrix (PP) filled by mineral aggregates (rigid particles) were studied. Generally, the addition of rigid particles to a soft polymer matrix will have two main consequences. Firstly, the particulate composite will have out of doubt greater Young's modulus than self soft matrix. But secondly, rigid particles have an indispensable embrittling effect on the composite.

The presented work was focused mainly on the possibility of the particulate composite numerical modeling. Assuming that the particles in composite were regularly distributed in the matrix the Young's modulus for different types of composites was calculated. The configuration corresponding to base matrix (matrix without particles) was considered as a special case.

The comparison between numerical results and experimental data was evaluated (see Fig. 3 for VVF = 20 %). Numerical results were calculated for three different types of composites (see Tab. I). Almost ideal congruity experimental data with numerical results for SMS2 composite (polypropylene with 20 % modified MAGNIFIN H 10) were found. Same composite but with unmodified particles had slightly higher value of Young's modulus. Composite with company modified particles KISUMA 5AU had moderate differences with comparison to SMN2 composite. It can be due to different type of acid for particles modification.

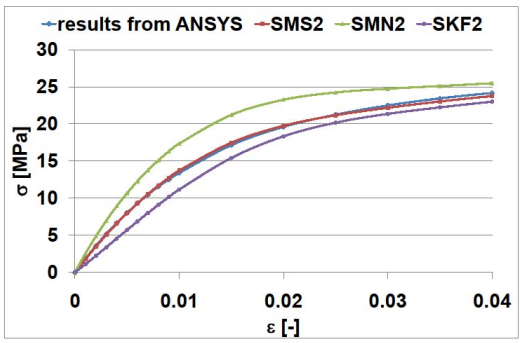

Fig. 3. **Comparison of results from ANSYS with experimental data of composite different type for volume filler fraction 20 %**

5. Conclusions

It is shown that mechanical properties of particulate composite using numerical calculations can be use. We are able qualitatively very well estimate the Young's modulus of particulate composite for various volume filler fraction.

In the case of polymer matrix with 20 % particles is shown that numerical results are very close to particulate composite with modified particles MAGNIFIN H 10.

This research was supported by grant P107/10/P503 of the Czech Science Foundation.

REFERENCES

1. Pukánszky B.: Eur. Polymer J. *41*, 645 (2005).
2. Nezbedová E.: Chem. Listy *101*, 28 (2007).
3. Veselý P., Nezbedová E., Vlach B.: Chem. Listy *102*, 1276 (2008).
4. Balac I., Milovancevic M., Tang Ch., Uskokovic P., Uskokovic D.: Mater. Lett. *58*, 2437 (2004).
5. Jančář J., Kučera J., Veselý P.: J. Mater. Sci. *26*, 4872 (1991).
6. Zuiderduin W. C. J., Westzaan C., Huétink J., Gaymans R. J.: Polymer *44*, 261 (2003).
7. Molíková E.: *Ph.D. Thesis* (2003) (in czech).

Z. Majer, and E. Novotná[a] *(Institute of Solid Mechanics, Mechatronics and Biomechanics,* [a] *Institute of Materials Science and Engineering, Brno, Czech Republic):* **The Effect of Various Non-Linear Matrix Types on Mechanical Properties of Particulate Composite**

The main objective of this contribution is the numerical investigation of the properties in polymeric particulate composite. The composite was modeled as a two-phase continuum (using representative volume element) and numerically simulated on a microscopic scale using finite elements method (ANSYS). For calculations of the composite Young´s modulus finite element model with respect the elastic-plastic model of polymer matrix (polypropylene) was used. The numerical results with experimental data were confronted as well as the data for modeling of primary matrix was determinate from experiment.

THE INFLUENCE OF SUBSTRATE BIAS ON NANOHARDNESS OF a-C:N FILMS DEPOSITED ON CoCrMo ALLOY

MARIÁN MARTON[a], DAVID KOVALČÍK[a], EVA ZDRAVECKÁ[b], MARIÁN VARGA[a], LENKA GAJDOŠOVÁ[a], ERIK VAVRINSKÝ[a], MARIAN VESELÝ[a], ROBERT REDHAMMER[a], and MARCUS HOPFELD[c]

[a] KME FEI STU in Bratislava, Ilkovičova 3, 812 19 Bratislava, [b] Department of Technologies and Materials, FME TU of Košice, Mäsiarska 74, 040 01 Košice, Slovak Republic, [c] Ilmenau university of technology, Institute of materials engineering, Ilmenau, Germany
marian.marton@stuba.sk

Keywords: DLC, Carbon nitride, Nanohardness, Raman spectroscopy, CoCrMo

1. Introduction

The biocompatibility along with mechanical properties and corrosion behavior plays an important role in feasibility of biomedical implants. Diamond like carbon seems to be the promising material in which all these requirements can be achieved. Covering the surface of artificial joints and implants by DLC thin film may lead to extension of lifetime of the implants, improvement of implants acceptance by human body and decrease of the organism immune system inflammation reactions[1]. The mechanical properties of DLC are directly affected by sp^3/sp^2 ratio. It is known that, the incident carbon ions energy is the key factor affecting the atoms hybridization. The application of substrate bias is frequently used to control the energy around 100 eV to promote the formation of sp^3 bonds in the film[2,3]. In this study nitrogen doped amorphous carbon (a-C:N) films were deposited on medical grade CoCrMo alloy. The influence of negative substrate bias on the thin films nanohardness was investigated.

2. Experimental

a-C:N thin films were deposited on cylindrical CoCrMo samples in a vacuum system UVNIPA-1-001 described previously[4] using a pulsed arc source for sputtering the graphite target. The substrates were cleaned for 10 min. with Ar ions prior to the deposition cycle. The sputtering frequency of the arc source pulses was 3 Hz and the total number of sputtering pulses was 3000. Background pressure was 10^{-4} Pa and working pressure was maintained at around 1 Pa according to gas flow. Argon to nitrogen (Ar/N) gas flow ratio was set up to 40/40 sccm. The temperature was kept below 150 °C. Negative substrate bias from 0 to −2.5 kV was applied during deposition process. Hardness measurements were performed using Fisher Picodentor HM500. The structural properties of a-C:N films were studied by Raman spectroscopy with 632.8 nm radiation from a He–Ne laser. The Raman spectra were fitted with a Gaussian line to obtain the D and G peak positions and I_D/I_G ratio.

3. Results and discussion

The Raman spectra for a-C:N films deposited with different substrate bias are shown in Fig. 1. Spectra of the films deposited under different conditions contain the typical diamond-like carbon D and G broad peaks attributed to the disorder-allowed optical zone mode (A_{1g}) of microcrystalline graphite sheets and optically allowed zone (E_{2g} mode) of the aromatic ring in graphite, sp^2 coordinated C-C bonds, C-N bonds and sp^2 C-N bonds, respectively[5]. The D peak arises owing to the limitation in the graphite domain size induced by grain boundaries or imperfections, such as substitutional N atoms and sp^3 coordinated carbon and nitrogen atoms.

A remarkable change in G peak position and I_D/I_G ratio with varying substrate bias can be observed in Fig. 2. The G peak position decreases from 1537 cm^{-1} to 1525 cm^{-1} with increasing negative substrate bias from 0 to −2.5 kV. As the incident carbon ion energy due to changing substrate bias increases, the I_D/I_G ratio decreases from 0 V and has a minimum value around −2 kV and then again increases. Robertson reported that, the I_D/I_G falls as the number of rings per cluster falls and the fraction of chain groups (disorder) rises. The I_D/I_G is also in direct proportion to in-plane correlation length L_a or domain size[3]. The increase of substrate bias leads to a rise in carbon ion kinetic energy that promotes the carbon ion bombardment on the substrate surface during the film deposition and favors the formation of sp^3 carbon bonding. However, when the ion energy is too high, the ions may damage the films surface and cause sp^3 bonds to transform into sp^2 bonds[6,7].

Fig. 3 shows the dependence of hardness and G peak full width at half maximum (FWHM) on negative bias for a-C:N on CoCrMo. We can see that the hardness has its maximum between 1 kV and 2 kV, whereas the G peak width decreases nearly linear. High hardness can be reached using the optimum ion energy for the formation of high concentration of sp^3 C-C and C-N bonds in the a-C:N film.

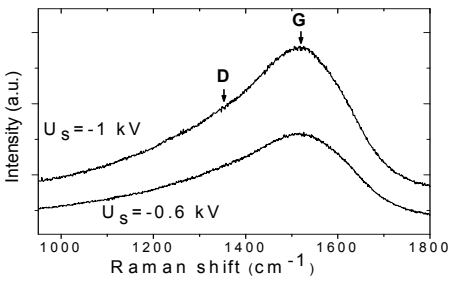

Fig. 1. **Typical Raman spectra of a-C:N on CoCrMo deposited with different negative substrate bias**

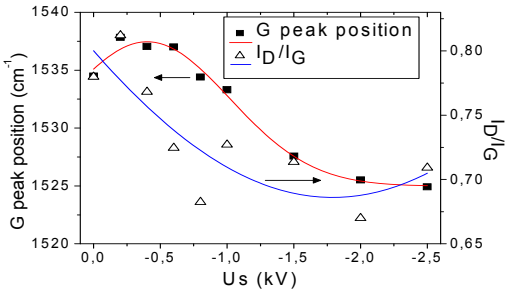

Fig. 2. **Dependence of raman G peak position and I_D/I_G ratio of a-C:N deposited with different substrate bias**

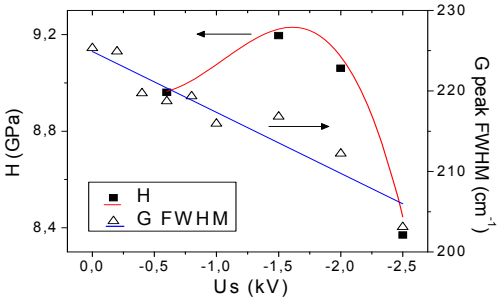

Fig. 3. **Dependence of hardness and I_D/I_G ratio of a-C:N deposited with different substrate bias**

4. Conclusions

Diamond like carbon thin films were deposited on medical grade CoCrMo alloys by glow discharge sputtering method with different substrate biasing and gas flow. Hardness of the coated samples was dependent on the value of connected negative substrate bias. The highest hardness on CoCrMo substrates was measured for negative bias between 1 kV and 2 kV, where the Raman spectroscopy showed the lowest I_D/I_G ratio and G peak position.

This work was done in Center of Excellence CENAM-OST (Slovak Research and Development Agency Contract No. VVCE-0049-07) and was financially supported also by grants APVV-0628-06, APVV-0548-07, SK-CZ-0139-09, LPP-0094-09, LPP-0246-06, LPP-0149-09, and VEGA 1/0807/08, 1/0857/08, 1/0390/08.

REFERENCES

1. Choi H. W., Lee K.-R., Park S. J., Wang R., Kim J.-G., Oh K. H.: Surf. Coat. Technol. 202, 2632 (2008).
2. Lifshitz Y.: Diamond Relat. Mater. *8*, 1659 (1999).
3. Robertson J.: Mater. Sci. Eng. *R37*, 29 (2002).
4. Marton M., Zdravecká E., Vojs M., Ižák T., Veselý M., Redhammer R., Varga M., Šatka A.: Vacuum *84*, 65 (2010).
5. Sui J. H., Zhang Z. G., Cai W.: Nuclear Instruments and Methods in Physics Research B *267*, 2475 (2009).
6. Surdu-Bob C., Vladoiu R., Badulescu M., Musa G.: Diamond Relat. Mater. *17*, 1625 (2008).
7. Sui J. H., Gao Z. Y., Cai W., Zhang Z. G., Mater. Sci. Eng. A *454–455*, 472 (2007).

M. Marton[a], D. Kovalčík[a], E. Zdravecká[b], M. Varga[a], L. Gajdošová[a], E. Vavrinský[a], M. Veselý[a], R. Redhammer[a], and M. Hopfeld[c] *([a] KME FEI STU in Bratislava, [b] Department of Technologies and Materials, FME TU of Košice, Košice, Slovak Republic, [c] Ilmenau university of technology, Institute of materials engineering, Ilmenau, Germany):* **The Influence of Substrate Bias on Nanohardness of a-C:N Films Deposited on CoCrMo Alloy**

In this study nitrogen doped amorphous carbon (a-C:N) films were deposited on medical grade CoCrMo alloy substrates by vacuum glow discharge sputtering technique from graphite target using different deposition conditions. The influence of negative substrate bias on the thin films nanohardness was investigated. The structural properties of a-C:N films were evaluated by Raman spectroscopy.

NANOINDENTATION INTO PMMA AND FUSED SILICA BY SPHERICAL AND POINTED INDENTERS – A COMPARISON

JAROSLAV MENČÍK[a], **and JIŘÍ NOHAVA**[b]

[a] *University of Pardubice, Studentská 95, 532 10 Pardubice, Czech Republic,* [b] *CSM Instruments, Rue de la Gare 4, CH-2034 Peseux, Switzerland*
jaroslav.mencik@upce.cz

Keywords: Nanoindentation, spherical indenter, pointed indenter, viscoelasticity, calibration

1. Introduction

The paper compares characteristic features of low-load indentation into two different homogeneous materials: fused silica and polymethyl-methacrylate. FS has high elastic modulus and hardness, and its response to load is instantaneous. PMMA is more compliant, with response depending also on time. For each material, two indenters were used: pointed, with high stresses, leading always to irreversible deformations, and spherical, where the stresses grow gradually. Under low loads, fully reversible deformations thus can be attained, suitable for the study of elastic or viscoelastic properties.

2. Experiments

All tests were done by nanoindenters NHT and UNHT from CSM Instruments, Switzerland, with a Berkovich indenter and a spherical indenter of nominal radius R = 200 μm.

2.1. Polymethyl-methacrylate (PMMA)

Creep tests and load-unload tests were done with a spherical indenter and a Berkovich indenter.

Creep test with a spherical indenter

The load grew to the nominal value F = 5.12 mN during 5.7 s and then it was held constant till indenter stopping (≈ 1050 s, Fig. 1). The growth of indenter depth in time, $h(t)$, was approximated by a model consisting of a spring (C_0) in series with three Kelvin-Voigt bodies[1]:

$$[h(t)]^m = K F\{C_0 - \Sigma C_j[1 - \rho_j \exp(-t/\tau_j)]\} \quad (1)$$

where m = 3/2, $K = 3/(4\sqrt{R})$, and constants C_1, C_2, …C_n are compliances pertaining to the relaxation times τ_j; n = 3. The constants $\rho_j = (\tau_j/t_R)[\exp(t_R/\tau_j) - 1]$ correct the fact of that the load grows to the nominal value during some time t_R; see Ref.[2]. The instantaneous compliance C_0 is related to the reduced instantaneous modulus as:

$$C_0 = 1 / E_r \quad (2)$$

E_r is related to the specimen modulus E and indenter modulus E_i as $1/E_r = [(1 - \nu^2)/E + (1 - \nu_i^2)/E_i]$; ν is the Poisson´s ratio. The constants were as follows:

$C_0 = 2.75{\cdot}10^{-10}$, $C_1 = 2.29{\cdot}10^{-10}$, $C_2 = 1.72{\cdot}10^{-10}$, $C_3 = 1.10{\cdot}10^{-10}$ (all m^2/N), τ_1 = 1.6 s, τ_2 = 19.5 s, τ_3 = 195.0 s.

The reduced instantaneous elastic modulus E_r, calculated via Eq. (*2*) as $1/C_0$, is E_r = 3.64 GPa.

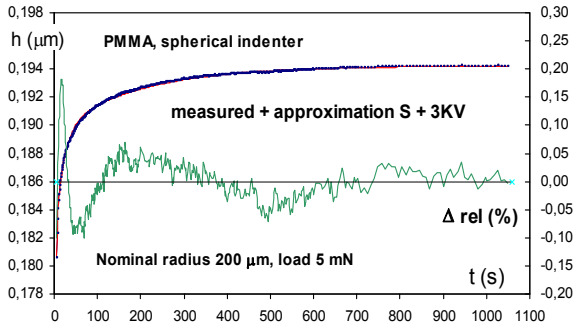

Fig. 1. **Indentation creep of PMMA under constant load. Δ rel – relative difference between the measured and calculated values**

The apparent reduced modulus was also calculated from the depth of penetration using Hertz formula[3]

$$E_r = (3/4)F R^{-1/2} h^{-3/2} \quad (3)$$

In this case, E_r was 3.53 GPa for the end of load growth (depth h = 181 nm), and 3.18 GPa for the end of dwell under constant load (with h = 194 nm).

The mean contact pressure, calculated from[3]

$$p_m = \pi^{-1}[(16/9)FE_r^2/R^2]^{1/3} \quad (4)$$

for F = 5.12 mN, E_r = 3.6 GPa and R = 200 μm, was only p_m = 45.7 MPa. For such low streses, the deformations were mostly viscoelastic and reversible.

Creep test with Berkovich indenter

The load increased during 18 s to F = 201 mN and then it was held constant 3700 s, without a sign of indenter stopping. The indenter displacement $h(t)$ during the dwell was fitted by several rheological models. The constants were again calculated from Eq. (*1*), now with m = 2 and $K = \pi/(2 \tan \alpha)$. Similarly good fits were obtained by the model „Spring + Dashpot + 2Kelvin-Voigt bodies" and „S+3KV". However, the contact pressure was much higher than under spherical indenter and caused irreversible plastic and viscous deformations. Thus, the S+D+2KV model is more appropriate. For the same reason, also the „instantaneous" compliances (C_0 = 2.9–3.1·10^{-10} m^2/N for the model S+D+2KV, and 3.4–4.0·10^{-10} m^2/N for S+3 KV) were higher than in the low-load tests with spherical indenter. Thus, elastic modulus cannot be determined in this way.

Load-unload tests with Berkovich indenter

The load increase to the nominal force of 300 mN lasted 23 s, the dwell under nominal load lasted 62 s, and the unloading lasted 20.6 s; the maximum depths were 8.12–8.20 μm. The elastic reduced modulus E_r, was calculated using Oliver & Pharr[4] approach:

$$E_r = (\pi^{1/2}/2\beta)\, S/A^{1/2} \qquad (5)$$

where $S = dF/dh$ is the contact stiffness at the beginning of unloading, A is the contact area calculated from the contact depth h_c ($= h - 0.75F/S$), and β is a constant ($\beta = 1$ for spherical indenter and 1.034 for Berkovich one).

In five tests[1], E_r varied between 3.62–3.67 GPa, close to the values from creep tests with Berkovich indenter. These values were also close to those obtained by J.M. for sheet PMMA in bending tests with relatively fast loading (3.7–3.9 GPa at 0.45 s, decreasing to 3.0 GPa after 1000 s).

Mean contact pressure (hardness), obtained from load-unload tests with Berkovich indenter[1] was about 205 MPa. This value has caused irreversible viscoplastic deformations in the polymer.

2.2. Fused silica

Tests with Berkovich indenter

A simple load-unload cycle was used, with the parameters: 32 s increase to the maximum load F = 20.1 mN, 15 s dwell, and unloading to 0; the maximum depth was h = 433 nm. The reduced modulus, calculated using Oliver & Pharr approach, was E_r = 70.9 GPa. The mean contact pressure (hardness) was H = 9.99 GPa.

Tests with a spherical indenter

A load-unload cycle as above was used, with two nominal loads: 51.4 mN and 5.0 mN. For F = 51.4 mN, the depth was h = 132.7 nm. The modulus, determined according to O&P, was E_r = 60.0 GPa, and the contact mean pressure p_m (hardness H) was 641.7 MPa. E_r was also calculated from the maximum indenter displacement using Hertz´ formula (*3*), with the result E_r = 56.4 GPa.

For the lower load, 5.02 mN, the depth was h = 37.0 nm, and the reduced modulus (Oliver&Pharr[4]) was E_r = 47.7 GPa and mean contact pressure p_m = 163.2 MPa. The reduced modulus via Eq. (*3*) was 37.4 GPa. The contact pressure was much lower than the yield stress Y for fused silica (several GPa), and the deformations were only elastic.

Indenter calibration

The elastic modulus of fused silica (FS), obtained from the tests with spherical indenter, was significantly lower than literature values ($E_r \approx$ 70 GPa). In our calculations, the tip radius R = 200 μm was assumed. However, it is known that for small radii the tip shape often deviates from an ideal sphere. If – vice versa – the elastic modulus of the sample is known, it is possible to calculate the apparent (or effective) radius coresponding to the load and penetration.

For example, for F = 51.4 mN, h = 132.7 nm and E_r = 70 GPa, the effective tip radius is R = 134 μm (instead of 200 μm). In this way, the calibration curve, giving the effective radius as a function of penetration depth, $R_{eff}(h)$, may be constructed from the $F(h)$ curve as[5]

$$R_{eff}(h) = (9/16)\, F^2\, E_r^{-2}\, h^{-3} \qquad (6)$$

Fig. 2 shows the calibration curve made for this indenter on FS under the assumption E_r = 70 GPa.

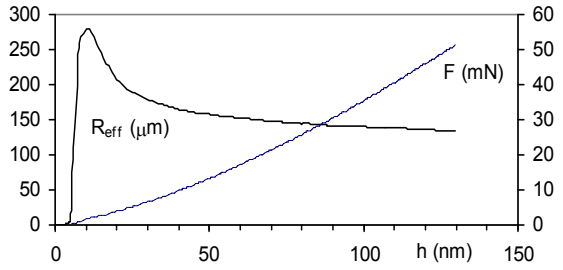

Fig. 2. **Effective radius R_{eff} of the spherical indenter as a function of penetration h. Nominal radius R = 200 μm. Thin curve: $F(h)$**

3. Discussion and conclusions

Streses below a spherical indenter grow gradually with indenter load, and can thus be kept below the onset of irreversible changes. The elastic modulus of PMMA, obtained in this way by spherical indenter, was similar to the values obtained by other means.

For fused silica, the elastic modulus obtained with spherical indenter for very small depths of penetration, differed significantly from the known values. A reason may be the tip deviation from ideal shape. Calibration of spherical indenters is thus necessary. This issue exceeds the scope of this paper (a role can also be played by the indented material) and will be studied more in the future.

This work was supported partly by the Grant Agency of Czech Republic, projects No. GAČR 103/08/1340 and GAČR 103/08/1197.

REFERENCES

1. Menčík J., He L. H., Němeček J.: Polym. Test *30*, 101 (2010).
2. Oyen M.: Philos. Mag. *86*, 5625 (2006).
3. Johnson K. L.: *Contact mechanics*. Cambridge University Press, Cambridge 1985.
4. Oliver W. C., Pharr G. M.: J. Mater. Res. *7*, 1564 (1992).
5. Menčík J.: Chem. Listy *105*, s680 (2011).

J. Menčík[a], and J. Nohava[b] *([a] University of Pardubice, Czech Republic, [b] CSM Instruments, Switzerland):*
Nanoindentation into PMMA and Fused Silica by Spherical and Pointed Indenters – a Comparison

The paper compares characteristic features of low-load indentation into two different materials: fused silica and polymethyl-methacrylate. FS has high hardness and elastic modulus, and instantaneous response to load. PMMA is more compliant, with response depending also on time. For each material, two indenters were used: pointed, with high stresses, causing always irreversible deformations, and spherical with gradual stress growth.

INFLUENCE OF STRAIN RATE ON AUTOMOTIVE STEEL SHEET BREAKING

MÁRIA MIHALIKOVÁ*, MIROSLAV NÉMET, PAVOL ZUBKO, and MAREK VOJTKO

Department of Materials Science, Faculty of Metallurgy, Technical University of Košice, Letná 9, 042 00 Košice, Slovak Republic
maria.mihalikova@tuke.sk

Keywords: automotive steel sheet, dynamic tests

Introduction

Strain rate is a significant external factor and its influence on material behavior in forming process is a function of its internal structure[1,2]. Increasing strain rate increases material's resistance against deformation, but also increases tendency to brittle fracture. Increasing strain rate results in changes to the microstructure and substructure of deformed material.

In practical terms, this means that it is necessary to know the impact of strain rate on mechanical properties of specific material, which are the basis for the calculation of the deformational resistance, but also the processes taking place during forming.

Prediction of strain rate impact on material's properties is quite complicated. It is related to the fact that intensity of strain rate impact is a function of material's internal structure, and also the interpretation of test results is very difficult at high rates.

Increasing strain rate also increases the critical flow stress, yield strength grows strongly, tensile strength increases, and deformation characteristics of the material are changed[3–9] . At the same time also values of forming criteria derived from these characteristics are changed[5,6].

2. Experimental material and methods

Experiments were performed on samples taken from the cold rolled strips and then hot dip galvanized H340 LAD grades intended for the production of stampings in automotive industry.

The tested material was 1.0 mm thick. Samples of the material were taken in rolling direction and flat test specimens for tensile test were produced. Tensile test was carried out on INSTRON 1185 tensile testing machine at loading speed of 1–1000 mm min^{-1}. Dynamic tests were carried out on PSW type pendulum impact tester at max. speed of 24 m s^{-1}.

3. Results and discussion

According to references[3,4], increasing strain rate increases the resistance of tested steel to plastic deformation, yield strength and tensile strength increase (Fig. 1).

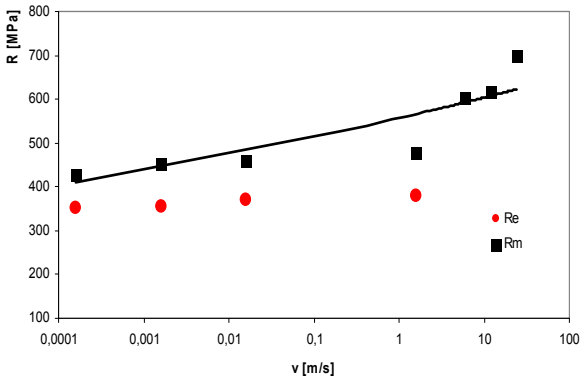

Fig. 1. **Effect of loading rate on the yield stress R_e and the tensile ultimate strength R_m of steel H340 LAD**

In the static loading is progress of R_m linear. For the dynamic speeds is observed high growth of R_m.

At static loading speed of 1.6×10^{-4} m s^{-1} a transcrystalline ductile failure with dimple morphology can be observed on fracture surface, while the shape and symmetry of dimples is related to the stress at failure spot. The size and layout of the dimples depends on the grain size. At low rates, (Fig. 2) it is a ductile failure with equiaxial dimple morphology, where the dimples are deep.

The generation of fracture surface is accompanied by significant plastic deformation associated with increasing the number of active slip systems at a higher strain rate. Fracture surface obtained at loading speed of 1.6 m s^{-1} has similar characteristics (Fig. 3).

On the fracture surface, the number of secondary cracks and voids that are generated in direction of lines, has increased. Increase of plastic deformation is clear from the shape of dimples. Dimples are elongated with a strong presence of striation on the walls. Coalescence of cavities is seen

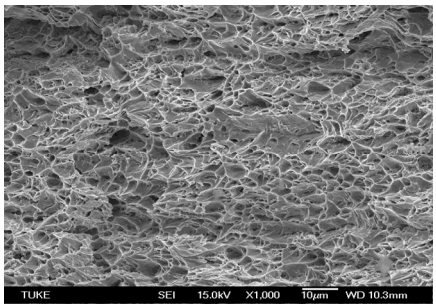

Fig. 2. **Fracture surface at a loading rate 1.6×10^{-4} m s^{-1}**

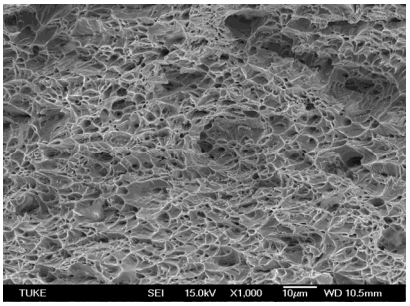

Fig. 3. **Fracture surface at a loading rate 1.6 m s^{-1}**

more significantly in direction perpendicular to tensile stress direction. At loading speed of 24 m s^{-1}, the angle of rupture increases (Fig. 4), uneven surface is generated, dimples are shallower. At the void growth in the process of ductile failure, coalescence bridges are getting narrow. Bridges are breaking by gradual stretching. Formation of ductile fracture takes place in the phase of micro-defect nucleation, void growth and contraction of bridges between the voids. Micro-defects nucleation in ductile failure was generated by decohesion of inclusions and other particles from the matrix.

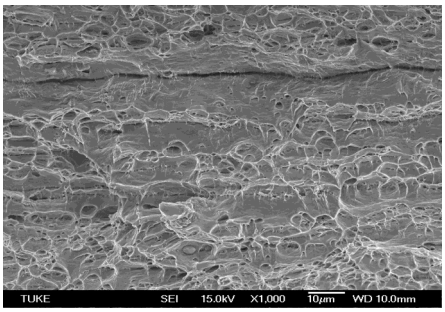

Fig. 4. **Fracture surface at a loading rate 24 m s^{-1}**

Microscopic observation of strain-strengthened steel structure confirmed that with increasing strain rate, also inhomogenity of deformation plasticity increases in the volume of deformed steel. It follows that the resulting properties of strain-strengthened material are influenced by strain rate.

4. Conclusion

The document analyzes the impact of strain rate of H340 LAD steel sheet on the change of mechanical properties and fracture appearance. Based on the results of tensile tests and dynamic tests at the loading speed range from 1.6×10^{-4} m s^{-1} to 24 m s^{-1} for the tested steel, it can be stated:

- At increasing strain rate up to about 3 s^{-1}, there is no deterioration in material characteristics of deep drawing, but deformation resistance increases.
- In case of the tested HSLA steel of H340 LAD grade it is the ductile failure, which is generated by void mechanism.
- At all speeds (rates), the material fails by transcrystalline ductile fracture with dimple morphology.
- With the increasing strain rate, plastic deformation becomes more significant and there is greater number of voids that are oriented in the direction of lines, dimples are shallower.

This study was supported by the Grant Agency of Slovak Republic, grant project APVV No. 0326-07.

REFERENCE

1. Micheľ J., Buršák M.: Komunikacie *5*, 34 (2004).
2. Lis J., Lis A., Kolan K.: J. Mater. Process. Technol. *162*, 350 (2005).
3. Čižmárová E., Micheľ J.: Acta Metallurgica Slovaca *9*, 90 (2003).
4. Micheľ J., Buršák M., Mihaliková M.: Acta Metallurgica Slovaca *11*, 134 (2005).
5. Wang H. R., Wang W., Gao J. O.: Mater. Lett. *64*, 219 (2010).
6. Zhao H., Gary G.: Mater. Sci. Eng. *A 207*, 46 (1996).
7. Buršák M., Mamuzič I., Micheľ J.: Metalurgija *46*, 37 (2007).
8. Vadasová Z., Mihaliková M.: J. Metals, Mater. Minerals *16*, 15 (2006).
9. Kormaníková E., Kotrasová K.: J. Int. Sci. Publ. Mater., Methods & Technologies *3*, 117 (2009).

M. Mihaliková, M. Német, P. Zubko and M. Vojtko *(Department of materials science, Faculty of metallurgy, Technical University of Košice, Slovakia):* **Impact of Strain Rate on Automotive Steel Sheet Breaking**

This analysis is aimed at impact of loading speed from 1.6×10^{-4} m s^{-1} to 24 m s^{-1} on changes in breaking of steel sheet used for automotive body components. Experiments were performed on samples taken from H340 LAD grade strips produced by cold rolling and hot dip galvanizing. Material strength properties were compared based on measured values, and changes to fracture surface character were observed.

THE INFLUENCE OF SURFACE PROTECTION ON CORROSION RESISTANCE OF ALUMINIUM ALLOY

ANETA NĚMCOVÁ*[a], MARTIN ZMRZLÝ[b], and BOHUMIL PACAL[a]

[a] *Institute of Material Science and Engineering, Faculty of Mechanical Engineering, Brno University of Technology, Technická 2, Brno,* [b] *Institute of Materials Science, Faculty of Chemistry, Brno University of Technology, Purkyňova 118, Brno, Czech Republic*
ynemco00@stud.fme.vutbr.cz

Keywords: aluminium alloy, corrosion, salt spray test, coating, surface protection

1. Introduction

The resistance of Al against corrosion in aqueous media can be attributed to a rapidly formed surface oxide film, which is composed of Al_2O_3, $Al(OH)_3$ and AlO(OH) phases. Nevertheless, the presence of aggressive ions like chlorides causes significant attack[1,2]. The main corrosion process that is developed on the surface of Al alloys in a NaCl solution is the localized alkaline corrosion in the Al matrix surrounding Al (Mn, Fe, Cr) cathodic intermetallics[3].

In this work is compared the corrosion resistance of AlCu4Mg1 alloy in the basic state and with surface treatment used for protection against extraneous influences in the aircraft industry. This is due to extreme danger of accidents if the local corrosion attack induces a reduction in strength (e.g. in the rivet joints).

2. Experimental material

The experimental material was received as a L-beam with dimensions 14 × 14 mm with length 150 mm and thickness 2 mm. The chemical composition was measured by glow discharge optical emission spectroscopy (GDOES) using Spectrumat GDS-750 device (see Tab. I).

Further material under study was the same alloy, however with protective coating. Fig. 1 shows microstructure of this material with coating containing organic polymer (epoxy resin with unspecific mineral fiber and aluminium particles).

Table I
The chemical composition in wt.% of AlCu4Mg1 alloy

Si	Fe	Cu	Mn	Mg	Zn	Ti	Al
0.21	0.31	4.10	1.08	1.71	0.03	0.02	Balance

3. Experimental procedure

For the assessment of the corrosion behaviour of the specimens of an Al alloy in a spray of neutral aqueous solution of sodium chloride the corrosion chamber Angelantoni DCTC 600 P was used. The course of the corrosion resistance test was in accordance with the standard EN ISO 9227 (ref.[4]). The experiments were carried out with increasing exposition time of 48, 96, 240, 480, 720 and 1000 hrs. Every cycle was conducted in the test environment of 5% NaCl aqueous solution with pH 6.9 and temperature 35±2 °C.

Final cleaning of the specimens after exposition was carried out by dipping in a solution of $CrO_3 + H_3PO_4 + H_2O$; according to Czech standard ČSN 03 8452 (ref.[5]). The weight loss was measured at analytical balances (d = 0.1 mg) after each experiment and calculated in g m^{-2} and mm/year.

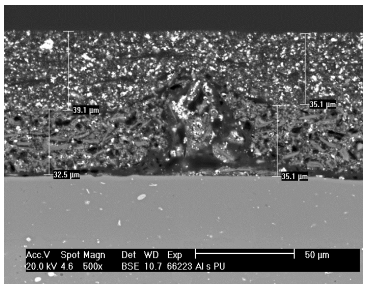

Fig. 1. **The AlCu4Mg1 alloy with protective coating, SEM**

4. Results

The corrosion rate calculated from weight losses versus time exposure are presented in Fig. 2.

Metallographic evaluation was performed according to applicable standard ČSN 03 8137 (ref.[6]). The corrosion attack after representative time of exposition observed by scanning electron microscope on metallographic cross-section cuts is shown in Fig. 3.

The results of local chemical analysis of the friable layer of corrosion products on specimens after 168 h exposure on spots 1 and 2 in Fig. 4 are presented in Tab. II. XRD analysis revealed presence of, $Al(OH)_3$ and large amount of non-

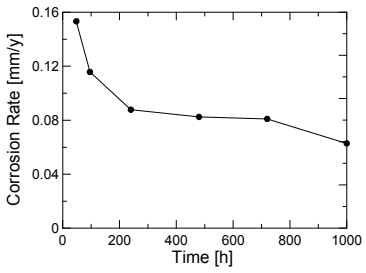

Fig. 2. **Corrosion rate of AlCu4Mg1 as a function of exposure time in corrosion chamber**

crystalline phase, that can be ascribed to mixture of hydrated compounds, including hydrated chlorides of substrate elements etc. There was no corrosion attack observed after 1000 hours exposure on the specimens with protective coating.

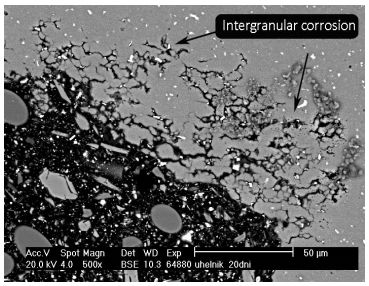

Fig. 3. **Corrosion attack after exposure 480 hours, the AlCu4Mg1 alloy without protective coating, SEM**

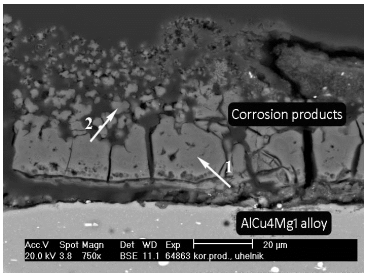

Fig. 4. **The corrosion products on AlCuMg1 alloy after 168 hours exposure, SEM**

Table II
The local chemical analysis by EDX of corrosion products on the surface of AlCu4Mg1 alloy

	Al [wt.%]	O [wt.%]	Cl [wt.%]
Spot 1	39.7	58.7	1.6
Spot 2	38.7	56.4	4.9

5. Discussion

The AlCu4Mg1 alloy was used for testing in neutral salt spray test. The chemical analysis by EDX has shown that the structure composed phases based on Al-Cu-Mg and Al-Cu-Fe -Mn.

The dependence of corrosion rate on exposure time (see Fig. 2) shows the greatest drop between 48 and 240 hours. Further progress was only slightly decreasing. This is type of corrosion when the corrosion attack is markedly localized. The corrosion pits are then filled by corrosion product that act as the partial barrier between metal and corrosion environment.

Pitting was observed after every exposure time with different average depth. Some differences were also obsereved in the depth on the edges and on the planes. After time of 480 hours and longer the intergranular corrosion (see Fig. 3) started to occur besides the corrosion pitting. The intergranular corrosion progressed along the grain boundaries and was observed mainly below the surface, starting from the edges of specimens.

Fig. 1 shows experimental material with protective coating. There wasn´t observed any corrosion attack even after 1000 hours exposure on these specimens.

6. Summary and conclusions

The AlCu4Mg1 alloy was used for salt spray tests in 5% NaCl aqueous solution with neutral pH. The dependence of corrosion rate on exposure time shows the greatest decrease between 48 and 240 hours and further progress was only slightly decreasing. Metallographic evaluation of corrosion attack identified corrosion pitting after every time of exposition and the intergranular corrosion after 480 hours and longer. The main cause of its occurrence was the evolution of corrosion microcells between the matrix and the Al_2CuMg phase which has a cathodic behaviour in the particular environment.

There was no corrosion attack was observed on specimens with protective coating even after 1000 hours exposure.

Result of this work will be utilized for detailed research of strength of rivet joints after corrosion degradation. Morphology and and form of corrosion attack will be very useful for explanation of strength differences at microstructural scale.

This research was supported by project of MIT of the Czech Republic no. FR TI 1/274 and project of the MEYS of the Czech Republic no. 1M2560471601.

REFERENCES

1. Ghali E.: *Corrosion resistance of Aluminium and Magnesium Alloy*. p. 719. Wiley 2010.
2. Mishra A. K., Balasubramaniam R.: Mater. Chem. Phys. *103*, 385 (2007).
3. Szklarska-Smialowska Z.: Corros. Sci. *41*, 1743 (1999).
4. ČSN EN ISO 9227. Prague (2007).
5. ČSN 03 8452. Prague (1989)
6. ČSN 03 8137. Prague (1990).

A. Němcová, M. Zmrzlý, and B. Pacal *(Brno University of Technology, Czech Republic):* **The Influence of Surface Protection on Corrosion Resistance of Aluminium Alloy**

This paper deals with the corrosion resistance of AlCu4Mg1 alloy. The corrosion behaviour was assessed after exposition in the neutral salt spray of 5% NaCl aqueous solution. The weight losses were measured and calculated in g m^{-2} and mm/year. The type of corrosion attack was observed by SEM on the cross-sectioned cuts. The corrosion products were analysed by local chemical analysis using SEM. Further, the corrosion resistance of Al alloy with protective coating were tested.

INITIATION AND GROWTH OF FATIGUE CRACKS IN INCONEL 713LC WITH AL COATING AT 800 °C

SIMONA POSPÍŠILOVÁ[a]*, KAREL OBRTLÍK[b], MARTIN JULIŠ[a], and TOMÁŠ PODRÁBSKÝ[a]

[a] Brno University of Technology, Technická 2896/2, 616 69 Brno, [b] Institute of Physics of Materials, Academy of Sciences of the Czech Republic, Žižkova 22, 616 62 Brno, Czech Republic
pospisilova@fme.vubr.cz

Keywords: low cycle fatigue, IN713LC, aluminide coating, crack initiation, crack propagation rate

1. Introduction

Ni-based superalloy IN713LC is used for gas turbine integral wheels in aircraft industry. The high temperature components are exposed to high temperature fatigue and creep and their interactions, high-temperature oxidation and corrosion in aggressive environment. Protective coatings are used to improve high temperature performance[1]. Low cycle fatigue and high cycle fatigue of the material were studied rarely[2,3]. The diffusion coatings do not affect the creep life of Ni-based superalloys[4] but the effect on the fatigue life depends on number of factors[5]. Both the positive and detrimental effect of coatings was observed.

The aim of the present work is to study the fatigue crack initiation and propagation in superalloy IN713LC with Al coating and without coating at 800 °C. Microstructure characteristics and microhardness of Al coating are documented. Fatigue crack propagation rates from striation spacing observed on fatigue fracture were correlated with the stress intensity factor.

2. Experimental details

The chemical composition of experimental material is following: 0.04 % C; 11.85 Cr; 0.72 % Ti; 5.80 % Al; 2.27 % Nb; 4.54 % Mo; < 0.05 % Mn, Co, Ta; rest Ni.

Low cycle fatigue (LCF) tests were performed on button -end specimens having gauge length and diameter of 15 and 6 mm. The Al diffusion coating was applied to one half of specimens (on the gauge length) by out of pack technique at 1050 °C for 5 hours. Next samples were used without the protected coating. All specimens were fatigued in a computer controlled electro-hydraulic testing system at total strain rate of 0.002 s^{-1} with fully reversed total strain cycle ($R_\varepsilon = -1$) at 800 °C in air. Based on previous research[3] it was found that the application of the Al diffusion coating results in changes of the fatigue behaviour of Inconel 713LC. Particularly, the stress response and the fatigue life of the coated material are different from those of the uncoated material. Light microscopy (LM) and scanning electron microscopy (SEM) were used to study fracture surface and specimen sections. The microstructure, microhardness, and thickness of the coating were obtained. The fatigue crack propagation rate was estimated from the striation spacing in fracture surfaces.

3. Experimental results and discussion

The microstructure of Al coating is documented in Fig. 1 that shows the fracture surface at the specimen surface. The Al diffusion coating consists of the outer layer (OL) and the diffusion layer (DL). The thickness of the coating and the diffusion zone in as-coated state was 45–70 μm and 20–25 μm, respectively. The average microhardness of the outer layer and the diffusion layer in as-coated state was 512HK0.1 and 610HK0.1 (the Knoop microhardness test, load 0.1 kg), respectively.

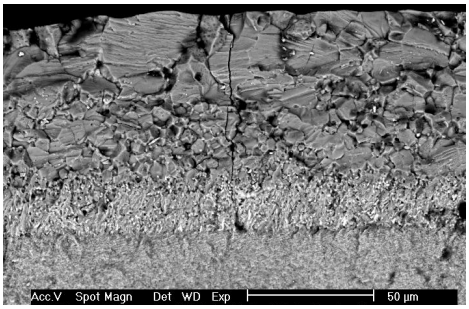

Fig. 1. **Detail of Al coating on fracture surface (SEM)**

The fracture surface of all studied samples is relatively rugged. The casting defects, most often shrinkage pores (up to 0.4 mm in diameter) occurred in fracture surfaces. In all cases, the fatigue crack initiation was observed at the surface both of coated and uncoated specimens. It was accelerated by shrinkage pores and carbides. Striations were observed in fatigue fractures in all specimens. Comparatively high incidence of carbides (type MC) was observed both in the fatigue fracture and final unstable fracture. The number of initiated cracks increases with growing plastic strain amplitude.

The fatigue crack shape was approximated by a semi-elliptical surface crack with a maximum crack depth b and surface crack length $2a$. Fatigue crack propagation rate db/dN was determined by assuming that each striation corresponds to a load cycle. Then, the distance between neighbouring striations s is equal to db/dN, where b is the crack length and N is the number of elapsed cycles.

Fatigue crack propagation rate was correlated with stress intensity factor amplitude K_{aI}. To evaluate stress intensity factor, the linear elastic fracture mechanics was applied. The specimens with the total strain amplitudes ε_a (0.43 and 0.45 %) were chosen, see Tab. I. The stress intensity factor amplitude K_{aI} was obtained from equation (1)[6] valid for semi-elliptical surface crack in the round bar under uniform ten-

Table I
The calibration function F_I and parameters of LCF

Specimen	ε_a[%]	σ_a [MPa]	N_f	b/r	b/a	F_I
1	0.45	582	397	0.08	1.23	0.65
2a*	0.43	651	195	0.33	0.54	0.89
2b*	0.43	651	195	0.52	0.9	0.72

*a,b are two cracks in the same specimen

sion. σ_a is the remote stress amplitude and F_I is the dimensionless stress intensity factor (the calibration function). F_I depends on the ratio *b/r* and *b/a* where *r* is the specimen radius. F_I shown in Tab. I was obtained using the data[6] for the crack depth corresponding to the striation location.

$$K_{aI} = F_I \sigma_a \sqrt{\pi . b} \qquad (1)$$

$$\frac{db}{dN} = A K_{aI}^{m} \qquad (2)$$

$$N = \frac{1}{A \cdot \left(\sigma_a F_I \cdot \sqrt{\pi}\right)^m} \left(\frac{b_f^{1-\frac{m}{2}} - b_1^{1-\frac{m}{2}}}{1-\frac{m}{2}} \right) \qquad (3)$$

Fatigue crack propagation rate *db/dN* versus stress intensity factor range ΔK ($2\,K_{aI}$) is plotted in Fig. 2. The crack propagation rate (square symbols in Fig. 2) were approximated using the Paris-Erdogan law (*2*) and material parameters $A = 5.4 \cdot 10^{-9}$ m cyclus^{-1} (MPa m$^{1/2}$)$^{-m}$ and $m = 2.2$ were evaluated with regression analysis.

It is noted that crack growth data found from striation spacing correspond well with literature data obtained in CT specimens of superalloy IN 713C at 600 °C at R=0 (ref.[7]) (dashed line in Fig. 2). The crack propagation data of the present work are also in a good agreement to fatigue crack propagation rates of surface cracks acquired from cylindrical samples at 600 °C (ref.[7]).

The number of cycles necessary to semi-elliptical surface crack extension from the initial crack depth b_1 to the final crack depth b_f was determined from equation (*3*) based on the integration of the relation (*2*) using (*1*). The initial crack depth is equal to the defect size observed on the fracture surface. b_f is the crack depth at the fatigue failure. The calculation shows that 300 cycles (76 % of fatigue life) are needed for crack propagation in specimen 1. Similarly, fatigue cracks propagates 127 cycles (65 % of fatigue life) in specimen 2. It means, major part of the fatigue life of specimens is spent in fatigue crack propagation from surface defects.

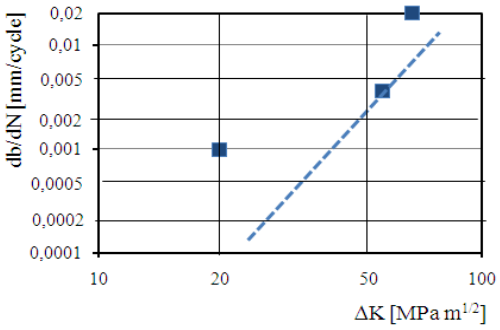

Fig. 2. **db/dN versus ΔK for material IN713LC at 800 °C (squares, present work) and for IN713C at 600 °C (dash line)** [7]

4. Summary

The fatigue crack initiation was observed on the free surface both in coated and uncoated specimens. The fatigue crack propagation rates determined from striation spacing can be approximated by the Paris-Erdogan law.

Research was supported by Czech Science Foundation (project 106/09/P522 and P107/11/2065), Ministry of Education, Youth and Sports (project MEB0810123), Brno University of Technology (project of specific research FSI-S-10-46), Ministry of industry and Trade (project FR-TI1/099).

REFERENCES

1. Čelko L., Klakurková L., Švejcar J.: Mater. Manufacturing Processes *24*, 1155 (2009).
2. Juliš M., Obrtlík K., Pospíšilová S., Podrábský T., Polák J: Procedia Eng. *2*, 1983 (2010).
3. Obrtlík K. et al.: Key Eng. Mater. *452-453*, 265 (2011).
4. Juliš M., Pospíšilová S., Podrábský T.: Chem. Listy *S/102*, 880 (2008).
5. Rahmani K., Nategh S.: Mater. Sci. Eng. *A486*, 686 (2008).
6. Murakami Y.: *Stress Intensity Factors Handbook*. pp 659 -665. Pergamon Books Ltd, 1987.
7. Sonsino C. M., Brandt U., Bergmann J.: Elsevier Applied Science, London and New York 1992.

S. Pospíšilová[a], K. Obrtlík[b], M. Juliš[a], and T. Podrábský[a] *([a] Brno University of Technology, [b] Institute of Physics of Materials AS CR):* **Initiation and Growth of Fatigue Cracks in Inconel 713LC with Al Coating at 800 °C**

This paper is focused on the study of initiation and growth of fatigue cracks in IN713LC with Al protective coating and without coating. Microstructure characteristics and microhardness of Al coating are documented. Fatigue crack initiation and fatigue crack growth mechanisms were identified. The crack propagation rates were obtained based on striation spacing in fracture surfaces.

INDENTATION TOUGHNESS OF Al_2O_3-CNT NANOCOMPOSITES

VIKTOR PUCHÝ[a]*, JÁN DUSZA[a], FAWAD INAM[b], and MICHAEL J. REECE[b]

[a] *Institute of Materials Research, Slovak Academy of Sciences, Watsonova 47, 04353 Košice, Slovakia,* [b] *Centre for Materials Research and School of Engineering and Materials Science, Queen Mary, University of London, Mile End Road, London E1 4NS, UK*
vpuchy@imr.saske.sk

Keywords: indentation toughness, Al_2O_3, carbon nanotube, carbon black

1. Introduction

In the last few years new ceramic/carbon nanotube composites have been developed and a number of authors have reported improved mechanical and functional properties in the case of ceramic/CNT composites compared to the monolithic materials[1]. According to the results reinforcing by CNTs in many cases improved the fracture toughness of Al_2O_3, however, this toughening is not evident, and some of the variations may purely arise from using different testing techniques[2]. The improvement in fracture toughness is due to bridging of the crack surfaces by CNTs during the crack propagation by CNT pullout mechanism, which strongly depends on the interfacial bonding between CNTs and the matrix.

The aim of the present work is to investigate the effect of addition of carbon nanotubes and carbon black on the indentation toughness of alumina-CNT and alumina-carbon black nanocomposites.

2. Experimental materials and methods

The experimental materials were prepared by spark plasma sintering at the Queen Mary University of London[3].

The microstructure and fracture surfaces of the investigated materials were studied using scanning electron microscopy (SEM). The small specimen size did not allowed to use standard fracture toughness test, therefore indentation fracture toughness test was performed at loads of 50 and 100 N using a Vickers indenter, and the calculation were made using Anstis equation:

$$K_{IC} = 0.016\left(\frac{E}{H}\right)^{1/2}\left(\frac{P}{c^{3/2}}\right)$$

where E is the modul of elasticity, H is the hardness and c the radial crack length generated by Vickers's indentation. At least 10 indentation have been made for all investigated materials. The grain size was measured on polished/etched surface and fracture surface of specimens using standard statistical methods.

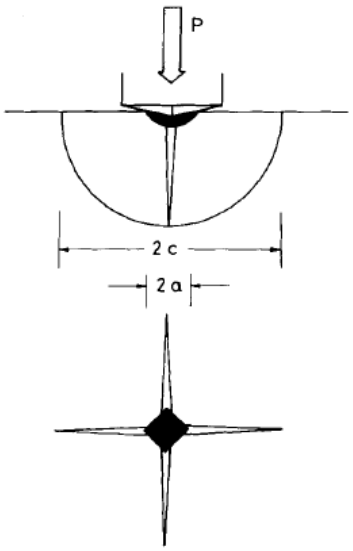

Fig. 1. **Schematic illustration of the indentation cracks used for the calculation of the indentation toughness**

3. Results and discussion

The microstructure of the monolithic Al_2O_3 consists of large, micron sized grains with randomly placed submicrometer sized pores. The grain size of the matrix is lower in the Al_2O_3 + 2 % CB composite and even lower in the Al_2O_3 + 5 % CB composite. Relatively large numbers of CNF clusters were observed on the polished and fracture surfaces of the Al_2O_3 + 5 % CNT composites. This material has even finer matrix with relatively well distributed carbon nanotubes with diameter several of nanometers and very high aspect ration. The smaller matrix grain size in the composite suggests that the carbon black and the CNTs hinder the grain growth during the sintering.

The CNTs in the Al_2O_3-CNT composite were located mainly in the intergranular places and they were well attached to the alumina grains.

The indentation toughness of monolithic alumina is approximately 3.25 MPa $m^{1/2}$ which is comparable with similar materials in the literature. The addition of 2 % carbon black increased the indentation toughness, but after increasing to 5 % decreased to the similar level as the indentation toughness of monolithic material. The addition of 5 % CNTs increased the indentation toughness up to 4.14 MPa $m^{1/2}$ which is the highest value obtained for the materials investigated.

Well-dispersed CNT-reinforced Al_2O_3 nanocomposites have been recently prepared with reasonably high density using hot pressing[4]. According to the results 2 wt.% of CNT addition increased the hardness, flexural strength and fracture toughness of nanocomposites (from 3 to 4.3 MPa $m^{1/2}$), how-

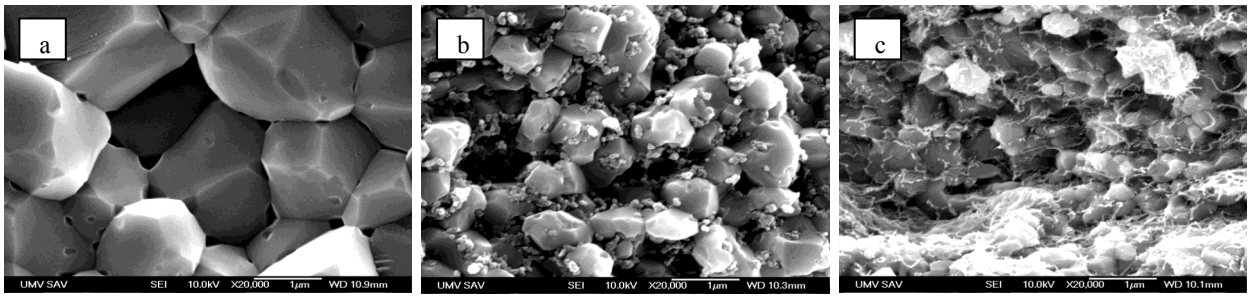

Fig. 2. **Microstructure of the investigated materials, Al_2O_3 (a), Al_2O_3 + 5 % CB (b) and Al_2O_3 + 5 % CNT (c)**

Table I
Indentation toughness and grain size of investigated materials

Sample	K_{IC} [MPa $m^{1/2}$]	Grain size [nm]
Al_2O_3	3.24 ± 0.15	1802 ± 339
Al_2O_3 + 2 % CB	3.84 ± 0.5	1065 ± 120
Al_2O_3 + 5 % CB	3.44 ± 0.25	536 ± 61
Al_2O_3 + 5 % CNT	4.14 ± 0.62	383 ± 45

ever further CNT addition up to 5 wt.% slightly decreased the hardness, reduced the flexural strength but improved the toughness up to 4.5 MPa $m^{1/2}$. The increase in toughness is believed to be associated with the strong interface connections between the CNT and the matrix, resulting in pullout resistance, bridged the crack gaps and hindered the crack propagation by exploiting CNTs elasticity, leading to improved fracture toughness.

In monolithic alumina the toughening mechanisms during the crack propagation are in bridging zone of the propagating crack in the form of frictional and mechanical bridges arising as a result of crack deflection at the Al_2O_3/Al_2O_3 boundaries. These toughening mechanisms are effective in large grain sized ceramics and by decreasing grain size are less important. From this is evident that in composites, investigated in this study, for the improved indentation toughness different toughening mechanisms are responsible. These are probably the carbon based bridges between the alumina grains, which mainly in the case of Al_2O_3 + CNT composite are strong enough to increase the resistance again the crack propagation. These results are in good agreement with the results of recent investigations.[4]

4. Conclusion

The effect of addition of carbon nanotubes and carbon black on the mechanical properties of alumina-CNT and alumina-carbon black nanocomposites has been investigated. The addition of carbon black decreased and approximately 20 %. The increased toughness is probably connected with the interfacial bonding between the CNTs and the matrix and with the bridging effect of the CNTs during the crack propagation.

This work was partly supported by APVV LPP-0174-07, APVV-0034-07, VEGA No. 2/0088/08 and MNT-ERA.NET HANCOC.

REFERENCES

1. Hirota K., Takaura Y., Kato M. and Miyamoto Y.: J. Mater. Sci. *42*, 4792 (2007).
2. Padture N. P.: Adv. Mater. *21*, 1767 (2009).
3. Fawad I., Haixue Y., Daniel D. J., Peijs T., Reece M. J.: J. Eur. Ceram. Soc. *30*, 153 (2010).
4. Ahmad, Unwin M., Cao H., Chen H., Zhao H., Kennedy A., Zhu Y. Q.: Comp. Sci. Technol. *70*, 1199 (2010).

V. Puchý[a], J. Dusza[a], P. Hvizdoš[a], F. Inam[b], and M. Reece[b] *([a] IMR SAS Košice, Slovakia, [b] University of London, UK):* **Indentation Toughness of Al_2O_3-CNT Nanocomposites**

Indentation toughness behavior of Al_2O_3 based nanocomposites with addition of carbon nanotubes and carbon black prepared by spark plasma sintering (SPS) has been studied by Vickers indentation technique. Vickers hardness and cracks were measured and recorded, indentation toughness were calculated. The microstructure, CNT/CB dispersion and fracture surface were studied using optical and electron microscopy and its mechanisms were identified.

NANOSCALE DYNAMIC MECHANICAL ANALYSIS OF SOFT TISSUE AND ITS FINITE ELEMENT MODELING

JOSEF ŠEPITKA*, JAROSLAV LUKEŠ, JIŘÍ KUŽELKA, and JAN ŘEZNÍČEK

Czech Technical University in Prague, Faculty of Mechanical Engineering, Dep. of Mechanics, Biomechanics and Mechatronics, Technická 4, 166 07 Prague 6, Czech Republic
Josef.Sepitka@fs.cvut.cz

Keywords: nanoindentation, end plate, nanoDMA, intervertebral disc, FEM

1. Introduction

According to recent studies the nanoindentation seems to be very effective tool to analyze mechanical properties of biomaterials especially in case of hardly accessible soft tissue. Machining of biological material to normalized shaped samples for tensile testing is quite difficult

This paper presents a study of implementing the experimental data from nanoscale dynamical mechanical analysis (nanoDMA) of bovine intervertebral end plate (EP) to the material library of commercial software Abaqus and nanoDMA experiment modeling.

1.1. End Plate

Cartilaginous end plate (EP) (Fig. 1) is a part of intervertebral disc that creates the transition zone between hard vertebral body and soft annulus fibrosus (AF). The process of calcification within AF lamellae and EP is crucial for mechanical behavior of intervertebral disc. It is observed as the clinical syndrome in childhood and elderly population. Sometimes the etiology is unclear. The previous trauma, surgical intervention or overloading are suggested. Calcification of end plate has critical influence on salute flow to avascular annulus fibrosus end nucleus pulposus and initiates the IVD degeneration[1]. Nanoindentation is an experimental method, which can tell us more about tissue mechanics of end plate[2].

2. Methods

2.1. Samples preparation

Sagittally halved bovine spine was obtained from the butchery. The lumbar spine motion segments were immediately dissected and five millimeter thick plates of vertebral body, end plate and annulus fibrosus were cut and polished under running water condition. Samples were placed into the physiological solution right after. The plate of the sample was glued to the bottom of the Petri dish and surrounded by physiological solution again. The surface was water free and ready to be indented.

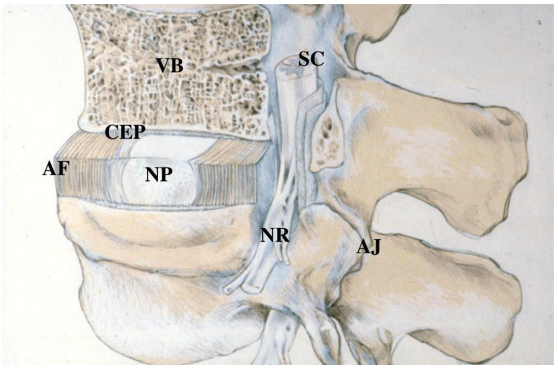

Fig. 1. **A schematic view of a spinal segment and the intervertebral disc. The figure shows the organization of the disc with the nucleus pulposus (NP) surrounded by the lamellae of the annulus fibrosus (AF) and separated from the vertebral bodies (VB) by the cartilaginous end-plate (CEP). The figure also shows the relationship between the intervertebral disc and the spinal cord (SC), the nerve root (NR), and the apophyseal joints (AJ). Adopted from Urban et al. (2004)[1]**

2.2. Testing conditions

NanoDMA load controlled experiment was performed with Hysitron TriboIndenter™ system with Berkovich diamond tip at the temperature 21.4 °C.

Harmonic loading $P_0 = sin(\omega t)$ with dynamic load amplitude P_0 = 20 μN was specified for the harmonic frequency range 5–295 Hz. During nanoDMA experiment was applied static load with maximum force P_{max} = 800 μN. That corresponded to the contact indentation depth h_c= 360.49 ± 129.73 nm. Configuration of measurement was assumed from Lukeš et. al. (2010)[3] The amplitude of the displacement oscillation X_0 and Φ the phase shift of the displacement with respect to the driving force are recorded by the nanoindentation system. The machine compliance C_i and the stiffness value K_i were determining during air indent calibration. The procedure was adopted from Asif et. al. (1999)[4] as well as the analysis of dynamic data.

The reduced storage modulus (E_r'), the storage loss modulus (E_r'') and $tan\delta = E_r'/E_r''$ depending on compliance and stiffness of the sample are given by

$$E_r' = \frac{K_s\sqrt{\pi}}{2\sqrt{A}} \qquad E_r'' = \frac{\omega C_s\sqrt{\pi}}{2\sqrt{A}} \quad \text{and} \quad \tan\delta = \frac{C_s\omega}{K_s}$$

where A is the contact area based on tip area function related to the contact depth at quasistatic loading[5]. The storage and loss modulus of the sample E_s' and E_s'', respectively, are related to the reduced storage and loss modulus by

$$\frac{1}{E'_r}=\frac{\left(1-\nu_i^2\right)}{E_i}+\frac{\left(1-\nu_s^2\right)}{E'_s} \quad \text{and} \quad \frac{1}{E''_r}=\frac{\left(1-\nu_i^2\right)}{E_i}+\frac{\left(1-\nu_s^2\right)}{E''_s}$$

where subscripts *i* and *s* refer to the indenter and sample materials, respectively, and *v* is the Poisson's ratio.

The storage modulus and the loss modulus are related to the complex modulus $E_s^* = E_s' + iE_s''$ and indicate the ability of the sample to store and return energy (recoverable deformation; E_s') and dissipate energy (E_s''). The ratio of the loss modulus to the storage modulus (i.e., *tan δ*) reflects the viscoelastic behavior of the material. It is a material parameter independent of the tip-sample contact area.

3. Numerical methods

3D FEM model was created for a verification of the nanoDMA method. The model was composed by the sample and Berkovich tip. Commercial software Abaqus 6. 9. 2 was used for modeling and analysis. The sample was modeled as compliant cylinder with elastic modulus E = 2 GPa and with Poisson´s ratio $v = 0.4^2$. Indenter tip was modeled as discrete rigid material. Tip radius was R = 100 nm. Hundred micron deep indent was simulated in the first step (quasistatic preload). Harmonic loading was applied on indenter tip using displacement amplitudes in the range of frequencies, which we measured by the nanoDMA experiment. Calculations were using perturbation steps (steady oscillations were solved).

Two material models were defined. The first model considered deviatoric components of deformation only and the second model considered deviatoric and volumetric components of deformation.

4. Results and conclusions

FEM calculation data correlated with nanoDMA experimental data that is shown in the Fig. 2. Figure 2. indicates an agreement between model and experiment in obtained data *tan δ* vs. frequency. *Tan δ* represents ratio of loss modulus and storage modulus. The imaginary and real parts of reaction forces correspond to these moduli in FEM analysis. The first material model that was defined for numerical simulation (deviatoric components of deformation only) is not in such an agreement as the second material model (deviatoric and volumetric components of deformation). A friction was not included in FEM simulation which could be explanation of difference between nanoDMA experiment and FEM simulation. It is possible to implement the experimental data to the Abaqus library successfully.

This work was supported by the Grant Agency of the Czech Technical University in Prague, grant No. SGS10/247/OHK2/3T/12.

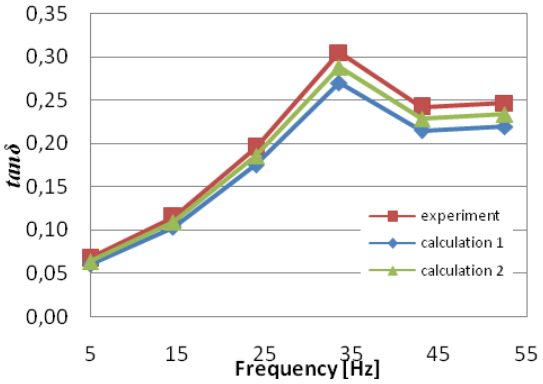

Fig. 2. **Loss tangent vs. frequency. Comparation of the experiment data with the FEM calculation**

REFERENCES

1. Urban J. P. G., Roberts S.: Arthritis Res. Therapy *5*, 120 (2003).
2. Lukes J., Mares T., Nemecek J., Otahal S.: *IFMBE Proceedings 23*, 1792 (2009).
3. Lukeš J., Šepitka J., Němeček J.: Chem. Listy *104*, s341 (2010).
4. Asif S. A. S., Wahl K. J., Colton R. J.: Rev. Sci. Instrum. *70*, 2408 (1999).
5. Oliver W. C., Pharr G. M.: J. Mater. Res. *7*, 1564 (1992).

J. Šepitka, J. Lukeš, J. Kuželka, and J. Řezníček *(Czech Technical University in Prague, Faculty of Mechanical Engineering):* **Nanoscale Dynamic Mechanical Analysis of Soft Tissue and Its Finite Element Modeling**

Hysitron Triboindenter™ TI950 system has been used for studying the viscoelastic properties of bovine intervertebral disc's end plate (EP) by means of nanoscale mechanical dynamic analysis (nanoDMA). NanoDMA offers several testing modes in which is a harmonic function prescribed to the indentation force $P(t)=P_0 \sin\omega t$. The resultant displacement amplitude [nm] and phase shift are measured. Then the storage (*E'*) and loss (*E''*) moduli can be calculated as well as their ratio *tanδ* and complex modulus (*E**). These parameters provide the viscoelastic description of our tissue. NanoDMA experimental data were used for Abaqus material card creation and were employed to the mathematical simulation of nanoDMA experiment.

NANOINDENTATION OF VERY THIN HARD COATINGS

JOSEF ŠEPITKA*, JAROSLAV LUKEŠ, VLADIMÍR JECH, FRANTIŠEK ČERNÝ, and JAN ŘEZNÍČEK

Czech Technical University in Prague, Faculty of Mechanical Engineering, Dep. of Mechanics, Biomechanics and Mechatronics, Technická 4, 166 07 Prague 6, Czech Republic
Josef.Sepitka@fs.cvut.cz

Keywords: nanoindentation, DLC, partial unloading

1. Introduction

Nanoindentation technique is being widely used for measuring intrinsic mechanical properties of hard thin coating. However, we are limited by the size of tip radius, geometry of tip, system sensitivity, quality of sample's surfaces etc. How does the rule of 1/10 rule (EN ISO 14577-1:2002) influence our testing? Does this rule take into the account different tip geometry?

This paper presents a study of actual limits for nanoindentation of very thin coating by two types of diamond tips.

2. Methods

2.1. Samples preparation

Multilayer surface was deposited on tool steel known as a Vanadis to increase wear resistance. TiN coating (50 nm) was deposited by IBAD (Ion Beam Assisted Deposition) method for the improvement of the adhesion of the very top layer of carbon (100 nm). High-voltage device (90 keV) was used for IBAD method for TiN deposition. Then low-energy device (1 keV) was employed for deposition of carbon coating. Ion Beam Mixing (IBM, 90 keV) method was applied on samples to improve the adhesion. IBM mixes the atoms from separate layers and substrate as well. However, it also sputters the surface, which reduces the final thickness of the coatings <150 nm in our case[1]. Our thin coating was approximately 100 nm thick. Thickness was measured by Si quartz during deposition.

2.2. Testing conditions

Quasistatic load controlled experiments were performed on Hysitron TriboIndenter™ system with fluid Berkovich and Cube Corner diamond tips using a partial unloading function[2] consisting of 100 cycles, each composed by loading segment, dwell and unloading segment (1×2×1 second) with maximum force P_{max} = 7300 μN (Fig. 1) and P_{max} = 3000 μN, respectively for Berkovich and Cube Corner tip, respectively. Applied loads corresponded to the contact indentation depths h_c = 145 ± 15 nm at the temperature 22.6 °C. The grids of 7×7 indents with 5 μm separation were applied on four areas for each tip (392 indents overall).

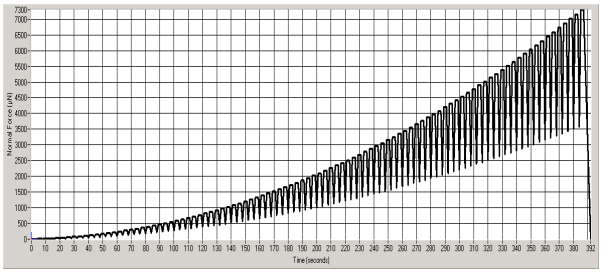

Fig. 1. **Load-displacement graph of the nanoindentation for partial unloading function that consists from 100 cycles using for Berkovich tip**

2.3. Quasistatic indentation

Elastic modulus (*1*) is determined from the unloading segment of indentation curve.

$$E_r = \frac{\sqrt{\pi}}{2}\frac{S}{\sqrt{A}} \qquad (1)$$

where E_r is reduced modulus, A is contact area and S is measured stiffness. Hardness is defined:

$$H = \frac{P_{\max}}{A} \qquad (2)$$

where P_{max} is the peak of indentation load and A is the projected area of the tip imprint[3].

Tip area functions were made for both tips on the fused quartz sample[3] by fitting the A vs. hc to the relationship implemented to TriboScan´s software:

$$A(h) = C_0 h_c^2 + C_1 h_c^1 + C_2 h_c^{1/2} + C_3 h_c^{1/4} + C_4 h_c^{1/8} + C_5 h_c^{1/16} \qquad (3)$$

where C_0 = 24.5 stands for Berkovich and C_0 = 2.598 for Cube Corner tip, respectively. We fitted the polynomial function *A (h)* (3) with $C_{0\text{-}4}$ and $C_{0\text{-}3}$ for Berkovich and Cube Corner tip, respectively.

3. Results

Both tips, Berkovich and Cube Corner tip area functions (*3*) were obtained according to ISO 14577 using the known material parameters (E_r, H) for fused quartz Er = 69.6 GPa and hardness H = 9.25 GPa. The average values from our calibration procedure were: Er = 68.47 ± 4.69 GPa and hard-

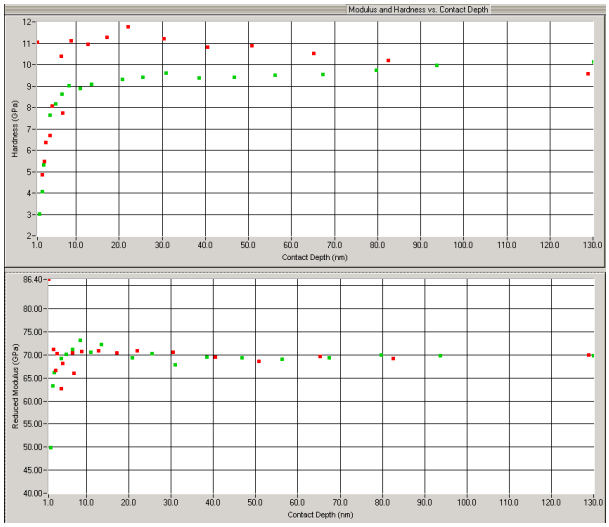

Fig. 2. **Modulus and Hardness vs. Contact Depth Berkovich (green) and Cube Corner (red) tip obtained for fused quartz as calibration of area function**

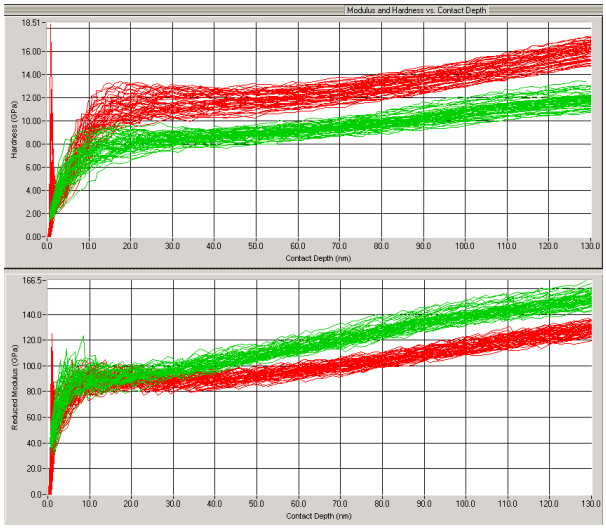

Fig. 3. **Modulus and Hardness vs. Contact Depth Berkovich (green) and Cube Corner (red) tip obtained for the sample for 1–130 nm depth**

ness H = 8.56 ± 1.98 GPa and Er = 69.39 ± 5.57 GPa and hardness H = 7.54 ± 2.85 GPa for Berkovich and Cube Corner tip, respectively, from 1 to 192 nm of contact depths (Fig. 2).

4. Discussion and conclusion

Cube corner tip is more suitable for measuring of a reduced elastic modulus Er of a very thin coating than Berkovich tip. If we look at the Fig. 3, cube corner data are stable for the rage of depths 10 to 40 nm which means that there is no influence of substrate. Berkovich tip data were unaffected in the range from 10 to 15 nm only. The values of Er in these ranges for both tips are reliable intrinsic properties of our thin coating because the tip area calibration uses the Er data measured on fused quartz. However the values of hardness from dataset obtained by cube corner were already higher than expected values of hardness for fused quartz (Fig. 2). It means that cube corner is not ideal for measuring the hardness except for very thin films, where Berkovich indenter cannot be applied due to either very shallow indents (no development of plastic deformation) or immediate influence of substrate (unsatisfaction of 1/10 rule). Fig. 3 shows that the substrate effect starts influencing the results at depth 15 nm for Berkovich and at 40 nm for Cube corner tip in case of our thickness of coating 100 nm. It means that nanoindentation with Berkovich tip has to really respect the rule of 1/10. Sharper Cube corner indenters are usable for thinner coating then 100 nm because the plastic deformation is developed even for very shallow indents and plastic zone beneath the tip is smaller which means that the influence of substrate comes later on in deeper depths.

This research work was supported by the Ministry of Education project: Transdisciplinary research in Biomedical Engineering II. No. MSM 6840770012.

REFERENCES

1. Černý F., Pitter J., Konvičková S., Jech V.: Surf. Coat. Technol. *203*, 2566 (2009).
2. Dietiker M. Nyilas R. D., Solenthaler Ch., Spolenak R.: Acta Mater. *230*, 499 (2004).
3. Oliver W. C., Pharr G. M.: J. Mater. Res. *7*, 1564 (1992).

J. Šepitka, J. Lukeš, V. Jech, F. Černý, and J. Řezníček *(Czech Technical University in Prague, Faculty of Mechanical Engineering):* **Nanoindentation of Very Thin Hard Coatings**

Nanoindentation technique is being widely used for measuring intrinsic mechanical properties of hard thin coating. However, what are the limits of the nanoindentation methods if we have to follow 1/10 rule according to EN ISO 14577-1:2002. How we can analyse very thin coatings about 100 nm thicknesses if we have to follow that rule? We are limited by the size of tip radius, system sensibility, quality of sample surfaces etc. Our paper will be focused on these limits of nanoindentation technique.

EVALUATION OF LOCAL MECHANICAL PROPERTIES IN P23/P91 DISSIMILAR WELDS AFTER CREEP EXPOSURE AT 500–600 °C

LUCIE STŘÍLKOVÁ*, ZDENĚK KUBOŇ, and VLASTIMIL VODÁREK

MATERIALS AND METALLURGICAL RESEARCH Ltd., Pohraniční 693/31, 706 02 Ostrava - Vítkovice, Czech Republic
lucie.strilkova@mmvyzkum.cz

Keywords: heterogeneous weld, P23 steel, P91 steel, creep, HV10, HV0.02

1. Introduction

P23/P91 dissimilar welds are candidate joints for applications in modern boilers. Redistribution of interstitial elements (C, N), known as up-hill diffusion, represents a significant degradation mechanism of dissimilar welds during creep service. This phenomenon is controlled by activity differences of elements across the fusion boundary[1]. In the vicinity of the fusion boundary the carbon/nitrogen depleted zone forms in a low alloy steel and the carbon enriched zone arises in the adjacent layer of a high alloy steel. These changes of chemical composition and microstructure occurring during the creep exposure lead to degradation of mechanical properties of dissimilar weldments.

2. Experimental material and results

Two types of dissimilar P23/P91 welds were studied. These welds were fabricated in SES Tlmače, in the Slovak Republic[2]. For *Weld A* filler metal with chemical composition corresponding to the P91 base metal was applied. *Weld B* was made using the type P23 filler metal. Weldments were prepared by combination of the shielded metal arc welding (SMAW) and the gas tungsten arc welding (GTAW), earlier reported as TIG. The post-weld heat treatment (PWHT) of both welds was performed at 750 °C for 2 hours. Cross-weld samples for creep rupture tests involved base materials, heat affected zones and weld metal. Creep tests to rupture were carried out in air at 500, 550 and 600 °C in the stress range between 55 and 200 MPa.

Weld A (P23/WM91/P91)

The results of creep rupture tests carried out at 500 and 550 °C were close to the –20 % scatter band of standardized creep strength curve for P23 steel[2]. The most pronounced decline of creep strength was observed during the exposure at 600 °C. The highest reduction area values were achieved in the case of specimens tested at 500 and 550 °C and the highest stresses.

Metallographical investigations revealed several localities prone to the development of creep damage. At testing temperatures of 500 and 550 °C final rupture occurred in intercritical area of the P23 heat affected zone (HAZ) or in the fusion zone (FZ) on the side of the P23 steel – in this coarse grain area a partial decarburization took place during the both PWHT and creep exposure. After exposure at 600 °C failure locations were identified in the partly decarburized FZ on the side of the P23 steel and in some specimens in intercritical part and/or fine grain regions of the P91 HAZ. Creep damage could simultaneously develop in several parts of the weldment, often in both HAZ′s of the weld. Final fracture occurred in the "weakest" locality for the given testing parameters[3].

Hardness profiles were evaluated on longitudinal sections through the ruptured cross-weld specimens. Table I summarises maximum and minimum HV10 values together with their allocation for both the weldment after PWHT and for individual creep ruptured specimens. Results proved that hardness of the P91 weld metal (WM) higher than that of the P91 base metal (BM).

Table I
Maximum and minimum HV10 values and locations of their occurrence in the creep ruptured specimens, *Weld A*

Temp. [°C]	Stress [MPa]	Time to rupture, [h]	HV max.	Locality of max HV 10 messure-ment	HV min.	Locality of min HV 10 messure-ment
after PWHT			285	CG HAZ P91	185	IC HAZ P23
500	200	18 802	339	WM	183	BM P23
550	150	9 715	287	WM	157	IC HAZ P23
550	140	8 665	281	CG HAZ P91	167	IC HAZ P23
600	110	1 384	343	WM	182	BM P23
600	100	4 056	319	WM	167	BM P23
600	90	5 171	260	WM	153	IC HAZ P23
600	75	9 852	294	WM	171	BM P23

where CG HAZ is the coarse grain part of the heat affected zone and IC HAZ is the intercritical part of the heat affected zone.

Fig. 1 shows a longitudinal section through the ruptured cross-weld specimen after creep exposure 600 ° C/75 MPa/9852 h. The specimen failed in the IC part of the P91 HAZ. Microhardness profile across the WM91/ P23 interface shows hardness changes due to carbon redistribution. A big scatter in microhardness values can be attributed to the presence of creep cavities and precipitates in the metal matrix. HV0.02 values in the P91 HAZ continuously decreased from the fusion line up to the fracture line. Partial austenitization of the P91 steel in the IC HAZ was responsible for a drop and heterogeneity of hardness in this part of the HAZ. As a result, during subsequent creep exposure creep deformation was localized in this region.

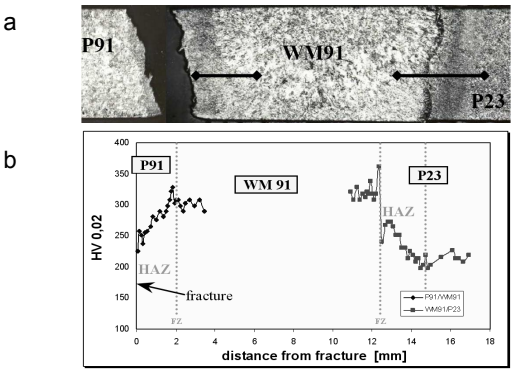

Fig. 1. **Macrostructure (a) of the specimen after creep exposure 600 °C/75 MPa/9852 h and HV0.02 profiles (b) across the HAZs of the cross-weld specimen – locations are marked in (a), Weld A**

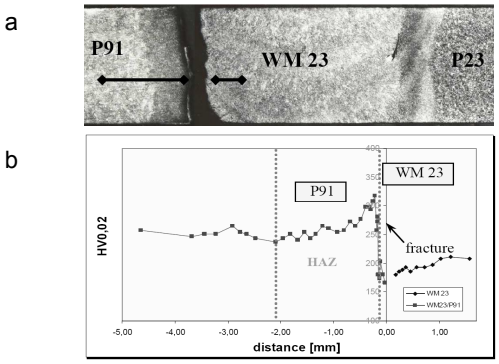

Fig. 2. **Macrostructure (a) of the specimen after creep exposure 600 °C/75 MPa/6550 h and HV0.02 profiles (b) across the P91 HAZ and WM23 – locations are marked in (a), Weld B**

Weld B (P23/WM23/P91)

The results of creep rupture tests performed at 500 and 550 °C were close, or slightly below the –20 % scatter band of standardized creep strength curve for P23 steel. The most pronounced decline of creep strength was observed, as in the case of *Weld A*, during creep exposures at 600 °C. In the course of creep at temperature of 500 °C the critical locus of the *Weld B* specimens was the IC HAZ on the side of the P23 BM. At temperatures of 550 and 600 °C the preferred failure location was the partly decarburized layer of the WM23 in the vicinity of the WM23/P91 fusion zone[3]. Fig. 2 shows for the specimen after creep exposure 600 °C/75 MPa/6550 h macrostructure and HV0.02 profile in the vicinity of fracture line.

Table II
Maximum and minimum HV10 values and locations of their occurrence in the ruptured creep specimens, *Weld B*

Temp. [°C]	Stress [MPa]	Time to rupture, [h]	HV max.	Locality of max HV 10 messurement	HV min.	Locality of min HV 10 messurement
after PWHT			260	CG HAZ P91	175	IC HAZ P23
500	200	2 327	256	BM P91	183	WM,BM P23
500	170	18 679	216	CG HAZ P91	143	BM P23
550	140	6 390	236	CG HAZ P91	146	BM P23
550	125	7 778	235	BM P91	147	IC HAZ P23
600	110	1 090	238	BM P91	168	BM P23
600	100	1 538	236	BM P91	168	IC HAZ P23
600	90	2 917	216	BM P91	136	IC HAZ P23
600	75	6 550	231	BM P91	150	IC HAZ P23

Table II summarises maximum and minimum HV10 values together with their allocation for the Weld B after PWHT and for individual creep ruptured specimens. Hardness of the WM23 in the *Weld B* was comparable with that of the P23 BM[3]. The preffered failure location in *Weld B* specimens corresponded to the partly decarburized part of the WM23 adjacent to the P91 HAZ. Microhardness profile across the fusion zone in the specimen after 600 °C/75 MPa/6550 hours exposure proves hardening of the carburized P91 HAZ and at the same time softening of the partly decarburized WM23 on the opposite side of the fusion line.

3. Conclusions

Creep rupture strength of both welds was close to the lower bound of the ±20 % scatter band around the mean creep rupture strength curve of P23 steel. Creep damage can develop simultaneously in several parts of weldments, fracture then occurs in the "weakest" locality. Microhardness data are useful for the detection of local degradation of dissimilar welds.

The authors would like to express thanks for the financial support from the project MSM 2587080701.

REFERENCES

1. Pilous V., Stránský K.: Structural Stability of Weldments for Power Plants, *ČSAV Study*, Academia Praha, 1989, p. 185 (in Czech).
2. Vodárek V., Kuboň Z.: *Proc. of 5th International Conference on Mechanics and Materials in Design*, p. 267. Porto 2006.
3. Vodárek V., Kuboň Z., Foret R., Hainsworth S. V.: *Proc. of the IIW International Conference Safety and Reliability of Welded Components*, (P. Mayr et al., ed.), pp. 233–238. Graz 2008.

L. Střílková[a], Z. Kuboň[a], and V. Vodárek[b]
([a] MATERIALS AND METALLURGICAL RESEARCH, Ltd., [b] Technical University of Ostrava, Ostrava, Czech Republic):
Evaluation of Local Mechanical Properties in P23/P91 Dissimilar Welds after Creep Exposure at 500–600 °C

The experience indicates, that in majority of cases where high temperature failure of power plant components occurs, defects predominate in the vicinity of weldments. P23/P91 dissimilar welds are perspective weld joints for applications in boilers of modern power plants. This contribution deals with studies on creep behaviour and local mechanical properties of P23/P91 dissimilar welds tested at 500, 550 and 600 °C.

EFFECT OF VARIOUS GRAIN BOUNDARY PHASES AND SiC ADDITION ON THE FRACTURE CHARACTERISTICS OF Si_3N_4 BASED CERAMICS

PETER TATARKO[a,*], MONIKA KAŠIAROVÁ[a], JÁN DUSZA[a], and PAVOL ŠAJGALÍK[b]

[a] *Institute of Materials Research, Slovak Academy of Sciences, Watsonova 47, 040 01 Košice,* [b] *Institute of Inorganic Chemistry, Slovak Academy of Sciences, Dúbravská cesta 9, Bratislava, Slovak Republic*
tatarko.peter@gmail.com

Keywords: nanoindentation, silicon nitride, composite, rare-earth oxides, grain boundary phases

1. Introduction

In silicon nitride ceramics the microstructure with elongated β-Si_3N_4 grains as the reinforcing agent is a necessary but not a sufficient condition for the improvement of the fracture resistance. Silicon nitrides prepared with different densification additives and processing conditions that exhibit selfreinforced microstructures can have very different fracture resistances[1].

In silicon nitride a continuous, amorphous intergranular film is formed at the boundary between two Si_3N_4 grains and its composition varies with the oxides used as sintering additives[2,3]. The bond strength across the interface is significantly influenced by the chemistry of the intergranular phase[2]. This bond strength determines where the crack propagates, at the grain/intergranular phase boundary or inside the intergranular phase. Because the coefficient of thermal expansion (CTE) of the grain boundary phase varies when the sintering additives are modified, residual stresses will be a function of the chemistry at the grain boundary[3]. These residual stresses, together with the residual stresses introduced to the composites Si_3N_4-SiC due to the different physical properties of the silicon nitride and silicon carbide, also influence the crack propagation and the fracture toughness.

The aim of this work is to investigate the effect of various grain boundary phases and SiC addition on the local deformation and fracture characteristics of Si_3N_4 based ceramics using indentation and micro-indentation technics.

2. Experimental procedure

The starting mixtures of the set of five Si_3N_4-SiC nanocomposites consisted of the following powders: α-Si_3N_4, amorphous SiO_2, carbon black and different rare-earth oxides RE_2O_3 (RE = La, Nd, Y, Yb, or Lu). All compositions contained the same atomic amount of RE element. Amount of SiO_2 and C was calculated to achieve 5 vol.% of SiC after "*in situ"* carbothermal reduction process. Simultaneously, the set of five reference monolithic Si_3N_4 materials with the same composition of additives were prepared. Bulk bodies were then hot-pressed at 1750 °C with a load of 30 MPa and 0.15 MPa pressure of nitrogen during 1 hour.

The instrumented indentation was used to yield both hardness and elastic modulus of the materials. These tests were performed using TTX-NHT nanoindenation tester (CSM Instruments, Switzerland) with a Berkovich indenter. A standard loading/unloading test mode was used with a maximum load of 100 mN and with loading/unloading rate of 200 mN min^{-1}.

The fracture toughness was measured using Vicker´s indentation. The indentation fracture toughness (IF) was determined by the measurement of the crack lengths created at the load of 98 N. The fracture toughness was calculated using the equation proposed by Anstis[4].

3. Results and discussion

All studied materials exhibited the typical bimodal microstructures composed of large elongated β-Si_3N_4 grains distributed in a fine β-Si_3N_4 matrix. Samples with a heavier (smaller) RE^{3+} cations (Y, Yb, or Lu) showed larger diameter elongated β-Si_3N_4 grains and finer β-Si_3N_4 matrix grains in comparison with the samples with a lighter (larger) RE^{3+} cations (La or Nd).

The XRD results revealed β-Si_3N_4 as a major phase and $RE_2Si_2O_7$ (where RE = Y, Yb or Lu) as a secondary phase in both monolithic and composite materials. This crystalline phase was not found in ceramics with La- and Nd additives. All Si_3N_4 materials also contain SiO_2 as a minor phase, whereas the Si_3N_4-SiC additionally contained SiC phase and also SiO_2, Si_2N_2O.

Fig. 1 and Fig. 2 illustrate the hardness and indentation modulus values measured at a load of 100 mN as a function of the cation size of the rare-earth elements, respectively. It is obvious that chemical composition of grain boundary phases strongly influences the values of hardness and elastic modulus of Si_3N_4 based materials. Both the hardness and the elastic modulus increased with decreasing ionic radius of RE^{3+}. This is related to the fact that hardness of RE-oxynitirde glasses is

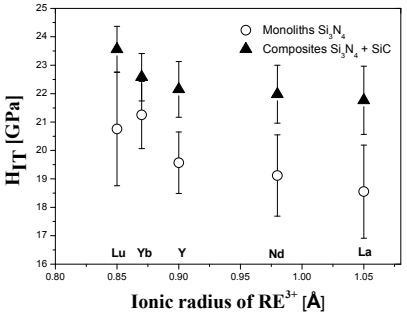

Fig. 1. **Hardness values measured at a load of 100 mN**

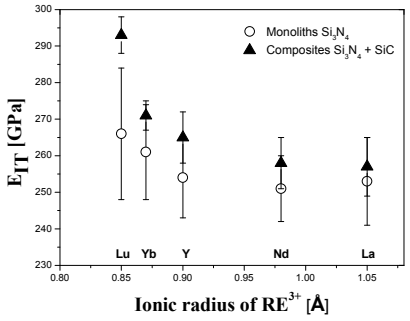

Fig. 2. **Indentation modulus measured at load of 100 mN**

strongly affected by nitrogen content and by the cationic field strength (CFS), which increases with decreasing ionic radius of RE[5]. Higher hardness of composite is attributed to the finer microstructures as well as to the presence of the harder SiC particles.

It is evident that the indentation modulus values are significantly lower than the typical values of Young's modulus [317-342 GPa (ref.[6]), 280–315 GPa (ref.[7])] for both kinds of materials given in the literature.

The values of fracture toughness also increased with decreasing ionic radius of RE^{3+} (Fig. 3). The materials doped with smaller RE exhibited higher aspect ratio of β-Si_3N_4 grains (i.e. ratio of grain length to grain width) and also higher fracture toughness in both the monoliths and the composites. This can be attributed to the fact, that toughening mechanisms were observed more frequently in the materials with higher aspect ratio.

The fracture toughness values of the composites were always lower than those of monolithic Si_3N_4 because of the finer composite microstructures. It is well known that in the case of finer microstructures there are limited possibilities for toughening mechanisms (crack deflection at the boundaries of elongated Si_3N_4 grains).

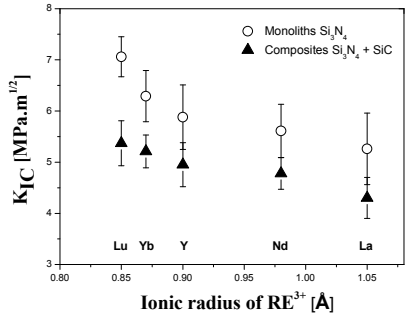

Fig. 3. **Indentation fracture toughness values measured at 98 N**

4. Conclusions

Influence of various grain boundary phases on the microhardness and fracture characteristics of Si_3N_4 based ceramics has been investigated. According to the results the indentation modulus as well as the indentation toughness increased with decreasing ionic radius of RE. Composites exhibited higher microhardness and indentation modulus, however lower indentation toughness in comparison with the monoliths. The indentation modulus is significantly lower than the typical values of Young's modulus for both materials.

This work was supported by VEGA 2/0156/10, by APVV 0171-06 and by LPP 0203-07.

REFERENCES

1. Sun E. Y., Becher P. F., Plucknett K. P., Hsueh C.-H., Alexander K. B., Waters S. B.: J. Am. Ceram. Soc. *81*, 2831 (1998).
2. Satet R. L., Hoffmann M. J.: J. Am. Ceram. Soc. *88*, 2485 (2005).
3. Wang C. M., Pan X., Hoffmann M. J., Cannon R. M., Rühle M.: J. Am. Ceram. Soc. *79*, 788 (1996).
4. Anstis G. R., Chantikul P., Lawn B. R., Marshall D. B.: J. Am. Ceram. Soc. *64*, 533 (1981).
5. Lofaj F., Hvizdoš P., Dorčáková F., Satet R., Hoffmann M. J., de Arellano-López A. R.: Mater. Sci. Eng. *A357*, 181 (2003).
6. Guo S., Hirosaki N., Yamamoto Y., Nishimura T., Mitomo M.: J. Eur. Ceram. Soc. *23*, 537 (2003).
7. Miyazaki H., Hyuga H., Yoshizawa Y., Hirao K., Ohji T.: J. Eur. Sci. Soc. *29*, 1535 (2009).

P. Tatarko[a], M. Kašiarová[a], J. Dusza[a], and P. Šajgalík[b] *([a] Institute of Materials Research, SAS, Košice; [b] Institute of Inorganic Chemistry, SAS, Bratislava, Slovakia):*
Effect of Various Grain Boundary Phases and SiC Addition on The Fracture Characteristics of Si_3N_4 Based Ceramics

Effect of various grain boundary phases and SiC addition on fracture characteristics of the Si_3N_4 based ceramics has been investigated by indentation technics. Strong influence of different rare-earth oxide additives on the hardness, indentation modulus and indentation toughness was found in both the Si_3N_4-SiC composites and Si_3N_4 monoliths. These values increased with decreasing ionic radius of rare-earth elements. Composites exhibited the higher hardness and elastic modulus values compared to monoliths, while monoliths exhibited higher values of fracture toughness.

MICROSTRUCTURAL AND MICROMECHANICAL STUDY OF GYPSUM

PAVEL TESÁREK*, and JIŘÍ NĚMEČEK

Czech Technical University in Prague, Thákurova 7, 166 29 Prague, Czech Republic
pavel.tesarek@fsv.cvut.cz

Keywords: nanoindentation, gypsum, micromechanical properties, deconvolution

1. Introduction

Gypsum is a structural material known for several thousands years which is commonly used for building purposes. Hardened material consists of two components – gypsum and water. In general, it is assumed that properties of gypsum, its hydration and hardening is well-known due to its relatively simple chemistry compared to more complicated systems like in case of e.g. cement. However, similar chemical composition of two gypsum mixtures can result in very different behavior and properties[1]. Many authors take gypsum as simple two-component system for modeling of hardening processes and other effects like water to gypsum ratio, porosity on macroscopic properties of gypsum[2].

From the chemistry point of view, every gypsum binder is composed of three main components – calcium sulphate anhydrite ($CaSO_4$) in different modifications, calcium sulphate hemihydrate ($CaSO_4 \cdot ½H_2O$) – α- or β-gypsum, and calcium sulphate dihydrate ($CaSO_4 \cdot 2H_2O$)[1]. The gypsum binder consists also some impurities and additives in case of natural sources.

As mentioned above, other effects than chemical composition can affect on the resulting behavior of the hardened gypsum. Therefore, it is necessary to take into account macrostructural properties[3] as well as microstructural effects[4] (amount of bound water, crystal orientation, porosity, etc.) for predicting and modeling of macroscopic properties. Our aim was to describe micromechanical behavior of hardened gypsum on a simplified model system consisting of a low-porosity α-gypsum which is used for dental purposes[5]. Although, the dental gypsum will probably never be used in building industry, it is assumed that its microstructure (e.g. crystallography) and mechanical properties are analogous to the real structural gypsums (that are mainly composed of β-gypsums).

2. Materials and tested samples

Commercially available dental gypsum Interdent® (with compressive strength 250 MPa after 24 hours) was used in our study. It was assumed that water to gypsum (w/g) ratio will have influence on its micromechanical properties. Therefore, five different types of samples with w/g=0.18, 0.19, 0.20, 0.21 and 0.22, further denoted as G0, G1, G2, G3 and G4, were prepared. Fig. 1 shows typical sample surface after polishing with easily visible large capillary pores (in black). Lighter parts in Fig. 1 and Fig. 2 are composed of non-hydrated gypsum grains.

3. Nanoindentation

Micromechanical properties of samples were measured using CSM Nanohardness tester. Each sample was tested on arbitrary position by a rectangular grid of ~12×15 = 180 indents. Quasi-static loading consisted of 10 s of linear loading (rate 30 mN min^{-1}), 10 s of holding period at constant peak force 5 mN and 10 s of unloading (rate 30 mN min^{-1}). The distance between individual indents was set 15 μm to avoid mutual influences. The size of the tested area 165×210 μm was considered to be representative enough and to contain all solid material phases for this particular case.

Elastic constants (Young's modulus) were evaluated for individual indents by standard Oliver and Pharr methodology[3]. Poisson's ratio was estimated to be 0.2 (Ref.[3–6]) for all cases.

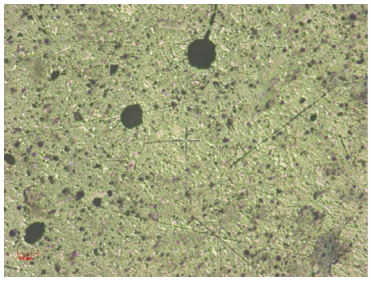

Fig. 1. **Optical image of a gypsum sample G2 with w/g = 0.2 (capillary porosity appears as black circles, non-hydrated gypsum particles are light colored)**

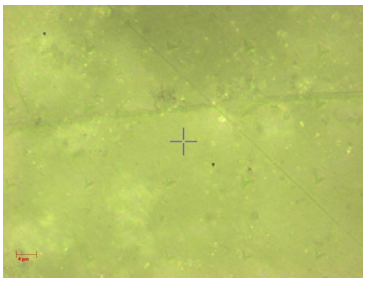

Fig. 2. **High magnification optical image of a gypsum sample G2 with w/g = 0.2 (indentation imprints are in circles)**

4. Evaluation of experimental results

Evaluated Youngs' moduli E were merged for each sample and analyzed statistically. Results in the form of probability density function are depicted in Fig. 3. Significant peak of

E appears around ~40 GPa which is considered to be characteristic value for a dominant part of the system. Minor peaks can be found around ~20 GPa (lower stiffness phases) and ~60 GPa (higher stiffness phases, probably non-hydrated grains). As the w/g ratio increases slight shift towards lower E can be found in Fig. 3, especially for G4 sample. This could show on the effect of increased porosity caused by higher water amount.

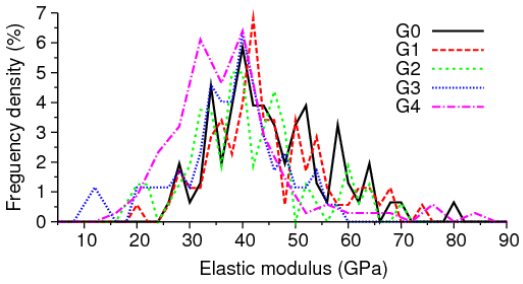

Fig. 3. **Experimental probability density function of Young's modulus for all tested gypsum samples**

In order to better characterize the differences in E between the samples, deconvolution procedure[6,7] was employed. The ill-posed problem of deconvolution was determined by a fixed number of phases. The number was set to three which corresponds to one lower stiffness, one dominant and one higher stiffness phase, respectively. In case of G0 and G4 the lower stiffness phase is almost lacking, so the deconvolution was performed just for two phases (dominant and higher stiffness). Results from deconvolution in the form of mean phase values and volume fractions are given in Tab. I.

Table I
Elastic moduli and volume fractions from deconvolution

Materials	Phase	Mean [GPa]	St. Dev. [GPa]	Vol. frac.
G0 w/g=0.18	1	-	-	0
	2	38.283	5.109	0.656
	3	58.360	9.656	0.344
G1 w/g=0.19	1	20.209	1.837	0.023
	2	40.892	6.689	0.801
	3	60.674	6.939	0.176
G2 w/g=0.20	1	19.357	3.539	0.044
	2	37.234	5.189	0.713
	3	56.278	11.803	0.244
G3 w/g=0.21	1	19.788	4.740	0.103
	2	39.910	6.283	0.845
	3	58.805	6.035	0.052
G4 w/g=0.22	1	-	-	0
	2	35.871	7.295	0.884
	3	62.905	10.516	0.116

Note: 1 ≈ lower stiffness phase; 2 ≈ dominant phase; 3 ≈ higher stiffness phase.

It can be seen in Tab. I that the E-value of the dominant phase lies between ~36 to 41 GPa. Also, the volume fractions of the dominant phase are similar for all samples (65–88 %). From the micromechanical point of view it seems that the samples are very similar, too. There was no substantial difference found in the elasticity of all tested samples.

It can be assumed from the above results that macromechanical differences in elasticity of the samples with different water to gypsum ratios are caused by effects which take place on a higher level, e.g. large capillary porosity (Fig. 1).

5. Conclusions

Based on statistical evaluation of nanoindentation experiments and subsequent deconvolution it was found that gypsum samples exhibit similar micromechanical behavior in terms of elasticity of their dominant phases.

Support of the Ministry of Education of the Czech Republic (project MSM 6840770003) and the Czech Science Foundation (GAČR 103/09/1748) is gratefully acknowledged.

REFERENCES

1. Garg M., Jain N., Singh M.: Constr. Build. Mater. *23* (2009).
2. Šatava V.: Ceramics – Silikáty, *40*, 2 (1996).
3. Oliver W., Pharr G.: J. Mater. Res. *7* (1992).
4. Arslan A. T., Koca M., Aydogmus Y. T., Klapperich H., Yılmaz H. R.: Rock Mech. Rock Engng. *41* (2008).
5. Singh M.: Constr. Build. Mater. *19* (2005).
6. Němeček J., Lukeš J.: Chem. Listy *104*, (2010).
7. Němeček J., Šmilauer V., Kopecký L., accepted for publication in Cem. & Concr. Comp., ISSN: 0958-9465.

P. Tesárek, and J. Němeček *(Czech Technical University in Prague, Faculty of Civil Engineering, Czech Republic):*
Microstructural and Micromechanical Properties of Gypsum

Gypsum samples (dental gypsum Interdent®) with different water to gypsum ratios have been investigated with nanoindentation. Statistical evaluation and deconvolution into several phases showed on similar micromechanical behavior of all samples. Elastic modulus of the dominant phase which occupies 65–88 % of the sample volume reaches average values ~36–41 GPa.

EFFECT OF CORROSION ON THE MECHANICAL PROPERTIES OF MAGNESIUM ALLOY AZ91

JAKUB TKACZ*, MARTIN ZMRZLÝ, and JAROMÍR WASSERBAUER

Brno University of Technology, Faculty of Chemistry, Centre for Materials Research CZ.1.05/2.1.00/01.0012, Purkyňova 118, Brno, 61200, Czech Republic
xctkacz@fch.vutbr.cz

Keywords: magnesium alloy, corrosion, microhardness

1. Introduction

Magnesium alloys are characterized by excellent mechanical properties in comparison with low density. These properties are nowadays mainly used in the automotive and aerospace industry. The reason is construction relief and thereby reduced fuel consumption, leading to the reduced financial costs and environmental protection.

On the contrary to excellent mechanical properties the negative aspect is low corrosion resistance of magnesium alloys. This is the reason why the magnesium alloys are not used more often.

The various phases present in magnesium alloys are characterized by different electrochemical potential and different mechanical properties. Complicated phase structure of the magnesium alloy influences both corrosion processes, and interaction passivating agents with magnesium alloy.

2. Experimental

2.1. Sample preparation

Magnesium alloy AZ91 was studied. Its chemical composition (wt.%) was 8.90 Al; 0.68 Zn; 0.20 Mn and the ballance was Mg. Samples were polished with 600 grit SiC paper and degreased by STAR PN 75 in ultrasonic bath for 2 minutes. Than the samples were rinsed by distilled water and ethanol and dried by hot air.

2.2. Immersion test

The samples were hung on insulated wire and they were immersed into corrosion environment[1].

Corrosion environments were distilled water and sodium chloride solution (3%). Durations were 1, 8 , 48 and 168 hours, respectively.

The corrosion products were removed in suspension of 5 g silver chromate ($Ag_2Cr_2O_7$) in 15% aqueous solution of chromium trioxide (CrO_3). Temperature of the bath was 90–100 °C. Then the sample was rinsed by distilled water and by ethanol and dried by hot air.

2.3. Metallography

Corroded part of the samples were cut out by handsaw and mounted in resin. The samples were polished with 1200 grit SiC paper, then with 1 μm diamond paste. Polished samples were etched[2] (0.4 g picric acid; 0.7 cm^3 distilled water; 0.3 cm^3 acetic acid and 40 m^3 ethanol) and observed by microscope Neophot 21 (Zeiss Jena).

2.4. Vickers microhardness tests

Microhardness was studied with LECO LM247 AT with a square-based pyramid diamond[3].

The samples were polished with 1200 grit SiC paper. The microhradness was measured at nine points of cross sections of the samples. Tests were repeated several times. Distances between indentations were 250–300 μm.

3. Results

Magnesium alloy AZ91 corroded in distilled water and in sodium chloride solution (3%).

The corrosion damage in distilled water reached through all profile of the samples (Fig. 1) and affected microhardness (Fig. 3). Higher values correspond to α-Mg and lower values are caused by corrosion. Microhardness was measured twelve times because of large spread of values in this case (Table I).

Corrosion in sodium chloride solution (3%) took place by typical pitting mechanism (Fig. 2). The corrosion damage was situated on the surface. The value of microhardness (Fig. 3) at each point differs for α-Mg (lower values) or intermetallic phase $Mg_{17}Al_{12}$ (higher values). In comparison with sample corroded in distilled water (Fig. 3), this sample had different mechanical properties.

Microhardness of pure AZ91 can be compared to microhardness of magnesium alloy AZ91 corroded in sodium chloride solution (3%).

Table I
Microhardness (HV 0,3) of uncorroded AZ91 and corroded (48 hours) by distilled water and NaCl solution (3%)

Uncorroded	67.3	76.7	63.8	69.8	67.2	63.0	66.9	68.9	64.9			
Distilled water	60.5	60.5	54.7	39.3	58.5	29.0	59.0	42.1	56.5	54.7	60.2	60.0
3% NaCl	59.5	64.3	64.9	60.5	63.2	71.1	65.4	63.3	67.8			

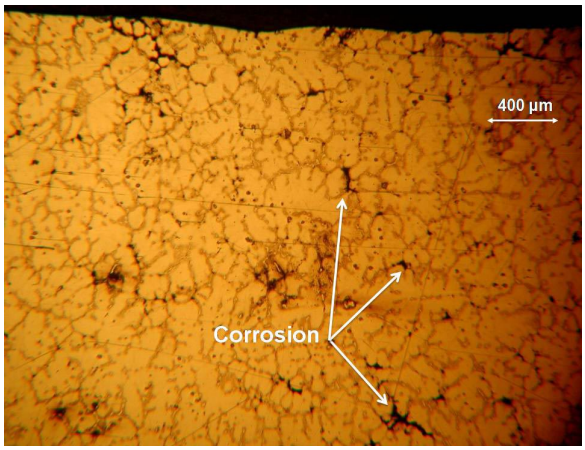

Fig. 1. **Corrosion through all profile in distilled water (48 hours)**[2]

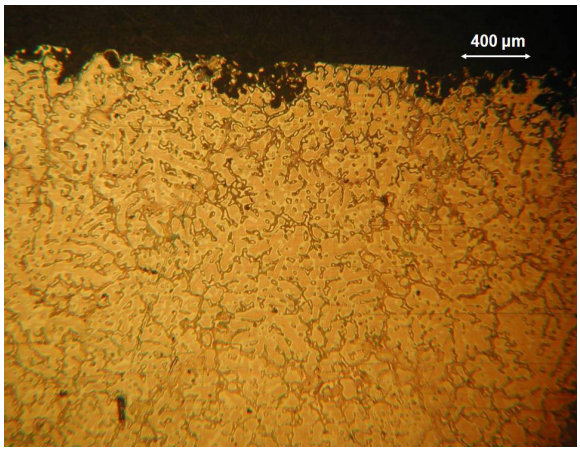

Fig. 2. **Corrosion in sodium chloride solution (168 hours)**[2]

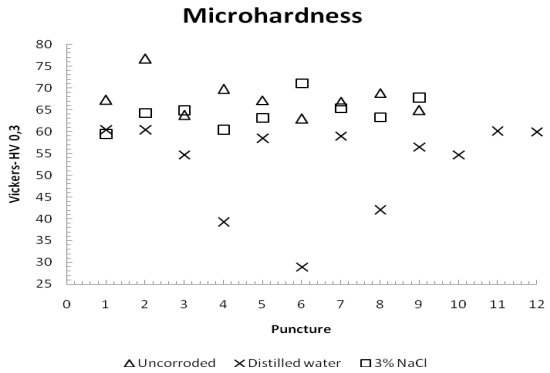

Fig. 3. **Microhardness after corrosion**

4. Conclusions

Corrosion of magnesium alloy AZ91 in distilled water affected mechanical properties (microhardness) more in comparison to corrosion in sodium chloride solution (3%).

Corrosion in distilled water passed through all the profile of the samples. Because of that the microhardness was affected in all profile of the sample. On the other hand, corrosion in sodium chloride solution (3%) affected only surface of the sample AZ91.

Studied alloy AZ91 was processed by gravity casting, during cooling probably rose intergranular stresses that made these regions more reactive. Then in distilled water, crevice corrosion with hydrogen depolarization (at relatively low value of pH) was more pronounced. It can be stated, that there was a large spread of values of the sample corroded in distilled water corresponding to heterogeneity of corroded material.

This work was supported by the project "Centre for Materials Research at FCH BUT" No. CZ.1.05/2.1.00/01.0012 from ERDF.

REFERENCES

1. Chen J., Wang J., Han E., Dong J., Ke W.: Corros. Sci. *50*, 1292 (2008).
2. Tkacz J.: *Reactivity and control of properties of metallic materials*, Brno 2010, 71.
3. Wasserbauer J.: *Local tests of mechanical properties of materials*, Brno 2009, 100.

J. Tkacz, M. Zmrzlý, and J. Wasserbauer *(Brno University of Technology, Faculty of Chemistry – Centre for Materials Research, Brno, Czech Republic):* **Effect of Corrosion on the Mechanical Properties of Magnesium Alloy AZ91**

Corrosion properties of magnesium alloy AZ91 were studied in distilled water and sodium chloride solution (3%). Corrosion resistance of $Mg_{17}Al_{12}$ phase was better than corrosion resistance of other Mg-phases. Microhardness profile was evaluated across the sample to show negative impact of the corrosion on the mechanical properties of magnesium alloy AZ91.

THE EFFECT OF DUPLEX COATING ON WEAR PROPERTIES OF TOOL STEELS

MARIE VÁLOVÁ* and JAN SUCHÁNEK

Czech Technical University, Technická 4, 166 07 Praha 6, Czech Republic
marie.valova@fs.cvut.cz

Keywords: Duplex Coating, Nanohardness, Tribological Properties, PVD

1. Introduction

This paper develops in more detail results listed in paper Characteristic of Duplex Coated Steels[1]. The requirements for materials used in the machine parts production, especially their functional characteristics and service life are currently increasing. Thin ceramic coatings deposited on the surface of tools and machine parts by PVD methods improve considerably their tribological properties. These hard brittle coatings can be damaged rapidly if a plastic deformation initiates in the substrate near the coating-substrate interface when subjected to relatively high intensity loading. Therefore, the strengthening of substrate surface layers, e.g. by plasma nitriding, appears to be a suitable solution for the low strength of the substrate[2].

2. Experimental procedure

The specimens from low-alloy steel 31CrMoV9 were austenitized, inert qas quenched and tempered. The duplex treatment proceeded in two phases. In the first phase the specimens were pulse plasma nitrided (further PN). In second phase different PVD coatings were deposited – a) TiN (thickness 1 and 3 μm), b) CrN (thickness 1 and 3 μm), c) TiAlN (thickness 3 μm) and d) multilayer 3×(TiN-CrN) (thickness 3 μm).

Nanohardness and elastic modulus of the coatings were measured. Evaluation of nanohardness was made by CSM method with maximum load *Pmax*=670 mN. The measurement methodics is described in ref.[3] and ref.[4]. The specimens were tested on tribometer „pin-on-disc". The experiments were realized at the temperature 22 °C and 350 °C, with load 1, 2 and 5 N, all under conditions of dry friction. Wear marks profiles were measured with profilograph Talysurf 6.

3. Results and discussion

The results of nanohardness and elastic modulus are shown in Table I. The results of wear marks measurement are shown in Table II. Records of wear marks` measurement on profilograph are shown at Fig. 1.

Table I
Modulus and hardness of coatings

Coating	Hardness [GPa]	E [GPa]
PN + TiN	35,8 ± 4,6	504 ± 80
PN + CrN	26,9 ± 3,4	327 ± 43
PN + TiAlN	32,9 ± 5,8	497 ± 98
PN + 3x(TiN-CrN)	34,2 ± 8,1	566 ± 83

Table II
Maximum surface roughness Rz [μm] of wear marks profile

Testing temperature	22 °C			350 °C	
Load	1 N	2 N	5 N	1 N	5 N
Coating PN + CrN	1,36	1,44	2,92	2,67	6,04
Coating PN + TiN	1,8	2,48	2,2	1,64	1,64
Coating PN + TiAlN	2,2	2,44	2,6	2	2,04
Co. PN+3×(TiN-CrN)	2,3	2,48	1,4	2,8	3,12
Parent material(PM)	0,72	1,2	-1,36	-3,4	1,2

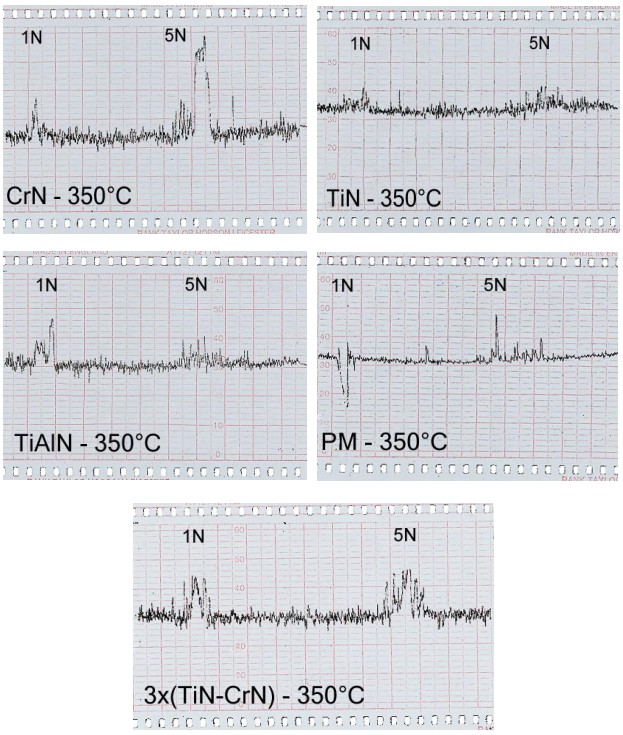

Fig. 1. **The record of measurement on profilograph Talysurf 6 for particular coatings after testing on tribometer Pin-on-Disc at temperature 350 °C**

Fig. 1 shows the change of surface roughness Rz with deposited PVD coating compared with only nitrided sample. The only nitrided sample, PM, has markedly lower roughness than all PVD coated specimens, though all specimens had the same roughness before PN. Reason is creation of „clusters", which are created using PVD treatment by arc.

At Table III the wear of ball (countepart) after "pin on disc" test is shown. At temperature 22 °C and load 1 N maximum wear was reached with TiAlN coating. Under load 5 N the wear is for all coatings similar. Only nitrided PM had the wear of the ball much lower. Results of friction during pin on disc measurement are shown at Fig. 2 and 3. The lowest friction coefficient had CrN coating. The friction coefficient of PM, at 22 °C, increased with friction distance because of adhesion.

Table III
Wear of the ball [μm] after "pin on disc" testing

Temperature	20 °C		250 °C
Load	1 N	5 N	5 N
PN + TiN	514	650	586
PN + CrN	535	676	592
PN + TiAlN	850	675	653
PN + 3x(CrN-TiN)	450	683	592
PM	90	370	505

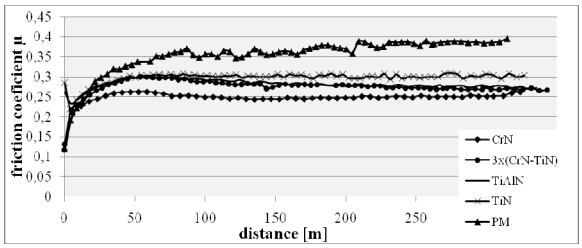

Fig. 2. **Graph of friction coefficient and distance, load 5 N and temperature 22 °C**

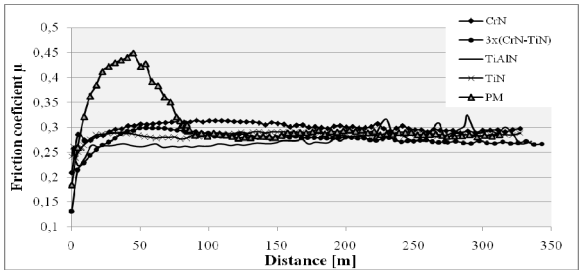

Fig. 3. **Graph of friction coefficient and distance, load 5 N and temperature 350 °C**

Experimental results show that the friction coefficients of the samples with duplex coatings firstly increases and consequently settles during testing. The mechanism of deterioration of the duplex coated steel is a combination of adhesive and abrasive wear. The adhesive wear took place on the disk during experiment while the ball was worn down in an abrasive manner. The evidence of abrasive wear can be seen on the grooves formed on the ball during experiment.

4. Conclusion

The conclusions drawn from the experiment show that duplex treatment is a useful way to increase the die service life and that the most suitable coating is the TiN coating. This coating in combination with a nitrided substrate had a low friction coefficient and a small wear.

As far as the coating hardness is concerned, the most favourable is the coating CrN and multilayer coating 3×(TiN-CrN), because it has the gentle increase of microhardness in depth profile. The max hardness is higher for TiN and TiAlN coatings, so there is steeper change of hardness between nitrided layer and PVD layer, causing risk of the coating cracking, but it did not occur in our measurement. So these coatings exhibit better service life and friction coefficient.

Current thin abrasion-resistant surface layers and duplex coatings bring remarkable extension of service life and reliability to parts, tools and dies as confirmed by this research. Still most technologies have not managed to reach the limits of their possibilities so far.

The research was financed by the Czech Ministry of Education, Youth and Sport within the frame of project SGS CVUT 2010 – OHK2-038/10.

REFERENCES

1. Válová M., Suchánek J., Bláhová O.: Chem. Listy *104*, s378 (2010).
2. Suchánek J., Jurči P., Zdravecká E.: *Proc. of the 2nd European Conf. on Tribology. Pisa, Uni.Pisa, 2009*, vol. 2, p. 791–796.
3. Lukeš J., Šepitka J., Němeček J.: Chem. Listy 104, s338 (2010).
4. Eichlerová R., Lukeš J., Konvičková S., Bradna P.: Human Biomech. p. 49–55. TU of Liberec, Liberec 2010.

M. Válová and J. Suchánek *(CTU in Prague, Prague, Czech Republic):* **The Effect of Duplex Coating on Wear Properties of Tool Steels**

The paper resumes partial results of tribological testing of duplex coatings of tool steel. Steel samples (31CrMoV9) were nitrided and subsequently treated by PVD process. There were deposited different coatings (TiN, CrN, TiAlN and multilayer 3×(CrN-TiN)) with 1 μm and 3 μm thickness. Samples were tested and their nanohardness, hardness of duplex coating, coefficient of friction, coating thickness (calotest), resistance against adhesive wear (scratch test) and abrasion size (HEF) were measured. Results of friction coefficient measured by "pin on disc" tribometer and wear marks measured by contact profilometry were are summarized.

PROPERTIES OF RENOVATION LAYERS APPLIED BY SUBMERGED ARC WELDING

JÁN VIŇÁŠ*, JANETTE BREZINOVÁ, ANNA GUZANOVÁ, and DENISA LORINCOVÁ

Technical university of Košice, Faculty of Mechanical Engineering, Department of Technology and Materials, Mäsiarska 74, 040 01 Košice, Slovakia
jan.vinas@tuke.sk

Keywords: wear, repairing, cladding, submerged arc welding-on (SAW), microhardness

1. Introduction

Continuous steel casting lines are one of the key facilities in steel processing. Steel mill rolls play a vital part in the production of steel products. Lifespan of rolls, which provide movement of slabs along the line, is very important for ensuring their reliable operation. During steel production, rolls are loaded with the combination of wear with thermal fatigue caused by thermal shocks when moving slabs in the temperature range 1280 °C to 850 °C and also with high-temperature corrosion. The combination of these stresses causes rapid wear on the surface of new rolls. Currently, the renovation of continuous steel casting rolls used to be carried out by submerged arc surfacing technology[1–7].

2. Materials and methods

Experimental works were aimed on the evaluation of rolls repaired by submerged arc welding (SAW). Worn roll comes from curved sector of continual steel casting line and was made of material 41CrMo4 EN 10083-1-91 by forging.

Welding position used according to STN EN ISO 6947-PA. This position is most suitable for repairing of rotary surfaces and by using a flux it is usable without other technology modifications of welding machine. There were three cladding layers deposited on the roll surface. The first layer deposited on the base material was the interlayer, welding wire UP5-GF -200-C DIN 8555 in combination with aluminous – basic flux S F AB 1 65 AC H5 EN 760 was used. Cladding hardness provided by welding wire producer is 190 HV. Flux was dried 1 hour at 300 °C before cladding. Properties of flux used are as follows: basicity index 1.3, flux granularity 0.2–2.0, density 1.2 kg dm^{-3}, suitable for AC and also DC welding current supply, hydrogen content ≤ 5 HDM.

Next there were two cover layers deposited using welding wire UP5-GF-45-C DIN 8555 and the same aluminous – basic flux as in previous S F AB 1 65 AC H5 EN 760 by SAW technology on interlayer. Cover cladding hardness provided by welding wire producer is 450 HV. Welding parameters are given in Table I. Roll preheating temperature: 260–270 ºC. During welding process the interpass temperature was kept up with the help of gas-burners at 200–380 ºC. After cladding the roll was treated by stress revealing at 520 ± 10 ºC), held there for 4–5 hours and finally cooled slowly (cooling rate 40 °C per hour) to the temperature of 210 ºC in isothermal wrap. When the roll temperature was 210 °C, next cooling continued in the air. According to STN EN 25 817 required quality rank was „B“. Cladding quality was evaluated by visual test according to STN EN 970 together with the capillary test according to STN EN 1289 and ultrasonic detection according to STN EN 1712.

Table I
Parameters of roll cladding

Layer	Welding wire diameter [mm]	Current [A]	Voltage [A]	Oscillation speed [cm/min]	Welding speed [cm/min]	Weldboad width [mm]
1	3,2	480–500	30–32	45	31	35
2,3	2,8	360–400	28–29	45	29	34

Metallographic analysis was carried out according to STN EN 1321 on cross sections of particular cladding layers.

Abrasive wear of repaired rolls was compared with the reference material of new roll with surface hardened layer thickness 4mm. Abrasive wear test based on weight analysis was performed on a laboratory device APGi, VEB Leipzig. Two corundum abrasive papers with different granularity marked as P 200 and P 800 were used. Surface exposed to abrasive wear was functional roll surface – cover cladding layer.

3. Results

Fig. 1a shows microstructure of roll base material – fine -grained martensite. Fig. 1b shows influence of heat introduced by welding on martensitic microstructure. The heat caused change of grain size and highlighting of grain boundaries. The increased occurrence of inclusions and precipitates on grain boundaries was observed. Transition from the base material to HAZ (heat affected zone) is continuous. This region can be designated as critical. Interlayer, Fig. 1c, has structure with characteristic epitaxial grain growth. Structure of interlayer is martensite-ferrite, also called semi-ferritic structure. Structure of cover layer, Fig. 1d, is martensite-ferrite. Thickness of cover layers after cutting operations to required dimension varied in the range of 3.0–3.5 mm.

Maximum microhardness value 410 HV0.01 was found in cover layer in 1mm distance from the surface. The lowest hardness values (from 239 HV0.01 to 243 HV0.01) were found in base material. Interlayer hardness is affected by cladding metal shuffle with cover layer metal, Table II.

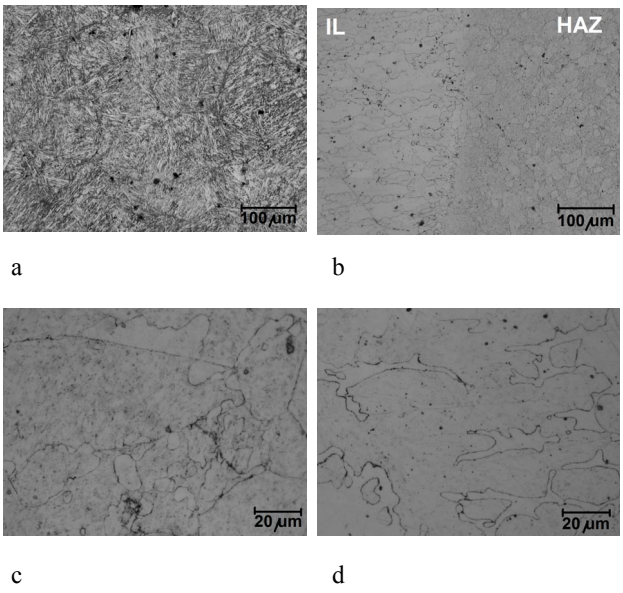

Fig. 1. **Microstructure of a) base material, b) transition region interlayer – HAZ, c) interlayer (IL), d) cover layer**

Table II
Microhardness of layers

Distance from surface [mm]	Cover layers		Inter layer		HAZ		Base material	
	1	2	4	5,5	7	10	30	58
HV 0.01	410	396	310	270	360	273	243	241

Larger abrasive effect on the sample with claddings showed corundum abrasive paper P 200, Fig. 2.

Lower abrasive effect was observed for corundum abrasive paper P 800. The measured values of weight losses are consistent with the hardness of the contact surfaces of samples exposed to abrasive wear.

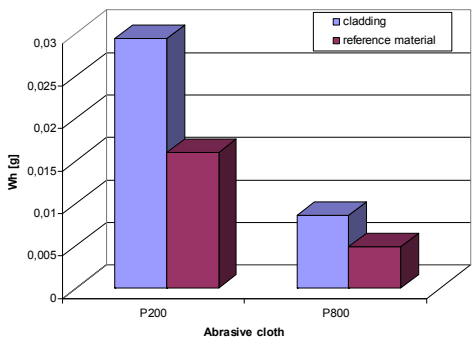

Fig. 2. **Weight loss of cladding and reference material**

4. Conclusion

Metallographic analysis identified structure of the base material and particular cladding layers. The highest average hardness was measured in the cover layer at a distance of 1 mm from the surface, 410 HV0.01. The lowest hardness is shown by the base material, 239–243 HV0.01.

New hardened cylinder showed higher abrasive wear resistance in comparison with renovating layers.

Rolls will wear differently from machine to machine and within machines. When choosing a surfacing alloy, a balance between each wear factor with the focus on the primary wear factor, should be considered.

This work was done within the scientific project VEGA No. 1/0510/10.

REFERENCES

1. Loosen B.: *Surfacing contiounous casting rollers*. Belgium: S.A. ESAB N.V, 1995, Svetsaven No. *2.*
2. Sanz A.: Surf. Coat. Technol. *177–178* (2004).
3. Paschold R.: Submerged-arc strip cladding of contiuous casting rollers using OK Band 11.82 and OK Flux 10.07. Solingen: ESAB GmbH, Svetsaren No.*1*, s. 17–19, (2001).
4. Sanz A.: Surf. Coat. Technol. *146 –147* (2001).
5. Boile R., Frick J.: La Metallurgia Italiana *1* (2005).
6. Schneider W.: *Continuous casting*, Wiley-VCH, Germany 2000.
7. Lenard J. G.: *Primer on flat rolling*. Elsiever, London 2007.

J. Viňáš, J. Brezinová, A. Guzanová, and D. Lorincová *(Technical university of Košice, Faculty of Mechanical Engineering, Department of Technology and Materials, Slovakia):* **Properties of Renovation Layers Applied by Submerged Arc Welding**

The paper presents an analysis of the quality of cladding layers deposited on continuous steel casting rollers made of material 41CrMo4 EN 10083-1-91 using destructive methods. The research works were aimed on the effect of chosen welding wire on the tribological properties of claddings. There was also monitored mixing of cladding metal with the base material at welding parameters used together with the effect of heat input in the process of cladding. Weldability and influence of the chemical composition of welding wires on resulting properties of cladding were also evaluated. There are presented proceedings that are necessary to be taken into account at rollers renovation process, and also the development of research in the studied area.

CONTENTS

Invited Papers

Regular Papers

Posters

AUTHOR INDEX

Universal testing machine

Electromechanical
High precision UTM AG-X (up to 1500 kN)

Standard precision UTM AGS-J (up to 10 kN)

Table top UTM (up to 5 kN) EZ test

Servohydraulic UTM
Hydraulic UTM UH (up to 32 000 kN)

Hardness tester

High Speed Video Camera

Capilary Rheometer

Thermal Analyzers

SALD

SHIMADZU

Solutions for Science

since 1875

měřicí technika - morava

messtechnik - moravia

measurement technic - moravia

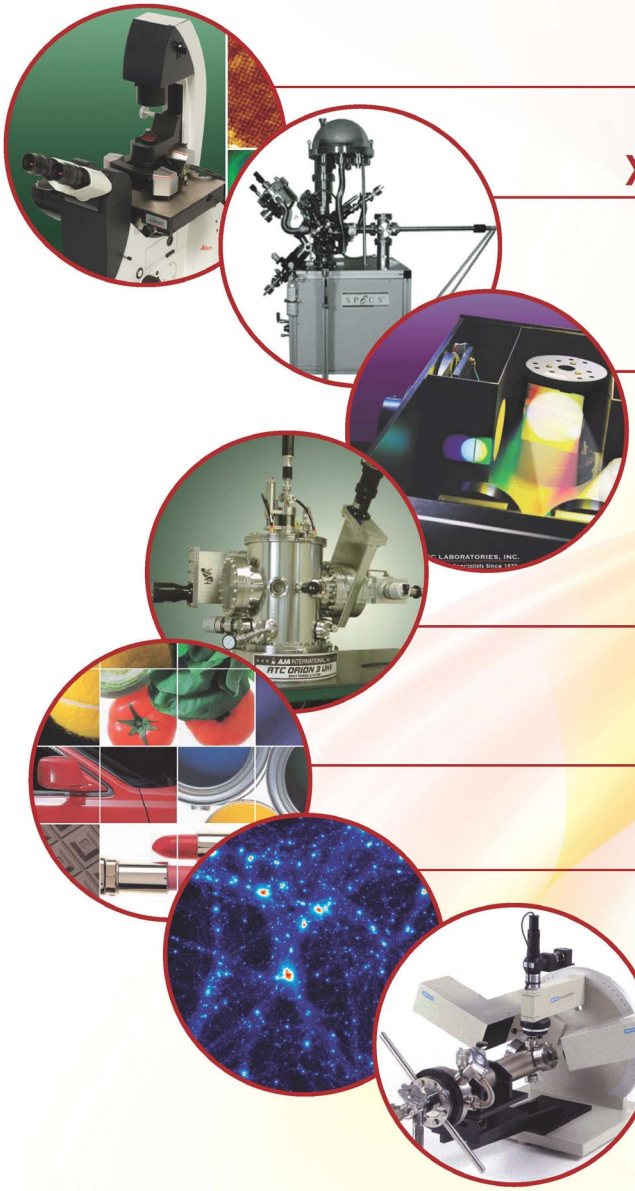

AFM , profilometry

XPS, UPS, SAM, LEEM…

Měření světla

Depozice tenkých filmů

Hodnocení barevnosti

Analýza částic

Elipsometrie

Zastoupení firem:
Bruker • Specs • Avantes • Gooch & Housego
Sentech • Bestec • Brookhaven Instruments

www.mt-m.eu

Třída 1.Máje 102, 664 84 Zastávka u Brna, Česká republika | tel: +420 **513 034 408** | e-mail: **info@mt-m.eu**

CHEMICKÉ LISTY • ročník/volume 105 (S), čís./no. Symposia • LISTY CHEMICKÉ roč./vol. 135, ČASOPIS PRO PRŮMYSL CHEMICKÝ, roč./vol. 121 • ISSN 0009-2770, ISSN 1213-7103 (e-verze), ISSN 1803-2389 (CD verze) • evidenční číslo MK ČR E 321 • Vydává Česká společnost chemická jako časopis Asociace českých chemických společností ve spolupráci s VŠCHT Praha, s ČSPCH a ÚOCHB AV ČR za finanční podpory Nadace Český literární fond a kolektivních členů ČSCH • IČO 444715 • Published by the Czech Chemical Society • VEDOUCÍ REDAKTOR/EDITOR-IN-CHIEF: B. Kratochvíl • REDAKTOŘI/ EDITORS: J. Barek, Z. Bělohlav, P. Drašar, J. Hetflejš, P. Holý, J. Horák, P. Chuchvalec, J. Podešva, P. Rauch, J. Volke; Bulletin: I. Valterová; Webové stránky: R. Liboska, P. Zámostný • ZAHRANIČNÍ A OBLASTNÍ REDAKTOŘI/FOREIGN AND REGIONAL EDITORS: F. Švec (USA), Z. Kolská (Ústí nad Labem) • KONZULTANT/ CONSULTANT: J. Kahovec • TECHNICKÁ REDAKTORKA/EDITORIAL ASSISTANT: R. Řápková • REDAKČNÍ RADA/ADVISORY BOARD: K. Bláha, L. Červený, E. Dibuszová, J. Hanika, Z. Havlas, J. Káš, M. Koman, J. Koubek, T. Míšek, V. Pačes, O. Paleta, V. Růžička, I. Stibor, V. Šimánek, R. Zahradník • ADRESA PRO ZASÍLÁNÍ PŘÍSPĚVKŮ/MANUSCRIPTS IN CZECH, SLOVAK OR ENGLISH CAN BE SENT TO: Chemické listy, Novotného lávka 5, 116 68 Praha 1; tel./phone +420 221 082 370, +420 222 220 184, e-mail: chem.listy@csvts.cz • INFORMACE O PŘEDPLATNÉM, OBJEDNÁVKY, PRODEJ JEDNOTLIVÝCH ČÍSEL A INZERCE/INFORMATION ADS: Sekretariát ČSCH, Novotného lávka 5, 116 68 Praha 1; tel. +420 222 220 184, e-mail: chem.spol@csvts.cz, chem.ekonom@csvts.cz • PLNÁ VERZE NA INTERNETU/FULL VERSION ON URL: http://www.chemicke-listy.cz • TISK: Rodomax s.r.o., Rezecká 1164, 549 01 Nové Město nad Metují • Redakce čísla Symposia (ISSUE EDITOR): F. Lofaj • SAZBA, ZLOM: ČSCH, Chemické listy • Copyright © 2011 Chemické listy/Česká společnost chemická • Cena výtisku 170 Kč, roční plné předplatné 2011 (12 čísel) 1730 Kč, individuální členské předplatné pro členy ČSCH 865 Kč. Roční předplatné ve Slovenské republice 92 EUR (doručování via SCHS), individuální členské předplatné pro členy ČSCH 70 EUR (doručování via SCHS), 258 EUR (individuální doručování), ceny jsou uvedeny včetně DPH • DISTRIBUTION ABROAD: KUBON & SAGNER, POB 34 01 08, D-80328 Munich, FRG; Annual subscription for 2011 (12 issues) 225 EUR • This journal has been registered with the Copyright Clearance Center, 2322 Rosewood Drive, Danvers, MA 01923, USA, where the consent and conditions can be obtained for copying the articles for personal or internal use • Pokyny pro autory najdete na http://www.chemicke-listy.cz , zkratky časopisů podle Chemical Abstract Service Source Index (viz http://cassi.cas.org/search.jsp) • Chemické listy obsahující Bulletin jsou zasílány zdarma všem individuálním a kolektivním členům ČSCH a ČSPCH v ČR i zahraničí, do všech relevantních knihoven v ČR a významným představitelům české chemie a chemického průmyslu; v rámci dohod o spolupráci i členům dalších odborných společností • Molekulární námět na obálce: P. Holý • Dáno do tisku 10.6.2011.